VOLUME DIFFUSERS FOR ARCHITECTURAL ACOUSTICS

Richard James HUGHES

School of Computing, Science and Engineering

University of Salford, Salford, UK

Submitted in partial fulfilment of the requirements of the
Degree of Doctor of Philosophy, June 2011

CONTENTS

LIST OF FIGURES

LIST OF TABLES

GLOSSARY OF SYMBOLS AND ABBREVIATIONS

Symbols

a	Cylinder radius
A	Scaling term
$\mathbf{A}_{l,m}$	Matrix of surface interactions
A_n , $A_{m,n}$	Set of amplitude coefficients
A_n'	Transmitted amplitude coefficients
A_n^i	Set of coefficients for a multiple scattering solution
A_S	Effective absorption area according to Sabine's equation
$\mathbf{A}_T$	Transformation matrix
c	Speed of sound (ms^{-1})
c_a	Ant in a labyrinth constant
c_1, c_2	Sound speeds during respective measurements (ms^{-1})
$C_a(\tau)$	One-dimensional Aperiodic Autocorrelation Function (AACF)
$C_A(\tau,\rho)$	Two-dimensional Aperiodic Autocorrelation Function (AACF)
$\mathbf{C}_{m,n}$	Matrix defining a Costas array
d	Distance (m)
d_e	Element width (m)
d_m	Depth of the mth layer (m)
d_{max}	Maximum layer depth (m)
d_{min}	Minimum layer depth (m)
d_n	Width of the nth element (m)
d_{run}	Width of continuous run of conjoined elements (m)
d_x	Grid spacing in the x direction (m)
d_y	Grid spacing in the y direction (m)
d_z	Grid spacing in the z direction (m)
$d\tau$	Time constant (s)
D	Diffuser width (m)
D_{max}	Maximum diffuser dimension (m)
e	Scattered polar pattern for an individual scattering element
$error(t)$	Cancellation error – time domain

E	Number of scattering elements
$Error(f)$	Cancellation error – frequency domain
$Error_{ref}(f)$	Normalised cancellation error – frequency domain
f	Frequency (Hz)
f_c	Cut-off frequency (Hz)
f_{max}	Diffuser upper limiting frequency (Hz)
f_s	Sampling frequency (Hz)
f_0	Diffuser design frequency (Hz)
F_{fill}	Fraction of line-of-sight through an array that is blocked
g_a	Ant in a labyrinth gradient
G	Green's function
$h_1(t)$	Impulse response of measurement with sample present
$h_1'(t)$	Time shifted version of measurement with sample present
$h_2(t)$	Impulse response of background measurement (without sample present)
$h_3(t)$	Impulse response of loudspeaker and microphone
$h_4(t)$	Deconvolved sample Impulse response
$H_n^{(1)}(x)$	Hankel function of the first kind of order n
i	Integer
I_m	Back-scattered intensity ratio from the first m layers
$\mathbf{I}$	Identity matrix
j	Imaginary unit ($\sqrt{-1}$)
$J_n(x)$	Bessel function of the first kind of order n
k	Wavenumber (m^{-1})
k_1, k_2	Wavenumber during respective measurements (m^{-1})
l	Integer
L	Length of a Golomb ruler
L_r	Length of surfaces within a room
L_{IR}	Back-scattered intensity ratio (dB)
L_p	Sound pressure level (dB)
m	Integer
M	Number of modes
M	Number of columns in an array of scattering elements

n	Integer
$\mathbf{n}$	Normal to the surface (pointing out of the surface)
N	Number of rows in an array of scattering elements
N	Number of elements
p_b	Bond probability
p_{bc}	Bond percolation threshold
p_i	Incident pressure (Pa)
$p_{i,ref}$	Incident pressure at the reference receiver (Pa)
p_s	Scattered pressure (Pa)
$p_{s,norm}$	Normalised scattered pressure
p_t	Total pressure (Pa)
$p_{1,n}$, $p_{2,n}$	Scattered pressure at the nth receiver for respective cases (Pa)
P	Number of elements per period
$\mathbf{P}_i$	Matrix of incident pressures
$\mathbf{P}_t$	Matrix of surface pressures
q	Prime number
r	Receiver distance (m)
$\boldsymbol{r}$	Receiver location
$\mathbf{r}_a$, $\mathbf{r}_b$	Arbitrary locations
$\mathbf{r}_i$	Centre of the ith cylinder
$\mathbf{r}_l$	Centre of the lth cylinder
r_{max}	Maximum distance between source and diffuser surface (m)
r_{min}	Minimum distance between source and diffuser surface (m)
r_{ref}	Source to reference receiver distance (m)
r_n	Distance to the centre of the nth scattering element
$\mathbf{r}_n$	Centre of the nth scattering element
$\mathbf{r}_s$	Point on surface
$\mathbf{r}_0$	Source location
r_0	Source distance (m)
R	Set of receivers
R	Pressure reflection coefficient
$R_a(\tau)$	One-dimensional periodic Autocorrelation Function (ACF)

$R(\Delta t)$	Reduction factor (dB)
s	Surface
S	Source
S_r	Area of 2D room
$S^{'}$	Image source
t	Time (s)
T_E	Reverberation time predicted using Eyring's equation(s)
T_S	Reverberation time predicted using Sabine's equation(s)
u	Primitive root
v	Primitive root
x	Cartesian coordinate (m)
x	Variable
x_t	Transformed x Cartesian coordinate (m)
y	Cartesian coordinate (m)
y_t	Transformed y Cartesian coordinate (m)
z	Cartesian coordinate (m)
z	Specific acoustic impedance ($kgm^{-2}s^{-1}$)
z	Bethe lattice number
Z_n^i	Set of coefficients determined by boundary conditions
α	Absorption coefficient
α	Integer
$\overline{\alpha}$	Mean absorption coefficient
β	Surface admittance – inward facing normal ($rayl^{-1}$)
β	Integer
β'	Surface admittance – outward facing normal ($rayl^{-1}$)
δ	Delta function
δ	Diffusion coefficient
Δc	Difference in speed of sound (ms^{-1})
Δr	Difference in distance (m)
Δt	Time shift (s)
θ	Angle of azimuth (radians)
θ_i	Angle between the ith cylinder and receiver (radians)

$\theta_{l,i}$	Angle between the ith and l^{th} cylinder (radians)
$\theta_{l,0}$	Angle between source and l^{th} cylinder (radians)
θ_0	Source angle (radians)
λ	Wavelength (m)
ρ	Autocorrelation lag (x dimension)
ρ_0	Density of air (kgm^{-3})
τ	Autocorrelation lag (y dimension)
τ_1, τ_2	Time of flight for respective measurements (s)
φ	Solid angle defining the shadow zone behind a diffuser (radians)
φ	Angle of elevation (radians)
φ_0	Source angle of elevation (radians)
Ω	External region (to the scattering objects)
Ω	Angular variable (radians)
Ω_0	Internal region (of the scattering objects)
ψ	Allowed angles of reflection
$\psi(f)$	Solid angle defining the interfering scattered zone behind a diffuser
ϵ_n	Neumann symbol

Abbreviations

AACF	Aperiodic Autocorrelation Function
ACF	Autocorrelation Function
ASSR	Average Sidelobe to Specular Ratio
BAD	Binary Amplitude Diffuser
BEM	Boundary Element Method
BSZ	Back-Scattered Zone
DFT	Discrete Fourier Transform
FT	Fourier Transform
FSZ	Forward-Scattered Zone
GSZ	Geometric Shadow Zone
GVZ	Geometric Visible Zone
IFT	Inverse Fourier Transform
MLS	Maximum Length Sequence

MS	Multiple Scattering
PRD	Primitive Root Diffuser
QRD	Quadratic Residue Diffuser
RT	Reverberation Time
SZ	Specular Zone

ACKNOWLEDGEMENTS

It would not have been possible to have written this thesis without the help and support of many people. It is not possible to mention each and every one of them here, though I will endeavour to include those to which I am particularly grateful.

Above all I wish to express thanks to my partner Lucy for her patience, support and words of encouragement. I am also extremely grateful for the support of my immediate family, my parents Kathryn and Gareth and my sisters Laura and Alex; and to my closest friends. I also include in this Lucy's parents Brian and Pam, who have shown great support to me throughout.

I would like to express my gratitude towards Professor Trevor Cox and Professor Jamie Angus for the help they provided throughout my studies. In particular, I would like to thank Professor Trevor Cox for his encouragement, guidance and dedication towards helping me complete this project; his knowledge and expertise providing a wealth of input.

I wish to acknowledge the input of the staff and my fellow postgraduates in the Acoustics Research Centre at the University of Salford for many helpful discussions and words of advice. There are too many to mention in person, though in particular I am grateful to Konstantinos Dadiotis for his help on the subject, notably through our many hours of discussions on diffusers which have proved invaluable to my research.

For there help with the construction of measurement samples I would like to express my thanks to Mike Clegg and Phil Latham of the University of Salford.

I would like to thank the Engineering and Physical Sciences Research Council (EPSRC) for funding the initial project on which the thesis is based (EP/D031745/1).

Finally I would like to dedicate this thesis to Steve Hoare who, through his passion for acoustics, encouraged me to start this whole journey.

DECLARATION

This is a declaration that the contents of this thesis are, except where due acknowledgement has been made, the work of the author alone. The following provides a list of publications associated with the research:

Publications

Hughes, R. J., Angus, J. A. S., Cox, T. J., and Umnova, O., "Volumetric Diffusers," *Proc. 124th Convention Audio Eng. Soc., Amsterdam, The Netherlands, May 17-20*, Convention Paper No. 7432 (2008)

Hughes, R. J., Angus, J. A. S., Cox, T. J., Umnova, O., Whittaker, D. M., Gehring, G. A., and Pogson, M., "Volumetric Diffusion from Pseudorandom Periodic Cylinder Arrays," *Presented at the 8th European Conference on Noise Control (Euronoise), Edinburgh, Scotland*, October 26-28 (2009)

Hughes, R. J., Angus, J. A. S., Cox, T. J., Umnova, O., Gehring, G. A., Pogson, M., and Whittaker, D. M., "Volumetric diffusers: Pseudorandom cylinder arrays on a periodic lattice," *J. Acoust. Soc. Am.*, Vol. 128(5), pp. 2847-56 (2010)

ABSTRACT

Most conventional diffusers are used on room surfaces, and consequently can only operate on a hemispherical area. Placing a diffuser in the volume of a room may provide greater efficiency by allowing scattering into the whole space. There are very few examples of volume diffusers and they tend to be limited in design; subsequently a suitable method for their development is lacking.

2D volumetric diffusers are investigated, considering a number of design concepts; namely arrays of slats, percolation structures and cylinder arrays. An experimental technique is adapted for their measurement, and the results are used to verify prediction models for each type. Diffusive efficacy is assessed through a new metric based on an existing surface diffuser coefficient and a measure of scattered power requiring half of the energy to be back-scattered.

Single layer slat arrays are formed from optimal aperiodic sequences, though due to the directional scattering from individual slats at higher frequencies, performance is heavily dependent on line-of-sight through the array. This limits the operational bandwidth to approximately 1.5 octaves. Multi-layer structures offer improvements by allowing cancellation of the back-scattered lobe, though at high frequency the specular reflection from an individual slat still dominates. Percolation fractals use slats orientated in multiple directions and by scattering laterally can channel sound and diffuse at lower frequencies. Low frequency diffusion however is limited and the best structures are those which provide a broad range of geometric reflection paths.

Through application of number theoretic concepts, arrangements of cylinders are shown to offer more enhanced diffusing abilities than slat and percolation structures. At low frequency scattered power is controlled by cylinder size and at high frequency diffusion is dominated by their spacing. By minimising structural similarity and including cylinders with circumference comparable to wavelength, significant diffusion is achieved over an approximate 5 octave bandwidth.

1. INTRODUCTION

1.1. Introduction

The design of a room, including surfaces and contents, can have a dramatic effect on the acoustic quality of the space. An acoustic environment determines the blend of direct and reflected sounds from sources, and ultimately how the sound in a space is perceived [1].

The use of diffusers as an acoustic treatment is well established, for example to reduce the effect of echoes. Problems such as strong echoes introduce distortion (unwanted artefacts caused by a listening environment) such as colouration (an uneven response with frequency); however it is often desirable to reduce such artefacts without removing energy from the room. Acoustic diffusers aim to both spatially and temporally distribute their scattered energy in an optimal manner over a desired bandwidth, and therefore reduce these unwanted effects without the need for absorption [2]. Diffusion has therefore become an important feature in the design of many acoustically sensitive locations, such as concert halls, studios and auditoria.

The research presented in this thesis investigates a new type of diffuser, one which operates in the volume of a space. This 'volume diffuser' is different to most conventional diffusers which generally take the form of a surface based treatment.

Although some volumetric diffusers do exist, the design process behind them has so far been limited, and installations tend to be application specific. Any device would ideally therefore take the form of a versatile ready-to-install stand alone unit, intended for a variety of room types and applications, which would add to the tools at the disposal of the acoustic engineer. To date however no one has designed, tested, or examined the potential application of such diffusers in any depth. Consequently there is a lack of an appropriate methodology for their design, measurement and analysis, and it is this that forms the basis of the work.

This chapter, in the context of architectural acoustics, considers existing diffuser technology in use today, and outlines the motivation behind the development of a volumetric equivalent. A short section details existing literature and its relative significance to the field so far. A brief discussion is given highlighting current examples of volume diffusers in acoustics. A

statement of the aims and objectives of the work are presented. Finally an outline of the thesis structure as a whole is given.

1.2. An introduction to architectural acoustics

In most environments the sound that we hear is a combination of the direct sound from a source or sources, and the indirect sound from reflections off the surfaces and objects within a space. This combination of direct and reflected sound determines how the space is perceived [1]. Architectural acoustics is concerned with this relationship in the built environment; for example in a large concert hall the walls, ceiling, floor and objects within the space will provide many reflections which determine the overall acoustic. By manipulating the reflections from these surfaces and/or objects, along with other important factors such as room volume and shape, the acoustic environment may be altered to best suit the intended use [3].

The design of architectural spaces as listening environments has a long and rich history. Examples stretch from the fan and elliptical arenas of ancient Greece and Rome, through to the classic theatres, opera houses and concert halls of the 18th and 19th Centuries [4]. The birth of modern architectural acoustics however is often cited as occurring a little over a century ago, with Sabine's discovery of the relationship between the random incidence absorption coefficient and Reverberation Time (RT) [5]. This led to a considerable effort being devoted to the study of both surface absorption [3] and the required reverberation time of spaces such as auditoria [4; 6].

For effective noise control absorption is naturally used since the focus is on removing sound energy. In architectural acoustic environments such as auditoria however it is often desirable to maintain the level of sound in a space, for example to allow the sound from a stage to carry to an audience, or to provide a sense of envelopment. Plane reflecting surfaces allow this; though can produce strong echoes or early reflections, which can lead to timbral colouration. More recently, since the seminal papers of Schroeder [7; 8], the use of diffusing surfaces have been investigated [3]. Diffusers allow reflections to be broken up by scattering sound into many directions, redistributing the reflected energy from a surface rather than removing it from a space. In general good architectural acoustic design involves finding the right combination and placement of reflecting, absorbing and diffusing surfaces [3].

The work presented here investigates the design of diffusing structures. Many early (and perhaps accidental) examples of diffusers can be seen in the intricate decorative architectural features of classical halls; such as plaster mouldings, statuettes and coffered ceilings [4]. These irregularly shaped surfaces diffuse perhaps more by accident than design, though have later helped to inspire the installation of more purpose built structures, for example the ceiling of the Beethovenhalle in Bonn which comprises a series of arbitrarily arranged shapes such as hemispheres, pyramids and truncated cylinders [4]. Such structures provide diffusion due to their varying depth, absorbing properties, and scattering angles; however apart from very simple constructions they do not scatter sound in a predictable manner [9]. Sparked by the work of Schroeder [7; 8], modern diffusers which scatter in a more controlled manner are now widely used [3]. Relevant examples of these to the work presented here are introduced in Section 1.3.

1.3. Surface diffusers: important developments, concepts and limitations

Acoustic diffusers are currently predominantly surface based, and a variety of designs are available for which the scattering behaviour is well understood and a large body of knowledge exists [3]. Unlike the volume diffusers presented in the following chapters, they are designed to be installed on walls and ceilings, and consequently will both receive from and scatter into a hemispherical (rather than spherical) area. Figure 1.1 shows examples of a typical planar (left) and hemispherical (right) surface diffuser, so called as they have been designed to spread energy spatially into a single plane and the full hemispherical space respectively. Since the design concepts behind many existing surface diffuser types may be relevant to the development of a volumetric diffuser and the work presented here, a short discussion is presented below which highlights some of their key features. These include some of the inherent limitations of surface diffusers which help form the motivation behind designing a volume equivalent.
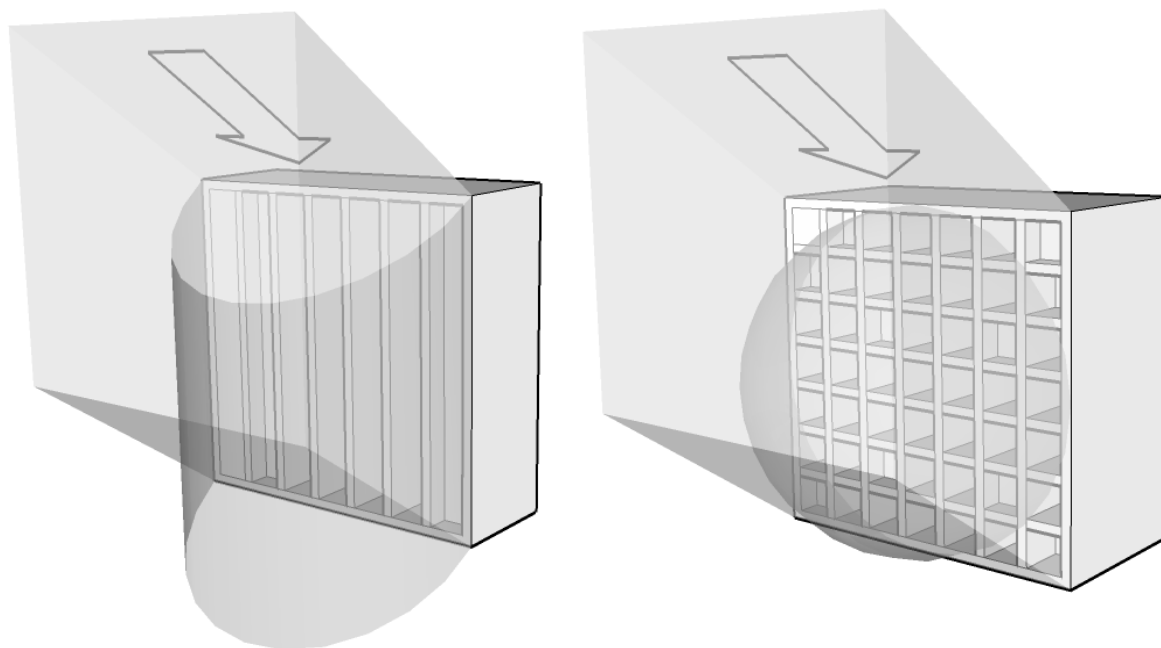
Figure 1.1: Scattering from a 1D planar (left) and hemispherical (right) surface Schroeder diffuser (after D'Antonio and Cox [2]*)*

1.3.1   Schroeder diffusers

In his seminal paper of 1975 Manfred Schroeder posed the question:

"What wall shape has the highest possible sound diffusion, in the sense that an incident wave from any direction is scattered evenly in all directions?" [7]

In this work Schroeder introduced the concept of a new type of diffuser to improve sound diffusion in concert halls and reverberation chambers; the phase grating diffuser. These diffusers were based on number theoretic pseudorandom sequences such as binary Maximum Length Sequences (MLS), which were later improved upon with integer based designs such as the Quadratic Residue Diffuser (QRD) [8] and the Primitive Root Diffuser (PRD) [10]. Often referred to as Schroeder diffusers, examples of which are depicted in Figure 1.1, these surfaces scatter sound in a controlled way.

A Schroeder diffuser comprises a series of equal width wells of varying depth, d_n, separated by narrow fins. Assuming no losses, an incident wavefront will travel down each well and reradiate with the same pressure magnitude, though with different phase due to distance

travelled (a concept particularly relevant to the slats and percolation diffusers presented in Chapters 4 and 5). This then results in dispersion due to interference between the reradiated waves. The well depths are usually determined by an appropriate number theoretic sequence, s_n, which when repeated periodically is designed to emphasise the energy scattered into the grating lobes. A QRD for example scatters equal energy into these lobe directions, resulting in what Schroeder described as 'optimal' diffusion' [8]. Figure 1.2 shows a cross-section through an example of a Schroeder diffuser: a planar length 7 QRD, highlighting a single period where the well depths are proportional to the quadratic residue sequence $s_n = [0\ 1\ 4\ 2\ 2\ 4\ 1]$. Here p_i is the pressure incident from a source and p_s is the scattered pressure.
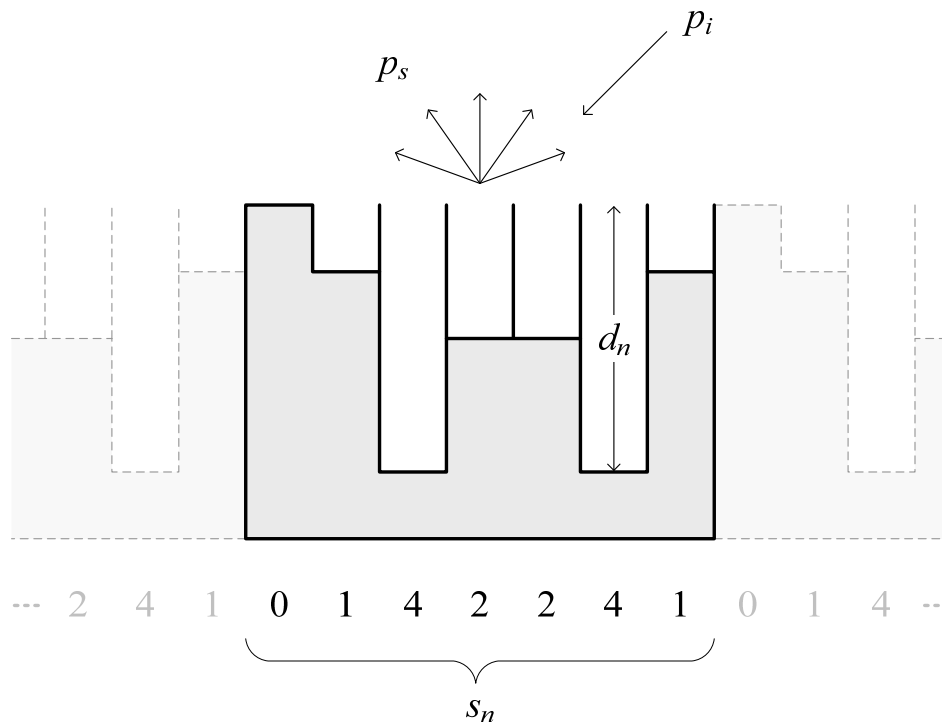
Figure 1.2: Cross-section of a Schroeder (phase grating) diffuser highlighting one period of a repeated sequence; depths d_n determined according to the quadratic residue sequence $s_n = [0\ 1\ 4\ 2\ 2\ 4\ 1]$

Limitations

Schroeder diffusers can be highly effective in dispersing sound, scattering equal energy into the grating lobes at the design frequency, f_0, and multiples thereof, though also resulting in

significant diffusion between multiples of the design frequency. Their bandwidth of operation however can be limited by a number of factors, and these are considered below.

Low frequency – Performance is inherently restricted by available depth, since sufficient phase change is required on reflection. The lower cut-off frequency is often quoted as being equal to the design frequency, since this is the first point at which even energy diffraction lobes are achieved. The period width (width of a single diffuser) however must be greater than a wavelength to ensure that there is more than one grating lobe in the polar response, thus taking advantage of their equal energy [3]. Dependent on sequence choice a low frequency limit generally equates to a wavelength on the order of approximately twice the maximum depth, though scattering behaviour usually differs from that of a plane rigid surface for an octave or two below this [11].

High frequency – The design theory assumes that plane wave propagation dominates within the wells. Consequently this breaks down when a half wavelength becomes equal to the well width, and cross-modes begin to occur in the wells. This does not stop dispersion, but is a limit to how the theory is applied and hence when diffusion is achieved in a controlled manner. In addition to this the use of integer based sequences results in critical frequencies, occurring when all of the well depths are integer multiples of half a wavelength and their phase change on exit is equal. These are often referred to as plate frequencies, since this causes the diffuser to behave like a plane surface and reflect in a specular manner.

1.3.2 Amplitude diffusers

In order to create dispersion, a diffuser must break up a reflected wavefront. With a Schroeder diffuser this is achieved by altering the phase of an incoming sound; however this is not the only way to perturb a wavefront, as any alteration in surface impedance will result in a change to the reradiated energy distribution. One alternative is to create a surface comprised of both absorbing and reflecting patches. Energy incident upon the surface structure is either absorbed or reflected depending on which patch type is encountered. Consequently the reradiated wavefront is altered in amplitude and not in phase [3] resulting in dispersion due to interference between the reradiated waves and edge effects due to impedance discontinuities [12]. This concept is important in the design of much of the work presented here, since a volume array of scattering elements acts much like an amplitude diffuser.

As with Schroeder diffusers, the use of number theoretic sequences allows the design of amplitude diffusers that scatter in a more controlled manner. These are referred to as amplitude grating diffusers [13], though due to both their absorbing and diffusing properties are also often referred to as hybrid diffusers. This concept was first used by Angus [13; 14] in the development of the Binary Amplitude Diffuser (BAD); so called as their surface arrangement is determined by a unipolar binary sequence, with values of 1 and 0 representing total reflection and total absorption respectively. An example of this is illustrated in Figure 1.3, where the MLS $s_n = [1\ 1\ 1\ 0\ 0\ 1\ 0]$ has been used. Like the Schroeder diffuser of Figure 1.2 the sequence is periodic, and hence s_n represents a single period (highlighted).
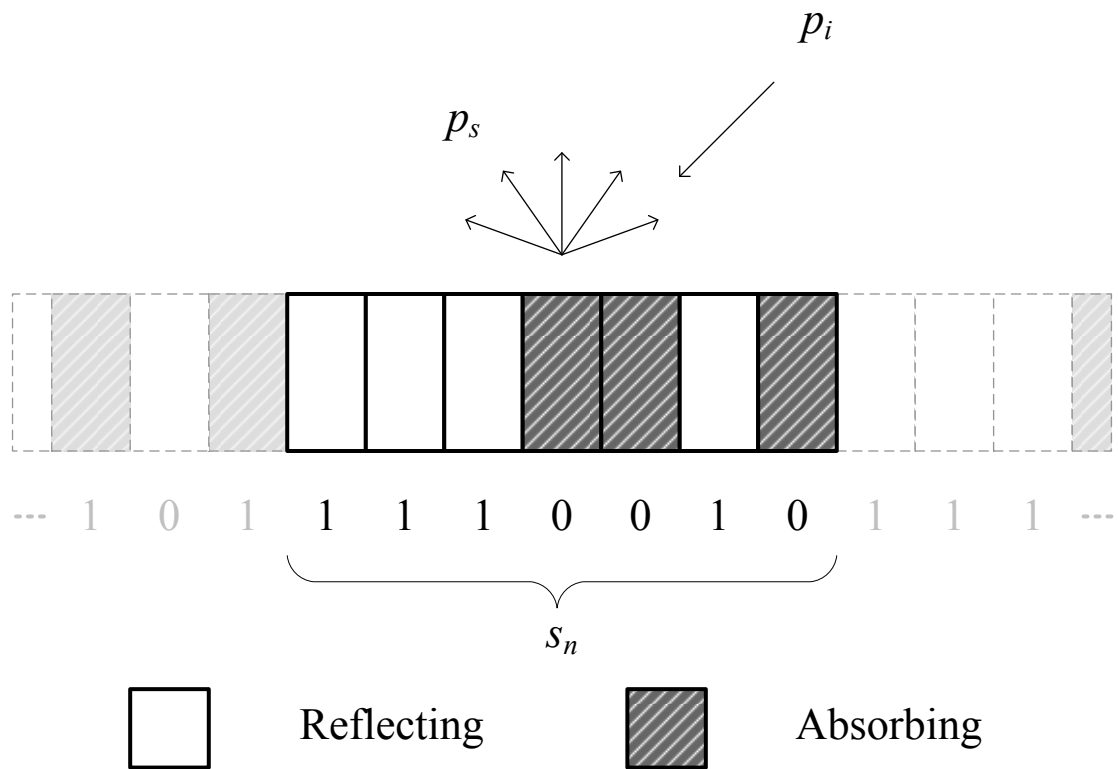
Figure 1.3: Cross-section of an amplitude grating diffuser highlighting one period of a repeated sequence; surface patches arranged according to the Maximum Length Sequence $s_n = [1\ 1\ 1\ 0\ 0\ 1\ 0]$

Limitations

One of the major drawbacks of an amplitude diffuser is the inherent absorption, meaning energy is removed upon reflection. This has led to their use in areas where a combination of both diffusion and absorption is desirable, and they are generally unsuitable for spaces such as

large auditoria where preservation of energy is required. One potential advantage is that unlike a welled diffuser there is (theoretically) no depth requirement (other than that required to fit the absorbent material). Since no phase change is introduced however, there is an inherent coherent specular reflection (though of a reduced amplitude relative to a rigid panel of the same size due to the use of absorption). Consequently sequences such as MLS often used in BAD panels are only able to scatter equal energy into the remaining (non-specular) grating lobes. Attempts have been made to reduce this effect, such as using curved surfaces [3], and more recently through a varying size patch design [15]. There are however several underlying limitations to performance:

Low frequency – Diffusive performance is limited by the properties of the absorbent material used. In practice the absorption must be on the order of a quarter wavelength deep to effectively remove energy, meaning that the theoretical lack of required depth does not hold true. Strictly speaking the slower sound speed of the absorption will mean that the depth requirement is reduced [3], though the need for depth is still an issue. Also, like the Schroeder diffuser, the period width must be greater than a wavelength to ensure the device works correctly when periodically repeated.

High frequency – Performance is limited by the directivity of the flat patches, since once wavelength is comparable to patch size an increasingly specular reflection results. Note this is also true for Schroeder diffusers, though their ability to alter the phase of a reflection means that this is less of a problem.

1.3.3 Other relevant surface diffusers

In Chapter 6 arrays of cylinders are considered; similar in concept to previously studied arrays of semi-cylinders. Single hemi-spheres and semicylinders are efficient at spatially dispersing in the back-scattered direction, however their temporal diffusion is poor and can cause comb-filtering [3]. Alternatively by creating an array of semi-cylinders the pressure distribution is determined more by that of the array configuration, and colouration effects introduced by a single semi-cylinder are less prominent. Using modulating techniques, a pseudorandom arrangement can reduce the effects of periodicity and aid dispersion in the mid-frequency range. Such an arrangement however is limited at low frequency by the diffuser depth and repeat distance and at high frequency by the large number of grating lobes.

Geometric shapes such as triangles / pyramids can be used to perturb an incident wavefront by redirection and modulation [3]. Redirection may be of particular interest in the development of the volumetric diffuser for channelling of energy through a structure, in particular the percolations structures presented in Chapter 5.

1.4.   A volume diffuser

1.4.1   Why a volume diffuser?

Most conventional acoustic diffusers take the form of a surface treatment, such as those discussed in Section 1.3 above. This means that they can only operate in 2π (hemispherical) space, with the remaining scattering paths being blocked off since these lie outside of the room. By considering a structure placed in the volume of the room, it becomes possible to operate on the full 4π (spherical) space, receiving from and scattering into all possible directions [3]. Such a structure forms a volume diffuser, an example of which is illustrated by Figure 1.4. This provides a potentially more efficient method of dispersing sound [3; 16], allowing a theoretical fourfold increase in efficiency relative to an equivalent sized surface diffuser. This occurs since the area received from and scattered into both double; a diffuser sees a twofold increase in both the rate at which it may interact with the sound incident upon it and the area over which it may spatially spread its reflections.

An important concept in the volume diffuser approach is that any device will likely be introduced into a location that was previously empty, thus introducing additional scattering surfaces. This is intrinsically different to the mechanism of a surface diffuser, which aims to alter the scattering characteristics of the surface it replaces. This was explained eloquently by Kuttruff in the statement:

"Quite a different method of achieving a diffuse sound field is not to provide for rough or corrugated walls, and thus to destroy specular reflections, but instead to disturb the free propagation of sound in the space." [16]
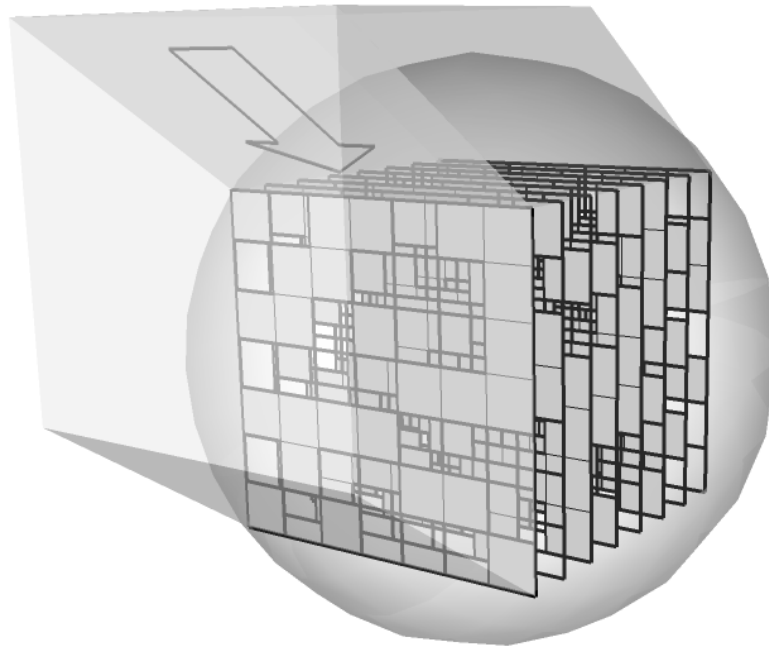
Figure 1.4: Scattering from a 3D spherical volume diffuser

For example objects may be placed in the paths of strong echoes to scatter energy before an echo occurs; or in the paths of modal propagation, breaking up standing waves and creating a more uniform sound field both spatially and with frequency [3]. The latter is a solution adopted in many reverberation chambers, discussed in more detail in Section 1.4.3 below. If these elements were to interfere with the functionality of a room, for example being situated in the line-of-sight from an audience to a stage in an auditorium, then this solution would be impractical. Kuttruff [16] noted however that the method can be quite efficient even when only applied to parts of a room.

Volume diffusers may be advantageous for a number of other reasons, including being more flexible in their geometry. Section 1.3 discussed how surface diffusers are often restricted in their bass response by available depth. Any increase in depth of a surface diffuser unavoidably removes valuable space from a room; it may be possible however with volume devices to utilise 'redundant' space, for instance high above the audience in auditoria, well out of the way of seating and access aisles. In addition to this, by providing many reflection paths a volume device may promote multiple scattering, spreading energy temporally as well as spatially and potentially bypassing the low frequency limitation (see Sections 5.4.2 and 5.5.2). This for instance could be achieved by an arrangement of scattering elements akin to

those seen in reverberation chambers; a construction which would likely be impractical for any surface diffuser.

Some surface diffusers rely on periodicity to produce their 'optimum' diffusion, which can be restricting as they only scatter evenly into the grating lobe angles, and periodicity is otherwise considered undesirable [3]. The use of periodicity has largely found favour due to reasons of practicality, since treating a surface is most easily achieved through a tiling based approach. Conversely a volume diffuser would be positioned in a spatial void, and consequently no longer needs to diffuse in conjunction with a series of neighbouring diffusers. This means that the restriction of periodic repetition of a base unit may be removed and the structure may form a diffusing object in its own right. Note this is not to say that a volume diffuser cannot be periodically repeated, though is a statement of their flexibility of placement.

1.4.2 Defining the volume diffuser

A volume diffuser may be defined as any object (or collection of objects) located in the volume of a space that alters the propagation of sound in a manner that promotes diffuse reflections and/or a diffuse field. The last part is important here, since to what extent a structure diffuses is a matter of definition. A surface diffuser for example promotes diffuse reflections to spread reflected energy both spatially and temporally, helping reduce unwanted artefacts that result from strong specular reflections. This is distinctly different to the approach adopted in many reverberation chambers, where a number of scattering surfaces hung within the space aim to create a diffuse field by redistributing energy, though do not necessarily promote diffuse reflections themselves.

To clarify the discrepancy above, in the context of the work presented here a more specific volume diffuser is referred to; one which forms a single stand alone unit that promotes diffuse reflections and acts as a diffuser in its own right. Ideally this would form a ready-to-install device suitable for application in a variety of room types. This definition is much more in keeping with that of a conventional surface diffuser, though with any need for repetition removed.

Volumetric diffusers, whether by accident or design, are not an entirely new topic. Chandeliers for example may be considered to be volume diffusers, or even 'sculptures' such

as the art installation shown in Figure 1.5, though these are analogous to the ornate surface decorations found in early auditoria which do not scatter in a controlled way. Conversely, whilst more purpose built structures (discussed in more detail in Section 1.4.3) scatter in a more predictable manner, they tend to be application specific and do not form a generic volume diffuser as defined above.

The design of a volume diffuser will essentially be limited only by size, which in turn is determined by available space. One constraint on these structures is that they cannot be placed where they interfere with a room's functionality, for example in the line-of-sight of an audience. Examples such as absorbers being hung in large auditoria to control reverberation [3], or of chandeliers as mentioned above, suggest that dependent on the use of the space, it may be possible to find a number of suitable locations for volume diffusers. In reality additional factors such as practicality of construction, weight, and aesthetics will also be important, though these are not considered here.

Figure 1.5: Cornelia Parker's "Cold Dark Matter: An Exploded View" (1991) [17]

1.4.3 Existing examples of acoustic volume diffusers

Reverberation chambers

Reverberation chambers often make use of suspended scattering surfaces hung within the room to promote a diffuse field by redistributing energy and breaking up modal propagation [3; 16], an example of which is shown in Figure 1.6. These may be viewed as a form of volume diffuser, for which current guidance on their application is given in Appendix A of international standard BS EN ISO 354:2003 "Acoustics – Measurement of sound absorption in a reverberation room" [18]. This recommends introducing a number of diffusing elements; specifically thin non-absorptive panels varying in size from 0.8-3m^2 (for one side). These may be slightly curved and of random orientation and location. The actual number of diffusing panels to be used is essentially based on a trial and error process; a method which involves measuring the absorption coefficient of a test sample (assuming a diffuse field in accordance with Sabine's equation [19]), and introducing diffusing panels until the average coefficient remains constant. In general the panels (considering both sides of each) should account for approximately 15-25% of the total surface area within the room.

In the context of reverberation chambers, volume diffusion can have significant advantages over surface diffusion [3]. Cox [3] for example points out that for a reverberation room to achieve a diffuse field via surface diffusion, at least three of the boundaries must be treated (e.g. at least one of each pair of surfaces directly facing one another). This implies a diffusing area of approximately 50% of the total surface area of the walls. Introducing diffusing panels that account for approximately 15-25% of the total surface area of the room on the other hand, as recommended by BS EN ISO 354:2003, equates to a volume diffusing area equivalent to 18-33% of the total surface area of the walls. Furthermore, this value considers the surface area of both sides of the panels, and so their total area considering only a single side is halved to 9-17% of the wall surface area. Whilst these improvements in efficiency do not necessarily carry over directly to more conventional spaces, they do however suggest the potential of a volume diffuser to at least pass on some of these gains.

Figure 1.6: Reverberation chamber with suspended scattering panels

The above guidance is given for the measurement of absorption coefficients over a frequency range of 100Hz-5kHz, which implies a maximum panel size (assumed to have a width of $3^{1/2} \approx 1.73\text{m}$) on the order of half a wavelength for the lowest measured frequency. The use of simple rigid panels is largely due to cost and practicality reasons, though alternative shapes could potentially be used. These scattering panels are often referred to as volume diffusers, though it could be argued that they form a single volume diffuser since independently they will have little effect, and it is their combined interaction that results in a more uniform sound field. In contrast to the volume diffusers considered here, however, the sound field is sampled within this diffusing structure. It is likely though that an arrangement which results in a uniform internal sound field would also provide dispersion external to the structure when placed in a free-field environment.

Overhead stage canopies

Overhead stage canopies have been investigated for their effectiveness in controlling reflected sound to enhance intelligibility and clarity [20]. They are usually found suspended above a stage or audience in auditoria to reflect sound back into the space, for example back towards the musicians to allow them to hear what is being played and keep in time with one another [3]. A common criterion for their design is to achieve an even distribution of reflections over a defined area [21], and as such are similar in concept to surface diffusers. Since they are located in the volume of a space however, these may be viewed as a type of volume diffuser.

Some canopies have virtually no open area and are curved to direct reflections sideways to promote lateral reflections and reduce colouration [8]. Of most interest to the work presented here however are canopy arrays, composed of a series of reflecting panels separated by intermediate gaps. By introducing these gaps the sound directed back to the stage may be controlled, whilst also permitting some sound to pass through the structure to be heard by the audience and to add to the general reverberance [3]. These arrays usually form a single layer of scattering panels, and as such are similar in concept to the 1D array volume diffusers presented later on in the thesis, in particular the 1D slat arrays presented in Section 4.2.

Rindel [22] determined that small elements were required in a canopy array so that diffracted energy was received in locations where there is no specular reflection, concluding that low frequency performance is determined by density and high frequency performance by panel size and spacing. Later Cox and D'Antonio [21] considered the effect of the density, size, shape and location of canopy elements using optimisation techniques, concluding that for high levels of support dense arrays of large simple shaped panels are best.

Much of the work above considers the near-field response of an array, though some investigations have been carried out for far-field conditions. Here at low frequency the response is dominated by the scattering characteristics of a single panel, and at high frequency by strong specular reflections, with the sidelobes of the array configuration being largely suppressed [3]. This behaviour is demonstrated for arrays of slats in Section 4.2 and is discussed further.

Other volume devices

Sonic crystals are periodic devices, ordinarily composed of cylinders (2D) or spheres (3D) with locations determined by a square or cubic lattice respectively. Consequently they are similar to the cylinder arrays of Chapter 6 whose arrangement is based on a periodic grid. Previous work in this area has predominantly focused on attenuation by arrays at specific frequencies, known as band-gaps [23-25], rather than on the spatial distribution of its scattered field. A typical sonic crystal will spread energy temporally, but produces inherent grating lobes and therefore makes a poor diffuser whose behaviour varies significantly with position and frequency [26]. Consequently they must be altered significantly if they are to provide diffusion.

1.5.   Aims and objectives of the research

The aim of the research is to investigate the design and analysis of volumetric diffusers as an acoustic treatment, for use in acoustically problematic environments such as train stations or large auditoria. Existing diffuser design techniques may be unsuitable, therefore a primary objective is to develop ways for measuring and assessing performance. These are used to study a number of design concepts, using existing surface diffuser design and number theory as a starting point.

An overriding question is "can a structure be created that sits in the volume of a space and improves the acoustics through 'diffusion'?" In terms of subjective analysis this is generally outside of the scope of the work presented here. Subsequently the aim is to set about objectively designing a structure that provides a likely candidate for achieving this.

Following from the original pioneering work of Manfred Schroeder, an adapted volume equivalent to the question quoted in Section 1.3.1 [7] is:

"What volume diffuser has the highest possible sound diffusion, in the sense that an incident wave from any direction is scattered evenly in all directions?"

This will ideally be a device which spreads energy temporally as well as spatially and over an appropriate bandwidth.

The aims may be summarised as follows:

- To develop a design methodology for modelling / prediction.

- To devise a measurement procedure to validate these predictions.

- To derive suitable metrics to test effectiveness.

- To investigate the links between existing surface diffuser designs and their potential applications towards a volumetric equivalent.

- To determine – for each of the concepts presented and in general – the key parameters that affect performance – e.g. size, shape, density, arrangement etc.

1.6.   Contributions to the field

The work presented is novel, in that it considers the effective design of a new type of diffuser; a single ready to install diffuser that is placed in the body of a room. This diffuser type is inherently different to existing conventional surface based diffusers, or more application specific examples of volume diffusers such as overhead stage canopies or curved panels suspended in reverberation chambers. The thesis presents a number of original contributions of knowledge to the field. These include:

- Demonstrating the applicability of a number of models for the accurate prediction of scattering from a number of volume diffuser structure types.

- The extension of existing surface diffuser measurement techniques in order to accurately measure the scattering around a volume diffuser, including notably the development of a cross-correlation oversampling technique to obtain accurate results for the scattering towards the back of a structure.

- The extension of existing diffusion metrics for the analysis of scattering uniformity, specifically through a volume diffusion coefficient metric which allows the forward scattered field to be included in the analysis.

- The application of a number of concepts taken from surface diffuser design, specifically number theoretic concepts, to the design of a volume diffuser.

- The extension of number theoretic concepts to include multi-layered structures, utilising sequences previously not applied to diffuser design.

- Obtaining a number of the key parameters that determine what makes an effective volume diffuser.

1.7.   Structure of the thesis

The thesis is broken down into three parts; methodology, design and discussion of outcomes. Chapter 2 details the prediction methods used for modelling the volume diffusers, which are then verified through measurements. Subsequently Chapter 3 develops a set of suitable metrics and methods for assessment of diffusive efficacy. A number of proposed diffuser types are developed and are presented in Chapters 4-6; investigating the merits of slat arrays, percolation structures, and cylinder arrays respectively. Chapter 7 discusses the findings from the design concepts used; the success of the methodology; and highlights potential further work. Finally Chapter 8 presents the conclusions.

2. PREDICTION AND MEASUREMENT

2.1. Introduction

Chapter 1 discussed the research objectives and the motivation behind the work. An important aspect of this process involves the development of both accurate and reliable prediction and measurement routines. In order to design an effective diffuser, it is necessary to be able to confidently quantify how it behaves. Techniques for analysing the scattering from surface diffusers are well known, with, in particular, direction for best practice being set out in international standard BS ISO 17497-1:2004 [27] and the Audio Engineering Society guidance document AES-4id-2001 [28] respectively. Here this work was extended and built upon to develop a new approach necessary for volume diffusers. This chapter sets out a method for obtaining both predicted and measured data for the free-field acoustic scattering of a structure located in the volume of a space. The performance of this structure as a diffuser is not considered at this point, and shall be covered in Chapter 3.

With existing surface diffusers, the scattered field is commonly represented by a series of polar responses, describing the spatial distribution of the reflected sound for a given frequency (or frequency range) [3]. This concept is extended to a volume equivalent which includes the full space, in a manner similar to the characterisation of the directional behaviour of transducers such as loudspeakers or microphones.

A brief overview of the geometry under consideration is given. Two types of prediction process are presented: both simplistic and highly accurate, and these are employed throughout the following chapters. The simplistic model is defined to help inform potentially suitable arrangements, which aids understanding of the design process and helps minimise computational time. For structures that demonstrate sufficient promise, a number of more accurate but more computationally expensive models are presented. These include both Boundary Element Method (BEM) and Multiple Scattering (MS) routines, with application dependent on structure type. While these techniques have been employed for prediction of scattering before, they have not previously been applied to the volume diffusers considered here.

Finally, a 2D volume measurement technique is developed, based on a conventional boundary plane technique. A novel refinement using oversampling is needed to allow accurate measurement in the forward-scattered region. This is the first time that modern diffuser evaluation techniques have been applied to measurements from volume diffusers. The natures of the diffuser structures introduced in Chapters 4 to 6 are described, and selective measurements representative of each proposed structure type allow verification of the more accurate modelling techniques.

2.2.   Defining the geometry

Often, whether it be an array of transducers or a crystal subject to a beam of X-rays, it is desirable to understand how an object spatially distributes its energy. In surface diffuser design this is usually achieved by obtaining the polar pattern for a given angle of incidence. This describes how the scattered energy is spatially distributed, sampling the scattered field at a fixed distance from the scattering object over a range of angles of reflection. Ordinarily at the design stage this would be carried out for a range of single frequency values.

In order to obtain the polar response it is necessary to define the setup. The following section defines the geometry that will be used throughout the remaining sections in the chapter, both for measurement and prediction. Much of the content here will be loosely based upon the existing guidelines for the measurement of surface diffusers set out by the Audio Engineering Society standard AES-4id-2001 [28], which is currently at the committee stage for consideration as international standard ISO:17497-2.

2.2.1   A typical 1D planar surface diffuser setup

In the case of a conventional planar diffuser the surface varies in one direction only, and is simply extruded in the orthogonal direction, an example of which was shown in Figure 1.1 (left). This produces scattering in one plane only (assuming the extruded dimension is large relative to wavelength) and so only scattering in this plane is considered. Furthermore, a surface diffuser need only be considered in the half-plane space containing the source, as it is intended to form part of a rigid wall structure which does not allow transmission. The receiver locations required therefore simply lie on a semicircular arc, and along with the source, lie on the plane whose normal is parallel to the extruded dimension. This allows the structure to be

approximated by a 2D cross-section, such as that shown in Figure 1.3, significantly reducing complexity relative to a conventional hemispherical diffuser like that shown in Figure 1.1 (right), i.e. one whose surface varies in more than one direction where it is necessary to consider appropriate source and receiver locations within the full hemispherical back-scattered space.

For clarity, the following surface diffuser definitions defined in Table 2.1 apply throughout the text:

Table 2.1: Surface diffuser type definitions

Diffuser type	Scattering type	Measurement / model type	Arrangement description
Planar	Single plane	2D	Surface varying in one direction only
Hemispherical	Hemispherical	3D	Surface varying in more than one direction; arbitrary surface

The basic setup for a planar surface diffuser is depicted in Figure 2.1, where a 1D Schroeder diffuser similar to that of Figure 1.1 (left) is shown as an example. The scattered pressure is obtained for an arc of receivers R, of radius (and hence receiver distance) r, and with individual receiver angles given by θ, the angle of reflection. The source location, S, is described by its polar coordinates r_0 and θ_0, the source distance and angle of incidence respectively. The origin of the coordinate system is taken as being the centre of the diffuser face (of maximum dimension visible from the source, D). By convention $\theta = 0°$ is taken as being in the direction normal to the surface (hence the term normal incidence), with the scattered field being limited to $-90° \leq \theta \leq 90°$.
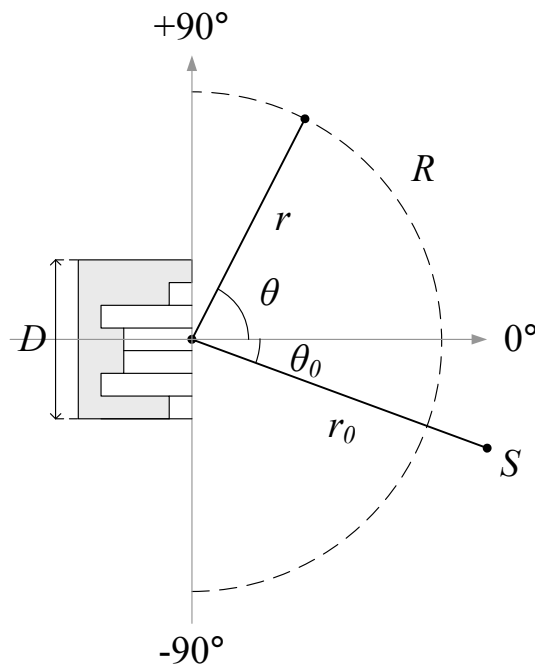
Figure 2.1: Typical planar diffuser geometry

2.2.2   1D and 2D planar volume diffusers

Unlike a surface device, a diffuser situated in the volume of a space allows sound to be received from and scattered into all directions, as was depicted in Figure 1.4 showing a 3D spherical volume diffuser. Consequently the full space must be evaluated, and the number of source and receiver locations necessary to provide the equivalent polar response resolution (relative to the surface diffuser analogue, in this case hemispherical) both double. This produces a potential fourfold increase in requisite measurements.

A planar 2D diffuser is hence preferred to reduce the complexity of both modelling and measuring the structures, whilst having the added benefit that the approach may aid understanding in the early design process. It is likely that the design principles developed in 2D are transferable to 3D designs in a similar manner to which more conventional surface diffusers have been extended from planar to hemispherical devices [8; 14].

By considering the volumetric analogue of the planar surface diffuser the structure is simplified to a 2D planar case, and is again assumed to continue to plus and minus infinity in the direction normal to the measurement/modelling plane. A circle of receivers centred on the structure is hence required to describe the scattered field. Figure 2.2 shows the necessary

setup, where angles and distances are defined as per Figure 2.1. This is essentially the same as the setup described in Section 2.2.1, though with angular variables unrestricted within the scattering plane, and unless otherwise stated this design type shall be assumed throughout the thesis.
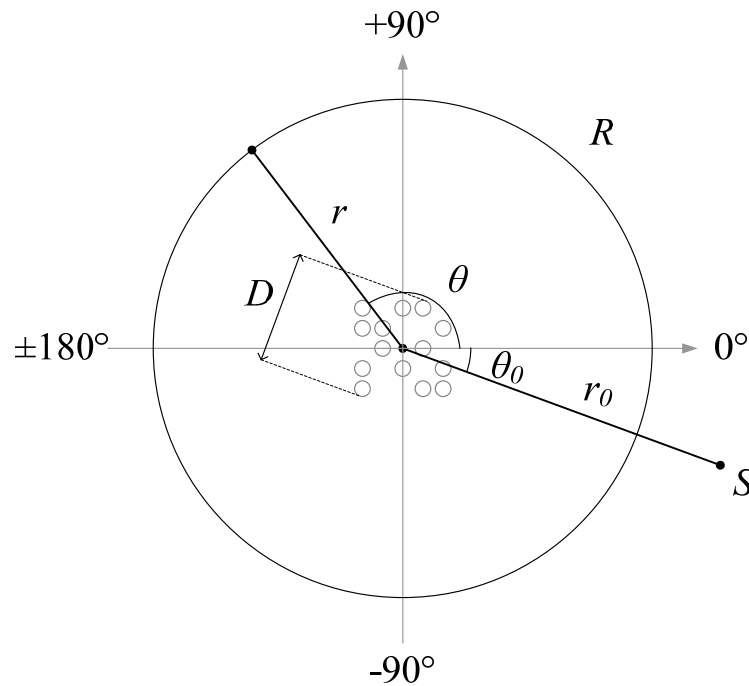
Figure 2.2: Planar volume diffuser setup

For clarity, the volume diffuser definitions defined in Table 2.2 apply throughout the text.

Table 2.2: Volume diffuser type definitions

Diffuser type	Scattering type	Measurement / model type	Arrangement description
1D			Varying in one direction only; collinearly arranged
2D	Single plane	2D	Varying in more than one direction; arbitrarily arranged
3D	Spherical	3D	Arbitrary arrangement

2.2.3   Free-field and far-field assumption

Free-field

The setups described in Sections 2.2.1 and 2.2.2 assume free-field conditions; that is, there are no additional reflecting boundaries such that no outgoing waves will return to the scattering object. This means that the only sound incident upon the diffusing object is from the single source, *S*, and from itself via multiple scattering. This in reality is not likely, since most diffusers are used as a room acoustic treatment and therefore interact with numerous sound waves varying both in time and direction of arrival. In diffuser design however it is common to represent a diffuser in this way [7], breaking down the problem into 'single reflections' for a variety of frequencies and angles of incidence. In this way the physical mechanisms that determine the overall behaviour can be more accurately understood. These structures may then if required be tested in a more application specific/realistic scenario at a later point in the design process.

Far-field

Ideally the scattered pressure from an object would vary only with angle and wavelength (relative to the object size). All free-field measurements however, and hence all polar response data, will be dependent on distance between the scattering object and both source and receivers. Consider the geometry as shown in Figure 2.3, showing a scattering surface of maximum dimension, D_{max}, subject to a sound from a source, *S*. The minimum and maximum distance between source and surface are given as r_{min} and r_{max} respectively, with their difference given as $\Delta r = r_{max} - r_{min}$. This difference in path length will approach $D_{max}/2$ for distances close to the surface where the curvature of the cylindrical wavefront is observed, whilst for large distances will become asymptotically close to zero with the incident wavefront becoming planar. This is frequency dependent, with plane wave behaviour resulting when energy incident upon the surface is coherent. This is approximately the case when the surface is within the same Fresnel zone, that is $\Delta r < \lambda/2$, where λ is the wavelength.
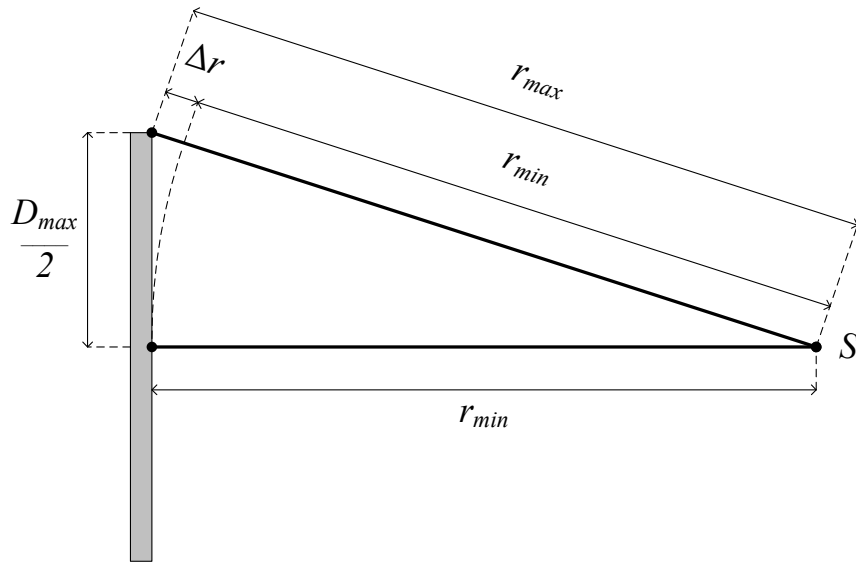
Figure 2.3: Geometry in estimating the extent in the near-field (after Kinsler et al. [29])

The above is for an on-axis source position, which represents the worst case (considering a change in phase only), and applies equally to receiver position also. Following from the Fresnel zone definition, the following far-field criterion may be derived [29]:

$$r_0 > \frac{D_{\max}^{\;2}}{4\lambda} \qquad\qquad 2.1$$

$$r > \frac{D_{\max}^{\;2}}{4\lambda} \qquad\qquad 2.2$$

Eqs. 2.1-2.2 therefore provide an approximate condition for far-field behaviour. A combination however of both source and receiver distance can be obtained to provide one characteristic distance [22], r_c, and resulting far-field criterion given as:

$$r_c = \frac{2r_0 r}{(r_0 + r)} \qquad\qquad 2.3$$

$$r_c \gg \frac{D_{\max}^{\;2}}{\lambda} \qquad\qquad 2.4$$

Note the more stringent definition of Eq. 2.4, ensuring incident and scattered regions of the observed wavefront are well within one Fresnel zone. This is to compensate for the fact that in

reality there is no definitive boundary between the near and far-field, with behaviour becoming asymptotically more and more 'far-field' in nature with increasing distance.

In this simplified approach (which describes behaviour in terms of relative phase only) the amplitude of the wavefront due to (in the 2D case) cylindrical spreading has so far been neglected. The worst case due to a change in amplitude is at grazing angles – angles which describe a trajectory close to being parallel to a surface (for example, $\theta_0 = \pm 90^\circ$ in Figure 2.1) – where the maximum path length difference is D_{max}. Consequently an additional criterion is used, given as:

$$r \gg D_{max} \hspace{8cm} 2.5$$

Eq. 2.3-2.5 form the standard far-field definition as per AES-4id-2001 [28]. It is worth noting that Eq. 2.5 above is particularly relevant to volume diffusers as they may contain depth, which in terms of path length is the equivalent to considering a surface diffuser at grazing incidence. Consequently at high frequencies, large distances are required to approximate true far-field behaviour.

There is another criterion for far-field conditions – that distance must be greater than wavelength, since for distances closer to the scatterer there will be additional reactive energy which does not radiate [30]. This is in contrast to the far-field behaviour where the energy radiates outward at the speed of sound. In practice however satisfying the criteria of Eqs. 2.3-2.5 means that for a diffuser of typical size and operational bandwidth this condition is usually met.

For distances satisfying the above, the scattered polar response becomes approximately consistent in envelope, and varies only in scale due to cylindrical spreading, falling by 3dB per doubling of distance. An example of this is shown in Figure 2.4, predicted using the thin panel Boundary Element Method (BEM) routine introduced in Section 2.3.2, where the scattering from a flat plate of width $D = 0.4$m at a frequency of 4kHz is shown. Note: for ease of comparison the effect of cylindrical spreading has been removed by normalising the scattered pressure following the procedure outlined in Section 2.5.2. With increasing distance the scattered field tends towards the asymptotic far-field case, which following from Eq. 2.4 for the plate shown becomes apparent when $r_c \gg 1.86$m.

In some situations however due to restrictions with space it is not possible to meet these requirements, and so an alternative less stringent criterion may be applied. AES-4id-2001 stipulates that no more than 20% of receivers must be situated within the specular zone (SZ), defined as being the region over which a geometric reflection occurs. This in the context of volume diffuser analysis is revisited in Chapter 3. For the flat plate shown in Figure 2.4, all of the characteristic distances except for the $r_c = 0.5m$ case have less than 20% of their receivers in the specular zone. Note, since this definition applies to surface diffusers the 20% criterion refers to one half of the scattered field, and consequently refers to 10% of the full scattered field, that is a solid angle of $36°$.
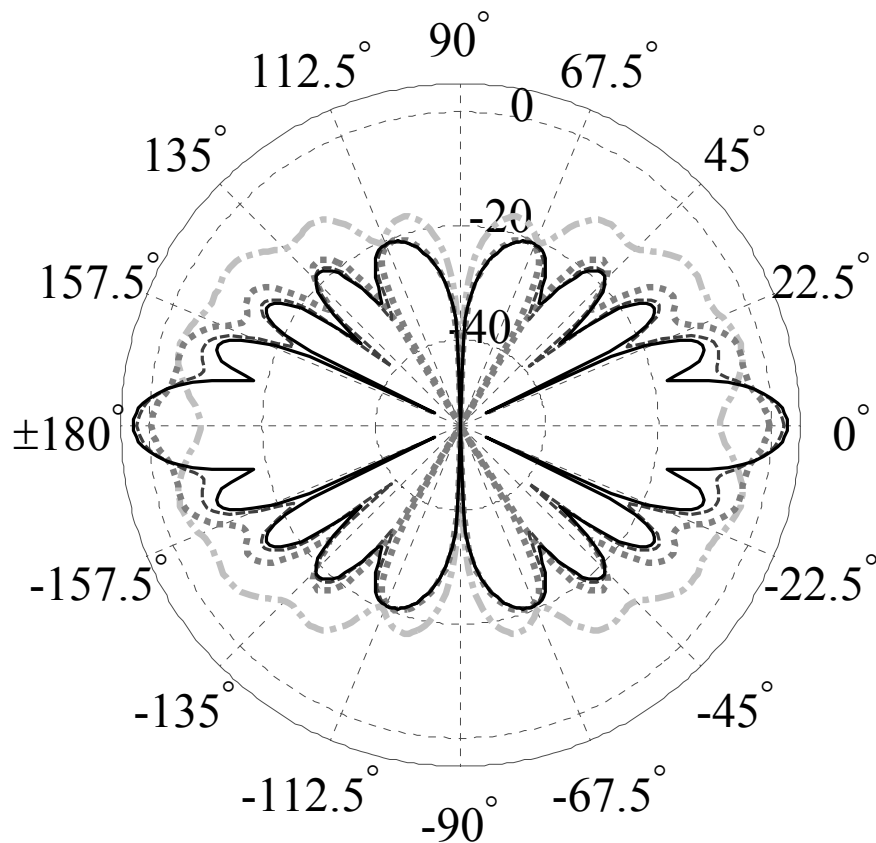
Figure 2.4: Normalised scattered pressure polar pattern for a flat plate modelled using the thin panel BEM of Section 2.3.2; D = 0.4m, f = 4kHz, r₀ = 25m, θ₀ = 0°; r_c = 0.5m (– –), 2.0m (- - -), 5.0m (– –), and 20.0m (▬)

Most diffuser measurements aim to achieve as close to far-field conditions as is practical, utilising the maximum amount of space that allows a measurement at a fixed distance from the centre of the diffuser surface (note: for a volume diffuser this is now defined as the centre

of the diffuser itself). In the case of the measurements considered here, this was restricted by the dimensions of the semi-anechoic chamber (discussed in further detail in Section 2.5). Again, more application specific/realistic scenarios may be considered later in the design process. This may include near-field aberrations such as focusing [28], particularly at high frequency.

Unless otherwise stated, all models / measurements assume free-field conditions and are evaluated for far-field source and receiver positions throughout.

2.3. Prediction: most accurate methods

All of the accurate methods presented below in theory produce exact solutions of the wave equation, neglecting numerical errors and finite discretisation, and provided a few simple assumptions are valid. This therefore should allow highly accurate prediction of the scattering from the modelled diffusers.

2.3.1 A boundary element method

For an arbitrarily shaped scattering object with a potentially non-rigid surface, a general prediction model is required. An example of this is a Boundary Element Method (BEM), which has been shown previously to provide accurate predictions of the scattered pressure from a variety of diffusing surfaces [3; 7-9]. This method is employed at various points throughout the text, including for comparison with the thin panel BEM presented below in Sections 2.6.1-2.6.2; and when modelling a surface diffuser including absorption in Chapter 4.

The BEM model uses the Helmholtz-Kirchoff integral equation, expanded using Green's first and second theorems, to formulate the pressure at a point as the addition of the incident pressure direct from any source(s) and the surface integral of the pressure and its derivative over the reflecting surfaces [3]. For simplicity, one source only is assumed throughout.

For the single frequency case, the total pressure $p_t(\mathbf{r})$ for a receiver located at $\mathbf{r} = (x, y)$ may be given by [31]:

$$\left.\begin{array}{cc} \mathbf{r} \in \Omega & p_t(\mathbf{r}) \\ \mathbf{r} \in s & \frac{1}{2} p_t(\mathbf{r}) \\ \mathbf{r} \in \Omega_0 & 0 \end{array}\right\} = p_i(\mathbf{r}, \mathbf{r}_0) + \int_s p_t(\mathbf{r}_s) \frac{\partial G(\mathbf{r}, \mathbf{r}_s)}{\partial \mathbf{n}(\mathbf{r}_s)} - G(\mathbf{r}, \mathbf{r}_s) \frac{\partial p_t(\mathbf{r}_s)}{\partial \mathbf{n}(\mathbf{r}_s)} ds \qquad 2.6$$

Where $p_i(\mathbf{r}, \mathbf{r}_0)$ is the incident pressure from a source located at $\mathbf{r}_0 = (x_0, y_0)$; $\mathbf{r}_s = (x_s, y_s)$ is the vector for a point on the surface, s; partial derivatives are taken with respect to the surface normal, $\mathbf{n}$ (pointing outwards); Ω and Ω_0 are the regions external and internal to the surface; and G is the appropriate Green's function. A graphical illustration of the above is given in Figure 2.5 for the case where the point of observation, $\mathbf{r} \in \Omega$.
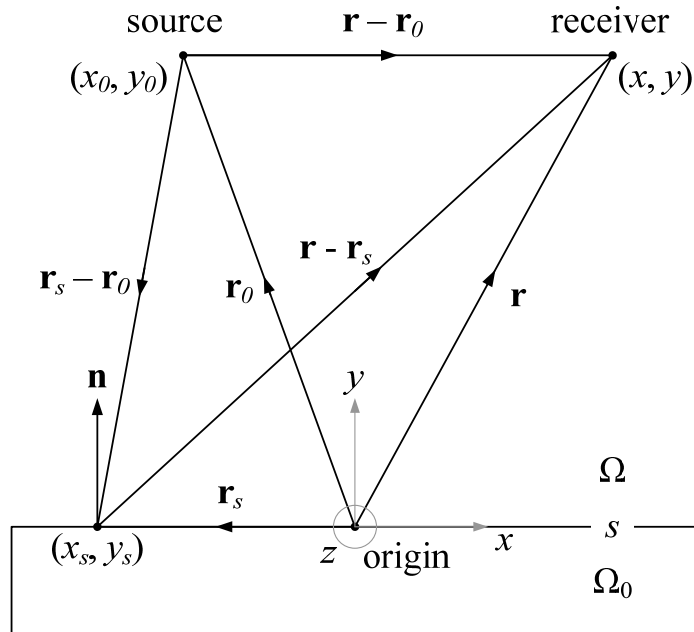
Figure 2.5: Geometry for the BEM prediction model (after Cox and D'Antonio [3]*)*

For a 2D solution, Eq. 2.6 essentially forms a line integral, and the following Green's function is used:

$$G(\mathbf{r}_b, \mathbf{r}_a) = \frac{-j}{4} H_0^{(1)}\left(k|\mathbf{r}_b - \mathbf{r}_a|\right) \qquad 2.7$$

Where $H_0^{(1)}$ is the Hankel function of the first kind of order zero; $k = 2\pi/\lambda$ is the wavenumber; and the Green's function describes how the pressure (and its derivative) propagate between two arbitrary points $\mathbf{r}_a = (x_a, y_a)$ and $\mathbf{r}_b = (x_b, y_b)$.

The surface is assumed to exhibit local reaction; that is the normal velocity of any point on the surface boundary depends only on the pressure at that point. This means that the surface pressure derivative – the second part of the integral equation in Eq. 2.6 – will be related to the surface pressure and the local surface admittance by the following [3]:

$$jkp_t(r_s)\beta'(r_s) = \frac{\partial p_t(r_s)}{\partial \mathbf{n}(r_s)} \qquad 2.8$$

Where β' is the surface admittance pointing out from the surface into the external domain $\mathbf{r} \in \Omega$. Note, β' here is the negative of the more conventional surface admittance β, where the more usual inward pointing normal is used. Unless otherwise stated however, for maximum preservation of energy, it is assumed that all surfaces are acoustically rigid. This means that the surface admittance $\beta' \rightarrow 0$, and the pressure derivative component can be omitted, thus simplifying the solution and reducing computational time.

To obtain the pressures at an arbitrary point Eq. 2.6 must be applied twice, firstly to find the surface pressures and secondly to determine the pressures at any number of desired receiver positions. As this is a numerically computed solution, the sample surface must be discretised into a number of elements. These must be small relative to wavelength, typically less than an eighth of a wavelength in length, such that the pressure and its derivative across the element may be considered approximately constant. To find the surface pressures a set of N simultaneous equations is set up, where N is the number of elements, forming a matrix representation of Eq. 2.6 where $\mathbf{r} \in s$, given as [3]:

$$\left(\frac{1}{2}\mathbf{I} + \mathbf{A}\right)\mathbf{P}_t = \mathbf{P}_i \qquad 2.9$$

$$\mathbf{A}_{l,m} = \int_{s_m} \frac{\partial G(\mathbf{r}_l, \mathbf{r}_{s,m})}{\partial \mathbf{n}_m(\mathbf{r}_{s,m})} - G(\mathbf{r}_l, \mathbf{r}_{s,m})jk\beta'_m \, ds_m \qquad 2.10$$

Where $\mathbf{P}_i$ is a ($N{\times}1$) matrix of incident pressures; $\mathbf{P}_t$ is a ($N{\times}1$) matrix of surface pressures; $\mathbf{I}$ is an ($N{\times}N$) identity matrix; and $\mathbf{A}$ is a ($N{\times}N$) matrix describing the surface interactions, that is the influence of the mth element on the lth element surface pressure where l and m are matrix indices referring to element number. By calculating the coefficients of matrix $\mathbf{A}$, including performing the required numerical integrations for each element combination, Eq. 2.9 may be solved obtaining the total pressures on the surface. Finally a numerical integration is performed over the entire surface using the now known surface pressures, in order to obtain the pressures at any arbitrary location for the region $\mathbf{r} \in \Omega$.

The above routine has been implemented throughout using a BEM executable routine, courtesy of Professor Cox of the University of Salford [32].

2.3.2   A thin panel boundary element method

Chapters 4 and 5 consider the use of slat array and percolation fractal diffusing structures, examples of which can be seen in Figure 2.21 and Figure 2.23 respectively, each comprising a series of thin panels. For very thin surfaces, the standard BEM routine in Section 2.3.1 will no longer provide accurate results. This is due to the front and back of the surface having elements very close to one another, causing a singularity in the equation and the result to become ill-conditioned [33]. An alternative approach however is to reformulate the problem in terms of the pressure difference and sum across the thin surface, considering it as an infinitely thin panel. This method has been shown to be accurate for a number of surface types [8; 11], whilst conveniently approximately halving the number of required elements, hence reducing computation time. Terai [34] showed that this thin panel variation on the standard BEM may be achieved by the use of both Eq. 2.6 and its derivative. Considering the specific case of rigid panels, the problem may be reduced to a single equation expressed in terms of the pressure difference across each panel [3], and is given by Eq. 2.11 as:

$$0 = \frac{\partial p_i(\mathbf{r},\mathbf{r}_0)}{\partial \mathbf{n}(\mathbf{r})} + \iint\limits_s \{p_t(\mathbf{r}_{s,1}) - p_t(\mathbf{r}_{s,2})\}\frac{\partial^2 G(\mathbf{r},\mathbf{r}_{s,1})}{\partial \mathbf{n}(\mathbf{r})\partial \mathbf{n}(\mathbf{r}_{s,1})}ds \qquad 2.11$$

Where the observation point is on the front of the surface, $\mathbf{r} \in s_1$; and the 1 and 2 in the subscripts refer to the front and back of the infinitely thin panel respectively.

The integral is performed over the front face to obtain the pressure difference, $p_t(\mathbf{r}_{s,1})$ - $p_t(\mathbf{r}_{s,2})$, between the front and back of each individual element in a similar manner to the procedure given by Eqs. 2.9-2.10. Once this is achieved, the following equation is used to obtain the pressures at an arbitrary location in the external region, $\mathbf{r} \in \Omega$ [3]:

$$p_t(\mathbf{r}) = p_i(\mathbf{r},\mathbf{r}_0) + \iint_s \left\{ p_t(\mathbf{r}_{s,1}) - p_t(\mathbf{r}_{s,2}) \right\} \frac{\partial G(\mathbf{r},\mathbf{r}_{s,1})}{\partial \mathbf{n}(\mathbf{r}_{s,1})} ds \qquad 2.12$$

The above routine has been implemented throughout using a thin panel BEM executable routine, courtesy of Professor Cox of the University of Salford [32].

2.3.3 Multiple scattering between cylinders

The BEM models presented in Sections 2.3.1-2.3.2 are versatile techniques, being able to model an essentially arbitrary arrangement, though can be computationally expensive. For some structure types where the physical construction is to a certain extent predefined, and limited to scattering bodies for which an analytical solution exists, it may be possible to significantly reduce computation time by using an alternative Multiple Scattering (MS) approach. This is the case for an array of cylinders such as those considered in Chapter 6, an example of which is shown in Figure 2.27.

A MS solution expresses the total pressure $p_t(\mathbf{r})$ at a given point $\mathbf{r}$, as a summation of the incident pressure $p_i(\mathbf{r}, \mathbf{r}_0)$ and the scattering from each individual scattering object. For cylinders this is broken down further into the cylindrical modes scattered by an individual cylinder. Assuming the use of the Green's function given by Eq. 2.7, the MS solution for an arbitrary arrangement of E cylinders may be expressed as [35]:

$$p_t(\mathbf{r}) = p_i(\mathbf{r},\mathbf{r}_0) + \sum_{i=1}^{E} \sum_{n=-\infty}^{+\infty} A_n^i Z_n^i H_n^{(1)}\left(k|\mathbf{r}-\mathbf{r}_i|\right) e^{jn\theta_i} \qquad 2.13$$

Where k is the wavenumber; n is the cylindrical mode number; $\mathbf{r}_i = (x_i, y_i)$ is the vector for the centre of the ith cylinder; θ_i is the angle between the ith cylinder and the receiver; $H_n^{(1)}$ is the Hankel function of the first kind and of order n; Z_n^i is a set of values determined by the boundary conditions; and A_n^i is a set of unknown coefficients. A graphical illustration of the above is given in Figure 2.6.

receiver
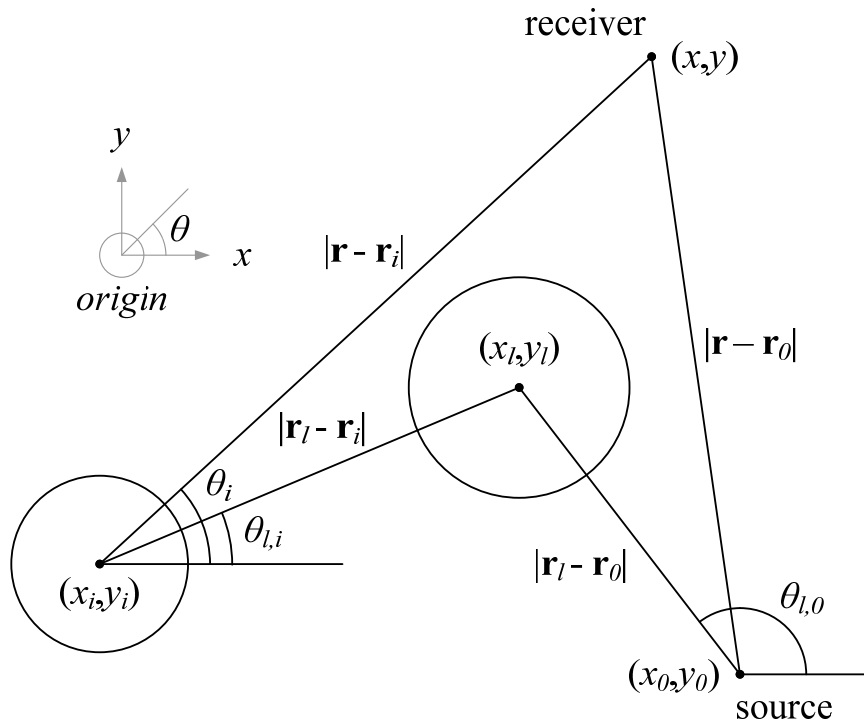
Figure 2.6: Geometry for the MS prediction model (after Umnova et al. [35]*)*

For the case of rigid cylinders, which shall be considered here, the matrix Z_n^i may be given as [35]:

$$Z_n^i = \frac{J_n{'}(ka_i)}{H_n^{(1)'}(ka_i)} \qquad 2.14$$

Where a_i is the radius of the ith cylinder; and J_n' and $H_n^{(1)''}$ are the derivatives of the Bessel function and Hankel function of the first kind, both of order n, respectively. Eq. 2.13 represents the summation of the scattered pressure for each cylindrical mode for each cylinder. In order to obtain a solution however, the set of unknown coefficients A_n^i must be determined. By setting the observation point to the centre of each cylinder, it can be shown that the following holds [35]:

$$-\frac{j}{4} H_m^{(1)}\left(k\left|\mathbf{r}_l - \mathbf{r}_0\right|\right) e^{-jm\theta_{l,0}} = A_m^l + \sum_{\substack{i=1 \\ i \neq l}}^{E} \sum_{n=-\infty}^{+\infty} A_n^i Z_n^i e^{j(n-m)\theta_{l,i}} H_{n-m}^{(1)}\left(k\left|\mathbf{r}_l - \mathbf{r}_i\right|\right) \qquad 2.15$$

Where $\mathbf{r}_l = (x_l, y_l)$ is the vector for the centre of the lth cylinder; m is the cylindrical mode number of the lth cylinder; $\theta_{l,0}$ is the angle between the source and the lth cylinder; and $\theta_{l,i}$ is

the angle between the ith and l^{th} cylinder. This forms a set of $E \times M$ simultaneous equations, where M is the number of modes used, and expresses the pressure at the centre of the lth cylinder as a function of the incident pressure and the contribution from each of the remaining cylinders. This is similar to the solution presented in Eqs. 2.9-2.10, only now solving for a finite (truncated) set of cylindrical modes as opposed to a finite number of elements. Once the set of coefficients, A_n^{i}, have been found, the pressure at an arbitrary point may be found through use of Eq. 2.13.

Provided that the number of modes used in a multiple scatter solution and the number of elements used in a BEM solution are sufficient, the solutions should be very similar. The multiple scatter solution however is preferred for the specific case of an array of cylinders, since the lack of required integration, and the generally smaller number of modes relative to elements needed results in faster computation times. Consequently new multiple scattering code was developed for the modelling of cylinder arrays.

2.3.4   Non-unique solutions

For the BEM routines above there is the potential for non-unique solutions; spurious resonances associated with the eigensolutions internal to the structure which have no physical meaning [36]. The can potentially be minimised through the use of techniques such as the Combined Helmholtz Integral Equation Formulation (CHIEF) method [37] which uses an overdetermined solution to force the pressure at defined internal points to be zero. No such method has been applied here, though the use of BEM has been verified both against the MS routine for cylinders and against measurements (see Sections 2.6.1-2.6.2). The problem here is only of concern for percolation structures, since arrays of slats have no enclosed spaces, and internal problems and the MS routine (used for all cylinder array models) have no non-unique solutions. The occurrence of non-unique solutions for percolation structures however was found to be rare, with false results being self-evident when they did occur due to a sharp rise/fall in scattered power. In addition where possible, enclosed spaces in percolation structures were avoided.

2.4.   Prediction: The Fourier approximation

The methods presented in Section 2.3 provide (asymptotically) exact solutions for the scattering behaviour of an array. Whilst these should produce reliable and trustworthy results, the solution may often be slow and computationally expensive, particularly for larger structures and for higher frequencies. There is a need therefore for a more simplistic approach, which aids physical understanding and provides very fast predictions. The models presented below are employed throughout; though in particular are used extensively for the slat array diffusers of Chapter 4 and the cylinder array structures considered in Chapter 6, incorporating the scattering from a flat plate and cylinder respectively.

2.4.1   Scattering from an array

This section considers the scattering from a given arrangement of infinitely small point scatterers; an approximation analogous to the systems often considered in antenna design, crystallography and general array theory [38-40]. This is a single scatter approximation which neglects the influence of shadowing due to neighbouring objects, and describes the scattering behaviour due to the array shape. At this point the boundary conditions are essentially ignored, and are assumed to be modelled by the scattering behaviour of an individual scattering element, considered in Section 2.4.2.

1D array of scatterers based on a periodic lattice

Section 1.3 introduced the periodic surface diffuser, examples of which were shown in Figure 1.2 and Figure 1.3, comprising a series of equal width strips each with individual reflection coefficient. Whilst the mechanisms used by some of these diffuser types may differ, there are some important similarities. Each may be thought of as spatially varying impedance surface, with the reflection coefficient assumed to be constant across each element (well/patch). Each element may then be represented as a point scatterer situated at its centre, with polar pattern determined by element type. Consider the arrangement shown in Figure 2.7, depicting a line of N point scattering elements spaced d_y apart, subject to an incident plane wave p_i of wavenumber k, arriving from angle θ_0.
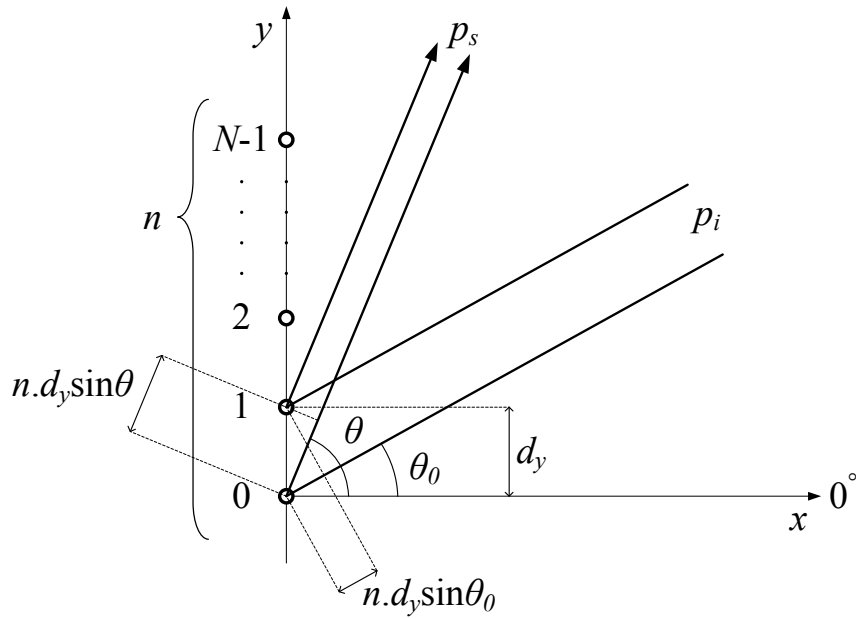
Figure 2.7: Far-field single scattered pressure p_s at receiver angle θ, from a 1×N periodically spaced line of point scatterers with unit spacing d_y in the y direction, subject to a plane wave p_i incident from angle θ_0

Far-field conditions are assumed meaning that, as was discussed in Section 2.2.3, the envelope of the scattered pressure distribution is no longer dependent on source and receiver distance. If all elements are assumed to have the same individual polar response for all angles of incidence and reflection, $e(\theta_0, \theta)$, with individual amplitude coefficients independent of angle, A_n, then for a given far field receiver angle θ, the following holds [38]:

$$p_s(\theta_0, \theta) = e(\theta_0, \theta) \sum_{n=0}^{N-1} A_n e^{jknd_y(\sin\theta + \sin\theta_0)}$$

2.16

Where p_s is the scattered pressure, and for simplicity only first order reflections are considered in this model. This follows from the well known theory in optics and crystallography that the diffraction pattern of a periodic structure is equal to the product of the diffraction pattern of the base element and that of the array [41]. For surface diffusers the scattering due to the element, $e(\theta_0, \theta)$, is determined by the response of a flat strip of width $d_e \equiv d_y$, which shall be introduced in Section 2.4.2. To avoid ambiguity the use of amplitude coefficients, A_n, has been introduced here, since the reflection coefficient is usually defined for plane surfaces and its use is therefore dependent on element type. The above model is employed throughout each of the design Chapters 4-6.

2D array of scatterers based on a periodic lattice

By extending the single layered concept, a multilayer structure based on a rectangular lattice may be envisaged. Such an arrangement is considered for arrays of slats in Chapter 4, though is used more extensively for periodic cylinder arrays in Chapter 6. Consider the arrangement shown in Figure 2.8, depicting an $M{\times}N$ rectangular grid of point scattering elements, with element spacing of d_x and d_y in the x and y directions respectively. If all elements are again assumed to have the same individual polar response for all angles of incidence and reflection, $e(\theta_0, \theta)$, then the following can be derived [38]:

$$p_s(\theta_0,\theta) = e(\theta_0,\theta)\sum_{m=0}^{M-1}\sum_{n=0}^{N-1} A_{m,n}e^{jk\left[md_x(\cos\theta+\cos\theta_0)+nd_y(\sin\theta+\sin\theta_0)\right]} \qquad 2.17$$

Where now the amplitude coefficients are defined as the $M{\times}N$ rectangular array, $A_{m,n}$; and again only first order reflections are considered. This structure now contains depth, and consequently there will be scope for shadowing of elements and increased multiple scattering / surface interactions. As a result this approximation will be most valid at low frequency when diffraction around individual elements is greater and for low fill factors when multiple scattering is weak.
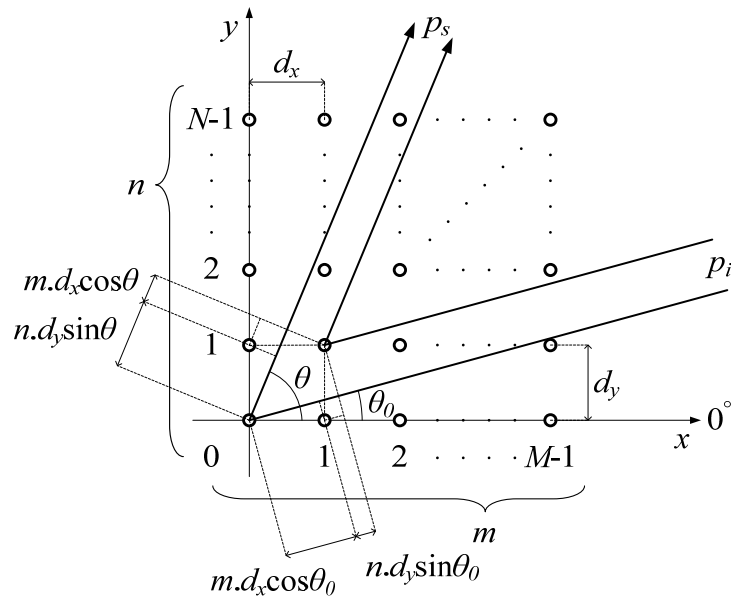
Figure 2.8: Far-field single scattered pressure p_s at receiver angle θ, from an $M{\times}N$ periodically spaced rectangular grid of point scatterers with unit spacing d_x and d_y in the x and y directions respectively, subject to a plane wave p_i incident from angle θ_0

2.4.2   Scattering from individual elements

In Section 2.4.1, it was shown that the scattering from an array of point scatterers could be combined with the scattering from an individual element $e(\theta_0, \theta)$, provided that the size, shape and orientation of each element type were the same. Two types of element will be used within the thesis: flat plates and cylinders, relevant for the structures presented in Chapters 4-5 and Chapter 6 respectively.

Scattering from a flat plate

The scattered pressure from an infinitely thin flat plate may be modelled exactly through use of Eqs. 2.11-2.12. For such a simple structure however an approximation may be used which results in reasonable accuracy [42]. For a large plate with uniform surface impedance, the pressure on the surface $p_t(\mathbf{r}_s)$ may be assumed to be:

$$p_t(\mathbf{r}_s) = \left[1 + R(\mathbf{r}_s)\right] p_i(\mathbf{r}_s, \mathbf{r}_0)$$

2.18

Where $R(\mathbf{r}_s)$ is the pressure reflection coefficient on the surface at $\mathbf{r}_s$. This is referred to as the Kirchoff boundary condition, and assumes that the Green's function and its derivative are unaltered upon reflection; valid when the surface is large relative to wavelength such that the edge diffraction is not significant. For the rigid case this implies that the surface pressure is simply double the incident pressure. By substituting Eq. 2.18 into Eq. 2.6, and assuming far-field conditions, it can be shown that for a flat plate of width d_e whose normal is parallel to the x axis the following approximation can be derived [3]:

$$p_s(\mathbf{r}) \approx -\frac{1}{8\pi\sqrt{rr_0}} e^{jk(r+r_0)} \int_{-d_e/2}^{+d_e/2} \left[1 + R(\mathbf{r}_s)\right] e^{jkx(\sin(\theta)+\sin(\theta_0))} \times$$

2.19

$$\left[\cos(\theta) + \cos(\theta_0)\frac{R(\mathbf{r}_s)-1}{R(\mathbf{r}_s)+1}\right] dx$$

Where p_s is the scattered pressure from the flat plate.

Assuming the reflection coefficient to be constant across the panel, this simplifies to:

$$p_s(\mathbf{r}) \approx -\frac{d_e}{8\pi\sqrt{rr_0}}\mathrm{sinc}\left(\frac{kd_e}{2}\left(\sin\theta + \sin\theta_0\right)\right)e^{jk(r+r_0)} \times$$

$$\left[R(\cos(\theta)+\cos(\theta_0))+(\cos(\theta)-\cos(\theta_0))\right]$$

2.20

Where $\mathrm{sinc}(x) = \sin(x)/x$; and the $(\cos(\theta)$-$\cos(\theta_0))$ term is often ignored [3], since this will only be significant for receiver angles away from the specular reflection where the influence of the sinc function tends to result in low values anyway. For the rigid case where $R = 1$, the equation again simplifies giving:

$$p_s(\mathbf{r}) \approx -\frac{\cos(\theta)}{4\pi\sqrt{rr_0}}d_e\,\mathrm{sinc}\left(\frac{kd_e}{2}\left(\sin\theta + \sin\theta_0\right)\right)e^{jk(r+r_0)}$$

2.21

The above is most accurate for higher frequencies when the wavelength is small relative to plate size, with the main source of error at low frequency being due to neglecting the pressures on the rear of the panel. At higher frequencies the approximation is limited by the inability to represent the finite sized edges of the panel (though this is also the case for the thin panel BEM of Section 2.3.2), and for angles close to grazing due to omitting the interactions across the surface [42].

Scattering from a cylinder

Section 2.3.3 gave the MS solution for an arbitrary arrangement of E cylinders. By combining Eq. 2.13-2.15 it can be shown that for a single cylinder centred on the origin, the scattered pressure $p_s(\mathbf{r})$ reduces to:

$$p_s(\mathbf{r}) = -\frac{j}{4}\sum_{n=-\infty}^{+\infty}Z_n H_n^{(1)}(kr_0)H_n^{(1)}(kr)e^{jn(\theta-\theta_0)}$$

2.22

This produces an analytically exact solution (excluding truncation of modes), and hence the Fourier approximation for an array of cylinders will combine both exact and approximate solutions. It can be shown that for far-field conditions using the asymptotic expansion of the

Hankel function [43], and through manipulation of modal symmetry [44] that the following approximation may be derived:

$$p_s(\mathbf{r}) = \frac{e^{jk(r_0+r)}}{2\pi k\sqrt{r_0 r}} \sum_{n=0}^{+\infty} \in_n (-1)^n Z_n \cos(n(\theta-\theta_0))$$

$$\in_n = \begin{cases} 1, & n = 0 \\ 2, & n \neq 0 \end{cases}$$

2.23

Where $\in_n$ is the Neumann symbol, and the above is in a similar form to that presented in the literature [30; 44].

2.5. Polar response measurements

In order to validate the models presented in Sections 2.3-2.4, in particular the accurate models upon which the design process throughout the remaining chapters will rely, it is necessary to carry out measurements for each of the structure types presented. As was stated in Section 2.2, AES document AES-4id-2001 [28] provides the most commonly used existing guidelines for the measurement of surface diffusers, upon which much of the measurement procedure outlined below will be based.

2.5.1 Measuring a 1D surface diffuser

The measurement setup for obtaining the polar response for a 1D planar surface diffuser was presented in Section 2.2.1. Due to the planar nature of the diffuser, the structure is assumed to be extruded in the dimension orthogonal to the plane. This makes a boundary plane technique possible, a method which allows measurements to be made on a solid floor (assumed to be acoustically rigid) which acts like an acoustic mirror [3]. This creates an image source equivalent, as shown in Figure 2.9, where the effective measurement is for a sample twice as high and with source and receiver located at the midpoint. The assumption is made that both source and receiver distances from the floor are small relative to wavelength.

To ensure free-field conditions the measurement must be carried out in either a semi-anechoic chamber or by utilising a boundary layer technique [28]. Due to restrictions in space it is usually necessary to use scale model measurements to allow far-field conditions, since the required characteristic distance is determined by the size of the diffuser as given by

Eqs. 2.3-2.5. The sample height must also be large relative to wavelength, ensuring that diffraction from the top of the diffuser is minimised.
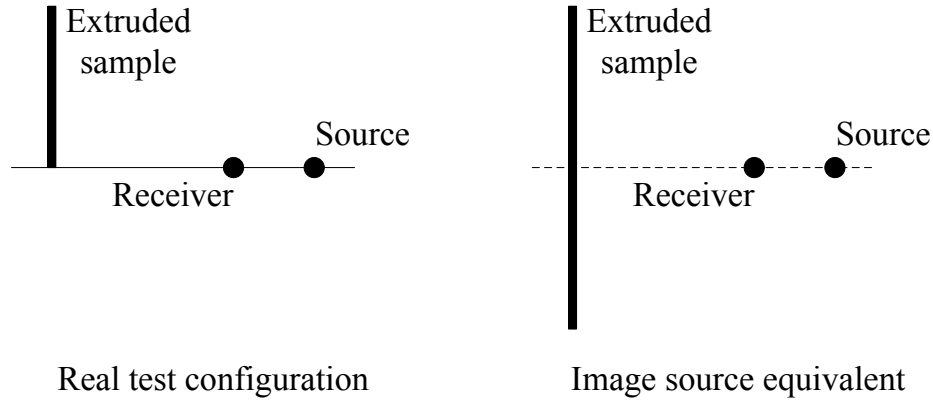
Figure 2.9: Boundary plane measurement and equivalent image source configuration (after Cox and D'Antonio [3])

A single source is used to provide the incident sound, whilst the arc of receivers comprises a series of microphones at radial positions separated by a (usually) equal angular step. By selecting an appropriate signal such as a Maximum Length Sequence (MLS) for the source [45], the pressure impulse responses are gained through synchronous acquisition of the response at each microphone. Once this is achieved, time gating is used to separate the incident and scattered sound. The pressure impulse response both with $h_1(t)$, and without $h_2(t)$, the sample present is measured, with the background measurement then being subtracted from the sample measurement. This helps to eliminate unwanted reflections common to both measurements such as reflections off neighbouring microphones. Finally each resultant response is deconvolved with the loudspeaker-microphone response, $h_3(t)$, for the respective receiver angle to remove the effects of the response of the transducers and measurement system. This is obtained by placing the source at the centre of the sample position facing the appropriate receiver such that the on-axis response of both microphone and loudspeaker are coincident with one another.

The process above may be expressed as:

$$h_4(t) = IFT\left[\frac{FT[(h_1(t) - h_2(t))]}{FT[h_3(t)]}\right]$$

2.24

Where $h_4(t)$ is the resultant deconvolved sample response. The subtraction and time windowing process is depicted pictorially in Figure 2.10.
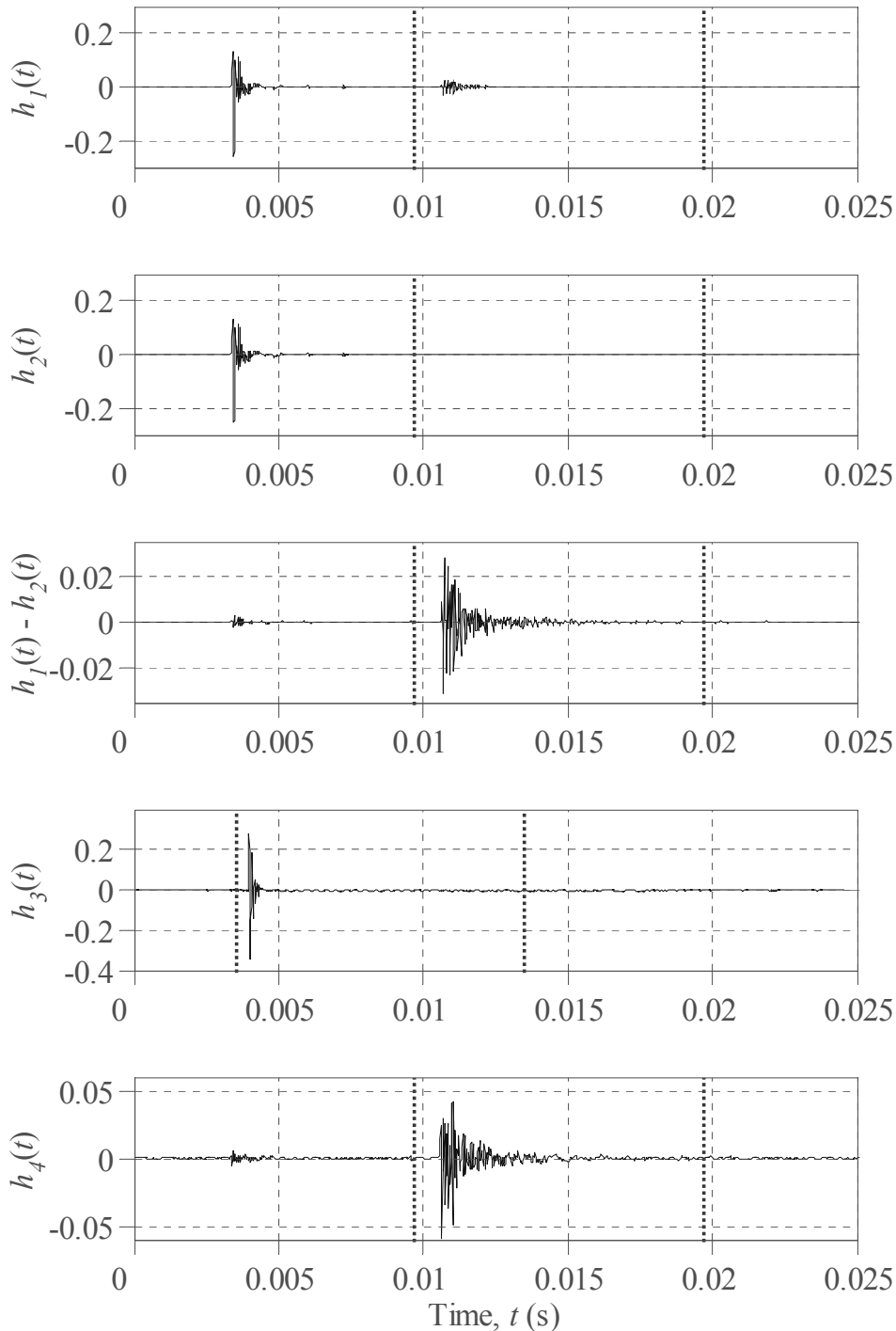
Figure 2.10: The subtraction method, including time windowing (■ ■ ■), for obtaining the scattered pressure; from top to bottom: sample, background, sample minus background, loudspeaker-microphone response, and deconvolved sample minus background measurements

2.5.2   A 1D and 2D volume diffuser measurement technique

The measurement procedure for a volume diffuser is in principal the same as the method outlined above, though with additional receiver angles as shown in Figure 2.2. The procedure adopted was broadly as follows.

Scattered pressure distributions were measured in a semi-anechoic chamber following the procedure outlined in Section 2.5.1. The lower cut-off frequency for the room, determined by the depth of the wall mounted foam, was approximately 250Hz. The samples were fixed into a central 600mm×600mm sample plate that slotted into a fake floor, comprising a series of plywood boards connected by tongue and groove edges. These were unvarnished, though were of a high quality finish, and were assumed to be acoustically rigid. This was replaced with a flat board of the same dimensions for background measurements. Receivers were placed in a circle of radius $r = 1.35$m from the centre of the array, with an angular step of 9° starting from $\theta = 0^{\circ}$. An MLS signal (of length $2^{13}-1 = 8191$ samples) was produced by a source located a distance of $r_0 = 2.5$m from the array centre. Figure 2.11 shows the measurement setup for an array of aluminium cylinders of 1m in height, arranged according to an optimised sequence introduced in Chapter 6 and shown later in Figure 2.27.

Due to the rectangular shape of the room the angle of incidence was restricted to $-30^{\circ} \leq \theta_0 \leq +30^{\circ}$, though by using source angles of $\theta_0 = \{-30^{\circ}, 0^{\circ}, +30^{\circ}\}$ and rotating the square sample board through steps of 90°, all angles of incidence in angular steps of 30° are effectively allowed, starting from $\theta_0 = 0^{\circ}$. All distances were restricted by the maximum dimensions of the room, which for the samples measured resulted in a characteristic distance, $r_c \approx 1.75$m. This meant that in order for approximate far-field conditions to be met, as given in Section 2.2.3, measurements were normally carried out at either 1:3 or 1:4 scale. For the intended frequency range (after scaling) of 400Hz-4kHz, this meant that for higher frequencies the far-field conditions as defined by Eqs. 2.3-2.4 were not possible, which for the samples used corresponded to cut-off frequencies (when scaled) of approximately 1.7kHz, 4.0kHz, and 1.0kHz for the 1:1, 1:3 and 1:4 scale models respectively. Using the criterion of no more than 20% of receivers in the specular zone however resulted in a maximum diffuser size, D_{max}, of approximately 410mm. Whilst for diffusers of this size the start of potential

near-field behaviour may be observed at higher frequencies, as the main purpose of the measurement was to validate the prediction models, this was deemed acceptable.
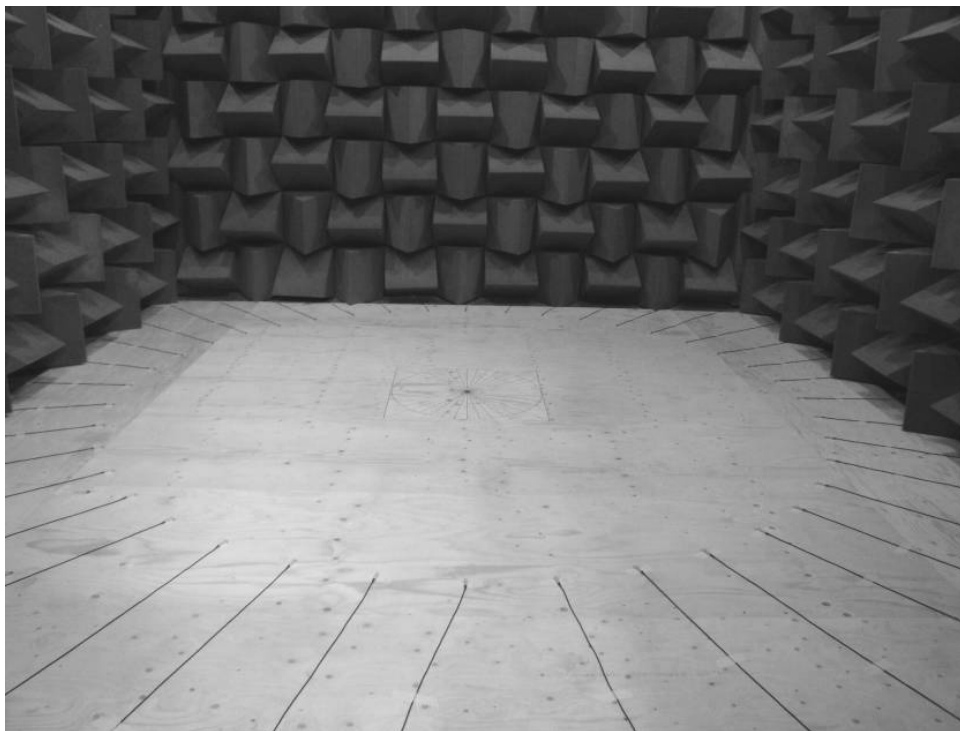
Figure 2.11: Semi-anechoic measurement setup both with (top) and without (bottom) a 2D planar volume diffuser as per Figure 2.27 constructed at 1:4 scale (source off bottom of shot)

The measurement equipment used was as follows:

- Source –Visaton 50mm diameter SC-4-ND-4Ω tweeter loudspeaker.

- Receivers – 40 custom-made Bridge 3/16" diameter piezoelectric microphones.

- Acquisition unit – 01dB NetdB PRO-121 and NetdB PRO-132 12 channel and 32 channel real time analysers respectively, in chain mode for synchronous acquisition of 40 channels at sampling frequency, f_s = 51.2kHz.

To allow comparison between real world measurements and the 2D prediction models used each scattered pressure result is converted to a normalised scattered pressure, $p_{s,norm}$, which unless otherwise stated shall be assumed in all scattered pressure plots throughout. This was achieved using the following method. Both measured and modelled results were divided by that of the incident pressure at a reference receiver, $p_{i,ref}$, taken from the background measurement. This eliminates the influence of source strength and the frequency dependent magnitude of the 2D model. The reference was taken to be the back receiver, that is $\theta = \theta_0 + 180^\circ$, which has the advantage that during measurements the source will always be on-axis to the rear receiver, ensuring that the high frequency directionality of the transducers is not an issue. In addition for the reference receiver used, scaling factors of $\sqrt{r_c / 2}$ and $r_c/2$ may then be applied to the 2D model and 3D measurement results respectively, where the characteristic distance r_c is defined by Eq. 2.3. This removes the effects of cylindrical and spherical spreading respectively to account for difference in behaviour due to distances used in the setup.

For convenience, throughout the rest of the chapter it is assumed that where sample and background measurements are referred to all measurements have been deconvolved with their appropriate loudspeaker-microphone response, as described in Section 2.5.1. For reference, the average loudspeaker-microphone response from the 40 microphones used during the measurements is shown in Figure 2.12. Ideally this response would be flat across the measurement bandwidth, though this is clearly not the case. It would be expected that frequencies below approximately 1.0-1.5kHz (unscaled) may suffer from a low signal-to-noise ratio, which is due primarily to the response of the tweeter.
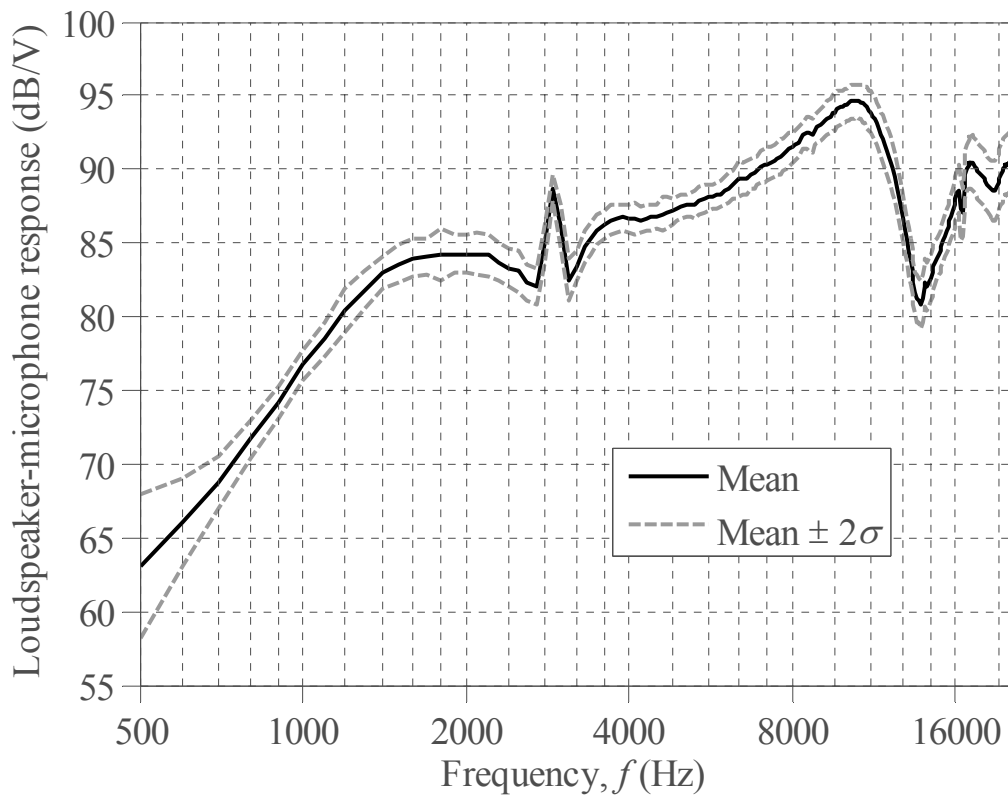
Figure 2.12: Average loudspeaker-microphone response used during the polar measurement for the 40 microphone setup shown in Figure 2.11

In addition to the low frequency limitations of the system, Figure 2.12 displays two further points at which there are potential signal-to-noise ratio / discontinuity problems. These frequency regions are centred on approximately:

▪ 3.0kHz (unscaled) – corresponds to the point at which approximately half a wavelength is equal to the source diameter. This may have been due to a zeroth order structural resonance.

▪ 13.5kHz (unscaled) – equates to the point at which sound radiating from the back and diffracting around the tweeter is out of phase with the sound propagating from the front. This was largely unavoidable since sealing the back of the tweeter would lead to a very low level output, whilst the use of any baffle / sealed enclosure on the tweeter may introduce unwanted reflections into the space.

2.5.3   Separation of the scattered field: potential errors

For surface diffusers the procedure is to separate the direct and scattered sound by considering time of arrival, as depicted by Figure 2.10, eliminating the incident sound entirely. Behind a volume diffuser however, progressive merging of the incident and scattered field in the impulse response makes this impossible.

Subtraction of the background impulse response is ordinarily performed in order to minimise the influence of any room interference [28]. This process should also in theory remove the incident sound, which is common to both measurements, leaving the scattered response from the diffusing structure only. In practice however, errors are introduced due to variations in response caused by a number of contributing factors. Assuming non-linear errors such as transducer distortion are negligible, any change in response may be described by a combination of the following:

1. A shift in arrival time – due for example to a change in the effective sound speed causing a difference in time of flight, caused predominantly by small changes in ambient temperature [46].

2. A change in signal amplitude – due to air movement, particularly when opening the door and moving sample diffusers in and out of the space, creating an inhomogeneous medium where local ambient conditions are a function of location. This amplitude change is assumed to be frequency invariant.

Both of the above effects will mean that complete cancellation is not achieved, and consequently substantial artefacts of the incident component can remain.

Consider the case where the measurement is performed both with and without a sample present, resulting in impulse responses $h_1(t)$ and $h_2(t)$ respectively. Considering the incident component alone, each may be represented by a Dirac delta function whose delay is determined by their respective times of flight τ_1 and τ_2, with the latter having an amplitude scaling factor, A, relative to the first measurement. Their difference is given as:

$$error(t) = h_2(t) - h_1(t) = \frac{A\delta(t-\tau_2)}{4\pi|\mathbf{r}-\mathbf{r}_0|} - \frac{\delta(t-\tau_1)}{4\pi|\mathbf{r}-\mathbf{r}_0|}$$

$$= \frac{1}{4\pi|\mathbf{r}-\mathbf{r}_0|}\left[\left(A\delta\left(t-\frac{r}{c_2}\right) - \delta\left(t-\frac{r}{c_2}\right)\right)\right]$$

2.25

Where c_1 and c_2 are the speeds of sound for their respective measurements; and δ denotes the Dirac delta function. Under ideal conditions the two impulse responses will be identical, and so subtracting one from the other would lead to complete cancellation. If the relative amplitude or speed of sound for each measurement varies however, then the measurements will be different and their difference will not be zero. Eq. 2.25 therefore, gives the theoretical error, $error(t)$, introduced due to the incomplete cancellation in the time domain. Since this is a superposition of two Dirac delta functions, the second of which is $180°$ out of phase, in the frequency domain this produces a comb filter effect [16] and may be represented as:

$$|Error(f)| = \frac{1}{4\pi|\mathbf{r}-\mathbf{r}_0|}\left|FT\left\{\left(A\delta\left(t-\frac{|\mathbf{r}-\mathbf{r}_0|}{c_2}\right) - \delta\left(t-\frac{|\mathbf{r}-\mathbf{r}_0|}{c_1}\right)\right)\right\}\right|$$

$$= \frac{1}{4\pi|\mathbf{r}-\mathbf{r}_0|}\sqrt{1+A^2-2A\cos((k_2-k_1)|\mathbf{r}-\mathbf{r}_0|)}$$

2.26

$$|Error_{ref}(f)| = 4\pi r_{ref}|Error(f)| = \frac{r_{ref}}{|\mathbf{r}-\mathbf{r}_0|}\left|\sqrt{1+A^2-2A\cos((k_2-k_1)|\mathbf{r}-\mathbf{r}_0|)}\right|$$

2.27

$$|Error_{ref}(f)| \approx \frac{r_{ref}}{|\mathbf{r}-\mathbf{r}_0|}\left|\sqrt{(A-1)^2+A(k_2-k_1)^2|\mathbf{r}-\mathbf{r}_0|^2}\right|; \ (k_2-k_1)|\mathbf{r}-\mathbf{r}_0| < 1$$

2.28

Where $Error(f)$ is the error in the frequency domain; $Error_{ref}(f)$ is the error in the frequency domain relative to the incident field at the reference receiver; r_{ref} is the distance from the source to the reference receiver; and k_1 and k_2 are the wavenumbers ($k = 2\pi f/c$) for their

respective measurements. Eqs. 2.25-2.28 represent the theoretical potential error, with the actual error being dependent on the phase relative to the scattered component. Eq. 2.28 is derived using the small angle approximation, and is valid when the change in wavenumber is small. These formulae have been expressed in terms of a change in wavenumber, though may easily be given in terms of a generic delay, due for example to a change in receiver distance or the response of the measurement system.

The error can broadly be divided into three separate regions:

Low frequency – The error will approximate the case where no shift in arrival time occurs, and a change in amplitude between measurements will dominate. A further approximation to Eq. 2.28 may then be expressed as:

$$\left| Error_0(f) \right| \approx \frac{r_{ref}}{\left| \mathbf{r} - \mathbf{r}_0 \right|} \left| A - 1 \right| \; ; \quad \left(k_2 - k_1 \right) \left| \mathbf{r} - \mathbf{r}_0 \right| << 1 \qquad\qquad 2.29$$

Figure 2.13 shows the effect of a change in amplitude for a fixed sound speed shift of 0.2ms^{-1}. As A is simply a scaling factor, the effect is to increase the noise floor, and therefore the minimum error at all frequencies.

Mid Frequency – Assuming the change in amplitude to be small, Eq. 2.28 simplifies to give:

$$\left| Error_{ref}(f) \right| \approx \left| \sqrt{A} \right| \left(k_2 - k_1 \right) r_{ref} \; ; \quad \left(k_2 - k_1 \right) \left| \mathbf{r} - \mathbf{r}_0 \right| < 1, \; A \approx 1 \qquad\qquad 2.30$$

Figure 2.13 and Figure 2.14 show the approximation of Eq. 2.30, following the initial slope of the comb-filter effect which becomes apparent at high frequency. The result is predominantly a linear function of frequency with an increase of +6dB/octave, and is independent of distance from the source.
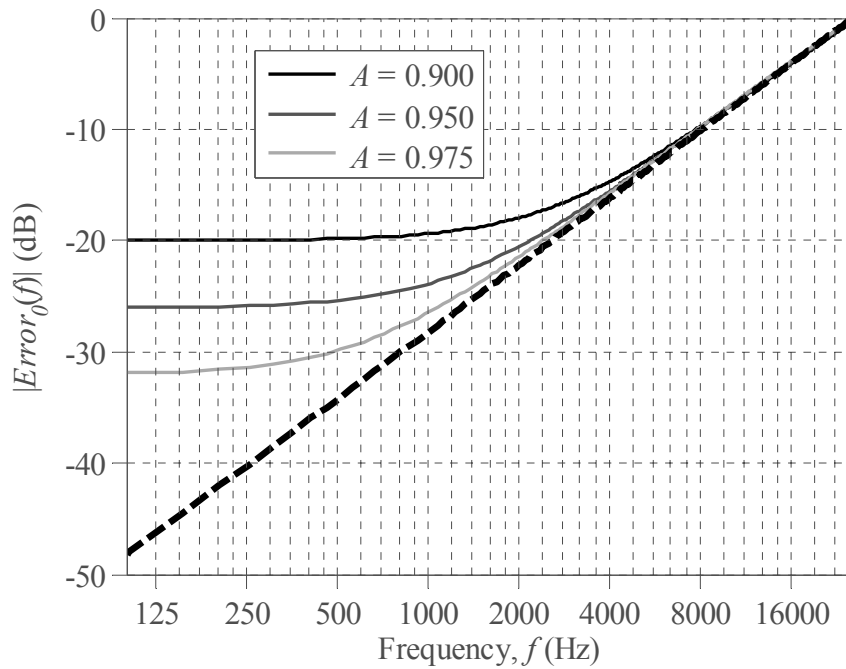
Figure 2.13: Potential error in cancellation of an incident pulse due to a change in amplitude with fixed sound speed change Δc = 0.2ms⁻¹ – original sound speed, c = 344ms⁻¹, |r - r₀| = r_ref = 3.85m (back receiver) – exact solution (solid lines); approximate solution as per Eq. 2.30 (dotted black line)
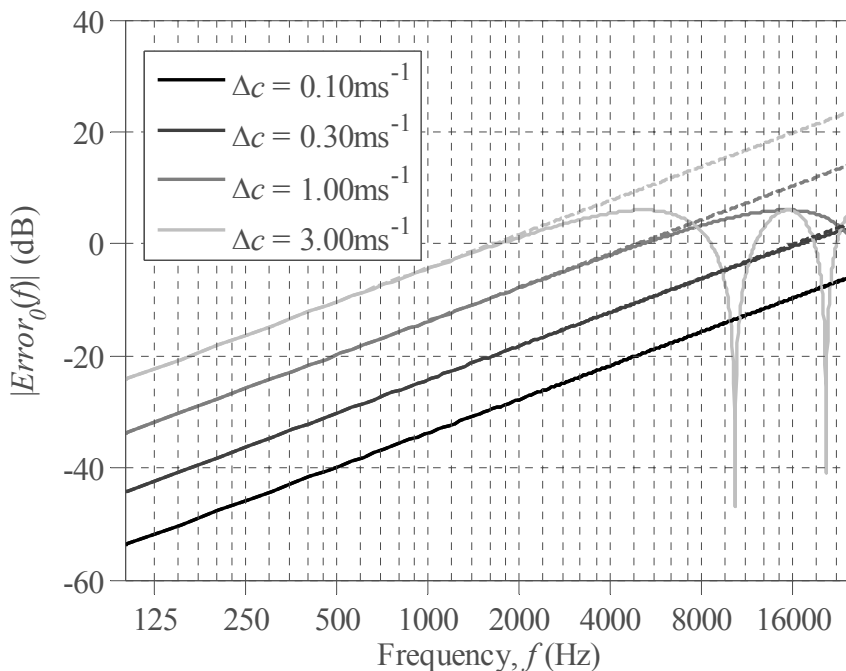
Figure 2.14: Potential error in cancellation of an incident pulse due to a change in sound speed – original sound speed, c = 344ms⁻¹, |r – r₀| = r_ref = 3.85m (back receiver) – exact solution (solid lines); approximate solution as per Eq. 2.30 (dotted lines)

High Frequency – Eq. 2.28 is no longer valid, and the comb-filtering effect becomes apparent, with periodicity determined by shift in sound speed and maxima and minima determined by:

$$\left|Error_{ref}(f)\right| = \begin{cases} \dfrac{r_{ref}}{\left|\mathbf{r} - \mathbf{r}_0\right|}\left|A+1\right|, & \text{maxima} \\[2em] \dfrac{r_{ref}}{\left|\mathbf{r} - \mathbf{r}_0\right|}\left|A-1\right|, & \text{minima} \end{cases} \qquad 2.31$$

This essentially forms a comb-filter with a raised noise floor. Figure 2.14 shows how the error changes with an increasing change in sound speed, and with no change in amplitude.

Based on the assumption that the air behaves as an ideal gas [29], which for small temperature shifts should provide a reasonable approximation, the sound speed changes of 0.1, 0.3, 1.0 and 3.0ms^{-1} from Figure 2.14 equate to an approximate 0.17, 0.50, 1.65 and $4.95°\text{C}$ change in temperature respectively. Laboratory temperature records indicate that temperature shifts on the order of $0.5°\text{C}$ were observed during the measurements. For most realistic changes to the speed of sound, Eq. 2.30 therefore provides a close approximation to the full solution at the upper limits of the measurement frequency range, and only the initial slope of the comb-filtering is observed.

Due to the use of scale modelling, the frequency range used for the measurements is increased, and therefore these effects will be more pronounced. For example at 8kHz (2kHz at 1:4 scale) the error in Figure 2.14 is given as -6dB relative to the reference receiver for a temperature shift of $0.5°\text{C}$. The scattered field may be significantly weaker than this, and the potential error would likely be significant for the majority of the measurement bandwidth. In general the severity is dependent on a number of factors, becoming worse with larger changes in sound speed; increasing frequency; and when scattering is comparatively weak. A technique is therefore required to reduce these effects.

2.5.4 Separation of the scattered field: an oversampling method

The method presented below forms a new technique using oversampling to allow accurate measurement in the forward-scattered region. A similar method has since been independently

developed by Robinson and Xiang [47] and this is also given, along with a short comparison of the two techniques.

The Method developed

In the time domain, the error in removing the incident sound is due to changes in time of flight and relative amplitude between measurements with and without the sample present. If the difference in arrival times, $\Delta t = \tau_2 - \tau_1$, and amplitude scaling factor, A, between these two measurements was known then it would be possible to shift and scale one measurement by the appropriate amount of time and magnitude relative to the other so that the two incident components align. This would then allow the incident field to be completely removed.

The above assumes we have an analogue signal; however the measured signal is digital and hence discrete, and is sampled with a resolution dependent on the sampling interval. To determine the shift required in samples there are two potential options:

1. A simplistic approach assumes that the time of arrival of an incident pulse may be accurately described by the sample number of its maximum absolute value. The difference between sample numbers from two measurements then represents the drift in arrival time (expressed in samples) relative to one another.

2. A more robust approach is to cross-correlate the two signals to determine where they are most 'similar'. The location of the peak then gives the change in arrival time (expressed in samples). To ensure (where possible) that the scattered component in a diffuser measurement has minimal effect on the outcome of the cross-correlation, the signal is only evaluated over a small region (approximately 0.2-0.5ms) either side of an initially estimated arrival time obtained as per method 1.

Any shift would be limited to multiples of the sampling interval – the reciprocal of the sampling frequency, $1/f_s$ – giving in this case approximately 20μs time steps. This is a relatively large step, equivalent to that caused by a temperature change on the order of 1°C based on the same assumptions as Figure 2.14. For smaller variations therefore, it is necessary to shift by fractions of a sample. To achieve this both diffuser and background measurements are oversampled in order to give a finer resolution in time of flight. This oversampling factor is ideally as large as possible, though is limited by available computational speed and

memory. For all measurements shown here an oversampling factor of 500 has been used. One of the measurements (typically the diffuser measurement) is then shifted by a number of samples determined using the cross-correlation method above and scaled to match their peak values, before both measurements are down-sampled back to their original sample rate. The final impulse response is then obtained through use of Eq. 2.24.

This method shall be referred to as the cross-correlation method, an example of which is shown in Figure 2.15, where a comparison of the results both with and without oversampling and scaling is shown for a receiver towards the rear of the diffuser. Note, all measurements have been deconvolved with the appropriate loudspeaker-microphone response. The shift applied in the cross-correlation method is minimal, being on the order of approximately 4μs or one fifth of a sample, with the time domain response in Figure 2.15 (top) appearing very similar. Regardless, there is a marked effect seen in the scattered response (bottom), with a significant reduction in pressure around the perceived time of arrival of the incident response. It is also clear that the sample and background measurements are extremely alike, that is the scattering is weak relative to the incident component, and hence the residual incident pressure in the scattered response without oversampling is significant. The method appears to be successful, though this is somewhat hard to quantify in the time domain.

Figure 2.16 shows the same measurement as Figure 2.15, though in the frequency domain. The effect of applying a time shift on the sound pressure level of the sample measurement (top) is simply to change the phase, and hence the only difference observed is the small change in magnitude due to scaling. The change in the scattered pressure response (bottom) however is considerable, resulting in an average deviation from the predicted response in the mid-to-high frequency range (above 2kHz) of 1.9dB for the cross-correlation method compared to an average of 7.3dB for the untreated case. The largest single frequency deviation is at high frequency, where a maximum difference of 10.3dB and 23.9dB occurs for the cross-correlation method and original case respectively. This is due to the increasingly sensitive nature of the scattered pressure with frequency to a change in time of flight, as predicted by Eq. 2.30, though also to factors such as transducer and sample positioning as the polar pattern varies much more rapidly with angle.
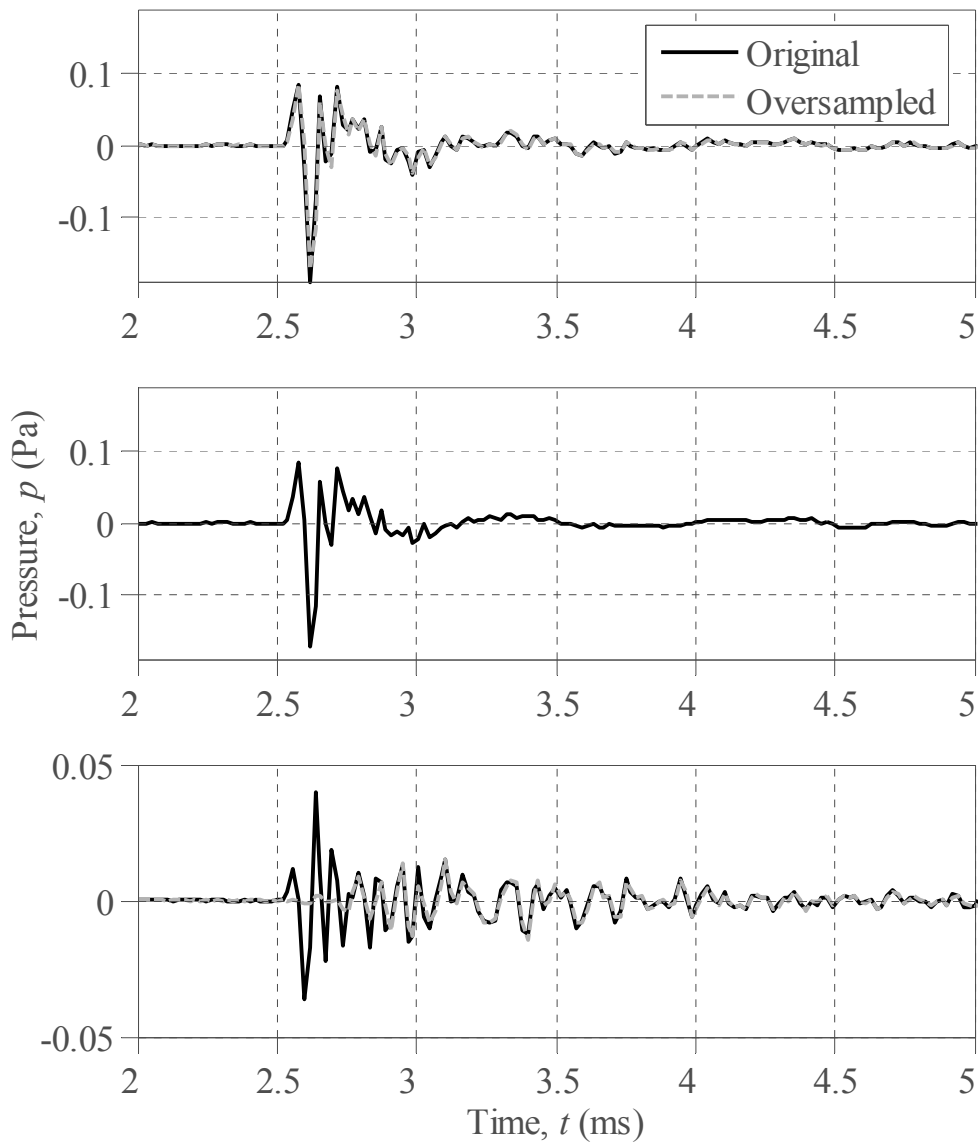
Figure 2.15: Time domain measurement of the cylinder array of Figure 2.11 using the subtraction method with and without the cross-correlation oversampling method applied; sample (top), background (centre) and their difference (bottom); $\theta_0 = -90°$, $\theta = \theta_0 + 144°$
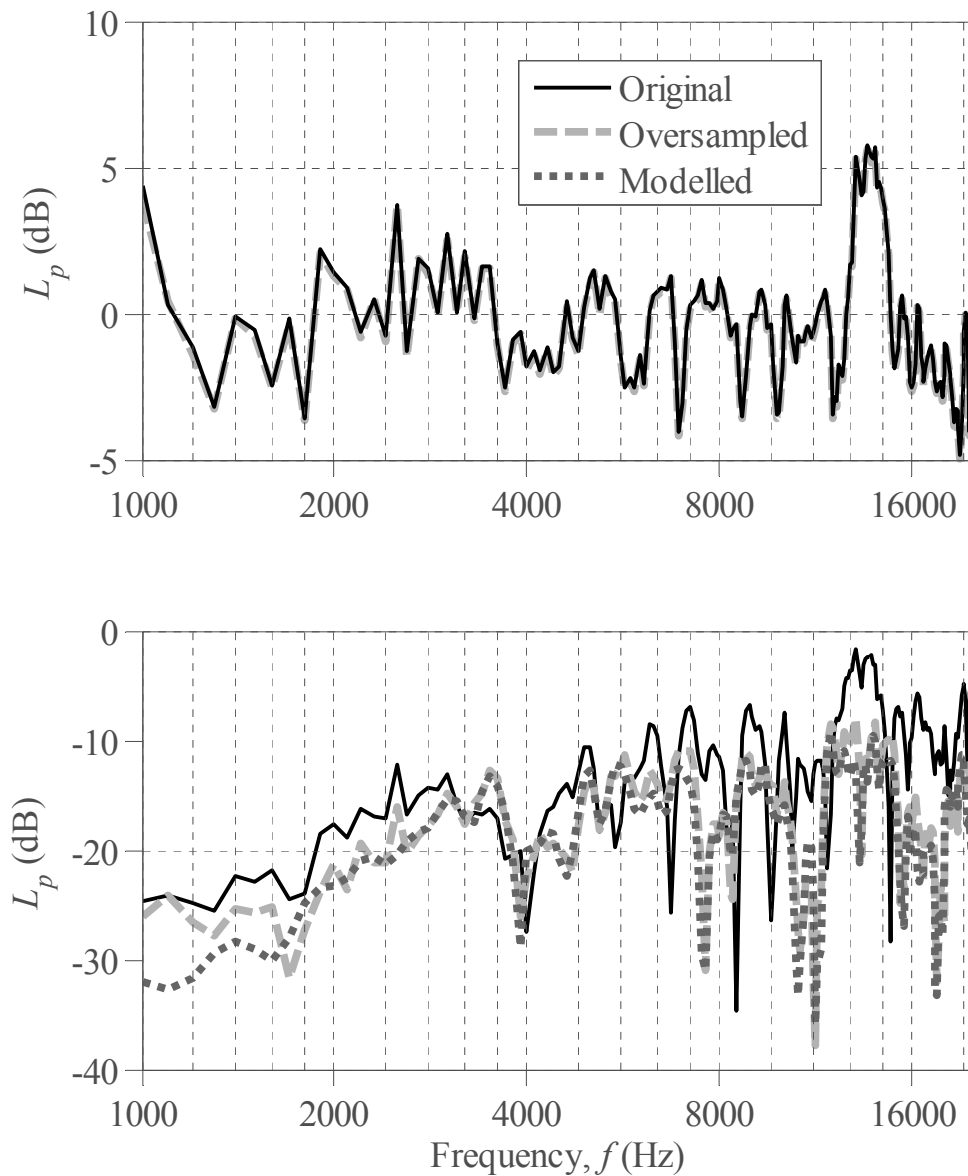
Figure 2.16: Frequency domain measurement for the cylinder array as per Figure 2.15 using the subtraction method with and without the cross-correlation oversampling method applied; sample (top), and sample minus background (bottom)

Figure 2.17 shows the difference (as pressures) between the original and cross-correlation method results from Figure 2.16. Assuming the cross-correlation method to provide accurate results, this should give the error in the original measurement due to any change in scaling or time of flight. This therefore can be compared to the predicted maximum error given by Eq. 2.30, where the estimated delay time ($\Delta t \approx 4\mu s$) corresponds to an approximate speed of sound shift of $0.13ms^{-1}$. Close agreement is observed, excluding two small deviations at

2.5kHz and 13.6kHz where the difference is larger than expected by approximately 3.4dB and 4.0dB respectively. These are potentially due to the loudspeaker-microphone response, as discussed in Section 2.5.2 and illustrated by Figure 2.12, where anomalies are observed around both of these frequencies.
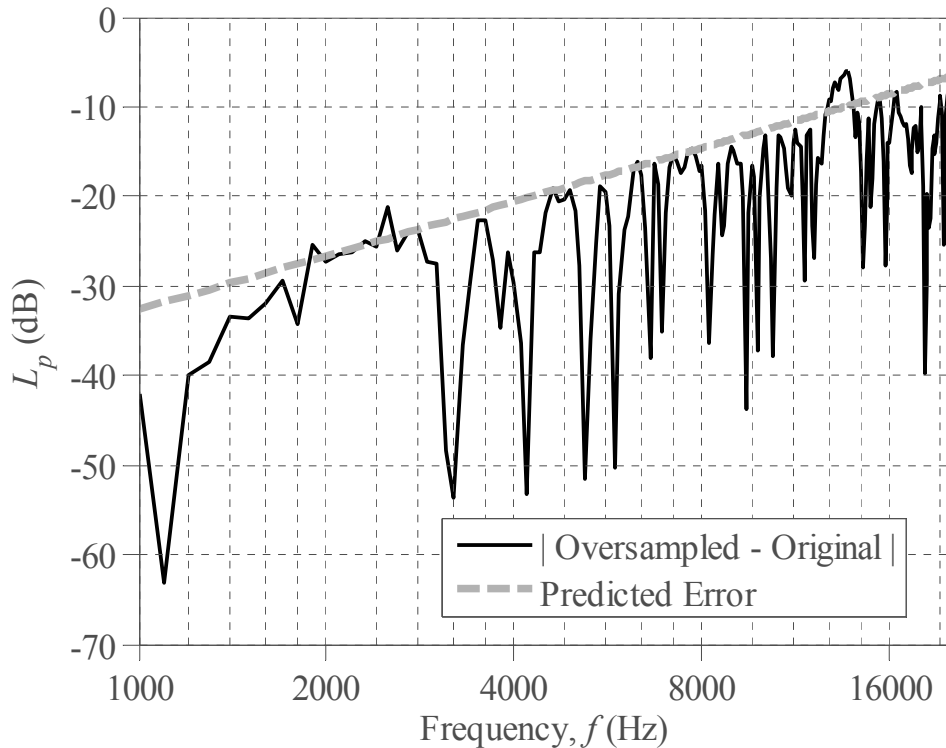
Figure 2.17: Difference in scattered pressure results using the subtraction method with and without the cross-correlation oversampling method applied; measurement as per Figure 2.16

Note that the frequency scale of Figure 2.16 and Figure 2.17 refer to the unscaled frequency; the actual frequency measured by the system. The results show good agreement here across the majority of the frequency range though at low frequency, below approximately 2kHz, there is a tendency to overestimate the scattered pressure. This was observed across all measurements, and is due mainly to the frequency response of the loudspeaker, resulting in a low signal-to-noise ratio. When using scaled frequencies however this is less of an issue.

Robinson and Xiang method

A similar method to the above has since been adopted by Robinson and Xiang [47], which proposed a routine to maximise a reduction factor, $R(\Delta t)$; the sum of the energy in the

background measurement relative to the sum of the energy from the subtraction method, given as:

$$R(\Delta t) = 10 \log_{10} \left(\frac{\sum_{t=\tau_2-d\tau}^{\tau_2+d\tau} (h_2(t))^2}{\sum_{t=\tau_2-d\tau}^{\tau_2+d\tau} \left(\frac{h_1'(t+\Delta t)}{A} - h_2(t) \right)^2} \right)$$
2.32

Where $h_1'(t+\Delta t)$ is the oversampled, shifted and downsampled version of the original measurement, $h_1(t)$; $d\tau$ is an appropriate time shift, suggested as $d\tau = 0.5$ms; and the ratio is evaluated over the region, $\tau_2-d\tau \leq t \leq \tau_2+d\tau$. This then essentially forms a signal-to-noise ratio. The method involves the use of a variety of oversampling factors, where for each the reduction factor is calculated for a shift of several samples either side of the shift indicated by the cross-correlation oversampling method, and with the inverse of the appropriate scaling factor applied. The final oversampling factor, sample shift and scaling are decided by the values that provided the largest reduction.

Figure 2.18 shows an estimate of the reduction factor for the cylinder array shown in Figure 2.11 for the $\theta = \theta_0 + 144°$ receiver for a number of angles of incidence, each having the same background response. The oversampling factor was set to 500, as opposed to selecting a range of smaller oversampling factors a suggested by Robinson and Xiang. In each case the sample shift obtained via the cross-correlation and Robinson and Xiang methods were virtually the same, with a maximum difference in reduction factor between the two of 0.004dB.
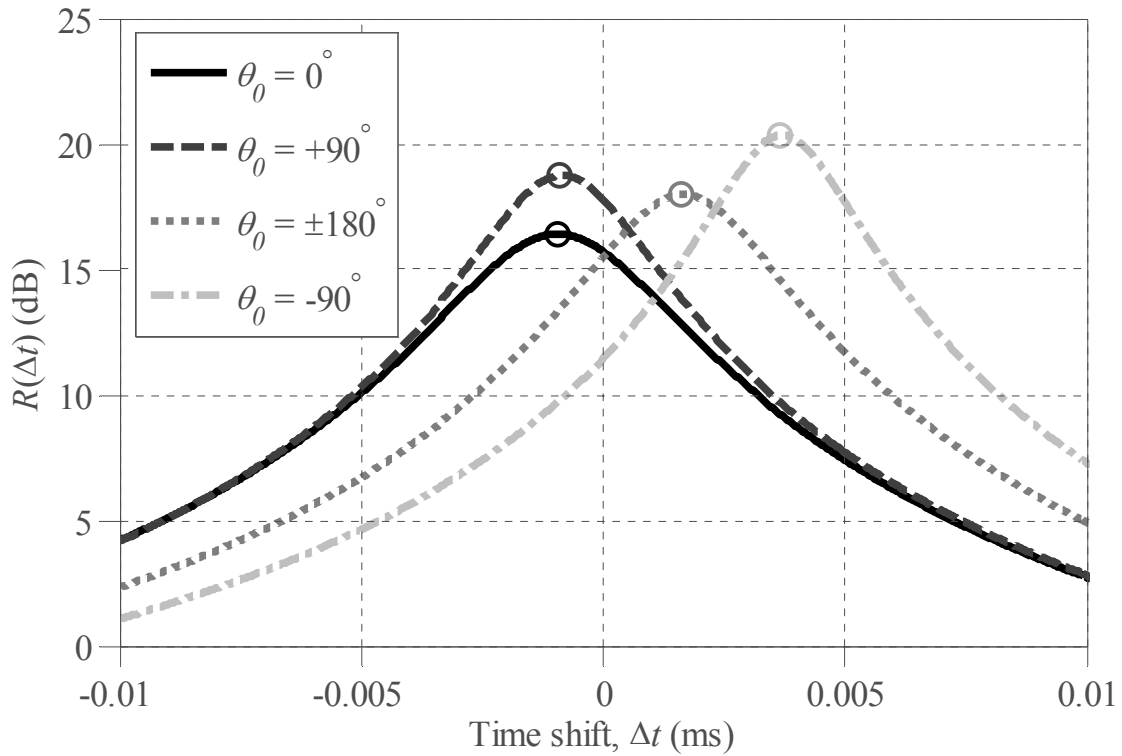
Figure 2.18: Reduction factor, R(Δt), for the cylinder array from Figure 2.11 measured for a number of angles of incidence; θ = θ₀+144°; cross-correlation values shown for reference (circles)

2.5.5   Separation of the scattered field: behind the diffuser

So far the removal of the incident field has been considered for angles close to the rear of the diffuser. This is equivalent to the problem posed by Robinson and Xiang whereby the specular reflection from surface diffusers was considered for angles of incidence close to grazing. For volume diffusers however it is necessary to consider receivers directly behind the structure, where the line-of-sight between source and receiver may be blocked. Here the time of arrival will be virtually equal, and the scattered field will form interfering rather than reflected waves [30] describing transmission and diffraction rather than progressive scattered waves. Consequently the scattered field here is generally large, and the total pressure measured with the sample present and the incident pressure obtained from the background measurement will lack similarity. As a result the time of flight cannot readily be determined, and both the cross-correlation technique and the Robinson and Xiang method break down. Furthermore, use of the Robinson and Xiang method would result in seeking maximum

cancellation in a region that includes the scattered field, and may even provide results worse than if no shift were applied at all.

To overcome this, the following was proposed. The remaining receivers where the incident pressure is easier to locate are used as a reference. By estimating the delay at each of these receivers, and using the appropriate distances from the source to each, an effective average sample drift per metre may be calculated. This is then used to determine the required shift for the receivers towards the back of the diffuser taking into account their distance from the source. The average scaling factor is found from a simple average with no correction for distance, and the appropriate time shifts and scaling are performed.

Figure 2.19 shows the estimated scaling factor and time drift per metre between sample and background measurements for the cylinder array of Figure 2.11, for a source angle of $\theta_0 = -90°$. The predicted values within the approximate region $\theta_0+150° \leq \theta \leq \theta_0+150°$ are similar, though not insignificant variation is observed. For the area towards the rear of the diffuser, as expected the estimation routine breaks down completely.

Applying a straightforward average time shift per metre should provide improvement, though it appears that a change in sound speed is not solely responsible for the observed delay. The most likely additional factor is slight movements in the boards that make up the fake floor shown in Figure 2.11 when placing and removing the sample. Since the method relies on the calculated distances from source to receivers (dependent on transducer placement) being accurate, and more crucially consistent between measurements, any shift in position would cause a shift in arrival time. The time shifts observed in Figure 2.19 for example correspond to a transducer movement in the region of 1mm, which could easily have occurred. A second possibility could be temperature gradients within the room, leading to different effective sound speeds observed at each receiver. Both of the above however should display one thing in common: that any shift in delay time at a given receiver should be similar to those surrounding it. An alternative therefore is to approximate the delay by a polynomial line of best fit, as shown on Figure 2.19. For similar reasons the same method can be applied to the scaling factor.
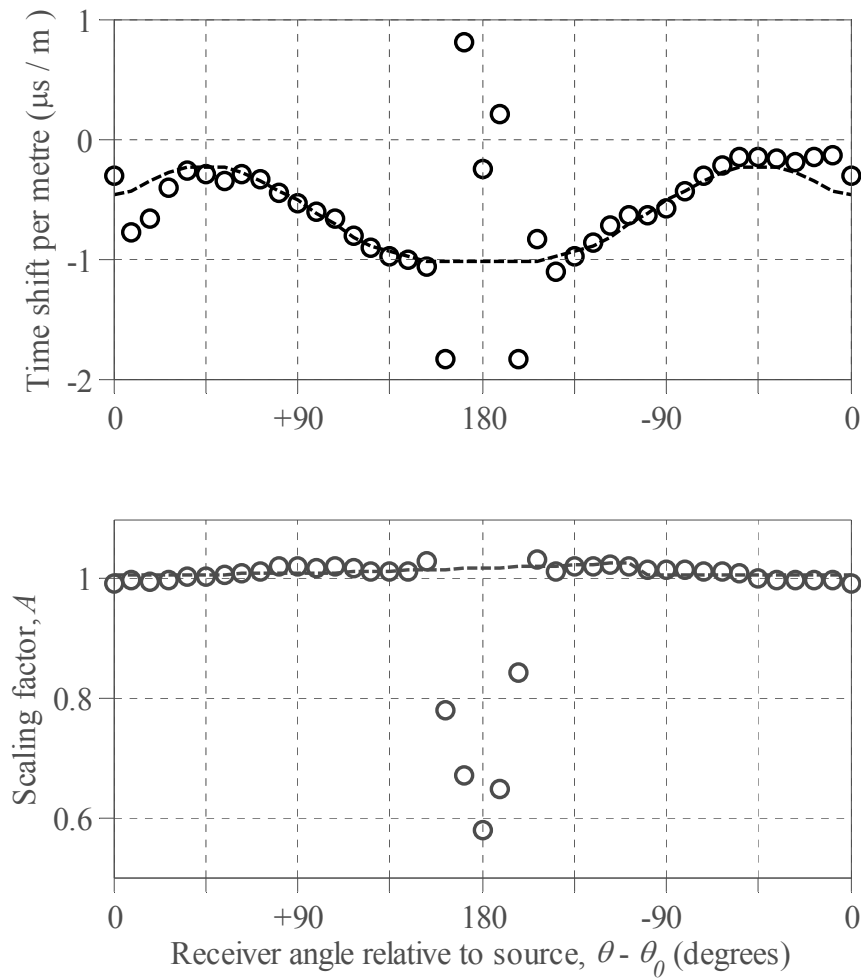
*Figure 2.19: Time shift per metre (top) and scaling factor (bottom), both estimated (**o**) and polynomial fit (▬ ▬) for the measurement of the cylinder array of Figure 2.11; $\theta_0 = -90°$*

Figure 2.20 shows the scattered pressure polar patterns at $f = 750\text{Hz}$ and $f = 3850\text{Hz}$, both with and without the amplitude scaling and time shift obtained from Figure 2.19 applied. It can be seen that for receivers close to the rear of the diffuser the change due to oversampling is small though noticeable, with average variations from the modelled results in the half-plane behind the diffuser ($\theta_0 + 90° < \theta < \theta_0 - 90°$) improving from 3.4dB to 1.4dB and from 5.6dB to 1.7dB for the $f = 750\text{Hz}$ and $f = 3850\text{Hz}$ case respectively. For the single receiver directly behind the diffuser these variations improve from 1.0dB to 0.0dB and 2.3dB to 0.2dB for the low and high frequency example respectively. Fortunately since scattering in this region tends to be quite large relative to the incident component, the errors introduced at the back receiver are less apparent.
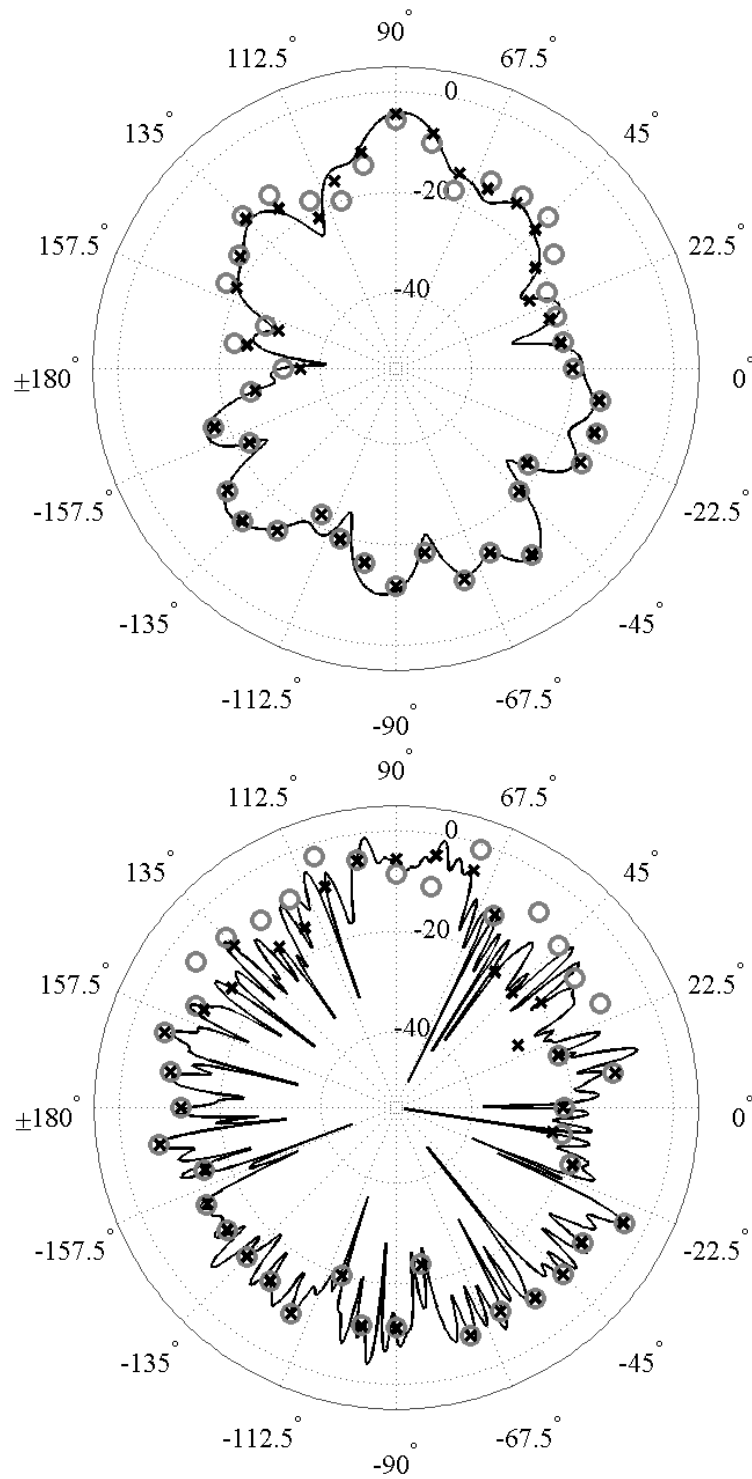
Figure 2.20: Modelled (━) and measured scattered pressure polar response for the cylinder array of Figure 2.11 using the subtraction method with (✖) and without (◉) the scaling and sample shifts obtained from Figure 2.19 applied; θ = θ₀+180°, θ₀ = -90°; f = 750Hz (top), f = 3850Hz (bottom)

2.6.   Verification of results

A comparison of measurement results with the appropriate model is offered below for each of the diffuser structure types presented throughout the thesis. All measurement results are obtained using the method described in Section 2.5, and are compared to the accurate model solutions given in Section 2.3. Approximate prediction methods are not considered here, since the intention is simply to determine whether or not the accurate models can be used throughout the remainder of the text to quantify behaviour without need for further experimental verification.

2.6.1   An array of slats

Arrays of slats shall be considered in Chapter 4, and comprise a series of thin, rigid, parallel strips. This therefore makes the thin panel BEM of Section 2.3.2 suitable for modelled predictions. For comparison with an existing equivalent surface diffuser considered in Section 4.2.1 the simple single layer array shown in Figure 2.21 was tested. Due to the partly absorbing nature of the surface diffuser, a 1:1 scale measurement was necessary.

The sample shown in Figure 2.21 (right) was constructed from 12mm thick high-density fibreboard (with smooth finishing process applied to both sides) of 600mm in height. Figure 2.22 shows the scattered pressure polar response for the $\theta_0 = 0^\circ$ case for a number of frequencies, including both thin panel BEM and the standard BEM prediction for reference.

At low frequency (400Hz-2.0kHz) both thin panel BEM and standard BEM predictions are very similar, since the depth of the structure is small relative to wavelength. The predicted energy scattered into the grazing angles ($\theta = \pm 90^\circ$ in Figure 2.22) is small and these shall be addressed separately below. For non-grazing angle receivers however, the average difference between modelled and measured results over this frequency range is 3.6dB for both prediction routines. The discrepancy here, particularly below approximately 1kHz, is largely due to the low signal-to-noise ratio caused by the frequency response of the loudspeaker, as described in Section 2.5.2 and illustrated in Figure 2.12. This is only really an issue for this particular sample due to the 1:1 scale, and hence the use of an unscaled frequency range.

In the mid-to-high frequency range (2.0-8.0kHz) the agreement generally improves (again excluding the grazing angles); with an average deviation from measurements of 2.6dB and

1.9dB for the thin panel BEM and standard BEM respectively. Here as wavelength becomes comparable to the finite depth of the structure, the standard BEM more closely matches the measured results since it is able to model scattering from the finite sized edges, though the difference is small.
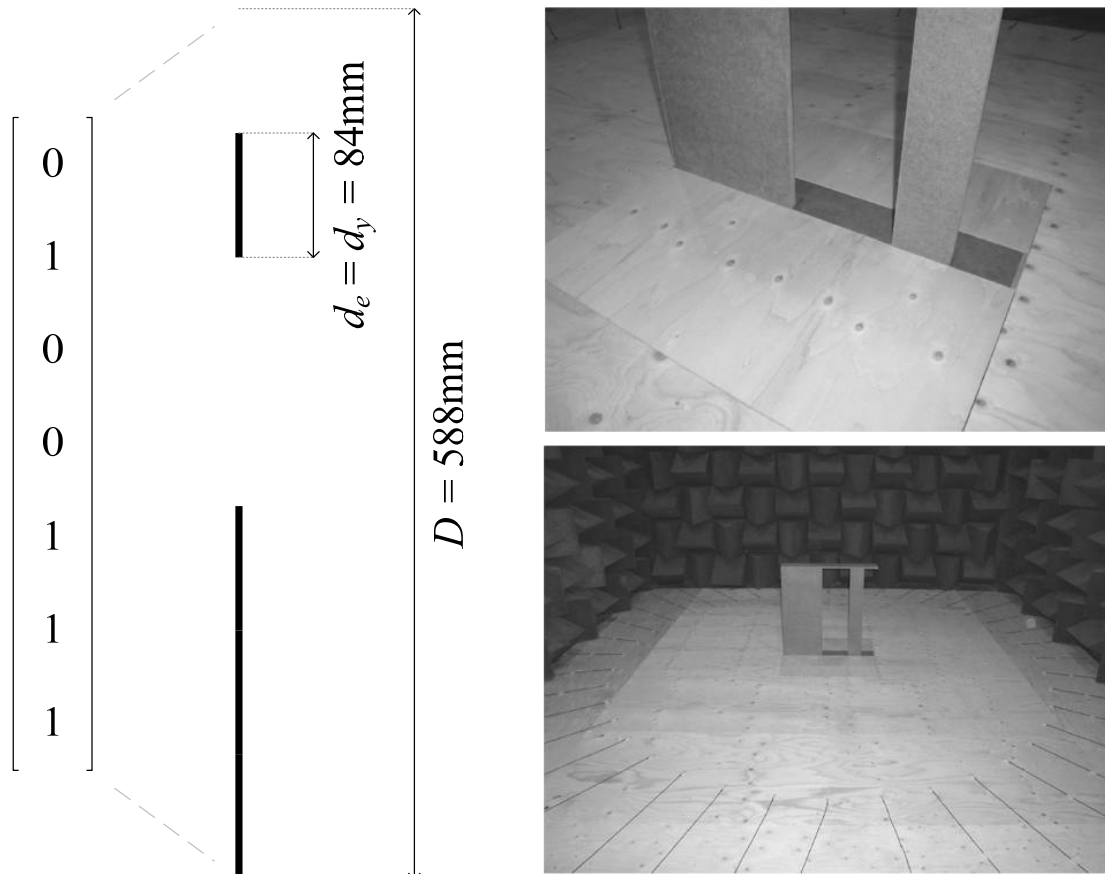
Figure 2.21: 1×7 array of slats arranged according to a Maximum Length Sequence (MLS) [1 1 1 0 0 1 0]; arrangement (left) and measurement sample constructed at full scale (right)

For the case of the grazing angles the agreement between modelled and measured results is less accurate. Here the standard BEM routine must be used since the thin panel BEM cannot model the finite edges of the structure and will always predict a complete pressure null at grazing receivers, which in reality cannot be measured. For the array of slats shown in Figure 2.21 the average difference between (standard BEM) modelled and measured results is 8.2dB and 2.6dB for the 400Hz-2.0kHz and 2.0-8.0kHz frequency ranges respectively. The discrepancies here are larger than for the remaining receiver angles as the scattered energy tends to be very low resulting in a low signal-to-noise ratio, an effect which at low frequency

is exacerbated by the low signal output from the loudspeaker (see Figure 2.12). In addition the often sharp drop in scattered pressure makes the measurement result highly sensitive to inaccuracies in transducer placement.

f = 1kHz

f = 2kHz

f = 4kHz

f = 8kHz
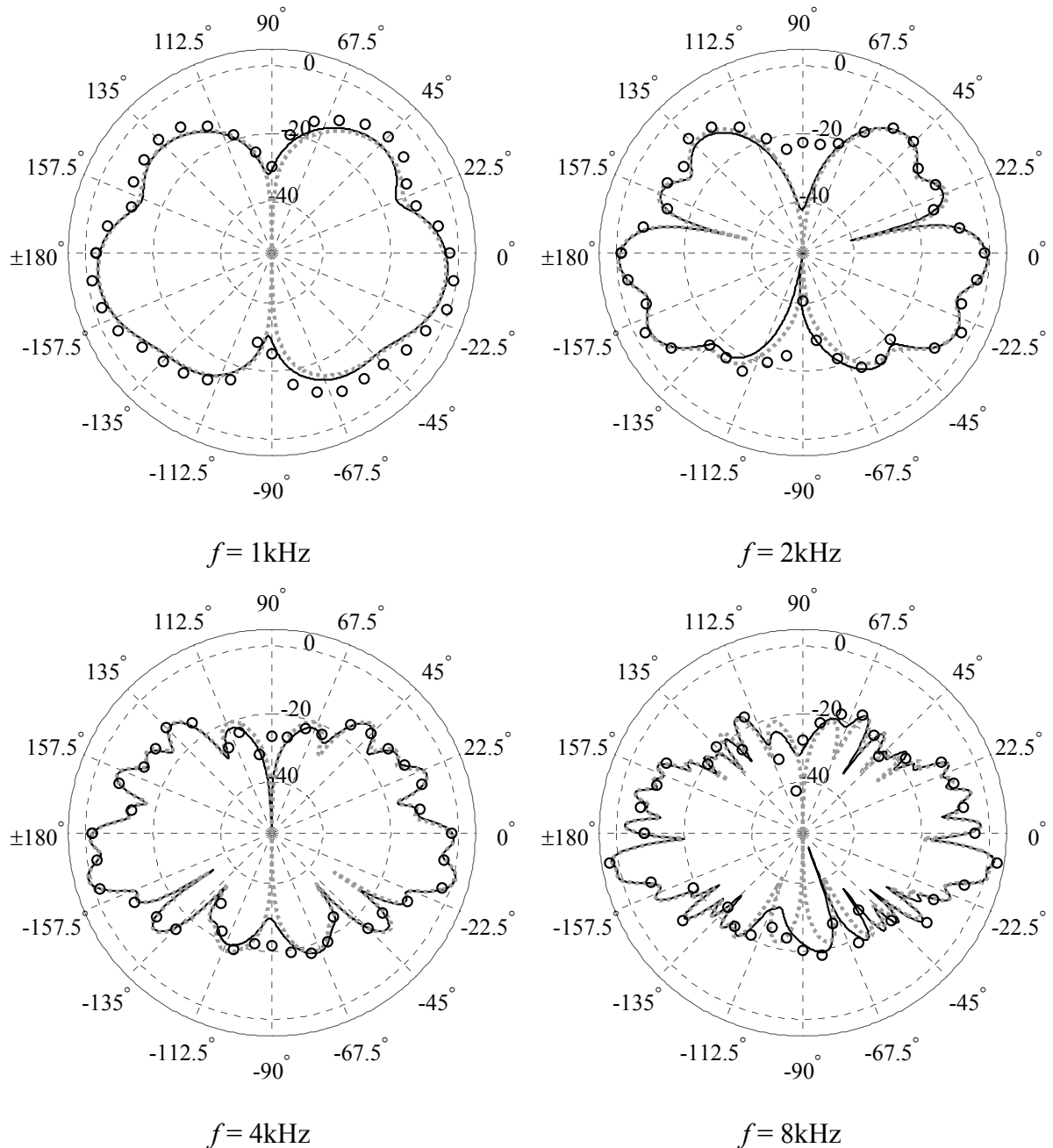
Figure 2.22: Measured (○) and modelled (BEM ▬, thin panel BEM ▪ ▪ ▪ scattered pressure polar response for the 1×7 array of slats as per Figure 2.21; θ₀ = 0°; frequencies as listed

Whilst the thin panel BEM fails to model the influence of the finite edges of the measured slats, evident for the receivers towards grazing angles where little or no scattering is

predicted, the routine provides a close approximation for the remaining receiver angles. In addition, where complete pressure nulls are predicted at grazing receivers, the scattered pressure from an array of slats will tend to be low and so the model will still adequately describe behaviour. This therefore makes the thin panel BEM a suitable model for prediction. In addition the thin panel assumption simplifies the design process since the effects of varying panel thickness is removed.

2.6.2 Percolation structures

Chapter 5 considers a percolation structure as a volume diffuser, an example of which is the sample tested shown in Figure 2.23, comprising a number of thin, rigid strips, which in this case is based on a square grid. Consequently like the slats diffusers, the thin panel BEM should provide a suitable prediction model.

The model was constructed at 1:3 scale, with the dimensions in Figure 2.23 representing the scaled case, and was made from ⅛" (≈5mm) thick aluminium strips of 600mm in height (15×1800mm when scaled) slotted into grooves in the sample board. To simplify construction, a structure based on a number of available square based aluminium channel cross-sections (e.g. flat bar, L and U cross-sections) was designed. Arrangement was determined by random selection, though with the restriction that the structure could be easily constructed from the cross-sections available. Shapes formed from a combination of cross-sections were fixed together by gluing along the length of the join(s) using a methacrylate adhesive to ensure an air tight seal between adjacent pieces.

Figure 2.24 shows the scattered pressure polar response for the $\theta_0 = 0°$ case for a number of frequencies, including both standard and thin panel BEM predictions. The standard BEM prediction here is perhaps close to its limits due to the very thin nature of the surfaces modelled, though displays very similar results to that of the thin panel model, only with a slight shift in behaviour to lower frequencies. This can be attributed to the small decrease in scattering path lengths within the structure due to the finite width of the panels.

The measured results display an average deviation of 3.5dB and 3.9dB from the standard BEM and thin panel BEM predictions respectively over the 400Hz-4.0kHz frequency range. Whilst these errors are not insignificant, Figure 2.25 demonstrates that the general trend in the

scattered pressure maps (which display the change in polar pattern with frequency) is very similar. Since the error for the two models are similar, the thin panel BEM model provides a suitable prediction routine, describing the general trend in behaviour whilst reducing computation time relative to that of the standard BEM routine.
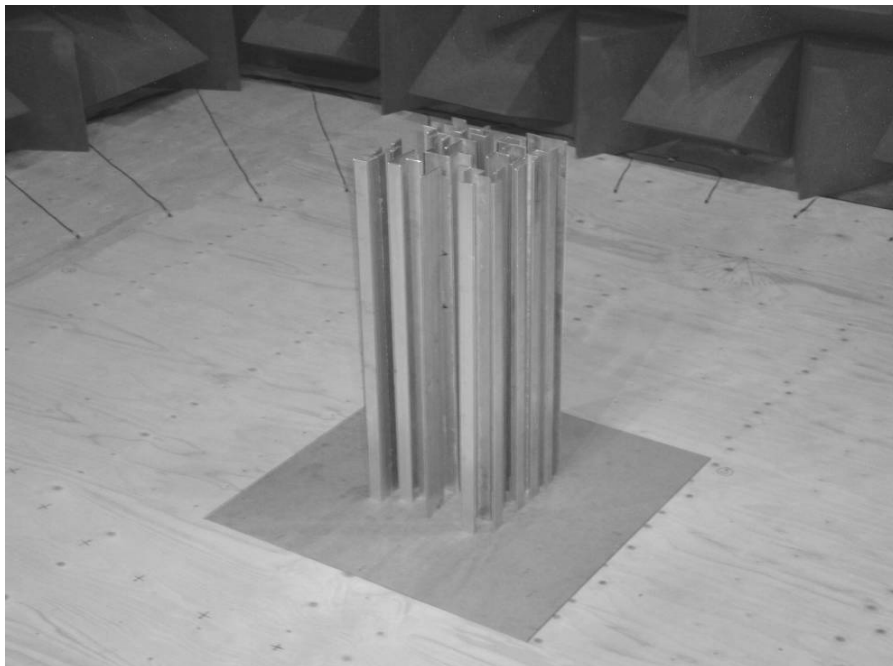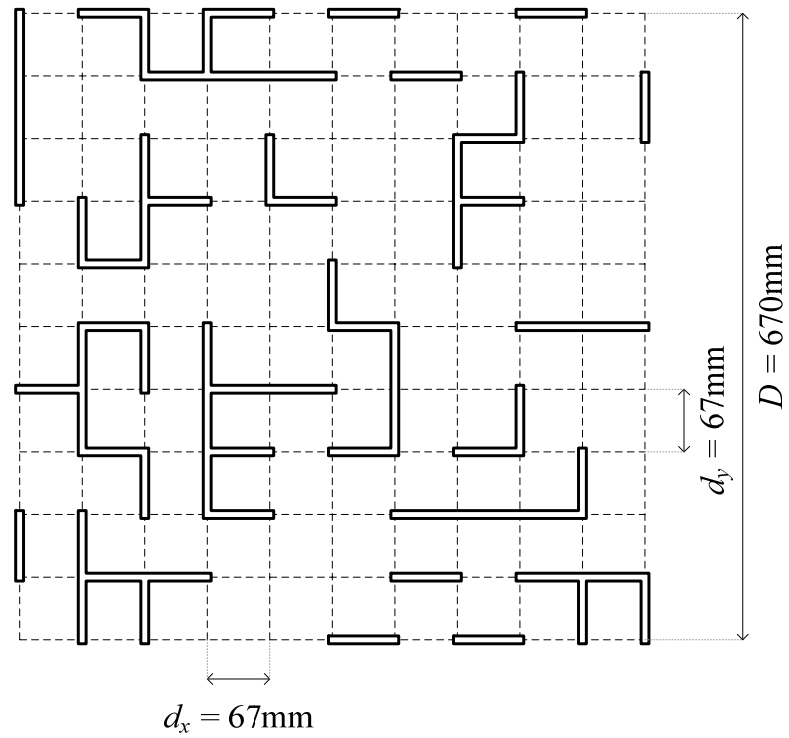
Figure 2.23: 10×10 channel percolation structure; arrangement (top) and measurement sample constructed at 1:3 scale (bottom)

f = 633Hz

f = 2.033kHz

f = 2.6kHz

f = 3.5kHz
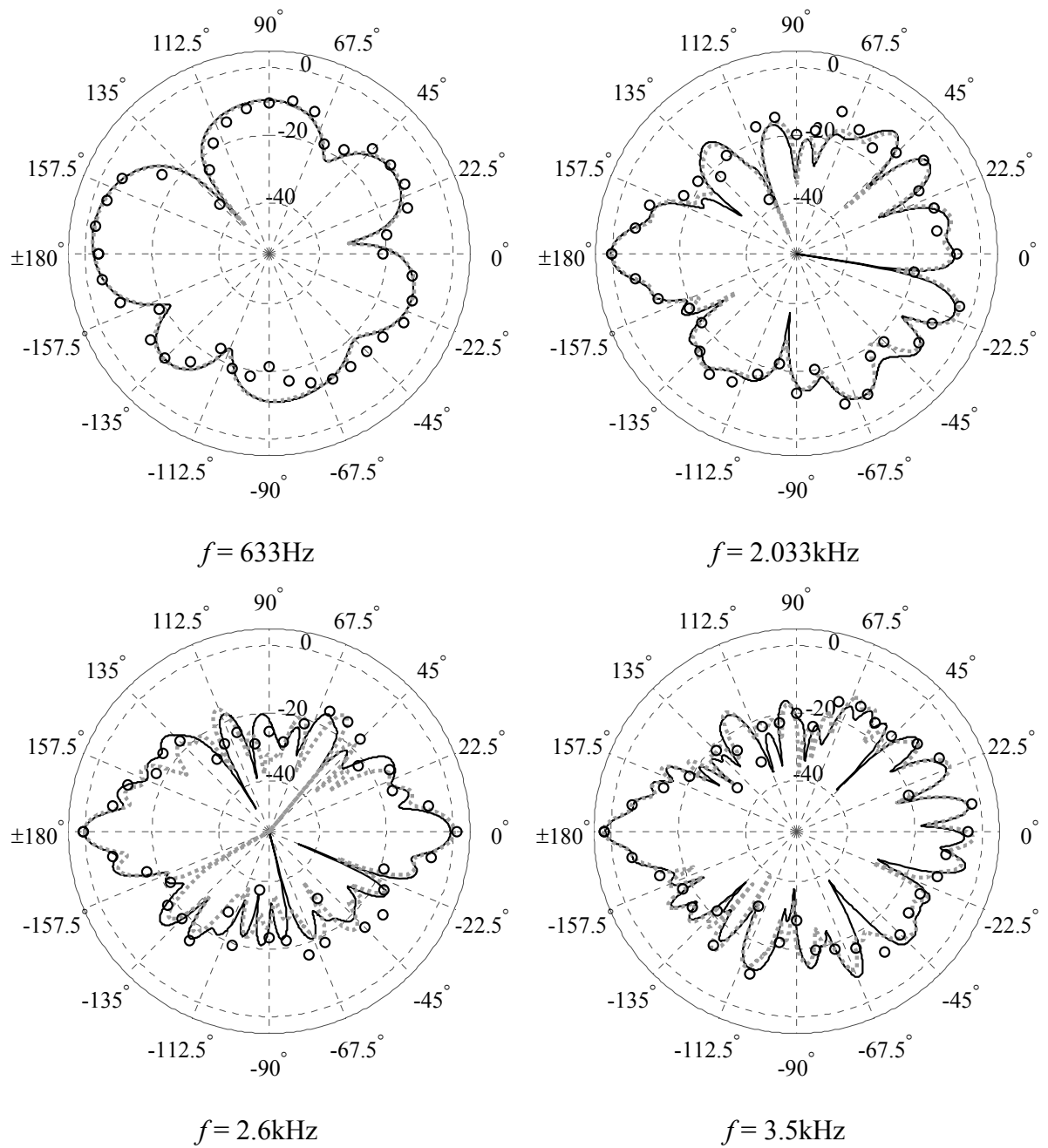
Figure 2.24: Measured (○) and modelled (BEM ▬, thin panel BEM ▪ ▪ ▪) scattered pressure polar response for the 10×10 channel percolation structure as per Figure 2.23; $\theta_0 = 0^°$; frequencies as listed
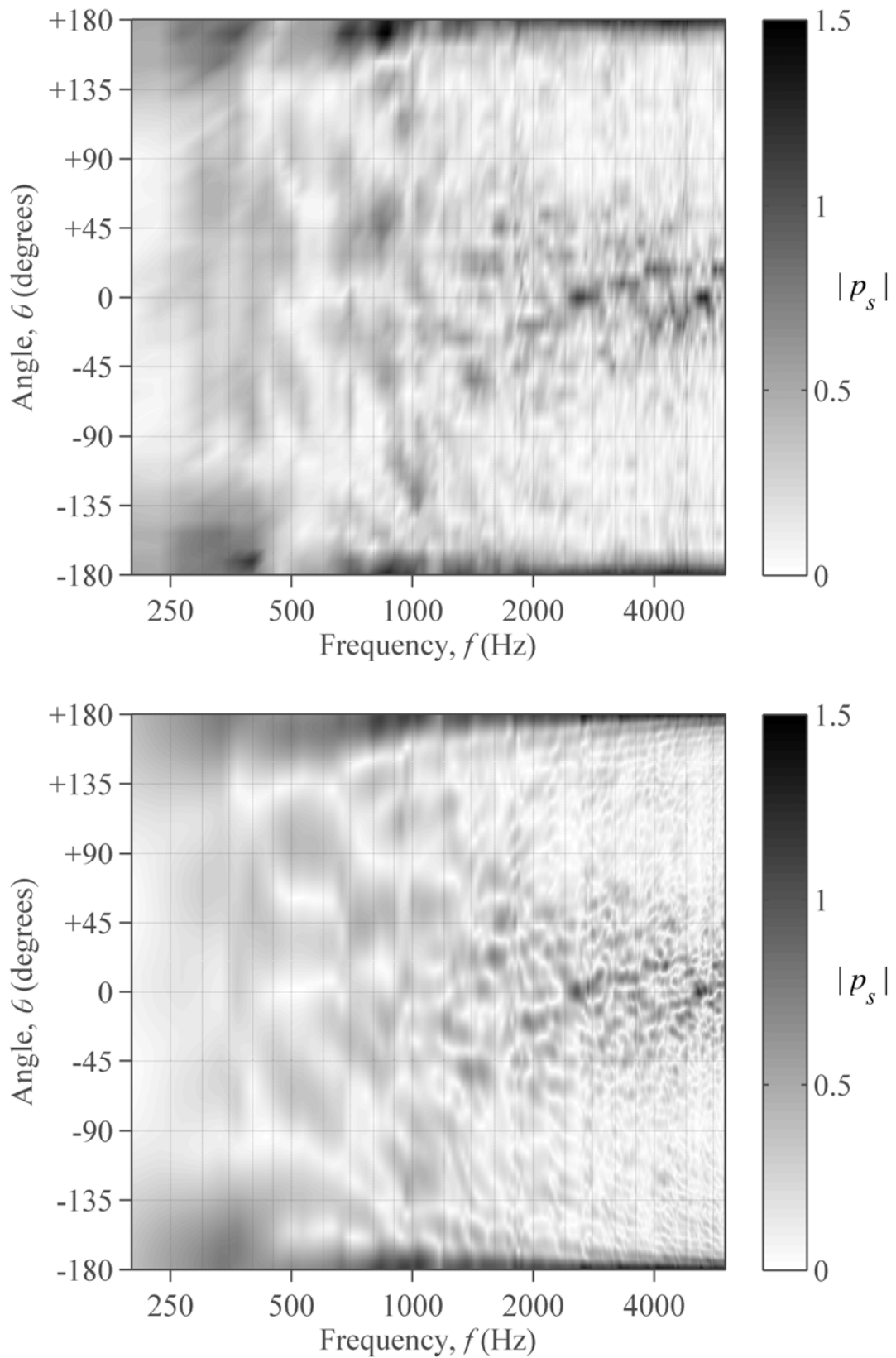
Figure 2.25: Measured and modelled scattered pressure for the 10×10 channel percolation structure as per Figure 2.23; $\theta_0 = 0^\circ$; measured (top), thin panel BEM (bottom)

2.6.3   Cylinder arrays

Chapter 6 considers an array of cylinders as a volume diffuser; an example of which is shown in Figure 2.26 and Figure 2.27 comprising a number of aluminium cylinders of 1m in height constructed at 1:4 scale. This is the same structure as the sample shown in Figure 2.11, and is a specific case based on a periodic lattice whose design is discussed in detail in Section 6.4. Such a structure, whether based on a periodic or more arbitrary arrangement, is suitable for modelling with the MS routine presented in Section 2.3.3; or where more appropriate, the BEM model given in Section 2.3.1.
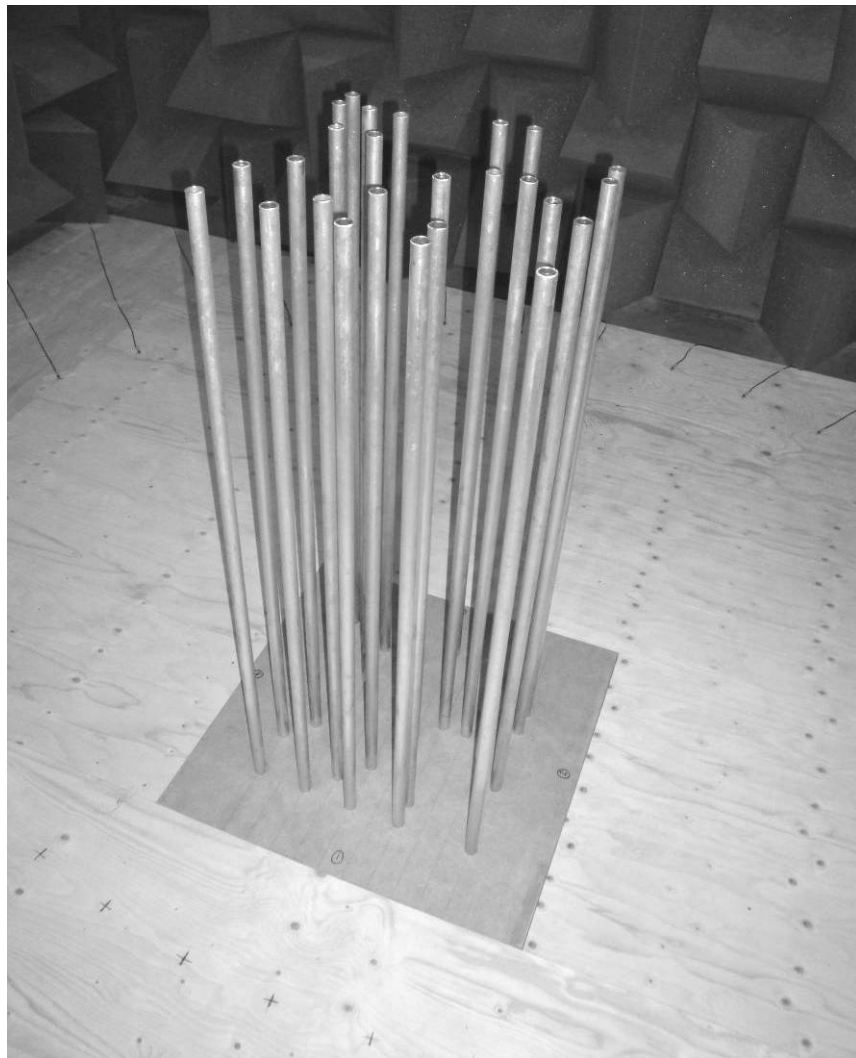
Figure 2.26: 10×10 optimised cylinder measurement sample constructed at 1:4 scale

$$\begin{bmatrix} 1 & 0 & 0 & 0 & 0 & 1 & 1 & 0 & 0 & 0 \\ 1 & 1 & 1 & 0 & 0 & 0 & 0 & 0 & 0 & 0 \\ 0 & 0 & 0 & 0 & 0 & 0 & 0 & 0 & 0 & 1 \\ 0 & 1 & 1 & 0 & 0 & 0 & 0 & 0 & 0 & 1 \\ 0 & 0 & 0 & 0 & 0 & 0 & 1 & 1 & 0 & 0 \\ 0 & 0 & 0 & 0 & 0 & 1 & 0 & 0 & 1 & 0 \\ 0 & 1 & 0 & 0 & 0 & 0 & 0 & 0 & 0 & 1 \\ 1 & 0 & 0 & 0 & 1 & 0 & 0 & 0 & 0 & 0 \\ 0 & 0 & 0 & 1 & 0 & 0 & 1 & 0 & 0 & 0 \\ 1 & 0 & 1 & 0 & 1 & 0 & 1 & 0 & 0 & 1 \end{bmatrix}$$
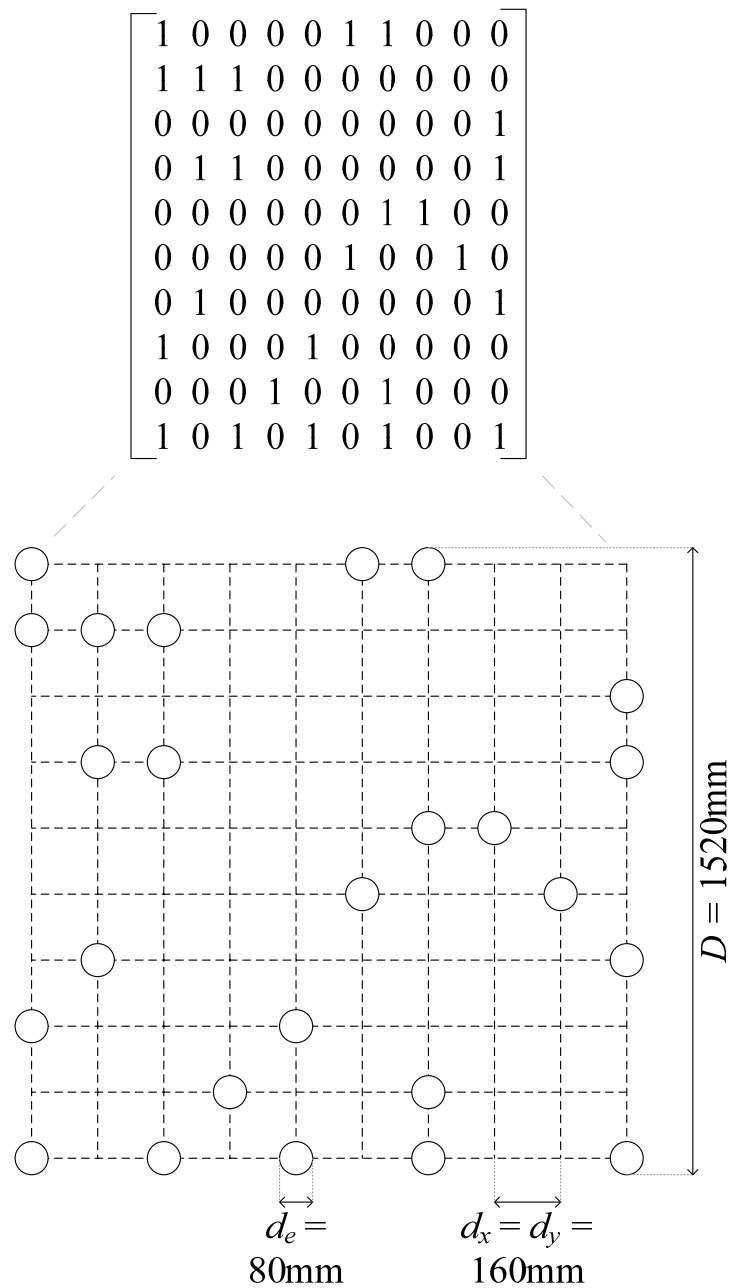
Figure 2.27: 10×10 optimised cylinder array arrangement

Figure 2.28 compares the measured and modelled polar plot results for the 10×10 cylinder array for a number of frequencies. Here only the MS modelled results are shown, since the BEM prediction gives very similar results. The agreement is generally good with an average deviation between measured and modelled results over the 400Hz-4.0kHz frequency range of 1.8dB and 1.9dB for the MS and BEM routines respectively.

$f = 400\text{Hz}$

$f = 1.05\text{kHz}$

$f = 1.65\text{kHz}$

$f = 2.8\text{kHz}$
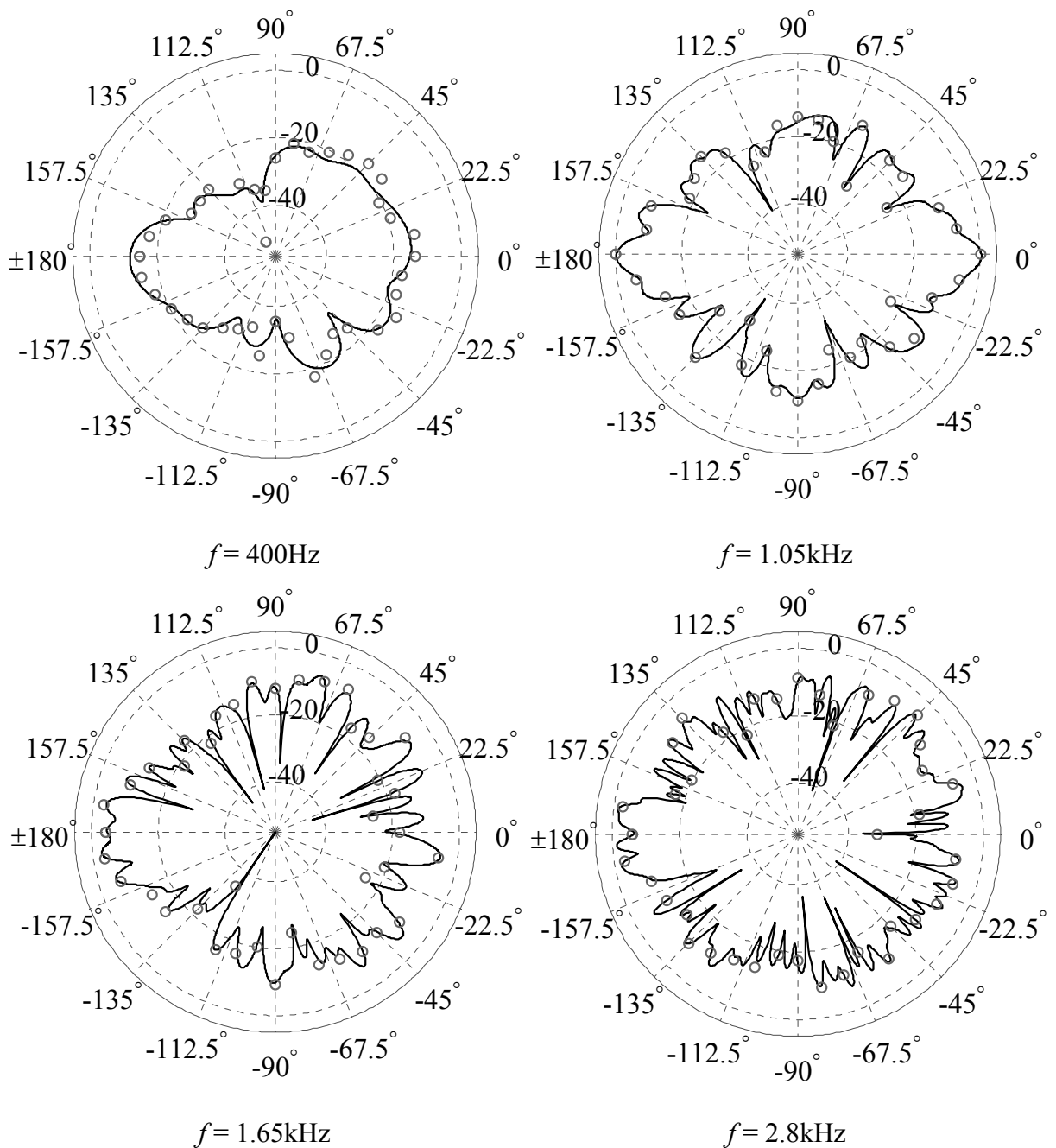
Figure 2.28: Measured (○) and modelled (▬) scattered pressure polar response for the 10×10 cylinder array as per Figure 2.27; $\theta_0 = 0°$ (left) and $\theta_0 = 30°$ (right); frequencies as listed

The largest average error per frequency of 4.1dB occurs at 3475Hz, which equates to a measured frequency (before scaling) of 13.9kHz. This however is likely due to the drop in the loudspeaker-microphone response discussed in Section 2.5.2. Consequently the model provides a reliable prediction routine for the cylinder array design.

2.6.4   General Comments

Agreement for the three structure types presented above is generally good, particularly for the simpler cylinder diffuser type which displayed an average error between measured and modelled results of 1.9dB across the 400Hz-4.0kHz bandwidth, and are in line with those seen in previous diffuser measurements [11; 42]. This is also the case for receivers towards the rear of the sample where the cross-correlation oversampling technique was applied.

There are some discrepancies at low frequency, predominantly due to a low signal-to-noise ratio caused by the low level output of the loudspeaker. Equally the signal-to-noise ratio can be problematic when scattering is weak since the measured pressures will fall into the noise floor. In addition, low frequency problems can occur when approximating a three-dimensional structure with a two-dimensional equivalent (or vice-versa) [31]. Errors also arise due to the highly sensitive nature of the structures to the sound speed used for the comparison model and also owing to uncertainty in source and receiver positioning. This is particularly evident at higher frequencies where the scattered field varies rapidly with angle, and consequently the inaccuracies in transducer placement become magnified.

2.7.   Conclusions

In this chapter the procedure for both modelling and measuring the scattering from a 2D planar volume diffuser has been presented, obtaining results as a set of free-field and far-field polar pattern responses. This extends the concept of the more conventional surface diffuser to a volume equivalent, obtaining the pressures scattered into all directions.

Both simplistic and highly accurate modelling procedures have been given; the former being a simple single scatter Fourier approximation and the latter including a standard BEM, thin panel BEM and MS routine, with application dependent on structure type.

The development of a new 2D volume measurement routine required the use of a cross-correlation oversampling method to ensure accurate time of flight estimation. This allows a more precise separation of the scattered and incident sound, necessary when conventional time windowing techniques can no longer be applied. Estimation of the scattered pressures towards the rear of the scattering object becomes particularly problematic, since

methods for calculating time of flight generally break down. A reasonable approximation may be made here however based on the more reliable data from the remaining receivers.

A selection of measurement results representative of each proposed structure have been presented, and are shown to agree well with predictions. This allows the accurate models to be confidently employed throughout the remainder of the thesis.

3.   CHARACTERISATION OF PERFORMANCE

3.1.   Introduction

Chapter 2 outlined the modelling process used to obtain the spatial distribution of the scattered pressure from a volume diffuser, and this was verified through measurements. This chapter addresses the way in which this distribution, or polar response, is analysed in order to obtain a measure of diffusive efficacy. Surface diffuser design has seen a number of metrics developed [48], though primarily it is the diffusion coefficient [28] and scattering coefficient [27] that are most commonly used today, the former being the more relevant to the work presented here. Building upon this, a number of new volume diffuser metrics are developed to allow an evaluation of performance.

The polar response is an important tool in diffuser development as it can tell a designer much about how an object scatters sound. For most practical purposes however, the amount of data involved in assessing multiple frequencies, potentially for a number of angles of incidence, is considerable. In order to assess the effectiveness of a diffuser therefore, it is necessary to adopt a (number of) suitable metric(s) which will characterise performance and reduce the data to a more manageable level.

Since a volume diffuser can scatter sound in all directions, this means that metrics designed for surface diffusers may no longer be appropriate. A discussion of the differences between a volume and surface diffuser is presented, along with how this affects the application of existing coefficients. Conventional metrics are considered, and where appropriate adapted to suit. A modification is required in the treatment of the forward-scattered region, since where a volume diffuser allows diffraction around or transmission through a structure, the behaviour of the scattered field is inherently different. A number of design metrics for a volume diffuser are proposed; specifically to consider scattering uniformity and scattered power. By applying suitable design targets, these are used to assess performance throughout the remaining chapters.

All results presented in this chapter are from predictions carried out using the relevant accurate scattering models as presented in Section 2.3.

3.2. Volume Scattering

To assess a volume diffuser's effectiveness it would be preferable to use a simple expansion on current metrics for more conventional devices. This would provide a measure of diffusive efficacy which would be easily understood and interpreted by those who are familiar with current surface diffuser analysis. As was discussed in Section 2.2.2 however, for a volume scatterer the full field must be taken into account. This raises a number of issues that are highlighted below.

3.2.1 Definition of the back-scattered and forward-scattered zones

Consider the setup shown in Figure 2.2 where a volume diffuser is subject to a sound from a source. Each receiver will observe the total sound field, p_t – a summation of both the incident sound direct from the source, p_i, and the scattered sound due to the presence of the diffuser, p_s. For surface diffusers the geometry is such that the scattered component usually arrives sufficiently separated in time from the incident sound so as to be considered independently. This was the case for the example given in Figure 2.10, which allowed a simple time windowing method to be used. As was discussed in Sections 2.5.3 however, and represented by the example given in Figure 2.15, towards the rear of the diffuser there is a gradual merging of the incident and scattered sound. Here it is unclear whether the scattered field can be treated independently, or whether the total field should be considered instead.

To help form a link between the two cases, the following regions are defined:

- Back-Scattered Zone (BSZ) – defined as the half-plane including the source, covering the angular region $\theta_0 - 90° \leq \theta \leq \theta_0 + 90°$.

- Forward-Scattered Zone (FSZ) – defined as the half-plane not including the source, covering the angular region $\theta_0 + 90° < \theta < \theta_0 - 90°$.

Both of the above are shown in Figure 3.1, and are the equivalent to the region considered for a surface diffuser (for a normal incidence source) and the additional region considered for the volume diffuser case respectively.
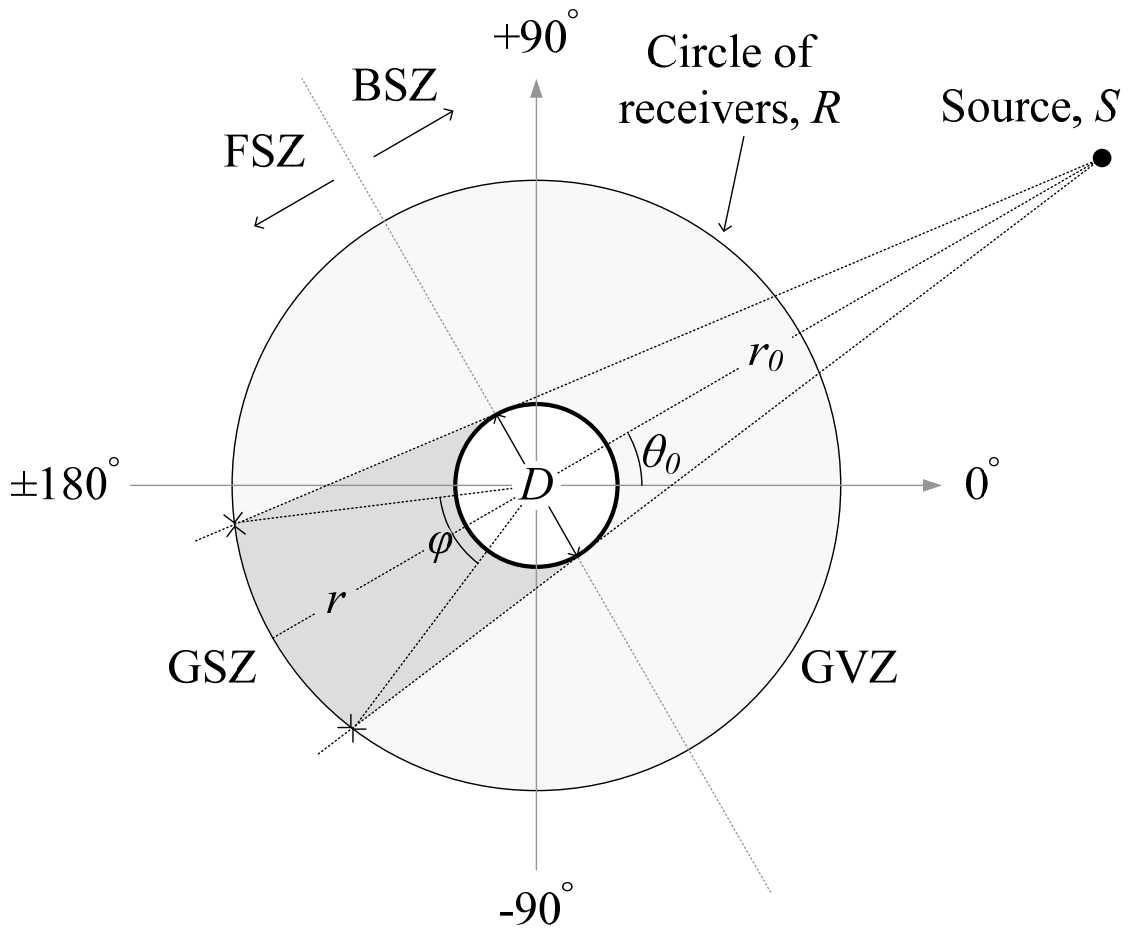
Figure 3.1: The scattered field around a 2D volume diffuser; definition of the Back-Scattered Zone (BSZ); Forward Scattered Zone (FSZ); Geometric Visible Zone (GVZ); and Geometric Shadow Zone (GSZ) around an array of width D.

3.2.2 Definition of the geometric visible and geometric shadow zones

Consider again the geometry defined in Figure 3.1. In the region directly behind the diffuser, where direct line-of-sight between source and receivers may be blocked, the incident and scattered sound will arrive at comparable times and their interference cannot be ignored. Here the total field must be considered as the scattered pressure alone becomes meaningless, forming interfering rather than reflected waves [30] as described in Section 2.5.5. For this reason the scattered pressure in this region cannot be included in a conventional scattered pressure diffusion metric. Sound scattered into the remaining angles however will continue to propagate and contribute towards a diffuse field, and so here uniformity is still desirable.

To differentiate between the above two cases the following regions are defined:

- Geometric Visible Zone (GVZ) – defined as the angular region in which all receivers have unobstructed views of the source when considering the diffuser as a solid object, covering the angular region $\theta_0 - \left(180° - \dfrac{\varphi}{2}\right) < \theta < \theta_0 + \left(180° - \dfrac{\varphi}{2}\right)$.

- Geometric Shadow Zone (GSZ) – defined as the angular region in which all receivers have obstructed views of the source when considering the diffuser as a solid object, covering the angular region $\theta_0 + \left(180° - \dfrac{\varphi}{2}\right) \leq \theta \leq \theta_0 - \left(180° - \dfrac{\varphi}{2}\right)$.

Where φ is the solid angle behind the diffuser representing the extent of the GSZ.

These regions, along with the BSZ and FSZ defined in Section 3.2.1, are shown in Figure 3.1. Their extent is a little harder to define, though an approximation for the extents of the GSZ may be obtained by considering the diffuser as a flat plate of width D, as illustrated in Figure 3.2. Here the shadow zone is numerically identical in size to the Specular Zone (SZ) as mentioned in Section 2.2.3. The extent of the solid angle, φ, behind the diffuser may then be derived as per Appendix A, which for the specific case of a source located at normal incidence (where the shadow region is at its largest) may be given as:

$$\varphi = 2\left[\sin^{-1}\left(\frac{D r_0}{2r\sqrt{r_0^2 + \dfrac{D^2}{4}}} \right) - \sin^{-1}\left(\frac{r_0}{\sqrt{r_0^2 + \dfrac{D^2}{4}}} \right) \right] + \pi \qquad 3.1$$
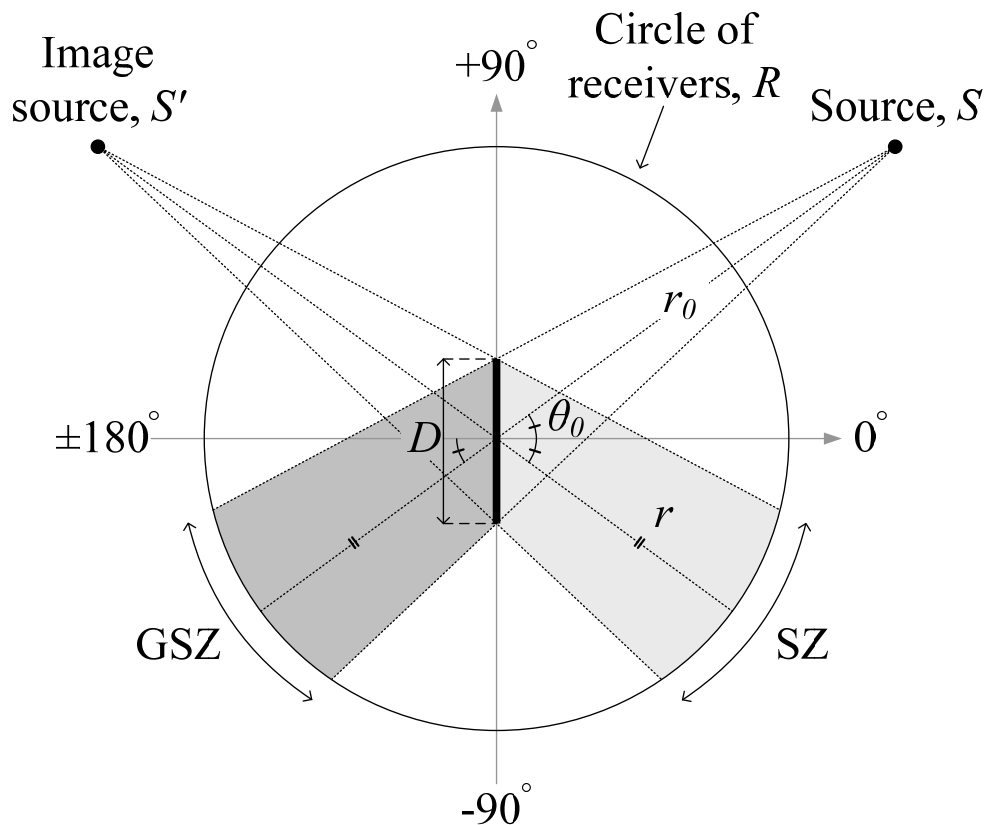
Figure 3.2: Geometry defining the extent of the Geometric Shadow Zone (GSZ) and Specular Zone (SZ) for a flat plate of width, D

3.3. Spatial diffusion

There are currently two main ways in which the scattering from a surface diffuser is analysed in order to quantify how well they perform: the scattering coefficient measured according to the ISO standard [27] and the diffusion coefficient presented in guidance document AES-4id-2001 [28]. The scattering coefficient provides a measure of the energy reflected in a non specular manner; a gauge of how well the diffuser redistributes its scattered energy relative to that of a plane surface of the same size. This however does not take into account how evenly this energy is redistributed, and is usually more suited to geometric room acoustic modelling [3]. The diffusion coefficient however is designed to measure scattering uniformity, and therefore generally provides a more suitable metric during the design process, as this aims to develop a diffuser whose scattered pressure magnitude is ideally uniform in all (appropriate) directions over the intended operational bandwidth.

A number of statistical figures of merit have been proposed to assess the spatial scattering uniformity of a surface [48; 49]. More recently however, since the introduction of AES-4id-2001 [28], it has become widely accepted that the autocorrelation diffusion coefficient provides the most representative single figure value.

Assuming an equal area per receiver is sampled, which for the 2D case simply means equal angular steps, the standard autocorrelation diffusion coefficient, δ, used to assess scattering uniformity may be given as [28]:

$$\delta = \frac{\left(\sum_{n=0}^{N-1}|p_{s,n}|\right)^2 - \sum_{n=0}^{N-1}|p_{s,n}|^2}{(N-1)\sum_{n=0}^{N-1}|p_{s,n}|^2} \qquad 3.2$$

Where $p_{s,n}$ represents the pressure scattered from the diffuser at the nth receiver over the evaluated region containing N receivers. This gives a value ranging between zero and one, representing completely directional (zero pressure at all receivers except one) and omnidirectional scattered pressure polar distributions respectively. This therefore shall be considered below, both in terms of a comparison with existing surface diffusers and as an equivalent metric for use with volume scatterers.

3.3.1 A diffusion coefficient for comparing volumetric and surface diffusers

For surface diffusers the region over which the coefficient of Eq. 3.2 above is evaluated is given as $-90^{\circ} \leq \theta \leq +90^{\circ}$. This area for the specific case of normal incidence will be equal in extent to the BSZ of a volume scatterer defined in Section 3.2.1. As with surface diffusers the scattered pressure in this half-plane may be considered independently from the incident field, and therefore uniformity is desirable. Consequently a back-scattered diffusion coefficient evaluated over the BSZ is proposed, given as δ_{BSZ}, allowing where appropriate a comparison with existing surface diffusers. This coefficient however will not take into account a volume diffusers ability to scatter energy into the FSZ, and consequently the coefficient definition needs revising.

3.3.2 A diffusion coefficient for volume diffusers

Since the standard diffusion coefficient is usually only evaluated over the equivalent of the BSZ, for volume diffusers it is necessary to extend the metric to take into account the forward-scattered component. Such a coefficient may encompass the whole space, though the distinction must be made between reflected and interfering waves since their nature is inherently different, and for reasons discussed above a metric combining the two no longer makes sense. Furthermore, the intention is to allow the design of a volume diffuser whose levels of scattered energy (discussed in Section 3.4) may be manipulated in order to satisfy an appropriate design target. This therefore requires the reflected and interfering scattering components to be considered separately.

A geometrically defined volume diffusion coefficient

Consider the simple case of a length seven Maximum Length Sequence (MLS) Schroeder diffuser with three periods and with a design frequency, f_0, of 500Hz. For this specific case the diffuser is situated in free space and for the purpose of analysis is considered as a volume diffuser. Figure 3.3 shows the diffusion coefficient evaluated over the BSZ, GVZ and the full circle of receivers respectively.

Figure 3.4 shows the polar response for the same structure at $f \approx 2\text{kHz}$ and $f \approx 2.4\text{kHz}$ respectively. The difference in the back-scattered diffusion coefficient between the two frequencies shown is large, since for reasons discussed in Section 1.3 they represent frequencies at which the diffuser back-scatters in a specular (flat plate frequency) and diffusive (odd multiple of the design frequency) manner respectively. A volume coefficient which includes the forward-scattered component though excludes the zeroth order lobe (seen in Figure 3.4 centred at $\theta = 180^\circ$) would be expected to provide similar results. This is indeed the case, though with generally lower diffusion coefficient values due to the scattering from the diffuser in the forward-scattered direction being of a relatively lower level. This is unsurprising, since this is a surface diffuser and is not designed to scatter energy into this region.
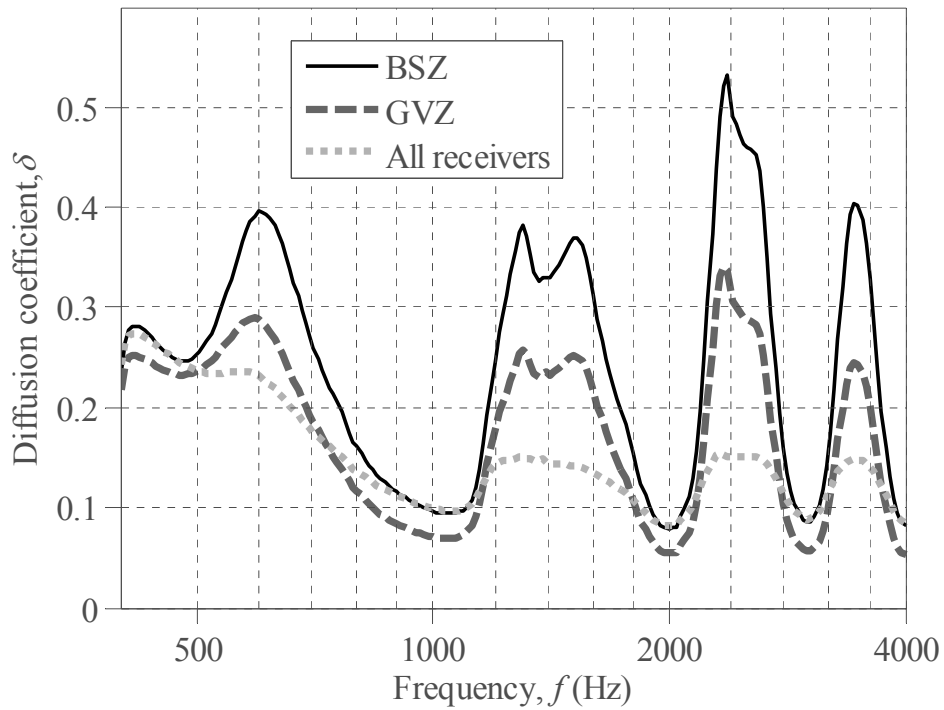
Figure 3.3: Diffusion coefficient for 3 periods of an MLS ([+1 +1 +1 -1 -1 +1 -1]) binary Schroeder diffuser evaluated over the BSZ, GVZ and full circle of receivers; D = 1.81m, $f_0 = 500Hz$, $\theta_0 = 0^\circ$, $r_0 = 20m$, $r = 10m$.
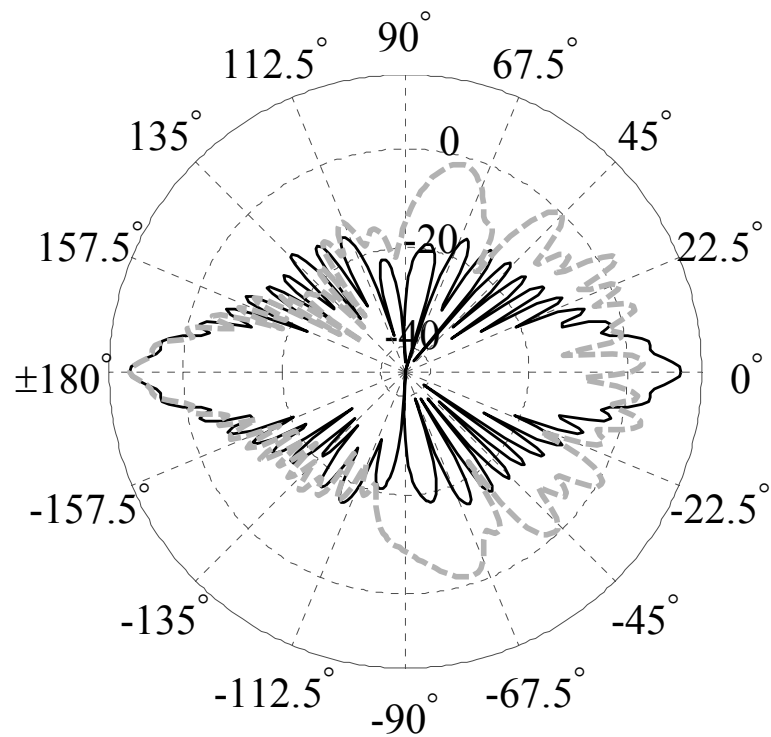
Figure 3.4: Normalised scattered pressure polar pattern for the diffuser as per Figure 3.3; f = 1998Hz (——), f = 2377Hz (– –)

In contrast to the above, including the pressure scattered into the GSZ includes the zeroth order lobe, which is present for all frequencies and determines attenuation due to the presence of the structure. This tends to be comparatively large and, as is found with the constant specular lobe produced by surface amplitude diffusers [14], will likely dominate any diffusion coefficient it is included in and produce low coefficient values. The variation in the coefficient obtained for the full field therefore varies very little.

Despite progressive merging of incident and scattered components, uniformity in the scattered field including receivers close to (but outside of) the GSZ is assumed to be desirable, since all reflected waves will contribute to a diffuse field. Based on the example above therefore, a diffusion coefficient evaluated over the GVZ may seem ideal. Unfortunately however the above definition is a little simplistic; since the assumption is that the border between reflectance and interference is formed by a basic geometric line-of-sight.

Figure 2.4 showed that in the far-field the distribution of the pressure scattered by an object at a given frequency (when normalised to account for cylindrical spreading) will become independent of receiver distance. Conversely Figure 3.5 (top) demonstrates that (for the same flat plate of width $D = 0.4$m) the scattered pressure varies significantly with frequency, with the main zeroth order lobe becoming progressively narrower with increasing frequency. Figure 3.5 (bottom) shows the effect this has on the total pressure for the same plate, demonstrating the complex nature of the interference between the incident and scattered fields. Here an area experiencing attenuation towards the rear of the plate can be seen, again becoming progressively narrower with frequency. This means then that, assuming far-field conditions, the envelope of the scattered pressure polar pattern will be dependent on frequency and independent of distance.

Following from the above, a frequency dependent descriptor of the shadow zone is desired that (assuming far-field conditions) is independent of receiver distance. The geometric description of the shadow zone however (whose extents are defined as per Eq. 3.1 and for the case of Figure 3.5 is highlighted by the central shaded region) is unsuitable, since it is determined by distance and is independent of frequency. This is due to the assumption that the size of the object is extremely large relative to wavelength; a very high frequency approximation valid in optics (hence the term line-of-sight), which for the acoustic case is less straightforward.
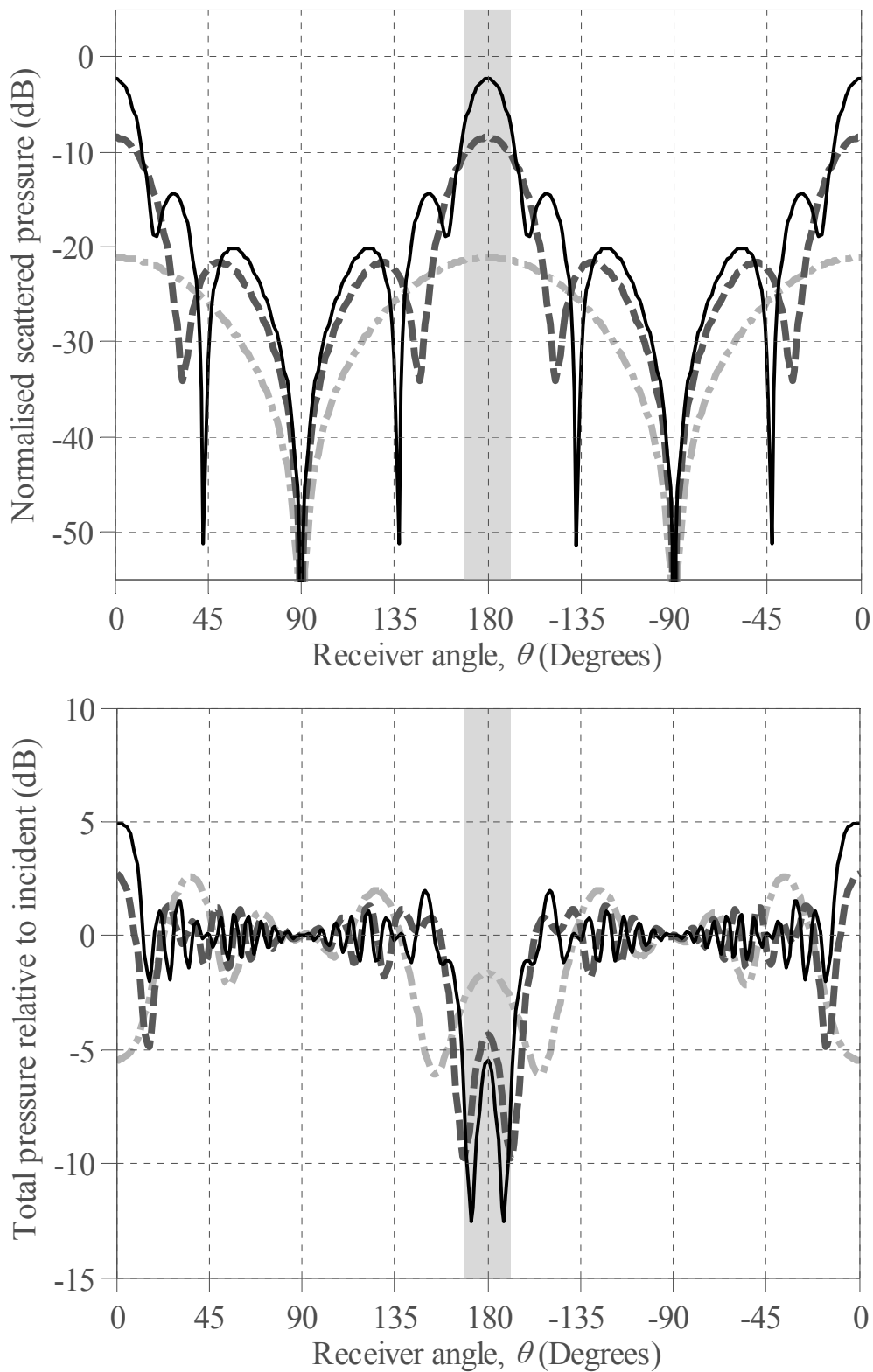
Figure 3.5: Normalised scattered pressure (top) and total pressure (bottom) for a flat plate;
D = 0.4m, r_c = 2m, r_0 = 5m, θ_0 = 0°; f = 500Hz (-·-), 1.5kHz (---), and 2.5kHz (——); central
shaded region depicts the approximate geometric shadow zone according to Eq. 3.1

The extent of the GSZ can perhaps be seen more clearly in Figure 3.6, showing the scattered pressure map in the FSZ for the same flat plate as Figure 3.5, for a frequency of $f = 2.5\text{kHz}$ and for a range of receiver distances. For clarity the scattered pressure has been normalised to remove the effects of cylindrical spreading as described in Section 2.5.2. For distances close to the object the geometric region, like in optics, defines a clear border in scattering behaviour. With increasing distance however the GSZ becomes progressively narrower, with more and more incident energy able to diffract around the plate, and the geometric assumption (dashed line) breaks down. It is again apparent, as with the case shown in Figure 2.4, that the extents of the main zeroth order lobe are independent of distance once far-field behaviour is observed.
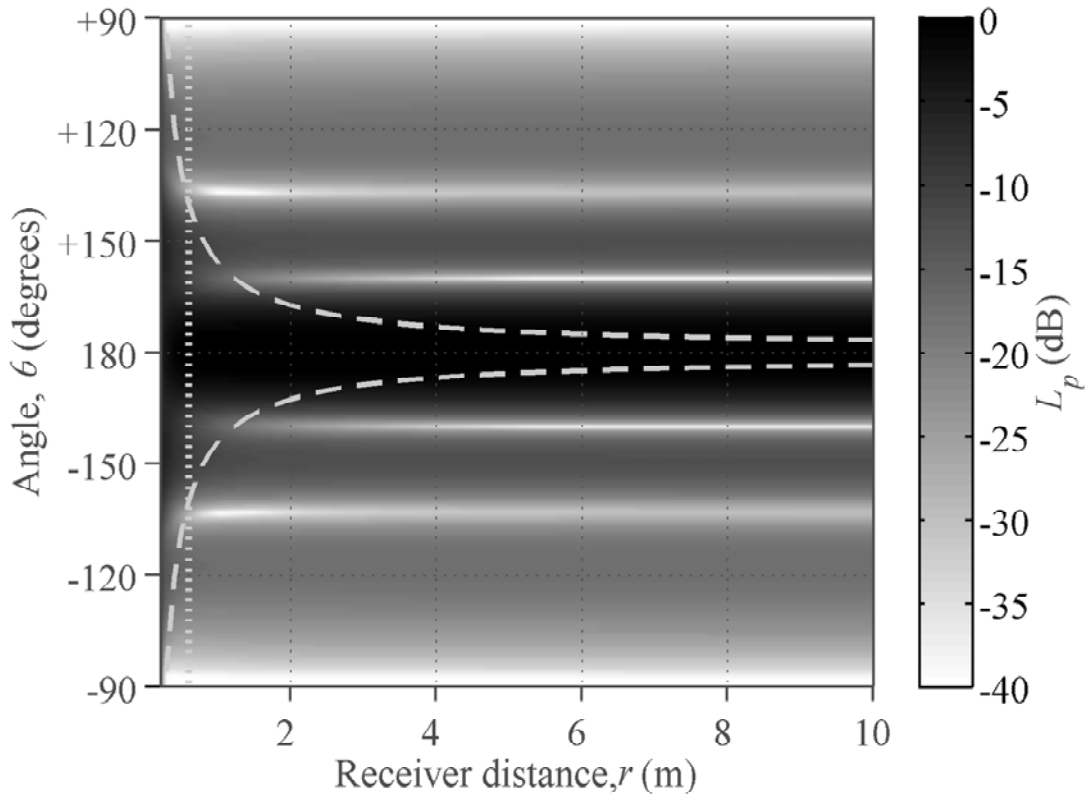
Figure 3.6: Normalised scattered pressure with receiver distance in the forward-scattered region for a flat plate; D = 0.4m, r_0 = 20m, θ_0 = 0°, f = 2.5kHz; geometric shadow zone according to Eq. 3.1 (– –) and far-field boundary as per Eq. 2.4 (- - -)

It would be expected then that any diffusion coefficient evaluated over the GVZ will vary significantly with distance. In order to illustrate this, the scattering from a cylinder of width $D = 1.6\text{m}$ is considered. Figure 3.7 shows the scattered pressure from the cylinder at $f = 1\text{kHz}$

(top left) and $f = 3\text{kHz}$ (top right) respectively, demonstrating the highly omnidirectional scattering behaviour of the structure in the back-scattered direction. Due to the far-field conditions the polar patterns with varying distance are (once normalised) near identical.

$f = 1\text{kHz}$

$f = 3\text{kHz}$
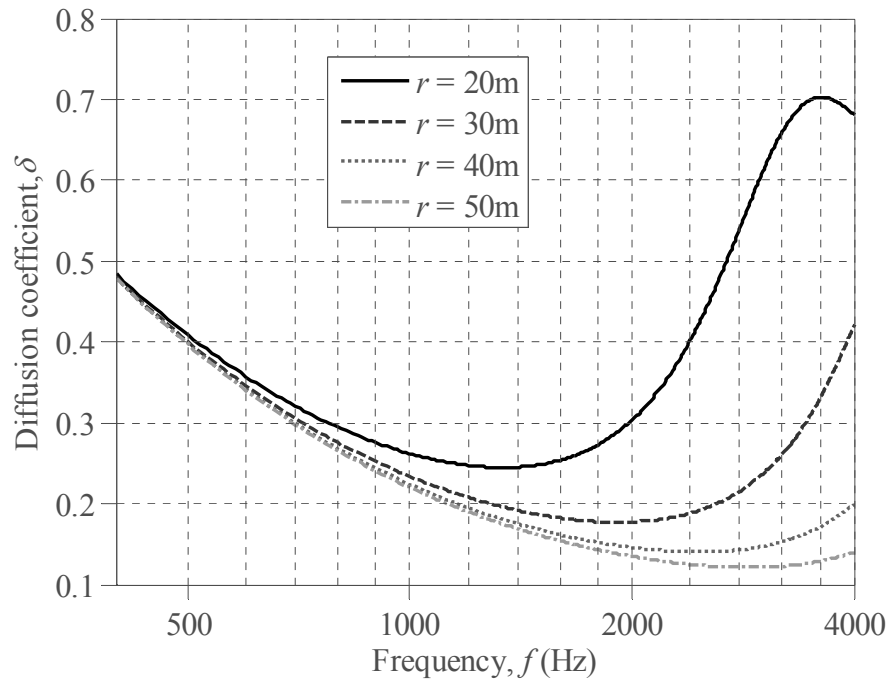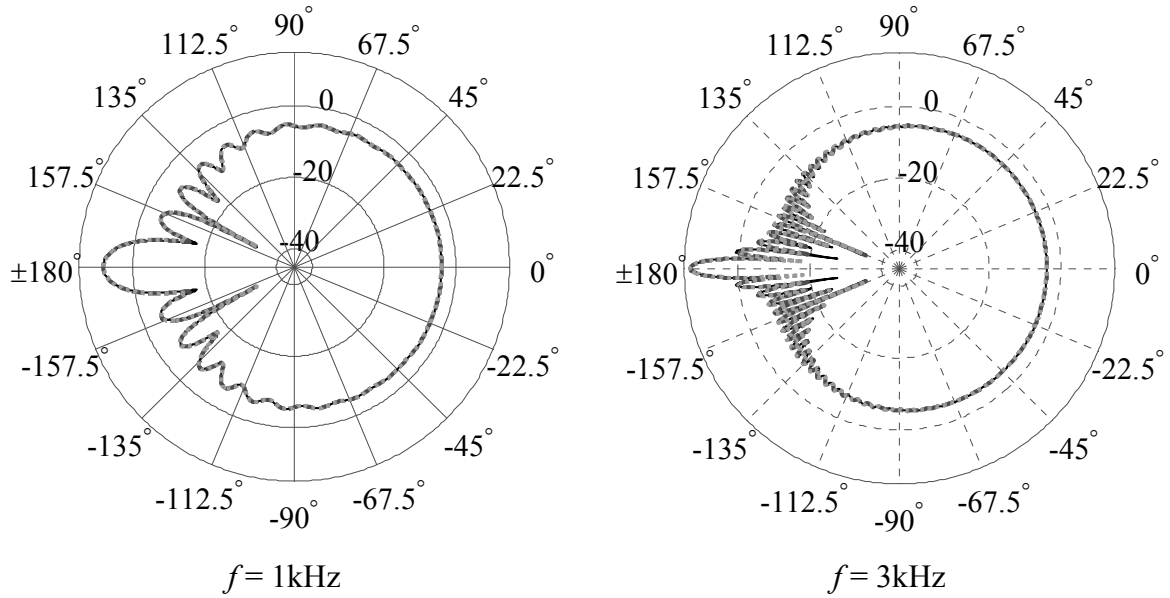
Figure 3.7 Scattering from a single cylinder of width D = 1.6m for a number of receiver distances; polar plots with frequencies as listed (top), and diffusion coefficient evaluated over the GVZ (bottom); $r_0 = 200m$, $\theta_0 = 0^\circ$

A more conventional back-scattered coefficient would result in a value close to one. The inclusion of the forward-scattered direction however, where the pressure distribution comprises a main zeroth order lobe and a series of sidelobes, makes evaluation less straightforward. A volume scattering coefficient that excludes this main lobe would have a similar rating to the back-scattered coefficient (though slightly lower due to the sidelobes in the FSZ), whilst a coefficient evaluated over the whole field would have a much lower value since the main lobe will dominate. Intuitively the former would make more sense, since the zeroth order lobe will primarily contribute to the interfering scattered field.

Figure 3.7 (bottom) shows the resulting diffusion coefficient for the cylinder evaluated over the GVZ for a range of receiver distances. At low frequency the coefficient is low as the zeroth order lobe is large compared to the GSZ, and consequently this dominates the outcome. With increasing frequency this lobe gradually narrows and disappears from the GVZ in a manner similar to that of the flat plate in Figure 3.5. This causes the diffusion coefficient to rise, though with the frequency at which this occurs varying with receiver distance.

It is clear from Figure 3.7 that the variation with distance observed in a coefficient evaluated over the GVZ is much too high to be of any use, and a more robust procedure is therefore required that allows more consistent results. Ideally, assuming far-field conditions, this would:

- Work equally well for all frequencies.

- Be invariant to source and receiver distance.

- Be invariant to diffuser size.

- Provide a frequency dependent descriptor of the boundary between reflected and interfering scattered waves.

For convenience two new regions shall be defined:

- Reflected-Scattered Zone (RSZ) – defined as the frequency dependent angular region in which the scattered field comprises reflected scattered waves, covering the angular region

$$\theta_0 - \left(180° - \frac{\psi(f)}{2}\right) < \theta < \theta_0 + \left(180° - \frac{\psi(f)}{2}\right).$$

- Interfering-Scattered Zone (ISZ) – defined as the frequency dependent angular region in which the scattered field comprises interfering scattered waves, covering the angular region $\theta_0 + \left(180° - \dfrac{\psi(f)}{2}\right) \leq \theta \leq \theta_0 - \left(180° - \dfrac{\psi(f)}{2}\right)$.

Where $\psi(f)$ is the frequency dependent solid angle describing the extent of the interfering scattered waves.

Fresnel zones: refining the definition of the shadow zone

It was shown above that a straightforward geometric definition of the shadow region may not provide consistent results with varying source and receiver distance. In surface diffuser design an existing analogue to the shadow zone is the specular zone, illustrated by Figure 3.2, which is important in surface diffuser analysis since including too many receivers in this region can dominate the outcome of any diffusion metric [28]. Cox and D'Antonio [3] suggested that in future revisions of guidance document AES-4id-2001 [28] a more suitable definition of the specular zone may be considered in terms of Fresnel zones. This for the case of the shadow zone is considered below.

Consider the case shown in Figure 3.8, illustrating the diffraction at a small aperture for a receiver located at a distance, r, away from a source.
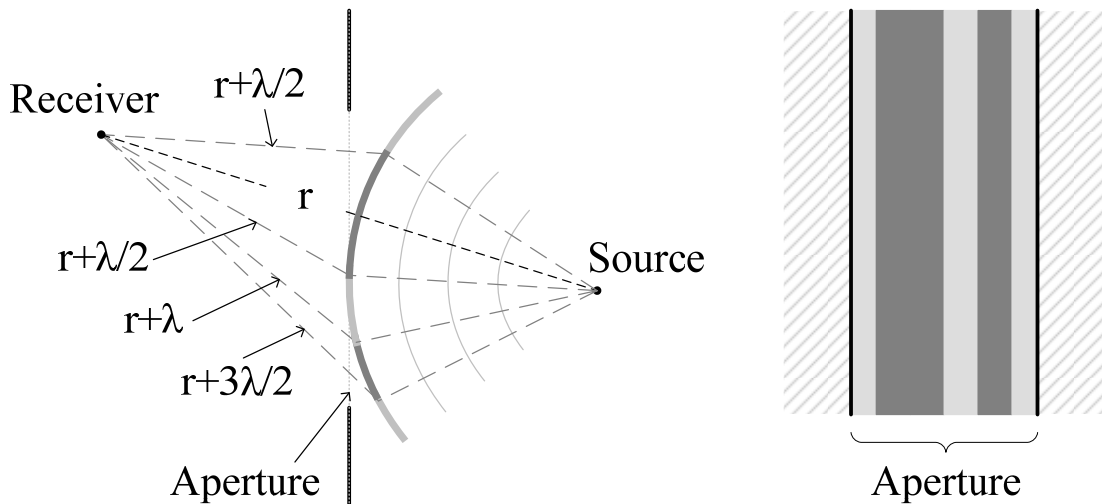
Figure 3.8: Pressure field at a receiver through a slit, considered in terms of Fresnel (half-period) zones; geometry (left), and as viewed by the receiver (right)

The wavefront is assumed to propagate according to Huygen's-Fresnel Principle, that is:

"Every unobstructed point of a wavefront, at a given instant, serves as a source of spherical secondary wavelets (with the same frequency as that of the primary wave)." [50]

The field considered at any point behind the obstruction may be obtained by summation of all the secondary wavelets, taking into account their respective amplitude and phase [50]. For the case illustrated in Figure 3.8, this simply implies a summation of the pressures incident upon the aperture, assuming the remaining incident field to be blocked by the rigid obstruction.

Following from this, Figure 3.8 shows the initial wavefront that will pass through the aperture divided into a set of regions. The extents of these regions is determined by the point at which a difference in path length to the receiver relative to the direct path is equal to an integer multiple of half a wavelength. These are therefore frequency dependent and are known as Fresnel zones or half-period zones [50], highlighted here by two alternating shades of grey, whose contributions will be successively in and out of phase with one another. Consequently their pattern, along with their respective amplitudes and obliquity factors, will help determine the resulting interference pattern observed at a receiver.

A full solution for the pressure at a point may be obtained via integration of the incident pressures across the aperture. The above however serves to demonstrate the influence of constructively and destructively interfering parts of the wavefront. Figure 3.9 (top) shows the far-field normal incidence equivalent to that shown in Figure 3.8 for a slit of width, D. At low frequency, and for receiver angles close to $\theta = 180^{\circ}$, only one Fresnel zone is observed and the result is constructive interference. With increasing frequency and/or angle however the number of Fresnel zones increases and the total field forms a fringe pattern, alternating between cancellation and sidelobes of decreasing amplitude.

When considering the extents of a shadow zone it is the diffraction around an object which is of concern; the inverted case where the slit is substituted for a flat plate of equal width, D, with free space either side as shown by Figure 3.9 (bottom). The total pressure at a given receiver may then be expressed as the integration of the pressure incident upon the aperture from minus to plus infinity with no obstacle present (the incident field), minus the integration evaluated over the extents of the slit (Figure 3.9 top). This means that the scattered pressure

behind the plate is simply equal to the negative version of the total pressure through a slit of equal size. Note here the switch in phase of the Fresnel zones illustrated in Figure 3.9 (bottom). This is analogous to the far-field scattering predicted by Eq. 2.21 for a rigid flat plate, where the forward-scattered pressure is given as the negative version of the back-scattered pressure. The scattered pressure behind the flat plate is hence, assuming far-field conditions, approximately proportional to the sinc function, an example of which was illustrated in Figure 3.5 for a number of frequencies.
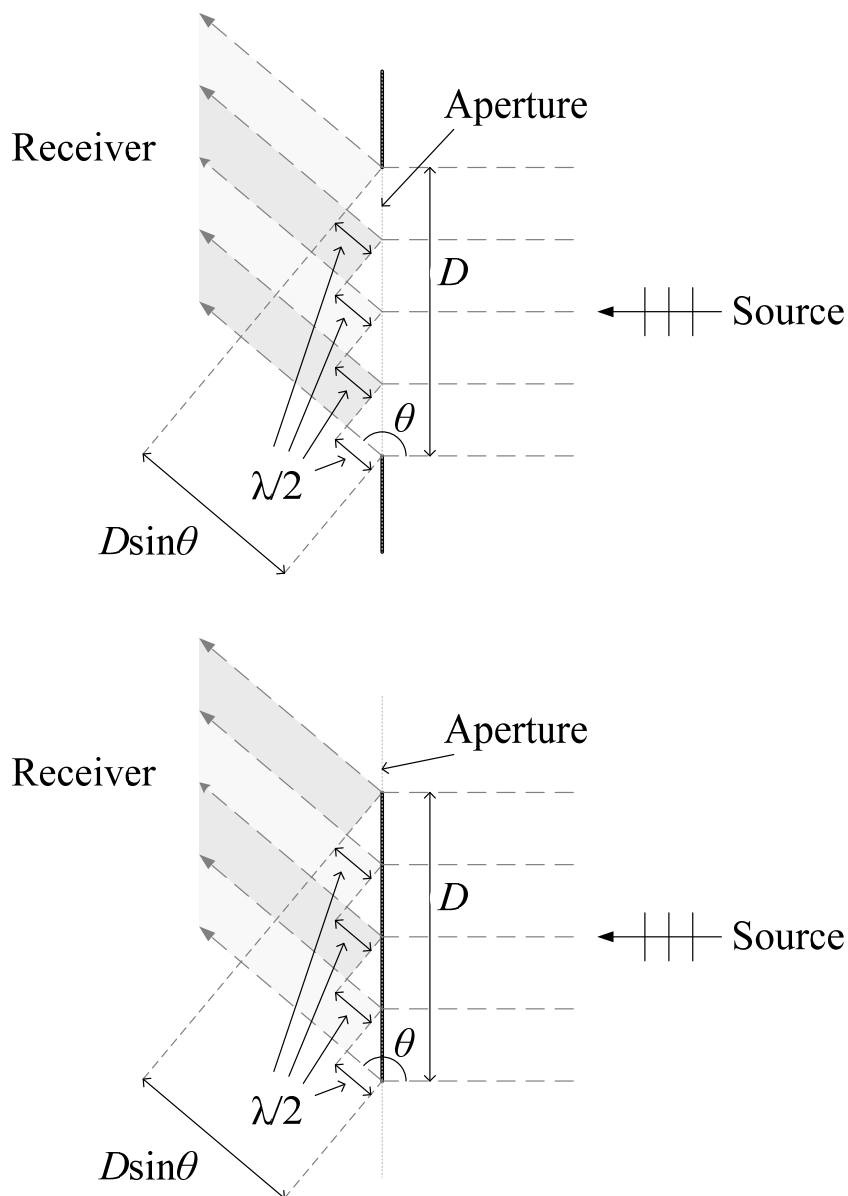
Figure 3.9: Diffraction through a slit – total field (top) and around a flat plate – scattered field (bottom), considered in terms of Fresnel zones

It is the extent of the interference zone however that must be defined. It is not possible to define these extents exactly as the border will likely be blurred, though an approximation may be given by estimating the size of the main (zeroth order) lobe. Following from Figure 3.9, assuming far-field conditions the frequency dependent receiver angles $\theta(f)$ defining the extent of the nth Fresnel zone may be given as:

$$\theta(f) = 180° \pm \sin^{-1}\left(\frac{n\lambda}{2D}\right) \qquad\qquad 3.3$$

Where n is an integer. The scattered pressure will display peaks and nulls when the plate width viewed from the source is equal to an odd and even number of Fresnel zones respectively. Consequently an approximation of the solid angle, $\psi(f)$, behind the diffuser encompassing the interfering scattered waves and defining the extents of the ISZ may now be given by:

$$\psi(f) = 2\sin^{-1}\left(\frac{\lambda}{D}\right) \qquad\qquad 3.4$$

Where the assumption has been made that the extents of the interfering scattered field may be described by the extents of the zeroth order lobe; that is $n = 2$ and the diffraction paths either side of the obstacle differ in length by one wavelength. The borders of this region hence occur when diffraction around either side of the object is coherent, resulting in little alteration to the incident field and consequently negligible scattered pressure.

The above has so far assumed that a diffusing object, when considered as an obstacle, may be approximated by the case of a flat plate of equal width, D. A diffuser however will likely have depth, leading to a maximum difference in diffraction paths greater than predicted. Figure 3.10 illustrates this for the case of a cylinder. Assuming the angle $\psi(f)$ to be small however, a high frequency approximation valid when $\lambda \ll D$, the cylinder will approximate the case of the flat plate.
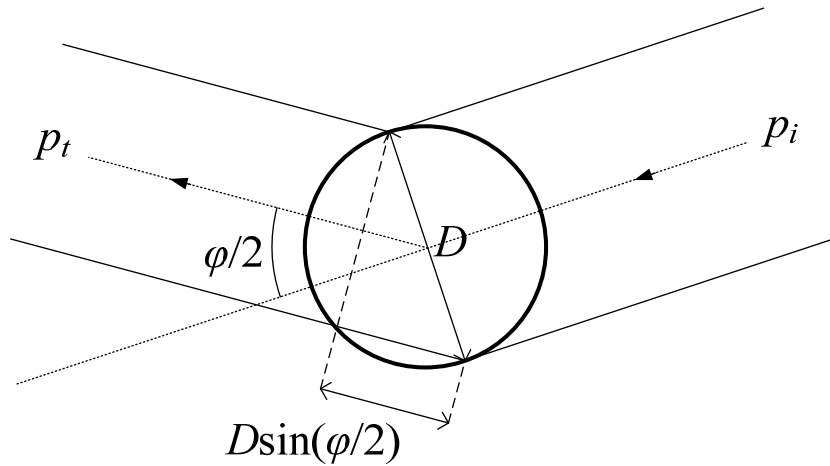
Figure 3.10: Error in approximating the diffraction around a cylinder by the diffraction around a flat plate

Figure 3.11 shows the scattered pressure map in the FSZ with distance for a cylinder of width, $D = 1.6$m, for frequencies of $f = 400$Hz (top) and 3kHz (bottom) respectively. The vertical dash-dotted line represents the approximate near-field / far-field boundary defined by Eq. 2.4; and the horizontal dotted lines represent the Fresnel zones according to Eq. 3.3, predicting the locations of pressure peaks and nulls either side of $\theta = 180°$ for odd and even values of n respectively.

For higher frequencies and for small angles, the Fresnel zones can be seen to accurately describe the locations of the peaks and nulls of the resultant fringe pattern. At low frequencies however, when wavelength becomes comparable to object size, the finite depth of the structure becomes significant, and here the predicted pressure peak / null angles are less accurate. For the $f = 400$Hz case shown this results in an error of approximately $6.5°$ in predicting the location of the first pressure null. Here though the error in terms of any diffusion coefficient will be less crucial, since with decreasing frequency the difference in diffracted path lengths around the object become small relative to wavelength. Furthermore the attenuation due to the structure will be low and consequently the interfering scattered waves are weak and the zeroth order lobe no longer dominates the scattered field. In the limit, when $D \leq \lambda$, the predicted pressure nulls either side of the zeroth order lobe occur at $\theta = \pm 90°$; that is $\psi(f) = 180°$, and the RSZ is identical to the BSZ.
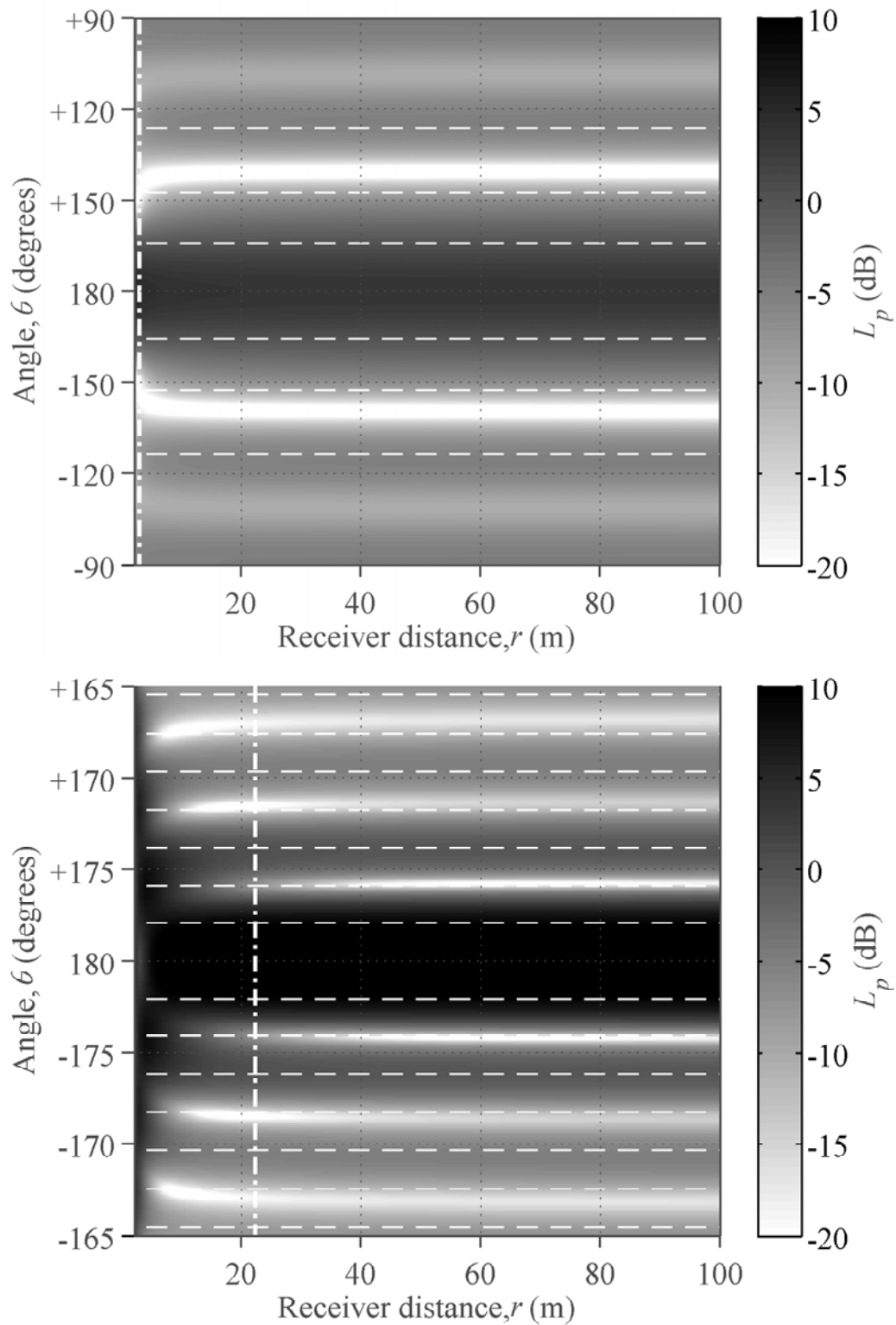
Figure 3.11 Normalised scattered pressure with receiver distance in the forward-scattered region for a single cylinder as per Figure 3.7, f = 400Hz (top) and f = 3kHz (bottom); Fresnel zone boundaries according to Eq. 3.3 (horizontal dashed lines) and far-field boundary as per Eq. 2.4 (vertical dot-dashed line)

Applying the above, a new coefficient may be considered evaluated over the RSZ. Figure 3.12 shows the variation in predicted diffusion coefficient for the cylinder as per Figure 3.11, evaluated over the BSZ, GVZ and RSZ for frequencies of $f = 1$kHz (top) and $f = 4$kHz (bottom) respectively. Ideally these should provide an asymptotic solution once far-field conditions are met, in a similar manner to that observed in guidance document AES-4id-2001 [28] when considering the maximum number of receivers allowed in the specular zone. The approximate boundary between near and far-field behaviour is illustrated by the vertical dash-dotted line.

For the back-scattered coefficient the result is consistent for virtually all distances tested. This is to be expected since as was shown in Figure 3.7 (top), the scattering from a cylinder in the BSZ is approximately constant once far-field conditions are achieved. Similarly the Fresnel zone coefficient tends toward a constant value, though of a slightly lower value due to the inclusion of the sidelobes in the forward-scattered direction. The geometrically defined coefficient however results in a value that decreases with distance, as the GSZ defined by Eq. 3.1 becomes progressively narrower, and more and more of the zeroth order lobe is included in the evaluation.

Based on the above a diffusion coefficient for volume diffusers is therefore proposed, considering all receiver angles within the RSZ. Unless otherwise stated, this coefficient is used throughout the results presented and hence shall be referred to simply as δ.
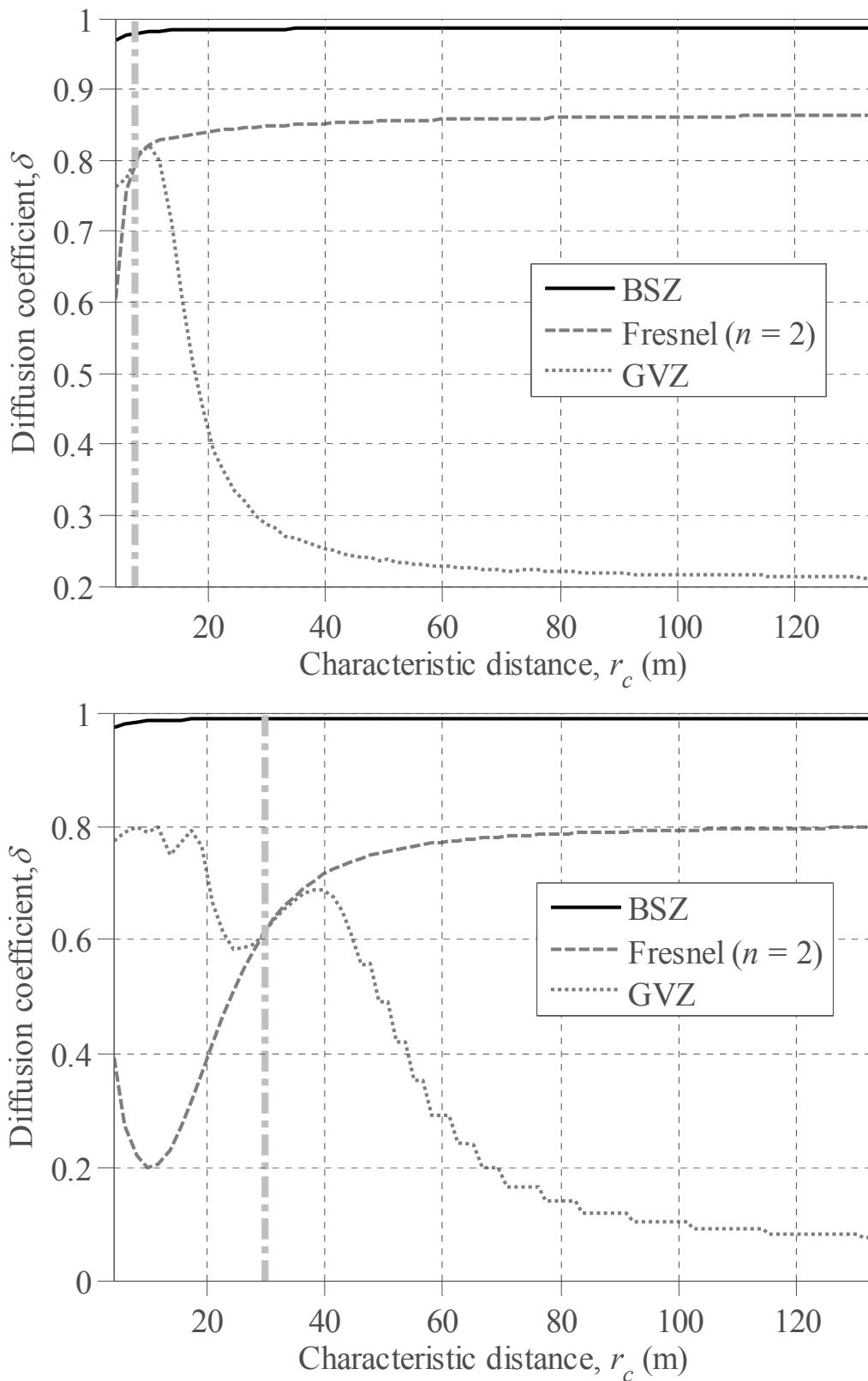
Figure 3.12: Diffusion coefficient with characteristic distance for the single cylinder as per

Figure 3.7, evaluated over the conventional back-scattered and proposed volume scattered

regions; f = 1kHz (top) and f = 4kHz (bottom)

3.3.3   A volume diffusion coefficient critique

Section 3.3.2 showed that it is necessary to differentiate between interfering and reflected scattered waves when considering a volume diffusion coefficient. For reasons discussed a straightforward geometric description fails to accurately separate the two and consequently a second coefficient was proposed, one evaluated over the RSZ. This has been considered in terms of a simple cylinder though it is necessary to test the coefficient on additional structures, particularly those that more accurately represent a volume diffuser, and this is considered below.

A single cylinder

Returning briefly to the case of a single cylinder, Figure 3.13 shows the new coefficient applied to the same case as Figure 3.7 (bottom) where the coefficient was evaluated over the GVZ.
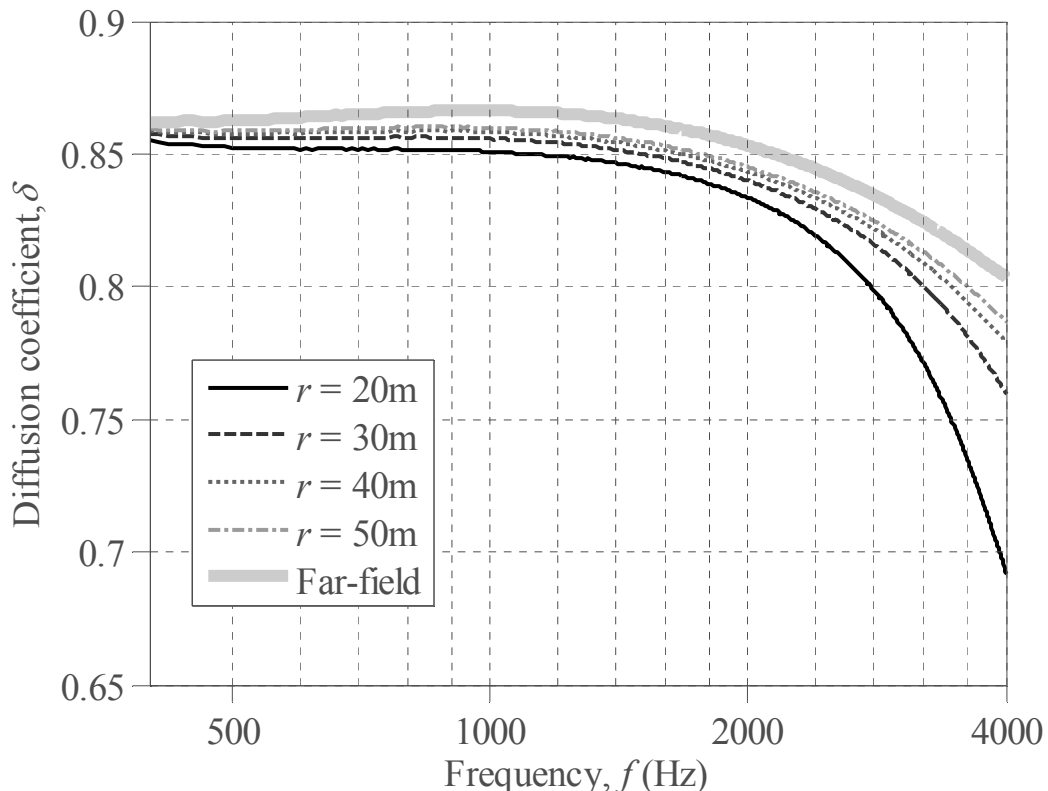
Figure 3.13: Diffusion coefficient for a single cylinder evaluated over the RSZ for a range of receiver distances; D = 1.6m, r_0 = 200m, θ_0 = $0°$; infinite far-field case modelled according to Eq. 2.23

With increasingly far-field conditions it can be seen that the RSZ coefficient tends toward the asymptotic far-field case, predicted using the far-field scattering from a cylinder formula given by Eq. 2.23. For frequencies less than approximately 2kHz the coefficient varies from that of the infinite far-field case by no more than 0.02. For higher frequencies however deviations of as much as 0.11 are seen for the smallest receiver distance. This is due to the pressure nulls in the forward scattered field to the rear of the cylinder, which require large distances before far-field behaviour is observed and the scattered pressure falls with 3dB per doubling of distance due to cylindrical spreading.

An array of cylinders

So far only solid structures have been considered, and so the above is an assumption based on the potential size of the attenuating lobe due to the diffraction around the extents of a structure. Most of the diffusers considered in the proceeding chapters however will allow transmission, and consequently their case is less straightforward. The effect of this however is generally to narrow the attenuating lobe in the shadow forming region.

Consider the case of the cylinder array arrangement given by Figure 2.27, subject to a normal incidence source. Figure 3.14 shows the normalised scattered pressure map with distance for the region towards the rear of a cylinder array, for frequencies of $f = 400$Hz (top) and $f = 3$kHz (bottom) respectively. As was described above, the effect of allowing transmission results in the zeroth order lobe in the shadow zone being slightly narrower than is predicted by the Fresnel zone estimate.

The effect on the diffusion coefficient evaluated over the RSZ is illustrated by Figure 3.15, showing consistent results for each of the receiver distances tested, with a maximum deviation between predictions of 0.08 occurring at high frequency. Note, the same source and receiver distances are used here as in Figure 3.13. In general it can be seen that the more random nature of the structure, coupled with its ability to allow transmission of energy, results in a coefficient exhibiting lower variation.
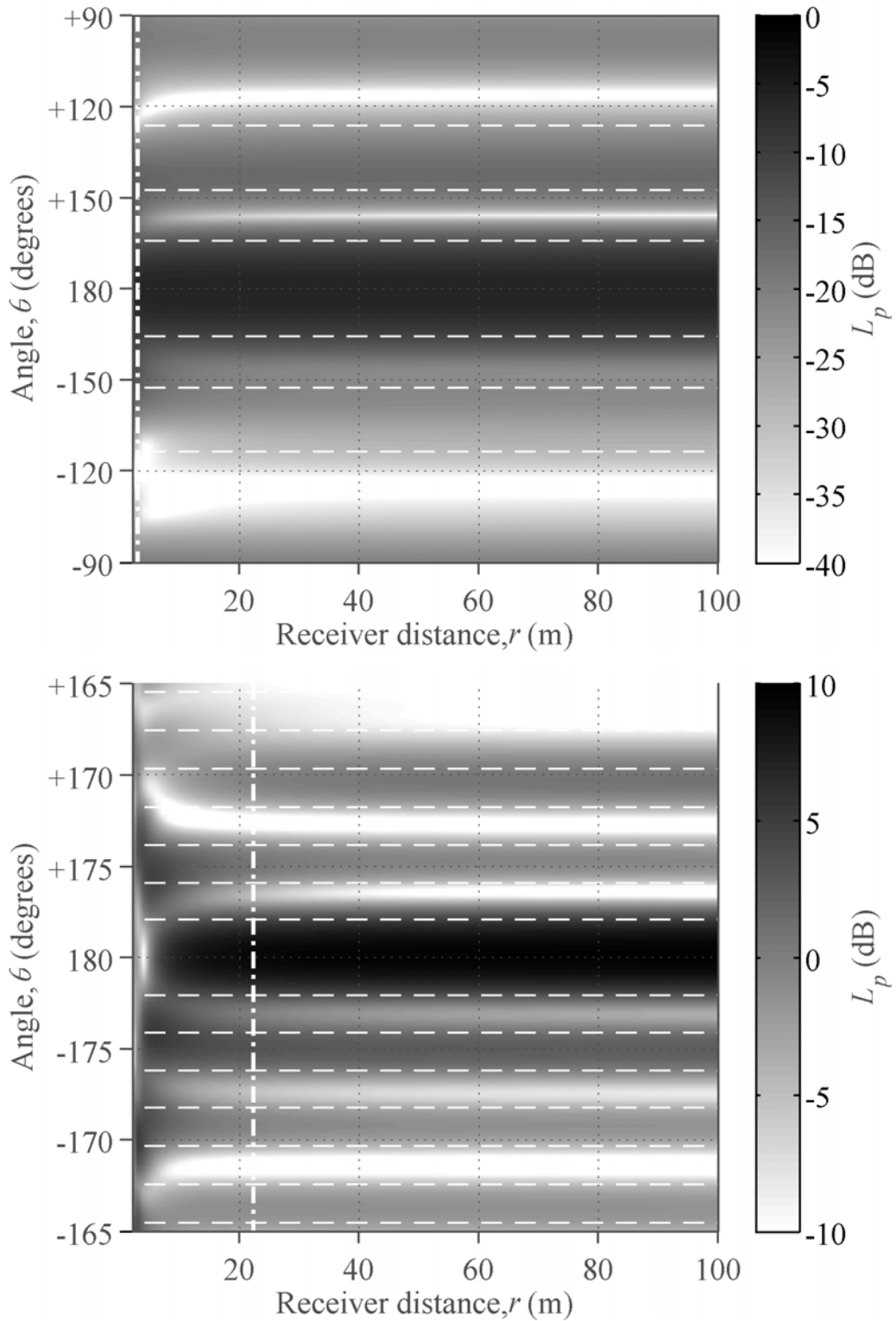
Figure 3.14: Normalised scattered pressure with receiver distance in the forward-scattered region for the cylinder array as per Figure 2.27; D = 1.52m, r₀ = 200m, θ₀ = 0°, f = 400Hz (bottom) and f = 3kHz (bottom); Fresnel zone boundaries according to Eq. 3.3 (horizontal dashed lines) and far-field boundary as per Eq. 2.4 (dot-dashed line)
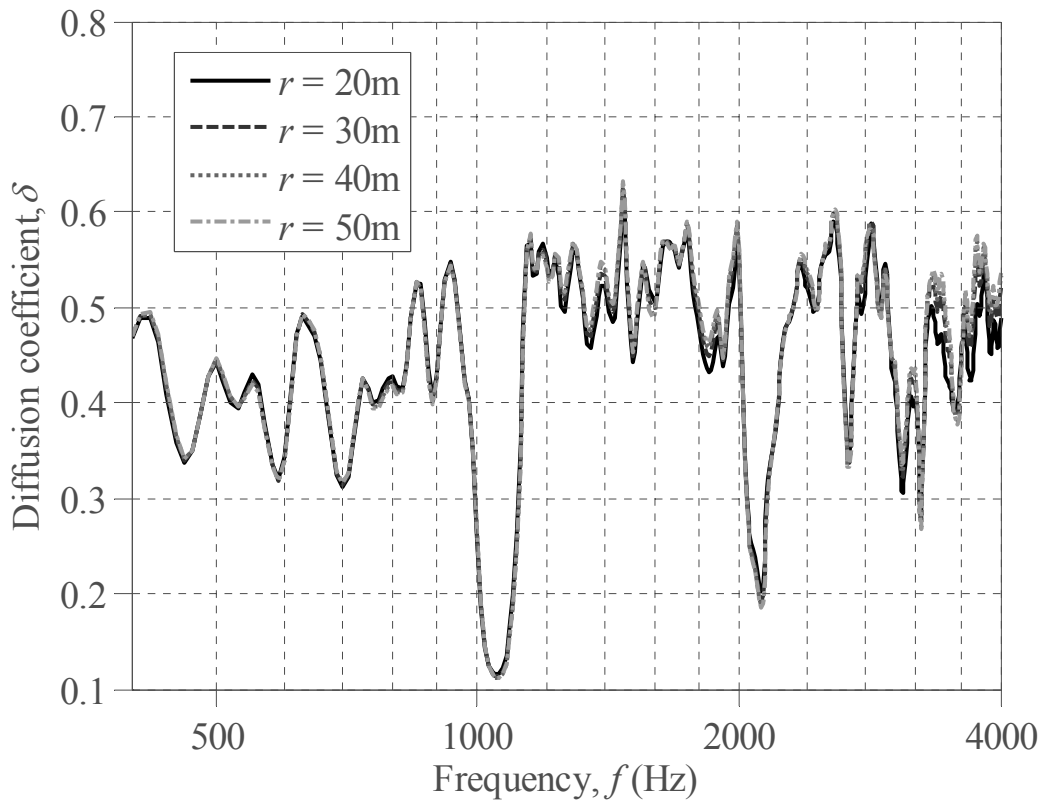
Figure 3.15: Diffusion coefficient for a cylinder array as per Figure 3.14 evaluated over the RSZ for a range of receiver distances

Percolation structure

Figure 3.16 shows the proposed diffusion coefficient for the percolation structure given by Figure 2.23. Much like the cylinder array, it is clear that the coefficient remains consistent across the frequency range considered. Note, due to the smaller nature of the structure the distances have been reduced. A maximum deviation in coefficient value of 0.06 is obtained for the distances tested, again providing generally consistent results for the majority of the bandwidth.
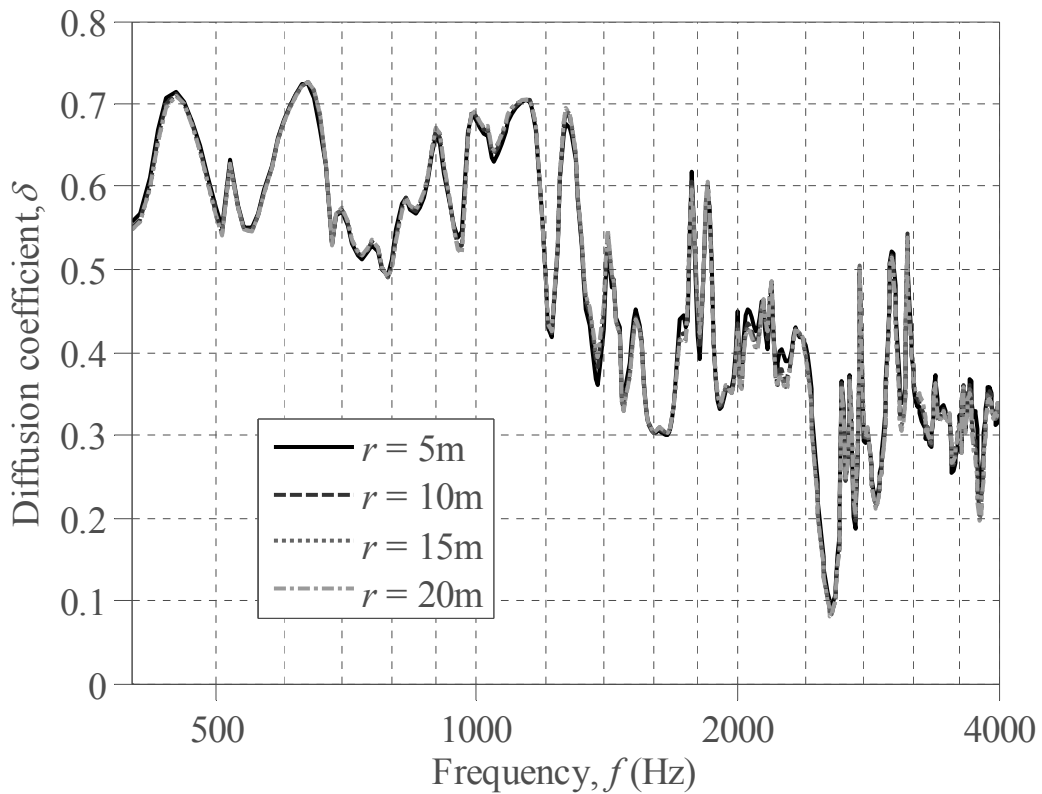
Figure 3.16: Diffusion coefficient for a percolation structure arranged as per Figure 2.23 evaluated over the RSZ for a range of receiver distances; D = 0.67m, $\theta_0 = 0°$, $r_0 = 40m$

Summary

In general the diffusion coefficient evaluated over the RSZ provides consistent results once far-field conditions are met, whilst providing a measure of the scattering uniformity over the majority of the scattered field. It should also be noted that these are single frequency values, and if for example one-third octave band results were to be calculated the variation would be significantly less.

It is apparent that the source and receiver distances required are greater than would be expected for a more conventional surface diffuser; that is more asymptotically far-field conditions are required. This is particularly evident for the single cylinder considered in Figure 3.13, due to the strong fringe pattern observed in the scattered field towards the rear of the object, and therefore the sensitive nature of defining a reflected / interfering boundary. It is important then to use large distances in calculations, however if measurements were to be performed in order to quantify diffusive performance, these distances would become

unrealistic and an alternative descriptor of the evaluated region may be required. This however is less of an issue once non-solid structures are considered; that is those that allow transmission.

An alternative would be to use the geometrically defined coefficient, though using closer source and receivers, since this increases the extents of the GSZ and tends to result in more stable coefficient values much closer to the Fresnel zone coefficient. This however is still inherently dependent on the distances used, and does not form a robust measurement procedure. A second alternative would be to define the solid angle $\psi(f)$ as a region encompassing a greater number of Fresnel zones by setting $n > 2$ in Eq. 3.3. This is possible, since in reality there will likely be a blurred boundary between reflected and interfering waves, and hence any region defined will be based on an inherent assumption of where best describes this boundary. This however would result in more of the scattered field being left out of the analysis. This is not ideal as the intention is to obtain a measure of volume scattering, where in terms of diffusion as much of the scattered energy as possible is assessed. Defining the interfering zone as per Eq. 3.4 however ensures that the majority of the scattered field is used in the analysis, whilst for the structures tested it has been shown that the interfering scattered component has little or no influence (adverse or otherwise) on the resulting coefficient.

3.4.   Scattered power

A diffuser whose elements are much smaller than the wavelength of an incident sound can scatter in a very even manner, however, it actually causes little perturbance to the sound field and is effectively almost acoustically transparent. For this reason the scattered power also needs to be considered. This is done via a scattered intensity ratio, L_{IR}. This compares the back scattered energy to that of a reference structure whose scattering properties are well understood – in this case a flat plate of equal width, D, to the diffuser - whilst normalising to account for differences in model setup.

The ratio is defined as:

$$L_{IR} = 10\log_{10}\left(\frac{\sum_{i=0}^{N-1}|p_{1,n}|^2}{\sum_{i=0}^{N-1}|p_{2,n}|^2}\right)$$

3.5

Where $p_{1,n}$ and $p_{2,n}$ are the scattered pressures at the nth of N receivers in the back scattered zone for the diffuser and reference structure respectively. It follows from the polar patterns illustrated by Figure 2.4 and presented in Sections 3.3.2-3.3.3, that if the envelope of the scattered pressure distribution in the far-field is independent of distance and alters only due to cylindrical spreading, then Eq. 3.5 will produce consistent results (assuming far-field conditions are met). This is illustrated by Figure 3.17, which shows the back-scattered intensity ratio defined in Eq. 3.5 for the cylinder array as per Figure 2.27 for a number of receiver distances. The maximum deviation between calculated L_{IR} values for the distances shown is 0.15dB.
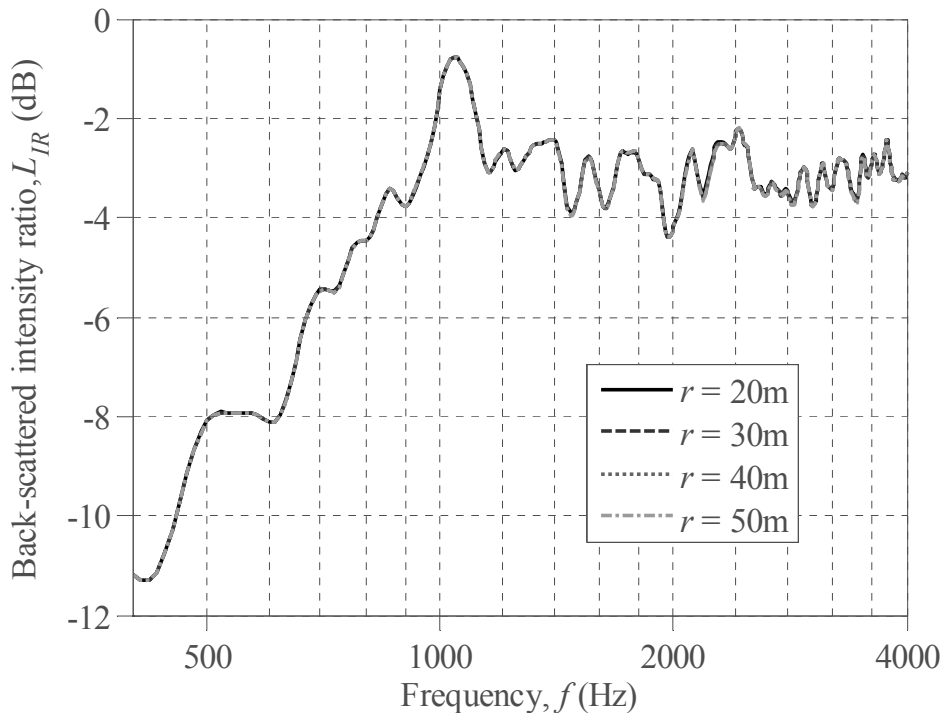
Figure 3.17: Back-scattered intensity ratio, L_{IR}, as defined by Eq. 3.5, for the cylinder array of Figure 2.27; D = 1.52m, r_0 = 200m, θ_0 = 0°

Design target

The choice of an appropriate scattered power target value will be dependent on application. Here a value of -3dB is suggested as a suitable design target for a volume array, since this means that half the incident energy relative to the reference plate is back-scattered. The reasoning behind this is that if half the energy is scattered into half of the space, and the scattering (evaluated over a region which includes this space) is uniform, then the diffuser should efficiently volume scatter all energy incident upon the structure in an even manner over all appropriate directions. It should be noted however that the choice of -3dB is somewhat arbitrary, and it would be possible to design for other target values.

3.5.   Conclusions

This chapter has presented suitable metrics for the analysis of the free-field polar response of a 2D planar volume diffuser in order to measure its diffusive efficacy. This builds upon existing metrics currently in use in surface diffuser design, presenting new coefficients that allow the concept to be extended to a volume equivalent. This allows the diffusive performance to be characterised in a way that reduces the amount of data to be analysed to a more manageable level.

A number of regions have been defined that help to highlight the key differences between a volume and surface diffuser. This in terms of more conventional metrics has been discussed. Based on this, three new coefficients have been proposed: a diffusion coefficient for comparison with surface diffusers; a volume diffusion coefficient, and a back-scattered intensity ratio.

A coefficient for comparison with existing surface diffusers is important, as this helps to provide a comparison of performance with structures that are well understood. The development of a new volume diffusion coefficient required a modification to the existing surface diffuser metric since, due to allowing diffraction around and/or transmission through a structure, the scattered field towards the rear of a volume diffuser is inherently different and cannot be used in the analysis. A simple geometric assumption was shown to be unable to describe the border between these two reflecting and interfering regions. To allow a more precise separation a frequency dependent descriptor was required, and is defined in terms of

Fresnel zones. This has been shown to provide consistent values once far-field conditions are met. Finally a measure of scattered power has been presented, allowing a measure of scattering efficiency.

4. PSEUDORANDOM ARRAYS OF SLATS

4.1. Introduction

In Chapters 2 and 3, a methodology for exploring the effectiveness of a volume diffuser was presented. In this chapter these techniques are used to assess the value of the first of the proposed new types of diffuser based on an array of slats, an example of which was introduced in Chapter 2.

An array of slats is a set of thin rigid, and usually parallel, strips arranged in some pre-determined way. This chapter firstly considers a single layer of periodically spaced slats, such as the array shown in Figure 2.21. The array is similar in concept to the canopy arrays introduced in Chapter 1, and may be thought of as a volumetric equivalent to the Binary Amplitude Diffuser (BAD). This allows an extension of the number theoretic concepts often applied in surface devices to a volumetric design, though now utilising transmission rather than absorption.

An extension to the above is a multi-layered concept, whereby each layer provides potential for 'additional diffusion' as sound propagates through the array. An example of this is shown in Figure 4.22. This structure type also provides depth, allowing the reflected wavefront to be altered in phase. Multi-layer structures spaced both periodically and aperiodically are investigated, and the effects of varying the slat size, structural dimensions, line-of-sight and spacing are discussed.

In this chapter it is shown that sequences whose spatial distribution is least self-similar tend to provide the greatest level of diffusion. Periodic spacing between layers however produces the equivalent to the flat plate frequencies observed in Schroeder diffusers, and therefore aperiodic or oversampled arrangements are preferred. At low frequency scattered power is determined by object size, whilst at high frequency is dominated by line-of-sight. This however implies a sparse array with large objects: two conflicting physical properties. A solution is proposed whereby slat size varies with structural depth, with layers being 'tuned' to a specific frequency range.

Unless otherwise stated, all results presented in this chapter are from predictions carried out using the thin panel BEM model presented in Section 2.3.2, shown in Section 2.6.1 to provide close agreement with experimental measurements.

4.2. A 1D slat array

4.2.1 A volumetric equivalent to BAD panels

Section 1.3.2 introduced the concept of amplitude diffusers; structures that perturb an incident wavefront by altering the amplitude of the reflected energy resulting in dispersion. A Binary Amplitude Diffuser (BAD) [13; 14] for example comprises a series of reflecting and absorbing strips arranged according to a unipolar binary sequence, s_n, with a value of 1 or 0 representing total reflection and total absorption respectively. An example of this is illustrated by Figure 4.1 (left), where the surface pattern is determined by a length 7 Maximum Length Sequence (MLS), a sequence type often used in BAD design [3].
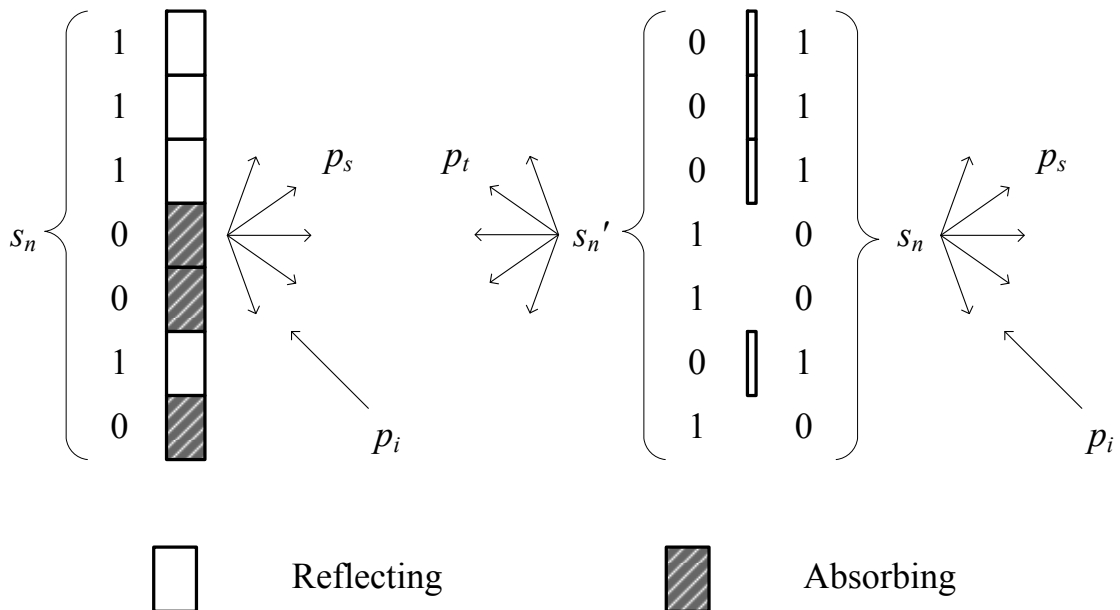
Figure 4.1: Cross-section of a BAD panel (left) and its volumetric slats equivalent (right); surface patches arranged according to the Maximum Length Sequence (MLS) [1 1 1 0 0 1 0]

Extending the concept of the BAD panel, a volume equivalent would be placed in the body of a room. The use of absorption in this case however is not necessary, as these elements may simply be omitted, allowing transmission rather than removal of energy. This is particularly

advantageous where preservation of energy is desirable because sound passing through the array is not lost, and will continue to propagate within the space. In addition to this the 'perfect absorber' assumed in conventional BAD theory – which in reality is not possible – is no longer required. This means that the array should more closely match the original design theory; the 'idealised' case with complete absorption. It should be noted that the incomplete absorption can in some cases actually lead to greater levels of dispersion [51], though this is not considered here.

The result of the above is a single layer of reflecting panels with intermediate gaps, similar in concept to the canopy arrays introduced in Section 1.4.3. Since there is no need for depth to achieve absorption, these panels can be chosen to be thin relative to wavelength, forming what shall be referred to as a one-dimensional array of slats. An example of this is depicted in Figure 4.1 (right); the volumetric equivalent to that of Figure 4.1 (left). In the back-scattered direction, as with the BAD panel, an incident wavefront will encounter a surface determined by the sequence, s_n. This means that both structures should display similar back-scattered pressure distributions. In the forward-scattered direction however the slats array will also have a sequence which determines transmission (neglecting diffraction around the sides), $s_n' = 1-s_n$; an orthogonal sequence where each 1 becomes a 0 and vice-versa. This however will act upon the total pressure transmitted through the layer.

Scattering from a real BAD panel

To enable a comparison between the scattering from a 1D slat array and its corresponding surface BAD, an equivalent BAD panel to the slats array in Figure 2.21 was constructed as shown in Figure 4.2. This was built using the same 12mm thick high-density fibreboard as the slats array, and was also 600mm in height. Absorption was achieved via strips of 50mm deep open-cell foam mounted in the 'wells' of the diffuser. The structure was set into the floor to minimise reflections off the base, and the centre of the front face of the structure was positioned at the origin of the coordinate system to most closely match the scattering from the slats. The diffuser was modelled using the standard BEM routine described in Section 2.3.1. The surface admittance for the absorption was assumed to have a value (when normalised to the characteristic impedance of air) of $1+0 \times j$ – that is all incident energy is absorbed – with the remaining surfaces assumed to be rigid. This was done to allow a comparison with the slat array, for which total transmission is the equivalent of total absorption.
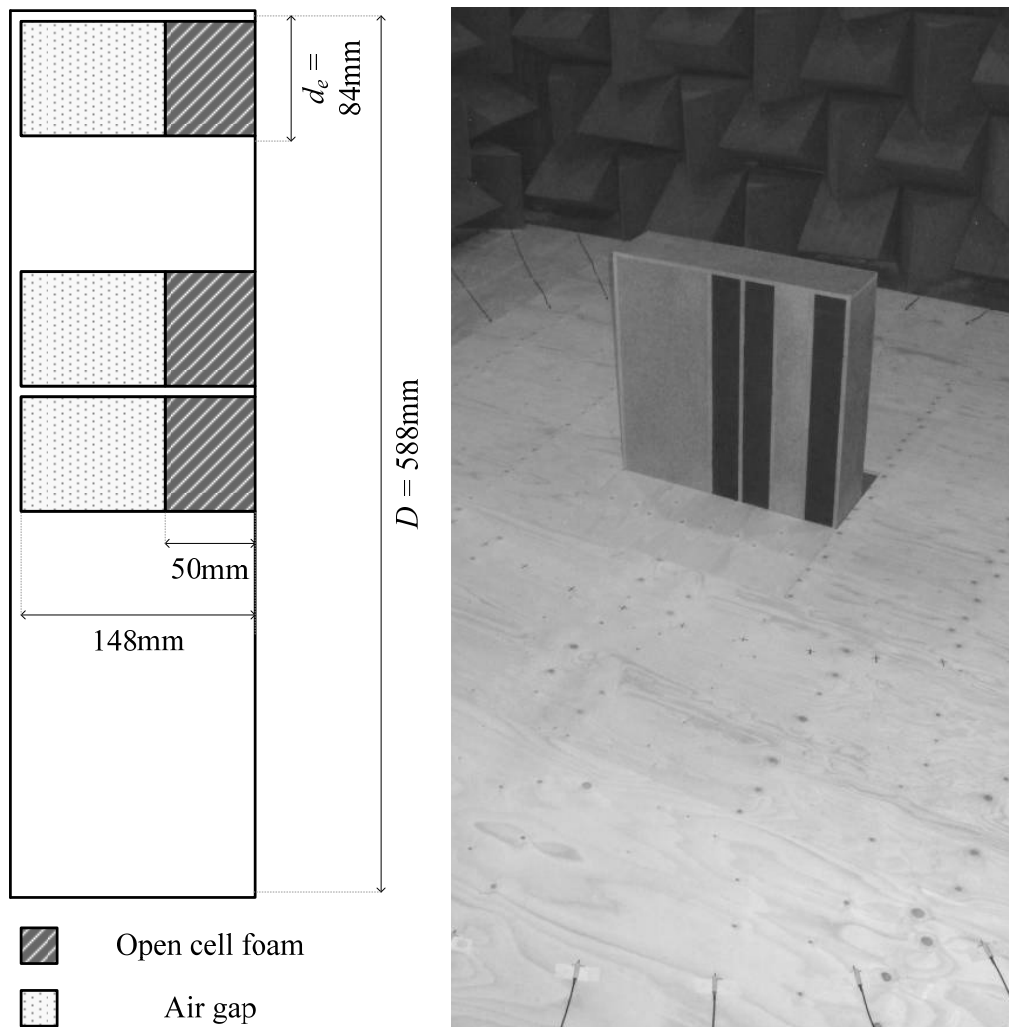
Figure 4.2: Binary Amplitude Diffuser (BAD) arranged according to a Maximum Length Sequence (MLS) [1 1 1 0 0 1 0], arrangement (left) and measurement sample constructed at full scale (right)

Figure 4.3 shows the BAD panel measured and modelled scattered pressure polar response for the $\theta_0 = 0°$ case for frequencies of $f = 2kHz$ (top) and $f = 4kHz$ (bottom) respectively. These also include the equivalent slat array modelled using the thin panel BEM, shown previously in Section 2.6.1 to agree well with measurements. Reasonable agreement is seen between the measured and modelled BAD results, with an average error over the frequency range 1.0-8.0kHz of 2.9dB, though accuracy is reduced at low frequency and at grazing receiver angles due in particular to the assumption that the foam strips provide total absorption. More accurate results should result if more realistic admittance values were used for the absorption, gained for example from an empirical approach such as the Delany and Bazley model [3] or from measurements in an impedance tube [51].
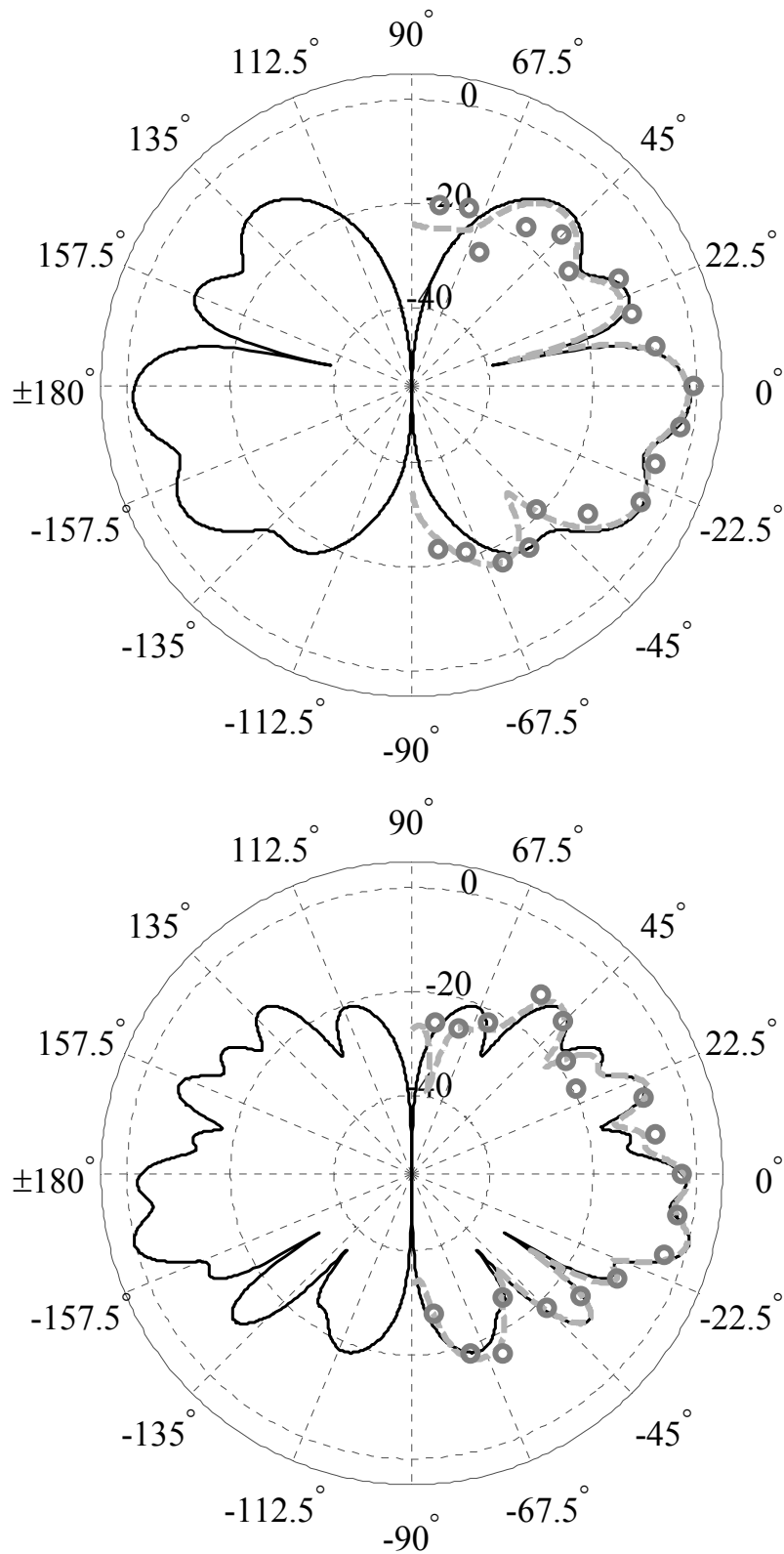
Figure 4.3: Measured (⊙) and modelled (– –) normalised scattered pressure polar response for the BAD of Figure 4.2, including equivalent slats array modelled using the thin panel BEM (──); $\theta_0 = 0°$; f = 2kHz (top) and f = 4kHz (bottom)

In the back-scattered direction, as expected, both the slats and the BAD panel display very similar behaviour. This demonstrates that the absorption of the BAD and open gaps of the slats are performing a very similar role, 'removing' back-scattered energy via absorption and transmission respectively. Since the BAD panel is a surface diffuser the scattered pressure in the forward-scattered region is not included. For the slats array however (due to the infinitely thin panel assumption) the polar pattern is symmetric about the *y*-axis, though with the forward-scattered pressure being of opposite phase to that of the back-scattered.

4.2.2 A simplified model of scattering

The above has modelled the scattering from a slat array using a thin panel BEM. In order to understand some of the basic principles behind the scattering from such an array however, a simplified model may be used. Consider the structure shown in Figure 4.1 (right). Assuming the strips to be spaced an equal distance, d_y, apart (centre to centre) this structure may be modelled according to the approximation given by Eq. 2.16, which considers a set of periodically arranged scattering elements. The amplitude coefficient for the nth scattering element (strip), A_n, is determined by the sequence, s_n; and the scattering from an individual element, $e(\theta_0, \theta)$, is given by the scattering from an individual strip, as approximated by Eq. 2.21. To compare the scattering with that of the normalised scattered pressure, using the method described in Section 2.5.2, the far-field approximation of the 2D Green's function given by Eq. 2.7 is required. This may be derived using the asymptotic expansion of the Hankel function [43]. In the far-field the incident pressure at the reference receiver, $p_{i,ref}$, is approximately given as:

$$p_{i,ref} \approx -\frac{(1+j)}{4\sqrt{\pi k(r+r_0)}} e^{jk(r+r_0)} \quad ; \qquad k(r+r_0) \gg 1 \qquad\qquad 4.1$$

An approximation to the normalised far-field scattered pressure, $p_{s,norm}(\theta_0, \theta)$, from an array of slats may therefore be given as:

$$p_{s,norm}(\theta_0,\theta) \approx d_e \cos(\theta)\frac{(1-j)}{\sqrt{2}}\sqrt{\frac{1}{\lambda}}\,\text{sinc}\left(\frac{kd_e}{2}(\sin\theta+\sin\theta_0)\right) \times$$
$$\sum_{n=0}^{N-1} A_n e^{jknd_y(\sin\theta+\sin\theta_0)} \qquad\qquad 4.2$$

Where since these strips can form a continuous surface (where adjacent slats are conjoined), the element width and element spacing are equal; that is $d_e \equiv d_y$. This method is often referred to as the Fourier approximation, as the summation in Eq. 4.2 represents a Discrete Fourier Transform (DFT) of the coefficients A_n, where $p_{s,norm}(\theta_0, \theta)$ is the angle dependent scattered pressure in the $d_y(\sin\theta+\sin\theta_0)/\lambda$ domain.

Optimal arrangements

To achieve even scattering with receiver angle a set of amplitude coefficients, A_n, is desired whose DFT is maximally flat. This is because the receiver angles of the Fourier Transform correspond to the grating lobe angles, and consequently when the sequence is periodically repeated these values will be emphasised [3]. The Wiener Khinchin theorem states that the power spectrum of a sequence is equal to the Fourier Transform of its Autocorrelation Function (ACF) [3]. This implies that a series of coefficients whose ACF is most like a Kronecker delta function is desirable, since this should result in a flat power spectrum and hence provide even scattering. An example of this is illustrated by Figure 4.4, showing the ACF (top) and power spectrum (bottom) for a length 7 MLS [1 1 1 0 0 1 0].
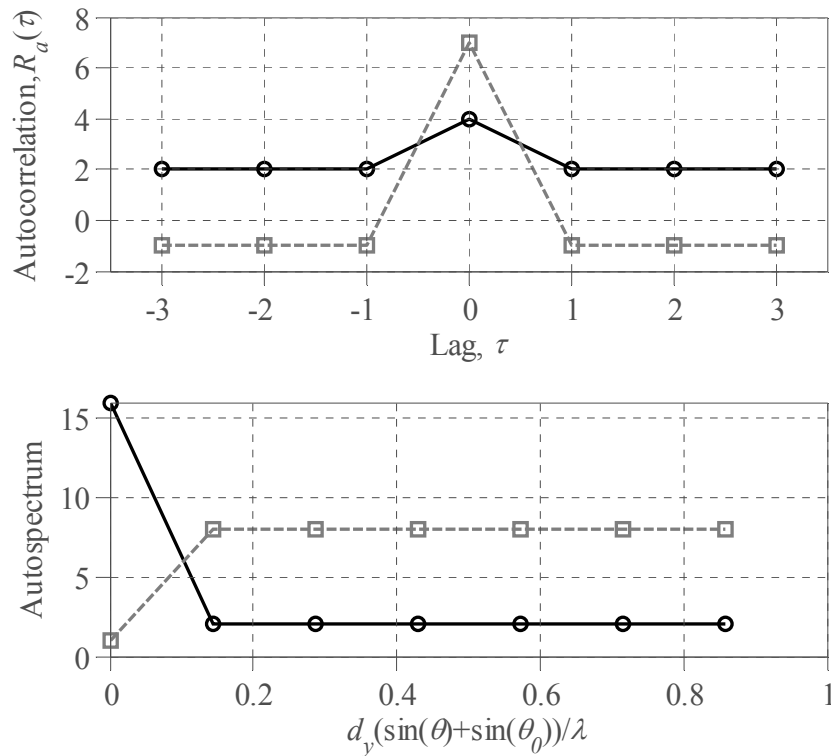
Figure 4.4: Autocorrelation function (top) and power spectrum (bottom) for a unipolar MLS [1 1 1 0 0 1 0] (━o━) and equivalent bipolar MLS [1 1 1 -1 -1 1 -1] (╍□╍)

A perfect ACF is one whose sidelobes ($\tau \neq 0$) are all equal to zero. Due to their unipolar nature however amplitude diffusers are unable to achieve this, and optimum sequences such as the MLS shown are those with a constant (positive non-zero) value for all out of phase ACF shifts. This is because unlike sequences which impart a phase change – an example of which is the equivalent bipolar MLS also shown in Figure 4.4 – they are unable to create cancellation. Consequently the DC peak in the power spectrum is large, which corresponds to a strong specular reflection [13]. This means that the best amplitude devices are those that disperse their reflected energy evenly into the remaining non-specular receiver angles.

Figure 4.5 shows a comparison of the predicted scattering from an array of slats modelled using both the thin panel BEM and the Fourier approximation. The array comprises three periods of the unipolar MLS sequence of Figure 4.4, with element width $d_e = 10$cm. The accuracy of the Fourier approximation is limited by the same factors that affect that of a single element, as discussed in Section 2.4.2. At low frequency when wavelength is much larger than the width of an individual element this results in a general overestimation of the scattered pressure, due to neglecting the pressures on the rear of the panel. For mid-to-high frequencies the Fourier method tends to underestimate the scattered pressure for receiver angles close to grazing, as the interactions across the surface are ignored [37]. For the slat array shown this results in an average difference of 6.2dB relative to the thin panel BEM over the frequency range 400Hz-4kHz; the shape of the scattered field distribution however is well predicted.

Diffusive performance

The diffusion coefficient for the above slats array is shown in Figure 4.6, along with a flat plate of the same overall width, $D = 2.1$m, for reference. Note this is the volume diffusion coefficient as defined in Section 3.3.2. The coefficient obtained from a simplified Fourier approximation is also included; one that models the structure as a set of point scatterers. At very low frequency the main specular lobe dominates and the slats array and flat plate behave similarly. The array begins to diffuse relative to the flat plate at approximately $f = 500$Hz; when the period width is equal to a wavelength and the first grating lobe appears (Figure 4.5, top right).

f = 250Hz

f = 500Hz

f = 1.0kHz

f = 2.0kHz
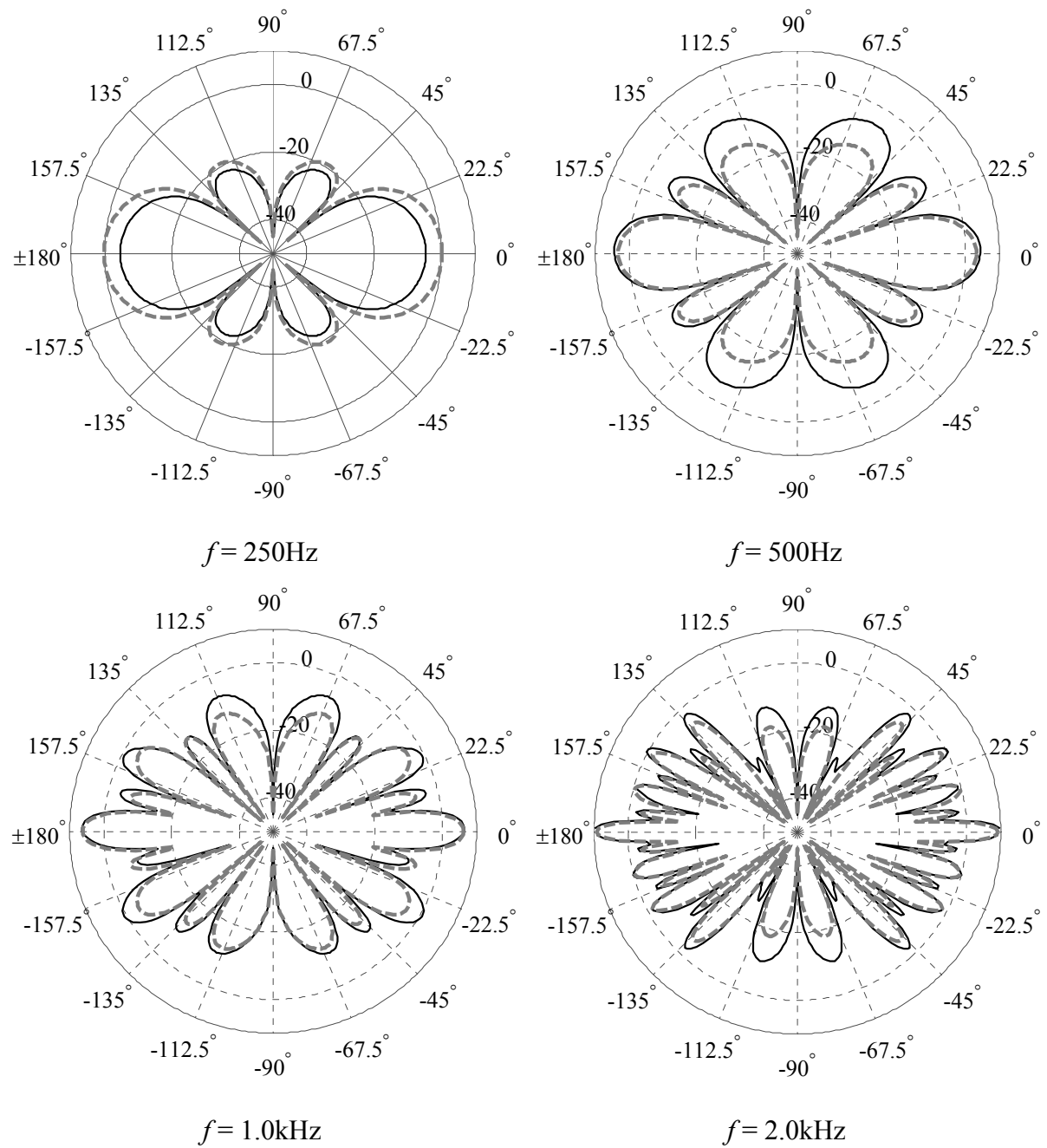
Figure 4.5: Normalised scattered pressure polar response for a 1D array of slats comprising 3 periods of the sequence s_n = [1 1 1 0 0 1 0]; thin panel BEM (━━) and Fourier approximation (━ ━); $\theta_0 = 0°$, $d_e = d_y = 10cm$; frequencies as listed
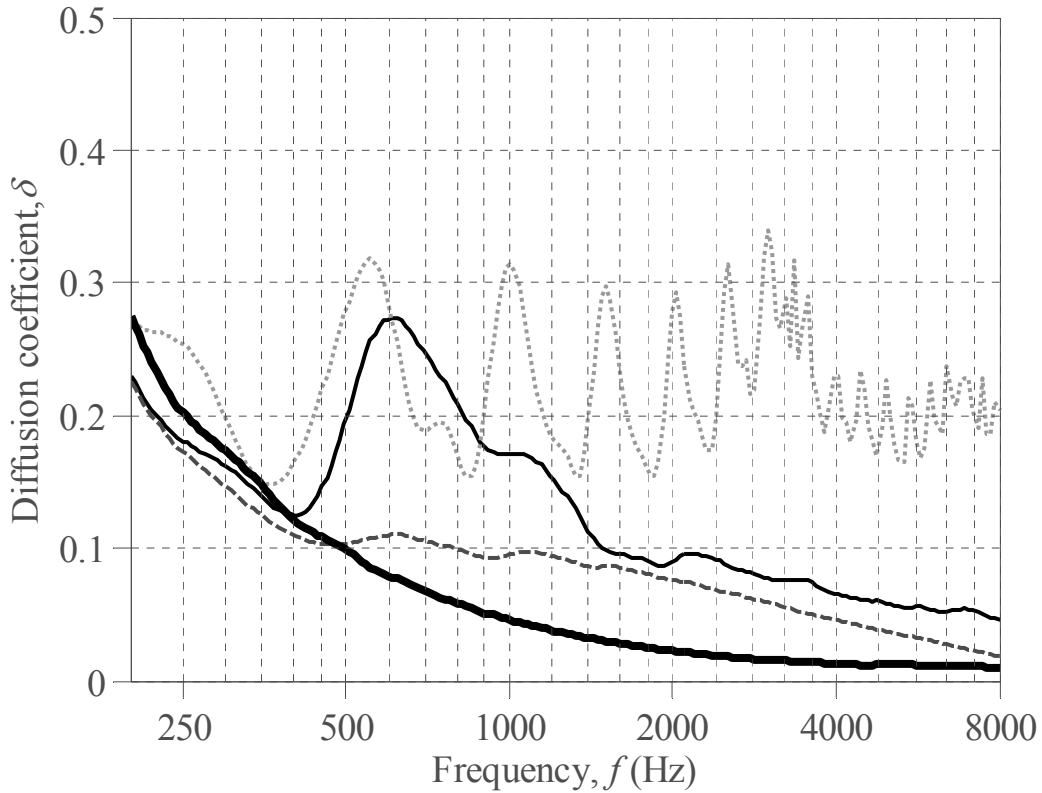
Figure 4.6: Diffusion coefficient for the slats array as per Figure 4.5; thin panel BEM (━), Fourier approximation (– –), simplified Fourier approximation (˗ ˗ ˗), and reference plate of width, D = 2.1m (▬)

Following from the above, a diffusing design frequency, f_0, may be given by:

$$f_0 = \frac{c}{P.d_e \lceil \sin(\theta_0) \pm 1 \rceil}$$

4.3

Where P is the number of slats per period, which for the example above is 7.

Due to the unipolar nature of the sequence the grating lobes are of a lower magnitude than the main specular component. Consequently the diffusion coefficient is generally lower in value than would be expected for a diffuser such as a Schroeder diffuser that allows cancellation. With increasing frequency progressively more of the grating lobes become visible, as can be seen in the polar plots of Figure 4.5, appearing at multiples of the design frequency. Due to the sequence repetition, the equal energy scattered into these angles is emphasised. For the Fourier approximation due to the reduced magnitude of the sidelobe behaviour predicted for angles close to grazing, the rate at which the diffusion coefficient increases is significantly

reduced relative to the thin panel BEM. Conversely the assumption of the simplified Fourier approximation that the slats scatter omnidirectionally results in an overestimate of scattering into the non-specular angles, and consequently predicts a much larger diffusion coefficient. In reality the magnitude of the scattering is somewhere between the two, though both provide an indication of relative diffusion between sequences.

For higher frequencies the scattering is dominated by the response of a single slat, with both the BEM and Fourier approximation predicting a progressively more specular reflection. This is an inherent limitation of conventional BAD diffusers, and leads to a gradual fall in the diffusion coefficient. To illustrate why this occurs Figure 4.7 considers the scattering predicted by Eq. 4.2 in terms of its sinc function (top) and summation components (centre), representing the response due to a single slat and the sequence arrangement respectively. Their combined response is given by Figure 4.7 (bottom). These (truncated) plots represent all frequencies simultaneously, with the area 'visible' in the scattered pressure polar response for a given frequency being dictated by the range covered by $d_y(\sin\theta+\sin\theta_0)/\lambda$. Due to spatial aliasing the scattering due to the arrangement repeats (Figure 4.7 centre), and consequently a simplified Fourier model predicts a series of peaks in the coefficient of Figure 4.6 occurring at multiples of the design frequency. The response of the element however, described by the sinc function (Figure 4.7 bottom), suppresses these grating lobes and progressively moves energy away from grazing receivers with increasing frequency. This causes the diffusion coefficient to fall.

Any upper boundary on diffusive performance will be less clear-cut than for the design frequency, f_0, given by Eq. 4.3, since the tail-off in diffusion is gradual. An approximate cut-off point however is given by the point at which the sinc function produces its first pressure null at grazing, which (for normal incidence) is when the slat width $d_e \equiv d_y$ is equal to wavelength ($d_y(\sin\theta+\sin\theta_0)/\lambda = \pm 1$ in Figure 4.7). This forms an approximate high frequency limit, f_{max}, of:

$$f_{max} \approx \frac{c}{d_e} \qquad\qquad 4.4$$
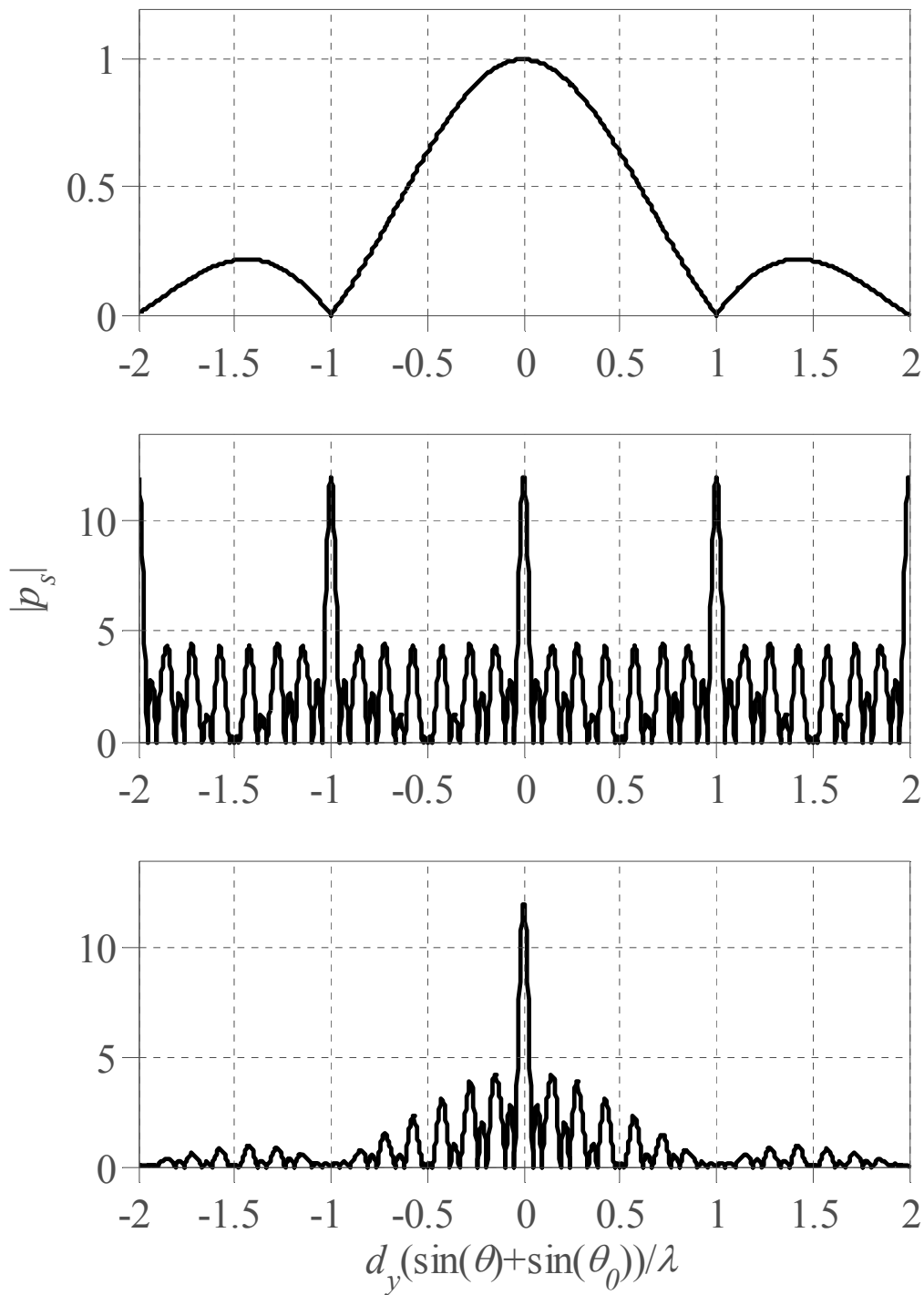
Figure 4.7: Approximation of the scattering from an array of slats comprising 3 periods of the sequence $s_n = [1\ 1\ 1\ 0\ 0\ 1\ 0]$; sinc function (top), array considered as point scatterers (centre), and their product (bottom)

The above results is an approximate $\log_2(P)$ octave bandwidth of diffusive performance over the frequency range $f_0 \leq f \leq f_{max}$, suggesting that a long sequence would be preferred. For the

$P = 7$ MLS shown in Figure 4.4-Figure 4.7 this results in an approximate 2.8 octave diffusive bandwidth over the frequency range $500\mathrm{Hz} \le f \le 3.5\mathrm{kHz}$. Note the upper frequency here is a measure of when diffusion begins to suffer and is not (as is the case with Schroeder diffusers for example) an upper limit to the design theory.

4.2.3 Optimal unipolar sequences

A flat Fourier spectrum as described above equates to scattering equal energy into the grating lobes, and this is what Schroeder described as 'optimal' diffusion [8]. Whilst this scatters in a controlled manner, this is not the same as even scattering into all angles. It is assumed here that a volume diffuser is not being placed alongside other identical units, and consequently it is the performance of a single sequence of length $N \equiv P$ that is important. In this case the Fourier approximation for the far-field polar pattern may be more accurately represented by the DFT of the amplitude coefficients padded with zeros (effectively representing free-space). The Aperiodic Autocorrelation Function (AACF) is therefore most appropriate to the work presented here, with a sequence whose AACF is most like a Kronecker delta function being most desirable.

Aperiodic sequences and the Golomb ruler

The AACF of a unipolar binary sequence can be described as the number of elements separated by each unique separation distance within a sequence [52]. An even spread of these separation distances is therefore sought. This is because any repetition will result in similarity between scattering from element pairs, leading to lobing and thus uneven scattering [53]. Conversely, an even spread of separation distances should avoid emphasis. Note, the ACF of a unipolar sequence may also be explained in this way, though this must be carried out in a circular fashion; that is modulo P.

In radar and sonar the AACF is often expressed in terms of redundancy [54]. A distance separation, or lag, is described as being redundant if it has one or more repetitions. An arrangement is described as being non-redundant if there are no redundancies, whilst a sequence with all possible distance separations with the least number of elements is said to have minimum-redundancy. One particular type of non-redundant sequence is given by the Golomb ruler [52], an example of which is shown in Figure 4.8 (left), an imaginary ruler

comprising a set of marks located at integer positions where no two marks are the same distance apart. The total number of marks on the ruler is defined as the order, and the maximum separation distance as the length, $L = N\text{-}1$. A Golomb ruler is said to be optimal if no shorter ruler of the same order exists, and is a special case of the non-redundant array referred to as the minimum hole array that minimises the number of holes (missing lags) in the AACF. A sequence with no holes is said to be a perfect Golomb ruler.
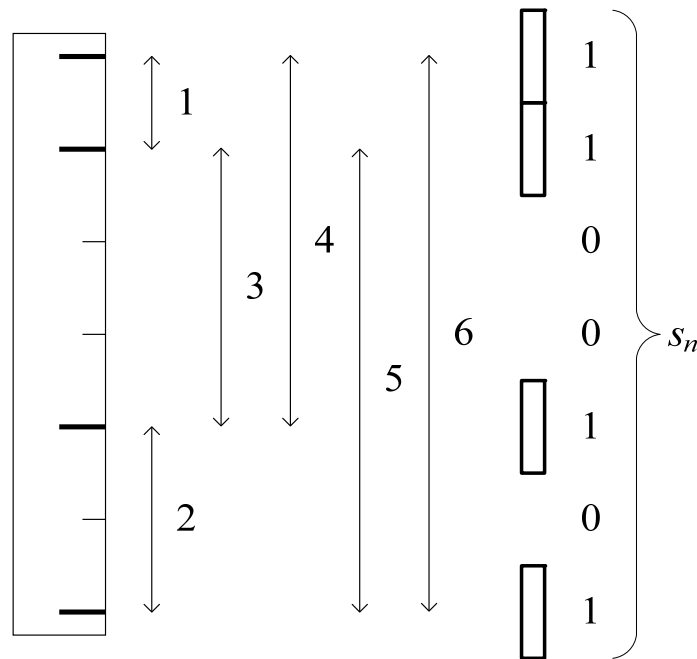
Figure 4.8: Slats array arranged according to an N = 7 (perfect) Golomb ruler

The corresponding slat array to the Golomb ruler above is given in Figure 4.8 (right), where each mark on the ruler corresponds to the inclusion of a slat. Figure 4.9 shows both the AACF (top) and power spectrum (bottom) for two cyclic variations of the same MLS, the first being the $N = 7$ perfect Golomb ruler of Figure 4.8. Whilst both sequences have an identical ACF their AACF is not the same; the Golomb ruler having a Kronecker delta like shape and the alternative MLS displaying both redundancy ($|\tau| = 3$) and missing lags ($|\tau| = 4$). The effect on the power spectrum (summation of Eq. 4.2 padded with zeros) is for the Golomb ruler sequence to produce a more even spread in its sidelobe energy, and consequently it would be expected to result in more even scattering.
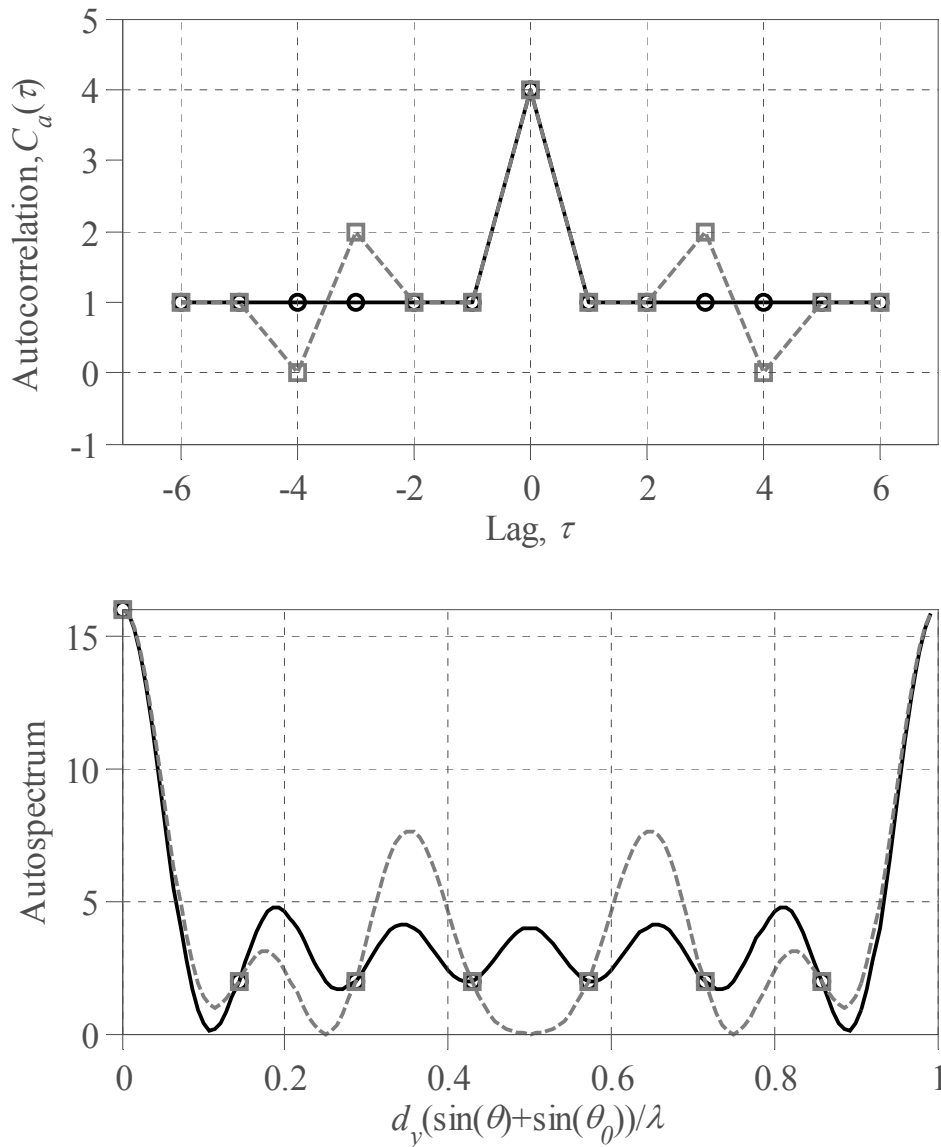
Figure 4.9: Aperiodic autocorrelation function (top) and power spectrum (bottom) for a
N = 7 Golomb ruler [1 1 0 0 1 0 1] (━o━) and MLS [1 1 0 1 0 0 1] (▪ □ ▪)

The resulting diffusion coefficient for an array arranged according to the two sequences above is shown in Figure 4.10. At low frequency the performance is similar to that of the reference plate, as the structures are small relative to wavelength. Both sequences however begin to diffuse relative to the flat plate at around the design frequency, f_0 = 500Hz. Note now the period length, P, and total sequence length, N, are equal since the sequence is not repeated, and diffusion results once wavelength is equal to the length of the whole array, D. Initially the Golomb ruler is outperformed due to producing a pressure null just before the appearance of the first grating lobe (see Figure 4.9, bottom). With increasing frequency however, and as

wavelength becomes comparable to the separation distances, progressively more of the sidelobe energy is seen and the Golomb ruler provides a more even spread of scattered energy. As with the periodic example of Figure 4.6, at higher frequencies a tail-off in diffusion occurs from approximately $f = f_{max} \approx 3.5$kHz due to the response of an individual slat, though the effect is gradual.
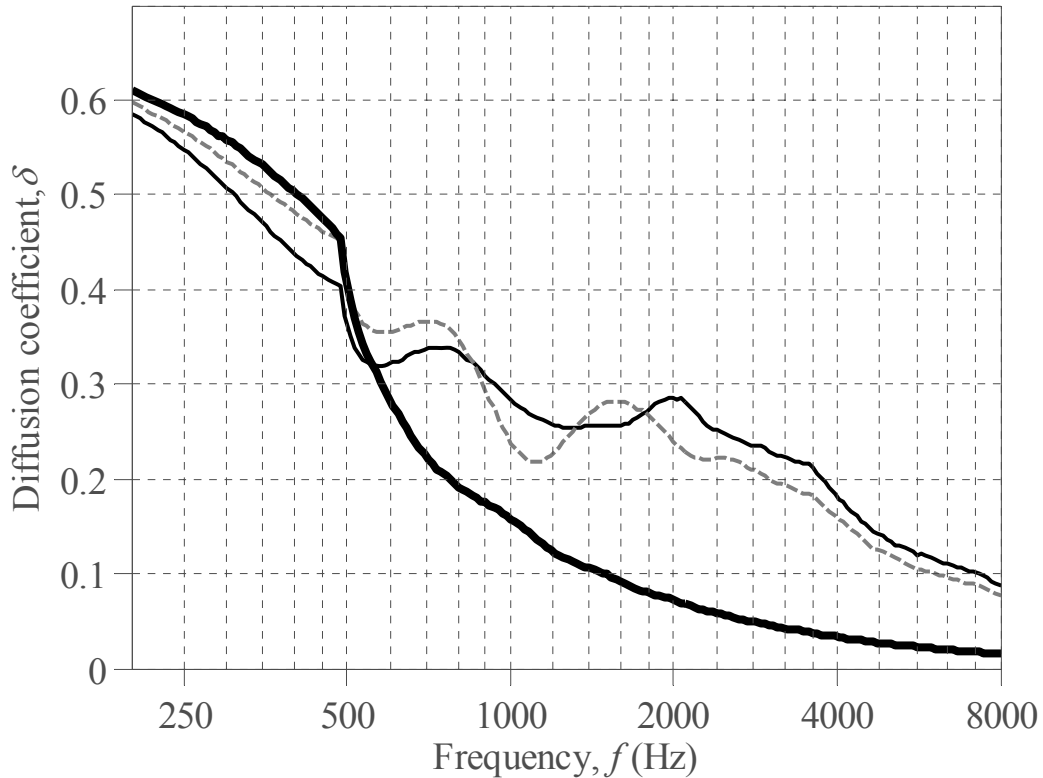
Figure 4.10: Diffusion coefficient for an array of slats arranged according to the N = 7 Golomb ruler [1 1 0 0 1 0 1] (━), and MLS [1 1 0 1 0 0 1] (– –); $\theta_0 = 0°$, $d_e = d_y = 10$cm; flat plate of width, D = 0.7m (━) shown for reference

Obtaining longer aperiodic sequences

The above demonstrates the diffusion achieved by a length $N = 7$ sequence though to improve the diffusive bandwidth, given for the aperiodic case as $\log_2(N)$, it is likely that longer sequences will be required. This however presents several problems:

- There are quite a few 1D sequences whose periodic autocorrelation properties are optimal, for example MLS, however aperiodic equivalents are less common.

- The longest possible optimal aperiodic sequence is the perfect $N = 7$ Golomb ruler presented above [52]. All sequences longer than this will contain at least one 'hole' or repetition in their AACF.

- In contrast to the often mathematically derived periodic sequences, aperiodic sequences such as those in non-redundant and minimum-redundancy arrays are usually found using (intelligent) exhaustive computational searching [55; 56].

- Since the focus in sequence design is generally on minimising redundancy, longer sequences tend to be very sparse.

In general it is easier to obtain a sparse aperiodic sequence with desirable aperiodic properties – for example Golomb rulers – than it is a dense one. A potential problem with this is that the density of an array will help determine the amount of energy it scatters, and hence sparse sequences may be less efficient. As shall be discussed later in Section 4.3 this may not always be a bad thing, though the ability to alter the scattering properties of an individual layer are still desirable. This is discussed in more detail in Section 4.2.5.

To compare the performance of larger less sparse sequences the following procedure was adopted. To provide a comparison with the example from Section 4.2.2 which comprised 3 periods of the periodic MLS sequence [1 1 1 0 0 1 0], a length $N = 21$ sequence was selected. In addition (also to match the previous example) the number of elements, E, in the sequence was set to 12. Each of the possible 293,930 sequence combinations was generated, and their respective AACFs and Fourier spectrums (padded with zeros) were calculated. For each AACF the standard deviation of the sidelobes $C_a(\tau \neq 0)$ was calculated. This gives an indication of the deviation of the sidelobe energy from the average, and consequently the deviation from the optimal AACF distribution; one with a constant value for all out of phase shifts. As a result a low value should result in more even scattering. Note a straightforward average is not used since the average sidelobe energy should remain constant for a fixed number of elements, E. As an initial indicator of potential diffusion, the diffusion coefficient of Eq. 3.2 was applied to the Fourier spectrum to assess uniformity. Strictly speaking this form of the diffusion coefficient assumes that the receivers are spaced at equal angular steps, which the Fourier spectrum is not since it is linearly spaced in the $d_y(\sin\theta + \sin\theta_0)/\lambda$ domain, though an idea of uniformity should still result.

Figure 4.11 compares the two metrics described above, and illustrates how the predicted diffusion rises as the spread in the AACF sidelobe energy falls, with a correlation coefficient between the two data sets of -0.9999. Also highlighted is the result for the periodically repeated MLS (grey circle). The AACF and autospectrum for both the MLS and (one of) the best performing sequences from Figure 4.11 ([1 1 1 1 0 1 0 1 0 0 0 1 1 0 0 1 0 0 1 1 1]) are compared in Figure 4.12. The flatter AACF of the optimal sequence can be seen to correspond to a more even spread in the autospectrum (expressed here in dB for clarity), as opposed to the equal energy lobing seen for the periodic sequence.
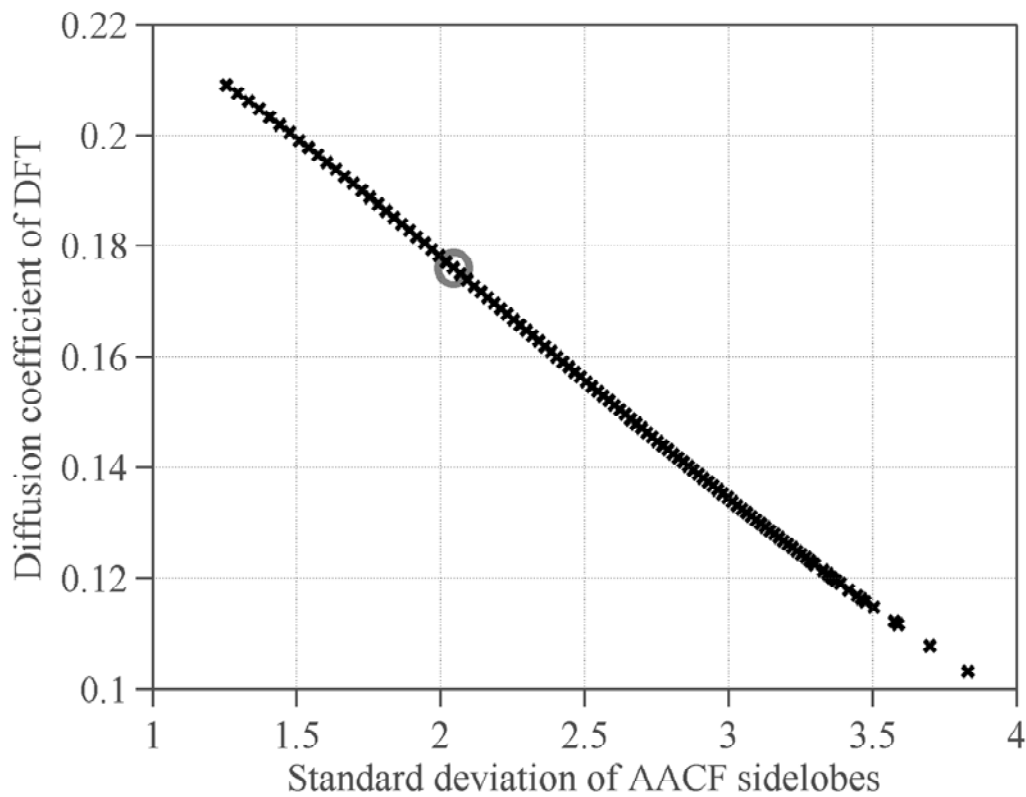
Figure 4.11: Relationship between the AACF sidelobe energy and the diffusion coefficient of the DFT; all combinations of the unipolar N = 21, E = 12 sequence (✖), and 3 periods of the

MLS [1 1 1 0 0 1 0] (◯)

The resulting diffusion coefficient for the above two sequences is shown in Figure 4.13 (top). As can be seen the optimal ($N = 21$, $E = 12$) sequence outperforms the periodically repeated MLS equivalent for all frequencies over the frequency range $200Hz \leq f \leq 8kHz$. This is particularly evident at low frequency, where the effective design frequency has shifted from

when the wavelength is equal to a single period of the MLS ($f_0 \approx 500$Hz) to when it is equal to the entire diffuser width ($f_0 \approx 165$Hz). An example of this is illustrated by Figure 4.13 (bottom) which shows the scattered pressure for a frequency of $f = 250$Hz, corresponding to a visible region in Figure 4.12 (bottom) of approximately $d_y(\sin\theta+\sin\theta_0)/\lambda \leq 0.07$. The first grating lobe of the periodically repeated MLS is not visible at this point, and consequently its scattering is similar to that of the reference plate though of a lower magnitude. The aperiodic optimal sequence however is able to spread its energy much more efficiently.
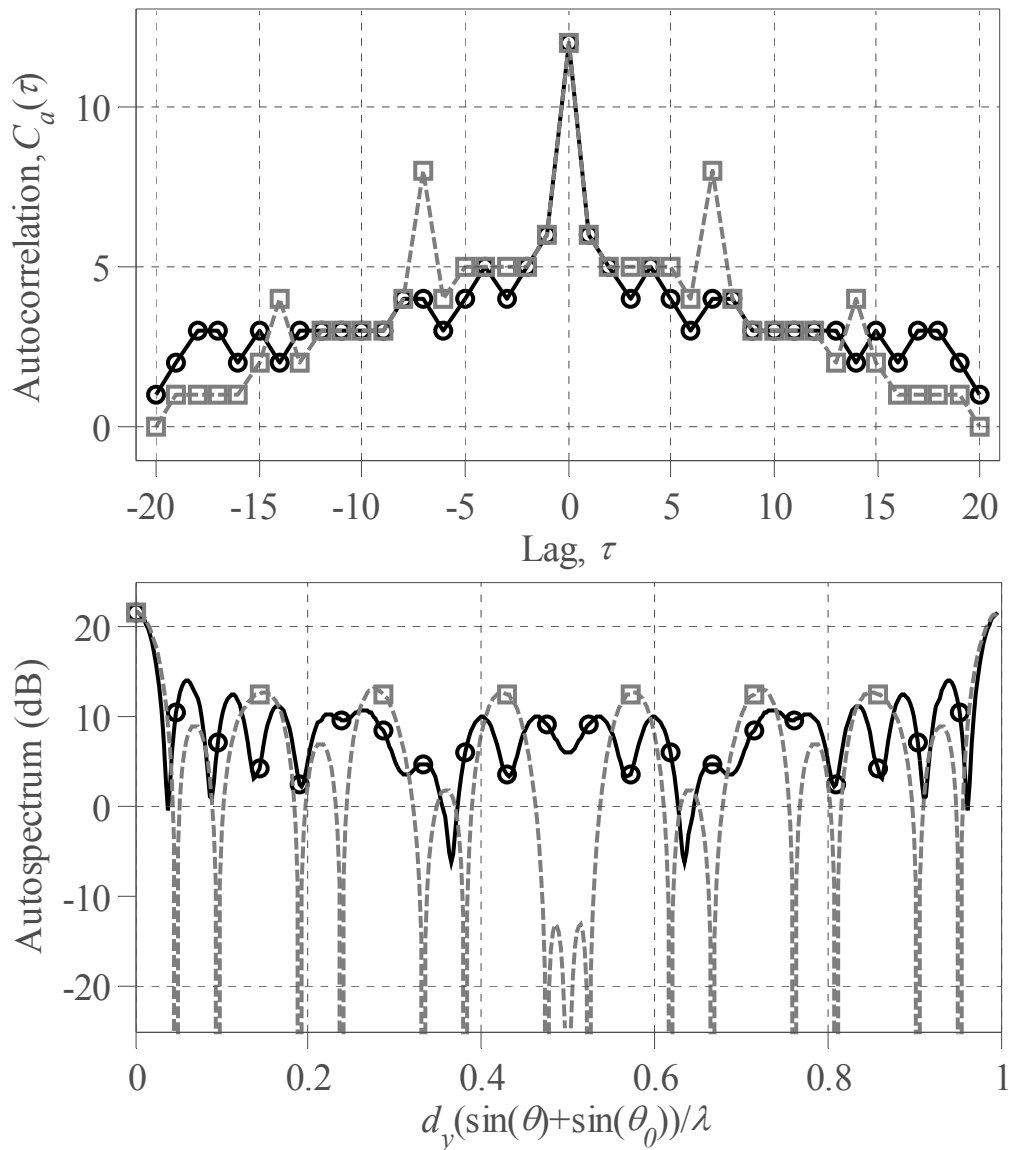
Figure 4.12: AACF (top) and power spectrum (bottom) for the best N = 21, E = 12 sequence found from an exhaustive search (━o━) and 3 periods of the MLS [1 1 1 0 0 1 0] (- □ -)
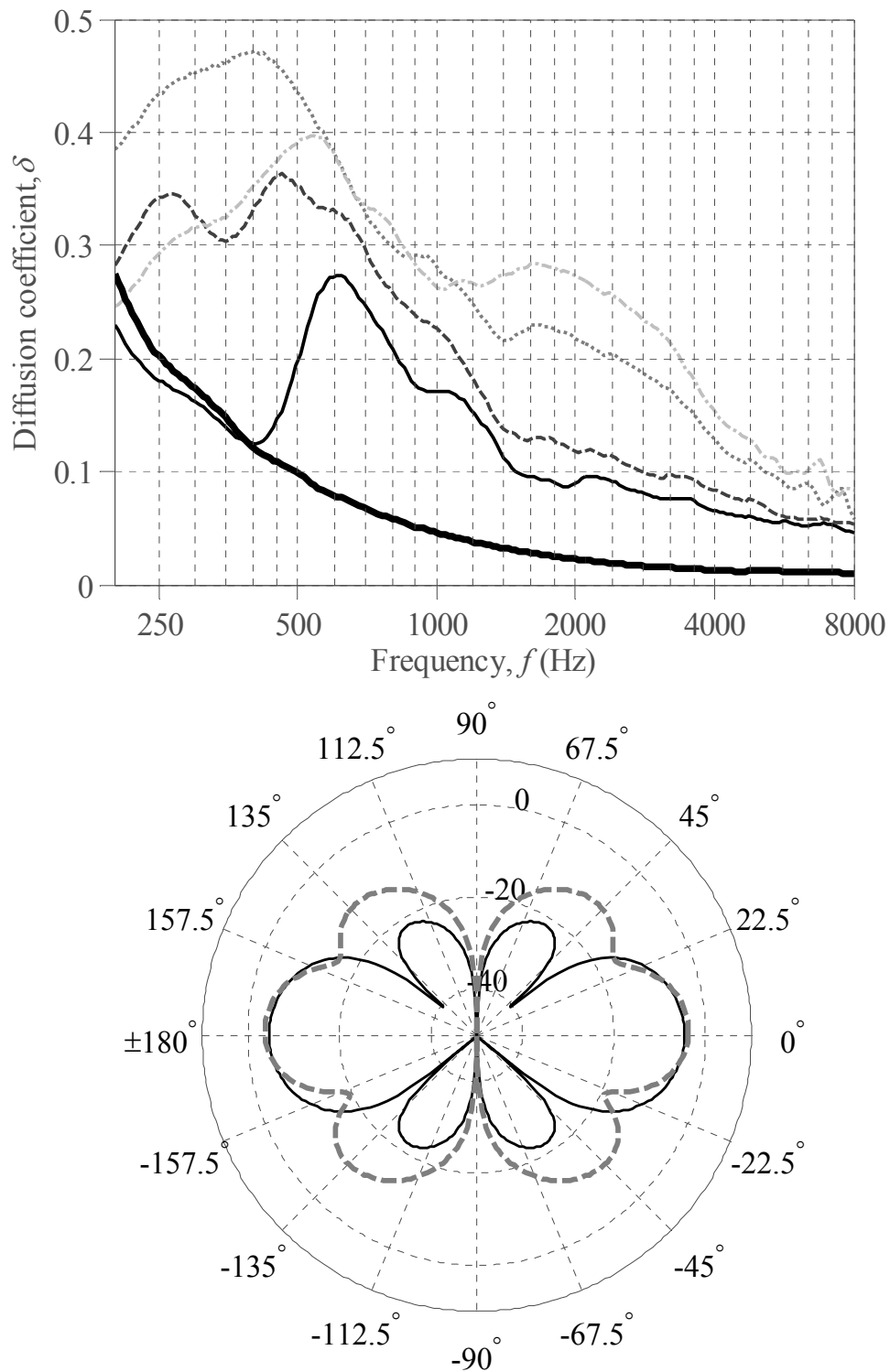
Figure 4.13: Diffusion coefficient (top) for an array of slats comprising 3 periods of the MLS
[1 1 1 0 0 1 0] (━━), the optimal N = 21, E = 12 sequence (━ ━), N = 18, E = 7
minimum-redundancy array (━ ━), N = 18, E = 6 Golomb ruler (━ ━) and flat plate (━━)
shown for reference; f = 250Hz normalised scattered pressure polar pattern shown for MLS
and optimal arrangements only (bottom); θ₀ = 0°, D = 2.1m

A denser array may be able to scatter more energy, though the level of diffusion that can be achieved is reduced. This is illustrated by Figure 4.13 (top) where two much sparser sequences are also included; a minimum-redundancy array ($N = 18$, $E = 7$) after Hopperstad and Holm [57], and a Golomb ruler ($N = 18$, $E = 6$) [58]. These sequences are slightly shorter than the $N = 21$ examples above, though have a different element size to ensure the same overall structure width. The reason for their more even scattering is that the ratio of the sidelobe energy to the DC (and hence specular) component in the Fourier spectrum of a sequence is not constant with the number of elements, E. Following from Parseval's relation [59] it can be shown that the ratio of the Average Sidelobe to Specular Ratio (ASSR) may be given by:

$$\mathbf{ASSR} = 10 \log_{10} \left(\frac{N - E}{E(N - 1)} \right) \qquad 4.5$$

Which as N becomes large may be approximated as:

$$\mathbf{ASSR} \approx 10 \log_{10} \left(\frac{1}{E} - \frac{1}{N} \right) \qquad 4.6$$

Consequently as E increases the specular component becomes large relative to the sidelobe energy and begins to dominate. With increasing sequence length N, this approaches the ratio of the summation of E random phase ($|p_s| \propto E^{1/2}$) to in phase ($|p_s| \propto E$) components, illustrating a dependence on the number of elements rather than their relative occupancy (E/N). An example of this is shown in Figure 4.14 which compares the scattering at $f \approx 1.8$kHz from the (dense) optimal sequence and (sparse) Golomb ruler array. Both sequences scatter efficiently away from the specular reflection, with their average sidelobe energy being very similar. The ASSR for the optimal sequence however is -14.3dB, compared with -9.3dB for the Golomb ruler, meaning that the specular component is more dominant. The result is a notably lower diffusion coefficient of 0.126, compared with the 0.279 value achieved by the Golomb ruler.

Note due to its lower number of elements (and similar Fourier properties) it would be expected that the Golomb ruler would result in a higher diffusion coefficient than that of the minimum-redundancy array. From Figure 4.13 (top) however, it can be seen that at low

frequency this is not the case. This is due to the Fourier spectrum of the minimum-redundancy sequence being more even close to DC, and consequently providing early scattering uniformity. With increasing frequency however, as more of the spectrum becomes visible the properties of the sequence become apparent and the Golomb ruler outperforms the minimum-redundancy array. This possibility of low frequency variation exists in general for all sequences, since the Fourier properties take into account the performance of a sequence for the range $0 \leq d_y(\sin\theta+\sin\theta_0)/\lambda < 1$ (which including repetition due to spatial aliasing encompasses all frequencies). As a result where multiple sequences with similar Fourier properties exist, those which provide the most even spectrum (when padded with zeros) close to DC may perform best.
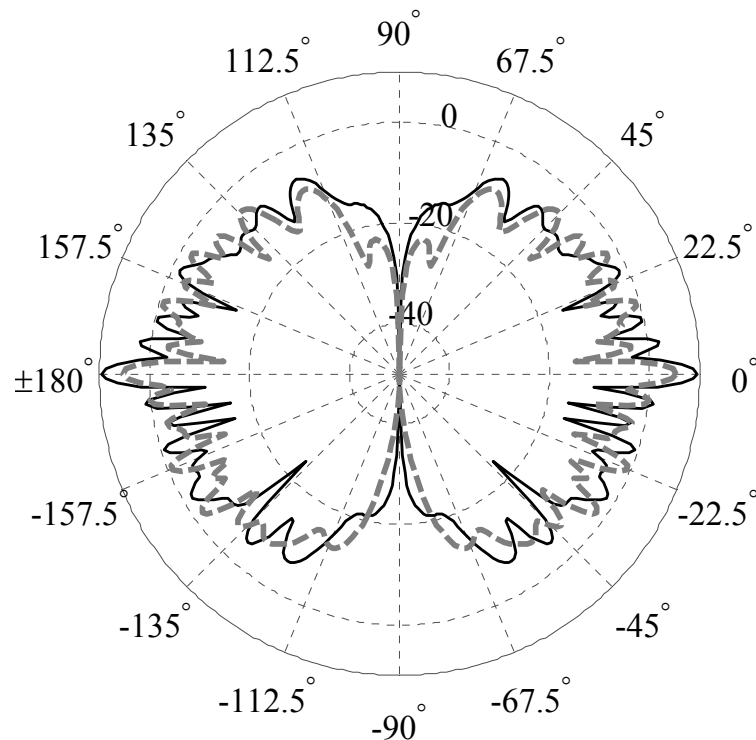
Figure 4.14: Normalised scattered pressure polar response for a 1D array of slats arranged according to an optimal N = 21, E = 12 sequence (━), and an N = 18, E = 6 Golomb ruler (━ ━); f ≈ 1.8kHz, θ₀ = 0°, D = 2.1m

4.2.4 Amplitude shading

An alternative approach to the design of an amplitude diffuser was suggested by Payne-Johnson *et al.* [15], who proposed a BAD comprising varying sized panels in an

attempt to remove the emphasis of the nulls produced by a single element. This emphasis is due to having a single element size, with the scattered pressure pattern described by the sinc function of Eq. 4.2 being the same for each. At low frequency, when wavelength is large relative to slat size, the scattering from a single element will be quite uniform. Consequently this is a high frequency effect, seen once $f \geq f_{max}$ (as defined by Eq. 4.4), the point at which the first pressure null is seen at grazing receivers.

To determine which arrangement will be most optimal, consider an array allowing varying sized slats of length, d_n, spaced an equal distance, d_y, apart (centre to centre). Since element size is no longer uniform across the array, Eq. 4.2 now becomes:

$$p_{s,norm}(\theta_0,\theta) \approx \cos(\theta)\frac{(1-j)}{\sqrt{2}}\sqrt{\frac{1}{\lambda}\sum_{n=0}^{N-1}A_n e^{jknd_y(\sin\theta+\sin\theta_0)}} \ ;$$

$$A_n = d_n \operatorname{sinc}\left(\frac{kd_n}{2}(\sin\theta+\sin\theta_0)\right)$$

4.7

Where the amplitude coefficient for the nth element, A_n, is now determined by the response of the nth slat. At low frequency and for receivers close to the specular reflection, the effect of the individual sinc functions will be negligible. Consequently the scattered pressure will be approximately proportional to slat size, and an arrangement whose distribution of slat lengths, d_n, has desirable Fourier properties is required. Unlike the unipolar sequence design these may be determined by any positive real sequence, and will ideally be non-integer based to prevent the nulls of the individual sinc functions coinciding at high frequency.

An analogous process to that described above comes from array theory, a procedure often referred to as amplitude shading. This typically involves the application of a windowing function to a full array in order to maximally suppress the sidelobes. Ideally however, a sequence / window is required that aims to achieve equal sidelobe energy rather than restrict their level, as it is this that determines diffusive performance. An example of this is the Chebychev window [60] which provides a series of weightings designed to achieve a specified attenuation. Figure 4.15 shows the AACF and power spectrum for an $N = 7$ Chebychev sequence designed to achieve equal energy sidelobes attenuated by 6.1dB. For scattered power reasons, as is discussed in Sections 4.2.5-4.2.6, this attenuation value was

selected in order to achieve a distribution with a 50% open area. The slat sizes for the array, d_n, are given in Table 4.1.
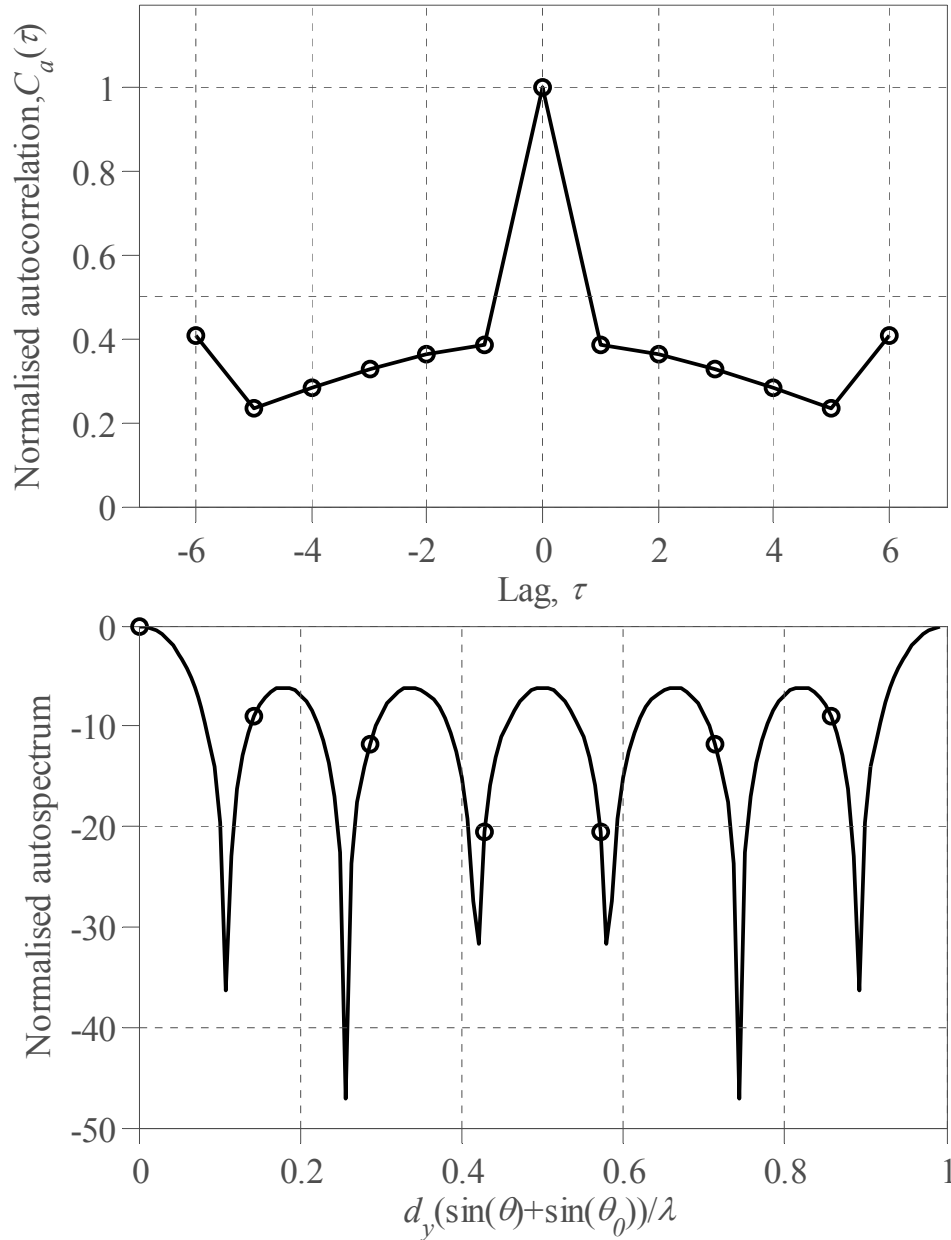
Figure 4.15: AACF (top) and power spectrum (bottom) for an N = 7 Chebychev sequence

One of the important benefits of this technique is that the nulls produced by the response of the individual elements will no longer necessarily coincide with the repetition of the zeroth order (specular) lobe due to spatial aliasing, as was previously demonstrated to occur for unipolar arrangements in Figure 4.7. This means that for frequencies above the previously defined f_{max} of Eq. 4.4 (though now with element spacing d_y substituted for d_e) scattering

towards receiver angles close to grazing becomes possible. This is illustrated by Figure 4.16 which shows the scattered pressure from the $N = 7$ Chebychev array of Figure 4.15 for frequencies of f $\approx$ 1.2kHz (top) and f $\approx$ 2.4kHz (bottom), corresponding to frequencies of f_{max} and $2 \times f_{max}$ respectively.
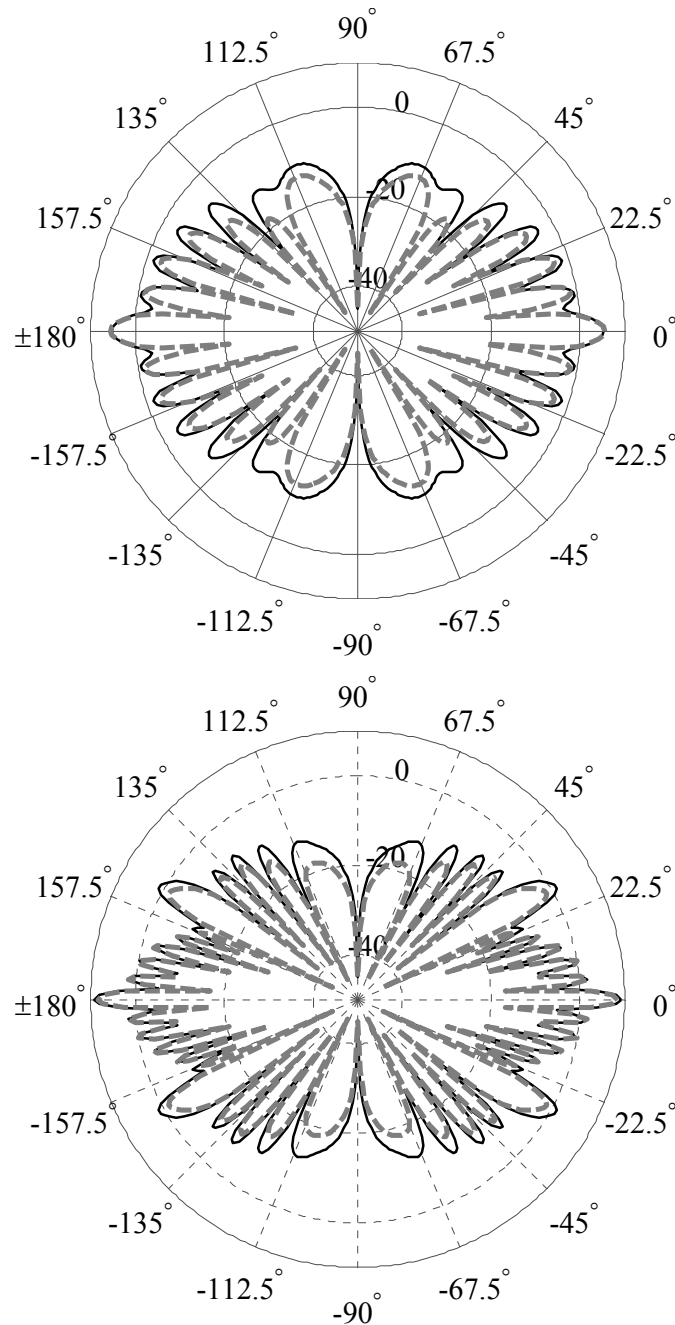
Figure 4.16: Normalised scattered pressure polar response for an N = 7 Chebychev slat array; thin panel BEM (▬), and Fourier approximation (‑ ‑); f ≈ 1.2kHz (top) and f ≈ 2.4kHz (bottom); θ₀ = 0°, D = 2.1m

Table 4.1: 1D Amplitude shading slat sizes

	Slat length, d_n (mm)						
Slat number, n	1	2	3	4	5	6	7
$N = 7$ Chebychev	300.0	85.9	92.0	94.2	92.0	85.9	300.0

The resulting diffusion coefficient for the above Chebychev array is shown in Figure 4.17, compared with the coefficient obtained for the optimal $N = 21$, $E = 12$ sequence from Figure 4.13 (top). The Chebychev array provides an almost constant boost in diffusion coefficient with frequency. It is worth noting however that their relative occupancy is different, and consequently the Chebychev array will produce a slightly lower magnitude specular reflection, resulting in an increase in diffusion. In general an amplitude shading technique will provide an at least equivalent level of diffusion to a unipolar design, though allows a degree of freedom in the selection of the size and density of the elements in an array.
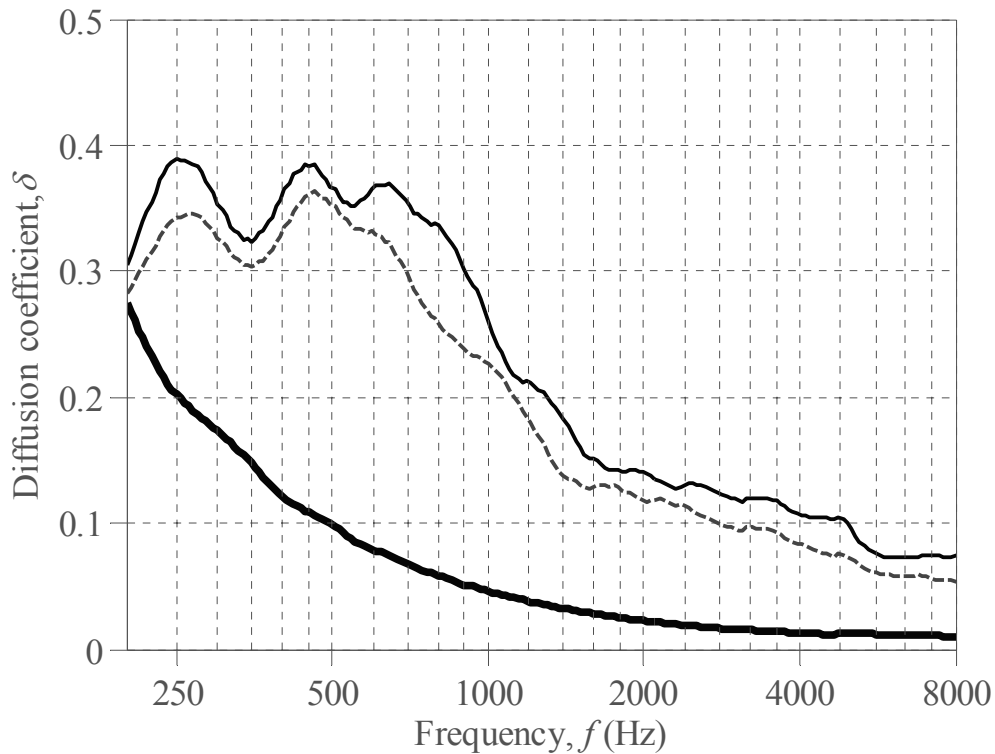
Figure 4.17: Diffusion coefficient for an N = 7 Chebychev slat array (━━), and an optimal N = 21, E = 12 sequence (━ ━); $\theta_0 = 0°$; D = 2.1m; flat plate (▬▬) shown for reference

4.2.5 Scattered power

In Chapter 2, Eq. 2.19 approximated the scattered pressure from a plane surface of width, d_e, as a function of the surface reflection coefficient, R. For the slats case, and considering the surface as a whole, this may be reduced to:

$$p_s(\mathbf{r}) \approx -\frac{\cos(\theta)}{4\pi\sqrt{rr_0}} e^{jk(r+r_0)} \int_{-D/2}^{+D/2} A(\mathbf{r}_s) e^{jkx(\sin(\theta)+\sin(\theta_0))} dx \qquad 4.8$$

Where the reflection coefficient, R has been replaced by the amplitude coefficient, $A = \{0, 1\}$ which can represent total reflection ($A = R = 1$) or total transmission ($A = 0$); and the integration is carried out over the whole surface of width, D. Note for the transmitted case there is zero scattering, which is not the same as no reflection ($R = 0$). The back-scattered intensity ratio, L_{IR}, as defined in Eq. 3.5 considers the sum of the squares of the scattered pressure, p_s. This expressed as an integral may be given as:

$$\int_{\theta_0-\pi/2}^{\theta_0+\pi/2} |p_s|^2 d\theta \approx \frac{\lambda}{16\pi^2 rr_0} \int_{\Omega} \cos^2(\theta) \left| \int_{-D/2}^{+D/2} A(\mathbf{r}_s) e^{j2\pi x\Omega} dx \right|^2 d\Omega$$

$$\Omega = \frac{(\sin(\theta)+\sin(\theta_0))}{\lambda} \qquad 4.9$$

Where the integration with angle is carried out with respect to Ω. Since this is a high frequency approximation, valid once wavelength becomes comparable to the width of the individual slats, d_e, the surface will produce a progressively more specular reflection. Consequently for source angles close to normal incidence the scattering will be greatest at small receiver angles, allowing the approximation $\cos^2(\theta) \approx \cos^2(\theta_0)$ to be made, with Eq. 4.9 therefore reducing to:

$$\int_{\theta_0-\pi/2}^{\theta_0+\pi/2} |p_s|^2 d\theta \approx \frac{\lambda \cos^2(\theta_0)}{16\pi^2 rr_0} \int_{\Omega} \left| \int_{-D/2}^{+D/2} A(\mathbf{r}_s) e^{j2\pi x\Omega} dx \right|^2 d\Omega \qquad 4.10$$

The remaining term inside the integral with angle is a form of power spectrum of the amplitude coefficient's distribution across the surface. Parseval's theorem states that the

integral of the energy of a signal is equal to the integral of its power spectrum [59]. Consequently the above may be simplified to give:

$$\int_{\theta_0-\pi/2}^{\theta_0+\pi/2} |p_s|^2 d\theta \approx \frac{\lambda \cos^2(\theta_0)}{16\pi^2 rr_0} \int_{-D/2}^{+D/2} |A(\mathbf{r}_s)|^2 dx \qquad 4.11$$

Which for a set of E uniformly spaced slats arranged according to a unipolar sequence again reduces to:

$$\int_{\theta_0-\pi/2}^{\theta_0+\pi/2} |p_s|^2 d\theta \approx \frac{\lambda \cos^2(\theta_0)d_e}{16\pi^2 rr_0} \sum_{n=0}^{N-1} |A_n|^2 = \frac{\lambda \cos^2(\theta_0)d_e E}{16\pi^2 rr_0} \qquad 4.12$$

This implies that the total back-scattered power will be proportional to the total length of the slats, $d_e{\times}E$. Consequently a high frequency approximation to the back-scattered intensity ratio, L_{IR}, given by Eq. 3.5 may be given by:

$$L_{IR} \approx 10\log_{10}\left(\frac{d_e E}{D}\right) = 10\log_{10}\left(\frac{E}{N}\right) = 10\log_{10}\left(F_{fill}\right) \qquad 4.13$$

Where F_{fill} is the fraction of the array that is occupied by a slat, and the reference plate has been modelled as a set of N slats of width, d_e. More generally F_{fill} is defined as the fraction of the line-of-sight through the array that is blocked (as viewed from the source), and may be thought of as a 1D fill factor or density. Eq. 4.13 therefore predicts an approximate 3dB drop in the scattered power for a halving in the fill factor. This is in contrast to the specularly reflected component, which predicts a 6dB drop in intensity per halving of slat occupancy.

Figure 4.18 shows the back-scattered intensity ratio for the optimal ($N = 21$, $E = 12$) set of slats from Section 4.2.3. This is compared to a flat plate of width, $D = 1.2$m; an equivalent total length plate. Since the total fraction of the array occupied for both slats and smaller plate is identical, their intensity ratio predicted by Eq. 4.13 is the same (-2.4dB, highlighted by dotted line in Figure 4.18). At high frequency this is approximately the case, though at low frequency their behaviour is very different. This is due to their arrangement; the slat array comprising plates of various lengths made up of adjacent slats, and the equivalent plate forming one continuous structure.
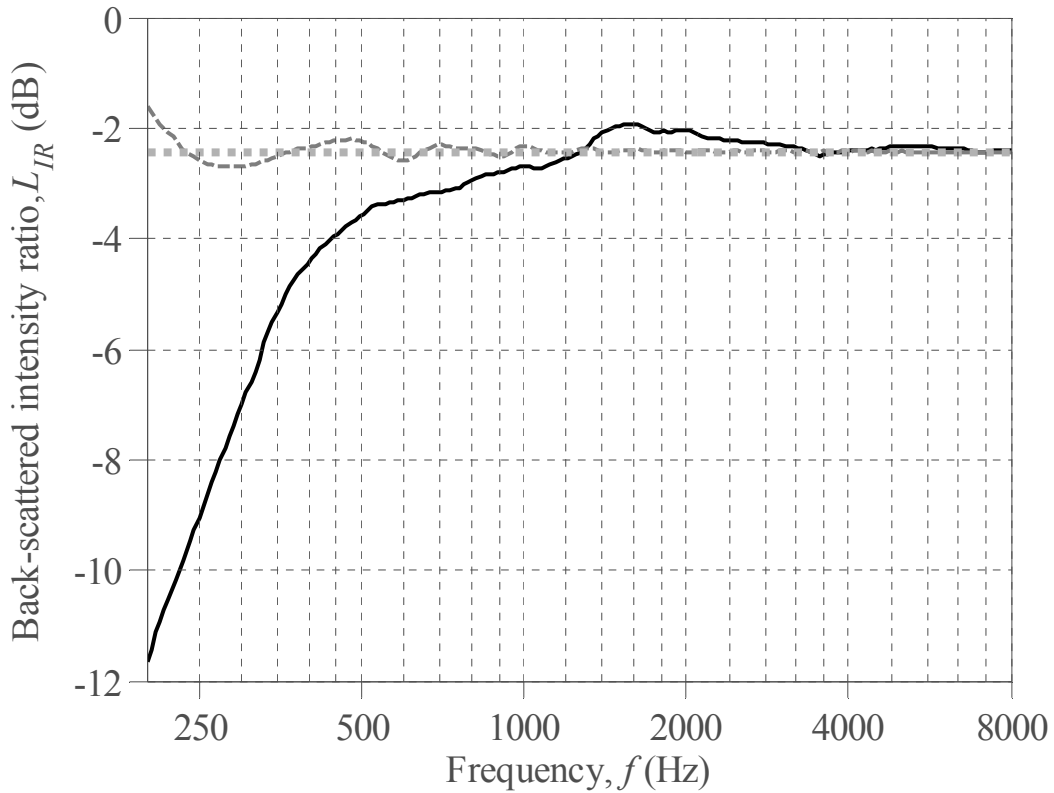
Figure 4.18: Back-scattered intensity ratio for an array of slats arranged according to the
N = 21, E = 12 optimal sequence from Section 4.2.3 (━), a flat plate of width D = 1.2m
(━ ━), and a high frequency approximation as per Eq. 4.13 (━ ━ ━); $\theta_0 = 0°$, D = 2.1m

Scattering from a single slat

To explain the scattered power from a slat array, consider first the case of a single slat. Figure 4.19 shows the back-scattered intensity ratio applied to a single slat of length d_e = 10cm. The frequency response can be seen to resemble that of a high-pass filter, agreeing with results found from previous studies into scattering from plane rigid panels [3; 22]. Consequently it would be expected that the scattered power from a single slat could be modelled using a simple roll-on and flat-shelf, separated by some cut-off frequency. This is illustrated in Figure 4.19, where the flat-shelf region of the high-pass response is determined by Eq. 4.13 (where $E = 1$) and a simple first order polynomial line of best fit is applied to the low frequency roll-on.
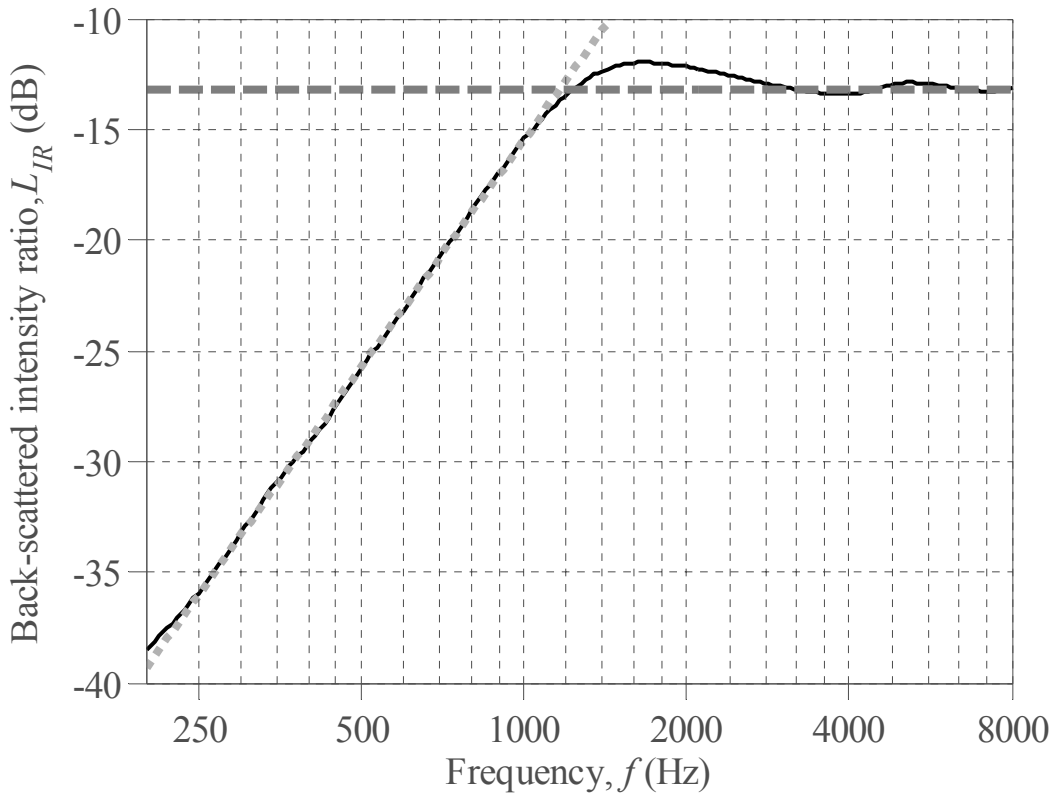
Figure 4.19: Back-scattered intensity ratio for a single slat of width $d_e = 10cm$ (━), the high frequency approximation as per Eq. 4.13 (━ ━), and a line of best fit for the roll-on (▪ ▪ ▪); $\theta_0 = 0°$, D = 2.1m

The high frequency approximation that the scattered power is a function of line-of sight assumes that the pressure contribution from the rear of a slat is insignificant. At low frequency however there is much greater diffraction around the structure, resulting in a significant contribution from the rear. When wavelength is large compared to slat length, d_e, this creates a dipole effect, with the scattering from the rear effectively being $180°$ out of phase with that from the front. The scattered field should therefore be proportional to the pressure, p_t, radiated from a dipole, which at low frequency may be approximated as [61]:

$$p_t(\theta) \propto jkd\cos(\theta); \quad kd << 1 \qquad\qquad 4.14$$

Where d is the separation distance between the front and back of the dipole. For the scattering case this will be determined by the diffraction path length around the panel, and consequently will be related to the panel length d_e. The scattered power will be proportional to k^2, implying a low frequency roll-on of +6dB/octave. This means the scattered power response should

approximate a first order high-pass filter shape. When normalised to the scattering from the reference plate however an extra +3dB/octave results since, assuming the reference plate to be larger relative to wavelength, Eq. 4.12 predicts a high frequency roll-off for the plate of -3dB/octave (due to the progressive narrowing of the specular lobe with frequency).

For very low frequencies ($k \times d_e \ll 1$) as predicted, the roll-on of Figure 4.19 is approximately +9dB/octave. A least-squares line of best fit analysis over the initial slope ($250\text{Hz} \leq f \leq 1\text{kHz}$) however yields an approximate +10.2dB/octave roll-on. This is due to the complex transition between low and high frequency behaviour, where the influence of edge effects are strongest [12]. In general however the roll-on may be modelled as a simple approximate +10dB/octave slope. Since the transition between low and high frequency behaviour is quick, forming a relatively sharp 'knee' frequency, a simplified model for the intensity ratio, L_{IR}, due to a single slat may be described by the combination of these two regions, given as:

$$L_{IR} \approx 10 \log_{10}\left(E_0 \left(\frac{f}{f_c}\right)^{\log_2(10)} \right) ; \qquad f < f_c \qquad\qquad 4.15$$

$$L_{IR} \approx 10 \log_{10}\left(F_{fill} \right) ; \qquad f \geq f_c \qquad\qquad 4.16$$

Where f_c is the cut-off frequency describing the transition between low and high frequency behaviour.

Cut-off frequencies for arrays of reflecting panels have been considered before. Rindel [22; 62] for example proposed a cut-off frequency below which the scattering from a canopy array was dependent on the density of the panels and not on their size, and above which performance was dependent on the panel size and distribution. For a single panel this equates to a transition between scattering effectively into all directions and producing a specular like reflection [3]. This cut-off frequency was given as:

$$f_c = \frac{c.r_c}{2d_e \cos(\theta)} \qquad\qquad 4.17$$

Where the reflection is considered at the specular reflection point, $\theta = -\theta_0$. As was observed for the single panel case of Figure 4.19, the frequency response resembles that of a high-pass

filter shape. Note, following this analogy the cut-off frequency here is defined as the -3dB point of the observed response when considered as a filter [3]. As was discussed in Section 2.2.3, in the far-field the shape of the scattered pressure should be independent of distance. The work presented by Rindel however was designed to work in the near-field, and in the limit as distance becomes large, gives a predicted cut-off frequency which goes to infinity. This means that due to approximations made in the derivation of Rindel's equation, in the far-field the formula does not work.

A more suitable far-field measure is given by the point at which the slat width is equal to half a wavelength. For the example of Figure 4.19, this equates to a frequency of $f = 1.72$kHz, and can be seen to correspond to the peak of the ripple during the transition phase. These ripples correspond to the frequencies at which the scattering from the rear of the slat constructively and destructively interferes with that from the front, and when the influence of edge effects are highest, though diminish with frequency as the level of diffraction around the slat falls. This cut-off can be shown to (asymptotically) agree well with the originally predicted +9dB/octave roll-on, though for the purposes of modelling a more appropriate cut-off frequency at and around the transition region may be given as:

$$f_c \approx \frac{c}{2\sqrt{2}d_e}$$

4.18

Where the factor of $2^{-1/2}$ has been found empirically. This equates to half of an octave below the point at which slat width is equal to half a wavelength.

Scattering from an array of slats

As was discussed above, an array of slats will comprise a series of panels of different length made up of runs of adjacent slats. Of course the cut-off frequency for these varying length sections will be different. Consider the case of a run of n adjacent slats forming one continuous panel of length $d_{run} = n \times d_e$. The intensity ratio for this run of slats may be modelled as per Eqs. 4.15-4.16, though with F_{fill} now determined by the fraction of the array that is occupied by the single panel. Similarly the cut-off frequency for this slat panel will be determined by Eq. 4.18, though substituting the slat length, d_e, for the length of the run of

slats, d_{run}. Carrying this out for each of the different sections, a combined response for an array of slats may then be obtained via a straightforward summation (of intensities), given as:

$$L_{IR} \approx 10\log_{10}\left(10^{\frac{L_1}{10}} + 10^{\frac{L_2}{10}} + 10^{\frac{L_3}{10}} + ...\right)$$

4.19

Where L_1, L_2, L_3, etc… represent the intensity ratios obtained separately for each run of slats. Figure 4.20 shows an example of the estimated intensity ratio of Eq. 4.19 (dashed line) for the optimal sequence from Figure 4.18; including the individually modelled runs of slats (dotted lines). The result is a steady merging of the response of the individual slat runs, with a gradual transition from low to high frequency behaviour types. The average deviation of the approximate model from the thin panel BEM result is 0.2dB, with the most notable source of error being an inability to account for the rippling behaviour at the cut-off points.
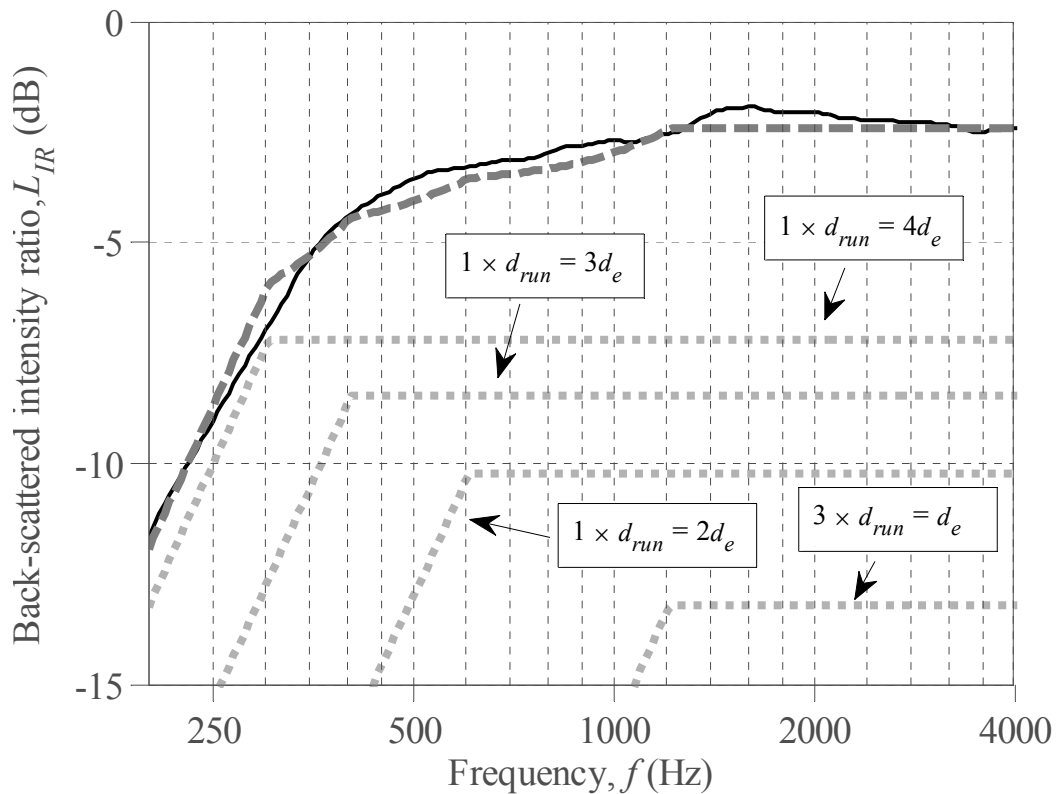
Figure 4.20: Back-scattered intensity ratio for an array of slats arranged according to the N = 21, E = 12 optimal sequence from Section 4.2.3 (——), approximate model – sum (– –), approximate model – individual runs of slats (· · ·); $\theta_0 = 0°$, D = 2.1m

The above suggests that efficient scattering will only occur once the cut-off frequency of the longest slat run is achieved. This gives an approximate minimum frequency, f_{min}, for the scattered power of:

$$f_{\min} \approx \frac{c}{2\sqrt{2}nd_e}$$

4.20

Where n is the maximum number of adjacent slats.

4.2.6 Design principles

From the findings presented throughout Sections 4.2 several key outcomes result. An individual run of slats will begin to scatter sufficient power when approximately a third of a wavelength fits into its length, though once it becomes comparable to wavelength an increasingly more directional reflection results. Consequently its bandwidth of operation is small and a range of slat runs of different sizes is required. Structures whose AACF is optimal, implying a lack of self-similarity, provide the greatest diffusive efficacy. Ultimately however the best arrangements for diffusion are sparse. A sparse array will tend to have smaller runs of slats, and consequently will scatter inefficiently at low frequency. The result is therefore a trade-off between scattered power and diffusive capability.

Ordinarily it is the bandwidth that will determine an arrangement, and consequently to design an array to operate over a frequency range of $f_{min} \leq f \leq f_{max}$, the following guidelines for construction apply:

- To achieve diffusion at low frequency (relative to a flat plate of the same size) the diffuser width should be larger than wavelength, giving:

$$D \geq \frac{c}{f_{min}}$$

4.21

- To ensure high frequency diffusion the slat size should be no larger than wavelength, giving:

$$d_e \leq \frac{c}{f_{max}}$$

4.22

- Following from Eq. 4.20, in order to scatter efficiently at low frequency at least one run of slats of minimum length on the order of $\lambda/(2\sqrt{2})$ is required:

$$d_{run} = nd_e \geq \frac{c}{f_{min}2\sqrt{2}} = \frac{D}{2\sqrt{2}}$$

4.23

- This implies a run of slats occupying approximately 1/3rd of the length of the array.

- Finally the required occupancy of the array is given as:

$$F_{fill} = 10^{\frac{L_{IR}}{10}}$$

4.24

For example a design frequency range of 400Hz $\leq f \leq$ 4kHz gives a diffuser with a maximum slat size $d_e = 8.6$cm, of minimum width $D = 86$cm, and with a minimum length run of slats $d_{run} = 30.4$cm. For a unipolar sequence d_{run} must be a multiple of d_e, and so the actual slat size becomes $d_e = 7.6$cm; the maximum run comprising 4 slats. The total width of the diffuser must also be a multiple of slat width and is therefore revised up to $D = 91.2$cm, where the sequence length is $N = 12$. To achieve an intensity ratio of -3dB a sequence with a 50% occupancy is required. Given these restraints an optimal sequence will have the longest run of elements at one end and a single element at the other, since this ensures the AACF will have elements separated by the largest lags. Consequently an optimal sequence may then be sought by considering the combinations of arrangements of the remaining elements. For the sequence length $N = 12$ here this is only a single element. Using this procedure an arrangement of slats based on the sequence [1 1 1 1 0 0 0 1 0 0 0 1] was obtained, and is shown in Figure 4.21 in terms of the resulting diffusion coefficient (top) and back-scattered intensity ratio (bottom) respectively.
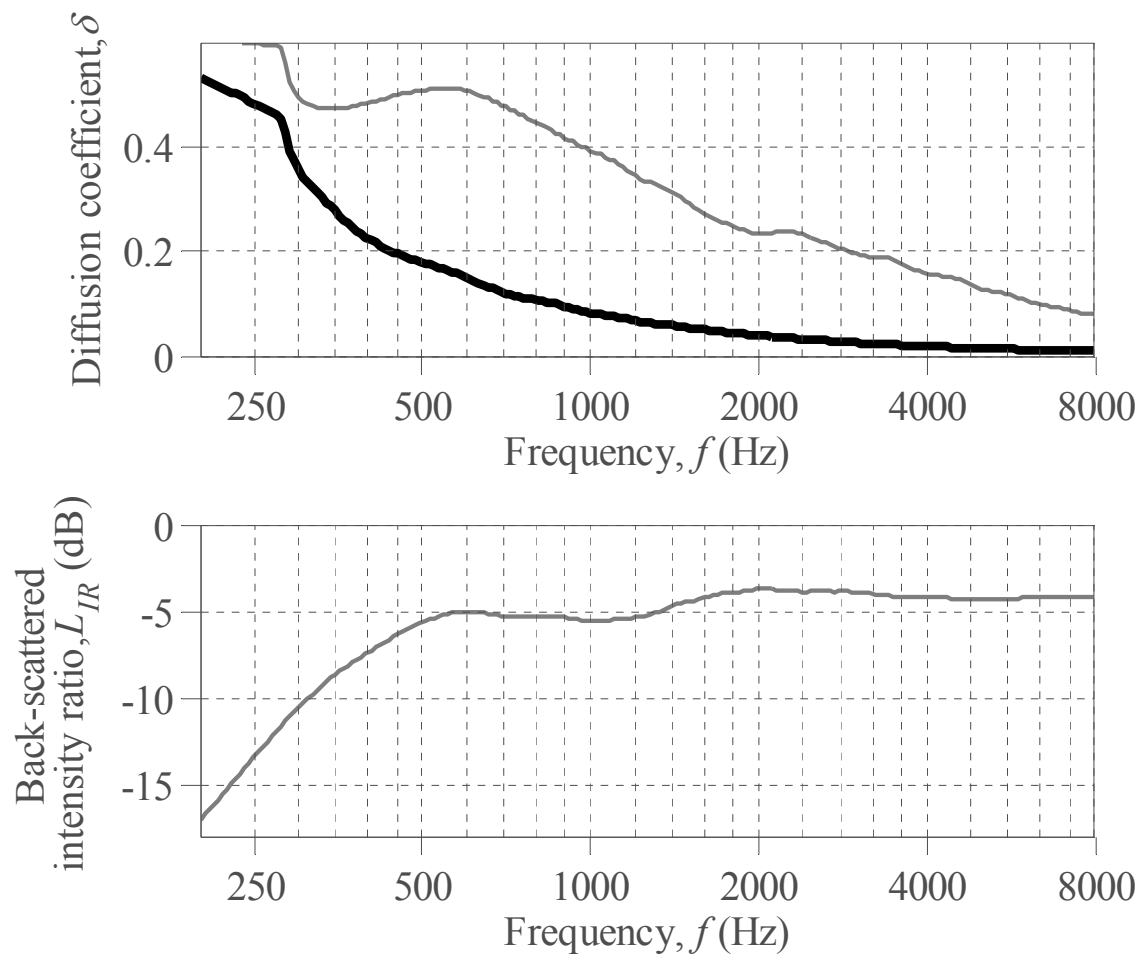
Figure 4.21:Diffusion coefficient (top) and back-scattered intensity ratio (bottom) for an array of slats arranged according to an N = 12, E = 6 sequence (——);θ₀ = 0°; diffusion coefficient of flat plate of width D = 0.912m (▬▬) shown for reference

More optimal sequences to the above may be found by increasing the diffuser length, *D*, and hence increasing the sequence length *N*, though this leads to a more dominant specular reflection as predicted by Eq. 4.5. Consequently the more 'optimal' diffusion is only relative to the larger reference plate.

This section has shown the merits of a 1D slat array, however due to the inherent specular reflection associated with amplitude diffusers they are limited in terms of their diffusive efficacy. To address this, the following section considers a new type of diffuser based on a multi-layered concept, introducing depth into the structure.

4.3.   A multilayered structure based on a periodic lattice

The design concept above was based on a single layer, where dispersion was caused by altering the amplitude of an incident wavefront. As was discussed however, these arrangements are limited, since the unipolar sequences on which they are based are unable to create cancellation. Consequently an inherent specular reflection results, with optimal arrangements being those whose remaining sidelobe distribution is most even. Figure 4.4 demonstrated the Fourier properties of a unipolar MLS, though also included here was a bipolar equivalent which demonstrated that by allowing negative values the ACF and Fourier properties could be significantly improved. Physically this requires a phase change on reflection, which for a rigid structure can be achieved through depth where the phase is altered due to distance travelled. This allows cancellation of the specular reflection, and is the mechanism by which Schroeder diffusers achieve their dispersion, an example of which was shown in Figure 1.2.

Building on the single layer slat designs, a multi-layer concept may be envisaged, whereby sound incident upon each layer is partially back-scattered and partially transmitted, with dispersion ideally occurring for both. In this manner each separate layer creates 'additional diffusion', which may then be further emphasised due to multiple scattering effects between layers. Since these structures will contain depth, the relative phase of the pressure scattered by each layer will be different, and consequently cancellation is allowed. This means that the specular lobe seen in a 1D array may be attenuated. In addition, the provision of different path lengths to provide a phase change and potential multiple scattering implies that the scattered field will be broken up in time, diffusing temporally as well as spatially. An example of a multi-layered array is shown in Figure 4.22, comprising $M = 5$ layers of slats each made up of a separate $N = 10$ sequence.
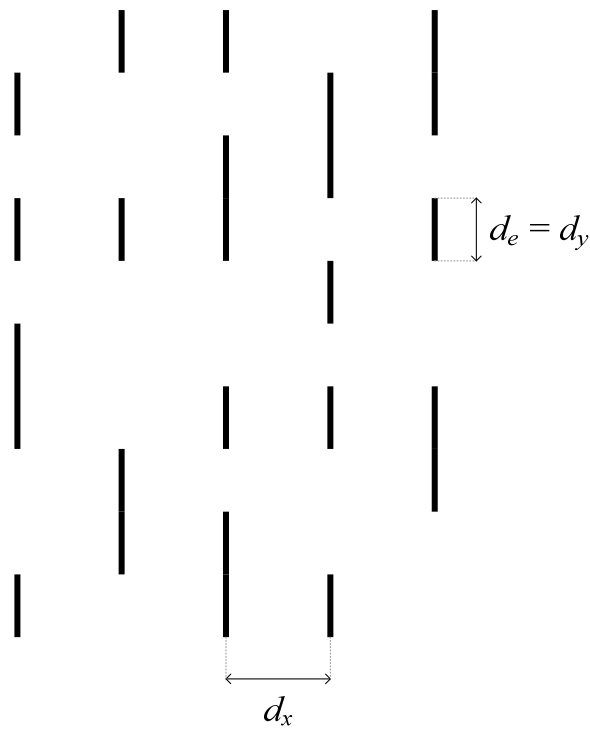
Figure 4.22: A 2D slat array comprising M = 5 layers separated by distance, d_x, each made up of an N = 10 sequence of slats separated by slat width, $d_e = d_y$

4.3.1 The importance of line-of-sight

Consider the simple two layered slat array shown in Figure 4.23, whose front layer is given by the $N = 12$ $E = 6$ diffuser designed in Section 4.2.6 and whose back layer is given by the orthogonal sequence where each 1 becomes a 0 and vice-versa. Due to the orthogonal arrangement the line-of-sight through the array is blocked for normal incidence. Figure 4.24 shows the back-scattered intensity ratio for the array where the spacing between the two layers is considered for two extreme layer spacings: $d_x = 5$cm (black line) and $d_x = 1$m (dashed line). The behaviour for the two layer spacings is very different, and may be described as follows.
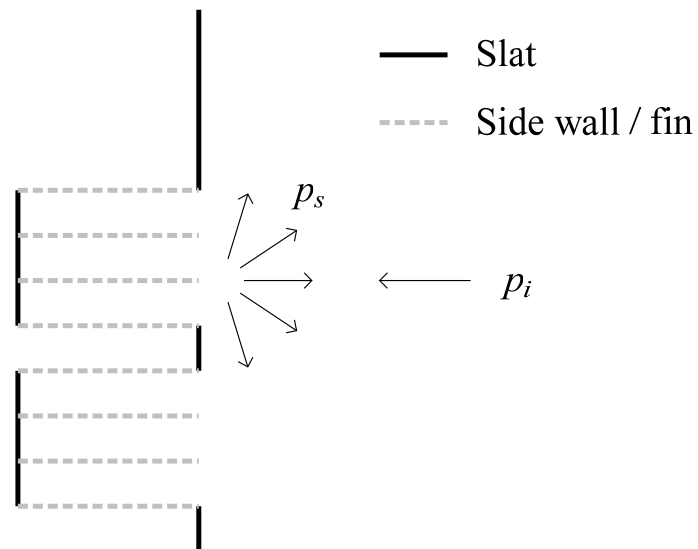
Figure 4.23: Example of a two layered slat array (slats only) and its Schroeder diffuser equivalent (slats and side walls / fins)
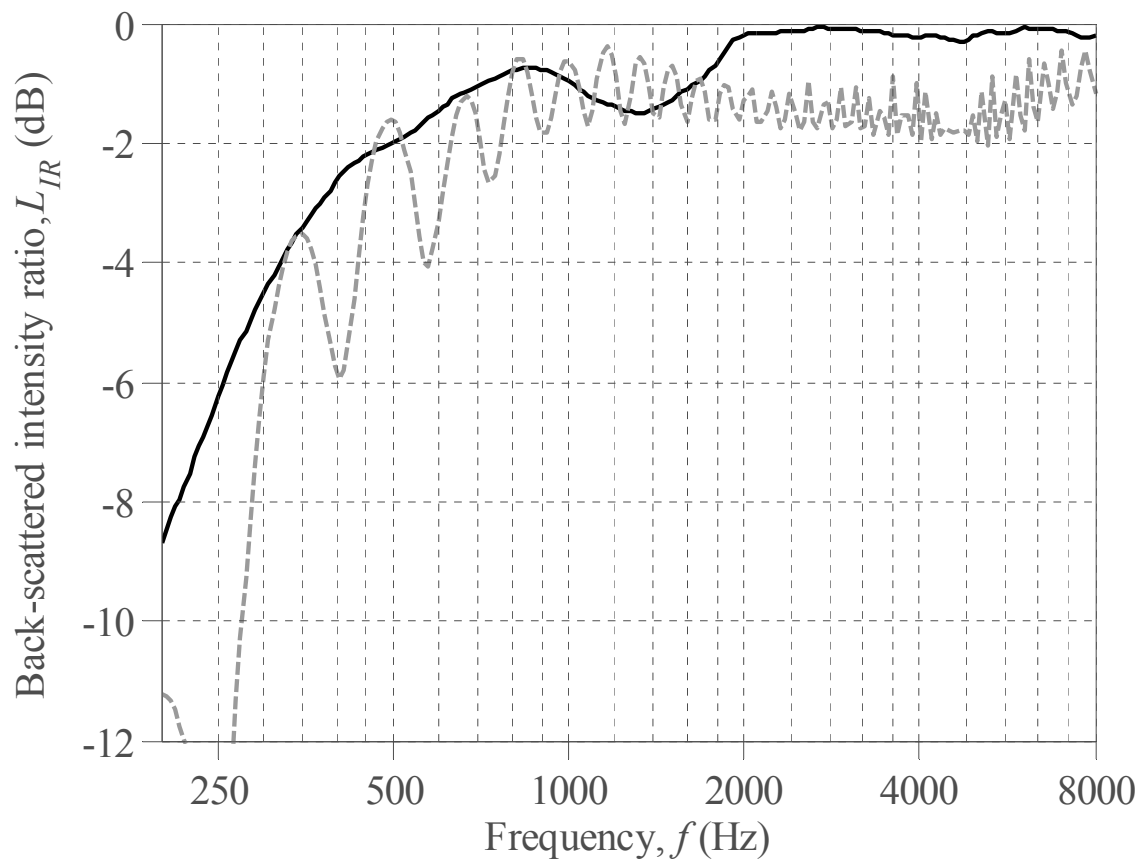
Figure 4.24: Back-scattered intensity ratio for an array of slats arranged according to the N = 12, E = 6 sequence from Section 4.2.6 with orthogonal layer at a distance behind of d_x = 5cm (━) and d_x = 1m (--); θ_0 = 0°, D = 0.912m

Small layer spacing

At low frequency when the layers are brought closer together and wavelength becomes large relative to their separation distance, d_x, the relative phase of the scattering from each layer will be small. This causes a coherent rather than incoherent summation of their scattered energy, and a roll-on of approximately +7dB results (shallower by a factor of 3dB relative to the single layer case).

An approximate boundary below which this behaviour occurs may be given as:

$$f \approx \frac{c}{4d_x}$$

4.25

For the d_x = 5cm array shown in Figure 4.24 this corresponds to a frequency of f = 1.72kHz.

For the high frequency case consider the case of a single gap in an array of width d. As was discussed in Section 3.3.2, for a plane wave incident upon an aperture the total field transmitted through the gap is proportional to the scattered pressure from a flat plate of the same width. At high frequency therefore when wavelength becomes small relative to d, the transmitted wave will form a narrow directional beam, similar to the sinc function of Eq. 4.2 (though strictly speaking this is a far-field assumption and the layers will likely be in the near-field of on another). For normal incidence this means that the energy transmitted through the layer will be directed towards the next slat located in the same position of any subsequent layers. In the same way the scattering off this slat will then be specularly reflected back through the gap and back towards the source. Consequently for small layer spacings where diffraction around this slat is limited, this will result in a back-scattered power determined by line-of-sight through the array. The back-scattered intensity ratio may be estimated in a similar manner to that of a single layer. Now however since diffraction around the smaller runs of slats is possible, with reference to the example array of Figure 4.25, this is carried out as follows:

- The length of slat runs in the array is calculated.

- The largest run closest to the source is considered first (Figure 4.25 (a), circled). The power scattered from this run is calculated as for a single run of slats using Eqs. 4.15-4.16

and the cut-off frequency from Eq. 4.18, though now with a roll-on of +7dB (the $\log2(10) = \log2(10^{10/10})$ is replaced with $\log2(10^{7/10}) \approx 2.3$).

- Since the scattering from the larger obstacle will dominate, all slats that share the same rows as the run (and hence line-of-sight when considering normal incidence) are omitted (Figure 4.25 (b), dashed lines).

- The process is repeated finding the largest remaining slat run closest to the source (Figure 4.25 (c), circled) until all the slats have been either modelled or omitted.

- The total back-scattered power is calculated as per Eq. 4.19.

(a)   (b)   (c)
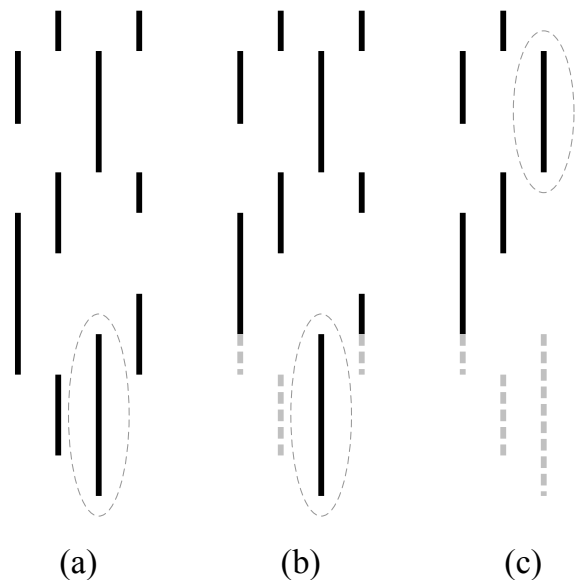
Figure 4.25: Illustration of the process for predicting the back-scattered intensity from a multi-layered array of slats with small layer spacing

For the example from Figure 4.24 the array comprises runs of $2 \times n = 1$, $2 \times n = 3$, and $1 \times n = 4$, where n is the number of slats in an individual run and all runs are visible to the source. Figure 4.26 shows the above prediction model applied to this array. The cut-off frequency for the runs of slats in a 2D array is the same as for a 1D array. Consequently objects (slat runs) on the order of approximately a third of a wavelength are required to efficiently scatter at low frequency. Once the line-of-sight is full however the higher frequency back-scattered power approaches 0dB. Consequently, any subsequent layers will have little influence and will essentially be redundant.
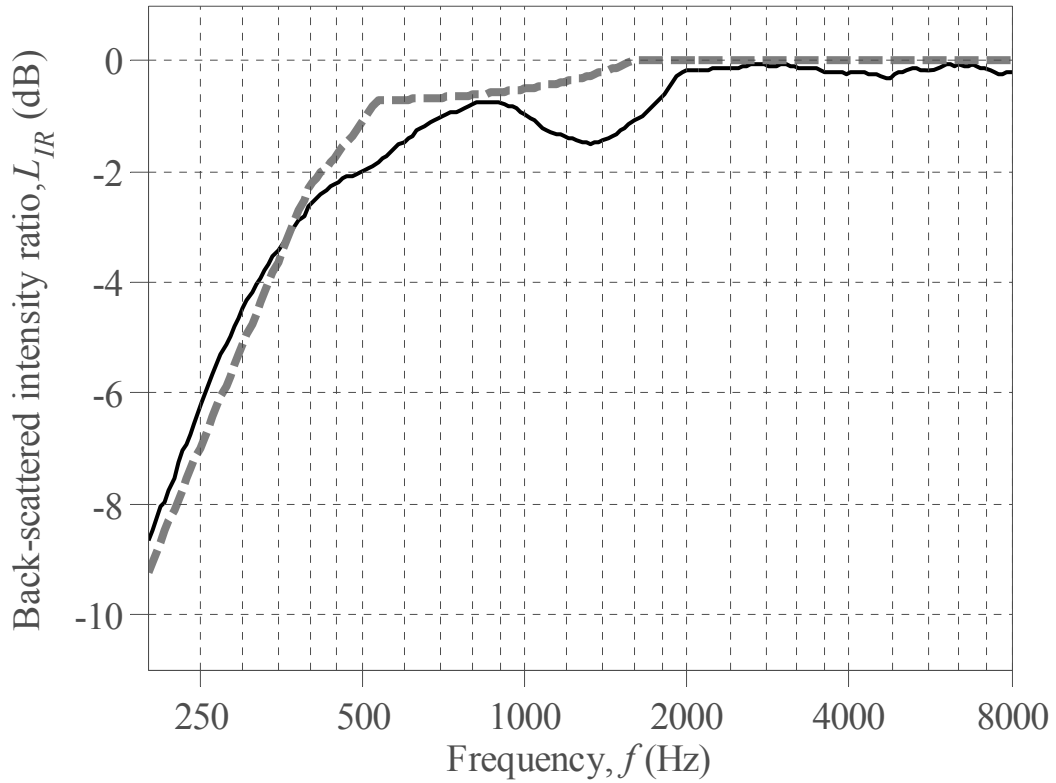
Figure 4.26: Back-scattered intensity ratio for the d_x = 5cm array as per Figure 4.24 (━)
and the small layer spacing prediction model presented above (╺ ╺); $\theta_0 = 0°$, D = 0.912m

To allow half of the incident energy to propagate through the array and to achieve a back-scattered power value of -3dB, an array with a 50% line-of-sight would be required (F_{fill} = 1-0.5 = 0.5).

For an $M \times N$ array, where each layer comprises E randomly placed elements, the fill factor F_{fill} will on average be given by:

$$F_{fill} \approx 1 - \left(1 - \frac{E}{N}\right)^M \qquad\qquad 4.26$$

From Eq. 4.26 this implies an average density of elements per layer of:

$$\frac{E}{N} \approx 1 - \frac{1}{2^{1/M}} \qquad\qquad 4.27$$

For example for an M = 5 layer structure the average layer density would have to be on the order of 13%. Since objects on the order of a third of a wavelength are required in order to

provide low frequency scattered power, this implies the use of long sparse sequences with an increased overall diffuser width.

Large layer spacing

Consider the case of the $d_x = 1$m array shown in Figure 4.24. Excluding the rapid fluctuations due to coherent and incoherent interference between the two layers, the low frequency roll-on is similar to that from an individual slat; that is approximately +10dB. This is due to the separation distance allowing the layers to act independently from one another, since at low frequency the diffraction around the individual slats will be large. Consequently the two layers act as independent sources. This is predicted by Eq. 4.25 which gives a frequency of $f = 86$Hz below which coherent interference will start to dominate. At high frequency, unlike the smaller spaced array, the back-scattered power does not approach 0dB. This is because with increasing layer spacing the width of a transmitted beam through the gaps in the array (and incident upon the following layer) increases, and subsequently the level of the specular back-scattered energy falls. For large spacings this beam will illuminate the whole of the succeeding layer and the two layers will act independently, with now the line-of-sight through the individual layers being of importance rather than through the whole array.

To demonstrate the above, Figure 4.27 show pressure maps of the total field (normalised to the on-axis incident pressure) with distance behind two very different slat arrays for a frequency of $f \approx 6.6$kHz. These comprise a single layer of slats of width $D = 10$m (to minimise diffraction around the sides) with a gap of width $d = 22.8$cm in the centre (top), and the front layer of slats from the example in Figure 4.24 (bottom). The pressure transmitted through the gaps in both arrays can be seen to form a beam that gradually widens with distance. This occurs despite the diffraction around the edges, even for the slat array of width $D = 91.2$cm.
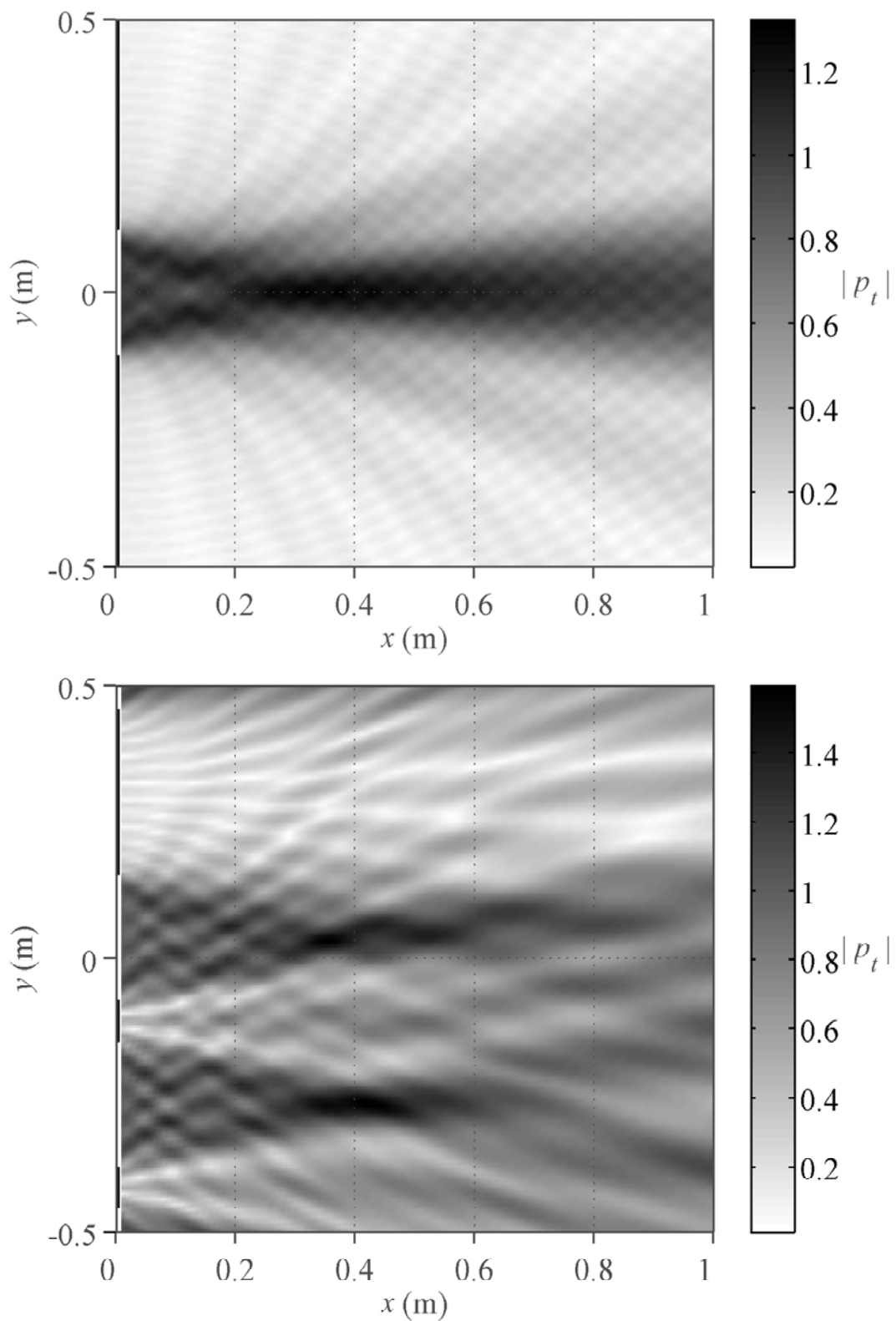
Figure 4.27: Total pressure behind a single layered slat array comprising a single hole of width d = 22.8cm in the centre of a plate of width D (top) and the N = 12, E = 6 sequence from Section 4.2.6 (bottom); f = 6617Hz, θ₀ = 0°

To approximate the point above which dispersion of the transmitted field becomes significant, consider the case shown in Figure 4.28, where a plane wave is incident upon a hole/gap of width d in a layer of slats. In a similar manner to that considered in Section 3.3.2, the extent of the main lobe incident upon a run of slats (also of width d) directly behind the gap may be estimated by the point at which a pressure null is predicted at its extents. Neglecting the effects of spherical spreading, this will occur when maximum path difference Δr is equal to wavelength; the point at which the slat (as seen by the edges) is illuminated by two Fresnel zones.
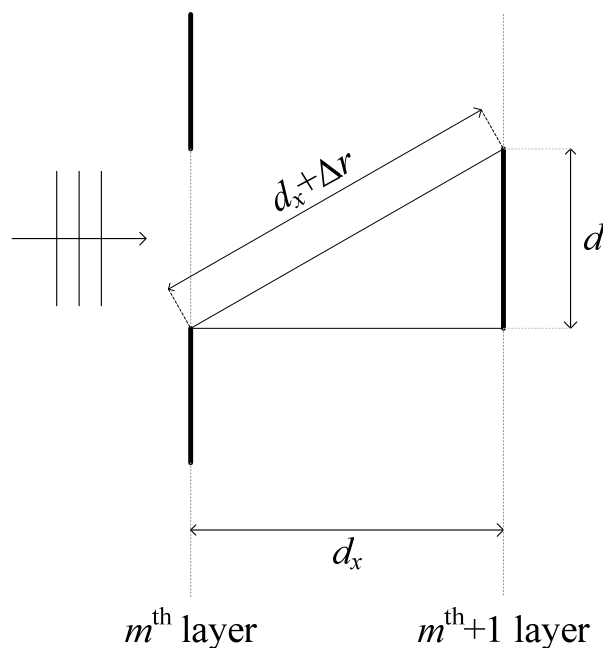
Figure 4.28: Geometry for determining the back-scattered intensity from a slat of width, d, situated at a distance, d_x, behind a slit of the same width

Above a certain frequency the main lobe (as defined above) transmitted through the gap will be narrower than the slat directly behind it, and consequently the majority of the incident energy will be redirected back towards the source. This case was illustrated by the small layer spacing example presented above. Below this frequency however the transmitted lobe will be wider than the slat and consequently part of the sound will miss the slat and be transmitted.

The above results in a predicted transition frequency of:

$$f \approx \frac{2cd_x}{d^2}$$

4.28

Where the frequency above is derived in the same manner as was presented for Eqs. 2.1-2.2 [29] which gave an approximate boundary between near and far-field behaviour. This gives an approximate frequency above which back-scattering will be dominated by line-of-sight, and below which the layers will behave independently from one another. For arrays with gaps of varying length this transition point will be somewhat blurred, though for the example from Figure 4.24 there are two gaps, each of length $d = 3 \times d_e = 22.8$cm. Consequently a transitional frequency of $f \approx 13.2$kHz is predicted for the $d_x = 1$m example, compared with a frequency of $f \approx 660$Hz for the $d_x = 5$cm layer spacing. For the pressure maps of Figure 4.27, the frequency ($f \approx 6.6$kHz) would correspond to a transitional frequency for a layer spacing of $d_x = 0.5$m.

Below the transition frequency given by Eq. 4.28 the array will (neglecting diffraction around the sides) begin to act like a set of independent barriers; each providing additional attenuation. If the mth layer considered separately provides an intensity ratio, I_m, predicted by using Eqs. 4.15-4.16 (though expressed in its linear rather than dB form), then an approximation to the back-scattered intensity ratio from a two layered structure may be given as:

$$L_{IR} \approx 10\log_{10}\left(I_1 + \left(1 - I_1\right)^2 \sum_{i=0}^{\infty} I_1^{\ i} I_2^{\ i+1} \right)$$

4.29

Where the $(1-I_1)^2$ term represents the attenuation passing and returning through the first layer, and the summation represents an infinite sum of multiple scatter reflections between the two layers. Note attenuation due to distance here is neglected. The above is a form of geometric series, and can be simplified to give:

$$L_{IR} \approx 10\log_{10}\left(I_1 + \frac{\left(1 - I_1\right)^2 I_2}{1 - I_1 I_2} \right)$$

4.30

For the $d_x = 1$m example of Figure 4.24 this implies a high frequency intensity ratio of -1.76dB, which when applied to the scattered power model is shown in Figure 4.29 to provide a much closer estimate.
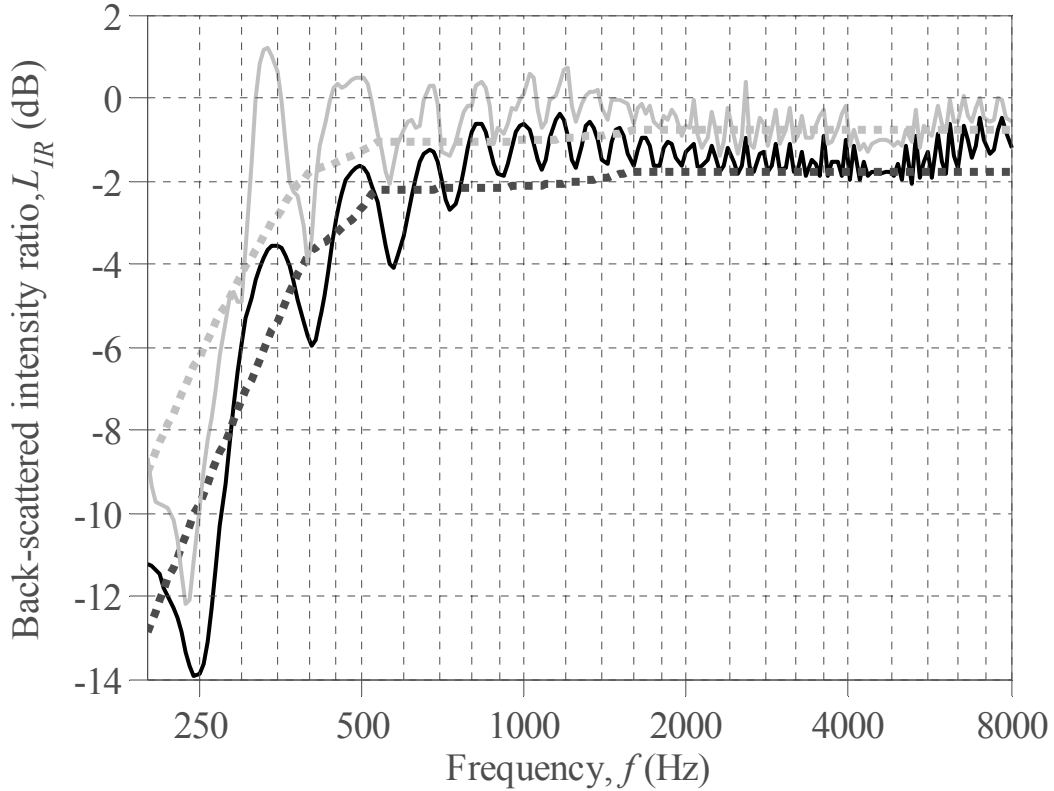
Figure 4.29: Back-scattered intensity ratio for a slats array comprising alternating orthogonal layers based on the N = 12, E = 6 sequence from Section 4.2.6; M = 2 (——), M = 5 (——), and their respective approximate models (▪ ▪ ▪ and ▪ ▪ ▪); θ₀ = 0°, d$_x$ = 1m, D = 0.912m

For additional layers it can be shown that the equation above can be expressed as follows:

$$I_t = I_t + \frac{(1 - I_t)^2 I_m}{1 - I_m I_t} \qquad\qquad 4.31$$

$$L_{IR} = 10 \log_{10}(I_t) \qquad\qquad 4.32$$

Where I_t is the total power scattered off the array, and is applied recursively until $m = M$. Note, multiple scattering is considered between adjacent layers only. Figure 4.29 also shows an example of an $M = 5$ layer array, and is constructed in a similar manner to the two layer

array, where the array is based on the same initial sequence and each subsequent layer is an orthogonal version of the layer in front. Excluding the rapid fluctuations, the approximation given by Eqs. 4.31-4.32 produces a suitable indication of the level of high frequency back-scattered power.

Based on the above it is evident that even for larger spacings, sparse layers would be required if a multi-layered structure is to achieve a -3dB back-scattered intensity ratio. For example, from Eq. 4.31 it can be shown that if all layers considered individually back-scatter the same intensity ratio, I, then the overall scattered power may be given as:

$$L_{IR} \approx 10 \log_{10} \left(\frac{IM}{1 + I(M-1)} \right)$$

4.33

To obtain a value of -3dB, the above reduces to:

$$I = \frac{1}{1+M}$$

4.34

Since the power scattered from a single layer is proportional to the fill factor E/N, a simple five layer structure for example would require a layer fill factor of just $1/6^{th}$. This a very similar value to that obtained from Eq. 4.27 for a random array with small layer spacing. In addition as layers become sparser, the transition frequency predicted by Eq. 4.28 decreases rapidly.

For very sparse arrays this transition frequency will be approximately given by:

$$f \approx \frac{2cd_x}{D^2}$$

4.35

Consequently for most practical layer spacings the back-scattered energy from sparse arrays will be dominated by line-of-sight, and an approximate 50% fill factor is required for a -3dB back-scattered power value. As with the small layer spacing therefore, this implies that the width of the array must be extended to ensure the maximum run size can be maintained whilst still providing low occupancy.

4.3.2   The effect of periodicity on diffusion

It was demonstrated above that once wavelength became comparable to the slat size then the specular reflection dominates. For the case of normal incidence this implies that the back-scattered energy will be similar to that from the equivalent Schroeder diffuser; the same arrangement though with side walls situated between adjacent slats to ensure plane wave propagation, an example of which was shown in Figure 4.23.

Following from Eqs. 2.16 and 2.20, which give an approximation to the scattering from a periodic line array and a single slat, an approximation to the normalised scattered pressure, $p_{s,norm}$, from a Schroeder diffuser may be given as:

$$p_{s,norm}(\theta_0,\theta) \approx d_e(1+\cos(\theta))\frac{(1-j)}{2\sqrt{2}}\sqrt{\frac{1}{\lambda}}\,\text{sinc}\left(\frac{kd_e}{2}(\sin\theta+\sin\theta_0)\right) \times$$

$$\sum_{n=0}^{N-1} R_n e^{jknd_y(\sin\theta+\sin\theta_0)}$$

4.36

$$R_n = e^{jk2d_n}$$

4.37

Where d_n is the depth of the nth well, as depicted in Figure 1.2, and determines the change in phase on exit due to distance travelled, described by the reflection coefficient, R_n. This is a Fourier approximation, equivalent to that often used in Schroeder diffuser design [3], and is similar to the model considered previously in Eq. 4.2 for 1D slat arrays / amplitude diffusers.

For the case considered in Figure 4.23 the well depths equate to $d_n = d_x \times [0\ 0\ 0\ 0\ 1\ 1\ 1\ 0\ 1\ 1\ 1\ 0]$, and forms a binary Schroeder diffuser. Figure 4.30 shows maps of the normalised scattered pressure with frequency for this array where $d_x = 20$cm, for both the thin panel BEM prediction (top) and Schroeder diffuser prediction as per Eq. 4.36-4.37 (bottom). Since this is compared to a surface diffuser the comparison is for the back-scattered region only. At low frequencies the two predictions deviate slightly due to diffraction around the slats, though with increasing frequency the trend becomes very similar.
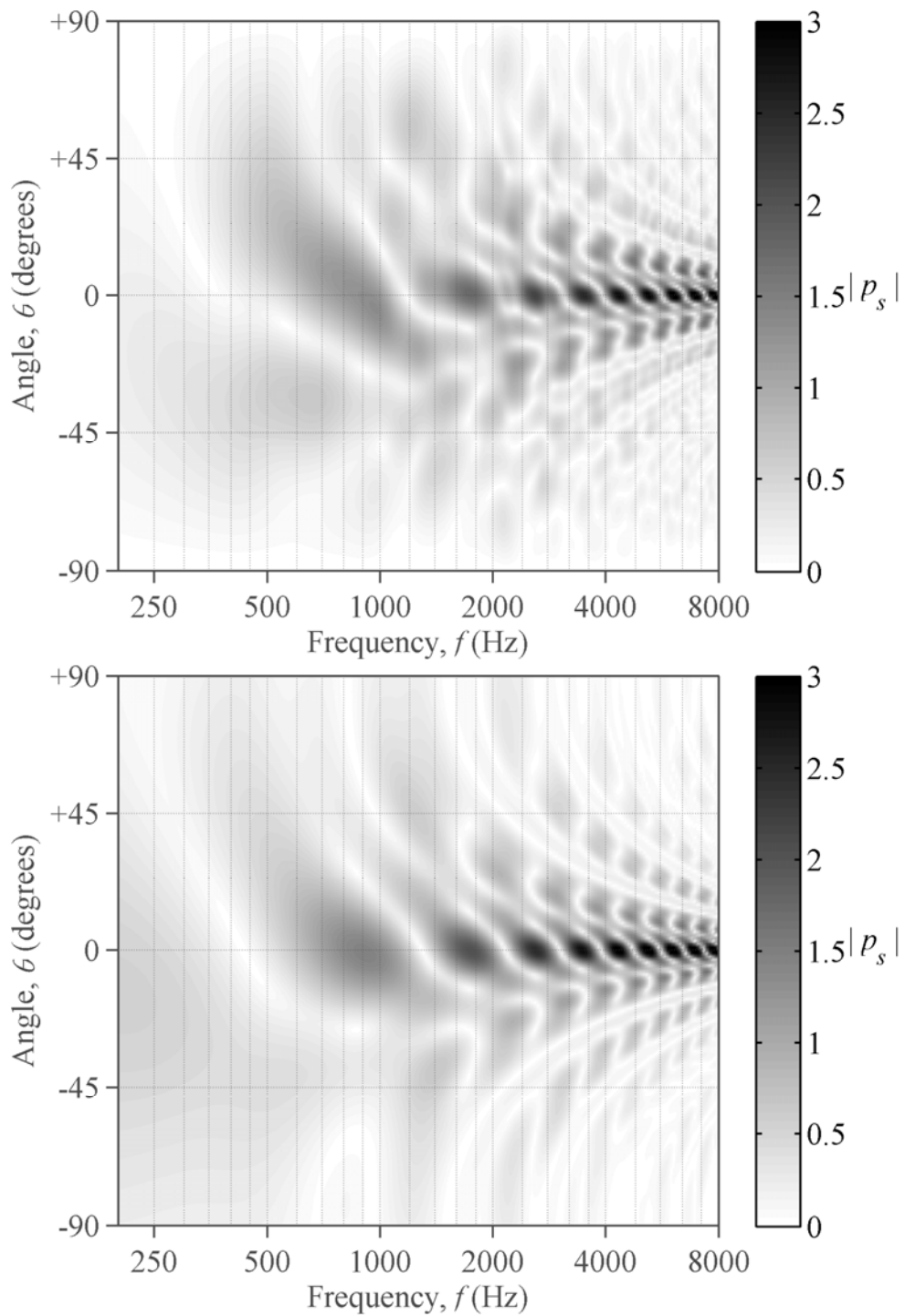
Figure 4.30: Normalised scattered pressure for the two layered slat array as per Figure 4.23 (top) and equivalent Schroeder diffuser modelled using a Fourier approximation (bottom); $\theta_0 = 0°$, $d_x = 20cm$, $d_y = d_e = 7.6cm$

The pressure scattered in the specular direction alternates between destructive and constructive interference; when odd and even multiples of quarter of a wavelength are equal

to the layer spacing. This equates to odd and even multiples of the frequency given by Eq. 4.25, which here is given as $f = 430$Hz. The diffusion coefficient for the two models is shown in Figure 4.31, where the fluctuation between cancellation and emphasis of the back-scattered specular lobe provides high and low values respectively; as would be expected for a bipolar Schroeder diffuser. Note for comparison with a surface diffuser, the standard back-scattered coefficient is considered here.
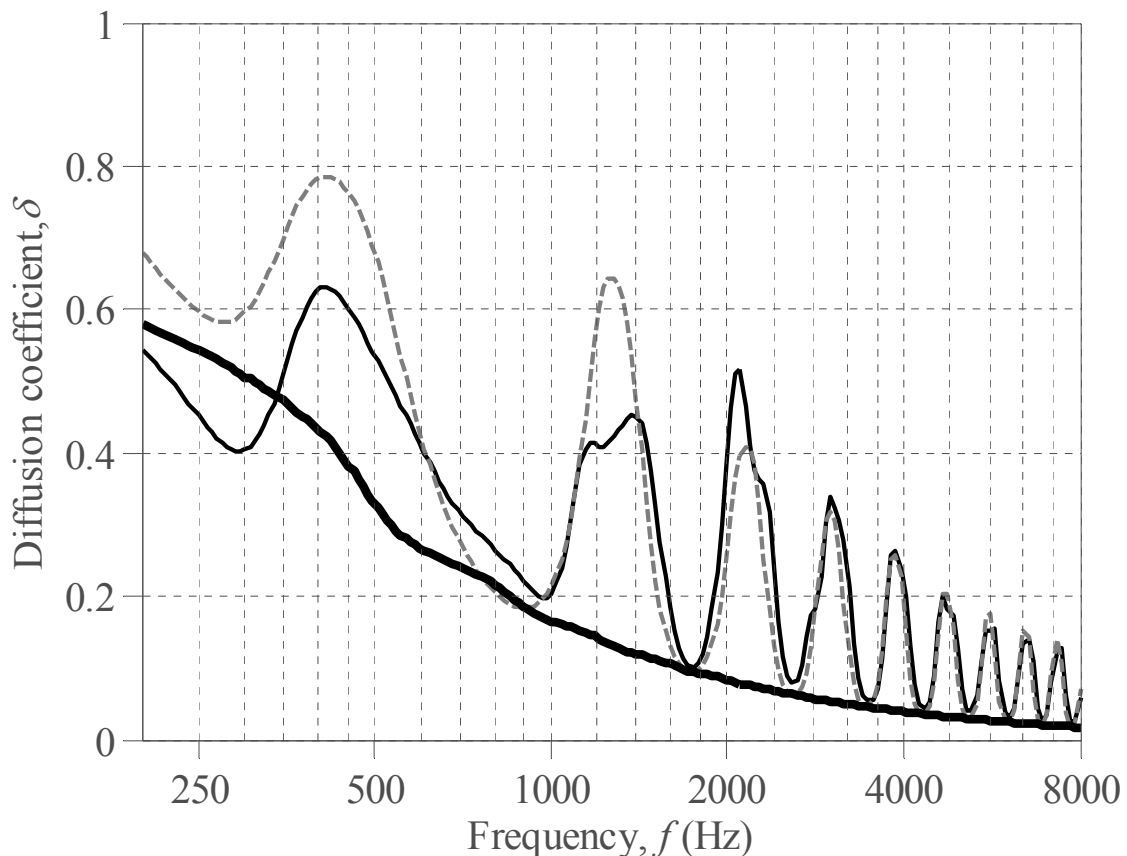
Figure 4.31: Back-scattered diffusion coefficient for the two layered slat array as per Figure 4.23 (━) and equivalent Schroeder diffuser modelled using a Fourier approximation (- -); $\theta_0 = 0^\circ$, $D = 0.912m$, $d_x = 20cm$, $d_y = d_e = 7.6cm$; flat plate (━) shown for reference

For the Schroeder diffuser the notches observed in the diffusion coefficient of Figure 4.31 are often referred to as the flat plate frequencies; when the scattering from the wells returns back in phase and the scattering mimics that of a plane surface. At low frequency the coefficients deviate for the reasons explained above. For all frequencies of interest however – when wavelength becomes comparable to slat size and sufficient scattered power can be achieved –

the trend in the diffusion coefficient pattern is largely the same. This occurs since, like the back-scattered power, the diffusion too is heavily dependent on line-of-sight.

Schroeder diffusers with multiple depths can achieve significant dispersion and so it could be argued that the bottoms of the wells of these devices would equate to an ideal slat array. An example of such an array is shown in Figure 4.32 where the depths of an $N = 7$ Primitive Root Diffuser (PRD) have been used to determine slat arrangement (solid lines only). This has been designed to achieve a diffusive design frequency of $f_0 = 400$Hz [3], with diffusion resulting when half a wavelength is equal to the total depth of the structure. Note only one period is used since the slat width has been selected to provide a scattered power cut-off frequency (following from Eq. 4.18) also of $f = 400$Hz, which for multiple periods would result in a very large structure. Whilst this means the energy scattered into the grating lobes will not be emphasised, dispersion is still significant. The resulting diffusion coefficient is shown in Figure 4.33 which, once wavelength becomes comparable to slat size, can be seen to agree well with the Fourier approximation. For lower frequencies the agreement is less accurate, since scattering from the rear of the structure results in significant scattering towards grazing receivers. At high frequency the flat plate frequencies observed previously for the two layer array are again seen, occurring when multiples of half a wavelength are equal to layer spacing, d_x. Here this corresponds to a frequency of $f = 2.4$kHz.
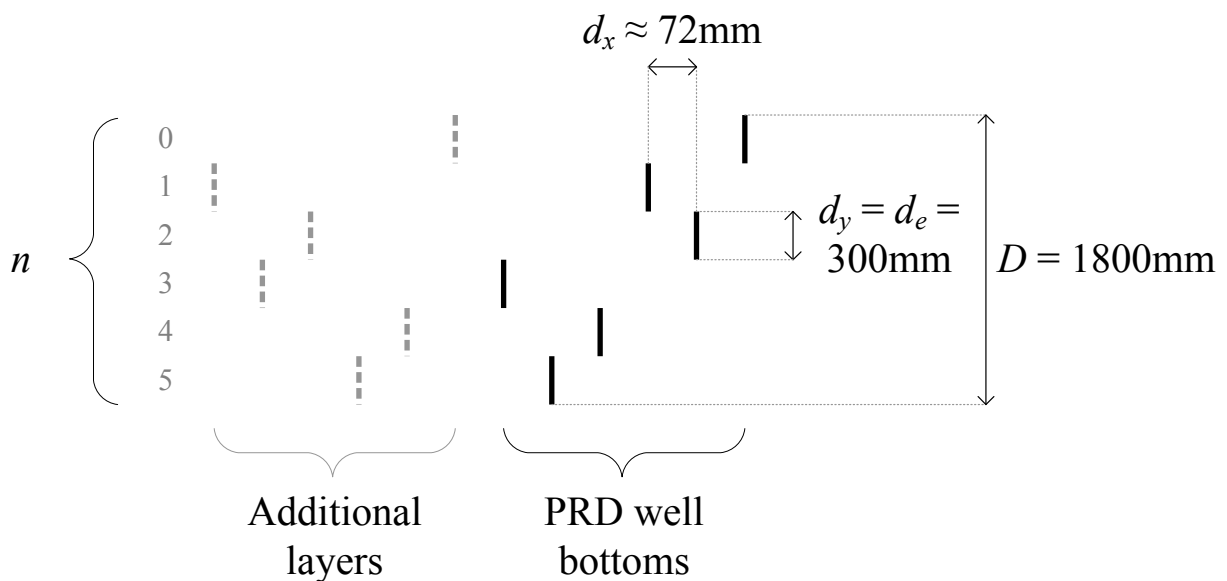
Figure 4.32: Slat array arranged according to the locations of the well bottoms of an N = 7 Primitive Root Diffuser (PRD) (solid lines) and additional layers (dashed lines)

Also included in Figure 4.33 is the coefficient for an array including additional slats to the rear of the PRD array (dashed slats in Figure 4.32). The diffusion coefficient for this array is very similar to that of the basic PRD slat structure, due to the view of these slats (as seen by the source) being completely blocked. This indicates a lack of propagation through the array; an inherent limitation of the specular reflection that results from the use of slats as a base element.
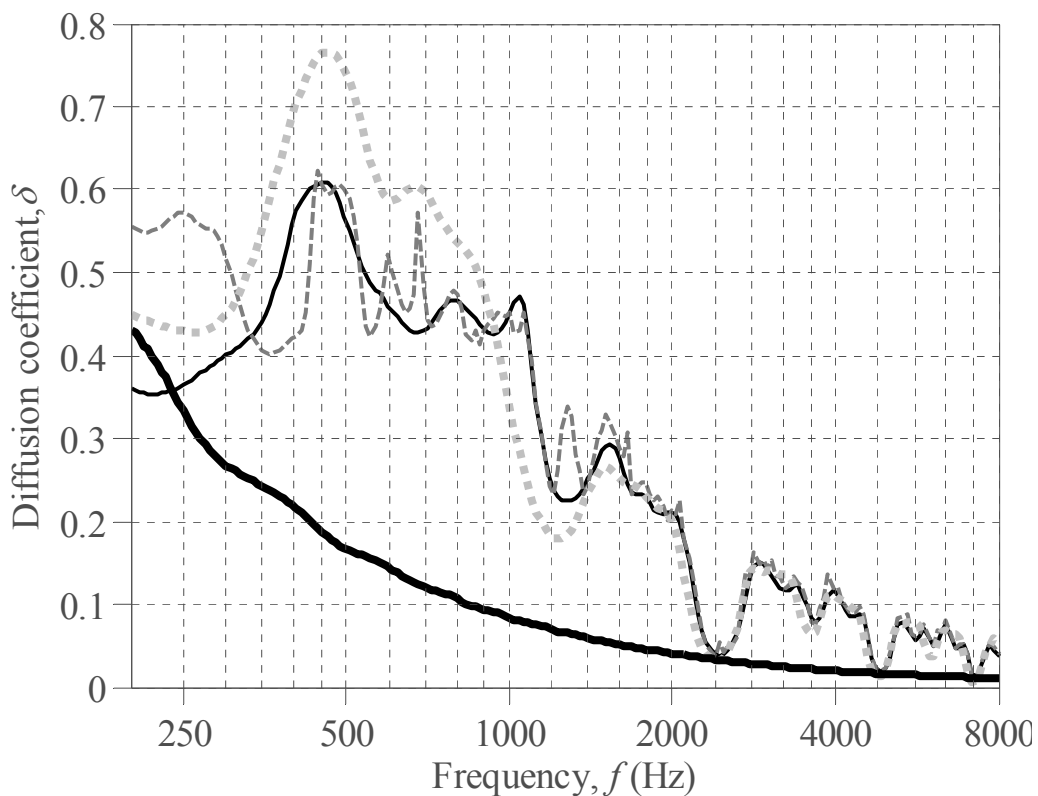
Figure 4.33: Diffusion coefficient (back-scattered) for the slat arrays as per Figure 4.32; PRD slats only (━━) including additional layers (╺ ╺) and equivalent Schroeder diffuser modelled using a Fourier approximation (╍ ╍ ╍); $\theta_0 = 0^\circ$, $D = 1.8m$, $d_x \approx 7.2cm$, $d_y = d_e = 30cm$; flat plate (■■■) shown for reference

Oblique incidence

Figure 4.34 shows the diffusion coefficient obtained for the same case as Figure 4.33, though for an angle of incidence of $\theta_0 = 30^\circ$. Also included is the Fourier approximation for the scattering from an equivalent Schroeder diffuser. The flat plate frequencies in the diffusion coefficient for the Schroeder diffuser appear at the same frequencies as for normal incidence,

since the incident energy must travel a fixed distance (relative to the front layer) determined by the well depths. For the slat array however there is a shift in the diffusion peaks. This is due to the change in path length which determines cancellation of the specular lobe.
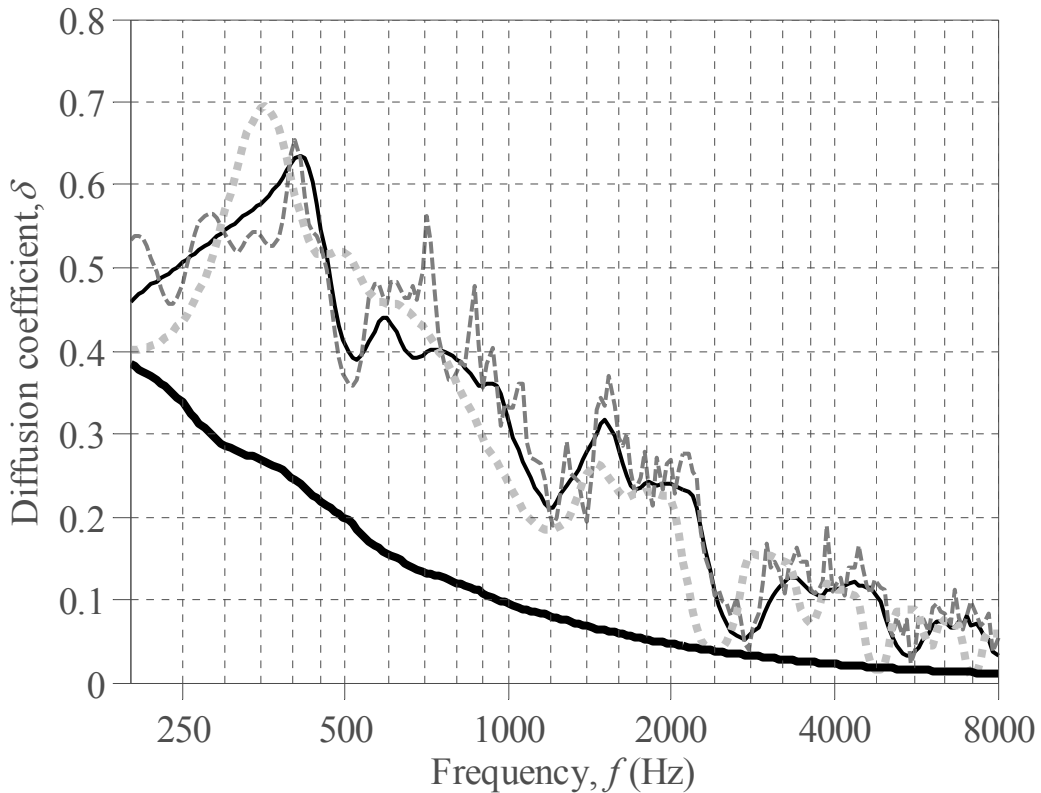
Figure 4.34: Diffusion coefficient (back-scattered) as per Figure 4.33 though with angle of incidence, $\theta_0 = +30^\circ$; flat plate (━) shown for reference is for normal incidence

The shift in the flat plate frequencies here may be described as follows. Consider the arrangement of point scatterers in Figure 2.8. Since each of the *M* layers comprises a series of slats, with increasing frequency the specular reflection ($\theta = -\theta_0$) will dominate. Constructive interference will occur when the path difference (there and back) between the scattering from these layers is equal to a multiple of a wavelength. In the direction of the specular reflection this will occur when:

$$f = \frac{\alpha\, c}{d_x\left(\cos(\theta) + \cos(\theta_0)\right)} = \frac{\alpha\, c}{2d_x \cos(\theta_0)} \qquad 4.38$$

Where α is an integer, and the above is a statement of Bragg's law [39]. Note Bragg scattering is more usually expressed in terms of the angle relative to the direction of the periodicity, and

consequently results in a sin term rather than the cos term seen here. Eq. 4.38 therefore predicts that for the $\theta_0 = 30^\circ$ example the diffusion should decrease when the frequency is a multiple of $f \approx 2.77$kHz, which is indeed the case. A more general description therefore for the frequencies at which diffusion will suffer due to the coherent specular reflections off layers can be described by Bragg scattering.

Acoustic iridescence

Since the frequencies at which a strong specular reflection results will be dependent on angle, the frequency response will alter depending on the point of observation. This is illustrated in Figure 4.35 where the scattering from the PRD array from above is considered for angles of incidence of $\theta_0 = 0^\circ$ and $\theta_0 = 30^\circ$. These display a form of harmonic series which alters with angle. An effective fundamental frequency is determined by Eq. 4.38, giving frequencies of $f \approx 2.40$kHz and $f \approx 2.77$kHz for angles of incidence of $\theta_0 = 0^\circ$ and $\theta_0 = 30^\circ$ respectively. The effect is essentially a form of acoustic iridescence [63], and would likely sound tonal; an undesirable effect for a diffuser. Consequently this should be avoided.
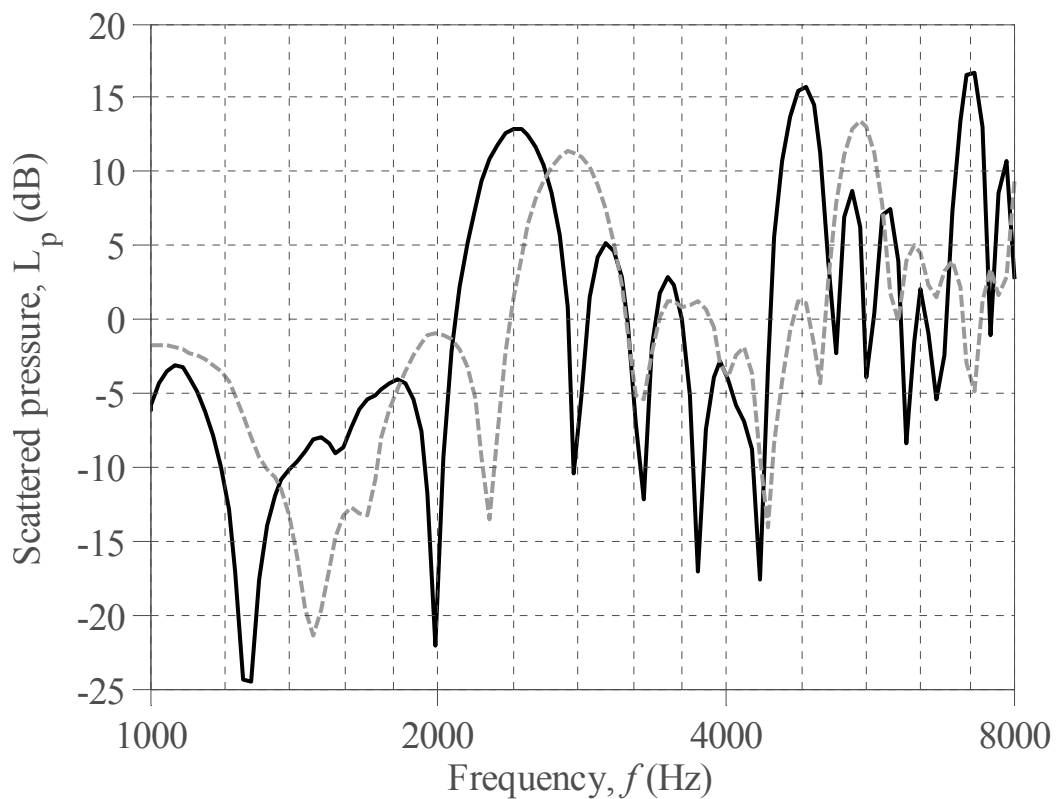
Figure 4.35: Scattered pressure specular reflection off the slat array as per Figure 4.32 (PRD slats only); $\theta_0 = 0^\circ$ (——), and $+30^\circ$ (– –); $d_x = 20$cm

4.3.3 Sparse arrays

The above illustrated how for fuller arrays once wavelength became comparable to slat size, the scattered response is heavily dependent on line-of-sight. To allow propagation through an array therefore, sparse sequences must be considered. In Section 4.2.3 Golomb ruler sequences were introduced; sequences that have a maximum out of phase AACF value of one. These sequences are ideal for a multi-layered structure since they both diffuse well and become gradually sparser with increasing sequence length, N. The required slat size for an array is determined by Eq. 4.23, which since by definition Golomb rulers can have no more than $n = 2$ consecutive elements, for a minimum frequency of $f_{min} = 400$Hz gives $d_e = 0.152$cm. To achieve the -3dB back-scattered power target an average layer density of approximately 0.13-0.17 is required (obtained from Eqs. 4.27 and 4.34). In order to achieve this, an optimal Golomb ruler on the order of $N = 72$ in length would be required. This however suggests a total diffuser width of $D \approx 11$m, which is clearly impractical. Since however an optimal Golomb ruler with elements removed is still a (non-optimal) Golomb ruler, it is possible to simply remove elements to obtain a suitable arrangement density, with each layer still having desirable Fourier properties. For the design here, shown in Figure 4.36 (a), a sequence length of $N = 26$ was selected; a length long enough to ensure a suitable number of elements per layer still remain, and for which five optimal Golomb rulers exist. The array was constructed by placing these five 'rulers' in an arbitrary order, before altering the structure through random element removal to allow a 50% line-of-sight.

Figure 4.37 and Figure 4.38 show the diffusion coefficient and back-scattered intensity ratio respectively for the $M = 5$ layered slat array constructed as described above. Also included for comparison is the results for an equivalent single layered array; one which appears the same as the multi-layered array as viewed by the source (Figure 4.36 (b)). At low frequency the single layer array provides more even scattering; with diffraction around the individual slats of the multi-layered structure resulting in less predictable behaviour. This agrees with the results presented in Figure 4.31 for a simple two layered array. With increasing frequency however, the multi-layered structures outperform their single layer equivalent.
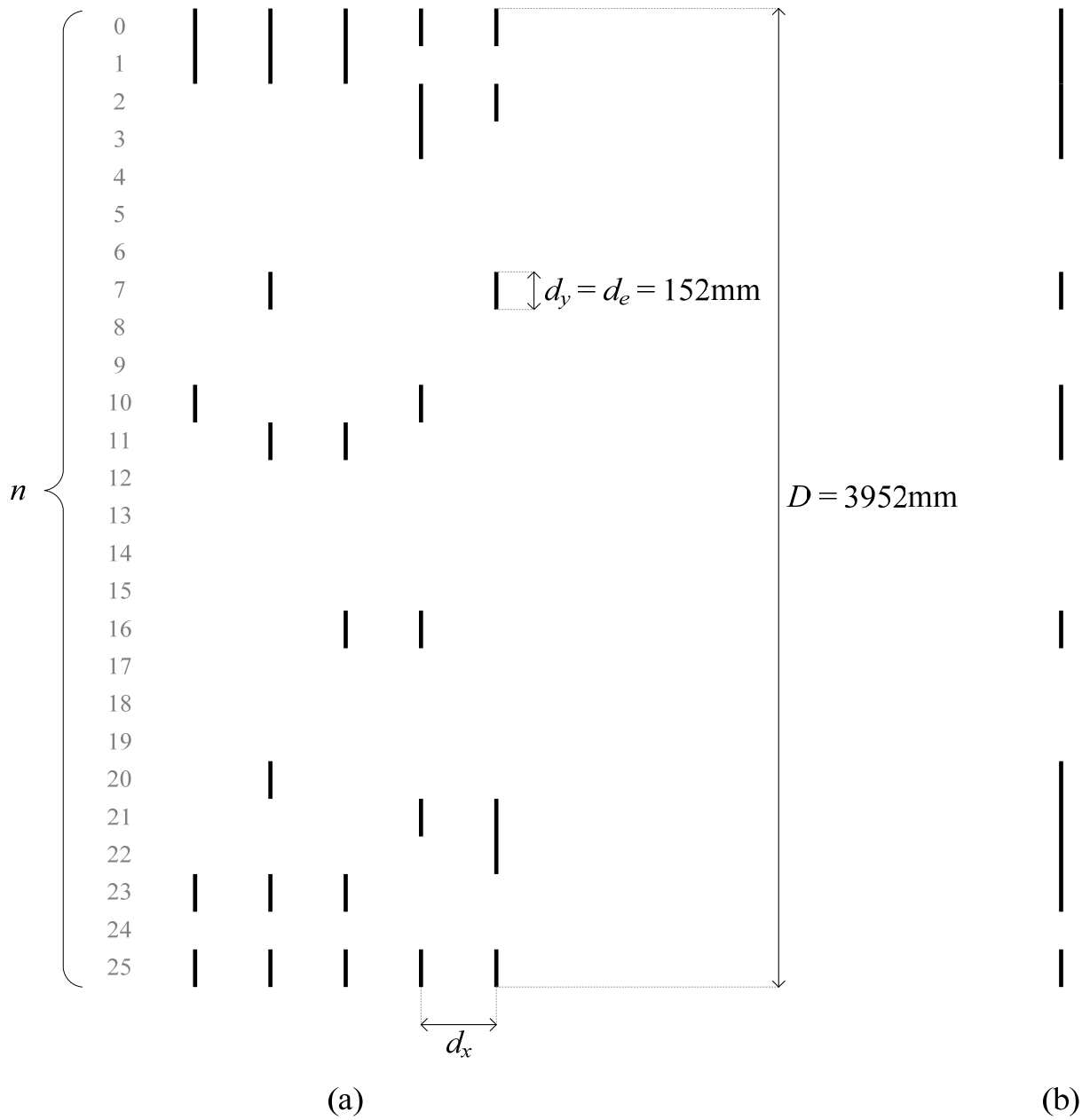
Figure 4.36: M = 5 × N = 26 Golomb ruler slat array arrangement (a) and single layer equivalent as viewed by normal incidence source (b)

At high frequency the first drop in diffusion due to coherent (Bragg) back-scattering off the layers, as predicted by Eq. 4.38, should occur at multiples of $f = 860$Hz and $f = 3.44$kHz for the $d_x = 20$cm and $d_x = 5$cm arrays respectively. The $d_x = 20$cm array displays these notches, though their severity is significantly reduced due to the sparse nature of the array. For the $d_x = 5$cm example this happens after the point at which the diffusion tails off due to the response of an individual slat, predicted by Eq. 4.4 to occur at $f \approx 2.26$kHz, and so any coefficient notches are largely unseen.
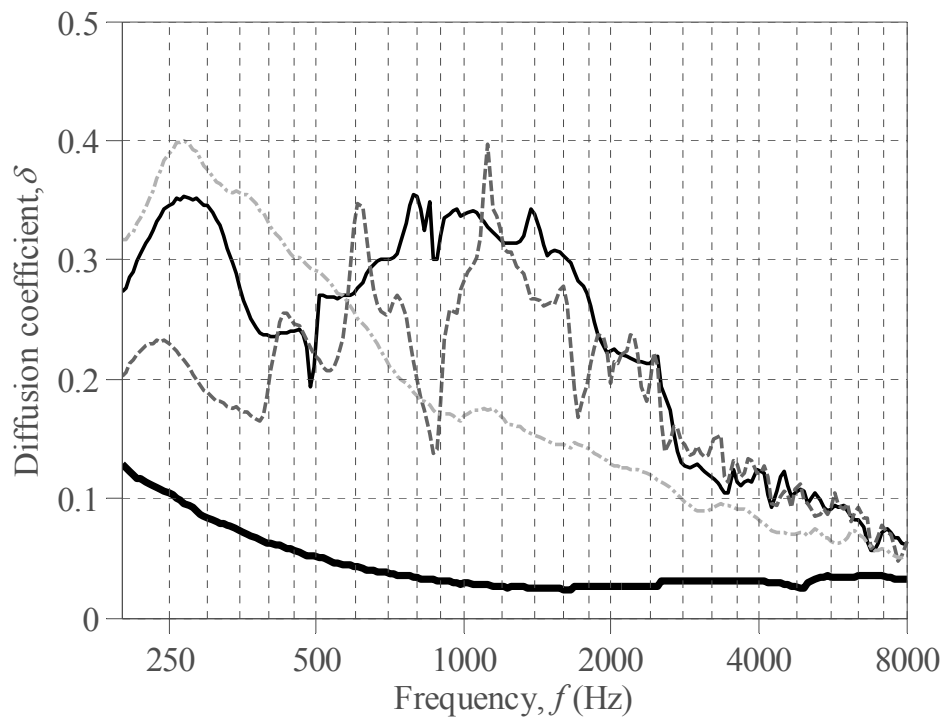
Figure 4.37: Diffusion coefficient for an M = 5 × N = 26 Golomb ruler array with layer spacing d_x = 5cm (━━) and d_x = 20cm (━ ━), and equivalent single layer array (━ ━); $θ_0 = 0^°$, D = 3.952m; flat plate (━━) shown for reference
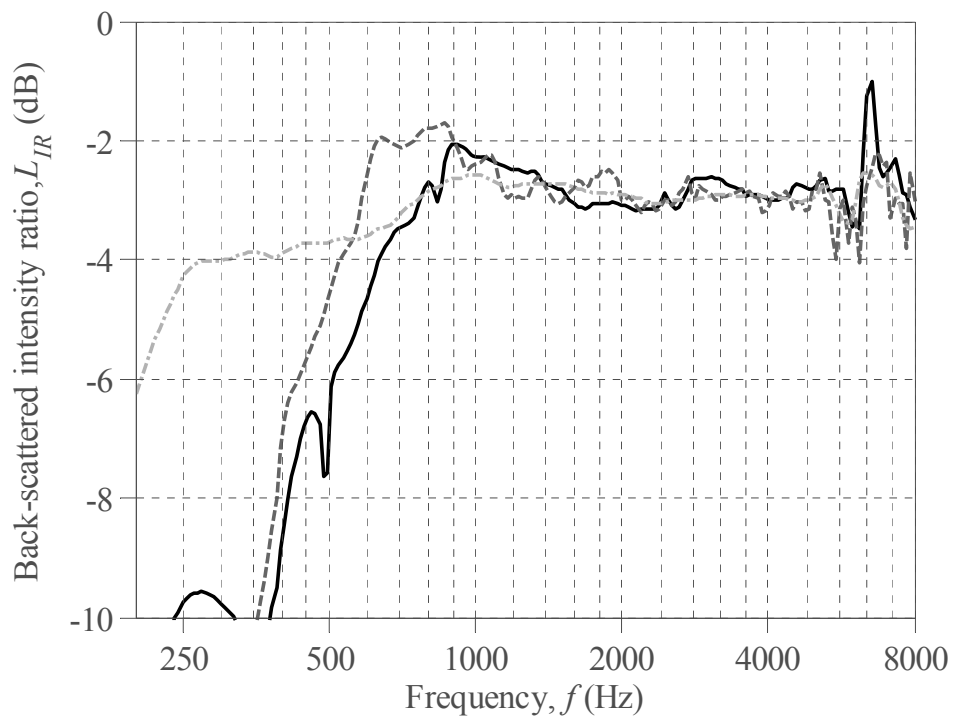
Figure 4.38: Back-scattered intensity ratio for the slat array as per Figure 4.37

Due to the small number of runs of two adjacent slats, their influence on scattered power at low frequency is minimal. Consequently the back-scattered power does not approach -3dB (as determined by the 50% line-of-sight) until the point at which the cut-off frequency for a single slat occurs; when $f = 800$Hz here. Coupled with the high frequency diffusive limit for a single slat, this limits the performance bandwidth to approximately $\log_2(2\sqrt{2}) = 1.5$ octaves; an inherent limitation of the need for large runs of slats with a low occupancy.

4.4. Alternative arrangements

4.4.1 An impedance matching approach

Since sparse arrays tend to have very few runs of adjacent slats, individual slats on the order of a third of a wavelength are required to scatter efficiently at low frequency. For a minimum design frequency of $f_{min} = 400$Hz this implies a slat size on the order of $d_e = 30$cm. Sparse layers based on this slat size will inherently be very large, for example based on the array from Figure 4.36 an approximate width of $D = 8$m would be required. Consequently these would likely make impractical constructions. In addition as was demonstrated above, due to the narrow frequency over which an individual slat scatters sufficient power whilst scattering in a non-specular manner, their bandwidth of operation is small.

One alternative to the above approach is to provide layers of varying slat size. As has been shown, if the front layers comprise elements large relative to wavelength then little energy will propagate into the array. If the array is designed to have small elements at the front and progressively larger elements towards the back of the array however, then each layer may be targeted to diffuse over a given frequency range. This forms an equivalent to impedance matching seen with absorbers [3]. For example consider a simple three layered array, comprising layers of small, medium and large elements from front to back; comparable in size to low, mid and high frequency wavelengths respectively. At low frequency the front two layers will have little effect, and an incident wavefront will effectively only see the back layer. At mid frequency the front layer will have little effect, and the incident energy will see a combination of the middle and back layers. Finally at high frequency the whole array is seen.

An example of the above is shown in Figure 4.39 for an $M = 5$ layered structure, where layers (from back to front) are based on Golomb ruler sequences of length $N = \{6, 10, 17, 29, 50\}$. The array has been designed to scatter efficiently from a lower frequency of $f_{min} = 400$Hz, with the individual scattered power cut-off frequencies for each of the layers being approximately given as 400Hz, 680Hz, 1.15kHz, 1.96kHz and 3.38kHz respectively. As with the sparse array from Section 4.3.3 the array comprises a set of Golomb rulers where some elements have been selectively removed in order to achieve an approximate 50% line-of-sight through the array. The structure has an overall depth from front to back of 0.5m.

$d_e = 300$mm

$d_e = 62$mm

$d_e = 36$mm

$D = 1800$mm

$d_e = 180$mm

$d_e = 106$mm

d_x
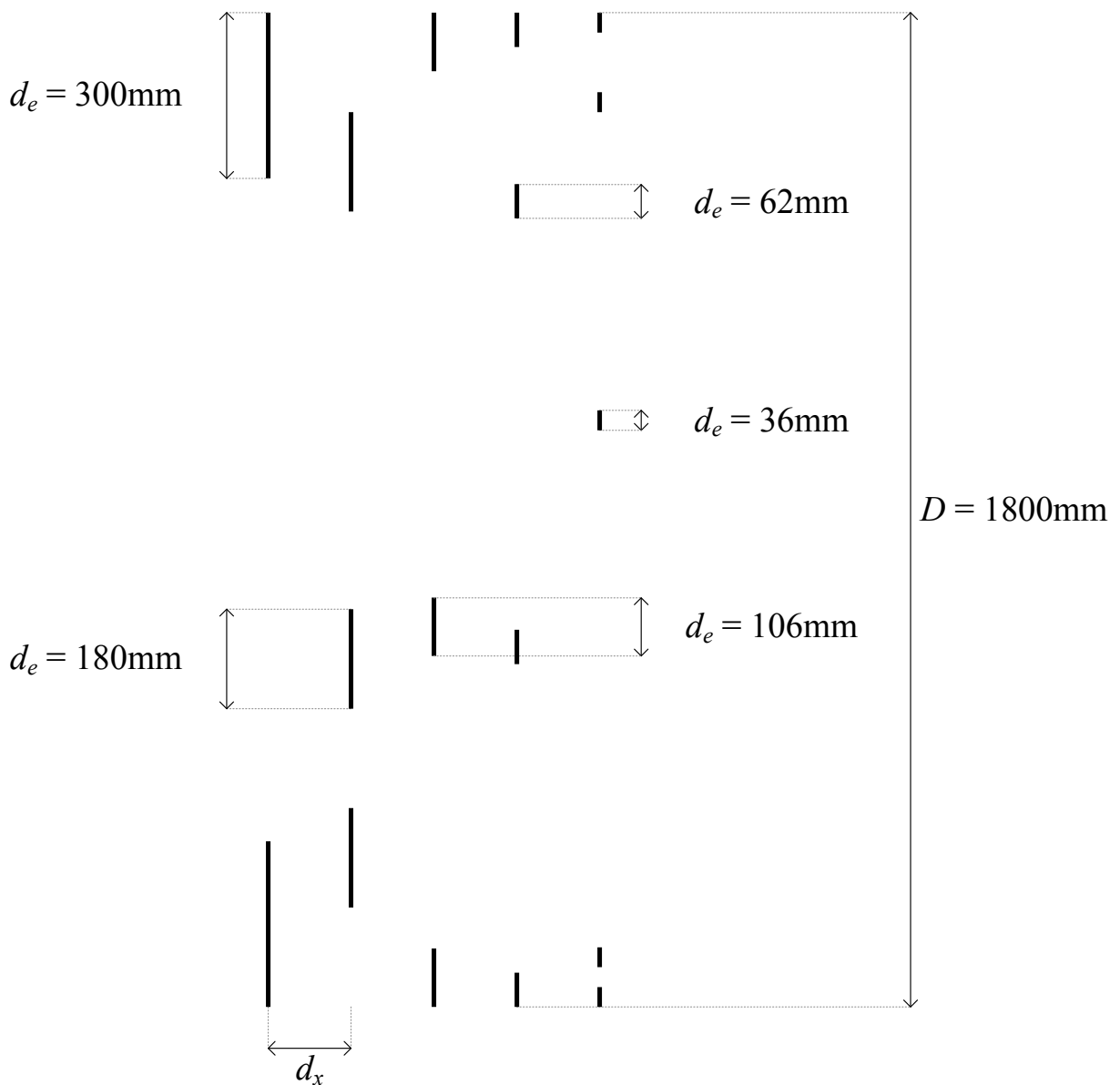
Figure 4.39: M = 5 layered Golomb ruler slat array arrangement based on an impedance matching approach (varying slat size with layer)

The diffusion coefficient (top) and back-scattered intensity ratio (bottom) for the array are given in Figure 4.40, though for a number of layer spacing methods: equal spacing (solid line), Golomb ruler spacing (dashed line) and logarithmic spacing (dotted line). For each of the arrays once the minimum design frequency ($f_{min} = 400$Hz) is reached, a back-scattered intensity ratio of -3 ± 1.1dB is achieved, as determined by the approximate 50% line-of-sight through the array. Each of the arrays provides reasonable diffusion for the majority of the frequency range shown, though as is expected at high frequency the use of equally spaced layers results in notch frequencies in the diffusion coefficient. Following from Eq. 4.38 for the equal layer spacing array (whose layers are situated $d_x = 12.5$cm apart) this occurs at multiples of $f = 1376$Hz. This is the case, though as with the sparse array from Section 4.3.3 the severity of these notches is reduced due to the sparse nature of the array. Improvements in diffusive performance are seen for both remaining arrays, and their construction is described below.

4.4.2 Oversampled and non-periodic layer spacings

Oversampled (Golomb ruler) spacing

Consider the arrangement of point scatterers in Figure 2.8. Due to the underlying periodicity and the inherent specular reflection produced by an individual slat, the limiting factor on diffusion will be the energy scattered in the specular direction ($\theta = -\theta_0$). Following from Eq. 2.17, the energy scattered into the specular reflection angle may be given by:

$$p_s(\theta_0) \propto \sum_{m=0}^{M-1} A_m e^{j2kmd_x \cos\theta_0} \qquad 4.39$$

Where $A_m = \{0, 1\}$ is the amplitude coefficient for the mth layer, where each layer is assumed to have either no elements ($A_m = 0$) or have a set of elements whose contribution is approximately equal to that of any other layers containing elements ($A_m = 1$). As with the summation of Eq. 4.2 describing scattering from a single layer of slats, Eq. 4.39 is a form of DFT. Subsequently in order to scatter evenly with frequency into the specular lobe direction a set of coefficients, A_m, are required whose aperiodic Fourier properties are desirable. As with the 1D arrays a suitable arrangement is given by the Golomb ruler.
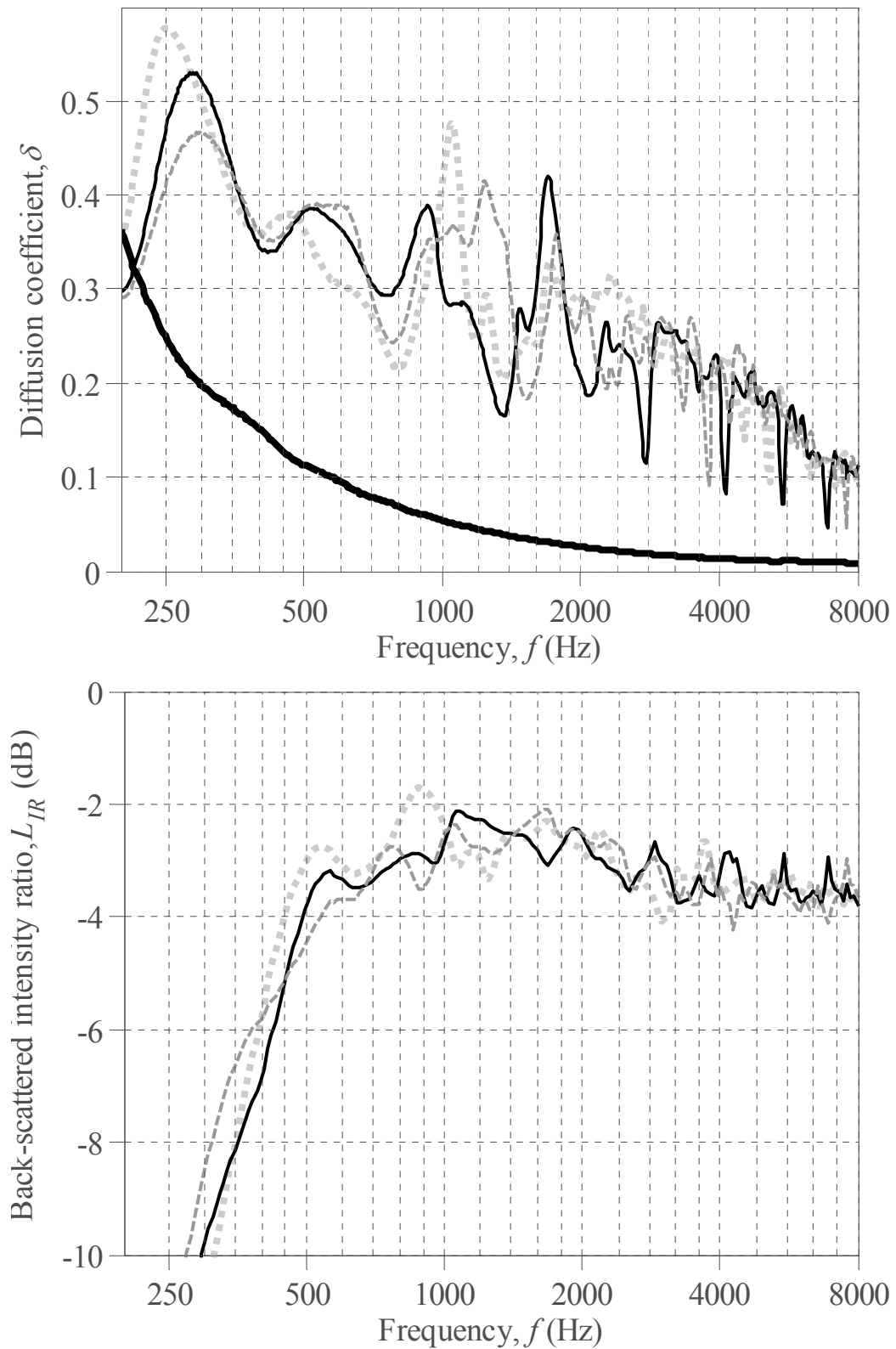
Figure 4.40: Diffusion coefficient (top) and back-scattered intensity ratio (bottom) for the slat array as per Figure 4.39; equal spacing (▬), Golomb ruler spacing (▬ ▬) and logarithmic layer spacing (▪ ▪ ▪); θ₀ = 0°, D = 1.8m; flat plate (▬) shown for reference on top figure

An example of a Golomb ruler spaced array is implemented in Figure 4.40 (dashed line) where the layer spacing is set to $d_x = 0.5/11 \approx 4.5$cm, and the layers are arranged according to the length 11 Golomb ruler [1 1 0 0 1 0 0 0 0 1 0 1]. The resulting layer depths (from front to back) are hence given as $d_x \times$[0 1 4 9 11]. This essentially forms an oversampled layer structure, with a much finer underlying periodic grid. Once half a wavelength (and multiples thereof) become equal to the layer spacing however spatial aliasing occurs and, like the equal spacing example, the array produces an inherent specular reflection. For the example here this first occurs at a frequency of $f = 3784$Hz. Due to the use of underlying periodicity these (Bragg) notch frequencies cannot be removed, though by using the above technique it is possible to push the first notch frequency up to a higher frequency, potentially outside of the design frequency range.

Non-periodic (logarithmic) spacing

Following from Eq. 4.39 above, a more arbitrary description for the back-scattering from an array of slat layers in the specular direction may be approximated by:

$$p_s(\theta_0) \propto \sum_{m=0}^{M-1} e^{j2kd_m \cos \theta_0}$$

$\qquad$ 4.40

Where d_m is the depth of the mth layer. The above is no longer a periodic DFT, though since the number of layers is small a potential exhaustive search may be performed in order to find an optimal arrangement. A complete exhaustive search will likely be very time consuming, however if information about the construction is known then a significantly faster result should arise. For instance in transducer array design it has been shown that the use of logarithmic spacing can result in a frequency independent directivity pattern [64]. These arrays both remove the requirement for periodicity and require only a single value to describe each arrangement, and so are ideal. A logarithmically spaced set of layers may be given as:

$$d_m = d_{max} \frac{e^{Am} - 1}{e^{A(M-1)} - 1}; \qquad 0 \le m \le M - 1$$

$\qquad$ 4.41

Where A is an arbitrary positive scaling factor, and d_{max} is the maximum array depth. Note, the search is performed until a predefined minimum spacing, d_{min}, between layers is achieved, which in this case was set to be equal to the spacing used for the Golomb array method above

(d_{min} = 0.5/11 ≈ 4.5cm). In a similar manner to the exhaustive search of Section 4.2.3, the above layer spacing description was used in conjunction with Eq. 4.40, where for each outcome the diffusion coefficient was used to asses the relative merit of each arrangement. A value of A = 0.354 was found to provide the highest coefficient for the range $0 \leq 2\cos(\theta_0)/\lambda \leq 1/d_{min}$ (which equates to the point at which half a wavelength fits into the minimum spacing and spatial aliasing occurs for a periodically arranged array). The layer depths are hence given as d_m = [0.0 6.8 16.5 30.3 50.0] cm.

It can be seen from Figure 4.40 that the notches relative to those observed for the periodic arrays are reduced. Since there are only five layers however there will inevitably be a degree of self-similarity relative to wavelength at certain frequencies. Consequently the improvement is noticeable, though small. Overall however an approximate 4 octave bandwidth of performance is observed, with a diffusion coefficient on the order of 0.1-0.4 above that of the reference plate being achieved.

4.5.   Conclusions

An investigation has been performed into the use of an array of slats as a potential volume diffuser. These were based on periodic arrangements and form an extension to surface amplitude diffusers, though replacing absorption with transmission. This for a simple BAD was demonstrated from measurements, with the back-scattered polar pattern displaying similar behaviour to an equivalent array of slats. Following from this, at first single layer structures were studied before later multi-layered structures were investigated. By selectively removing or varying the size of the individual slats based on number theoretic and array theory concepts, arrays have been created that result in reasonable performance over their intended bandwidth of operation. Typical diffusion coefficient values range from 0.1-0.4 relative to the equivalent reference plate, with scattered power values falling within approximately ±1dB of the -3dB target value.

For a 1D array optimal arrangements are those whose Fourier properties are most desirable. This implies a lack of self-similarity, and may be achieved through the use of both unipolar and amplitude shading arrangements. At low frequency the performance is restricted by slat size, with a maximum run of (conjoined) slats on the order of a third of a wavelength required in order to scatter efficiently. Above this frequency the level of back-scattered power is

controlled by line-of-sight through the array and consequently a 50% fill factor is required to achieve the -3dB target. At high frequency the scattering from an individual slat dominates and diffusion begins to suffer once wavelength becomes comparable to slat size; the larger runs of slats required to scatter efficiently at low frequency produce inherently directional scattering. Consequently the operational bandwidth is determined by the range in size of elements. The best arrangements for diffusive performance however are both short and sparse. These tend to have smaller runs of slats, and consequently scatter inefficiently at low frequency. There is therefore a trade-off between the degree of diffusion and the operational bandwidth.

By introducing layers it becomes possible to cancel the inherent specular reflection associated with an amplitude diffuser, and consequently increased levels of diffusion can result. As with the 1D arrays, slat runs comparable to a third of a wavelength are required to scatter efficiently at low frequency whilst a 50% line-of-sight is required to meet the -3dB scattered power design target. This is due to the inherent directional scattering from a single slat, with the scattering from an array being dominated by what the source can see. An example of this is illustrated by a slat array behaving similarly to an equivalent Schroeder diffuser, with flat plate frequencies resulting at high frequency due to spatial aliasing when half a wavelength is equal to layer spacing. To allow propagation through the array with increasing layers the array must be made sparser, though large objects are still required to scatter effectively at low frequency. Consequently single sized element arrays are limited, and result in an approximate 1.5 octave bandwidth.

An alternative approach has been presented whereby layers comprise progressively larger elements from front to back, similar in concept to impedance matching found in absorbers. This allows both a range of element sizes and a 50% line-of-sight through the array. Periodic spacing between layers is still undesirable. Through use of oversampling or non-periodic (logarithmic) arrangement techniques however the high frequency Bragg frequencies can be either moved outside of the design bandwidth or removed entirely. An example for the latter has been shown to result in an approximate 4 octave bandwidth of performance.

Though slat arrays can be formed that provide a reasonable level of performance, the directional scattering from a single slat is an inherent limiting factor, with performance being heavily dependent on line-of-sight through the array. In addition, due to the their arrangement

arrays of slats will perform very differently with changing angle of incidence; appearing effectively acoustically transparent for grazing source angles. Consequently alternative designs may be considered that aim to get around these restrictions, examples of which are considered in the following two chapters. These take the form of percolation structures in Chapter 5 which aim to channel energy through an array, and through arrays comprised of cylinders in Chapter 6 similar to the design concept presented here though using a base shape that naturally scatters sound more evenly. Both structures form more isotropic arrays, whose appearance is more consistent with angle of incidence.

5. VOLUME DIFFUSION FROM PERCOLATION STRUCTURES

5.1. Introduction

The concept presented in Chapter 4 was one of a layer based structure comprised of slats, where each layer provides 'additional diffusion', or is targeted towards diffusing over a particular frequency range. Slats comparable to approximately half of a wavelength are required to scatter efficiently at low frequency, which at high frequency results in an inherent specular reflection. Consequently arrays of slats have a narrow bandwidth of performance and are inherently limited by line-of-sight through the array. Whilst providing a number of (potentially multiple scattered) paths through the structure, channelling of energy and lateral reflection are not strongly promoted. This chapter introduces a similar though crucially different structure based upon a percolation fractal, which provides potential for promoting sound propagation through an array, encouraging both forward scattering and temporal diffusion.

Schroeder diffusers channel energy through the use of wells separated by fins, forcing plane wave propagation [9]. These produce highly effective diffusion, achieving scattering due to interference of the reflected waves from each well which display different phase shifts due to distance travelled. Low frequency diffusion however is inherently limited by available depth. More recently folded versions of Schroeder diffusers have been suggested [3; 65] which provide the necessary well depths for a given design frequency, though requiring a shallower structure. This can help to utilise some of the wasted space in a classic welled diffuser.

Extending this concept, a periodic lattice may be considered whose adjacent nodes are connected by walls (bonds), both vertically and horizontally. By selectively omitting some of these walls a 2D percolation fractal structure is formed, an example of which was shown in Figure 2.23, which has numerous propagation paths running throughout the structure. Varying the probability that any one bond may be omitted allows the degree of how open the structure is to be varied, and consequently the structure may be tailored to allow sound to navigate through with varying levels of ease. Such a structure essentially forms a waveguide with numerous impedance discontinuities and potentially tortuous paths, allowing multiple scattering and long delays, and hence temporal diffusion and large phase changes on exit. This makes significant improvements in low frequency performance possible compared to

that of a conventional Schroeder diffuser. In addition the structure will display roughness on various different scales, forming a diffuser similar in concept to that of a fractal Schroeder diffuser [66]. This provides scope for diffusion over a broad bandwidth.

This chapter firstly presents an initial investigation into the channelling of sound in channels / wells. A percolation structure as a surface diffuser is then investigated before the use of a volumetric equivalent is considered. This is done by process of a Monte Carlo simulation since the complexity of the structures is large. Later the effect of altering the lattice type is also assessed. Due to the complex nature of the structure a measure of tortuosity is developed, allowing a gauge of how intricate and convoluted the routes through the structure are. The effects of varying the physical properties of an array are examined, including its density, line-of-sight, geometric reflection paths and tortuosity.

Tortuous paths are shown to extend diffusive performance over the low frequency range. Conversely at higher frequencies sparse structures are preferred since, due to the inherent specular reflections off flat surfaces, the effect of line-of-sight through the array on scattered power is dominant. In addition the underlying lattice of a structure determines 'allowed' reflections, which for periodic percolation structures results in sound being predominantly scattered into the back-scattered direction. Due to spatial aliasing, this also causes the equivalent to the flat plate frequencies observed in Schroeder diffusers. Consequently lattice shapes are proposed which avoid periodicity and promote forward scattering and the channelling of energy into the structure. These are shown to offer better performance.

Unless otherwise stated all results presented in this chapter are from predictions carried out using the thin panel BEM model presented in Section 2.3.2, shown in Section 2.6.2 to provide close agreement with experimental measurements.

5.2.   Background to the design concept

5.2.1   Percolation fractals

Percolation structures are ordinarily based on some form of underlying network / lattice comprising a series of sites (nodes) and connecting bonds [67; 68]. The theory behind these networks has been applied to a wide range of 'fluid flow' topics, ranging from fluid transportation in porous media to forest fires and the spread of disease [68]. Of relevance here

is the case of bond percolation where the bonds of a network are either occupied (with probability p_b) or vacant (with probability 1-p_b), allowing or forbidding the propagation of energy between nodes respectively. When p_b is small the network will consist of small isolated clusters of bonds, and consequently for sufficiently large structures propagation from one side to the other will not be possible. Conversely when p_b is large, apart from some small holes the structure will be entirely connected and 'fluid' may pass from one side to the other with ease. As the structure increases in size, asymptotically there becomes a well defined probability value that describes the transition between these two behavioural regimes; the bond percolation threshold, p_{cb} [68]. This threshold is dependent on the network type.

A simple example of a percolation diffuser is shown in Figure 5.1; one based on a square grid lattice (for which the percolation threshold is given as $p_{cb} = 0.5$ [68]). The black lines represent an array of horizontal and vertical slats, forming a series of connected channels between which sound may travel. Consequently the bonds which allow propagation are denoted by the grey dashed lines, forming a network of interconnected nodes (grey circles) with propagation being forbidden or allowed depending on whether or not a slat is present. Since slats block potential propagation paths a structure with percolation threshold, p_{cb}, therefore is formed by placing slats with probability 1-p_b.

By varying the probability that a slat is included / number of slats in an array, the degree of propagation through the structure may be altered. If too few elements are included then sound will essentially pass through the array unperturbed. On the other hand if too many elements are present then energy will not be able to travel through the array and little change in phase will occur. For very large arrays it is likely that this probability value (1-p_b) would be approximately at or below the percolation bond threshold, since this would allow energy to propagate through the array. This however describes the behaviour of a very large network, and the structures considered here are on a much smaller scale. As such, a large range of fill factors may need to be considered.
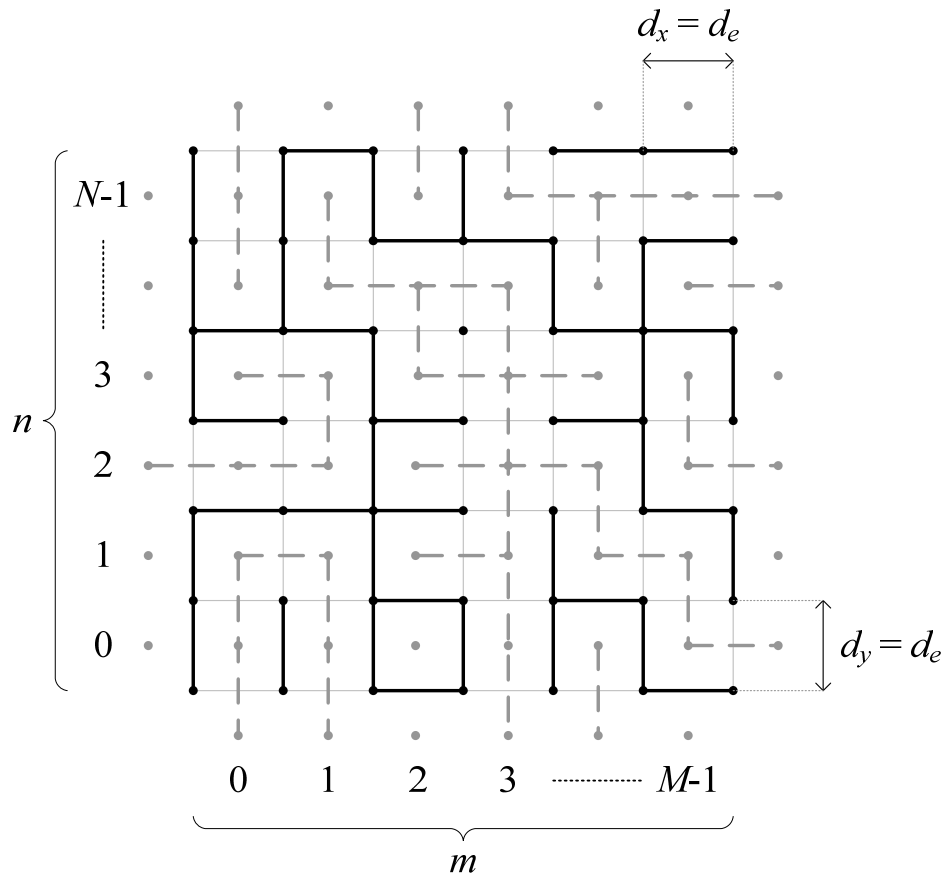
Figure 5.1: M×N Square grid bond percolation structure realised as a series of slats of width, d_e; slats (—), underlying grid (—), and propagation paths (- -); circles denote nodes

5.2.2   Brilliant whiteness in beetle scales

Recently in optics it has been discovered that there exists a species of beetle whose scales display an unexpected degree of whiteness given their depth [69]. This whiteness was shown to be due to an aperiodic structure of scattering interfaces, made up of a network of interconnecting cuticular filaments of varying orientation. This therefore forms a structure similar to that of a percolation network, acting as a waveguide. Whiteness in optics requires an even scattered response with frequency for a range of wavelengths (albeit over a somewhat narrower bandwidth than in acoustics) [50]. If a similar acoustic equivalent could be created then a device which scatters evenly and over a range of frequencies may be possible.

The scales of the beetle were approximately 5μm thick, with filaments on the order of 0.25μm in diameter and with a relatively high void fraction. Since the visible light spectrum contains wavelengths ranging from approximately 390nm to 780nm [50], the depth of a single scale

corresponds to approximately 6.7 times the maximum wavelength. This is actually quite deep; for example in acoustics for a minimum frequency of $f = 400$Hz this corresponds to a depth of approximately 5.8m. Despite this, the above does suggest that a disordered structure based on randomly interconnected elements will be able to scatter evenly over a wide frequency range.

5.3. Sound propagation through channels

In order to understand the mechanisms by which propagation within a structure occurs, it is necessary to consider a number of simple cases. These are presented below for arrangements based on a simple square grid lattice ($d_e = d_x = d_y$) such as that shown in Figure 5.1.

5.3.1 Propagation round corners

For a simple square grid lattice to be effective, it is essential that incident energy must be able to propagate through an array. Consequently this means sound travelling around corners. Consider the case of a wave propagating along a straight channel of width d_e (a single slat wide) that encounters a sharp 90$^°$ bend; the basis for the promotion of all energy channelling in a simple rectangular grid percolation structure. For generality the length of the channel either side of the corner is assumed to be infinite, so as to remove the effects of end reflections or cross-talk between open ends of the two sections. This may be approximately modelled (using the standard BEM routine of Section 2.3.1) as an L-shaped structure with a source located close to one end, and whose ends are terminated by total absorption. The source is placed far away from the corner (relative to the channel width) such that the incident field is approximately planar.

Figure 5.2 shows total pressure maps for an arrangement based on the above for $d_e/\lambda = 0.30$ (top) and $d_e/\lambda = 0.70$ (bottom) respectively. The channel width is set to $d_e = 10$cm, with the whole structure being 1m×1m ($10d_e \times 10d_e$) in size. The source is situated at the centre of the channel, 2.5cm from the end. Figure 5.3 shows the level of transmission round the corner with frequency. This was taken as being the ratio of the average absolute total pressure in the region $-0.2\text{m} \leq x \leq 0.2\text{m}$ (after the corner) relative to that in the region $-0.2\text{m} \leq y \leq 0.2\text{m}$ (before the corner).
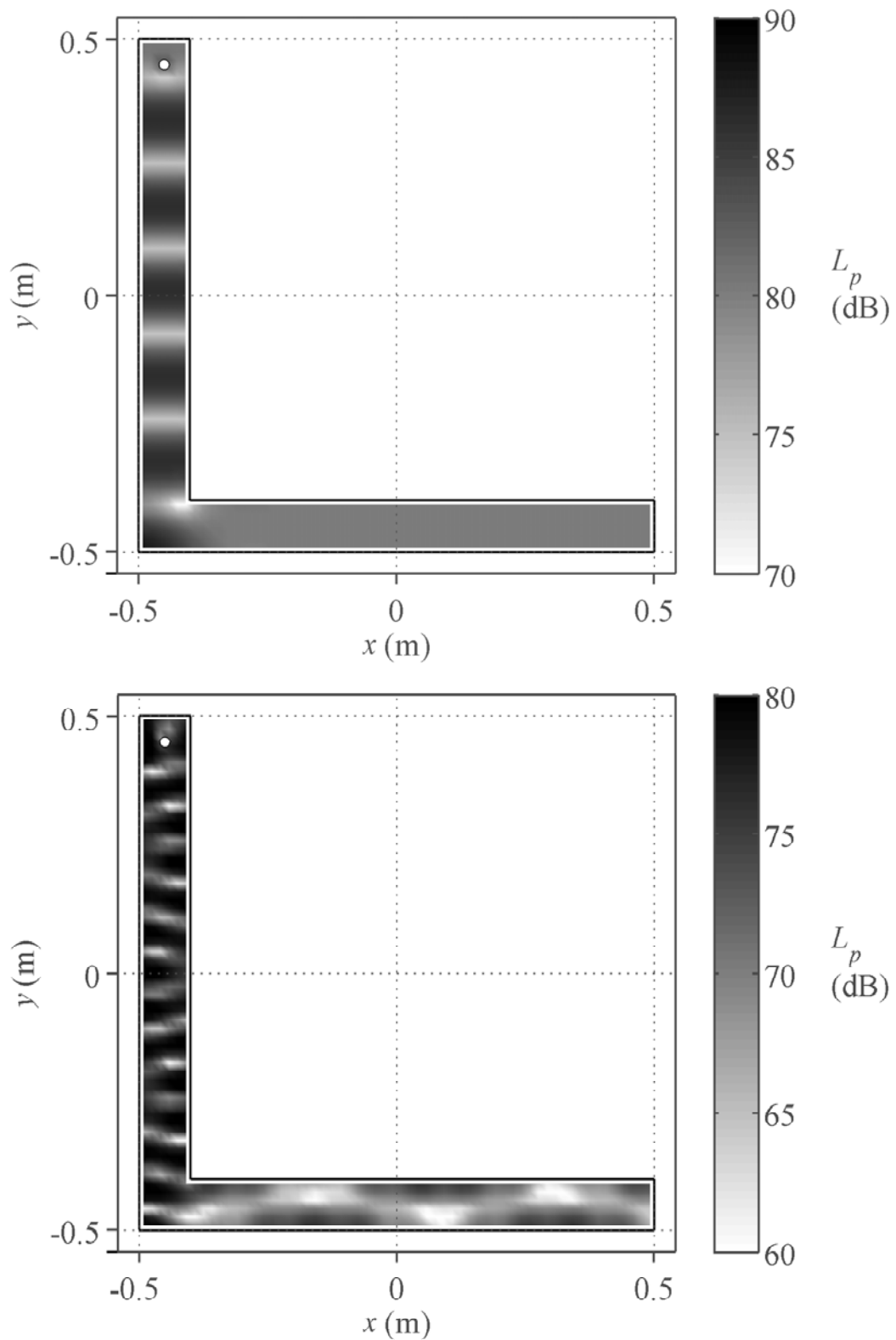
Figure 5.2: Total pressure in a closed pipe of width d = 10cm with a 90° corner and totally absorbing termination at both ends due to a source (white circle) located at (-0.45, 0.45); $d_e/\lambda = 0.30$ (top) and $d_e/\lambda = 0.70$ (bottom)
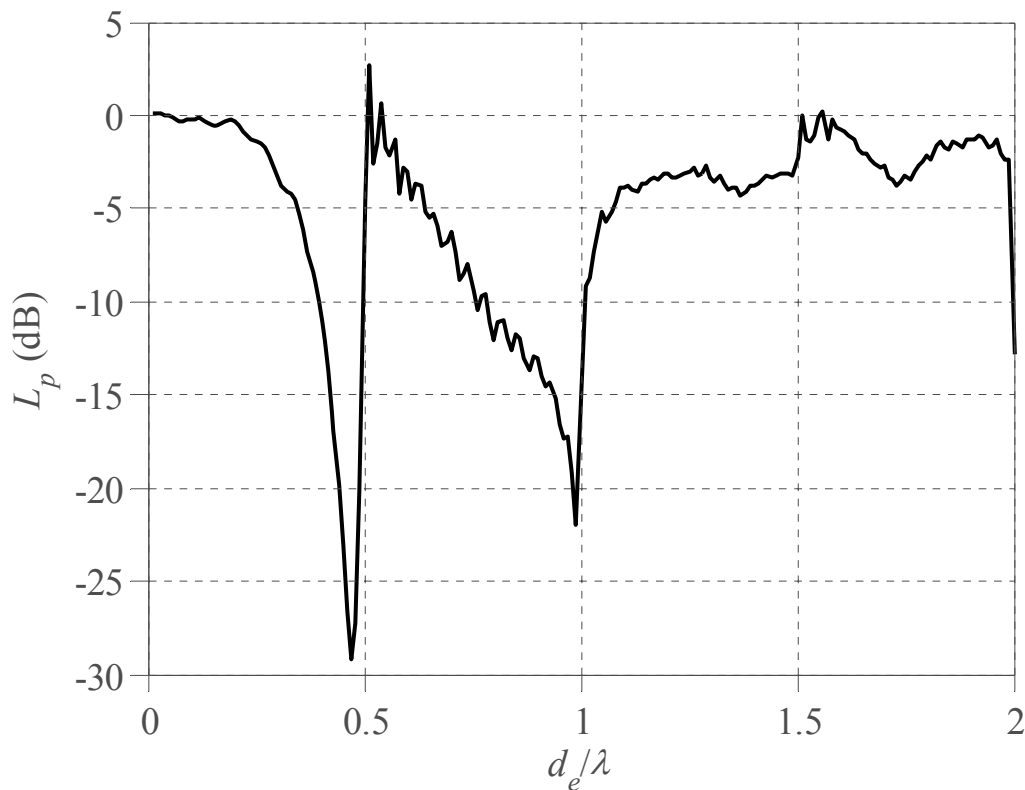
Figure 5.3: Transmission round a 90° corner in a pipe as per Figure 5.2

At low frequency, as with the wells of a Schroeder diffuser for example, plane wave propagation dominates [9] and much of the incident energy travels round the corner. Consequently the corner is essentially unseen, and the structure acts much like one straight channel. With increasing frequency the level of transmitted energy falls, and the corner acts like a low-pass filter, the approximate -3dB point being when $d_e/\lambda \approx 0.3$ (the example shown in Figure 5.2 (top)). Once half a wavelength becomes equal to the channel width ($d_e/\lambda = 0.5$) the first cross-mode appears and the transmitted pressure level increases dramatically. From this point, and with increasing frequency thereafter, a simple plane wave approximation breaks down and modal behaviour dominates. Here the performance becomes more complex, as shown in Figure 5.2 (bottom), and as illustrated by the transmitted pressure pattern of Figure 5.3.

Based on the above, provided that the wavelength is much larger than the channel width it should be possible to achieve large phase changes through the use of a simple square grid percolation structure. With increasing frequency however the behaviour will be more complex and will be dominated by modal patterns.

An approximate transition / cut-off frequency for energy channelling may be given as:

$$f = \frac{c}{2d_e}$$

5.1

Which gives an upper frequency limit to the plane wave assumption and corresponds to the cut-off frequency often given for the application of a Schroeder diffuser's design theory [9]. For significant propagation around the corner however a frequency below the -3dB point would be required, which occurs approximately an octave below this cut-off frequency.

5.3.2 The folded well Schroeder diffuser

Following from the above, the use of cornered channels may be used to create longer propagation paths that impart a phase change ordinarily not possible for a given maximum allowed depth, d_{max}. This concept has been applied previously to 'folded' well Schroeder diffusers [3], utilising much of the wasted space to the rear of the structure. An example of this is illustrated by Figure 5.4 which shows an $N = 7$ QRD (a) and folded equivalent (b). Note the structure is slightly different in dimension to that previously given in the literature due to setting the well width to be equal to the well step / minimum well depth ($d_e = d_x = d_y$).
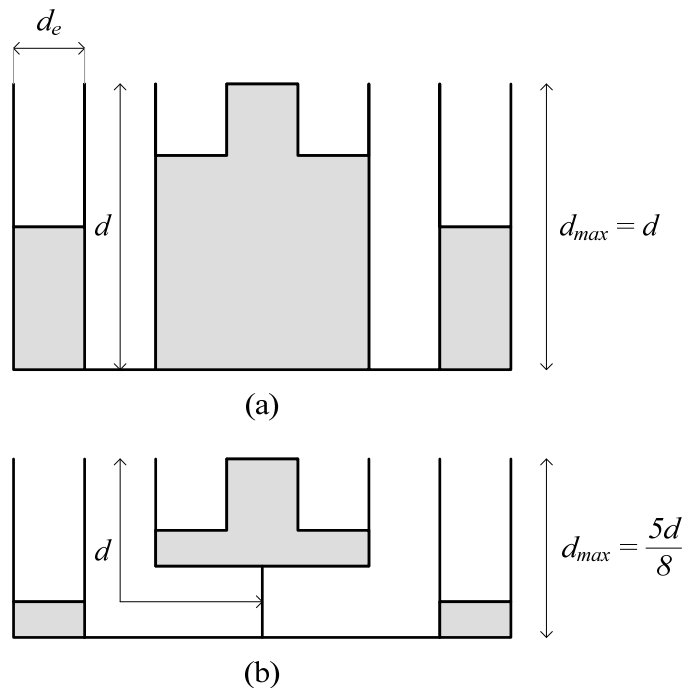
Figure 5.4: N = 7 QRD (a) and reduced depth folded well equivalent (b) (after Cox and D'Antonio [3]); total depth d_{max} expressed as a fraction of the maximum well depth, d

The effect of folding a well is shown in Figure 5.5, where the average (unwrapped) phase change on exit from the deepest well is shown for three periods of both the standard (a) and folded (b) structures of Figure 5.4. The well width of the diffusers was set to approximately 10cm ($d_e = c/(2 \times 250 \times 7)$), which is the same as the minimum depth and corresponds to a design frequency of $f_0 = 250$Hz. The phase change from the thin panel BEM prediction was estimated from the average scattered to incident pressure ratio across the mouth of the deepest well. This phase change is also compared to that predicted by a simple Fourier approximation for a Schroeder diffuser (introduced in Section 4.3.2), given by the phase of the reflection coefficient of Eq. 4.37.
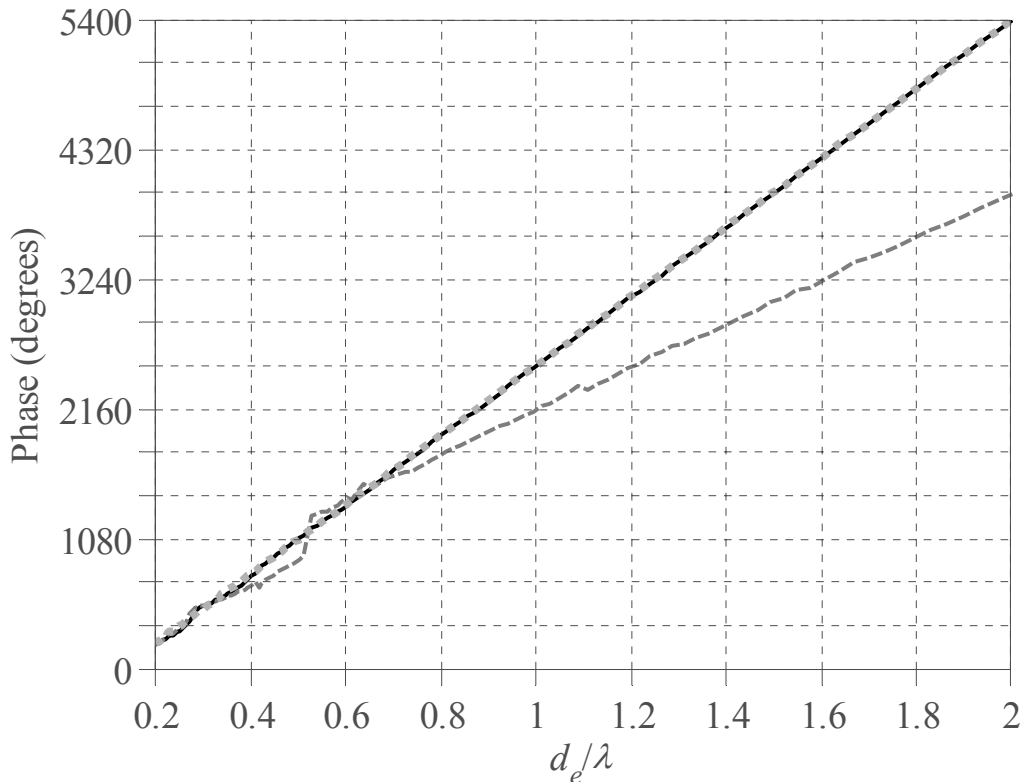
Figure 5.5: Average (unwrapped) phase change on exit from the deepest well of 3 periods of the N = 7 QRD diffuser as per Figure 5.4; standard arrangement (━), folded equivalent (━ ━) and simple phase change calculation using e^{2jkd} (╌ ╌)

The phase change from the standard Schroeder diffuser matches that given by the design theory well, even when the wavelength is much smaller than the well width. This agrees with previous finding where it was shown that a simple phase change model was valid up to at least $d_e/\lambda = 1/0.6 \approx 1.67$ [11]. For the folded well example however the agreement is not so

good. At low frequency plane wave propagation dominates and, as was illustrated by Figure 5.3, the majority of the energy travels around the corner of the folded well (and back). Consequently the phase change on exit is approximately equivalent to that of the standard diffuser (as determined by a distance traced out by the centre line of the well). At high frequency however the break down of the plane wave approximation means that, although modal patterns may form around the corner of the folded well (see Figure 5.2 (bottom)), the progressive wave which determines the reflected energy does not travel around the bend. As such an apparent shallower depth is seen [3]. This corresponds to the distance to the bottom of the well as seen by the source, which here equates to a depth of $d \times 5/8$.

The above indicates that, in a similar manner to that of an array of slats, once wavelength becomes comparable to element size a dominant specular reflection results from the effective bottom of the folded well. Consequently at high frequency the response of an array will be determined by what the source can see, with an approximate transition frequency for when this occurs being given by the cut-off frequency of Eq. 5.1.

5.3.3   Fermat's principle

In order for diffusion to occur, an incident wave must be able to travel far enough into the structure (relative to wavelength) for sufficient phase change to occur on exit. At mid-to-high frequency there will be many simple paths comparable to wavelength, formed in a similar manner to the simple folded well structures discussed above. At low frequency however, when wavelength is large compared to the diffuser dimensions, an incident wave must be able to penetrate deep into the structure via complex tortuous paths. These will comprise potentially many side branches and convoluted routes, often with multiple ways of travelling between two parts of an array. Consequently the following considers a number of potential scenarios illustrating the low frequency behaviour of different path arrangements.

Consider the examples shown in Figure 5.6, each comprising a well (or wells) of width $d_e = 5$cm situated in the centre of a baffle of 10m in length. A large baffle much greater than wavelength in size is used so that the contribution from the rear of the structure will be minimal for the range of frequencies modelled. The phase change on exit from the well is obtained in the same way as for the folded well Schroeder diffuser above. A simple e^{jkd} model is also used as above for the prediction of the phase change from each structure, where d is the

distance travelled along a specified path before exit. Of primary interest is the lowest frequency for which a significant change in phase occurs, an indication of which will be the first quarter wave resonance; when the reflected wave exits 180° out of phase. Beyond this point the structures will display complex interference patterns due to the various path lengths.

(a)   (b)   (c)
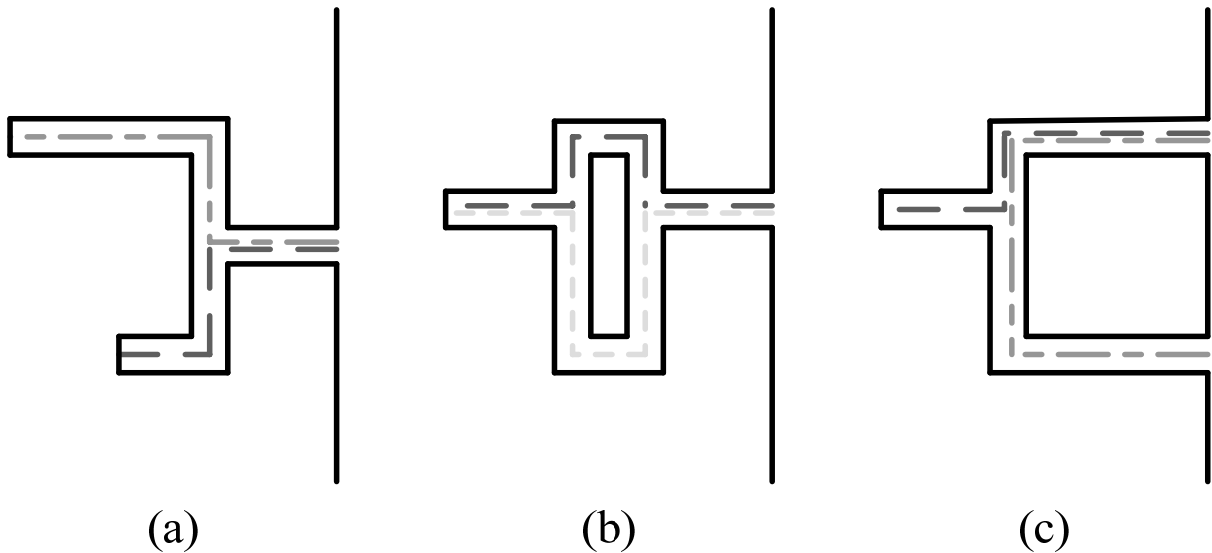
Figure 5.6: Baffled structures used to test the phase change on exit; d_e = 5cm, D = 10.0m, $\theta_0 = 0^{\circ}$; (dashed lines etc… indicate the propagation paths considered below)

Figure 5.7 shows the phase change on exit from the split well of Figure 5.6 (a). The simple model gives predictions for the phase change expected due to propagation (there and back) along the long (dashed line) and short (dash-dot line) branches respectively. It can be seen that the first quarter wave resonance (indicated by a sharp flip in phase) is seen at a point between the two predictions, suggesting that sound propagates down both of the dead end branches. This is illustrated by the model summing the contribution of the two simplified predictions above (dotted line), which is shown to provide a much closer approximation.
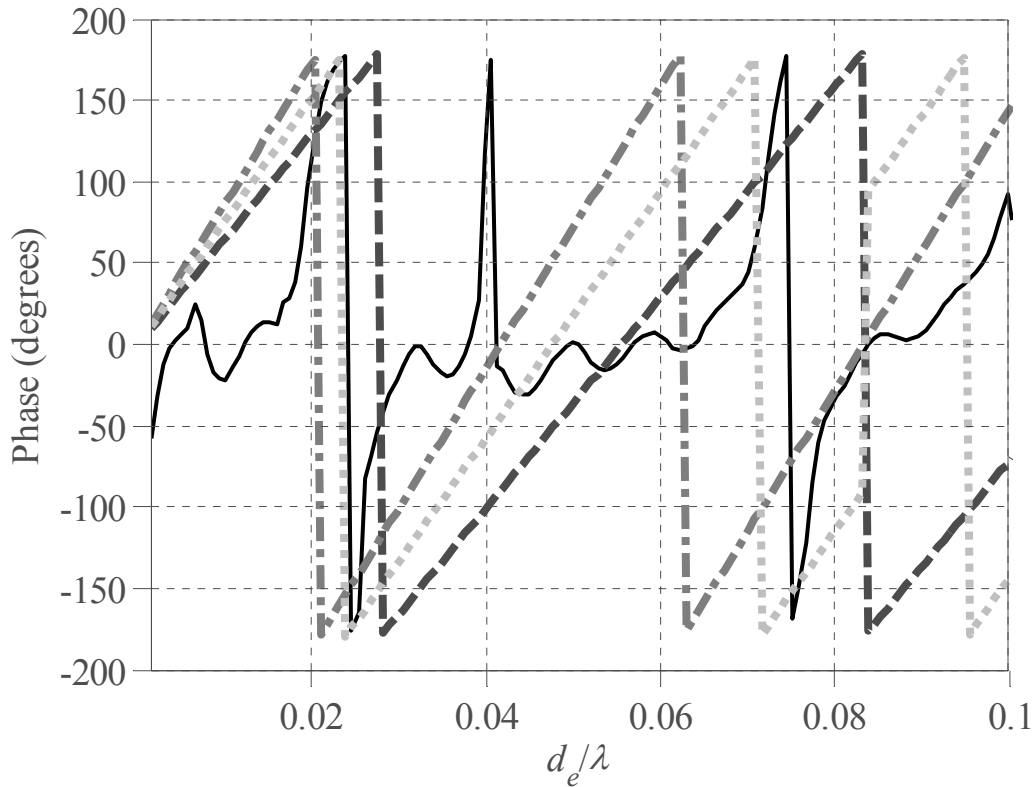
Figure 5.7: Phase change on exit from the structure of Figure 5.6 (a) (━━) compared to that predicted by e^{jkd} for the short branch (━ ━), the long branch (━ ·), and the sum of the two (· · ·)

A variation on the split branch structure is shown in Figure 5.6 (b); a channel that splits and then rejoins before terminating with a dead end. The resulting phase change for the structure is shown in Figure 5.8. The simple model provides predictions for the phase change expected due to propagation along the short (dashed line) and long (dash-dot line) branches to the dead end and back respectively. Note (ignoring multiple scattering up and down sections of the structure) there are two additional possible paths; those around the loop and back both with and without the dead end, both of which result in longer propagation paths than the two examples shown. It is evident that the model based on the shorter propagation path provides a much closer estimate to the point of the first quarter wavelength resonance. This implies that at low frequency where there are multiple routes to a dead end, sound incident upon the structure will want to follow the shortest possible path. This is in its simplified form is a statement of Fermat's principle, a principle from optics which states that a light wave travelling from one point to another via a reflecting surface will take the shortest possible route [50].
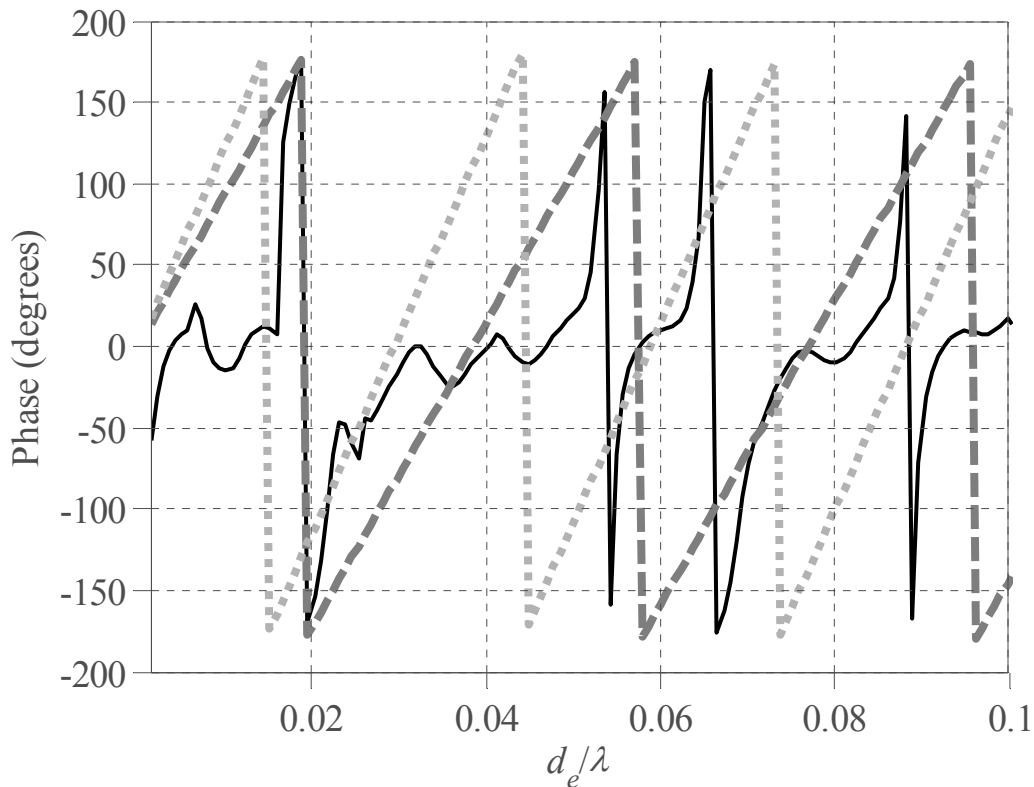
Figure 5.8: Phase change on exit from the structure of Figure 5.6 (b) (——) compared to that predicted by e^{jkd} for the short (— —) and long (- - -) routes to the dead end

Finally Figure 5.9 considers the case of the structure in Figure 5.6 (c); two separate channels that join before terminating with a dead end. Note the phase change shown is that at the mouth of the upper well, though for the frequency range shown the phase change from the two wells is near identical. This indicates that at low frequency the structure behaves as a lumped impedance system. Following from the above there are two paths that traverse the shortest possible route through the structure; the shortest path to the dead end via the top well and the loop entering one well and exiting another. The predictions using the two models are shown in Figure 5.9 (dashed line and dotted line respectively), along with their sum (dash-dot line). The latter combined prediction more accurately predicts the frequency of the first resonance, showing the importance of both propagation paths.
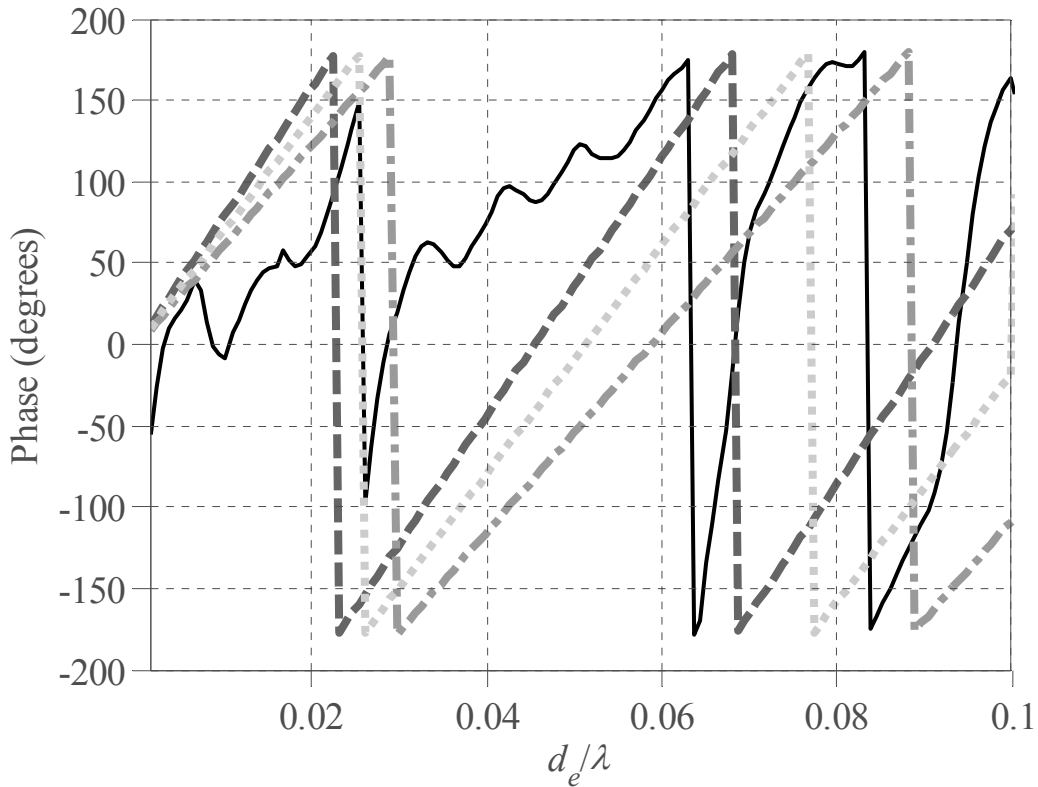
Figure 5.9: Phase change on exit from the structure of Figure 5.6 (c) (▬) compared to that predicted by e^{jkd} for the short route to the dead end (▬ ▬) the loop entering one well and exiting the other (▬ ▬) and the sum of the two (▪ ▪ ▪)

In summary the above implies that the lowest frequency at which a significant change in phase will occur will be determined by a combination of the longest paths in a structure for which no shorter alternatives exist. Here a path is defined as the distance either to a dead end (and back) or from entering one part of the structure to exiting at another. Consequently in order to force phase changes at low frequency it is necessary to channel energy via tortuous paths.

5.4.   A percolation surface diffuser

This section presents an initial investigation into a simplified version of the percolation diffuser; a surface diffuser equivalent with a rigid backing, an example of which is shown in Figure 5.10 (a). As with the above this is based on a simple square grid lattice ($d_e = d_x = d_y$). Since the structure is rigidly backed the back-scattered power can be ignored, and an indication of potential diffusive performance can be gained through use of the more standard back-scattered diffusion coefficient.
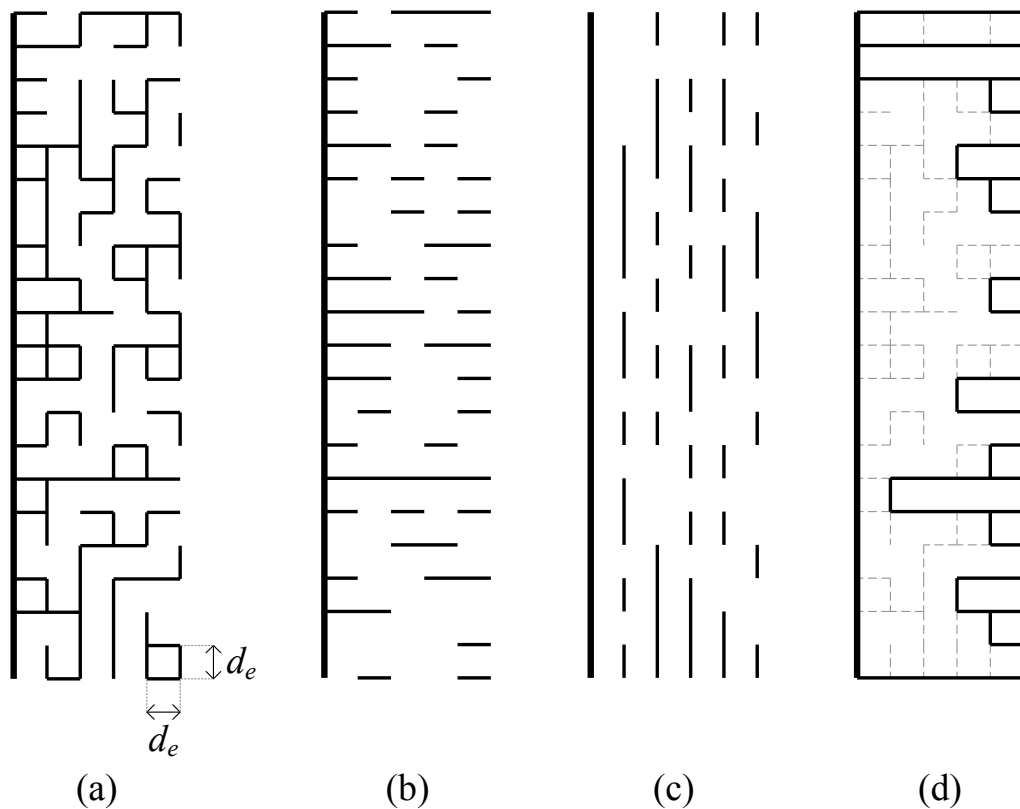
Figure 5.10: Bond percolation surface diffuser (a) and the same structure lacking vertical (b) and horizontal (c) elements; Schroeder diffuser equivalent (d)

5.4.1 A comparison with an existing case study using the Monte Carlo method

A recent investigation by Cox *et al.* [70] reported the initial findings of an investigation into the design of a surface percolation diffuser similar to the one shown in Figure 5.10 (a). The arrangement considered was based on a square percolation grid 0.6m wide by 0.12m deep, and with element size, $d_e = 3$cm. Since the task of considering all possible arrangements (of which there are 2^{164}) would be too large, a Monte Carlo simulation was run on a large number of randomly generated arrangements. The standard surface diffuser diffusion coefficient (for normal incidence) was calculated for each sample generated, and the influence of some of the basic characteristics of the device on diffusion was considered.

Initially three types of diffuser were considered by Cox *et al.* [70], examples of which are illustrated by Figure 5.10 (a-c); a percolation structure comprising both horizontal and vertical elements (a), a structure with only horizontal elements (b) and a structure with only vertical elements (c). A total of 1000 samples were generated for each structure type. Arrangements

with horizontal lines only were found to make very poor diffusers, since (for normal incidence) their elements run parallel to the incident sound, and consequently a diffuser appears very much like a plane surface. For diffusers with vertical lines only, a much broader range of average diffusion coefficient was observed. These structures are similar to the slat arrays of Chapter 4, though forming a surface diffuser equivalent. The best diffusers however were shown to be those with both horizontal and vertical lines, assumed to be due to the channelling of sound via complex tortuous paths. Consequently the full percolation structure was considered for further investigation.

A similar structure to that above has been considered here; a 5×10 percolation diffuser of total width 1.0m, of depth 0.25m and with element size $d_e = 5$cm. There are 2^{205} possible combinations of this diffuser, and so again a Monte Carlo simulation was run for 1000 randomly generated arrays. A wide range of fill factors (number of elements in the array) was considered in order to observe the effect that this would have, with the probability of including vertical and horizontal elements being determined by an unrelated random number to ensure independence. The average diffusion coefficient (obtained over the frequency range $85\text{Hz} \leq f \leq 4\text{kHz}$) is considered in Figure 5.11, showing the variation with percentage lattice lines filled, taking into account the vertical elements (top), horizontal elements (middle) and their combined fill factor (bottom). The best twenty average diffusion coefficient values are highlighted for reference (grey circles). It can be seen that the best diffusers are those with approximately 30-70% of the lattice lines filled (bottom). This is in close agreement with the findings of Cox *et el.* [70] who showed that an approximate 20-80% fill factor was most optimal; centring on the same value though encompassing a slightly narrower range. Note, assuming the number of samples generated is large enough to give an accurate representation of general behaviour, the deviation between the two sets of results is likely down to the slightly different structural dimensions and frequency range considered.
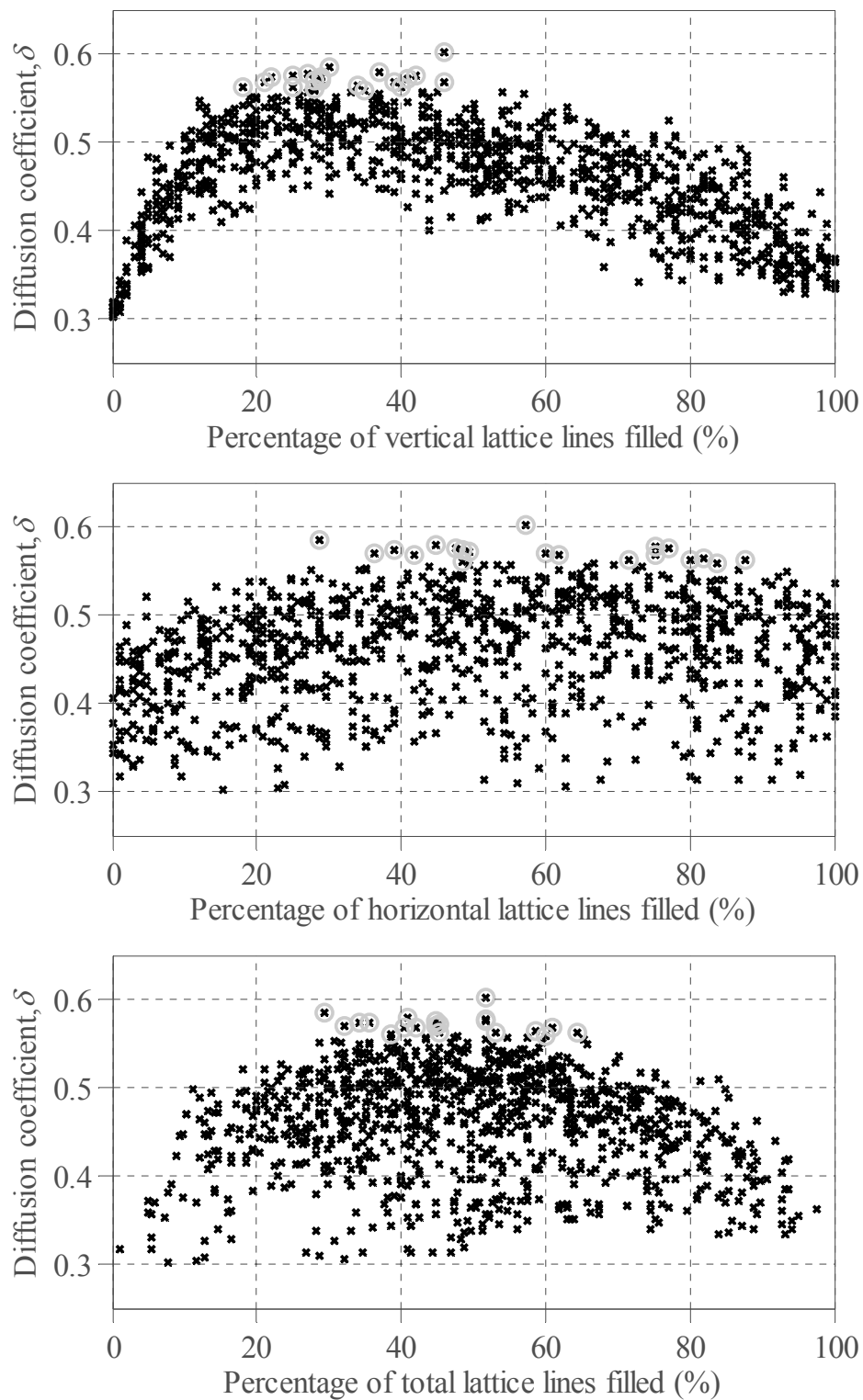
Figure 5.11: Average diffusion coefficient for 1000 randomly generated 5×20 percolation bond surface diffusers with percentage of lattice lines filled: vertical (top), horizontal (middle) and total (bottom); $d_e = 5cm$, $D = 1.0m$, $\theta_0 = 0°$; grey circles indicate best 20 diffusers

From the above it would be assumed that an approximate 50% fill factor of elements would be most optimal. The role of the vertical and horizontal slats in an array however will be different. Figure 5.11 top and middle show the effect on diffusion of both the vertical and horizontal element fill factors respectively. For the vertical slats the best diffusers are those whose fill factors are approximately 15-50%; considerably lower than for the total fill factor results. For the horizontal slats on the other hand the best performing arrangements are those with occupancies on the order of 30-90%; a much higher fill, though the spread is much broader and the effect on diffusion is less obvious. To consider these results in more detail it is necessary to assess the effect of occupancy with frequency.

Figure 5.12 shows maps of the diffusion coefficient with frequency (expressed as element spacing relative to wavelength). These illustrate the range in diffusion coefficient obtained as the number of vertical (top) and horizontal (bottom) elements within the array alters. At low frequency it can be seen that there is a slight preference towards a higher fill factor. Provided however the vertical element fill factor is not so sparse or dense so as to act like an effective plane surface, for both vertical and horizontal elements the best diffusers are obtained from a large range of fill factors. With increasing frequency the two cases behave very differently. For the horizontal elements there is a slight preference for a higher fill factor, forming a structure more akin to a conventional Schroeder diffuser by blocking off lateral propagation paths (as per Figure 5.10 (d)), though this preference is small and the variation with fill factor remains largely unaltered. For the vertical elements however with increasing frequency the best diffusers are those with a much lower fill factor; as wavelength becomes comparable to the individual element size the optimal range approximately halves to a 10-40% occupancy.

The above may be explained as follows. At low frequency vertical slats will promote lateral scattering and channelling of sound by forming longer propagation paths, and consequently their presence is desirable. This is illustrated by the slightly higher coefficient values seen for high fill factors of Figure 5.12 (top). Conversely at high frequency (approaching the cut-off point given by Eq. 5.1) less energy is able to propagate round the corners within the diffuser, and the phase change on reflection will become increasingly dominated by the 'apparent well depths'. This occurs in a manner similar to the 2D slat arrays presented previously in Section 4.3, and in the folded well Schroeder diffuser example of Section 5.3.2. As such a lower number of elements will likely be preferable in order to provide a range of these depths.

In contrast the horizontal slats will both channel energy into the structure and help create complex paths, and so their effect with frequency is less evident.
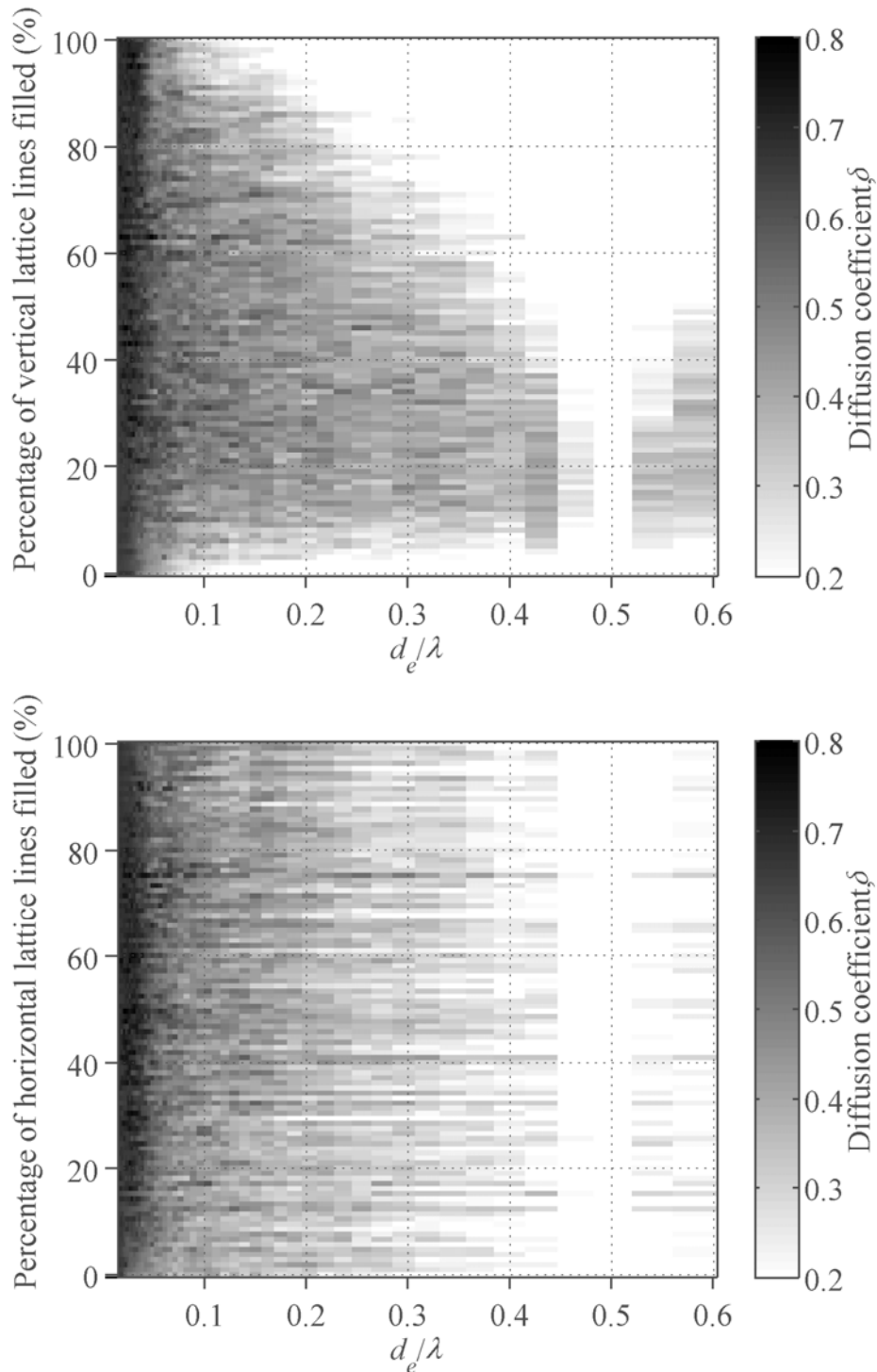
Figure 5.12: Diffusion coefficient for 1000 randomly generated 5×20 percolation bond surface diffusers with percentage of lattice lines in structure filled; vertical elements (top) and horizontal elements (bottom); $d_e = 5cm$, $D = 1.0m$, $\theta_0 = 0°$

In addition to the element occupancy, Cox *et el.* [70] also demonstrated how the level of diffusion depends on the line-of-sight through an array. This was expressed in terms of blocked line-of-sight; that is how much of the rigid back wall as viewed by the source is obscured by elements. It was shown that the most optimal arrangements were those whose blocked line-of-sight was approximately 65% or more. Figure 5.13 shows a similar coefficient map to those of Figure 5.12, though illustrating the effect of line-of-sight on diffusion with frequency. In general the best diffusers are those which cover a significant portion of the back wall, agreeing with the previous findings. It was suggested that the reason for this is because if too much of the back wall is seen then a diffuser will behave similarly to the structure of Figure 5.10 (b), and hence diffusion will be poor [70]. At high frequency however the optimal fill reduces marginally, which as wavelength becomes comparable to the lattice spacing results in the best diffusers having approximately 30-80% of the line-of-sight blocked. This suggests that for higher frequencies some of the back wall should be visible, thus providing at least one channel with the maximum (apparent well) depth.
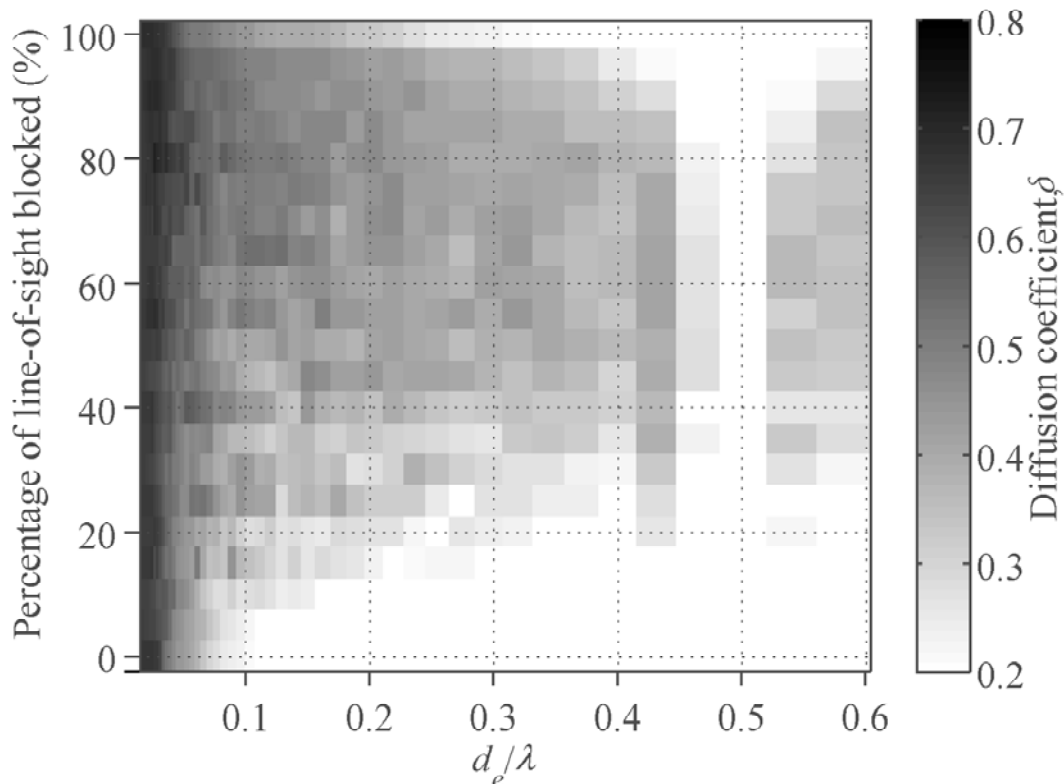
Figure 5.13: Diffusion coefficient for 1000 randomly generated 5×20 percolation bond surface diffusers with percentage of line-of-sight filled; $d_e = 5cm$, $D = 1.0m$, $\theta_0 = 0^\circ$

In general for the structure considered the above suggests that for diffusion across the bandwidth modelled (up until spatial aliasing occurs) an approximate 20-40% occupancy of vertical elements, 30-90% occupancy of horizontal elements and 65-80% blocked line-of-sight through the array is optimal. The variation of the diffusion coefficient with vertical element fill factor however suggests that there is a potential trade-off between low and high frequency diffusive efficacy.

5.4.2   Comparison with a conventional Schroeder diffuser

It was suggested that a percolation structure could be used to provide increased low frequency diffusive efficacy (relative to a more conventional diffuser) due to being able to provide potentially longer propagation paths and hence larger phase changes on exit. This theory is supported by the findings above which implied that at low frequency the best diffusers are generally those with a higher fill factor, indicating that a percolation structure is able to promote lateral scattering allowing sound to penetrate into the array via tortuous paths. To test this, the performance of a percolation diffuser may be compared to its Schroeder diffuser equivalent, an example of which was shown in Figure 5.10 (d); the same structure though with the horizontal elements filled in such that no lateral propagation may occur. An additional Monte Carlo simulation was therefore run, using the same samples as above to allow a direct comparison, though altered to form their Schroeder diffuser equivalent.

The low frequency performance of the equivalent Schroeder diffuser will be limited by the maximum available depth, $d_{max} = Md_e$, where M is the lattice size in the x dimension (allowing for $M+1$ possible depths, see Figure 5.1). By rearrangement of the more conventional design frequency equation [3] it may be shown that the effective design frequency, f_0, for the structure considered here may be given by:

$$f_0 = \frac{M}{(M+1)}\frac{c}{2\,d_{max}} = \frac{c}{(M+1)\,2\,d_e} \qquad\qquad 5.2$$

Which for the $M = 5$ structure considered results in a design frequency of $f_0 = 573$Hz. The diffusion coefficient for both structure types is given in Figure 5.14, showing the average (solid lines) and maximum (dashed lines). Note these values are obtained per frequency, and

as such represent the potential of the structure type to diffuse at a particular frequency rather than the performance of any one single diffuser.
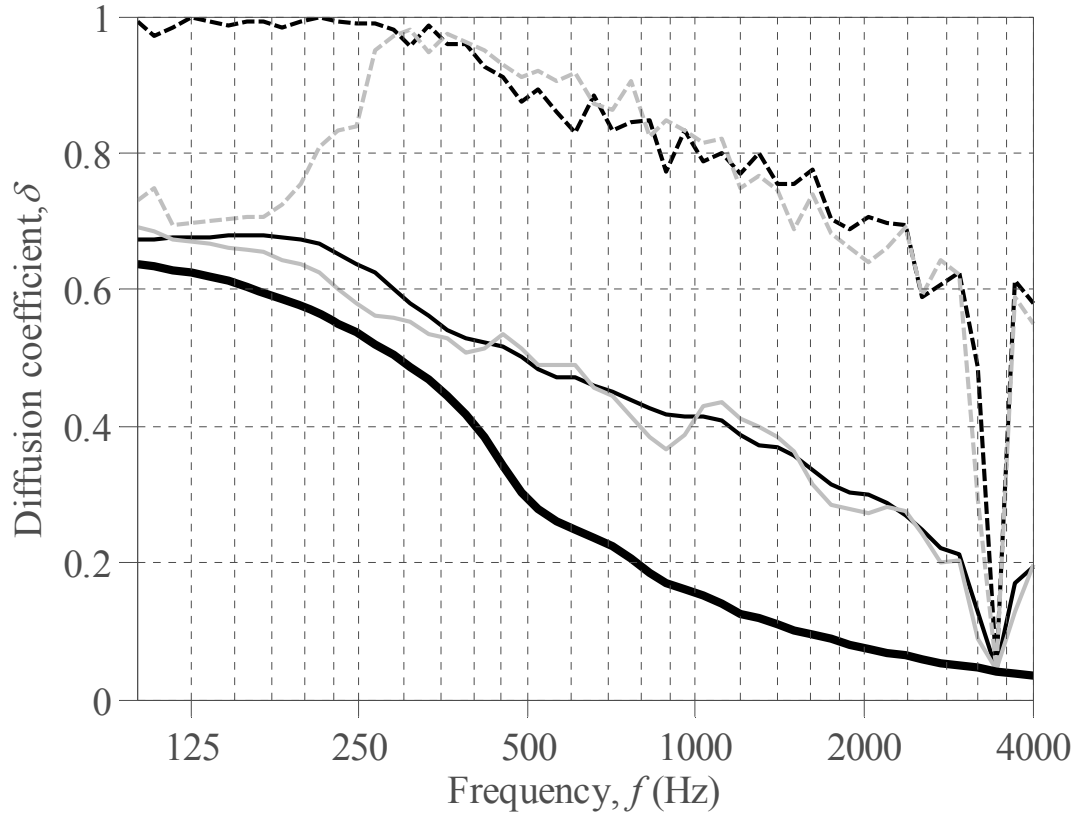
Figure 5.14: Average (solid lines) and maximum (dashed lines) diffusion coefficient obtained per frequency for 1000 randomly generated surface diffusers based on a 5×20 square grid lattice; bond percolation diffuser (▬)and equivalent Schroeder diffuser (▬); d_e = 5cm, $\theta_0 = 0^{\circ}$; reference plate of width D = 1.0m (▬)

From Figure 5.14 it is evident that the basic Schroeder diffuser is capable of achieving substantial diffusion from somewhere in the region of $f = 300$Hz. This corresponds to approximately a quarter of a wavelength fitting into the maximum depth, and agrees with previous findings for conventional Schroeder diffusers which have been shown to reflect differently to a plane surface an octave or two below the design frequency [11; 71]. The percolation diffuser however is able to provide high levels of diffusion at a much earlier frequency. This occurs from a frequency of $f = 85$Hz (the lowest frequency tested) and potentially lower; a frequency at least 3.5 times lower than its Schroeder diffuser equivalent. This therefore indicates a maximum path length on the order of at least 7 times (there and back) the maximum depth (1.75m), a route which must be formed from tortuous channels.

The above has considered the ability of a structure to diffuse at a specific frequency, however of most interest will be how well a single device performs. Figure 5.15 (bottom) shows the diffusion coefficient obtained for the percolation diffusers with the highest average diffusion coefficient at both low ($f < 287$Hz) and high ($f \geq 287$Hz) frequency respectively. This cut-off frequency was selected since this is one octave below the design frequency of the equivalent Schroeder diffuser; the point which, following from Figure 5.14, describes an approximate cross-over between diffusion due to tortuous channelling and that due to depth alone. The best low and high frequency diffuser structures are shown in Figure 5.15 (a) and (b) respectively.

It is evident that whilst the best low frequency diffuser is able to achieve significant low frequency diffusion, at high frequency the performance is not so good. Conversely the best high frequency diffuser makes a poor low frequency diffuser. This may be explained as follows. At low frequency, as was suggested by the Monte Carlo simulation results of Figure 5.12, a high percentage of vertical elements are required to create tortuous channels. This is illustrated by Figure 5.15 (a) which forms a complex structure of paths through the array. At high frequency however, above the approximate -3dB cut-off point for propagation around a corner (obtained from Figure 5.3), little sound will be able to penetrate into the array. This corresponds to a frequency of approximately $f = 2.1$kHz, though the effect is pronounced well before this frequency. In addition the high vertical slat occupancy tends to result in large plane surfaces occurring towards the front of the array. At high frequency, as with the slat arrays of Section 4.3, this results in strong specular reflections off these surfaces. Consequently this dominates the scattered polar pattern.

The diffuser of Figure 5.15 (b) displays the opposite effect to that described above. Close inspection reveals the diffuser to appear much like a more conventional Schroeder diffuser; the low percentage of vertical slats providing a range of 'apparent' well depths, with the much higher occupancy of horizontal slats helping to promote plane wave (Schroeder diffuser like) propagation in the 'wells'. Consequently the diffuser behaves much like a Schroeder diffuser. At low frequency however the closed off horizontal elements mean that lateral propagation is limited, and that very few (if any) tortuous paths greater than the maximum depth are created. As such, little diffusion results.
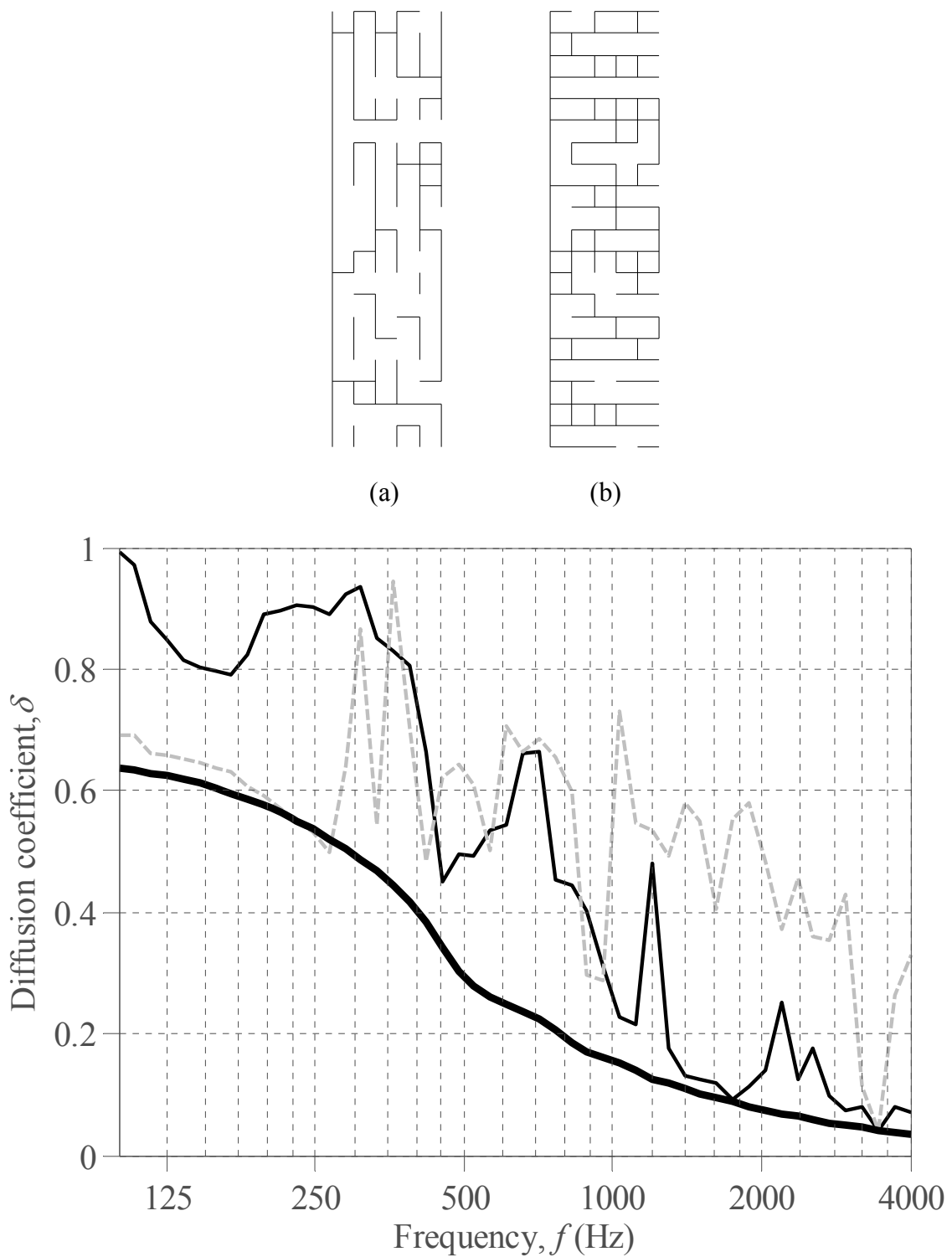
Figure 5.15: Best low frequency (a) and high frequency (b) diffusers from 1000 randomly generated percolation structures based on a 5×20 square grid lattice (top) and their diffusion coefficient (a ▬▬, b ▬ ▬) including plate of width D = 1.0m (▬▬▬) shown for reference (bottom); d_e = 5cm, θ_0 = 0°

The above indicates that for the structure considered it is possible to achieve significant low frequency diffusion at (no less than) approximately 2 octaves below that of a more conventional welled diffuser. In general however there is an inherent trade-off between low frequency and high frequency diffusive efficacy. It is likely therefore that a volume diffuser based on similar principles will also demonstrate this behaviour. This is considered in the following section.

5.5.   The 2D percolation volume diffuser

The previous section considered the case of a percolation fractal as a surface diffuser. This section builds upon this; extending the concept to that of a volume equivalent, an example of which was shown in Figure 5.1. As with the surface diffuser case this is based on a simple $M \times N$ square grid lattice ($d_e = d_x = d_y$). The findings from the surface percolation diffuser will likely give an indication as to the expected diffusive behaviour, though here it is the volume diffusion coefficient that is considered. Since a volume device no longer has a rigid backing it is possible for sound to pass through the structure. Consequently, as with the diffuser types from the previous chapters, it is necessary to also consider the back-scattered power.

5.5.1   A comparison with a percolation surface diffuser

The number of possible arrangements of an $M \times N$ square grid lattice diffuser is $2^{2MN+M+N}$. Consequently for all practical sized structures, as with the surface diffuser example, the task of considering each possible realisation will be too large. As such a Monte Carlo simulation is again useful, allowing an indication as to the structural traits most important to diffusive performance. This is again carried out by generating a large number of randomly generated structures, though now obtaining both the volume diffusion coefficient and back-scattered intensity ratio values for each.

A structure was considered based on an underlying 10×10 square grid lattice (for which there are 2^{840} different combinations). The total width and depth were set to 0.5m, with a lattice spacing of $d_e = 5$cm. As with the surface percolation diffuser examples from Section 5.4, 1000 diffusers were randomly generated, with results obtained for a frequency range of $50\text{Hz} \leq f \leq 4\text{kHz}$ and for normal incidence. Figure 5.16 shows diffusion coefficient maps for

these simulations, showing the variation with both vertical (top) and horizontal (bottom) percentage lattice lines filled.
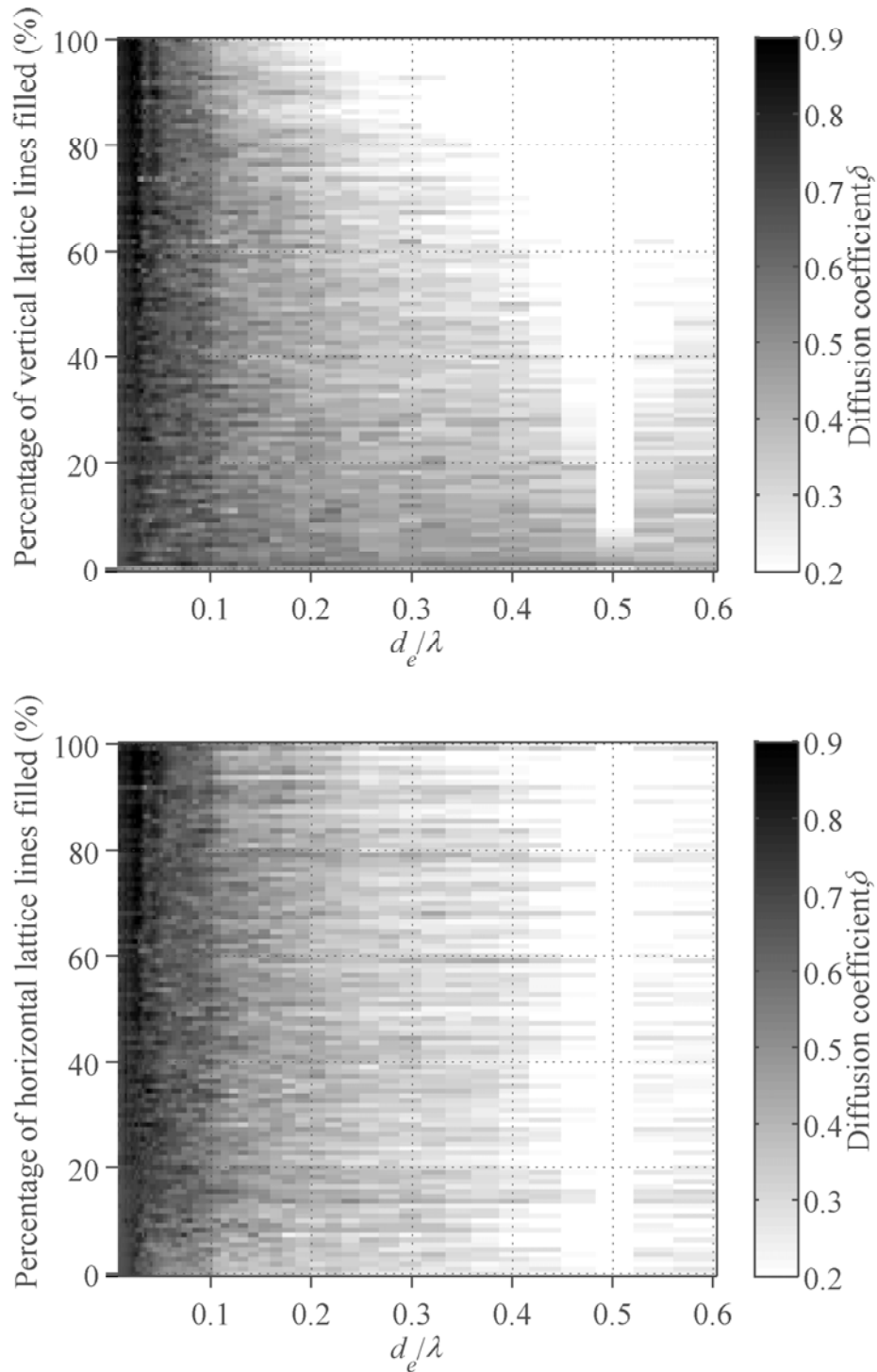
Figure 5.16: Diffusion coefficient for 1000 randomly generated 10×10 percolation bond volume diffusers with percentage of lattice lines filled: vertical (top) and horizontal (bottom); $d_e = 5cm$, $D = 0.5m$, $\theta_0 = 0°$

It is evident that the behaviour with frequency is similar to that of the surface diffuser example of Figure 5.12. At low frequency a high fill of both vertical and horizontal elements is desirable since complex channels can be formed, with a fill factor of approximately 60% or greater being best. With increasing frequency as wavelength becomes comparable to element size a much lower vertical element fill is required, providing varying 'effective' depths, with optimal fill factors being on the order of 40% or less. Again at higher frequencies the specular reflections from the vertical elements means that the horizontal fill factor is less important.

In Figure 5.13 it was shown that for a surface percolation diffuser the line-of-sight through the structure that is blocked (as viewed from the source) should be high to achieve significant diffusion. This is because if little of the line-of-sight is blocked then a large proportion of the back wall is seen and the diffuser will tend to behave like a plane surface. For a volume diffuser however, gaps through the structure mean that incident sound is able to pass through the device. Consequently a low fill in line-of-sight may now result in a much higher diffusion coefficient. This is illustrated by Figure 5.17, which shows the effect on the average diffusion coefficient for the volume diffuser case. The best twenty average diffusion coefficient values are again highlighted for reference (grey circles). The best diffusers are now spread over virtually all blocked line-of-sight values (excluding 0% since this implies a completely open array). Note the very best diffusers tend to be those for which the line-of-sight is nearly completely unblocked (e.g. 10%). These diffusers however will result in low back-scattered power and will likely be unsuitable. This is considered further in Section 5.5.4.

In general, as with the surface diffuser example, the above indicates a trade-off between low and high frequency diffusive performance. Consequently for a percolation structure based on a periodic square grid lattice it may be necessary to choose whether to design a diffuser that performs effectively at either low or high frequency respectively. The performance at both low and high frequency is therefore considered below.
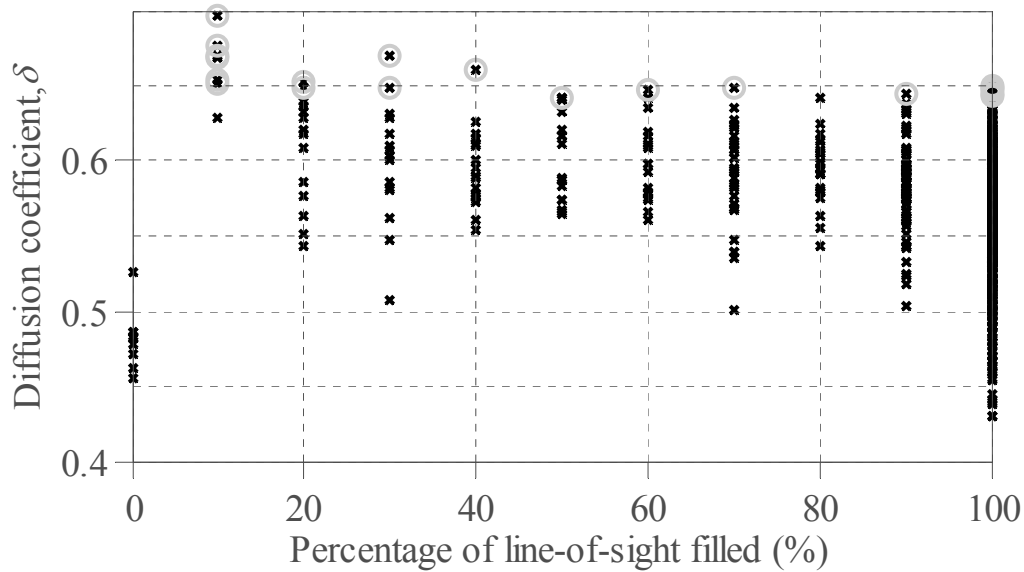
Figure 5.17: Average diffusion coefficient for 1000 randomly generated 10×10 percolation bond volume diffusers with percentage line-of-sight blocked; d_e = 5cm, D = 0.5m, θ_0 = 0°; grey circles indicate best 20 diffusers

5.5.2   Tortuosity and low frequency diffusion

For a surface percolation diffuser in Section 5.4.2 it was demonstrated that significant diffusion could be achieved for frequencies much lower than that of a more conventional welled device. It was suggested that this is due to the complex channelling of sound via tortuous paths; though to support this hypothesis a measure of tortuosity must be adopted.

Ant in a labyrinth algorithm

In percolation theory a lattice is often considered in terms of diffusion, where in this case diffusion refers to the dispersion of 'fluid' flow within a lattice [67]. If a lattice contains many connecting bonds (very few slats/elements) then this process will occur rapidly, since there are few paths along which the fluid cannot travel. Conversely if there are few connecting bonds (many slats/elements) then diffusion as defined here occurs more slowly with time, since the fluid flow is restricted to following many convoluted paths. Consequently, the rate at which this diffusion occurs may be used to indicate how tortuous a percolation structure is, and hence the degree of ease with which a fluid (in this case sound) may pass through.

One way of assessing this diffusion as defined above (and hence structural tortuosity) is through use of what is termed the 'ant in a labyrinth' algorithm. This is so called since it considers a random 'walk' through the structure; like an ant attempting to navigate its way through a maze. With reference to Figure 5.1, the method is broadly as follows [67]. A point in a percolation structure is selected as a starting point for the 'ant', e.g. a grey node (inside the array) of Figure 5.1. Upon every discrete time step the ant attempts to move to one of its four adjacent locations (grey nodes) by selecting one at random. If a path exists (grey line in Figure 5.1) then the ant moves to the new position, else if the path is blocked by an element (black lines in Figure 5.1) then the ant remains in the same place. In either case the time, t, is increased by one time step and the square of the displacement distance (considering the structure in unit steps, i.e. $d_e = 1$) is recorded. This is repeated for a set number of time steps, obtaining the square of the displacement (a measure of how far the ant travels) as a function of time. The simulation is repeated many times, and for many starting points, before the square root of the averaged square distance, $d(t)$, is calculated.

The above provides a measure of how hard it is for propagation through a structure to occur. This is given as a function of time, though what would be more useful is a single figure of merit that describes the structure. It can be shown that for sufficiently large t, and for a large number of averages the root mean square of the distance travelled by the ant, $d(t)$, may be given by the power law [67]:

$$d(t) = c_a t^{g_a} \qquad\qquad 5.3$$

Where c_a and g_a are constant variables. The behaviour of this distance with time however is more easily considered on a log-log plot, since the log of the distance may be given as:

$$\log(d(t)) = g_a \times \log(t) + \log(c_a) \qquad\qquad 5.4$$

Where g_a describes the gradient and c_a the (exponential of a) constant of a first order polynomial. Consequently for a set of discrete distances $d(t)$, both c_a and g_a may be obtained by a simple line of best fit analysis. Both give an indication of how easily the 'ant' may move through the labyrinth, varying from being unable to move (lowest values) to complete freedom of movement (highest values). These may therefore be used as a measure of structural tortuosity.

Note since the above is ordinarily applied to essentially infinite structures, two key differences are applied to the method adopted. For the finite sized diffusers very large values of t will not be possible, since the ant will keep 'escaping' the percolation structure. Consequently when the ant makes a move to a position outside of the structure the calculation for that starting position finishes and only the steps up until that point are included in any average. In addition the analysis of an infinite network considers the general properties of a structure, and does not differentiate between linked and closed off sections. For the acoustic case however there may be closed off sections where sound cannot reach, and which are essentially redundant. If these were included then the ant would become 'trapped', with any tortuosity measure likely indicating that the structure is more complex and tortuous than it effectively is. Subsequently these sections are excluded from any calculation.

Figure 5.18 (bottom) shows the above applied to three example structures from the Monte Carlo simulation of Section 5.5.1 (top). Diffuser (a) is relatively sparse, and consequently the 'ant' is able to move more easily throughout the structure, resulting in a steeper gradient ($g_a = 0.43$) and a higher offset ($c_a = 0.92$). This indicates that channelling of energy is unlikely and as such the array would be expected to make a poor low frequency diffuser. Diffusers (b) and (c) on the other hand have lower values, with gradients of $g_a = 0.35$ and $g_a = 0.38$ respectively, implying that movement through these arrays is slightly more arduous. Note, the lower gradient of diffuser (b) is due mainly to comprising many small sections that are cut off from one another, making it impossible to pass from one side of the array to the other. The offset values for diffusers (b) and (c) are $c_a = 0.74$ and $c_a = 0.70$ respectively. Since this is the value at $t = 1$ this represents the ease at which the ant moves locally, i.e. how easy it is to move from one position to the next. As such this suggests that diffuser (c) is more enclosed, comprising tighter channels.
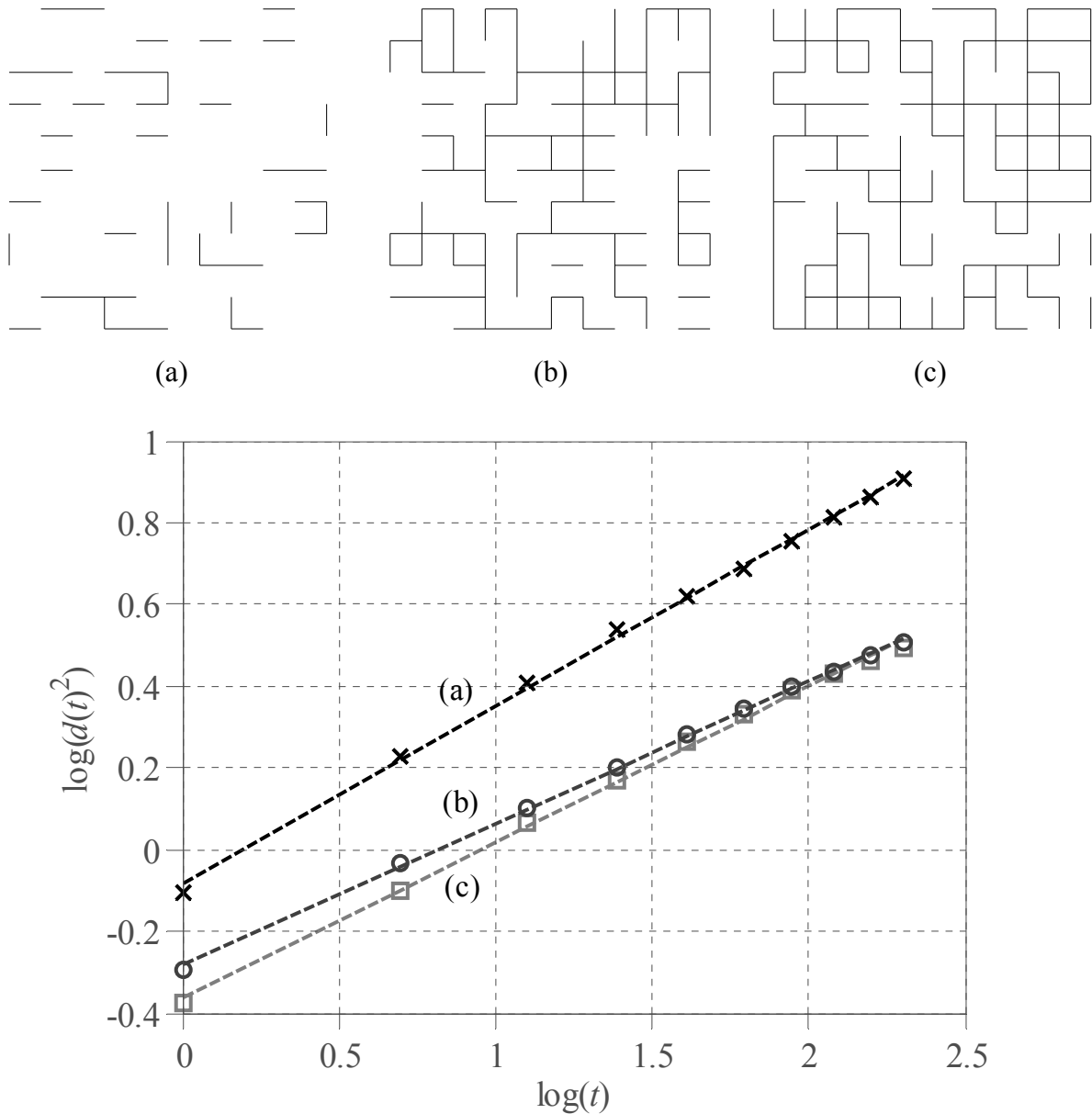
Figure 5.18: Example 10×10 percolation bond volume diffusers (top) and their corresponding 'ant in a labyrinth' results (bottom) including lines of best fit (dashed lines); $d_e = 5cm, D = 0.5m, \theta_0 = 0°$

Figure 5.19 shows the effect of the two tortuosity metrics on the average diffusion coefficient from the Monte Carlo simulation above. This average is taken for frequencies less than $f = 156Hz$, corresponding to an octave below the design frequency of the structures' equivalent Schroeder diffuser (as given by Eq. 5.2). The top plot illustrates the effect of the tortuosity gradient, g_a. The lowest of these values (high tortuosity) tend to result in a high level of diffusion, however the best diffusers actually have a much higher gradient (low

tortuosity). This is because, as was explained above, this metric may be affected by small sections in an array that are cut-off from one another. The best structures therefore are those with a tortuosity value approximately in the range 0.3-0.45, implying that the channels form longer paths.
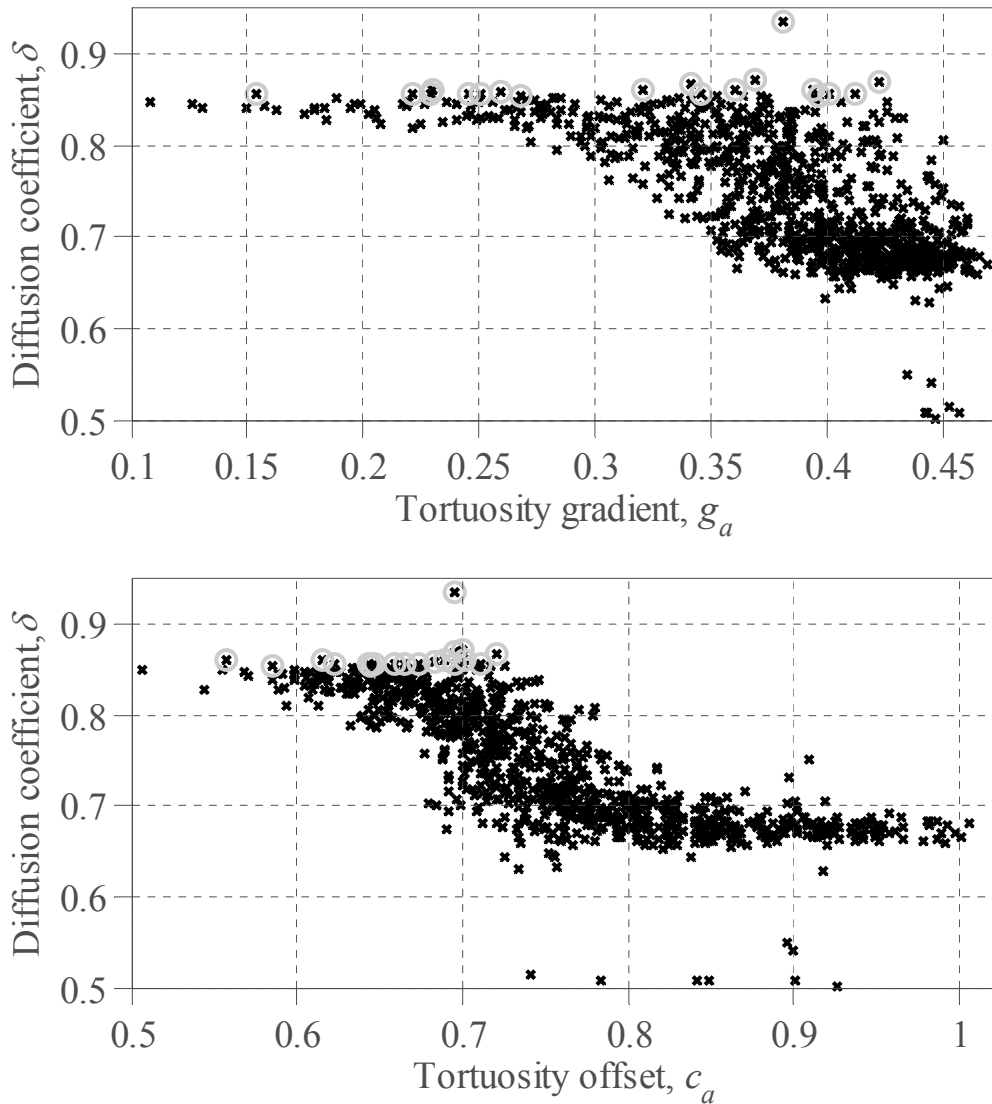
Figure 5.19: Average diffusion coefficient over the frequency range 50Hz ≤ f ≤ 156Hz with tortuosity gradient, g_a (top) and offset, c_a (bottom) for 1000 randomly generated 10×10 percolation bond volume diffusers; d_e = 5cm, D = 0.5m, θ_0 = 0°; grey circles indicate best 20 diffusers

Figure 5.19 (bottom) shows how the average diffusion coefficient at low frequency varies with the tortuosity offset metric, c_a. The best diffusers are shown to be those approximately in

the range 0.6-0.7. Since this provides a measure of how easy it is to perform a single step, this gives a gauge of how enclosed and tightly packed the channels (if any) in a structure are. For example in the ant in a labyrinth algorithm an ant placed in a part of an array surrounded by two elements, e.g. in an enclosed channel, will see two closed off and two open path options from which to choose. On average this situation will result in a root mean square displacement of 0.707. A location surrounded by three elements on the other hand will form a dead end and hence will have only one open path, resulting in an average root mean square displacement of 0.5. A value of 0.6-0.7 therefore implies a mixture of the two, forming a structure comprising a series of narrow channels and dead ends.

On the whole the very best diffusers are those with a c_a value close to 0.7, suggesting a structure with long tortuous channels. This is the case for the best diffuser found, shown in Figure 5.18 (c), which is largely comprised of one long continuous tightly enclosed section. This follows from the examples from Section 5.3.3 in which it was shown that at low frequency sound will propagate from one part of an array to another along the shortest possible path. Consequently a structure is desired that provides long complex channels for which no shorter alternatives exist.

Tortuous percolation structures through Eden growth

Generating arrays through an arbitrarily random generation process (like the method considered so far) will likely result in structures with less than optimal tortuous paths. Consequently it is necessary to consider a method for creating tortuous diffusers by other means. Ideally these diffusers will comprise long runs (clusters) of elements that wrap around one another to form channels, though which do not overlap since this shortens the potential channel lengths and blocks off part of the structure to sound propagation.

One way of achieving the above is to use an algorithm based on a type of Eden growth [72]; a process similar to diffusion limited aggregation and which was initially applied to modelling the growth of cell colonies in biology. The method considers the growth of an initial 'seed' placed on the central node of a lattice. An iterative process is then carried out where upon each iteration an unoccupied neighbouring node to those within the structure is selected at random, thereby extending the size of the colony. Since this is carried out on the nodes of the lattice, this forms a type of site percolation structure.

A similar procedure to the above may be adopted here for the bond percolation structure case; placing an initial element on a periodic lattice before allowing it to grow into a cluster of elements. Note here the bonds determine the arrangement of slats rather than propagation paths. Upon each iteration the cluster attempts to add an additional bond (slat) from one of its nodes. By allowing the cluster to grow and by forbidding the connecting of already existing elements, this will extend into a tortuous array that does not cross and/or form closed off sections into which sound cannot propagate. The growth of the cluster is restricted to a predefined area ($M \times N$ grid). When no further growth is possible the routine is terminated. Starting with only one seed will likely make a diffuser with many separate sections. By starting the process with a number of randomly placed elements however, a series of clusters will wrap around one another, forming tortuous paths between them. This is carried out by introducing an additional stage where for each iteration a cluster to grow is selected at random. This procedure is illustrated in Figure 5.20 for the case of a simple 4×4 lattice starting with 3 initial seeds (left) which grow around one another (middle) until no further growth is possible (right). Note though separate areas in the diffuser are formed, there are no completely blocked off sections.
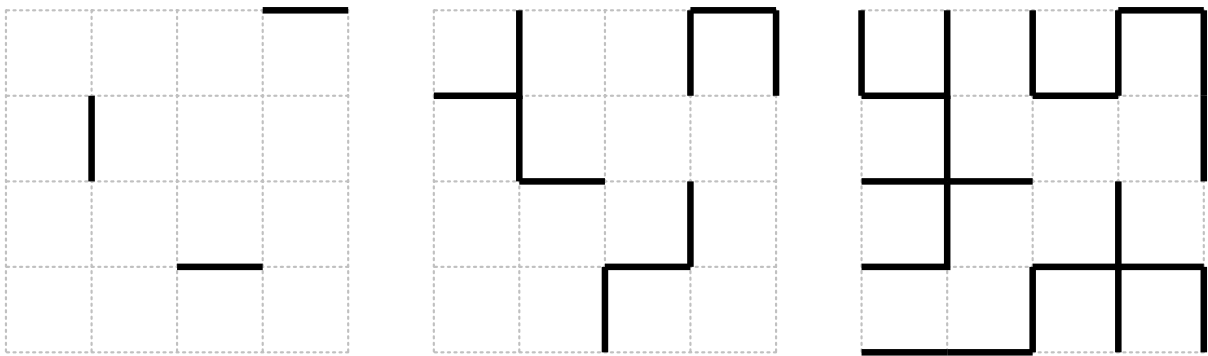
Figure 5.20: Illustration of the Eden growth algorithm (progressing from left to right) starting with 3 seeds for the construction of a 4×4 tortuous square grid percolation structure

As before, the above method was applied to a 10×10 square grid lattice comprising elements of length $d_e = 5$cm, forming a 50×50cm structure. A Monte Carlo simulation was run where 100 samples were generated for each of three different structures, grown from initial 'seed' numbers of 1, 10 and 40 respectively. An example of each of each structure type is shown in Figure 5.21 (top); each being the structure which achieved the highest average low frequency diffusion coefficient for its type. As above the average coefficient was taken for frequencies

an octave or more below that of the design frequency (of the structures equivalent Schroeder diffuser), f_0 = 313Hz results.

Figure 5.21 illustrates how, due to the tortuous nature of the structure, the diffuser type grown using the smallest number of seeds has the potential to diffuse effectively at the lowest frequency. The structures obtain tortuosity gradient values of g_a = 0.35 (a), 0.38 (b) and 0.42 (c) respectively, indicating that those with the shallowest gradient (and hence most tortuous paths) perform best. This illustrates how the gradient metric is more effective when applied to structures with little or no completely shut off sections. The tortuosity offset values for the three diffusers of Figure 5.21 are c_a = 0.70 (a), 0.73 (b) and 0.81 (c) respectively, implying that the best low frequency diffusers are again those with a value closest to approximately 0.7; structures comprising tightly packed channels.

The best diffusers were found to provide effective diffusion at approximately 2 octaves below the equivalent Schroeder diffuser design frequency. In general, however, though the tortuous structures above can provide high diffusion coefficient values at frequencies lower than would be expected based on their depth alone, this tends to be over a narrow bandwidth. This is likely due to the fact that with decreasing frequency the path lengths through the array required to create a phase shift larger enough to result in diffusion become large. Following from Fermat's principle (and the findings from Section 5.3.3), the need for paths for which no shorter alternative exists means that separate channels must be formed, hence taking up separate parts of an array. At very low frequency however a single path may occupy much of the array, which is undesirable since for effective broadband diffusion it is necessary to have a range of depths. This is because when a reflection from two parts of a structure arrive back in phase, there must be alternative reflected components from other parts of the structure that are out of phase in order to cause cancellation. This is the way in which Schroeder diffusers create diffusion.

In addition to the above, like the best low frequency surface percolation diffusers, once wavelength becomes comparable to the different length sections of slats toward the front of a diffuser, these surfaces will specularly reflect. Consequently for higher frequencies diffusion is poor. In addition, to form tortuous channels the best low frequency diffusers tend to have closed off backs to form the maximum path lengths. This means that diffusers similar to the

surface percolation diffusers of Section 5.4 are formed, which from other angles of incidence will look like a plane surface. Square lattice percolation structures capable of providing very low frequency diffusion will therefore likely make unsuitable broadband diffusers. Consequently it is necessary to consider the design of an array in the mid-to-high frequency range.
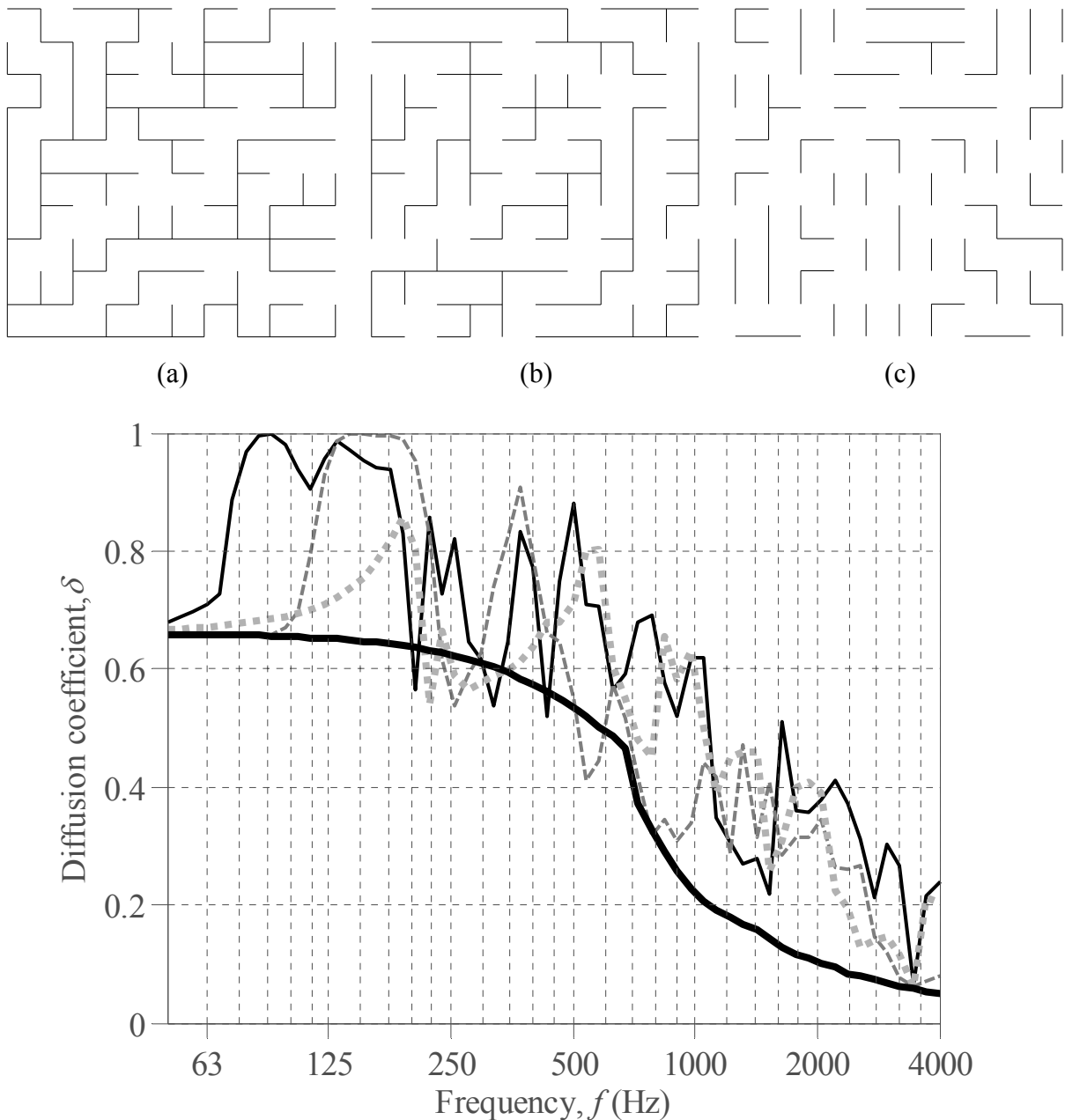
Figure 5.21: Best 10×10 percolation diffusers formed using the adapted Eden growth method grown from 1 (a), 10 (b) and 40 (c) seeds (top) and their diffusion coefficient (▬ (a), ▬ ▬ (b) and ▪ ▪ ▪ (c)) including reference plate of width D = 0.5m (▬) (bottom); d_e = 5cm, $\theta_0 = 0°$

5.5.3 The effect of the apparent well depths on high frequency diffusion

In Section 5.4.2 it was noted that with increasing frequency the distribution of the diffusion coefficients achieved by a Monte Carlo simulation of a surface percolation diffuser becomes much like that of its more conventional Schroeder diffuser equivalent. In a similar manner to the folded well diffuser results presented in Section 5.3.2, this suggests that the phase change on reflection from a percolation structure will become increasingly dominated by the 'apparent well depths'; the distance from the front of the structure to the first vertical element. This may be thought of as the well depth of a percolation structures equivalent Schroeder diffuser, an example of which is shown in Figure 5.10 (d) (though for a surface diffuser equivalent). As such this section considers the effect of these depths for the Monte Carlo simulation results presented in Section 5.5.1.

Figure 5.16 (top) demonstrated that with increasing frequency the best diffusers were those with a low number of vertical elements, suggesting that larger depths were important. Figure 5.22 shows a diffusion coefficient map similar to those shown previously, though considering the effect of the range of these depths (maximum minus minimum). At low frequency almost any depth range is sufficient to create diffusion, though the more optimal structures are those with a low depth range. This agrees with the vertical element occupancy findings discussed above, indicating that for higher fill factors more tortuous paths are created and that sound is being channelled into the structure by promoting lateral propagation. With increasing frequency however the most successful diffusers are those which have a greater range in depth. As with the folded well Schroeder diffuser example from Section 5.3.2, this is because as the frequency approaches the cut-off point given by Eq. 5.1, little sound will propagate laterally and the phase change will be determined more by the apparent depth as seen by the source. Consequently a range in depths is desirable.

Once half a wavelength becomes equal to the lattice spacing (given by the cut-off frequency of Eq. 5.1), spatial aliasing occurs and a sharp drop in diffusion results. This is similar to the behaviour observed in periodically spaced layers of slats discussed in Section 4.3.2, and is the equivalent to the flat plate frequencies seen with Schroeder diffusers. Due to the use of a square grid lattice structure (where $d_x = d_y$) this provides an upper limiting frequency, f_{max},

equivalent to the well cut-off frequency of Eq. 5.1, which for the structure here corresponds to a frequency of f_{max} = 3.44kHz.
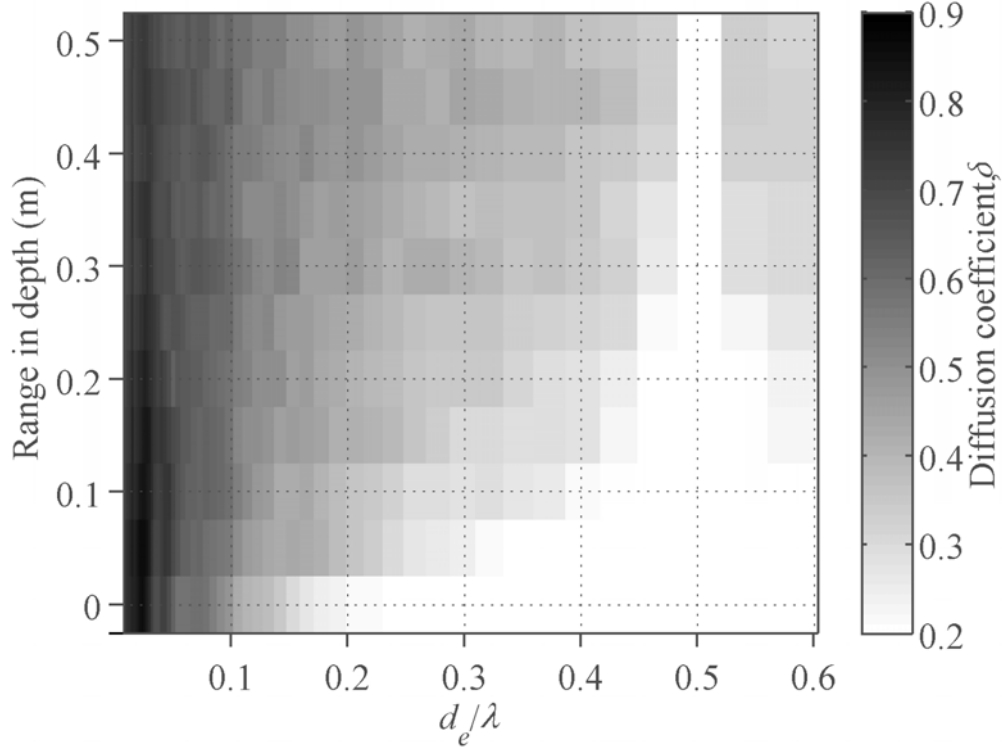
Figure 5.22: diffusion coefficient with range in effective well depth for 1000 randomly generated 10×10 percolation bond volume diffusers; , d_e = 5cm, D = 1.0m, θ_0 = 0°

Following from the above, the merits of a set of apparent well depths may be estimated using the same basic theory as for a conventional welled device. It was shown in Section 4.3.2 that an approximate model for the scattering from a Schroeder diffuser is given by the Fourier Transform of its reflection coefficients, R_n, as determined by Eq. 4.37. The reflection coefficients will be dependent on frequency, though at the design frequency (given by Eq. 5.2) through rearrangement of the more conventional well depth formula [3] they may be given as:

$$R_n = e^{j2\pi \frac{2d_n}{d_x(M+1)}}$$

5.5

Where d_n is the (apparent) depth of the nth 'well'. Note, where no depth can be obtained (due to line-of-sight through the structure) the magnitude of the reflection coefficient is set to zero.

In Section 4.2.3 it was shown that for a single period device it is the aperiodic properties of a sequence which is of most interest, with optimal sequences being those whose AACF is most like a Kronecker delta function, a measure of which was obtained by taking the standard deviation of the AACF sidelobe energy (an example of which was shown in Figure 4.11). Consequently the same method may be applied here to the reflection coefficients given by Eq. 5.5. The effect of this on diffusion is shown in Figure 5.23, demonstrating the influence on the average diffusion coefficient for all frequencies above that of the effective Schroeder design frequency of Eq. 5.2 ($f_0 = 313$Hz). In general the average diffusion coefficient can be seen to correspond to a low standard deviation of the AACF sidelobes values. Consequently at mid-to-high frequency the diffusion from an array is much like that expected from a conventional Schroeder diffuser. The very best diffusers occur for a standard deviation value of zero, though it should be noted that these correspond to very sparse structures with a high line-of-sight through the array. Consequently they comprise very few 'effective depths' and their scattered power will tend to be weak. This is discussed further in Section 5.5.4.
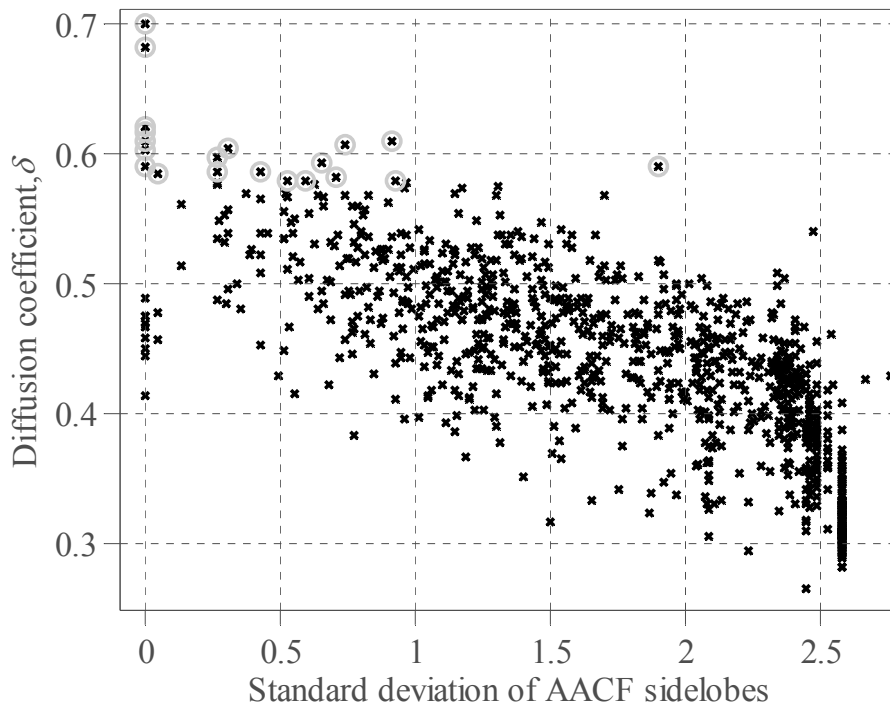
Figure 5.23: Average diffusion coefficient over the frequency range 313Hz $\leq f \leq$ 4kHz with the standard deviation of the AACF sidelobes for 1000 randomly generated 10×10 percolation bond volume diffusers; d_e = 5cm, D = 1.0m, θ_0 = 0°; grey circles indicate best 20 diffusers

5.5.4 The effect of line-of-sight on scattered power

It has been shown that with increasing frequency the scattering from a percolation diffuser will be increasingly dependent on the 'apparent' well depths. This is because, as was discussed in Chapter 4 for arrays of slats, as wavelength becomes comparable to element size a progressively more specular reflection results. Consequently the scattered power findings for slat arrays will likely also apply here. At high frequency, above the cut-off frequency given by Eq. 4.18, it was shown that the back-scattered power from an array of slats is approximately determined by the fraction of the line-of-sight through the array that is blocked, F_{fill}. This relationship is described by Eq. 4.13, which predicts that approximately 50% of the line-of-sight should be blocked in order to achieve the -3dB back-scattered power target. To illustrate this for the percolation structure case, Figure 5.24 shows the back-scattered intensity ratio (top) and diffusion coefficient (bottom) for the percolation diffusers shown previously in Figure 5.18 (a) and (c). Note diffuser (a) is the structure from the Monte Carlo investigation above with the highest average diffusion coefficient from all the arrays with exactly 50% line-of-sight.

It is evident that, as expected, at high frequency the structure results in a back-scattered power level close to -3dB. Based on the individual slat size the predicted transition frequency from which this will occur is $f = 2.43$kHz (as given by Eq. 4.13). As with the slat arrays however, the scattered power will be affected by the different length runs of adjacent vertical elements, since adjacent slats conjoin to form larger flat surfaces that will scatter power efficiently at a lower frequency. Figure 5.24 (top) also shows therefore the approximate model from Chapter 4, obtained by following the procedure outlined in Section 4.3.1 (as illustrated in Figure 4.25). It can be seen that at high frequency (above the transition frequency) the model agrees well with the thin panel BEM prediction. At lower frequencies however, due to the presence of horizontal slats, the structure produces a higher than expected level of scattered power. Figure 5.24 (top) also shows for reference the scattered power value for the percolation structure from Figure 5.18 (c), illustrating how for the fuller more tortuous arrays the scattered power approaches 0dB. Consequently for the design target presented here the scattered power from these diffusers is unsuitable.
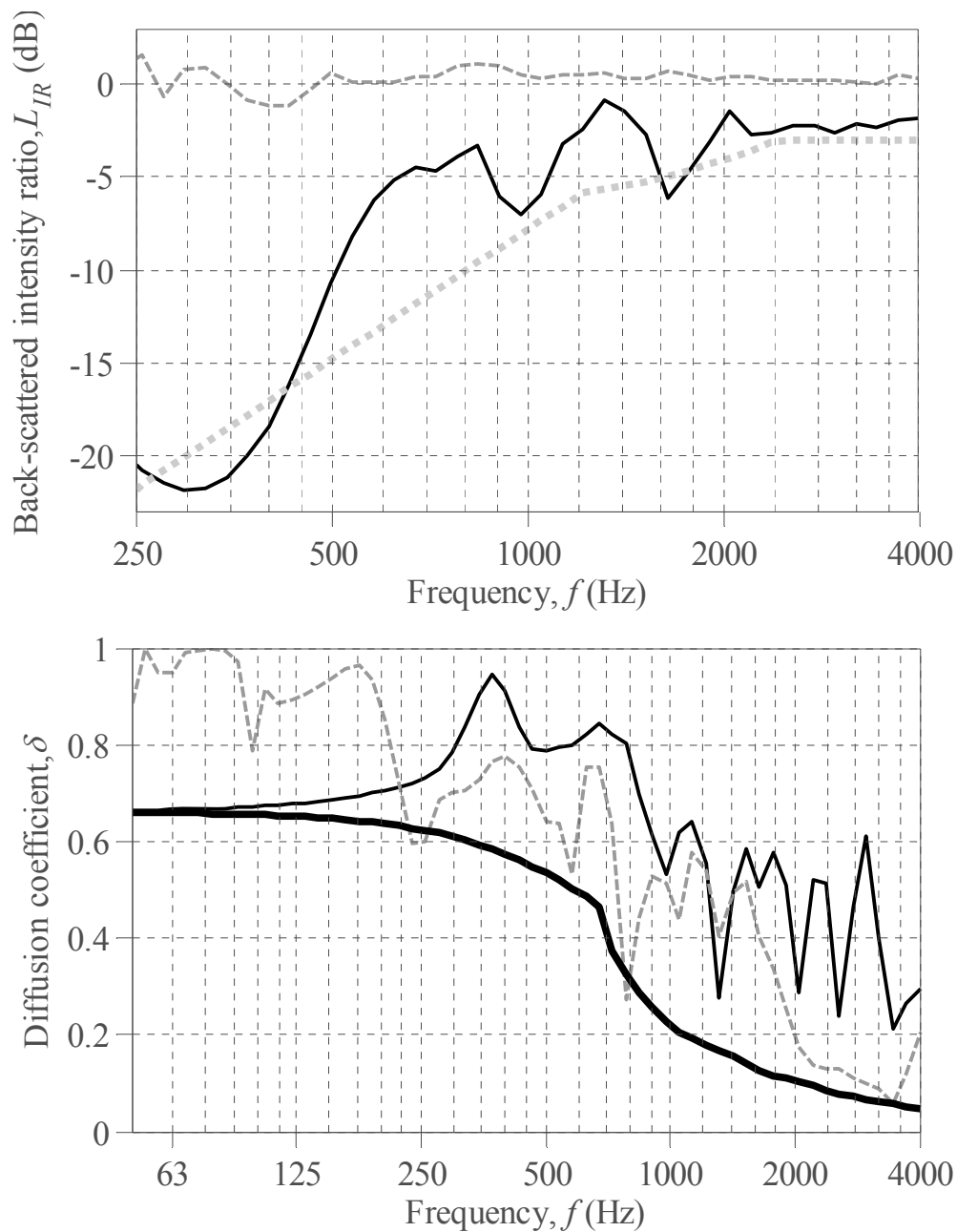
Figure 5.24: Back-scattered intensity ratio including approximate power model from Chapter 4 (- - -) (top) and diffusion coefficient including reference plate of width D = 1.0m (━━) (bottom) for the percolation bond surface diffusers from Figure 5.18 (a) (━━) and (c) (- -); d_e = 5cm, D = 0.5m, $\theta_0 = 0°$

Since the scattered power form a percolation structure is with increasing frequency progressively more dominated by line-of-sight (and hence what the source can see), this suggests that for higher frequencies little sound is able to propagate into the structures. To assess this, the percolation structure used for the verification of the prediction routine in

Section 2.6.2 (shown in Figure 2.23) was subject to a second measurement; one where absorbing foam was introduced to the centre of the structure. The measurement sample including foam is shown in Figure 5.25, showing both photograph from above (left) and the approximate location of the absorption in the array (right). The foam was the same as that used in the construction of the Binary Amplitude Diffuser (BAD) sample from Figure 4.2, though with thickness 10mm, and cut into sections that slotted into the whole length of the diffusers height.
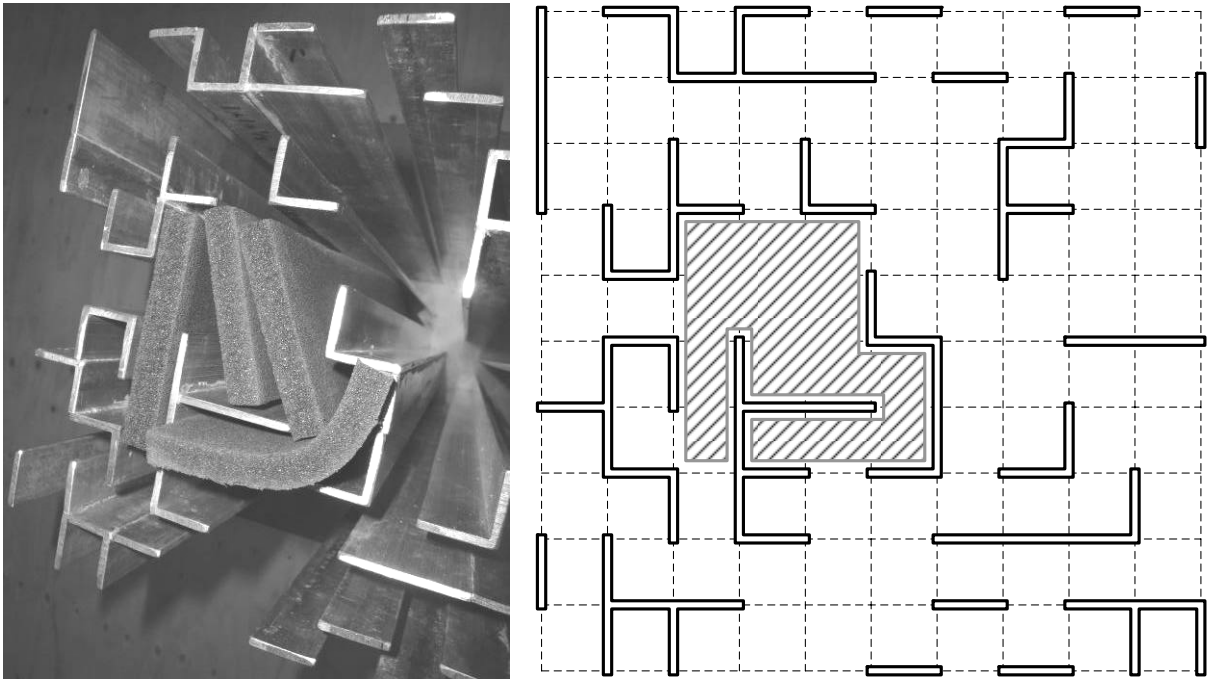
Figure 5.25: Porous foam placed in the centre of the measured percolation structure from Section 2.6.2 (left) and its approximate location within the structure (hatched area, right); $d_e = 6.7cm$ (when scaled), $\theta_0 = 0°$

Figure 5.26 shows the average (normalised) back-scattered pressure obtained for the measured percolation structure both with (dashed line) and without (solid line) foam respectively. This was taken as an average over all receivers in the $-90° \leq \theta \leq +90°$ region for a normal incidence source (from the right of Figure 5.25 (right)). It can be seen that at low frequency the back-scattered power is reduced, with a maximum deviation between the two measurements of approximately 5.7dB, occurring at $f = 400$Hz. Note at very low frequency the absorption effect is reduced, though this is likely due to the absorption properties of the foam. With increasing frequency however the effect is small, which for frequencies above

$f = 500$Hz results in a deviation of no more than ± 2.0dB. This is despite the foam being likely more effective in the absorbing of sound over this frequency range. This approximate 500Hz transition frequency corresponds to a wavelength of 0.69m, which equates to the approximate width of the array, $D = 0.67$m. This suggests therefore that for structures containing even relatively non-tortuous channels, little sound can penetrate far into the structure over the majority of the bandwidth.
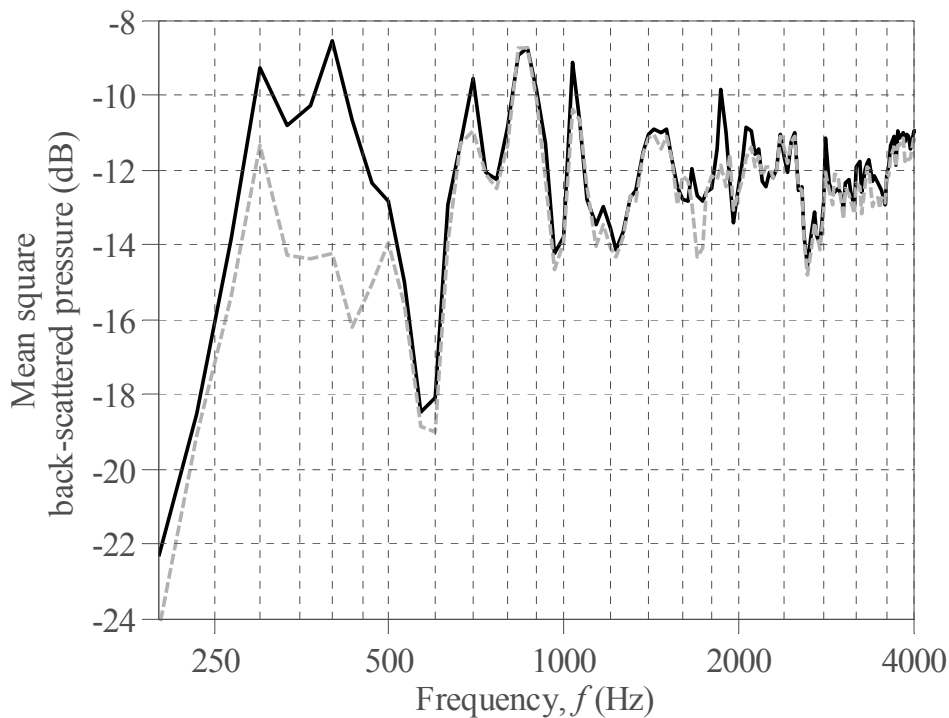
Figure 5.26: Average (normalised) back-scattered pressure from measurements for the
percolation structure of Figure 5.25 without (━) and with foam (━ ━)

The above implies that, whilst a percolation diffuser may be formed that achieves both reasonable levels of diffusion and the desired level of scattered power, the structure is not behaving as intended. This is because little sound may propagate through the structure, with at mid-to-high frequency tortuous arrays producing strong specular reflections in the back-scattered direction, resulting in poor diffusion and a back-scattered power approaching 0dB. To avoid this, a diffuser must have few vertical elements, though ideally a higher number of horizontal elements to encourage Schroeder diffuser like behaviour. This structure however when viewed from a source angle of $\theta_0 = \pm 90°$ will appear as the complete opposite; a diffuser with a high vertical and a low horizontal element occupancy respectively. Consequently a more isotropic array must have few vertical and horizontal elements,

potentially reducing diffusive efficacy. This array will appear more like a collection of scatterers rather than a percolation device, and will likely behave similarly to the slat arrays of Chapter 4.

The above is due to a combination of both the shape of the elements – which on their own will tend to redirect sound rather than cause diffusion – and their arrangement. For a square grid structure, due to the element orientation, this results in a strong back-scattered effect controlled by element density and line-of-sight through the array. Consequently alternative lattice types may be considered that attempt to redirect energy into the structure, allowing sound to be moved into the forward scattered region. This provides potential both for decreased back-scattered power and more even scattering.

5.5.5   A comparison with a triangular grid percolation structure

Above it was shown that for a square grid percolation diffuser, with increasing frequency the performance of an array will become increasingly dominated by line-of-sight through the structure. This is because once wavelength becomes comparable to element size an increasingly more specular reflection results. For normal incidence therefore, a square grid percolation will tend to direct much of the incident sound back in the direction of the source. This section therefore compares this case with that of a different type of percolation diffuser; one based on a periodic triangular lattice. This is comprised of slats of equal length, d_e, forming a grid of equilateral triangles. As before these may be included or omitted to alter the properties of an array.

To assess the effect of using a triangular lattice, a Monte Carlo simulation was run as previously, though for 400 randomly generated structures. This was performed for four different scenarios; percolation diffusers based on a square grid lattice, a square grid lattice rotated by 45°, a triangular lattice, and a triangular lattice rotated by 30°. Each structure comprised elements of length d_e = 10cm. To allow a more accurate comparison of behaviour, the dimensions of the structures (in all directions) were restricted to a width of no more than 1.05m, resulting in diffusers with an approximate width of D = 1.0m. Figure 5.27 shows the average (normalised) scattered pressure maps with frequency for the four structures. The lattice on which they are based is shown on each map for reference.
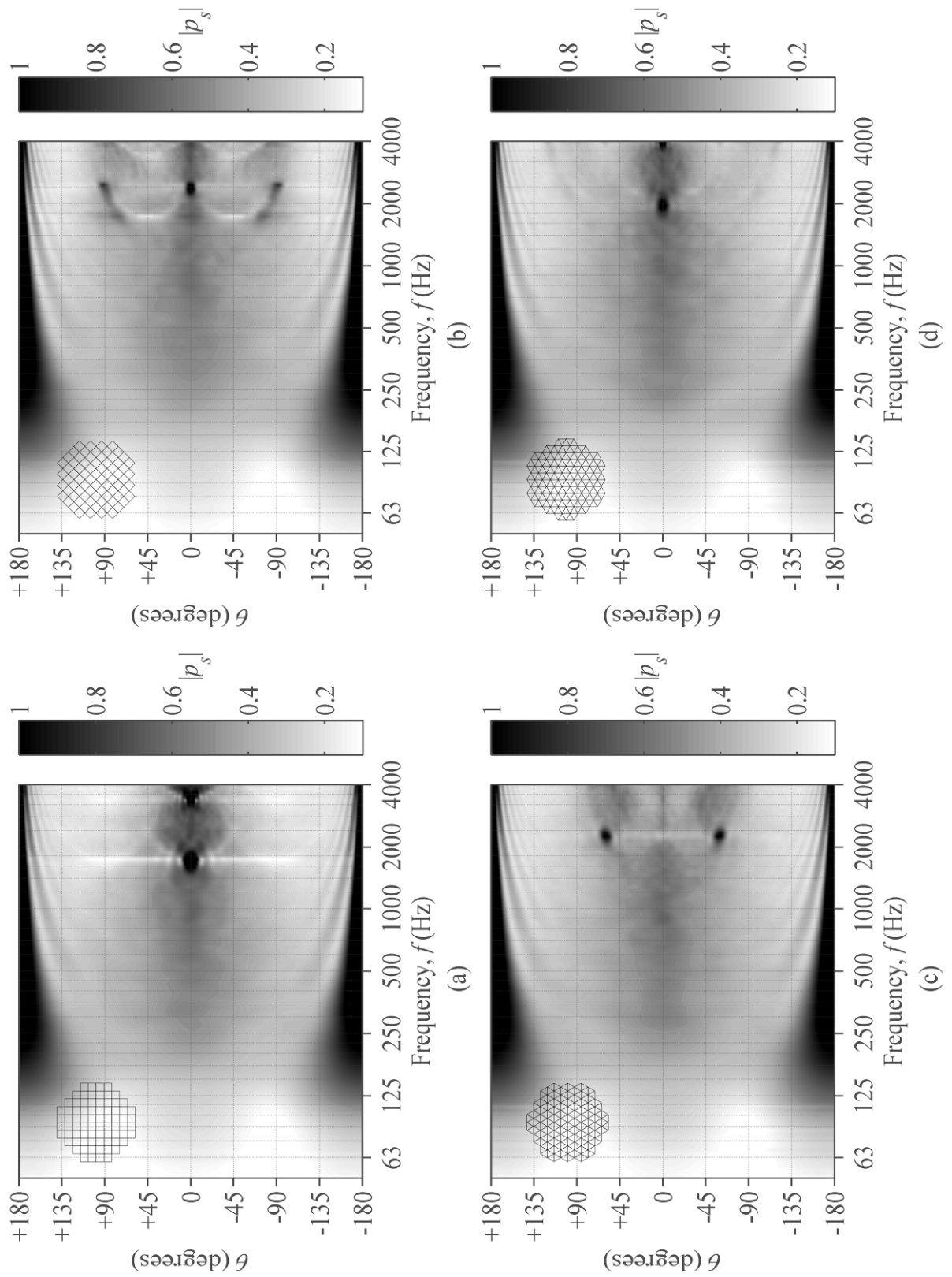
Figure 5.27: Average normalised scattered pressure with frequency for 400 randomly generated percolation bond volume diffusers based on the grid types shown; $d_e = 10cm$, $D = 1.0m$, $\theta_0 = 0°$

At low frequency, due to their approximately circular footprint, the average scattered pressures from the four structure types are very similar. This is also the case in the mid frequency range (before spatial aliasing occurs), the region in which the best diffusers generated above were those with the more optimal 'apparent' well depths. This is where the diffusers are able to spread their scattered energy most evenly, though this is generally restricted to the back-scattered direction. This is because the reflections from the plane surface elements in the array will be subject to Lambert's law which may be given as [3]:

$$|p_s|^2 \propto \cos^2\left(\frac{\theta}{2}\right) \qquad\qquad 5.6$$

Where a flat surface orientated at an angle of $\theta/2$ results in a geometric reflection toward the receiver angle, θ (as illustrated by Figure 5.28), and all angles are expressed relative to the angle of incidence. This is a simple statement of the size of the solid angle into which a surface both receives and reflects. Consequently as the angle of reflection moves from the specular direction toward the back of the array (as the surface is tilted from a vertical to a horizontal position in Figure 5.28) the scattered intensity falls.
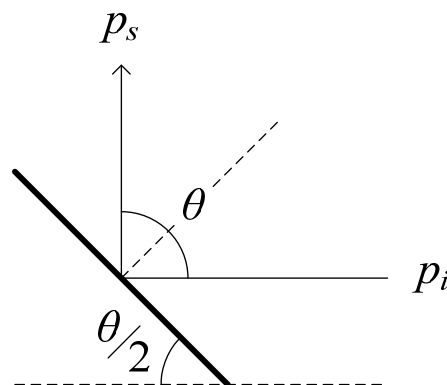
Figure 5.28: Geometric reflection from a flat surface

In contrast to the above, at high frequency the average pressure maps for the four structure types of Figure 5.27 differ significantly. This is because once element size becomes comparable to wavelength, and with increasing frequency thereafter, the elements produce an inherent specular reflection. An approximate frequency above which this occurs is given by Eq. 5.1, which equates to a frequency of $f = 1.72$kHz. This redirects the incident sound into distinct directions determined by the geometric angles of reflection in an array, dependent on

lattice shape (and angle of incidence). This is emphasised when spatial aliasing occurs; when the sound scattered into the directions constructively interferes and a (set of) strong specular reflection(s) results. It can be shown that for a lattice with elements whose angles of orientation may be given as $2\pi \times \alpha/\beta$ (modulo 2π), where α is an integer of any value (positive or negative) and β is a positive integer of fixed value, the potential geometric angles of reflection, may be given by:

$$\theta = \frac{4\pi\alpha}{\beta} - 2\theta_0 - \pi \qquad \text{odd order reflections} \qquad\qquad 5.7$$

$$\theta = \frac{4\pi\alpha}{\beta} + \pi \qquad \text{even order reflections} \qquad\qquad 5.8$$

Where θ is expressed relative to the angle of incidence, θ_0, and Eqs. 5.7-5.8 represent all possible odd and even angles of reflection respectively. The above corresponds to a lattice based on the periodic tiling of a regular polygon. A full derivation of the above is given in Appendix C. Consequently at high frequency a small number of allowed reflections results, with sound being scattered into distinct directions. For example the allowed reflections in a simple square grid array, where $\beta = 4$ (with element angles of orientation being given by 0°, 90°, 180° and 270°), at normal incidence may be given as $\theta = \{0^{\circ}, 180^{\circ}\}$ for both odd and even order reflections respectively. This can be seen from the example in Figure 5.27 (a), which with increasing frequency progressively focuses more of its scattered energy into these angles. For the square grid array rotated by 45° (the equivalent of the above though with a source angle of $\theta_0 = -45^{\circ}$) the above predicts allowed reflections of $\theta = \pm 90^{\circ}$ (odd order) and $\theta = \{0^{\circ}, 180^{\circ}\}$ (even order). Again the example in Figure 5.27 (b) can at high frequency be seen to direct the scattered sound into these specific angles.

The triangular percolation structures considered have element angles of orientation of 0°, 120° and 240°, where $\beta = 3$. The allowed reflections from the array of Figure 5.27 (c) are given as $\theta = \{\pm 60^{\circ}, 180^{\circ}\}$ for both odd and even order reflections. As with the square grid arrays from above, this is the case. For the triangular percolation structure rotated by 30°, the equivalent of considering a source angle of $\theta_0 = -30^{\circ}$ (Figure 5.27 (d)), the reflection angles are given as $\theta = \{0^{\circ}, \pm 120^{\circ}\}$ and $\theta = \{\pm 60^{\circ}, 180^{\circ}\}$ for odd and even order reflections respectively. Note

in this case the relatively weak scattering into the $\theta = 120°$ receiver direction, despite it being a first order reflection. This (as was described above) is again due to Lambert's law.

Following from the above and the findings from the previous sections, the behavioural trends of a percolation diffuser based on a periodic lattice may be summarised by Figure 5.29. This breaks down the behavioural regime into three sections; tortuous channelling (low frequency), Schroeder diffuser like diffusion (mid frequency) and geometric scattering (high frequency). The diagram represents the potential behaviour per frequency, though for reasons discussed above a single diffuser is unlikely to perform this well over all frequencies. In general the effectiveness of the diffusers considered so far is inherently limited by the use of an underlying periodic grid. This is largely due to the limited number of angles of orientation of the elements which tends to redirect sound into the back-scattered direction. Consequently alternative lattice types must be considered; ones which have elements with many angles of orientation.
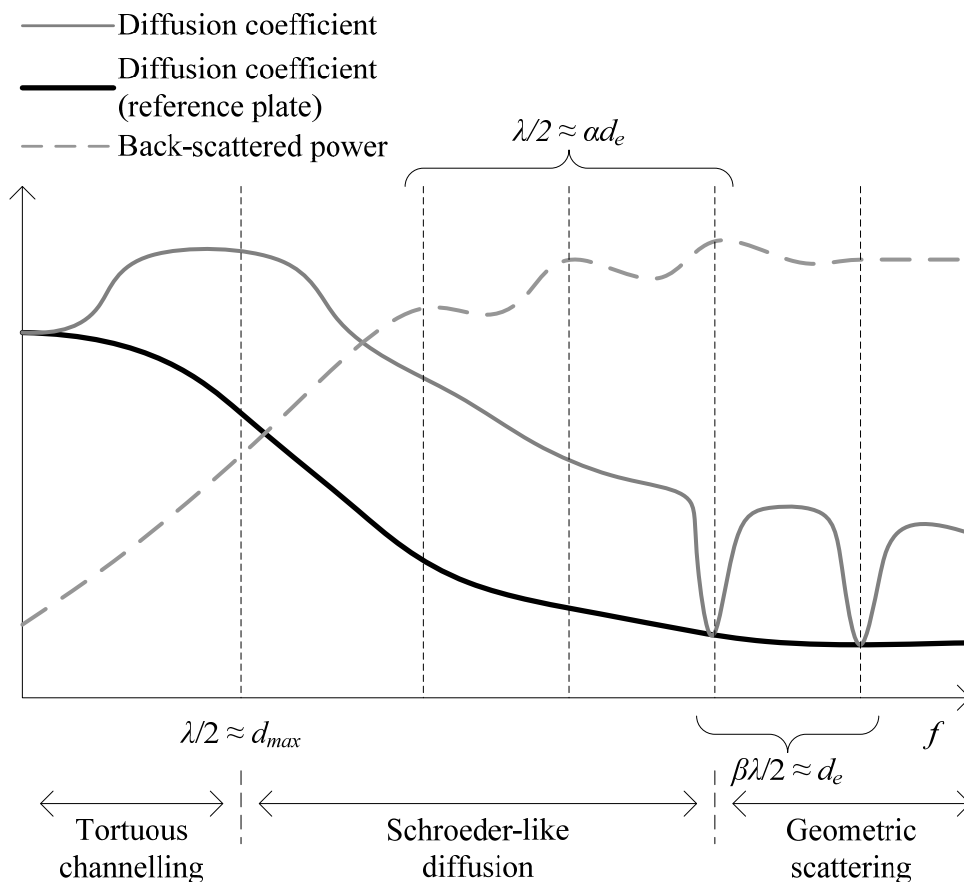
Figure 5.29: Behaviour of the diffusion coefficient and back-scattered intensity ratio of a generalised square grid volume percolation diffuser with frequency

5.5.6 A non-periodic lattice

Following from the above, it is clear that with increasing frequency the use of an underlying periodic lattice means that a structure will tend to scatter into distinct directions. This begins in the mid frequency region before spatial aliasing occurs, though becomes progressively more evident as the wavelength decreases and becomes comparable to or smaller than lattice spacing. The effect for fuller arrays was shown to result in an intensity ratio, L_{IR}, which tends towards 0dB, since the geometric reflection paths result in the majority of the sound incident upon a structure being directed into the back-scattered region. As such in order to create a more even scattered field, including in the forward-scattered direction, an alternative lattice type may be considered; one whose geometric reflection paths are capable of scattering in all directions. Following from the findings of Section 5.5.5, this may be achieved by providing elements of varying orientation. This is akin to the randomly orientated filaments of the brilliant white beetle scales [69] introduced in section 5.2.2. Two structure types were considered for investigation and are discussed below; a Bethe lattice and a randomised lattice, examples of which are shown in Figure 5.30 (left and right respectively).
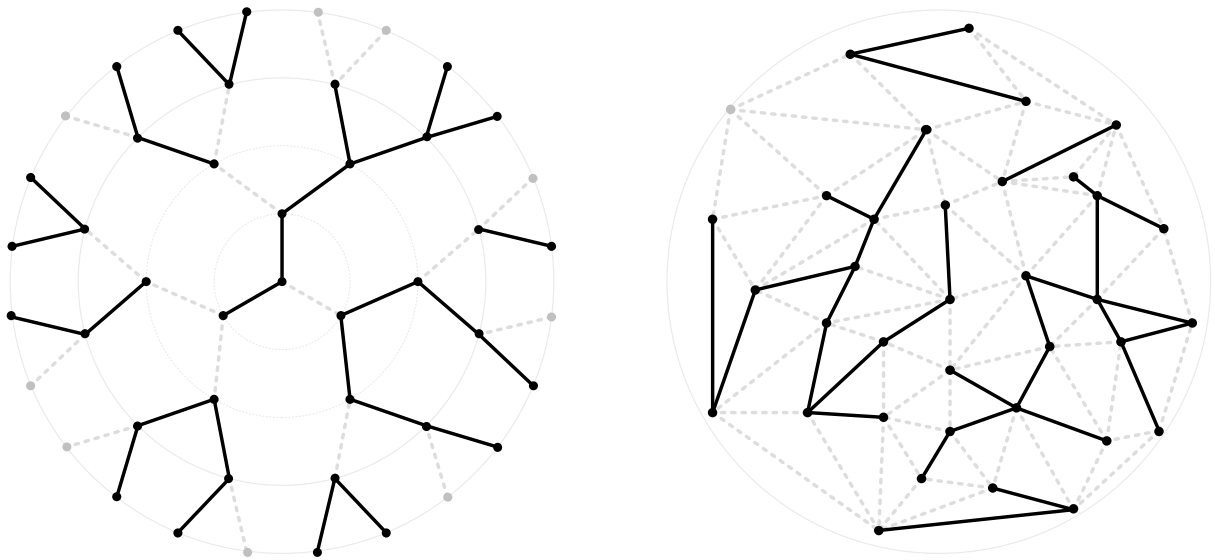
Figure 5.30: Examples of percolation volume diffusers based on a Bethe lattice (left) and a random node lattice with bonds determined by Delaunay triangulation (right); bonds are either occupied (━) or vacant (┄ ┄) based on random selection

The Bethe lattice

A Bethe lattice (or Cayley tree), an example of which is shown in Figure 5.30 (left), is a lattice often applied in percolation theory to the study of magnetism [67]. The lattice is defined as a network for which (excluding the effects of truncation at its extents) each site (node) is connected to z bonds [67]; the example from Figure 5.30 (left) having a value of $z = 3$. This forms an endlessly branching structure with no closed loops [68].

As was illustrated by Figure 5.1 for a square grid percolation structure, it is the lack of a slat that allows transmission paths in an array. Unlike the square grid structure however (whose propagation paths are also based on a square grid lattice) the 'bonds' in terms of sound propagation through a Bethe lattice of slats forms a very different structure; one comprising a series of closed off cavities of different sizes. By randomly removing some of these elements these cavities may interlink and form more tortuous paths. Of particular interest however is that when arranged as shown in Figure 5.30 (left) the slats will emanate from the centre of the array. Consequently a sound wave incident on the structure (from any angle) will first encounter slats that are approximately parallel to the direction of propagation, thus encouraging sound to travel into the array. As the incident sound approaches the centre of the array however the natural angles of reflection should result in sound being scattered back outwards again, though with direction dependent on which slat is encountered. Since there are numerous slat orientations within the structure this has the potential to scatter much more evenly. In addition, due to the rotational symmetry of the lattice the array should provide potential for more consistent behaviour with angle of incidence.

To asses the potential of the array a $z = 3$ Bethe lattice was constructed in a manner similar to the example of Figure 5.30 (left), though comprising five rather than four layers (grey dotted circles). The nodes within each layer were spaced with equal angle increments. Each layer was based on a circle centred on the central node, with the radii of each successive layer being increased in 10cm increments. The total width of the array therefore was $D = 1.0$m. Based on this lattice, as with the previous examples, a Monte Carlo simulation was run for 400 randomly generated structures. Figure 5.31 shows the average (normalised) scattered pressure map with frequency obtained from the simulation.
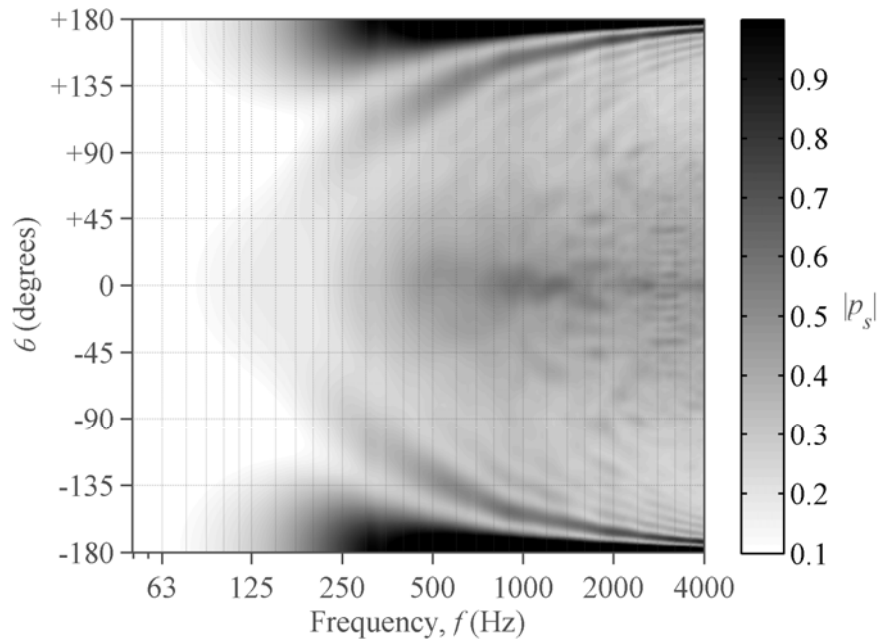
Figure 5.31: Average normalised scattered pressure with frequency for 400 randomly generated percolation bond volume diffusers based on a Bethe lattice; $\theta_0 = 0^°$, $D = 1.0m$

It can be seen that once approximately a wavelength fits into the structures' total width ($f = 344$Hz), the structure on average behaves similarly to the examples from Figure 5.27 for the square and triangular lattice structures respectively. With increasing frequency however it is evident that the scattered pressure does not strongly favour any one particular direction. The structure still reflects more energy into the back-scattered than forward-scattered region. This is due to Lambert's law [3] and may be explained as follows. An array comprising a large number of randomly orientated flat elements will with increasing frequency result in many randomly distributed specular reflections. Depending on slat orientation these reflections will be of varying magnitude due to the solid angle which they both receive sound from and scatter sound into. Consequently on average the scattered intensity, for a set of randomly orientated slats will be given by Eq. 5.6. This is equivalent to the high frequency approximation for the scattering from a cylinder, as given by Eq. 6.2 in the following chapter. Since at high frequency a single cylinder provides a highly uniform scattered field, this suggests that a percolation diffuser based on the Bethe lattice has the potential to diffuse well.

A random lattice

By providing a large range of slat orientations it was shown that the Bethe lattice structure above showed potential to scatter in a highly even manner. An alternative way in which this

could be achieved is through use of a more randomised lattice; one where the node locations are selected at random. Basing the slat locations of a percolation structure on this lattice, elements may then be randomly removed as for the previous percolation structures. An example of this is shown in Figure 5.30 (right), where the locations of the nodes of the lattice have been selected at random (though from within a defined area), and the elements connecting these nodes have been obtained via a simple Delaunay triangulation algorithm [73].

Based on the above a structure was considered whose lattice lay within a circle of $D = 1.0$m in diameter, restricting the maximum width of an array. The number of nodes was set to 462; the number of nodes required to achieve the same average density of nodes as an equivalent periodic triangular array. As with the Bethe lattice example a Monte Carlo simulation was run for 400 randomly generated structures, though with a different randomly generated lattice used for each. Figure 5.32 shows the average (normalised) scattered pressure map with frequency.
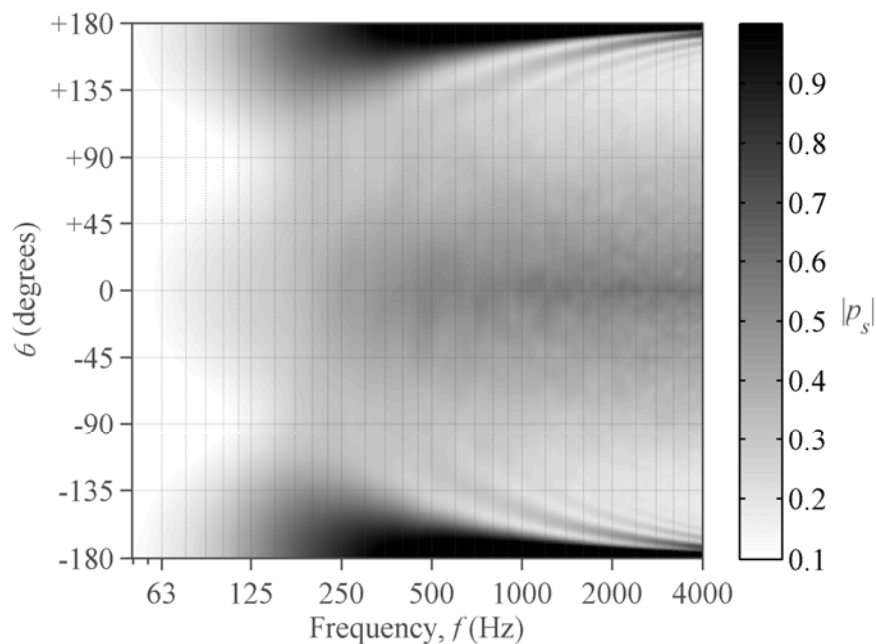
Figure 5.32: Average normalised scattered pressure with frequency for 400 randomly generated percolation bond volume diffusers based on the random Delaunay triangulation construction method; $\theta_0 = 0°$, $D = 1.0$m

It can be seen that the result is highly similar to that of the Bethe lattice above (Figure 5.31), which following from Lambert's law, at high frequency results in a scattered pressure field

approximately given by Eq. 5.6. Consequently, as with the Bethe lattice, the randomised structure also has the potential to diffuse well.

Results

Figure 5.33 shows the diffusion coefficient (top) and the back-scattered power (bottom) for the diffusers obtaining the highest average diffusion coefficient over all frequencies tested for both the Bethe lattice and randomised Delaunay triangulation lattice Monte Carlo simulations above. These diffusers are shown in Figure 5.34 (left and right respectively).

It can be seen from Figure 5.33 (top) that both Bethe lattice and randomised lattice structures are able to produce high levels of diffusion, obtaining average diffusion coefficient values of 0.66 and 0.69 over the frequency range $50\text{Hz} \leq f \leq 4.0\text{kHz}$ respectively. Overall an approximate diffusion coefficient of 0.3-0.5 above that of the reference plate is achieved. In addition both structures are capable of achieving close to the desired -3dB back-scattered power target. For the randomised array (solid line) this is achieved over the majority of the modelled bandwidth. This is due to providing a variety of element sizes, and hence having elements more comparable to wavelength at low frequency. Due to its relatively high occupancy the average value obtained is approximately -2.4dB, though this is still less than would be expected given the level of blocked line-of-sight. This likely due to the different slat orientations being able to redirect energy in the forward-scattered direction. The Bethe lattice diffuser on the other hand, due to its comparatively smaller clusters of elements, produces an even level of scattered power from approximately $f = 350\text{Hz}$ (when wavelength is approximately equal to structure size). This structure achieves an average back-scattered power value for all frequencies above $f = 350\text{Hz}$ of -3.7dB. Note the back-scattered power values at very low frequency are less reliable, since the scattered power metric assumes that the reference plate is relatively large compared to half of a wavelength. These less accurate results will occur below approximately $f = 122\text{Hz}$ since this is the approximate cut-off frequency for the reference plate (as given by Eq. 4.18).
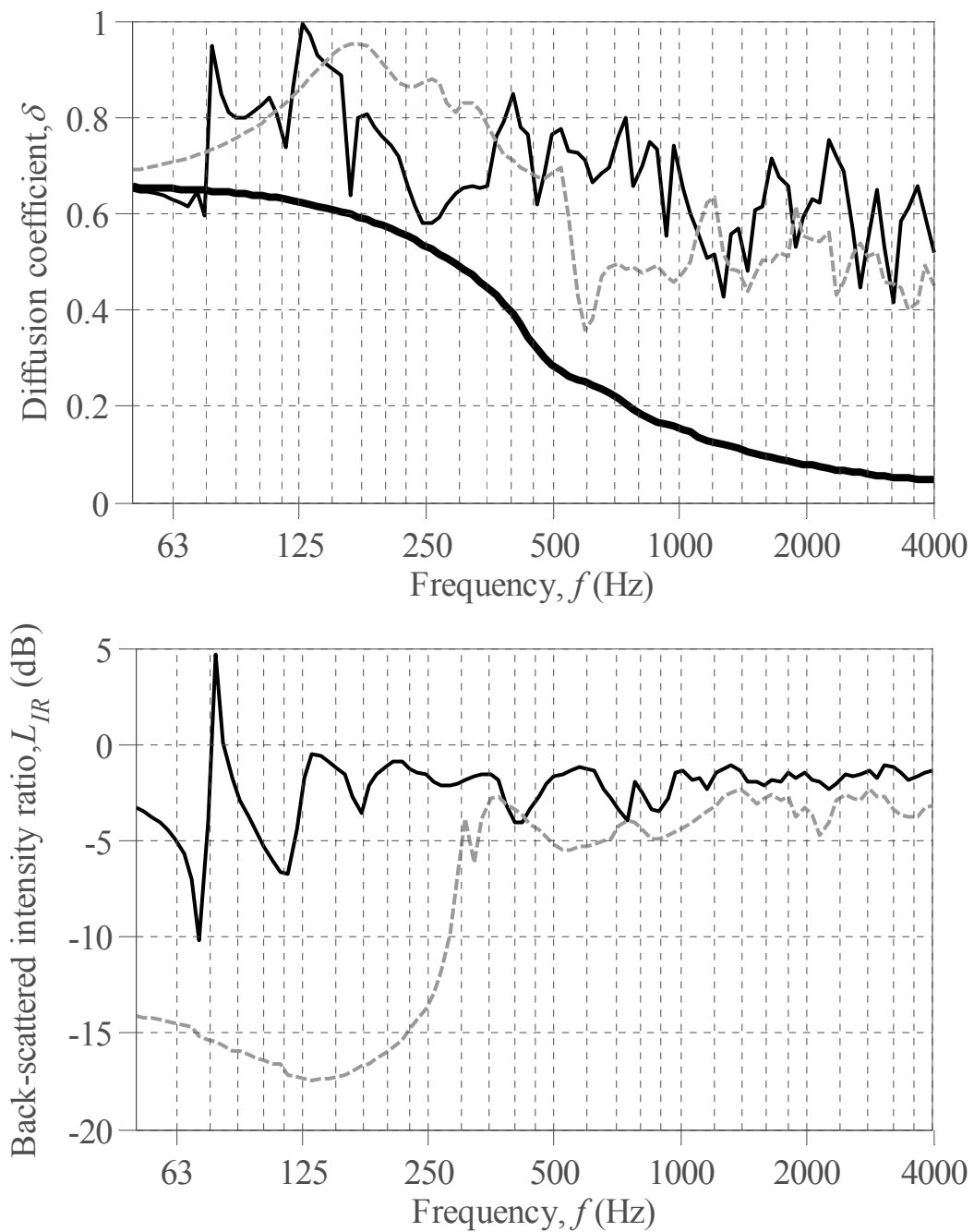
Figure 5.33: Diffusion coefficient (top) and back-scattered intensity ratio (bottom) for the best random Delaunay triangulation (━━) and Bethe lattice (━ ━) percolation structures obtained via Monte Carlo simulation; $\theta_0 = 0°$; top plot includes plate of width D = 1.0m (▬)
for reference
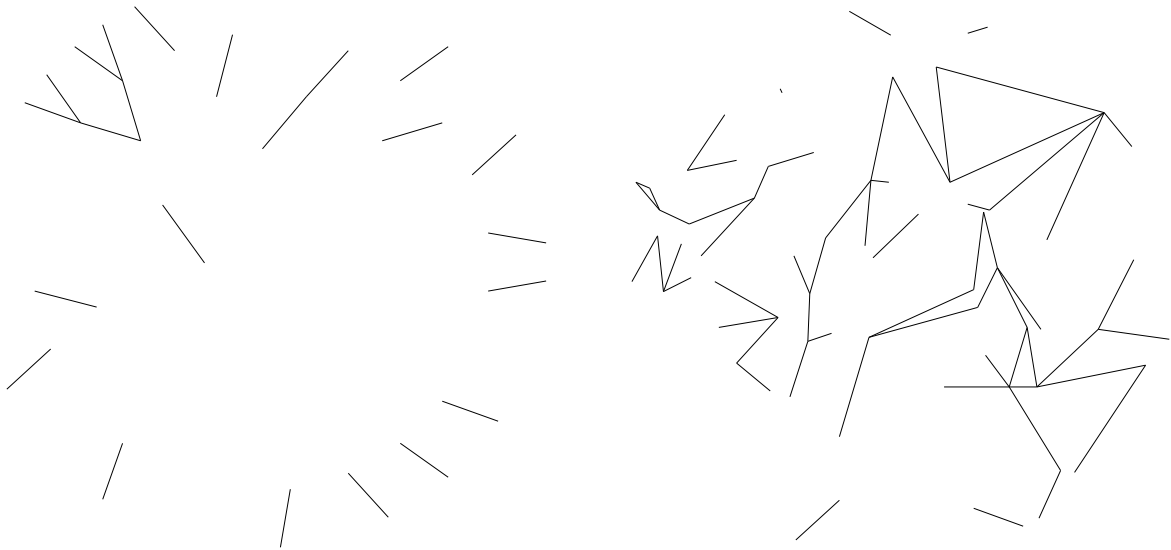
Figure 5.34: Best diffuser obtained from the Monte Carlo simulation of 400 randomly generated percolation structures based on a z = 3 Bethe lattice (left) and a randomised Delaunay triangulation lattice (right)

Based on the above, each of the structure types shown provides effective diffusion over an at least 3.5 octave bandwidth. This is due to their varying element orientation, providing angles of reflection that allow sound to propagate into the array, thus avoiding the inherent line-of-sight problems associated with a simple square grid lattice percolation diffuser. In addition due to the lack of periodicity these structures avoid the problem of spatial aliasing in periodic arrays. Substantial diffusion (relative to the reference plate) is seen from approximately f = 86Hz; the point at which a quarter of a wavelength fits in to the depth of the structure. This approximately matches the performance of a conventional Schroeder diffuser presented in Section 5.4.2, indicating that diffusion at this point may be achieved by depth alone, and consequently these structures are unlikely causing significant tortuous channelling. As can be seen from the Bethe lattice example of Figure 5.34 (left) this is because the best arrays are often sparse, and as such are behaving more like an array of scatterers than a tortuous waveguide. Consequently the most effective diffusers are those more akin to the brilliant white beetle introduced in Section 5.2.2 than a percolation diffuser.

5.6. Conclusions

A study has been carried out to investigate the potential use of a percolation structure as a volume diffuser. These structures are similar in concept to the slat arrays considered in Chapter 4, though including horizontal elements that channel sound into the structure in a manner similar to the fins separating the wells of a more conventional Schroeder diffuser. Considering structures based on a periodic square lattice, an initial investigation was carried out to consider some of the key principles of channelling sound. Percolation diffusers were then considered based on this arrangement. Due to the complexity of the structure a Monte Carlo method was adopted to allow an indication into potential performance. To simplify the design problem at first a surface percolation diffuser was considered. The concept was then extended to that of a volume percolation diffuser, before alternative lattice shapes – both periodic and non-periodic – were considered. It was shown that suitable levels of diffusion and back-scattered power across the modelled bandwidth could be achieved; with examples demonstrating a diffusion coefficient of approximately 0.3-0.5 relative to the reference plate and a back-scattered power value within approximately ±1.5dB of the -3dB target for all but the lowest frequencies.

At low frequency, below the point at which approximately a half of a wavelength fits into channel width, it was demonstrated that sound tends to propagate around corners formed in a square lattice structure. This can be used to obtain large phase shifts via complex tortuous paths, though following from Fermat's principle this will only occur when no shorter alternative route exists. Following from this, for a surface percolation diffuser it was shown that at low frequency the best diffusers were those with high vertical element occupancy, since these promote lateral propagation and the complex channelling of sound. This was illustrated by a surface percolation diffuser being shown to provide diffusion at a frequency approximately 2 octaves lower than its Schroeder diffuser equivalent; a structure whose change in phase upon reflection is due to depth alone. At high frequency however a much lower vertical occupancy was required since, once half of a wavelength becomes comparable to element size, little lateral propagation occurs and it is the range in depths in an array that are important. Consequently there is a trade-off between low and high frequency diffusion. For all frequencies a relatively high occupancy of horizontal elements was preferred since in both cases channelling into the array is desirable.

The surface diffuser findings above were shown to also apply to a volume percolation diffuser. Two diffuser types were therefore considered; a low and high frequency percolation diffuser respectively. For the low frequency arrays tortuous structures were preferred, illustrated by a measure of tortuosity that showed how structures with more tightly formed convoluted channels performed best. Due to the limited number of different paths through an array however, these tend to result in a narrow diffusive bandwidth. In addition due to their high element occupancy, these structures tend to produce a back-scattered power value of approximately 0dB.

For a high frequency array the scattering from an individual element dominates and it is the depths of the vertical elements that is important; the best diffusers being those for which the 'apparent' well depths result in a set of reflection coefficients with desirable AACF properties. Once half a wavelength fits into the lattice spacing spatial aliasing occurs and the equivalent to the flat plate frequencies seen in Schroeder diffusers is seen. Consequently this limits their bandwidth of performance. As with the slat arrays of Chapter 4, the level of back-scattered power is controlled by line-of-sight through the array. Consequently a 50% fill factor is required to achieve the -3dB target. This forms a very sparse structure which limits channelling into the array.

An alternative approach has been presented based on a number of alternative lattice shapes. At high frequency the angle of orientation of elements is important, which for a periodic array comprising very few orientations results in a distinct set of 'allowed' reflections. This produces very uneven scattering. Through use of structures made up of a large number of these orientations however, and by promoting reflection angles which channel sound into an array, more even scattering results. In addition the removal of any underlying periodicity eliminates the effects of spatial aliasing. This has been demonstrated for structures based on both a Bethe lattice and a randomised lattice, examples of which have been shown to provide a minimum 3.5 octave bandwidth of performance.

Though examples of diffusers have been demonstrated to provide a high level of performance, the structures tend to be sparse, and therefore will behave more like an array of scatterers than a complex waveguide. Diffusion through this method relies on redirection due to randomised orientation of the base element, a method which above has been reliant on Monte Carlo

simulation due to the structural complexity. An alternative however may be to use an element type that produces more even scattering. This is considered in Chapter 6, which investigates the use of an array of cylinders as a volume diffuser.

6. PSEUDORANDOM CYLINDER ARRAYS BASED ON A PERIODIC LATTICE

6.1. Introduction

Chapter 4 discussed the use of an arrangement of slats as a volume diffuser. In Chapter 5 this concept was extended to include elements which aim to channel energy by scattering laterally. Whilst some arrangements are effective, they are inherently limited by the use of flat surfaces which scatter in an increasingly more directional manner with frequency. This chapter introduces a different approach to designing a volume diffuser; an array of cylinders based on a periodic lattice, an example of which was shown in Figure 2.27. These have the potential to provide a more uniform scattered distribution due to the more even scattering from a single cylinder.

Periodic cylinder arrays are investigated, akin to a sonic crystal [22; 23]. Previous work in this area has predominantly focused on attenuation by arrays at specific frequencies, known as band-gaps, rather than on the spatial distribution of its scattered field.

A periodic array of scatterers will spread energy temporally but, unless wavelength is unrealistically small compared to lattice spacing, will also produce distinct grating lobes and therefore make a poor diffuser whose behaviour varies significantly with position and frequency. Conversely, a single cylinder will scatter sound in a very uniform manner, though temporally acts much like a flat plate, risking colouration. By removing or varying the size of some of the cylinders the scattering behaviour can be manipulated. This provides scope to achieve both spatial and temporal diffusion. Furthermore, by basing a structure on an underlying periodicity the application of number theoretic concepts is allowed, whilst also potentially making manufacture easier.

At first single layer diffusers are considered. These are similar to previously studied surface diffusing arrays of semicylinders [3], as well as their equivalent BAD and slat arrangements presented in Chapter 4. Later multilayer structures based on a rectangular lattice are explored, before alternative lattices are considered. In each case, sequences forming arrangements are assessed, and the effect of varying parameters such as lattice spacing, density, line-of-sight and individual cylinder size is examined.

It is shown that arrangements whose spatial distributions are least self-similar tend to provide the more optimal spatial diffusion. For fuller arrays however operational bandwidth can be limited, with low frequency scattered power being limited by object size and high frequency diffusion becoming affected by spatial aliasing. By reducing self-similarity the detrimental effects on diffusion are minimised, producing an effectively oversampled array whose element separations allow for larger cylinders to be used. Further improvements may also be gained through the use of lattice types which allow more isotropic behaviour, or by selecting a cylinder size that minimises scattering into the grating lobes.

Unless otherwise stated, all results presented in this chapter are from predictions carried out using the multiple scattering model presented in Section 2.3.3, shown in Section 2.6.3 to provide close agreement with experimental measurements.

6.2. Scattering from an individual cylinder

The structures presented in Chapters 4-5 showed that one of their limiting factors was the inherently directional scattering properties of flat surfaces at high frequency. When a slat for example becomes on the order of a wavelength in length, and with increasing frequency thereafter, a specular reflection dominates. One solution would be to use an element type that results in more even spatial scattering. A cylinder is an example of this, as illustrated in Chapter 3 by the scattered polar patterns of Figure 3.7 and the diffusion coefficient of Figure 3.13. The scattering from a single cylinder as a pressure map is shown in Figure 6.1, modelled using Eq. 2.23, and is expressed as a function of cylinder diameter, d_e, relative to wavelength. It can be seen that with increasing frequency that the cylinder is able to move more energy into the forward-scattered region (excluding close to the back of the cylinder where a distinct shadow is formed) and the scattering becomes progressively more omnidirectional. An approximate point at which this occurs is considered below.

At low frequency it can be shown that the scattered intensity from an individual cylinder subject to a source located at $\theta_0 = 0°$ is approximately proportional to [30]:

$$|p_s(\theta)|^2 \propto d_e{}^4 k^2 (1 + 2\cos(\theta))^2 ; \qquad kd_e \ll 2 \qquad\qquad 6.1$$

Consequently at low frequency the scattering from a cylinder is dominated by a main back-scattered lobe in the direction $\theta = \theta_0$.
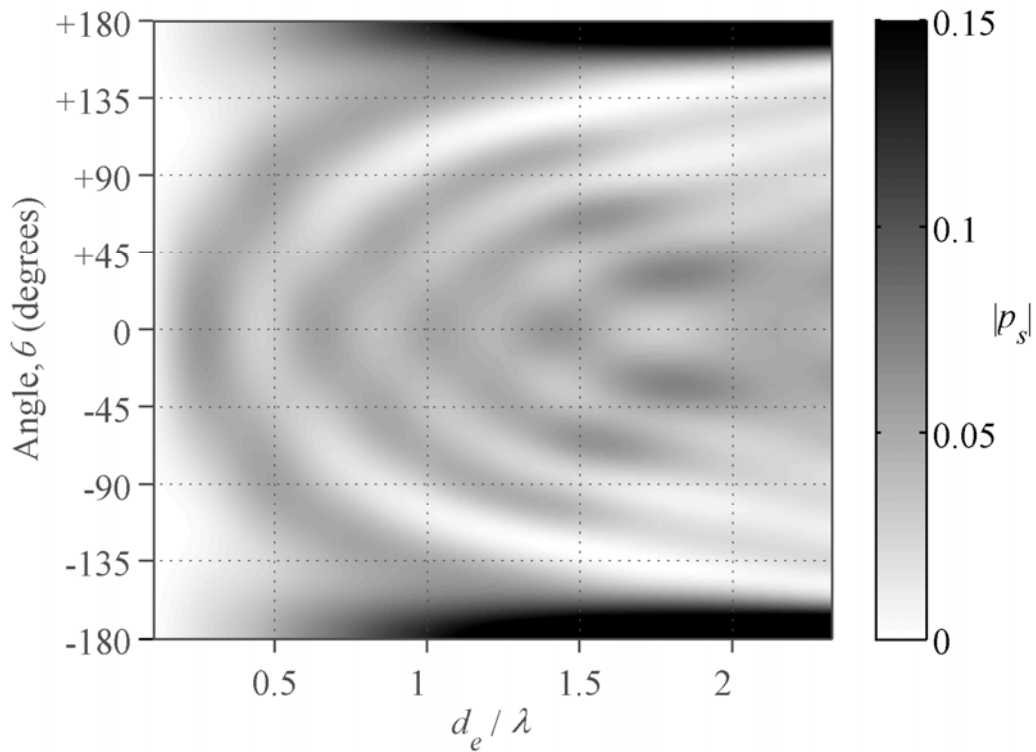
Figure 6.1: Normalised scattered pressure for a single cylinder of diameter, d_e, expressed relative to wavelength

At high frequency the scattered intensity from an individual cylinder, neglecting the shadow-forming beam (which determines attenuation) and small rapid fluctuations, may be approximated as [30]:

$$|p_s(\theta)|^2 \propto \frac{d_e}{k}\cos\left(\frac{\theta}{2}\right); \qquad kd_e \gg 2 \qquad\qquad 6.2$$

This gives a largely uniform scattering pattern over the angles of interest. An approximate frequency which divides these two behaviour types is therefore given as:

$$f_0 = \frac{c}{\pi d_e} \qquad\qquad 6.3$$

Where f_0 represents the approximate design frequency for even scattering from a single cylinder, and implies that scattering should be even once wavelength is less than its circumference. The above is in contrast to the scattering from a slat which scatters relatively evenly (though with little power) when wavelength is large relative to its perimeter ($2 \times d_e$) though provides an increasingly more specular reflection with increasing frequency. This is

due to the natural angles of reflection of a cylinder, which spatially results in a very even spread of energy. Since this is due to a simple geometric reflection however, like a single slat, a cylinder results in virtually no temporal smearing [3]. In addition a single cylinder large enough to scatter efficiently would likely remove a large volume from a space. Consequently an array of cylinders must be considered.

6.3.   Periodic line arrays

6.3.1   A simplified prediction of scattering

As with the slats of Chapter 4, a periodic line array of cylinders may be modelled using a simplified Fourier approximation given by Eq. 2.16, though with now the scattering from an individual element $e(\theta_0, \theta)$ given by the scattering from an individual cylinder. Again, the amplitude coefficient for the nth scattering element, A_n, has a value of 1 or 0 and determines whether or not an element (cylinder) is present. Modelling the scattering from a cylinder as per Eq. 2.22, and normalising to the incident field approximated by Eq. 4.1, the far-field scattered pressure, $p_{s,norm}(\theta_0, \theta)$, from a 1D array of cylinders may be given as:

$$p_{s,norm}(\theta_0, \theta) \approx \frac{-(1-j)}{\sqrt{\pi k}} \sum_{i=0}^{+\infty} \in_i (-1)^i Z_i \cos(i(\theta - \theta_0)) \times$$

$$\sum_{n=0}^{N-1} A_n e^{jknd_y(\sin\theta + \sin\theta_0)}$$

$$\in_i = \begin{cases} 1, & i = 0 \\ 2, & i \neq 0 \end{cases}$$

6.4

The summation above, as with the slats, represents a Discrete Fourier Transform (DFT) of the coefficients, A_n. Consequently the number theory presented in Sections 4.2.2-4.2.3 applies equally here if the effects of multiple scattering are small / ignored.

Figure 6.2 shows the normalised scattered pressure from an array of cylinders arranged according to the $N = 7$ Golomb ruler sequence, $s_n = [1\ 1\ 0\ 0\ 1\ 0\ 1]$. This sequence was introduced previously in Section 4.2.3. The assumed accurate predictions made using the MS method are compared to the results obtained from the Fourier approximation model as given by Eq. 6.4.

f = 500Hz

f = 1.0kHz

f = 2.0kHz

f = 4.0kHz
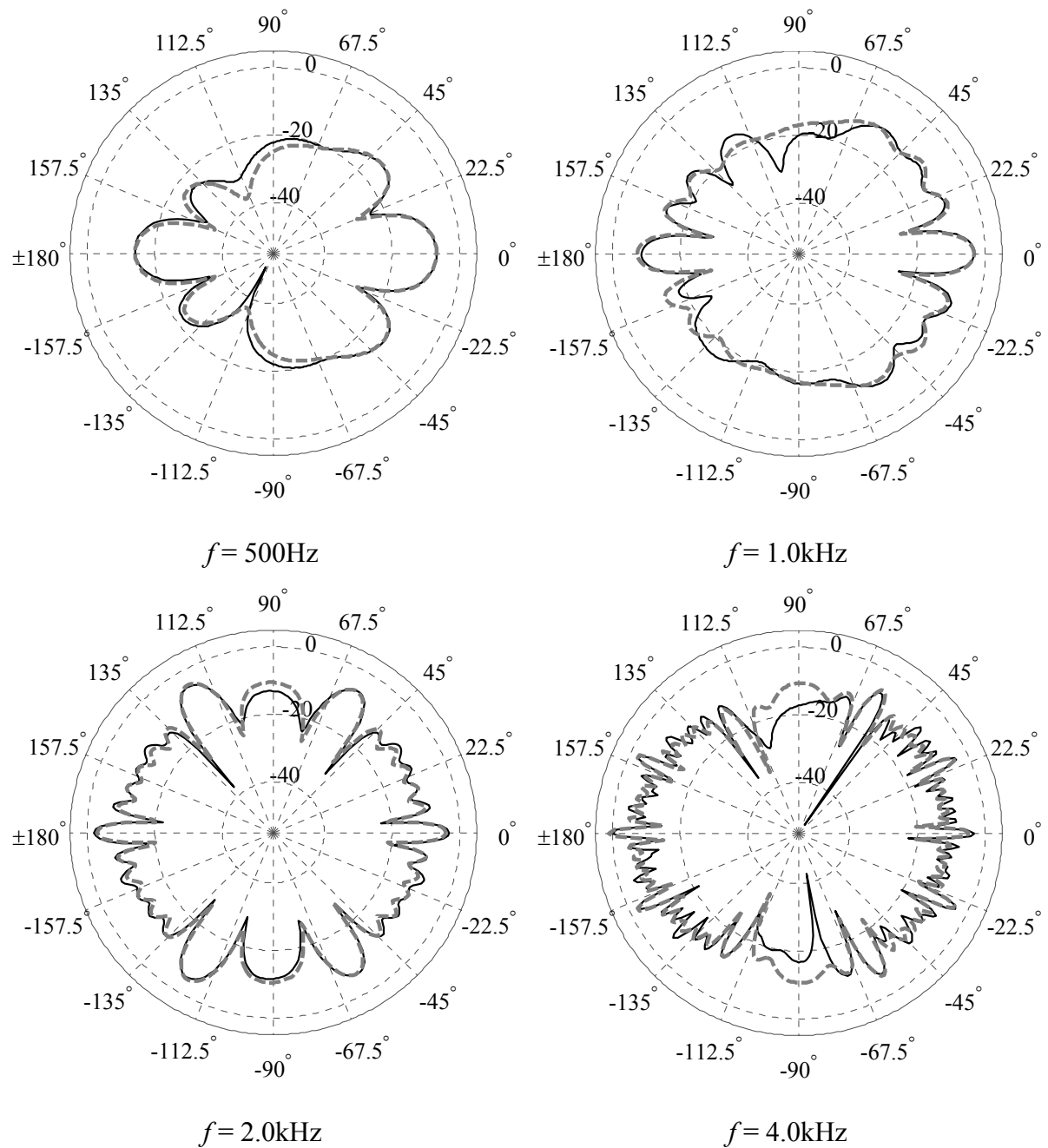
Figure 6.2: Normalised scattered pressure polar response for a 1D array of cylinders arranged according to an N = 7 Golomb ruler sequence s_n = [1 1 0 0 1 0 1]; MS (——) and Fourier approximation (‑ ‑); $\theta_0 = 0°$, d_e = 10cm, d_y = 20cm; frequencies as listed

For angles away from grazing the Fourier approximation in Figure 6.2 above is shown to agree very well with the more accurate model, since the modelling of an individual element is (excluding truncation of modes) exact. For receivers in the grazing angles this accuracy reduces due to the effects of multiple scattering, since the natural angle of reflection towards

these locations will (excluding the end cylinders) direct energy towards adjacent cylinders. This will of course be dependent on cylinder size, and is an effect not observed for slats due their thin construction. The overall result is an average difference of 1.9dB in the Fourier model relative to the MS routine over the frequency range 400Hz-4kHz, which is significantly more accurate than was observed for the slats (6.2dB).

6.3.2   Optimal sequences

Section 4.2.3 showed that a volume equivalent to the BAD could be formed from slats. Similarly this concept can also be applied to an array of cylinders, an example of which was considered in Figure 6.2 above. It was shown that due to their lack of self-similarity, diffusers based on unipolar binary sequences whose Aperiodic Autocorrelation Function (AACF) was optimal tended to provide the most even scattering. These correspond to arrays with an even spread of separation distances between elements. Consequently the same sequences may be used, allowing a direct comparison between the two structure types.

Figure 6.3 shows the diffusion coefficient for the length $N = 7$ perfect Golomb ruler from Figure 6.2, comparing the performance of equivalent slat and cylinder arrangements. The design frequency for diffusion for a sequence arrangement given by Eq. 4.3, and determined by the point (for normal incidence) at which a wavelength is equal to structural width, D, here equates to $f_0 \approx 250$Hz. For a slat array this is where diffusion begins to increase, though at this point the diffusion from a cylinder array is relatively poor and the slat array is able to slightly outperform its cylinder equivalent. This is because, as was mentioned in Section 6.2, the scattering from a cylinder only starts to become even once wavelength becomes small relative to its diameter. For the cylinder diameter $d_e = 10$cm here, this should occur for frequencies above a cut-off point of approximately $f_0 \approx 1.1$kHz. From Figure 6.3 it is evident that once this frequency is reached the diffusion coefficient increases dramatically relative to the slats. The scattered polar patterns of Figure 6.2 (bottom) above this frequency shows how, based on the Fourier properties given previously in Figure 4.9, the array is then able to display the sidelobe behaviour expected due to the structure's arrangement.
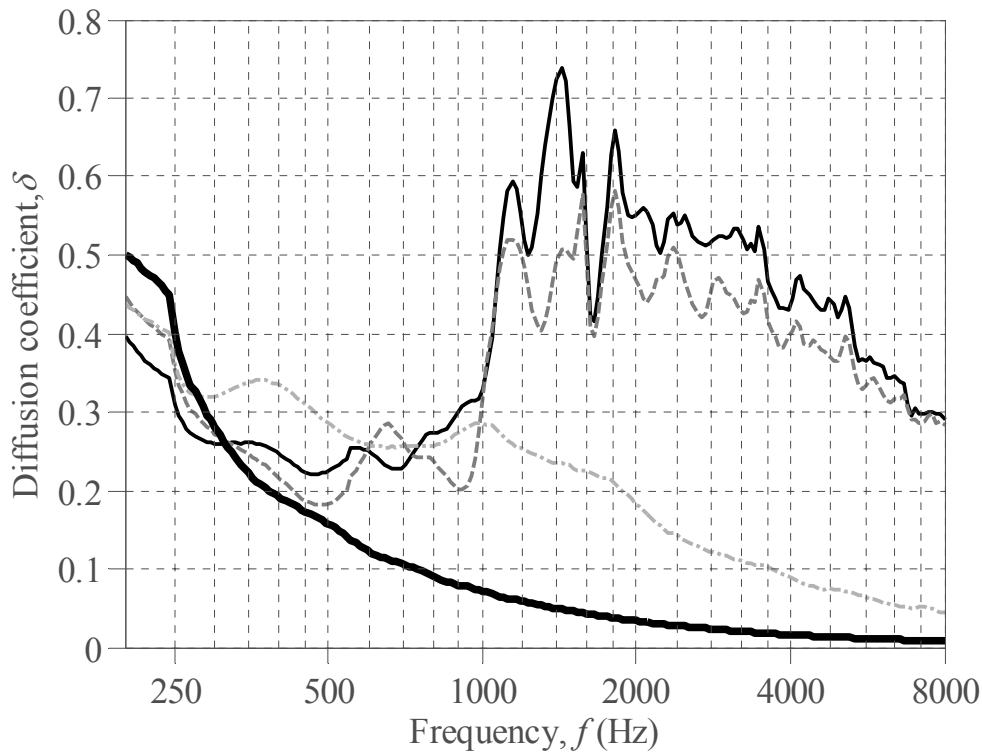
Figure 6.3: Diffusion coefficient for an array of cylinders of diameter d_e = 10cm arranged according to the N = 7 Golomb ruler [1 1 0 0 1 0 1] (——), and MLS [1 1 0 1 0 0 1] (– –); and an N = 7 Golomb ruler array of slats of width d_e = 20cm (– ·); θ_0 = 0°, d_y = 20cm; flat plate of width, D = 1.4m (▬) shown for reference

As with the slats, the Golomb ruler array in Figure 6.3 is compared to an equivalent MLS ([1 1 0 1 0 0 1]), whose Fourier properties were compared in Figure 4.9. It is evident that once past the cut-off frequency the Golomb ruler sequence is able to provide greater diffusion than the MLS sequence due to its more even scattered sidelobes. This illustrates that, as with the slats, sequences whose AACF is most like a Kronecker delta function tend to provide better diffusion. At higher frequencies repetition of the main specular lobe appear from the grazing angles due to spatial aliasing, which for the element spacing here occurs at multiples of f = 1.72kHz. This was illustrated previously for a slat arrangement in Figure 4.7, though were shown to be suppressed due to the response of an individual element. With increasing frequency the sequence arrangements begin to have little influence, agreeing with previous findings from studies into periodic arrays of semicylinders where the sidelobe behaviour becomes lost amongst the large number of closely spaced main lobe repetitions [3]. This is unavoidable for a 1D sequence.

In addition to the above, at high frequency the diffusion begins to tail-off due to the response of each cylinder. This is because the lobe which forms the shadow zone behind an individual cylinder, which becomes narrower and of comparatively greater magnitude with frequency, will be larger than the shadow zone lobe behind the array as a whole (as defined by Eq. 3.4). Consequently a volume diffusion coefficient will suffer, whereas a more conventional back-scattered coefficient will plateau and remains roughly constant in value. As a result a larger cylinder array will diffuse at a lower frequency (from a frequency approximately given by Eq. 6.3) though its diffusion coefficient will also tail-off at a lower frequency. This is to some extent, however, a matter of definition and a high level of diffusion should result for many octaves.

6.3.3 Amplitude shading: varying the cylinder size

In Section 4.2.4 it was shown that an alternative to the unipolar BAD design was to apply amplitude shading to an array; altering the length of the elements rather than using a fixed size. This technique can also be applied to cylinders, since in Eq. 6.2 it was shown that once wavelength is approximately less than the perimeter of a cylinder the scattered pressure is approximately proportional to the square root of the cylinder size, d_e. Consequently as with the slat case, the cylinder size may also be used to control the level of scattering from each element.

Considering an array allowing cylinders of varying diameter, d_n, spaced an equal distance, d_y, apart (centre to centre), an approximation to the scattered pressure may be given as:

$$p_s \propto \sum_{n=0}^{N-1} A_n e^{jknd_y(\sin\theta+\sin\theta_0)}$$

$$A_n \approx \sqrt{d_n}$$

6.5

Where individual elements are assumed to scatter omnidirectionally and only first order reflections are considered. Due to their desirable Fourier properties, as with the slats, the element size may be determined by a Chebychev sequence. Figure 6.4 shows the normalised scattered pressure from an amplitude shaded cylinder array determined according to (the square of) an $N = 7$ Chebychev sequence [60], designed to achieve an equal energy sidelobe attenuation of -9.8dB. This value was selected so as to obtain a fill factor of $F_{fill} = 0.5$. The

individual cylinder sizes, d_n, are listed in Table 6.1. It can be seen that the sidelobe distribution forms a distinct set of near equal energy lobes.
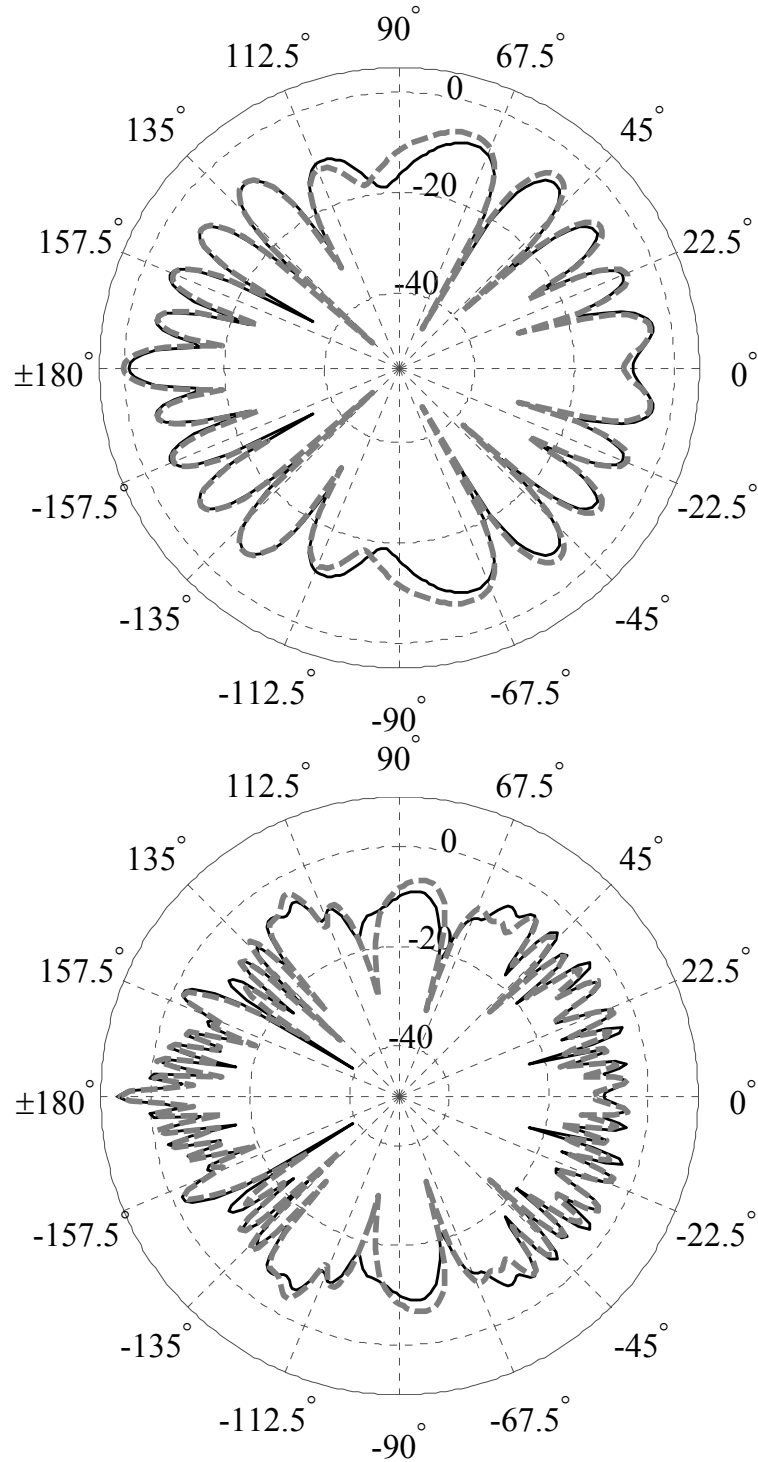
Figure 6.4: Normalised scattered pressure polar response for an N = 7 Chebychev cylinder array; MS (━━), and Fourier approximation (━ ━); f = 1.5kHz (top) and f = 4.0kHz (bottom); $\theta_0 = 0°$, $d_y = 20cm$, D = 1.4m

Table 6.1: 1D Amplitude shading cylinder sizes

Cylinder number, n	Cylinder diameter, d_n (mm)						
	1	2	3	4	5	6	7
(a) $N = 7$ Chebychev (-9.8dB sidelobe attenuation)	200.0	50.8	64.4	69.6	64.4	50.8	200.0
(b) $N = 7$ Chebychev (-12.5dB sidelobe attenuation)	200.0	94.2	129.2	143.2	129.2	94.2	200.0
(c) Fixed size ($F_{fill} = 2^{-1/2}$)	141.4	141.4	141.4	141.4	141.4	141.4	141.4

The diffusion coefficients for a number of cylinder arrays (listed in Table 6.1) are shown in Figure 6.5, including an $N = 7$ Chebychev sequence designed to achieve a sidelobe attenuation of -12.5dB and an equal sized cylinder array for reference. These form denser arrays which for reasons discussed in Section 6.3.4 were designed to achieve a fill factor of $F_{fill} = 2^{-1/2}$. The point at which an individual cylinder will scatter approximately proportionally to its size, and therefore a lower frequency limit to the design theory, is determined by the diffusive design frequency of Eq. 6.3. Since a number of cylinder sizes are used at low frequency the performance is complex. Due to the denser Chebychev array having very similar sized cylinders, its low frequency diffusion coefficient is similar to that for the equal sized cylinder array. Once the design frequency for the smallest cylinder is met however ($f \approx 1.9$kHz and $f \approx 1.0$kHz for the sparse and dense Chebychev arrays respectively) the properties of the sequence are fully realised and both Chebychev arrays diffuse well.
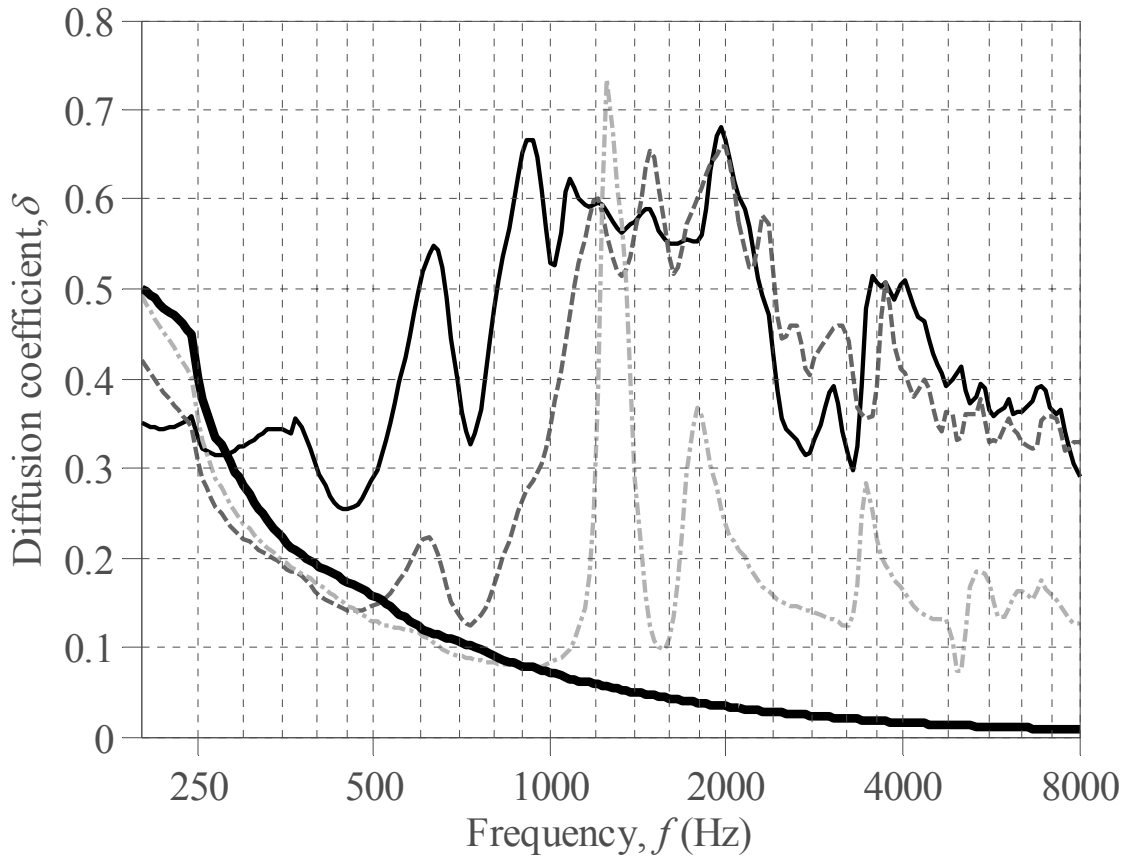
Figure 6.5: Diffusion coefficient for the cylinder arrays as per Table 6.1 (a ▬, b = =, and c = -); $\theta_0 = 0°$, $d_y = 20cm$, $D = 1.4m$; flat plate (▬) shown for reference

6.3.4   Scattered power

Figure 6.6 shows the back-scattered intensity ratio for the $N = 7$ Golomb ruler cylinder array considered above. As with the slat arrays of Chapter 4, an approximate high-pass filter shape is seen, and consequently a model similar to that given by Eqs. 4.15-4.16 should be possible. The intensity ratio obtained via the Fourier approximation provides a close fit to the MS routine, suggesting that multiple scattering has only a small influence on the overall back-scattered energy. Following from Eqs. 6.1-6.2 the scattered power from a cylinder, like an individual slat, should display an approximate +6dB/octave roll-on at low frequency and a -3dB roll-off at high frequency. When normalised to the scattered power from the reference plate, given by Eq. 4.12, this again results in a +9dB/octave roll-on and a high frequency shelf. For very low frequencies this is the case, though for frequencies close to the

transition / cut-off frequency, f_c, the observed slope is slightly shallower than this and is on the order of approximately +7dB.
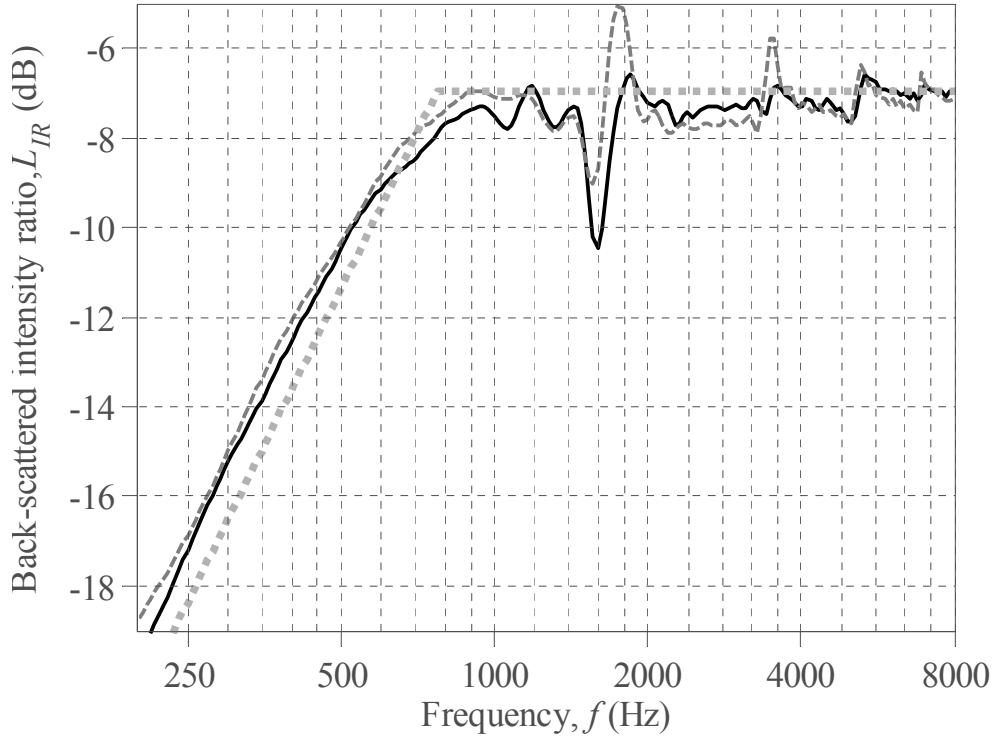
Figure 6.6: Back-scattered intensity ratio for an array of cylinders arranged according to the N = 7 Golomb ruler [1 1 0 0 1 0 1]; MS (▬), Fourier approximation (▬ ▬) and approximate model (▪ ▪ ▪); θ₀ = 0°, dᵧ = 20cm, dₑ = 10cm, D = 1.4m

At high frequency the geometric angles of reflection dominate, and the back-scattered power is again determined by line-of-sight. This time however an individual cylinder behaves effectively like a flat plate of length $d_e \times 2^{-1/2}$. The is because the curvature of a cylinder, as illustrated in Figure 6.7, will scatter sound incident upon its sides into the forward-scattered region. Consequently, following from Eqs. 4.15-4.16 in Section 4.2.5, an approximate model for the back-scattered intensity ratio of a 1D cylinder array may be given as:

$$L_{IR} \approx 10\log_{10}\left(\frac{F_{fill}}{\sqrt{2}}\left(\frac{f}{f_c}\right)^{\log_2\left(10^{7/10}\right)}\right) ; \qquad f < f_c \qquad\qquad 6.6$$

$$L_{IR} \approx 10\log_{10}\left(\frac{F_{fill}}{\sqrt{2}}\right) \; ; \qquad\qquad f \geq f_c \qquad\qquad\qquad 6.7$$

Where f_c is the cut-off frequency and F_{fill} is the fill factor (line-of-sight through the array that is blocked as viewed by the source).
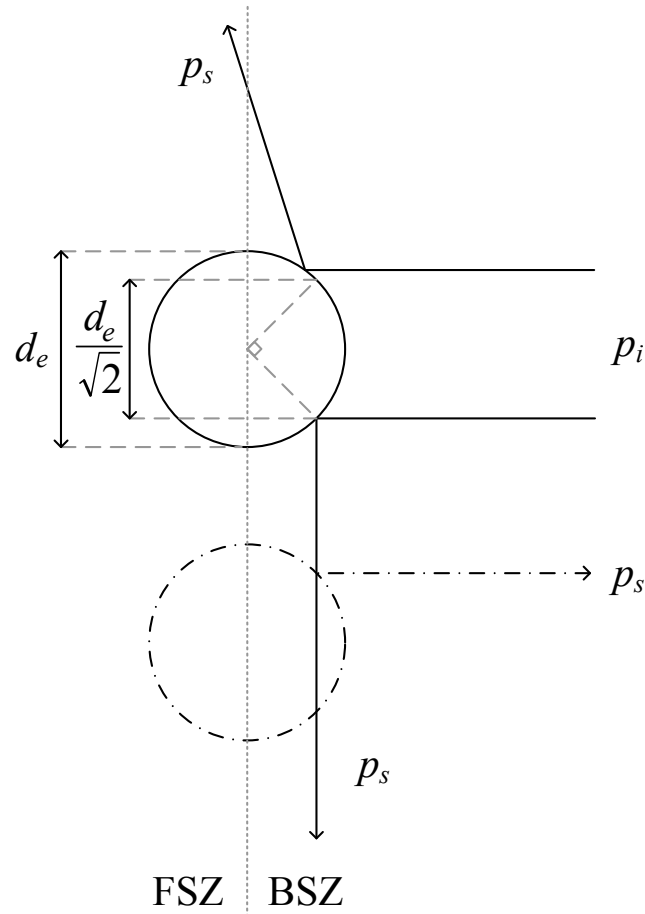
Figure 6.7: Geometric reflection from an array of cylinders

As with the slats, the cut-off frequency which describes the peak of the ripple is best described by the point at which a wavelength is equal to the cylinders perimeter, given previously in Eq. 6.3. Again however an empirical factor of $2^{-1/2}$ is included to best model the roll-on at, and just below the transitional phase. Consequently the cut-off frequency is given as:

$$f_c \approx \frac{c}{\sqrt{2}\pi d_e} \qquad\qquad\qquad 6.8$$

For the cylinder array of Figure 6.6 this results in a frequency of $f_c \approx 770\text{Hz}$, and the model is shown to provide a close fit. Note, due to the cut-off frequency being dependent on element size the above model is valid when all cylinders are the same size. As with the slats however the model can be used for an arrangement with a varying element size by considering each cylinder size separately and summing their contributions as per Eq. 4.19.

Based on the above, the scattered power from a 1D cylinder array below the cut-off frequency will be weak, and so cylinders comparable to approximately a quarter of a wavelength are required. In order to achieve the -3dB scattered power target a fill factor of $F_{fill} \approx 2^{-1/2}$ is necessary. Since cylinders cannot conjoin this implies a high number of large elements, which for all realistic cylinder sizes means a near full array. This would result in highly directional scattering due to the properties of the arrangement, as illustrated by Figure 6.5 (grey dash-dot line). For an amplitude shaded array however the fill factor may be altered by appropriate Chebychev sequence selection. For example Figure 6.8 demonstrates how the sparse and dense Chebychev arrays from Section 6.3.3 (Table 6.1), which have fill factors of $F_{fill} = 0.5$ (a) and $F_{fill} = 2^{-1/2}$ (b), result in an approximate high frequency plateau level of -4.5dB and -3.0dB respectively (as predicted by Eq. 6.7). At low frequency however the power model is inaccurate. This is due to the scattering from a full array of similarly sized cylinders being relatively similar, and consequently causing a boost in low frequency power.

The notch observed in the scattered power is due to multiple scattering between adjacent cylinders, an example of which is illustrated by Figure 6.7 (dash-dot line) where sound incident upon the structure is reflected back toward the source. When these multiple scattered reflections are out of phase with the sound reflected from the front of the cylinders their destructive interference causes a reduction in the size of the specular lobe. This is particularly evident for the equal sized cylinder array (the notch being observed at approximately $f = 1.3\text{kHz}$), which due to having equal sized cylinders has many repetitions of the same multiple scattered paths. Consequently this produces the effect at a more distinct frequency. Due to the reduction in the specular lobe, at this frequency a sharp increase in scattered uniformity results, as illustrated by the sudden increase in diffusion coefficient in Figure 6.5 (dash-dot line).
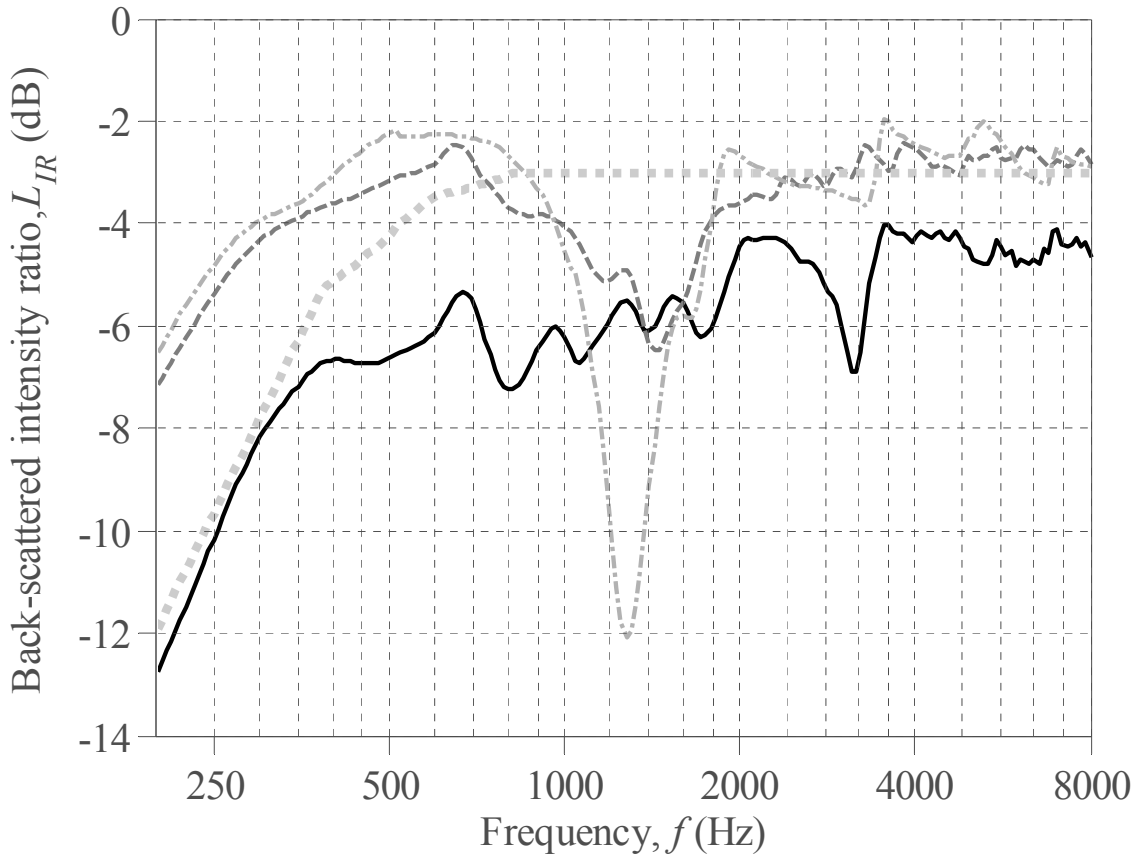
Figure 6.8: Back-scattered intensity ratio for an array of cylinders as per Table 6.1 (a ▬,
b ▬ ▬, and c ▬ ▪), and approximate model for array b (▪ ▪ ▪); θ₀ = 0°, dᵧ = 20cm, D = 1.4m

6.3.5   Design principles

Diffusion from a 1D array of cylinders will, like the slats case, be most optimal for sequences with desirable Fourier properties. The design however will likely be limited by the required back-scattered power, giving two options:

▪   Where less scattered energy is acceptable, unipolar sequence arrays provide a simple design concept. Since the scattered power cut-off frequency f_c (given by Eq. 6.8) is lower than the diffusive design frequency f_0 (given by Eq 6.3), it is the latter that dictates performance. Consequently the minimum cylinder size may be given as:

$$d_e \geq \frac{c}{\pi f_{min}}$$

6.9

Which for a minimum frequency of $f_{min} = 400$Hz equates to a minimum cylinder size of $d_e \approx 27$cm.

- If scattered power is an issue, achieving a level such as the -3dB target considered here will likely need a high fill factor, and hence amplitude sequences are best suited. At low frequency performance is again limited by the design frequency, though now considering the smallest cylinder size used. Defining a lower diffusive cut-off point is therefore complex, though in general for denser arrays where cylinder size is similar it is the notch in the scattered power that limits performance. Consequently this determines the minimum cylinder spacing, given as:

$$d_y \geq \frac{c}{f_{min}} \qquad\qquad 6.10$$

For example a frequency of $f_{min} = 400$Hz gives a minimum spacing of $d_y = 86$cm. This in turn dictates the individual cylinder size and length of the array. In reality however it may not be possible to design such an array to perform at low frequencies since the size of the array will be large and/or the number of cylinders will be low.

For both of the 1D array designs above, once sufficient scattering is achieved an array performs effectively over an approximate 3-4 octave bandwidth, though a high frequency cut-off point for diffusion is hard to define, and diffusion continues beyond this range.

The 1D cylinder array designs above demonstrate reasonable diffusive performance which, due to the more even scattering of a cylinder, are able to provide a substantial improvement on their slat array equivalents. As with the 1D slat arrays however, due to their lack of depth, their scattering uniformity is inherently limited by the strong back-scattered specular component. The next section therefore considers an improved design which adds depth to the structure.

6.4.   The rectangular lattice array

In a similar manner to that presented in Chapter 4 for an array of slats, the concept of the 1D structures above may be extended to a 2D equivalent: an arrangement of cylinders based on a periodic rectangular lattice. An example of such an array was shown in Figure 2.27, which

demonstrated the use of a 2D unipolar sequence to determine (like the 1D arrangements) whether or not a cylinder is included or omitted. Since elements do not conjoin (allowing transmission and diffraction), and cylinders inherently forward scatter, a more appropriate model may be used that considers the array as a whole. Considering the arrangement in Figure 2.8 for an $M \times N$ arrangement of scattering elements, an extension to the Fourier approximation of Eq. 6.4 may be given as:

$$p_{s,norm}\left(\theta_0,\theta\right) \approx \frac{-\left(1-j\right)}{\sqrt{\pi k}}\sum_{n=0}^{+\infty}\in_n \left(-1\right)^n Z_n \cos\left(n(\theta-\theta_0)\right)\times$$

$$\sum_{m=0}^{M-1}\sum_{n=0}^{N-1}A_{m,n}e^{jk\left[md_x\left(\cos\theta+\cos\theta_0\right)+nd_y\left(\sin\theta+\sin\theta_0\right)\right]} \qquad\qquad 6.11$$

$$\in_n=\begin{cases}1, & n=0\\2, & n\neq0\end{cases}$$

Where the summation is taken from Eq. 2.17, and represents a 2D DFT of the amplitude coefficients, $A_{m,n}$, in the $d_x(\cos\theta+\cos\theta_0)/\lambda$ by $d_y(\sin\theta+\sin\theta_0)/\lambda$ domain. The angular variables θ and θ_0 above are common to both orthogonal directions, and consequently are dependent on one another, resulting in an interfering product due to the periodicity in the two dimensions.

The above (as with the 1D diffusers) is in many ways analogous to array theory, as it considers the far-field polar response of a set of (usually linearly) distributed radiating elements. Linear arrays produce a main beam, with additional side lobes appearing with increasing frequency [74], as was illustrated for a (line) array of slats in Figure 4.7 (centre). A 2D diffuser array however is comparable to a planar array whose main beam is steered towards the back of the diffuser ($\theta = \theta_0+180°$) by application of a series of delays equivalent to that imposed by a source located at θ_0. This main beam, which for a 1D array produces a specular reflection, forms the forward-scattered component which interacts with the incident field and determines attenuation in the shadow zone. Consequently as with the 2D slat arrays in Chapter 4 the addition of depth allows cancellation of the back-scattered specular lobe, and it is the sidelobe and grating lobe behaviour which determine the remaining scattered field. This gives potential for more even scattering. In addition it is likely that with added depth the influence of multiple scattering will increase, which provides scope for temporal diffusion, though this may limit the accuracy of the single scatter Fourier approximation above.

6.4.1 Sequence selection: redundancy and the AACF in two dimensions

Like the 1D case presented in Section 6.3, an array is desired whose amplitude coefficients, $A_{m,n}$, form a sequence whose AACF is optimal. This however is now a 2D AACF, an example of which is shown later in Figure 6.16 (bottom). The AACF of a 2D unipolar binary sequence may be thought of as the number of elements separated by a given vector spacing; that is not only by the same distance (as illustrated by the Golomb ruler sequence of Figure 4.8) but also direction. Redundancy therefore refers to the repetition of these separation vectors. A sequence whose 2D AACF is most like a Kronecker delta function is therefore desirable, implying a structure with an even spread of vector separations between elements with little or no redundancy. There are quite a few 2D sequences whose periodic autocorrelation properties are optimal, for example perfect arrays [59], however aperiodic equivalents are less common. Furthermore unlike for periodic sequences, folding techniques such as the Chinese remainder theorem [75] cannot be applied because these assume periodicity. Consequently optimal sequences such as minimum hole arrays are often found using (intelligent) exhaustive computational searching [56], and so produce small arrays.

In order to obtain a larger sequence one alternative is to use an optimisation routine, and for this a genetic algorithm and the Fourier approximation given by Eq. 6.11 was used. This is a simplified version of the process adopted by Romero García *et al*. [76] where targeted band gaps were created in sonic crystals, and Hakansson *et al*. [77] where focusing arrays were generated. As the Fourier approximation is based on a simple summation of (scattering) sources it is particularly suited to this type of optimization, as elements are assumed to act independently. The optimisation process used was broadly as follows:

- An organism is defined by its genes, in this case cells in an array of amplitude coefficients, $A_{m,n}$ – a value of one or zero representing the two possible gene types: a cylinder being present or absent.

- An initial population of randomly generated parents (coefficients) is set up, and the next generation of children (new coefficients) is formed from combinations of the parent population's genes (though ensuring the same occupancy is kept).

- Occasional mutations are introduced to allow new genes into the gene pool. This allows children that are not formed by a straight forward combination of the parent population to be formed.

- By keeping only the fittest (arrays of coefficients with minimal side lobe AACF energy), successive generations gradually produce more successful individuals.

- The routine is repeated several times using new initial parent populations, with the overall fittest individual from all simulations being selected.

Using this method a sequence comprising a 10×10 grid with 25% occupancy was created; the cylinder array shown in Figure 2.27, used in Chapter 2 for experimental verification of the multiple scattering prediction routine. Note for a sequence of this size the process above is unlikely to find a global minimum, and so it is probable that sequences with more desirable Fourier properties exist. Scattered pressure maps from this array are shown in Figure 6.9, comparing the prediction using the Fourier approximation (c) with the MS solution (d). The effect of the sequence arrangement (a) and the cylinder size (b) on the Fourier approximation are also shown, breaking down the Fourier approximation of Eq. 6.11 into its summation and single cylinder prediction components respectively.

At low frequency, when wavelength is large compared to cylinder size, the Fourier approximation for the optimised array above provides highly accurate predictions of scattering. This occurs approximately below a frequency given by Eq. 6.3, which here equates to $f \approx 1.37$kHz, since below this point the diffraction around the cylinders will be high. For higher frequencies when wavelength becomes small relative to cylinder size the Fourier approximation is less accurate due to the effects of multiple scattering and shadowing (cylinders being in the line-of-sight of one another from the perspective of the source). Here the MS prediction of Figure 6.9 (d) results in a 'smearing' of the predicted response. Overall the average difference of the Fourier approximation (relative to the multiple scatter solution) over the frequency range 400Hz $\leq f \leq 4.0$kHz is 4.0dB. Since the genetic algorithm routine above is based on the Fourier prediction this therefore demonstrates the limitation on the optimisation process.
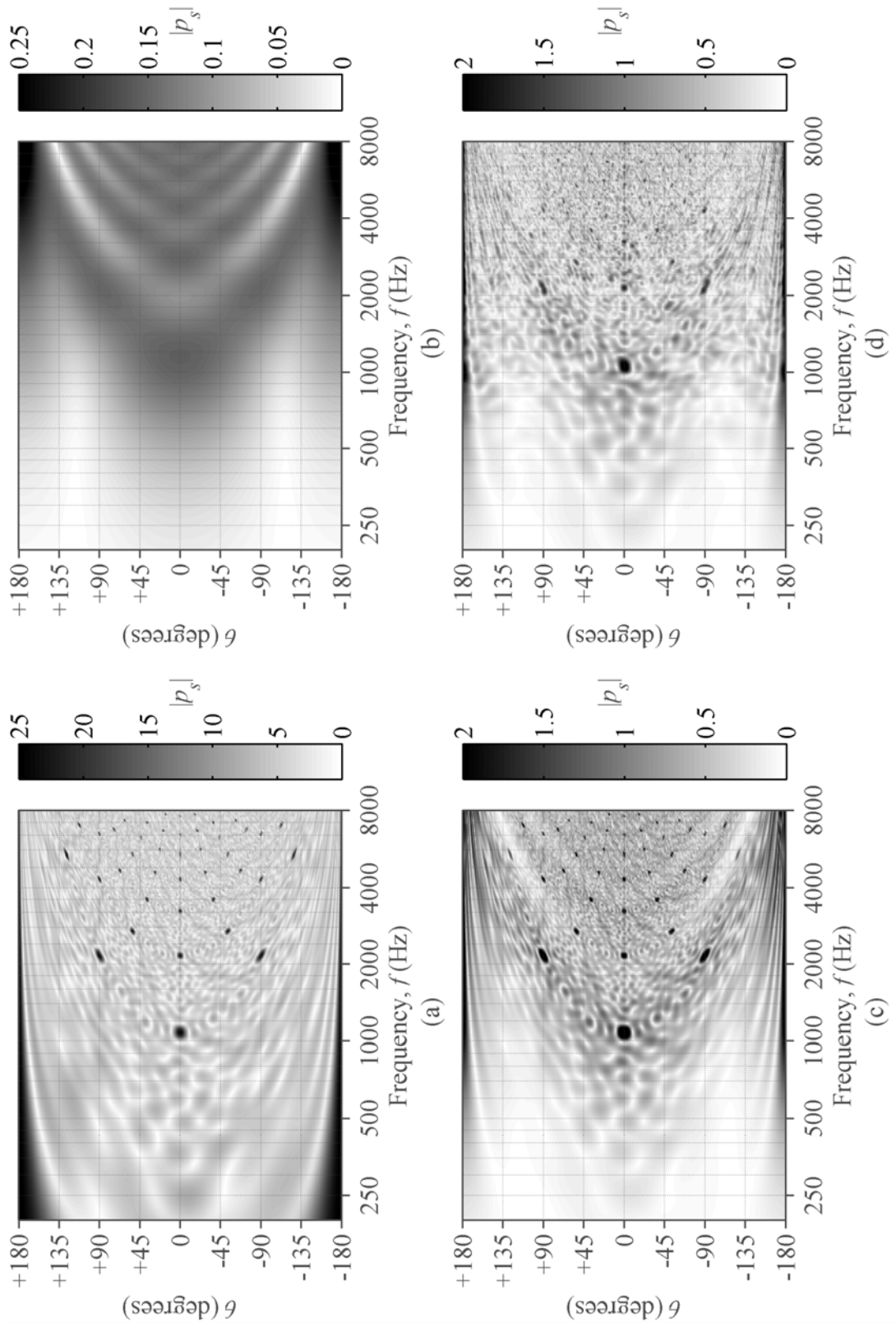
Figure 6.9: Normalised scattered pressure with frequency; optimised arrangement as per Figure 2.27 modelled as point sources with spacing $d_x = d_y = 16cm$ (a), single cylinder of width $d_e = 8cm$ (b), their product (c) and a full MS solution (d); $\theta_0 = 0°$

The diffusion coefficient for the optimised array is shown in Figure 6.10 which (excluding a series of notch frequencies discussed in Section 6.4.2) is generally high. Again it can be seen that at low frequency the agreement of the Fourier approximation with the MS solution is good. Due to the depth of the sequence the array is able to diffuse well before the diffusive design frequency, f_0, of a 1D array (given by Eq. 6.3, expressed above as an approximate point below which significant diffraction occurs and the Fourier approximation is most accurate). This is due to the scattered field no longer being dominated by a specular reflection. Consequently a more appropriate diffusive design frequency is given by:

$$f_0 = \frac{c}{D} \hspace{4cm} 6.12$$

Which follows from Eq. 4.3, and equates to when the first grating lobe appears in the scattered polar response. For the optimised array shown this corresponds to a frequency of $f = 226 Hz$.
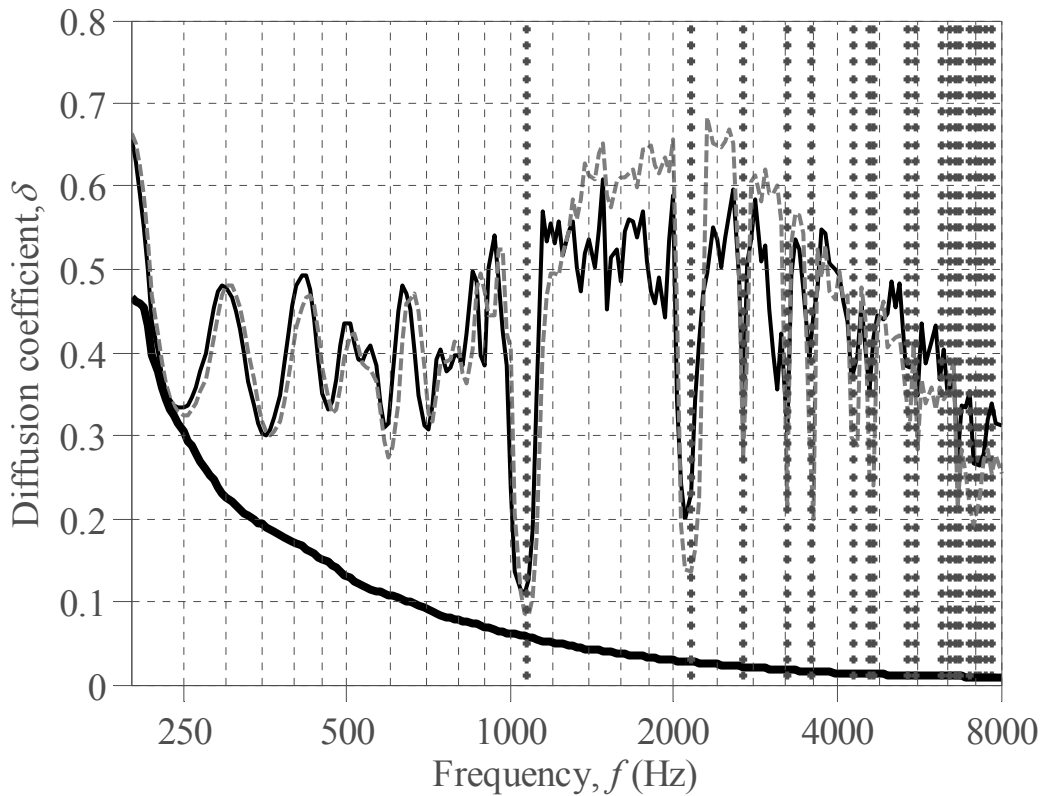
Figure 6.10: Diffusion coefficient for the optimised cylinder array as per Figure 2.27;
MS (━), Fourier approximation (= =) and predicted Bragg frequencies (•••); $\theta_0 = 0°$; flat
plate (▬) shown for reference

At higher frequencies the Fourier model tends to over predict the diffusion coefficient, since the effects of multiple scattering mean that the idealised scattered pressure pattern is altered, though the overall trend is still well matched. As with 1D arrays, a gradual tail-off in diffusion occurs at high frequency due to the response of each individual cylinder.

6.4.2 The effect of periodicity on diffusion

For a 1D array the lack of depth meant that the specular lobe could not be cancelled out. At low frequency this meant that the response was dominated by a single specular reflection, though as more repetitions of this lobe appeared due to spatial aliasing the diffusion coefficient increased. In contrast for a 2D array, the back-scattered lobe is attenuated and the sidelobe pattern due to the arrangement of the cylinders dominates. Consequently the appearance of main lobe repetitions reduce scattering uniformity. This is illustrated in Figure 6.11 where the scattering from the optimised array (considered as point sources) is represented in the 2D Fourier domain, as given by the summation from Eq. 6.11.
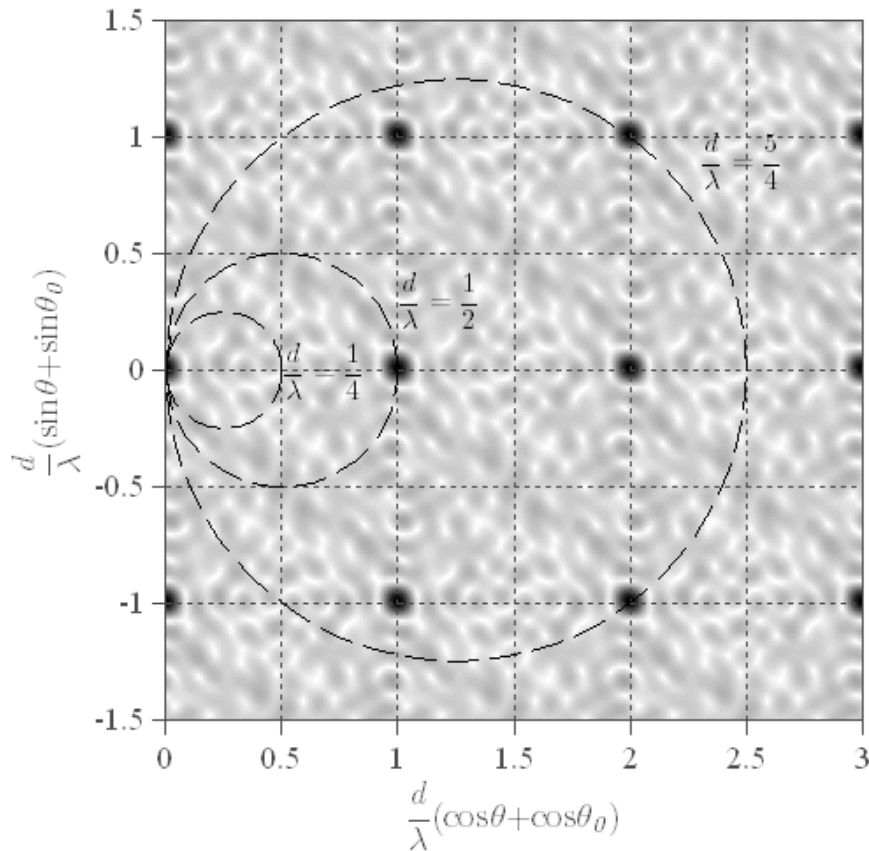
Figure 6.11: Fourier domain representation of the scattering from the arrangement as per Figure 2.27 (considered as point sources) for a number of wavelengths; $d = d_x = d_y$, $\theta_0 = 0°$

For a given frequency the polar pattern in Figure 6.11 is traced out by a (in this case since $d_x = d_y$) circular pattern whose location and size is determined by angular variables (θ and θ_0) and spacing relative to wavelength (d/λ) respectively. At low frequency only the sidelobe pattern is observed (excluding at DC, though this determines the attenuation behind the array). With increasing frequency however the spatial aliasing lobes are introduced, and consequently these dominate.

The spatial aliasing effect is an inherent property of the underlying periodicity, and happens when lobing due to periodicity in the x and y directions occur at the same angle and their product results in constructive interference, concentrating reflection in one direction. These reflections are known as Bragg peaks [39], and are analogous to the flat-plate frequencies observed in Schroeder diffusers when all reflection paths become equal to a multiple of a wavelength and all wells reradiate in phase. They are also intrinsically linked through conservation of energy to the attenuation band gaps observed in sonic crystals.

It can be shown that for a 2D rectangular array the Bragg frequencies are given by:

$$f = \frac{c\left(\dfrac{\alpha^2}{d_x^{\,2}} + \dfrac{\beta^2}{d_y^{\,2}}\right)}{2\left(\dfrac{\alpha\cos(\theta_0)}{d_x} + \dfrac{\beta\sin(\theta_0)}{d_y}\right)} \qquad\qquad 6.13$$

Where α and β are integers (including zero and negative values) and a full derivation of the above is given in Appendix B. The frequencies predicted by Eq. 6.13 for the optimised array are highlighted in Figure 6.10 (vertical dotted lines), where despite the relatively low occupancy, several sharp drops in diffusion result. Note the frequencies given here are similar to those for a 2D array of slats considered in Section 4.3.2 and given by Eq. 4.38, which described the constructive interference between periodically spaced layers at the Bragg frequencies.

An example of the scattering from the optimised array at (approximately) the first Bragg frequency predicted above ($f = 1075$Hz) was shown in Figure 2.28 (top right). Here it can be seen that in contrast to the remaining three example frequencies, for which scattering is quite even, the array produces a strong back-scattered lobe in the direction of the source. This in

Figure 6.11 corresponds to the $d/\lambda = \frac{1}{2}$ example highlighted. With increasing frequency more and more of these notch frequencies appear. Multiple scattering can help to reduce severity, though for arrays with higher occupancy these notches are broader and more defined and continue on to higher frequencies. Consequently sparser arrays are generally preferred.

6.4.3 Back-scattered power

In Section 6.3.4 it was demonstrated that the back-scattered power from a 1D array could be modelled as a summation of the contributions from the individual cylinders, where each cylinder is modelled by an approximate high-pass filter shaped response given by Eqs. 6.6-6.8. For a 2D array, as with the slat arrays of Section 4.3.1, the line-of-sight from the source to a cylinder can potentially be blocked. This means that with increasing occupancy the cylinders towards the back of an array will have less and less influence on the back-scattered power. Consequently a line-of-sight model may be adopted following the procedure outlined for an array of slats with a small layer spacing, illustrated in Figure 4.25.

Figure 6.12 shows the application of the above scattered power model to the optimised arrangement considered in the previous sections. As with a 1D array, at low frequency the scattered power is limited by cylinder size, determined by the cut-off frequency, f_c, given by Eq. 6.8. For the array here with cylinder size $d_e = 8$cm, this equates to a cut-off frequency of $f_c \approx 970$Hz. At high frequency the scattered power is determined by a function of element fill factor, though the relationship here is less clear. A simple (line-of-sight) fill factor model (dotted line) under predicts the level of back-scattered energy from the array, estimating the flat region to plateau at approximately -4.5dB. This is because unlike a slat a cylinder will also forward scatter energy. Consequently although cylinders with no direct view of the source will receive less energy than those which do, their influence via multiple scattering can still be important. Conversely the Fourier approximation (dashed line) over estimates the degree of back-scattered energy, predicting an approximate plateau level (excluding at the Bragg frequencies) of -1.3dB, given by the incoherent summation of $E = 25$ cylinders. This is due to the assumption that all cylinders are directly subject to the incident field, and hence neglects the effects of shadowing. The more accurate results provided by multiple scattering theory lies somewhere between the two more approximate predictions.
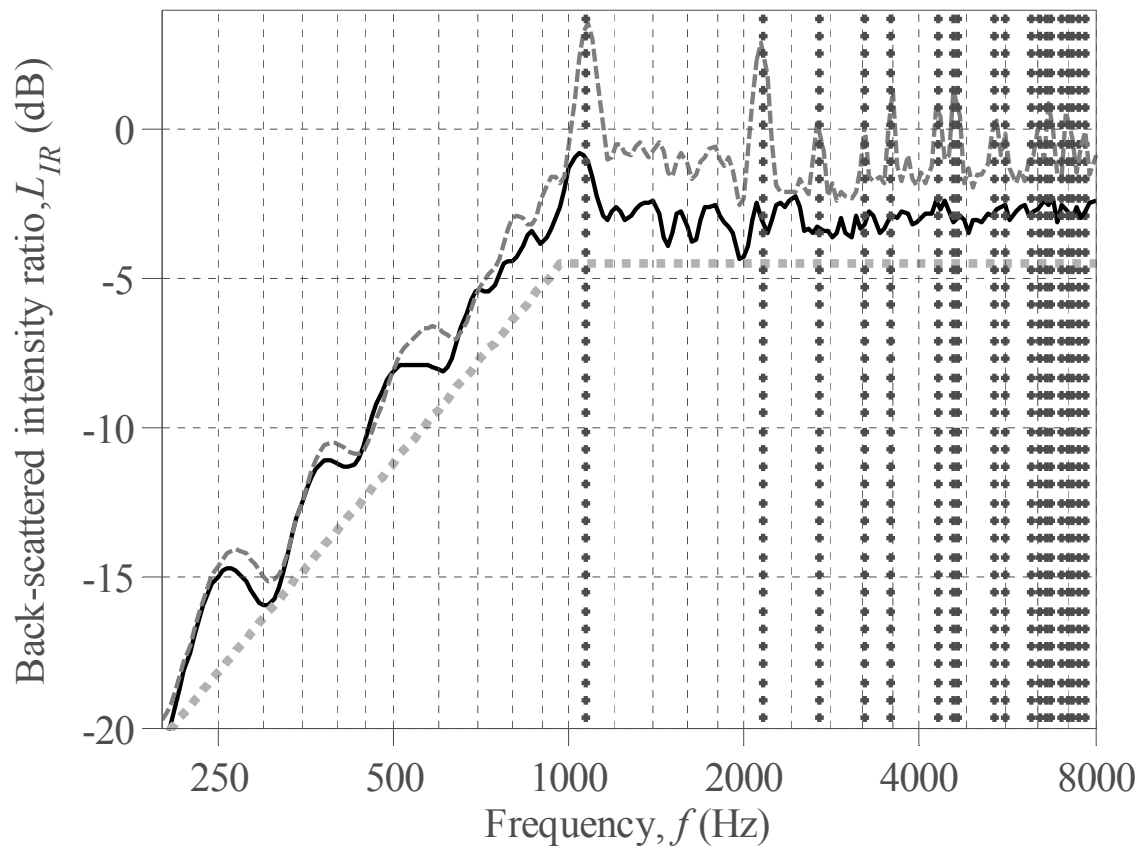
Figure 6.12: Back-scattered intensity ratio for the optimised cylinder array as per Figure 2.27; MS (▬), Fourier approximation (━ ━), approximate model (━ ━ ━) and predicted Bragg frequencies (•••); $\theta_0 = 0°$

Based on the above the required cylinder size / line-of-sight through the array will be to some extent dependent on occupancy. In general, however, to scatter efficiently at low frequency elements on the order of approximately a quarter wavelength are required. This tends to coincide with the first Bragg peak. Consequently at low frequency an array will diffuse well though with limited efficiency, whilst at higher frequencies sufficient power is scattered though diffusion suffers due to the underlying periodicity. The operational bandwidth is therefore small, and an array that allows larger cylinders or reduces the effects of periodicity is needed.

6.4.4   Amplitude shading: varying cylinder size

Since cylinders of approximately a quarter wavelength in diameter are necessary, one option is to use a variety of cylinder sizes; providing elements comparable in scale to a range of

wavelengths. In Section 6.3.3 it was shown that diffusion from a 1D varied cylinder size array may be achieved through amplitude shading. For the 2D case this is achieved by considering an array that allows cylinders of varying diameter, $d_{m,n}$, spaced an equal distance, $d = d_x = d_y$, apart (centre to centre). Following from Eqs. 6.5 and 6.11, a single scatter Fourier approximation to the scattering from a 2D amplitude shaded array may be given by:

$$p_s \propto \sum_{m=0}^{M-1}\sum_{n=0}^{N-1} A_{m,n} e^{jk\left[md_x\left(\cos\theta+\cos\theta_0\right)+nd_y\left(\sin\theta+\sin\theta_0\right)\right]}$$

$$A_{m,n} \approx \sqrt{d_{m,n}}$$

6.14

As with the 1D array a set of amplitude coefficients whose sidelobe pattern is even will be desirable, and consequently 2D Chebychev sequences are appropriate. Figure 6.13 shows a 10×10 array of cylinders (top) and scattered polar pattern examples (bottom) for a 2D Chebychev array designed to produce sidelobes all attenuated by 20dB. Cylinders for which the design frequency as determined by Eq. 6.3 is greater than 8kHz however have been omitted, corresponding to cylinder diameters of $d_{m,n} < 1.37$cm, since their contribution is insignificant over the frequency range considered.

From the scattered pressure plots of Figure 6.13 (bottom) it is evident that in general the equal energy sidelobe scattering seen for a 1D array is not observed. This is because the design theory is based on a high frequency approximation, and assumes that the diffusive design frequency for each of the cylinders is met; when cylinder diameter is equal to approximately a third of a wavelength resulting in scattering approximately proportional to its size. This will occur gradually as the individual cylinder sizes become comparable to wavelength. At the same time however the effects of multiple scattering and shadowing from these cylinders will become significant, and the single scatter approximation breaks down.

Despite the theory behind the design of a 2D Chebychev array being limited, significant dispersion still results. This is illustrated by the diffusion coefficient for the above array shown in Figure 6.14, with the array providing performance comparable to the optimised array of Figure 6.10. At the Bragg frequencies however, particularly the first, notches in the diffusion coefficient caused by spatial aliasing occur due to the high occupancy and hence redundancy (repetition of cylinder separation vectors).
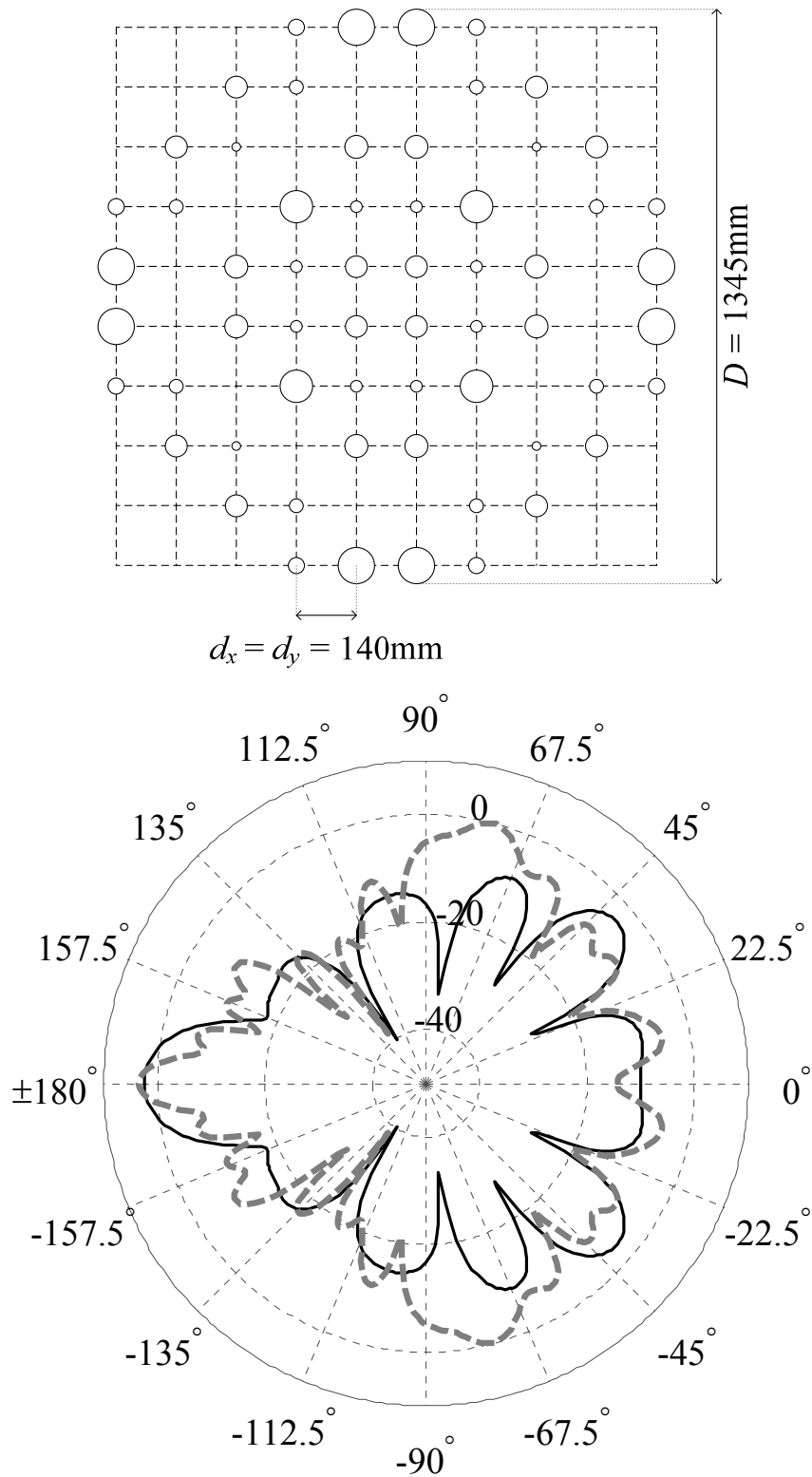
Figure 6.13: Amplitude shaded Chebychev cylinder array arrangement (top) and polar pattern (bottom) for frequencies f = 750Hz (———) and f = 1.5kHz (— —); $\theta_0 = 0°$
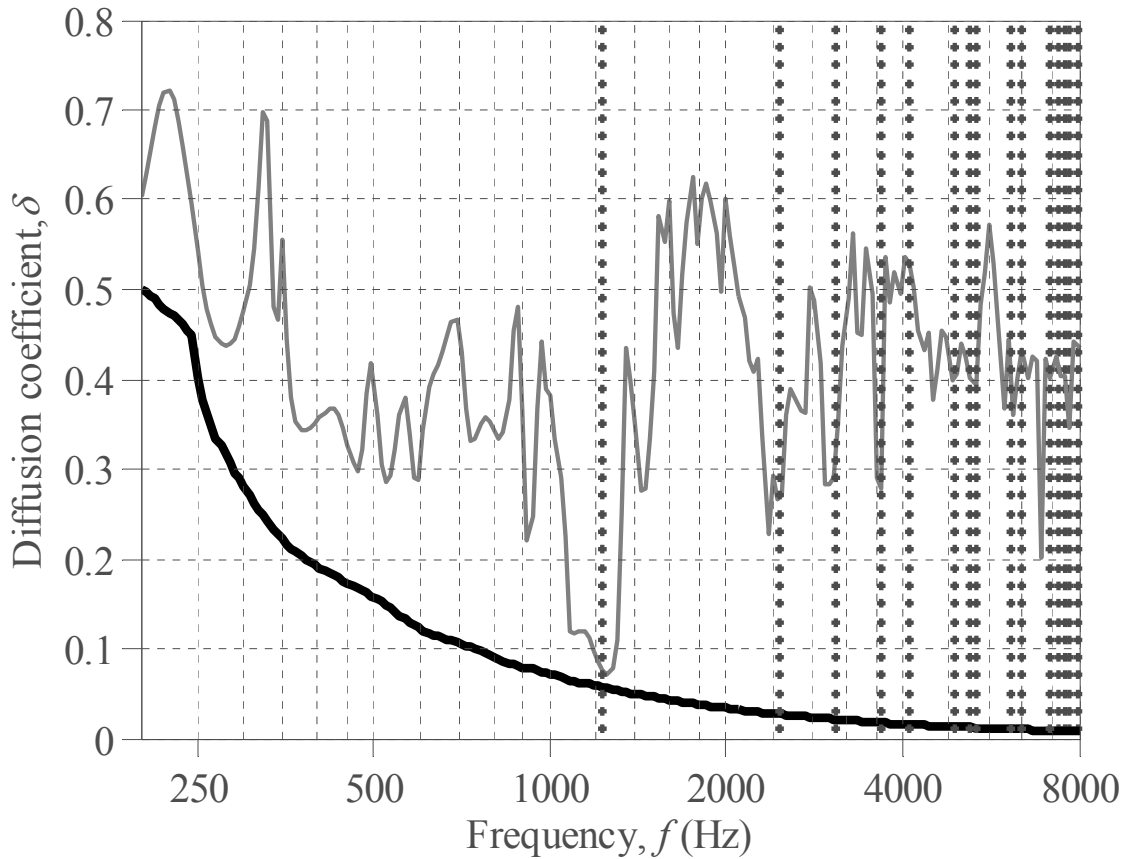
Figure 6.14: Diffusion coefficient for the amplitude shaded Chebychev array as per Figure 6.13; MS (━), and predicted Bragg frequencies (•••); $\theta_0 = 0^{\circ}$; flat plate (▬) shown for reference

Avoiding this first notch in the diffusion coefficient would require pushing the first Bragg frequency to below the minimum design frequency, f_{min}, which from Eq. 6.13 implies:

$$\{d_x, d_y\} > \frac{c}{2f_{min}} \tag{6.15}$$

This for a lower design frequency of $f_{min} = 400$Hz equates to a minimum element spacing of 43cm, which like the 1D case would result in an array that is very large and/or contains very few cylinders.

6.4.5 Non-redundant sequences: Costas arrays

An array ideally should have good AACF properties, implying little or no redundancy (the repetition of element separation vectors) to minimise periodicity effects. 2D non-redundant

sequences have no repetitions of these separation vectors and so should be ideal, providing they have a sufficient number and spread of elements for them to be useful. An example of this is the Costas array, defined as being a permutation matrix whose separation vectors between occupied cells are unique [78]. In other words, a square $N \times N$ grid containing N elements, with one element in each row and each column and a maximum out of phase AACF coincidence of one. An example of this is shown in Figure 6.15. Costas arrays may be thought of as a 2D semi-equivalent to the Golomb ruler used for 1D arrays, and are commonly used as frequency hop patterns for sonar or radar due to their optimum ambiguity function [78].

There are a number of methods for making Costas arrays, though particularly suited to this application is the Taylor T_4 variant to the Lempel L_2 construction [78]. This method ensures a minimum separation distance between elements, allowing larger cylinders for increased low frequency power. For a generating prime power, q^i, where q is any prime and i is a positive integer, the Lempel L_2 construction forms an $N \times N$ array, $\mathbf{C}_{m,n}$, where $N = q^i - 2$, and is defined as follows:

$$\mathbf{C}_{m,n} = \begin{cases} 1, & u^m + v^n = 1; \\ 0, & otherwise \end{cases} \quad 1 \le m \le N, \ 1 \le n \le N, \quad \quad 6.16$$

Where u and v are primitive roots of prime number q, and the operation is carried out modulo q^i. An important characteristic is that Lempel constructions have reflective symmetry about the main diagonal. This means that the nearest possible neighbouring elements lie one diagonal step apart either side of the main diagonal. A special case of this, of which the L_2 square array in Figure 6.15 is an example, is formed when $u^1 + v^2 = 1$ (and $u^2 + v^1 = 1$, though this is automatically satisfied due to the reflective symmetry) which places these two elements (highlighted by grey hatched squares) in the first two rows and columns. These elements then may simply be removed to form a new $N = q^i - 4$ Costas array known as the Taylor T_4 variant.

By definition the maximum out of phase AACF coincidence of the T_4 array must be one. With the closest element pair having been removed, the next nearest set of elements must therefore be further apart than a single diagonal step. The resulting array has the property of 'non-attacking chess kings' – that is no element lies within the eight surrounding cells of another. This makes it possible to form an oversampled array where the cylinder size can be greater than grid spacing, allowing sufficient scattered power to be achieved well before the

first Bragg frequency. This for a given cylinder size effectively pushes the first Bragg peak to a higher frequency.
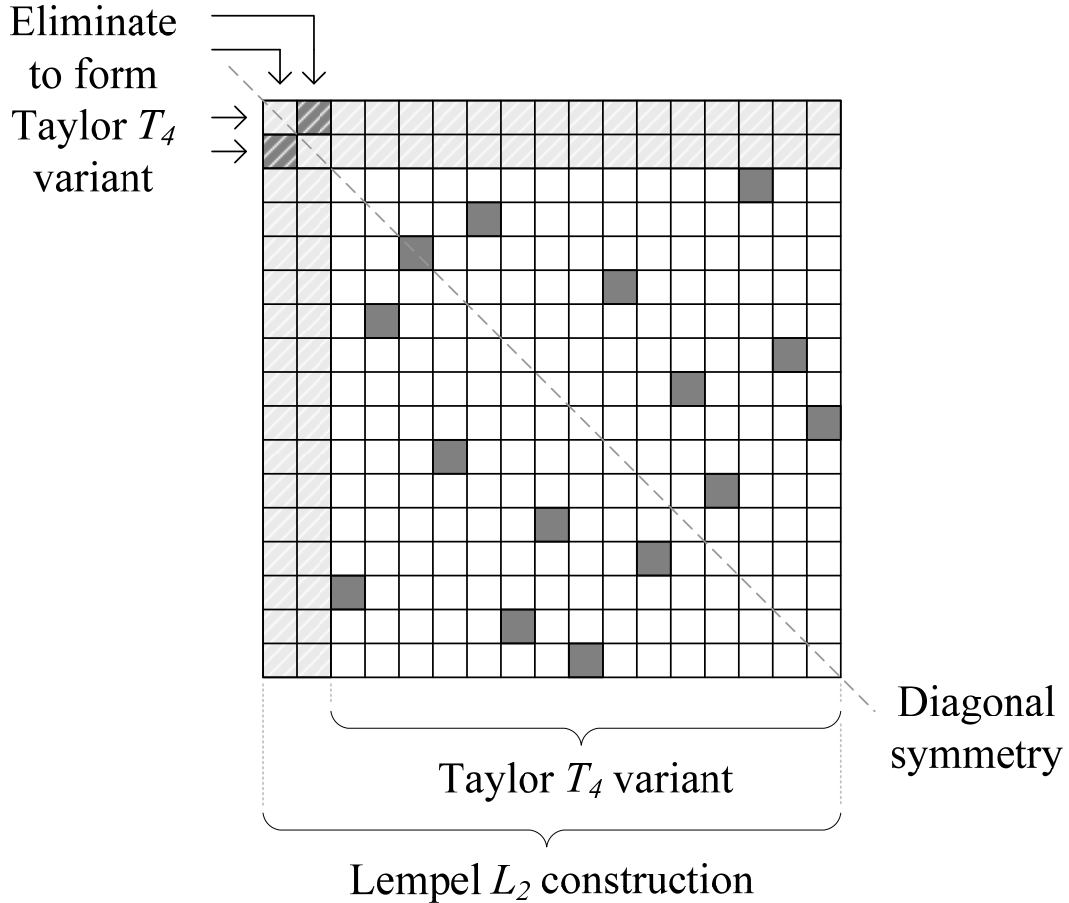
Figure 6.15: Construction of a Taylor T_4 variant (N = 15) Costas array from a Lempel L_2 (N = 17) construction

Figure 6.16 shows an example of a Taylor T_4 15×15 grid Costas array arrangement of cylinders with location determined as per Figure 6.15 (top) and AACF (bottom). The resulting diffusion coefficient and back-scattered intensity ratio are shown in Figure 6.17. It can be seen that due to the lack of redundancy the effects of periodicity are significantly (though not entirely) reduced, resulting in a diffusion coefficient varying between 0.28-0.66 over the frequency range $400\text{Hz} \leq f \leq 4.0\text{kHz}$. Due to the presence of larger cylinders the back-scattered power falls within ±1dB of the -3dB target for all frequencies above the 400Hz design frequency.
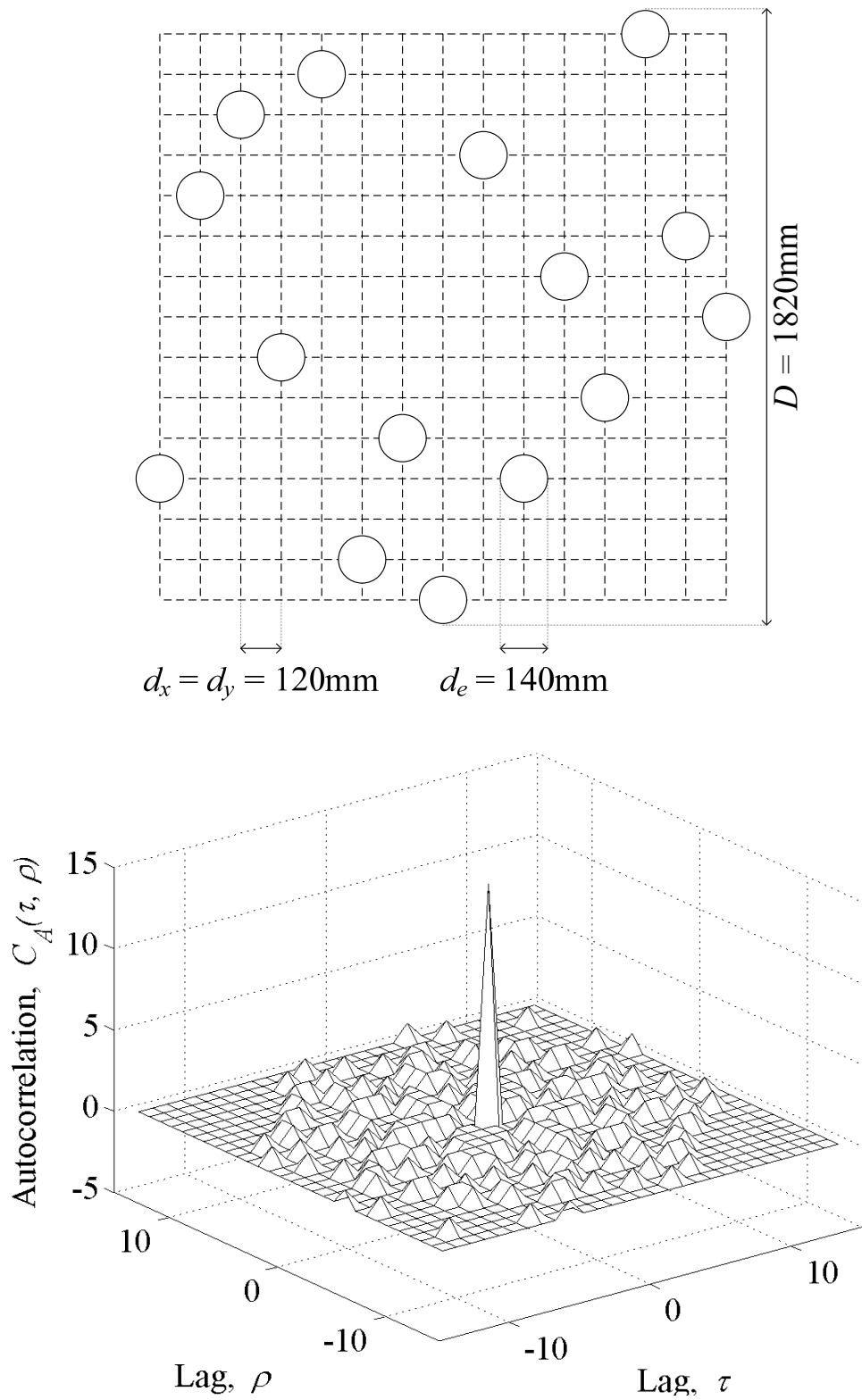
Figure 6.16: N = 15 Taylor T₄ Costas arrangement of cylinders (top) and AACF (bottom)
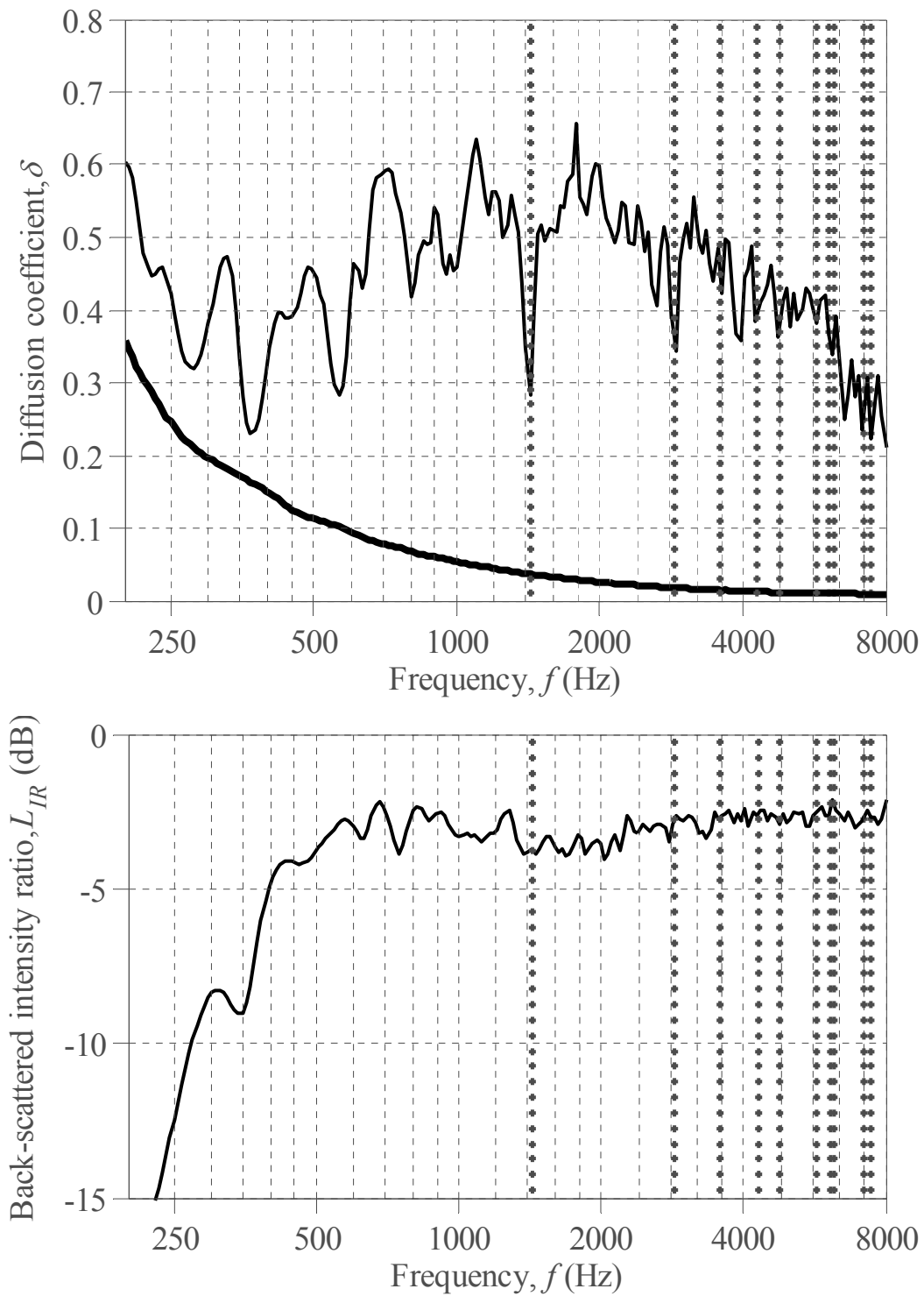
Figure 6.17: Diffusion coefficient (top) and back-scattered intensity ratio (bottom) for the
N = 15 Costas array of cylinders as per Figure 6.16 (━), and predicted Bragg frequencies
(•••); θ₀ = 0°; diffusion coefficient of flat plate (▬) shown for reference

6.4.6 The effect of cylinder size on diffusion for sparse arrays

In Figure 6.1 the scattered pressure from a cylinder was expressed as a function of its diameter, d_e, relative to wavelength. It is evident that although scattering is relatively even there are a series of troughs and peaks that occur which are dependent on angle. These appear to emanate from the direction of the reflection back to the source ($\theta = \theta_0$) and with increasing frequency gradually move towards receiver angles to the rear of the cylinder. Subsequently, if this behaviour could be counteracted, then diffusive performance could be improved.

For the arrays presented here the most limiting factor is the inherent spatial aliasing lobes, due to the underlying periodicity and hence the arrangement. To approximate the scattering due to this periodicity alone a simplified Fourier approximation (summation from Eq. 6.11) may be used, though considering a full array (all point scatterers present). An example of this is shown in Figure 6.18 for a 15×15 array demonstrating that (for normal incidence), like a single cylinder, the arrangement too results in a series of peaks and troughs emanating from the specular reflection direction. As illustrated by Figure 6.9, it is the product of the response of the array and that of a single cylinder which determines the scattered distribution. Consequently if the appropriate cylinder size (d_e) to spacing ($d = d_x = d_y$) ratio is chosen then the peaks of the arrangement response may be set to coincide with the troughs of the cylinder response (and vice-versa), thus reducing the severity of the spatial aliasing lobes. The effect of this is shown in Figure 6.19, which illustrates the change in diffusion coefficient with cylinder size (expressed as a map) for the $N = 15$ Costas cylinder array as per Figure 6.16. It can be seen that the notches in diffusion due to the Bragg peaks observed at $d/\lambda = \frac{1}{2}$ and $d/\lambda = 1$ experience a reduction for the $d_e/d \approx 0.9$ case and $d_e/d \approx 1.6$ case respectively.

It should be noted that the above is based on the case of normal incidence, and for other source angles the above technique may be less effective. This is because for other angles of incidence the scattered pattern due to the shape of the underlying grid shown in Figure 6.18 will be different. In addition selecting cylinder size based on this approach will inherently alter the level of back-scattered energy. Consequently there is a trade-off between increased diffusive performance and achieving the desired scattered power.
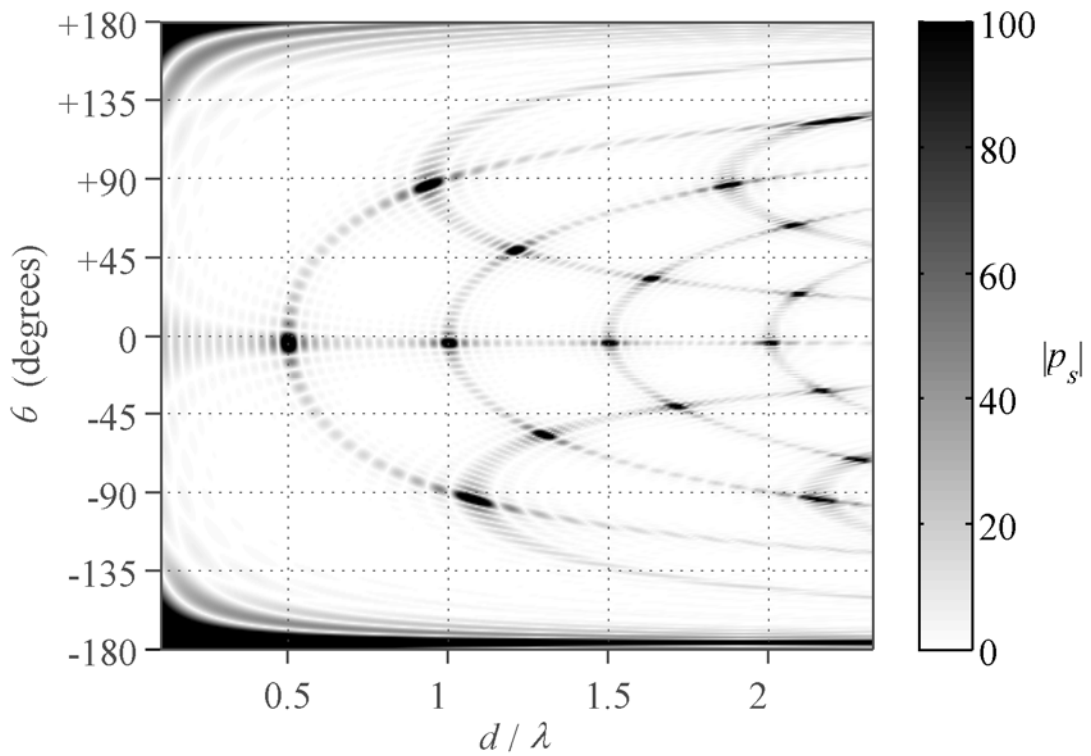
Figure 6.18: Scattered pressure for a 15×15 square grid array of point scatterers; $\theta_0 = 0°$,

$d = d_x = d_y$
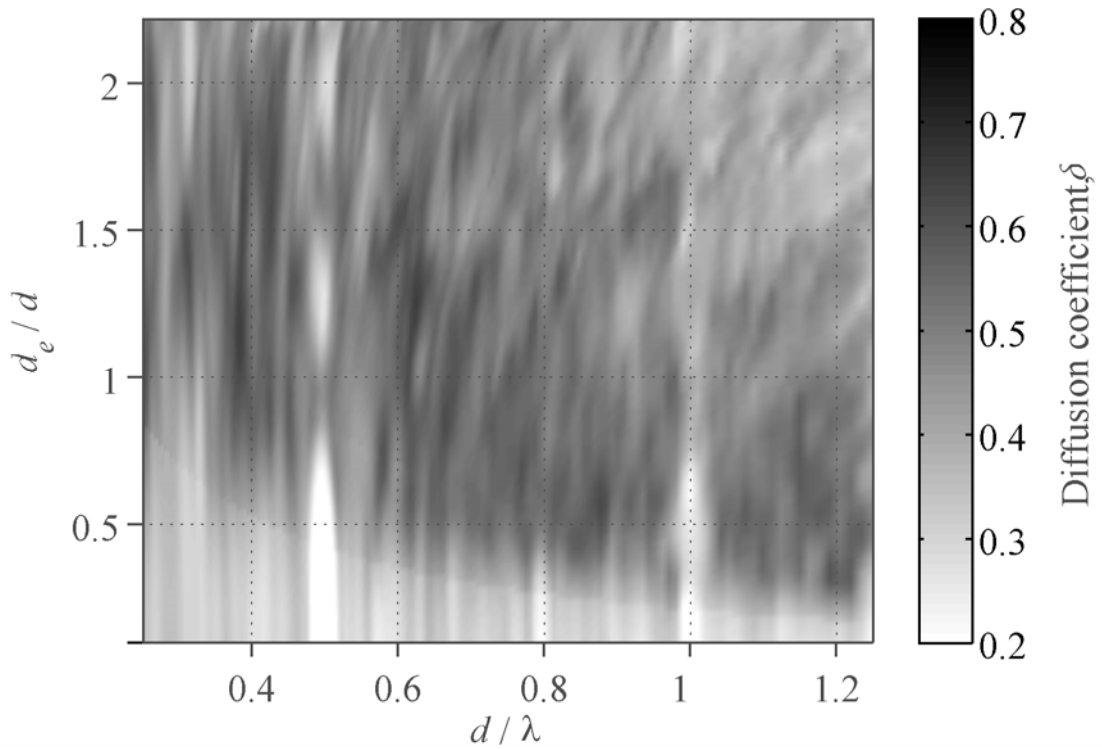
Figure 6.19: Diffusion coefficient for the N = 15 Costas cylinder array as per Figure 6.16

with varying cylinder size d_e (relative to cylinder spacing $d = d_x = d_y$)

6.5. The hexagonal / triangular lattice array

Ideally an array will display isotropic behaviour, meaning that performance is consistent for all angles of incidence. A potential downside of an arrangement such as that of Figure 6.16 is a changing appearance upon rotation, which can lead to variation in scattered power due to the change in line-of-sight and/or effective total width. Introducing rotational symmetry could help, as this may provide a more consistent appearance (as seen by the source) with varying angle. Even-fold rotational symmetry however (when an arrangement appears the same an even number of times upon one complete rotation) implies redundancy and so is undesirable.

An alternative to a rectangular grid is the hexagonal (or triangular) lattice, whose potential odd threefold rotational symmetry permits unique vector spacings. Although examples have been considered [3], these arrays do not lend themselves as easily to surface diffuser design, both in application of number theory and in terms of construction and practicality of installation, and consequently have received little attention.

6.5.1 Hexagonal Costas arrays

Golomb and Taylor [78] demonstrated that a hexagonal arrangement may be formed by a simple 'shear-compression' transformation of an existing square lattice array using the transformation given by:

$$\begin{bmatrix} x_t \\ y_t \end{bmatrix} = \mathbf{A}_T \begin{bmatrix} x \\ y \end{bmatrix} \quad , \qquad \mathbf{A}_T = \begin{bmatrix} 1 & 0 \\ 0 & \sqrt{3}/2 \end{bmatrix} \begin{bmatrix} 1 & 1/2 \\ 0 & 1 \end{bmatrix} = \begin{bmatrix} 1 & 1/2 \\ 0 & \sqrt{3}/2 \end{bmatrix} \qquad 6.17$$

compression   *shear*   *shear-compression*

Where x_t and y_t are the coordinates of the original x and y row vector element locations, when altered by transformation matrix, $\mathbf{A}_T$. This was applied specifically to Costas arrays, though is applicable to any arrangement, and is represented pictorially in Figure 6.20 for a 7×7 Lempel L_2 construction, where the array is first sheared in the horizontal dimension, then compressed in the vertical dimension.
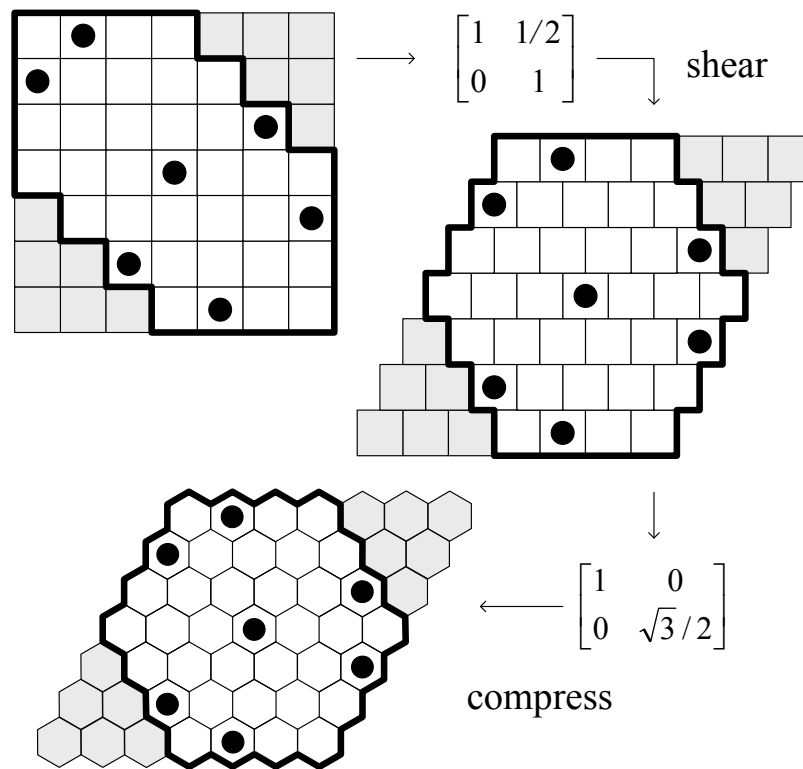
Figure 6.20: Transformation of a 7×7 Lempel L₂ Costas array from a square lattice to a hexagonal lattice via shearing and then compression (shear-compression) – after Golomb and Taylor [78]

Applying a spatial transformation to the element locations also applies the same transformation to the vector separations, and hence the AACF. This means that a non-redundant square grid arrangement will, when transformed, also produce a non-redundant hexagonal one. In order to form a more isotropic array therefore, a sequence is preferred whose elements fall close to the main diagonal, and consequently the Lempel L_2 construction introduced in Section 6.4.5 is well suited. This is evident from Figure 6.20 where it can be seen that a 'square footprint' array (including grey squares) would transform to a 'rhombus footprint' array, as opposed to the hexagonal array shown (excluding grey squares). The resulting arrangement has the property of 'non-attacking bee-rooks' (from the game of hexagonal chess), whereby no two elements lie on the same line of adjacent hexagons [78]. This, like the Costas array of Figure 6.16, ensures an increased minimum separation distance.

The above technique does not remove the underlying periodicity, though the transformation can lead to a more tightly packed, yet evenly spread AACF. This is demonstrated in Figure 6.21 where both original square grid (a) and transformed hexagonal array (b) for a 27×27

Lempel L_2 Costas array are shown, along with their respective AACF distributions (c) and (d). These are expressed as vector separation maps where no two separations coincide. The threefold rotational symmetry (and more consistent appearance with angle) of the hexagonal array is clear.
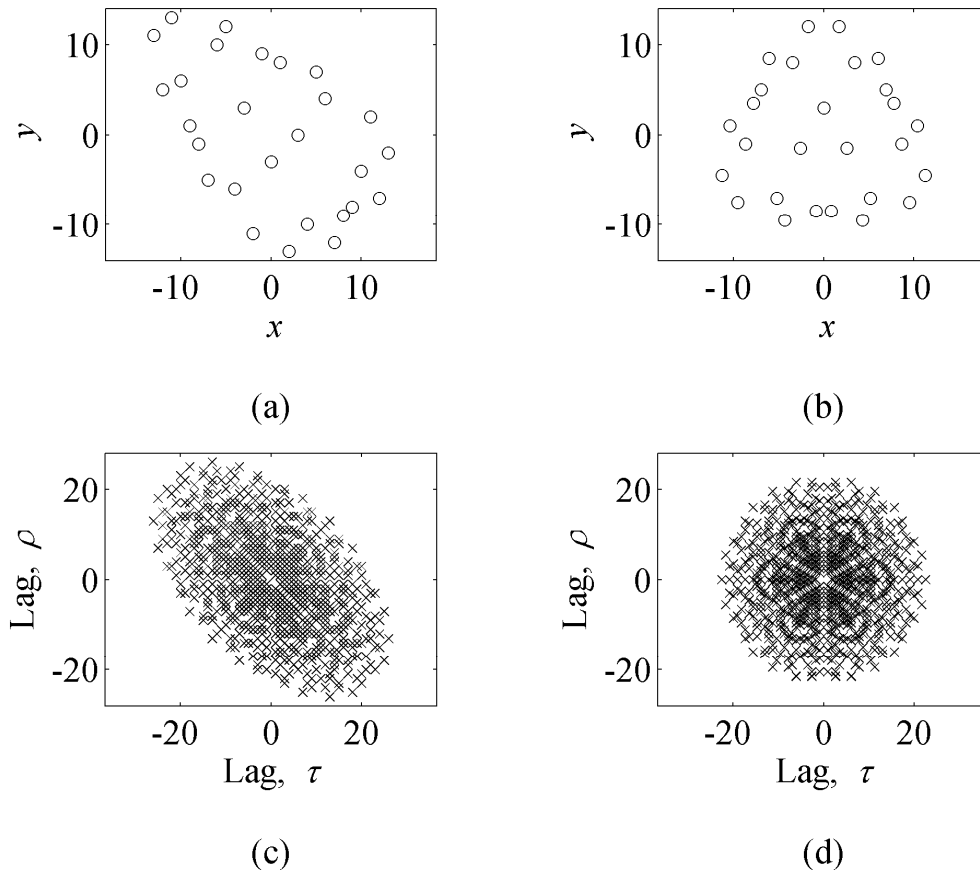
Figure 6.21: Square grid (a) and transformed hexagonal array (b) for a 27×27 Lempel L_2 Costas construction, along with respective AACF vector spacings (c) and (d).

The result in terms of diffusion and scattered power for an array based on the hexagonal arrangement of Figure 6.21 (b) is shown in Figure 6.22 (top and bottom respectively). Full details of the construction are given in the following section. An improvement in scattered uniformity occurs compared to a regular square grid due to the larger number of separation paths comparable to wavelength across the design bandwidth. This improvement however is slight (increasing the average diffusion coefficient by 0.02), and notches in the diffusion coefficient still remain, though shifted in frequency due to the spatial transformation. In general the performance is similar to that of a square grid array, though with more consistent behaviour with angle of incidence.
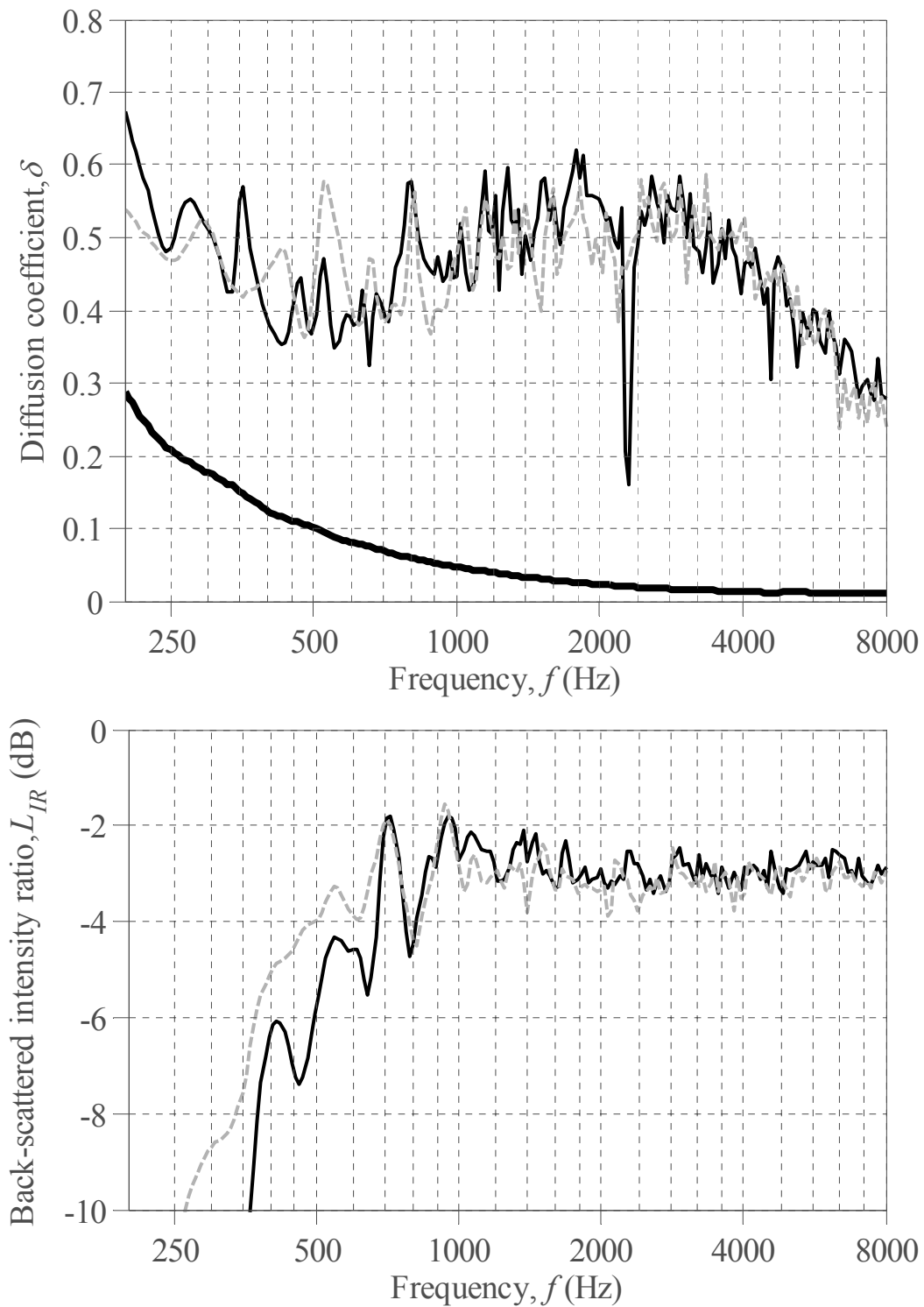
Figure 6.22: Modelled diffusion coefficient (top) and back-scattered intensity ratio (bottom) for a hexagonal Lempel L_2 Costas array of cylinders; equal sized cylinders, $d_e = 10cm$ (━━━) and amplitude shaded array as per Figure 6.23 (━ ━); $\theta_0 = 0^{\circ}$, $D = 2.04m$; diffusion coefficient of flat plate (━━━) shown for reference

6.5.2   Amplitude shading: a windowing approach

An alternative approach to the amplitude shading technique presented in Section 6.4.4 is to apply amplitude shading to an existing array by multiplying it with a chosen window in the spatial domain. This equates to convolution in the scattered polar (Fourier) domain. The objective is to smooth out the polar response by removing the more rapid fluctuations and so a window sequence shaped like a low-pass filter is desired, implying larger objects in the centre of the array and progressively smaller objects toward the extents. Conveniently, this allows low frequency energy to penetrate into the structure and higher frequencies to scatter off the smaller outer elements; a concept similar to the impedance matching approach discussed in Section 4.4. In addition, when windowed radially, a more isotropic array is formed since objects of the same size will occur at the same distance from the array centre.

A suitable arrangement for amplitude shading in this manner is the hexagonal grid Lempel L_2 Costas array such as that illustrated in Figure 6.21 (b), as these tend to be sparsely populated toward the centre. An arrangement was therefore designed based on the square grid array of Figure 6.21 (a) with original grid spacings set at $d_x = d_y = 86$ mm, before the transformation matrix in Eq. 6.17 was applied. To allow measurements to be carried out on the amplitude shaded array, three readily available cylinder sizes (when scaled) were selected: $d_e \approx 50$mm for the outermost six, $d_e \approx 200$mm for the innermost three, and $d_e \approx 100$mm for the remaining eighteen. These cylinder sizes were selected so that, following from Eq. 6.8, the largest cylinder size ($d_e \approx 200$mm) will begin to scatter efficiently at approximately 400Hz, with the remaining two beginning to scatter efficiently at an octave ($d_e \approx 100$mm) and two octaves ($d_e \approx 50$mm) above this point. The measurement sample used is shown in Figure 6.23, and like the optimised array used for verification of the MS model in Section 2.6.3, was constructed at 1:4 scale using 1m high aluminium cylinders.

Figure 6.22 shows the diffusion coefficient (top) and back-scattered intensity ratio (bottom) for the hexagonal array of Figure 6.23 obtained from prediction, both with (dashed line) and without (solid line) amplitude shading. The latter is shown for reference and follows from the previous section, using a single cylinder size $d_e = 10$cm. It can be seen that the general performance of the two arrays is very similar, though the notches in the diffusion coefficient observed for the single cylinder size case are significantly reduced for the amplitude shaded

equivalent (in particular at $f \approx 2.3\text{kHz}$). In addition the amplitude shaded array is able to provide a slight boost in low frequency scattered power due to the presence of larger cylinders. The result is a range in diffusion coefficient and back-scattered intensity ratio over the frequency range $400\text{Hz} \leq f \leq 4.0\text{kHz}$ of 0.16-0.62 and -7.4dB to -1.8dB for the standard array and 0.36-0.59 and -5.0dB to -1.6dB for the amplitude shaded equivalent.
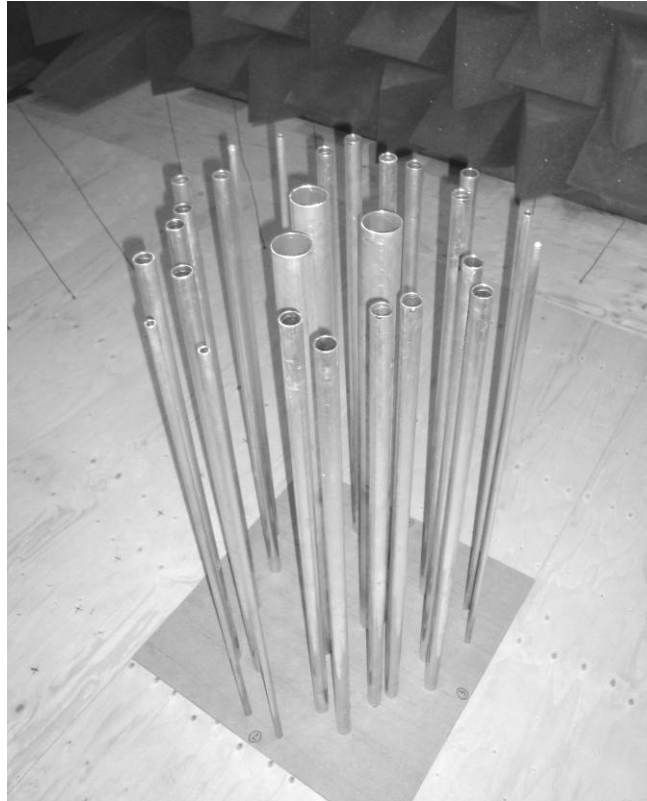
Figure 6.23: Hexagonal amplitude shaded cylinder measurement sample constructed at 1:4 scale

The above array is capable of performing efficiently over an approximate 4-5 octave bandwidth. Like the 1D case, the 2D diffuser is inherently limited by the high frequency tail-off in diffusion due to the forward-scattered response of an individual cylinder. As was explained previously, however, this is more a matter of definition of the volume diffusion coefficient, and effective scattering will continue well beyond this frequency range.

Figure 6.24 shows both measured and modelled random incidence back-scattered diffusion coefficient for the amplitude shaded array. Random incidence values were obtained by averaging results for source angles of $\theta_0 = 0^\circ$ to $\theta_0 = 330^\circ$ taken in steps of 30°. A

back-scattered coefficient is used here since, as was discussed in Section 3.3.3, the definition of the volume diffusion coefficient means that strict far-field conditions must be met and this was impractical for the measurements. Like the optimised array of Section 2.6.3, there is good agreement between measured and modelled results, with slight discrepancies in level at low frequency. The average error in the diffusion coefficient over the frequency range $400\text{Hz} \leq f \leq 4.0\text{kHz}$ is 0.02. The array demonstrates an overall reduction in severity of diffusion notches, both for random incidence and for specific angles of incidence. Performance might be improved further if the cylinder sizes were optimised.
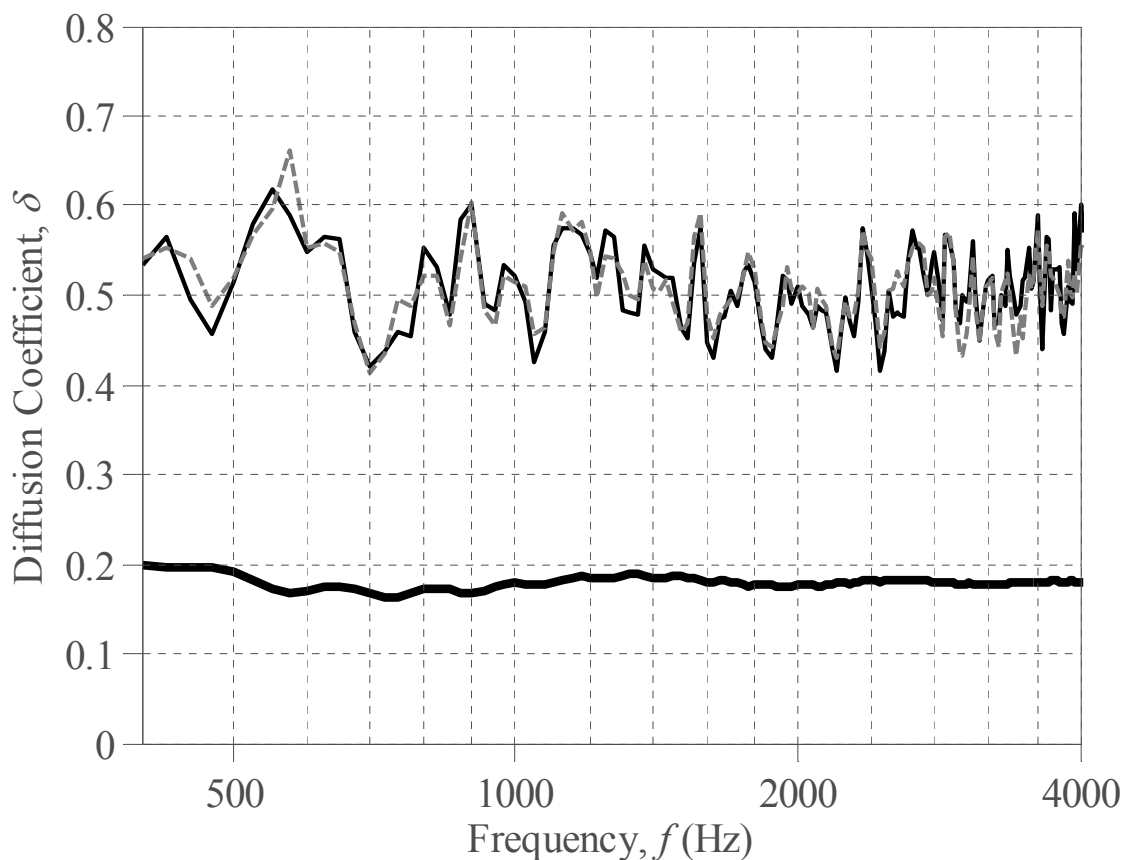
Figure 6.24: Random incidence (back-scattered) diffusion coefficient for the amplitude shaded array as per Figure 6.23; modelled (━) and measured (━ ━); D = 2.04m; diffusion coefficient of flat plate (▬) shown for reference

6.6.   Conclusions

This chapter has investigated the use of arrays of cylinders based on a periodic lattice as volume diffusers. Initially single layer structures were considered, before multi-layered

structures based on both rectangular and hexagonal lattices were studied. By removing or varying the cylinder size based on number theoretic sequences, a number of design concepts have been shown to create arrays that provide suitable levels of diffusion and back-scattered power across the design bandwidth. Typical diffusion coefficient values are on the order of 0.3-0.5 above that of the reference plate, whilst back-scattered power values fall within approximately ±1dB of the -3dB target.

Sequences whose AACF properties are optimal provide the most even scattering, with in general, a typical array being capable of performing over an approximate 3-4 octave bandwidth. For a 1D array the limiting factor is the performance of a single cylinder, since at low frequency their scattering is less even and their scattered power is weak. Once wavelength is on the order of the length of cylinder circumference, however, significant diffusion may be achieved despite the lack of depth. At high frequency, scattered power is dictated by line-of-sight through the array, which for optimal unipolar sequence arrangements means the -3dB intensity ratio target cannot be met. Use of amplitude shading (varying cylinder size) allows for fuller arrays that can achieve this objective, however this tends to compromise low frequency diffusion due to the limits of the design theory and the inherent structural similarity of a full array. Consequently performance is a trade-off between consistency in low frequency behaviour and efficiency in high frequency scattered power.

For a 2D array the introduction of depth means diffusion may both be increased and achieved at a lower frequency, occurring once an array is on the order of wavelength in size. Like the 1D array this may be attained through the use of sequences whose aperiodic Fourier properties are desirable. In order to scatter efficiently at low frequency, however, cylinders on the order of approximately a quarter wavelength in diameter are required. At the same time for fuller arrays when wavelength becomes comparable to lattice spacing the inherent redundancy produces strong directional reflections (Bragg scattering). These two frequencies tend to roughly coincide and consequently operational bandwidth is limited to less than an octave. The array diffuses well at low frequency though with limited efficiency, whilst at higher frequencies scatters sufficient power though with reduced diffusion due to the underlying periodicity.

By limiting structural similarity the detrimental effects on diffusion are significantly reduced (though not completely removed), producing an effectively oversampled sparse array. An example of this is the Costas array, which can allow cylinder size greater than lattice spacing, helping to extend the bandwidth of performance by effectively increasing the frequency of the first Bragg peak. Further improvements may be gained by transforming to a hexagonal lattice, providing more isotropic behaviour due to the threefold rotational symmetry. By applying amplitude shading, such as to hexagonal Costas sequences, an array can be tuned to provide both further improvements to diffusion.

Based on the above a selection of designs have been presented, performing effectively over an approximate 4-5 octave bandwidth; the principles behind them are flexible, and in theory could be used to create an array with arbitrary design targets (e.g. scattered power, diffusive bandwidth, structural dimensions etc…) although this has not been tested.

7. DISCUSSION AND FURTHER WORK

7.1. Introduction

In the previous chapters an investigation into the design and analysis of a volume diffuser has been presented, considering notably the prediction, measurement and evaluation of a number of suggested diffuser types. This chapter brings these together, considering the implications of the findings and enabling a comparison of the structures proposed in Chapters 4 to 6 in terms of their diffusive efficacy.

Whether or not one diffuser design is better than another will depend much on the analysis techniques adopted, the intended use and the feasibility of design; and these are considered. An appraisal of each diffuser type is given, before their relative merits are discussed and a number of key design guidelines are outlined.

A number of the designs put forward show potential for use as volume diffusers, however there are several areas in which further research could help expand and improve upon the work presented. A discussion of a number of these is therefore presented. In particular these include both the testing of volume diffusers in more realistic spaces and the extension of the findings to 3D.

7.2. Discussion

7.2.1 An appraisal of metrics used

A volume diffusion coefficient

A new type of diffusion coefficient introduced in Section 3.3.2 has been used for most of the diffusers considered in the thesis. This volume diffusion coefficient forms an extension to the more usual surface diffusion coefficient, assessing scattering uniformity over a wider area. As the coefficient was used in developing the volumetric diffusers, some limitations became apparent.

Section 3.3.3 discussed the need for very large source and receiver distances to get the proposed diffusion coefficient to provide consistent values. This was due to the pressure nulls in the forward scattered field, which at high frequency require large distances before far-field

behaviour is observed and the scattered pressure falls with 3dB per doubling of distance due to cylindrical spreading. This is not a problem for predictions where very large distances can be used. Obtaining a diffusion coefficient from measurements however would be more problematic, since the distances required for any measurement setup (even scaled) are unrealistic.

For some of the diffusers it was shown that at high frequency a gradual tail-off in diffusion coefficient occurs. For example, this was the case for the amplitude shaded cylinder array shown in Figure 6.23 whose volume diffusion coefficient was shown in Figure 6.22 (top). Figure 7.1 compares both the volume diffusion coefficient and back-scattered 'surface' diffusion coefficient (defined in Section 3.3.1) for this array. At low frequency the volume diffusion coefficient is lower than the back-scattered coefficient due to the weak forward-scattering from an individual cylinder, whilst at mid frequencies once an individual cylinder provides efficient forward scattering the two coefficients are very similar. At high frequency however, despite the relatively even scattering of an individual cylinder, a reduction in the volume diffusion coefficient occurs. The reason for this is due to an individual cylindrical element producing a wider zeroth order lobe in the shadow forming region than that of the structure considered as a whole (as defined by Eq. 3.4). Part of this lobe therefore is included in the evaluation. Due to its comparatively low level at low frequency this is less of an issue, though with increasing frequency the zeroth order lobe behind a cylinder becomes gradually larger relative to the remaining scattered field. Consequently its inclusion in a coefficient causes a gradual fall in value. This may be interpreted as a physical reality which limits diffusive performance, or as a limitation of the diffusion coefficient's definition, due for example to assuming that the extent of the shadow forming region behind an array of objects will be similar to a solid object of the same overall size.

Based on the above some aspects of the volume diffusion coefficient may need refining, and these are discussed in Section 7.3.1. In general, however, the coefficient has allowed a measure of scattering uniformity that is applicable across the majority of the frequencies considered. In addition the coefficient provides a value that is easily understood, and which gives a close comparison with the performance of more conventional surface diffusers.
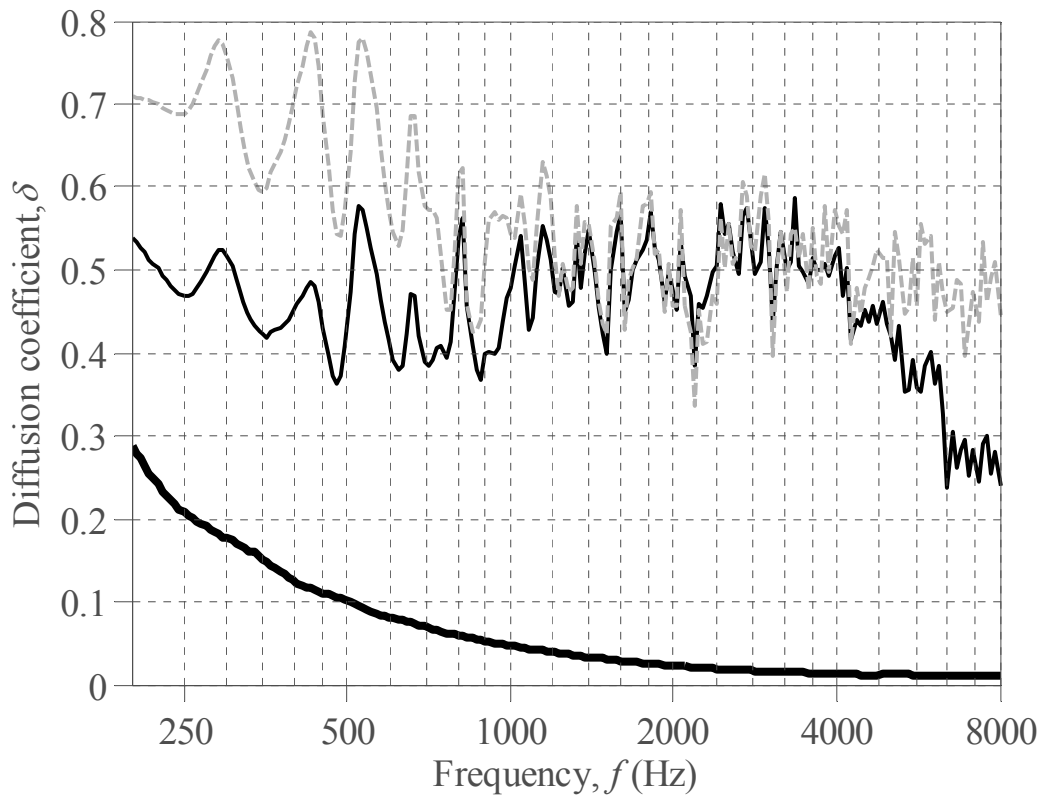
Figure 7.1: Volume diffusion coefficient (▬) and Back-scattered diffusion coefficient (▬ ▬)
for the amplitude shaded cylinder array of Figure 6.22 modelled using the multiple scattering
technique; $\theta_0 = 0°$, D = 2.04m; flat plate (▬) shown for reference

A Scattered power metric

The back-scattered power metric introduced in Section 3.4 has been used to assess the level of power scattered from an array. A target value of -3dB was set, though as was mentioned this is a somewhat arbitrary value, and a diffuser could just as easily be designed to meet an alternative target. This may be dependent on application type, and consequently ties in with the potential further research presented in Section 7.3.

The scattered power metric forms a relatively robust measure of scattered power, since it is independent of both source and receiver distance (assuming far-field conditions) and source strength. There are however limits to its application. One of these was briefly mentioned in Section 5.5.6 with reference to Figure 5.33 (bottom), where it was noted that at very low frequency the back-scattered power metric is less reliable. This is due to the assumption that the reference plate is relatively large compared to half of a wavelength; when the effects of

edge effects are minimal and the average back-scattered intensity demonstrates a smooth -3dB/octave roll-off. Before this the ripples seen at around the cut-off frequency, f_c, for the reference plate (as given by Eq. 4.18) will affect the outcome. Since the back-scattered power metric relies on the consistent behaviour of the reference plate with frequency, this limits the application of the metric applied here to approximately an octave or two above this frequency.

For most suitable sized arrays and for the majority of frequencies considered the above is not too much of an issue. For example a diffuser of width $D = 1$m has a cut-off frequency of $f_c = 122$Hz, and so from approximately $f = 250$-500Hz will produce a consistent reference value. For diffusers that need to be considered at lower frequencies however, for example the percolation structures of Section 5.5.6, the metric may be less reliable. One alternative may be to use a method that evaluates the power incident upon a diffuser and use this as a reference.

7.2.2 Slats array diffusers

Both single and multi-layer slat array diffusers have been shown to provide reasonable levels of performance. For a single layer array, however, diffusion is limited by the narrow bandwidth over which runs of slats scatter both in a relatively uniform manner and with sufficient power. These arrays therefore are inherently limited; the slat runs required at low frequency to scatter efficiently resulting in a directional specular reflection at high frequency. These findings have implications for structures such as both Binary Amplitude Diffusers (BAD) (i) and canopy arrays (ii).

(i) In Section 4.2.1 it was shown that in the back-scattered direction an array of slats performs very similarly to its equivalent BAD panel. Consequently the outcomes from the single layer investigation have implications for BAD design; the slat findings suggesting that more effective BAD panels may be formed by following a procedure similar to that for the design of a 1D slat array presented in Section 4.2.6. These slat sequences are aperiodic whilst BAD panels are usually arranged periodically, though unless large numbers of BAD repetitions are used the emphasis of the scattering into the grating lobes will not completely dominate. Consequently the scattering into the remaining directions will also be important and sequences which have both desirable periodic and aperiodic properties (such as the $N = 7$ Golomb ruler) may be preferable. In general, however, for reasons discussed above, both the lack of depth and use of flat surfaces results in a narrow bandwidth. There is a trade-off

therefore between the level of scattered power and scattering uniformity; the sparser sequences diffusing best though with little scattered power, particularly at low frequency. Techniques such as curving the surface of a BAD panel have been shown previously to improve diffusion at high frequency by spreading the specular reflection over a much broader area [3]. Similarly this is a technique often adopted for overhead canopy arrays [3], discussed further below. Consequently to provide better diffusion a slat array could be curved.

(ii) Unlike the alternative structure types presented, the slat arrays in Chapter 4 would likely make unsuitable arbitrary volume diffusers. This is because when viewed from angles close to grazing the array appears effectively acoustically transparent; the incident sound will travel parallel to the slats and little scattering will occur. Consequently they may be better suited to situations in which the primary concern is sound arriving from a more specific direction. Overhead canopy arrays are an example of this; the sound predominantly arriving from a stage below the diffuser. Canopy arrays are often designed so that the reflected pressure is the same for all source and receiver pairs on a stage below, redirecting sound back to the stage in an even manner. Diffusing slat arrays could therefore potentially be used for this purpose. A similar structure, coined the 3D-grid diffuser, has recently been applied to the Tonhalle St. Gallen Concert Hall in Switzerland [79], comprising a series of vertically hung orthogonal square plates. Unlike the slat arrays here, however, these are regularly arranged with no gaps based on number theoretic sequences or similar.

If flat surfaces were used, single layer arrays with slats horizontally suspended above a stage would likely make poor canopy arrays. This is because canopies comprising flat surfaces will for some source and receiver pairs produce a strong specular reflection, whilst for others (where the geometric reflection point lies between panels) at high frequency result in much weaker scattering [3; 22]. This produces an uneven distribution of sound on a stage; an effect that would likely be made worse by constructing an array from runs of both slats and gaps. This is why canopy arrays are usually made of curved surfaces; to spread the reflections spatially and fill in the missing gaps.

A multi-layered design may make a more effective canopy array since it could provide much fewer specular reflection gaps. Furthermore, through the addition of depth a more even scattered pressure distribution results and the potential to reduce colouration on a stage

through temporal smearing occurs. It is likely however that the use of flat surfaces will still result in strong specular reflections off the front layer of a structure, and the bandwidth therefore would be limited. Consequently, as with the BAD panels, it is likely that curved elements would perform better.

7.2.3 Percolation diffusers

Examples of successful percolation diffusers have been presented in Chapter 5. In general however these form structures more like an array of scatterers than a series of complex tortuous channels. This is because in order to meet the -3dB scattered power design target at high frequency, line-of-sight is required through the array. This restricts the channelling allowed in an array. One possible way around this would be to construct an array which becomes gradually denser with distance into structure. This would provide an open structure with good line-of-sight through the outer sections of the array, and a potentially more tortuous centre. In addition this forms an equivalent to the impedance matching approach of the multi-layered slat arrays of Section 4.4.1, whereby with decreasing frequency sound is able to penetrate further into the array past the smaller outer elements. Such an array, however, would likely be quite large and also complex in design. This would make both construction and the search for optimal arrangements extremely difficult.

Since for a surface diffuser (providing absorption is negligible) the back-scattered power may be ignored during design, the line-of-sight is not an issue. Consequently more tortuous structures can be formed with surface diffusers. This for example was demonstrated by the percolation surface diffuser shown in Figure 5.15 (a), which resulted in significant diffusion at a frequency at least 2 octaves lower than would be expected due to overall depth. In general, however (as was found for the volume arrays), the high vertical element occupancy that forms the more tortuous channels of an effective low frequency diffuser will tend at high frequency to specularly reflect and produce poor high frequency diffusion. One way around this may be to again adopt a varying density approach. This would likely be based on a highly oversampled lattice structure whose elements become increasingly more sparse with distance into the array, forming tortuous channels that promote energy channelling over a range of wavelengths.

7.2.4 Cylinder array diffusers

From the three structure types presented it is the cylinder arrays that demonstrate the most promise. Unlike slat arrays the single layer structures result in more even scattering due to the behaviour of an individual cylinder. Consequently it is possible that canopy arrays based on cylinders could be used. Amplitude shaded arrays may be more suited to this application since they can more easily be altered to provide the required level of back-scattered power. Another alternative may be the application of the concept to surface semi-cylinder arrangements using absorbent patches to replace transmission. Consequently this would form a structure more like a BAD panel, offering partial absorption, though with curved reflecting elements. This is similar to the BAD design described above, though using curved elements rather than a curved panel.

The main limitation of the designs presented is the underlying periodicity, which due to spatial aliasing at the Bragg frequencies causes a reduction in scattered uniformity. Whilst alternate designs may be possible (considered further in Section 7.3.3), a structure based on periodicity is often desirable; for example for ease of manufacture. One solution is to vary the cylinder size to limit the periodicity problem, as discussed in Section 6.4.6, though this limits the cylinder size (relative to lattice spacing). Consequently for many arrays the -3dB scattered power design target cannot be met. In general however a suitable reduction in the severity of the Bragg peaks can be achieved through use of optimal sequences which sufficiently reduce the structural similarity.

7.2.5 A generalised volume diffuser

In general it has been shown that the most successful diffusers are those whose aperiodic Fourier properties are most desirable. For arrays based on unipolar sequences, such as the slat and cylinder arrays of Chapters 4 and 6 respectively, this is described by the Aperiodic Autocorrelation Function (AACF); the best diffusers being formed from sequences whose AACFs were most like a Kronecker delta function. For both the multi-layer slat arrays and the percolation diffusers of Chapter 5 the AACF was applied to the effective reflection coefficients of the structures. Again, diffusers with the most desirable Fourier properties tend to perform best. In both cases the AACF gives an indication of structural similarity, with the least self-similar structures being most desirable. This is due to the lack of self similarity

causing the scattered sound from different parts of an array to be most effectively broken up in phase.

In all cases a general rule of thumb is that at low frequency objects whose perimeter is comparable to wavelength are required to scatter sufficient power. At high frequency it is often the line-of-sight through an array that is important, though more generally it is the geometric angles of reflection in an array that are of significance. For example, for a slat array or square grid percolation structure for normal incidence, once wavelength becomes comparable to element width an increasingly more directional reflection results. Since this is directed back toward the source the scattered power is dominated by what the source can see, and a 50% line-of-sight is required. Conversely for a cylinder array or non-periodic percolation structure the natural angles of reflection will also forward scatter sound, and consequently the relationship is not necessarily as simple. For these structures a higher blocked line-of-sight is required.

Following from the above with increasing frequency a structure with many geometric angles of reflection is preferable, since these angles will scatter sound in many directions. In addition the provision of many reflection angles tends to make a more isotropic array; a diffuser being able to scatter sound evenly for many angles of incidence. A cylinder array is an example of the above, since cylinders scatter both very evenly and appear the same regardless of angle of incidence.

For multi-layer arrangements based on some underlying periodicity one of the limiting factors is spatial aliasing; when wavelength becomes comparable to the periodic spacing and scattering is emphasised in a specific direction. This is comparable to the flat plate frequencies observed in Schroeder diffusers when all wells reradiate in phase. This causes a sharp drop in diffusion. As above, this is best remedied by reducing the structural similarity, as this reduces the magnitude of the spatial aliasing lobes and causes them to be less severe. For arrays with elements that emphasise the scattering in these directions however, this effect is worst; for example slat arrays and square grid percolation diffusers whose inherent specular reflection coincides with the first Bragg peak. Consequently these structure types are generally limited to working below this frequency. In contrast arrays which provide many reflection angles (such as cylinder arrays) tend to be sparse and do not provide sufficient

power until just below this frequency. These arrays therefore are based around limiting periodicity and providing elements that are relatively large relative to wavelength that spread their scattering over many angles.

7.3. Further work

7.3.1 Improving metrics

Diffusion

Following from Section 7.2.1, the application of a volume diffusion coefficient could be further investigated to determine whether an improved metric could be defined. This for example could be extended to include a distance term to allow more accurate determination of the Fresnel zone boundaries. Whilst in the true far-field the metric should be independent of distance (as is the case presented here), for realistic distances this may allow more accurate determination of the width of the zeroth order lobe towards the back of a diffuser. Consequently, this could permit the use of less strict far-field conditions, allowing the use of a volume diffusion coefficient for measurement results.

Attenuation / absorption

In addition to the metrics considered, since transmission is possible, it may also be of interest to know the level of attenuation and / or absorption a diffuser provides. This for example could be of importance if the diffuser were placed in the path of a strong echo where high attenuation might be desirable. One way of assessing this would be to consider a similar metric to that of the back-scattered power from Section 3.4, though taking the total pressure toward the back of the array relative to that for the reference plate. This would likely be taken as an average over the Interfering-Scattered Zone (ISZ). Alternatively a more straightforward insertion loss as used in sonic crystal design for example could be used [24]. If absorption were considered then a measure of total power may be more appropriate. This, if diffusers were assessed in real rooms (see Sections 7.3.2), would likely have implications on parameters such as the Reverberation Time (RT). As with all the metrics presented, any attenuation or absorption value would ideally be flat over the performance bandwidth. A target value however, much like the -3dB value used for the scattered power, may be largely arbitrary and dependent on the diffusers application.

Other metrics

The intention is to create a volume diffuser that breaks up the incident energy both spatially and temporally. Throughout the thesis the former has been considered in terms of a volume diffusion coefficient, however the latter has been largely neglected; the diffuser types proposed assumed to provide scope for multiple scattering or energy channelling, and hence breaking up the scattered field in time. Previous studies into the temporal behaviour of surface diffusers include analysis of the decay characteristics of the scattered pressure via backward integration [80] and a measure of colouration in the total field based on a weighted autocorrelation technique [16; 81]. These metrics (or similar) therefore could be assessed to see if they measure the temporal diffusion from a volume diffuser.

The autocorrelation method above is a technique first proposed by Bilsen [81], in which the time dependence of a reflections audibility is taken into account. Initial investigations into the use of this metric for one of the cylinder diffusers presented indicate that similar performance to a more conventional surface Schroeder diffuser can be achieved. An example of this is illustrated by Figure 7.2 (top) for the hexagonal amplitude shaded cylinder array from Section 6.5.2. This is compared to that for five periods of a length seven Quadratic Residue Diffuser (QRD) Figure 7.2 (bottom); a surface diffuser of the same width ($D = 1.6$m) and with a design frequency of $f_0 = 500$Hz. These are expressed as maps giving the colouration value over a 10m×10m area around the diffuser. Colouration values were acquired from time domain data, obtained via an Inverse Fourier Transform (IFT) of the frequency domain data [63]. Note this is a normalised version of the colouration metric proposed by Bilsen, and hence a value of one indicates audibility. For most receiver locations approximately 2m or more away from the cylinder array (excluding the shadow zone to the back of the diffuser) the volume diffuser results in either inaudible (<1) or relatively low (<2) colouration values. This in the back-scattered region is comparable to the values obtained for the Schroeder QRD of Figure 7.2 (bottom). Since a Schroeder diffuser is able to break up reflections in time, this suggests that a cylinder array can also do this. These however are only initial findings and the application of the metric itself is relatively untested and should be applied with caution [3]. Nonetheless there is scope for further investigation in this area.
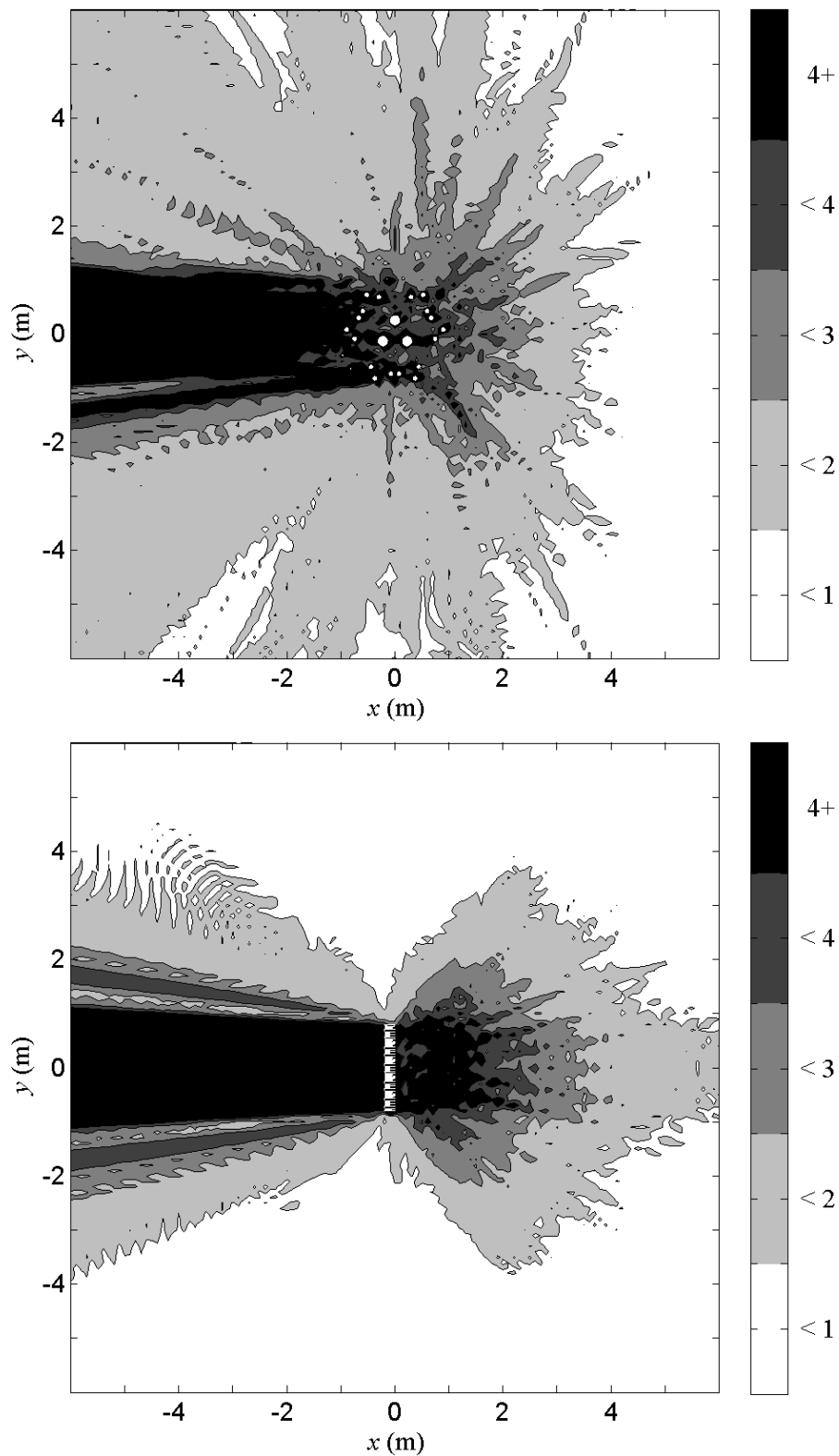
Figure 7.2: Bilsen's (normalised) colouration metric (from prediction models) for the amplitude shaded cylinder array shown in Figure 6.23 (top) and 5 periods of a length 7 QRD Schroeder diffuser (bottom); D = 1.6m, $\theta_0 = 0°$

7.3.2 Testing application

The diffusers considered throughout the thesis follow a design procedure that, as is often found in diffuser design, is based on a free-field assumption [3; 28]. For example in surface diffuser design the scattering is regularly considered for a diffuser alone; attempting to both understand and quantify behaviour, whilst allowing a more generalised design that is independent of any space that it may be installed within. The application of surface diffusers in enclosed spaces has been studied extensively [2; 3; 5] both subjectively and objectively, and have been found to reduce colouration and distortion, promote spaciousness and suppress the effects of strong reflections. In a similar way, if a volume diffuser is to be used as an acoustic treatment it is necessary to know what affect they might have in a room.

Simulated results: Diffusive efficacy and Lam's method

Whilst the more subjective effects of introducing a diffuser into a space are beyond the scope of this work, it is possible to perform an initial test on a modelled space to determine whether or not a volume diffuser shows promise. This is presented below in terms of diffusive efficacy; that is the ability to produce a diffuse field in an otherwise non-diffuse space.

Consider a rectangular room with absorption along one wall only. The space will be non-diffuse; some early energy will be removed from the space by the absorber, though there will be some sound propagation paths that never interact with the absorbent. Consequently the Reverberation Time (RT) for these reflection paths will be excessively long. By introducing diffusers to the room however, sound is scattered into the absorbent and the RT drops. This idea is the basis for Lam's method [49], which is broadly as follows. The RT of a physical space is both measured and modelled, adjusting the properties of the modelled space until the closest match is achieved. This is firstly carried out for the case with no diffuser(s) present in order to provide a baseline measurement and to allow the properties of the empty space used in the model to be tuned for optimal agreement. Once this is achieved the diffuser(s) is introduced and a second set of modelled and measured results is obtained, measuring how much more diffuse the sound field becomes. The model parameters for the diffuser(s) are then altered until the closest match is achieved.

Though the method above is intended to quantify the behaviour of an individual diffuser, it may also serve as a direct comparison between diffuser types. Hargreaves [49] for example noted that whilst the matching of modelled and measured results was subject to large uncertainties, the general effect of introducing a sample was to reduce the RT, and (providing the absorption of the samples is comparable) their values offer a form of empirical rank of diffusive efficacy.

To provide an indicator of effectiveness, a simulation comparing a volume diffuser to a more conventional surface diffuser was carried out using a non-diffuse space created according to Lam's method described above. Consider the 2D room shown in Figure 7.3. The top wall has an absorption coefficient of $\alpha = 0.95$, with all remaining surfaces (including diffusers) unless otherwise stated having an absorption coefficient of $\alpha = 0.05$. This was done so that energy was removed at each reflection, ensuring a finite decay. A number of separate models were run, each including either one of the diffuser types shown or no diffusion at all. The pressure field in the room was calculated using the Boundary Element Method (BEM) introduced in Section 2.3.1, with time domain values obtained via an Inverse Fourier Transform (IFT) of the frequency domain data [63]. One-third octave band results were obtained through use of a series of 6th order Butterworth band-pass filters, designed according to the ANSI S1.11-1986 standard [82] and implemented in MATLAB using a freely available routine [83]. The calculation of the RT broadly follows the procedure given in BS EN ISO 354:2003 [18], with valid receiver locations (being at least 1m away from the nearest surface) given by the shaded region in Figure 7.3. Due to computation time however, only one source position was used.

The diffuser simulations were as follows:

- Plain room – no diffusion.

- Schroeder diffuser 1 – eight periods of a QRD Schroeder diffuser with a design frequency of 500Hz installed on the central half of the far right wall.

- Schroeder diffuser 2 – sixteen periods of a QRD Schroeder diffuser with a design frequency of 500Hz filling the entire far right wall.

- Volume diffuser 1 – the cylinder array as per Figure 2.27 situated towards the right hand side of the room.

- Volume diffuser 2 – the cylinder array as per Figure 2.27 situated towards the right hand side of the room, with rigid cylinders ($\alpha = 0.00$).
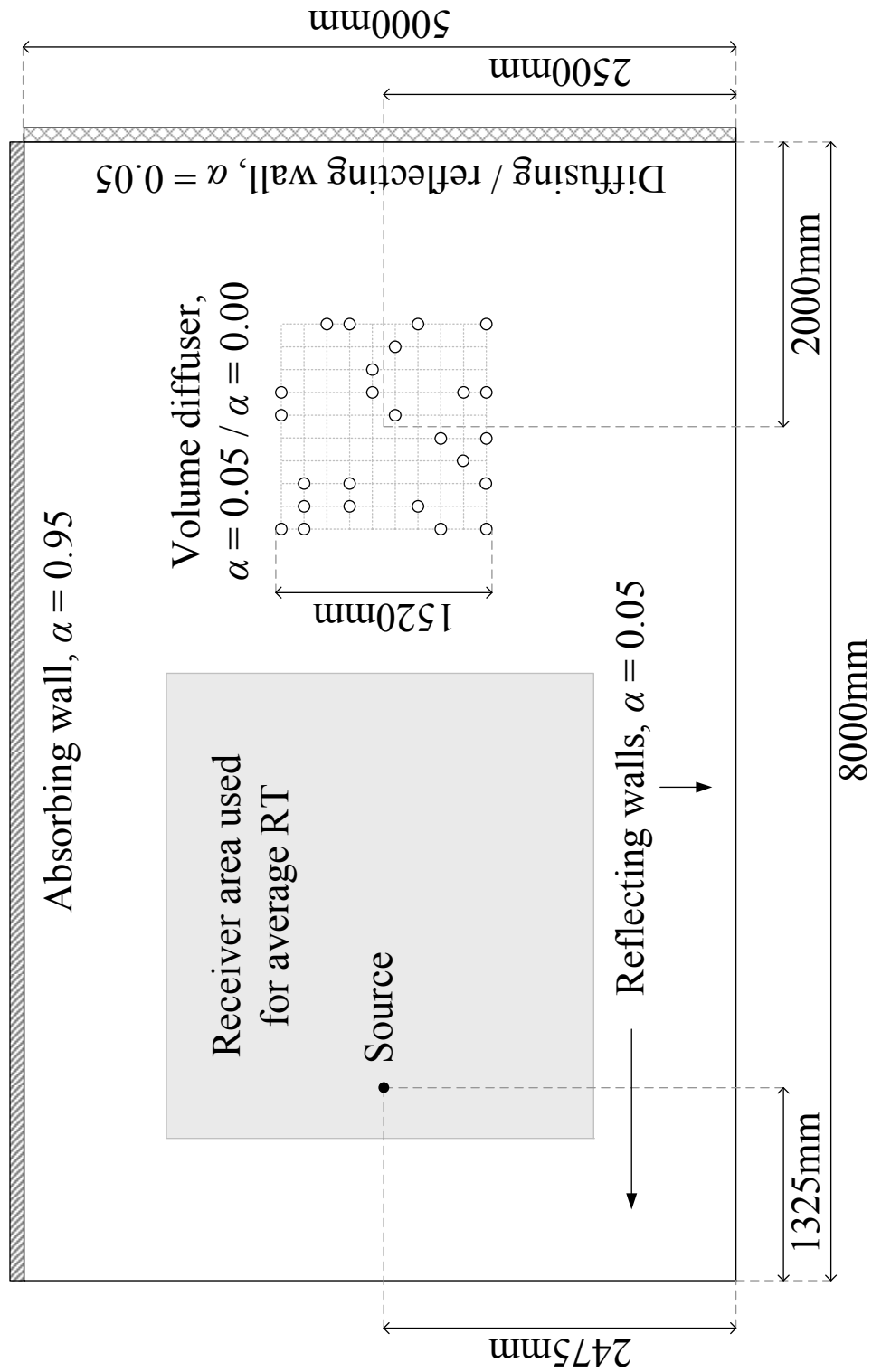
Figure 7.3: Rectangular room dimensions used for BEM simulation

Note the Schroeder diffusers here have been modelled using a spatially-varying impedance surface. This has been shown previously to provide a close approximation to a full thin panel BEM solution [3] for normal incidence, and below the cut-off frequency (when half a wavelength is greater than well width, which is the case for all frequencies modelled). The prediction will however be less accurate for oblique incidence sources due to failing to take into account the surface pressure interactions. Since in the model sound may be incident from all directions this is an inherent limiting factor. A spatially-varying surface though, whilst not predicting the exact behaviour of a physical QRD, will nevertheless provide spatial diffusion for these source angles. Consequently they should give an indication of the expected effect on the RT from a surface diffuser.

Figure 7.4 shows the effect on reverberation time for the modelled room. The plain room results agree with previous findings from Yasuda *et al.* [84] who found that (assuming an absorption coefficient independent of frequency) the RT in a room with unevenly distributed absorption will tend to increase with frequency. The introduction of diffusion results in a reduced RT in the mid-to-high frequency range, as was found by both Hargreaves [49] and Yasuda *et al.* [84], with the latter concluding that this occurred once a wavelength became comparable to diffuser dimensions. The volume diffuser shows that a diffusing structure in the centre of a room demonstrates promise, as like the conventional diffuser examples it too brings down the RT, indeed more so than the equivalent area of Schroeder diffusers on a wall.

It could be argued that since the objective is to create as diffuse a field as possible, the ideal RT would be that predicted based on a diffuse field assumption. This is most commonly obtained through the use of either Sabine's or Eyring's equations. Redondo *et al.* [85] and Wells *et al.* [86] independently demonstrated that the RT in two dimensions according to Sabine's and Eyring's formulations respectively may be given as:

$$T_S = \frac{\pi}{2} \frac{0.161 S_r}{L_r \overline{\alpha}}$$
7.1

$$T_E = \frac{\pi}{2} \frac{0.161 S_r}{L_r \ln\left(1 - \overline{\alpha}\right)}$$
7.2
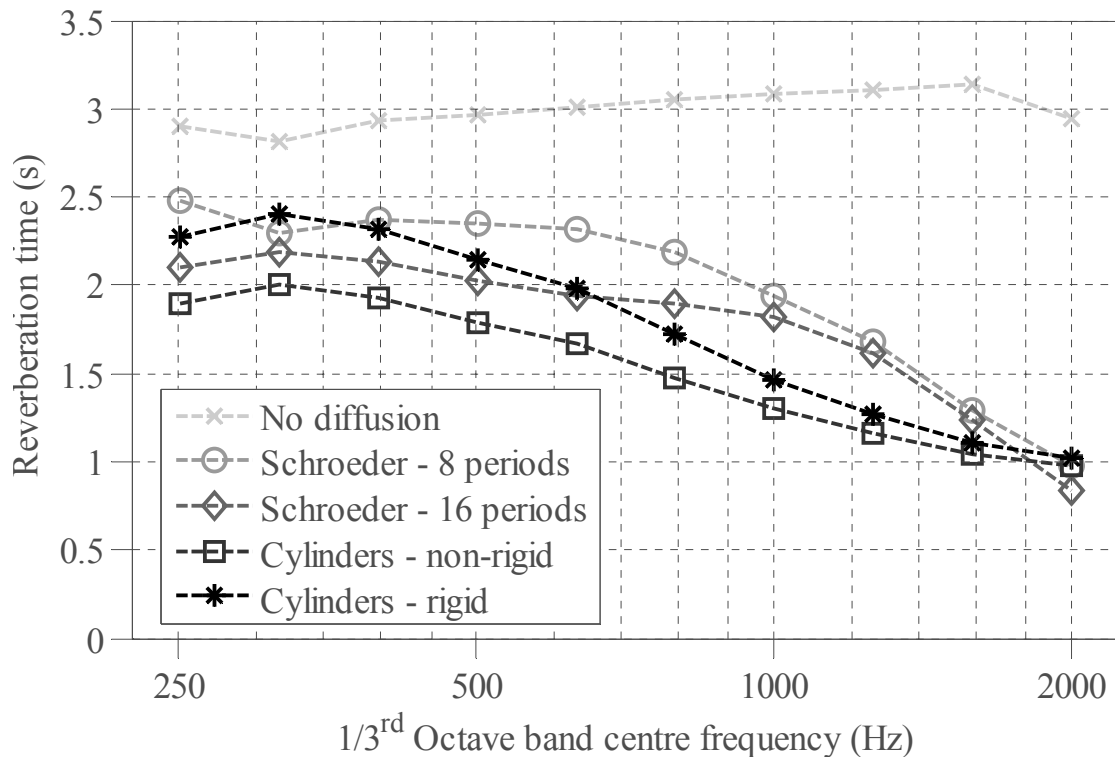
Figure 7.4: Effect on reverberation time when a number of diffuser types are introduced to a rectangular room with one near fully absorbing wall (Lam's method) as per Figure 7.3; predicted using the BEM model

Where S_r is the area of the 2D room (the equivalent to volume); L_r is the total length of the room surfaces (the equivalent to surface area); $\bar{\alpha}$ is the mean absorption coefficient of the room surfaces; and T_S and T_E are the reverberation time according to Sabine's and Eyring's equations respectively. The original form of the Eyring equation is used here which considers the arithmetic mean absorption coefficient, since the large absorption value of the absorbing wall will produce unreasonably low RT values when considering a Millington-Sette solution [16]. Note a simple adjustment of a factor of two has been applied to the formulae above, since their original derivations both assume a spherically radiating source. This is because for the case of a cylindrically spreading source used in the 2D model, the field will decay at half the rate. The predicted reverberation time for the empty modelled room is 1.19s and 0.98s for the Sabine and Eyring formulations of Eqs. 7.1-7.2 respectively. Strictly speaking the introduction of the volume diffuser both decreases volume and increases surface area, though the effect is only small, resulting in predicted RTs of 1.14s and 1.19s for Sabine's equation

and 0.98s and 1.02s for Eyring's equation for the part absorbing and rigid cylinder diffuser cases respectively.

At low frequency the diffusers are ineffective, since this is below the lowest frequency at which they are designed to operate. With increasing frequency the diffuser results tend towards an RT time approximately in the region of that predicted by the Sabine and Eyring formulae. In terms of reducing the RT, the volume diffuser examples are slightly more effective than the Schroeder diffuser examples across the majority of the bandwidth. This is despite having a higher design frequency of approximately 1kHz (see Section 6.4.3), compared with a design frequency of 500Hz for the Schroeder diffusers. In addition the width of the volume diffuser is less than both of the Schroeder diffusers.

It should be noted that care should be taken to ensure that any diffusing surfaces are as rigid as possible. This is particularly relevant if the efficiency of a volume diffuser is high, since if the interaction of the diffuser with the pressure field is large then it follows that so too is its potential to absorb. This is demonstrated in Figure 7.4 where it is clear that the partially absorbing array produces a somewhat lower RT relative to the rigid case than would be expected, particularly at low frequency. Of course these results alone are insufficient to draw any firm conclusions from, but they serve to demonstrate the potential of a volume diffuser.

Other simulation methods

The initial findings from the modelling of a volume diffuser in a room presented above indicate that a similar performance to that of a more conventional surface diffuser may be achieved. These however are initial findings, and further investigation is needed to draw more firm conclusions. Possible studies into more application specific scenarios include:

- The performance of an array close to a reflecting boundary – since a volume diffuser in a real room may be situated close to a wall or ceiling it would be useful to understand how this affects a sound field. For example when the distance to a surface is comparable to wavelength the interaction with the reflections from the surface may harm or even improve diffusion. Also, as sound has to pass through an array twice a more open structure which scatters less power may be required. This could be assessed by using a method similar to that used in overhead canopy design, where the scattered uniformity is

assessed over a number of receiver positions [3; 21]. For example a diffuser suspended from a ceiling in an auditoria would ideally create a more even sound field over an area representative of an audience below. This could be modelled using a Boundary Element Method (BEM) by using a modified version of the Green's function [3] allowing relatively fast prediction times. Additional metrics such as a measure of colouration or temporal decay as described in Section 7.3.1 above could also be considered.

- Performance in an enclosed space – this is similar to the investigation presented though it is likely that for large spaces, due to computation times, accurate methods such as the BEM will be limited to low frequencies. For higher frequencies a geometric room acoustic model could be used. This models the sound as a series of beams or rays, assuming the wavelength to be much smaller than any dimension within the room [3]. These models have been used to model the diffuse reflections from surfaces by modelling reflections according to Lambert's law [87]. It is possible however that a similar method could be applied, modelling a volume diffuser as a single structure which redistributes its energy following similar principles. This would require investigation into how best to model a volume diffuser in a geometric model, perhaps incorporating more accurate free-field BEM predictions. Whilst this would be less accurate, the predictions would be quick, and may help inform where the best place to locate a volume diffuser is. As with the above this method could be assessed in terms of uniformity of the sound field, both spatially and with frequency, as well as considering the effect on parameters such as the RT.

Physical measurements

In addition to the above if volume diffusers are to be used it will be necessary to consider how they perform in a real room. One example of this would be to consider the effect of introducing volume diffusers (as described in the thesis) to reverberation chambers, to see whether they could be more effective at creating a diffuse field than the current curved panel and/or rotating vane diffusers usually used. For large spaces such as auditoria if an installation was commissioned then full scale measurements would be possible, however initially scale model simulations [88; 89] would be most practical. This would allow the influence of a volume diffuser to be assessed in a similar manner to that described above, indicating where they may most effectively be used.

7.3.3   Improvements to existing designs

Slat arrays and percolation structures

As was suggested in Section 7.2.2, one of the principle problems behind the design of a slat array is their use of parallel flat surfaces. One solution, therefore, may be to investigate the curving of these arrays to spread the specularly reflected sound at higher frequencies. An additional restriction is that these arrays tend to be highly dependent on angle of incidence; a grazing incidence source seeing an effectively acoustically transparent array. Whilst curving an array may help, a more isotropic volume diffuser would ideally have rotational symmetry to its underlying structure, allowing a similar appearance regardless of the angle of observation. An initial study into layers of slats arranged in concentric circles has demonstrated the potential of such an array to provide much higher levels of diffusion. As with the slat arrays presented, layers were created based on unipolar sequences with desirable Fourier properties. This structure is similar in concept to the non-periodic percolation structures of Section 5.5.6, providing a range of reflection angles and propagation paths, though with the introduction of number theoretic sequences. Consequently slat / percolation arrays based on lattice shapes such as this provide scope for further work, in particular in the development of more intelligent methods for their construction.

Low frequency percolation diffusers

Percolation structures which provided very low frequency diffusion were shown in general to result in a narrow bandwidth. This however is to some extent limited by the frequency range over which effective channelling into an array occurs; when wavelength is large compared to channel width. Consequently by considering highly oversampled percolation lattices it may be possible to avoid this problem; providing tortuous paths comparable to a range of wavelengths. This, as was suggested previously may be best achieved through a varying density design to allow some line-of-sight through the array. This however would need investigating further.

Cylinder arrays

Whilst cylinder arrays have been presented which result in a high level of performance, their main restriction is due to spatial aliasing. The effect of the Bragg frequencies may be

significantly reduced by limiting spatial similarity; however they are not removed entirely. In addition the least self-similar structures tend to be sparse, reducing the influence of multiple scattering and hence the level of temporal smearing. Consequently structures based on a more arbitrary arrangement could be investigated. An initial study into such arrays has indicated that, as with arrays based on a periodic arrangement, the structures with the least self-similarity tend to perform best. An example of a few of the cylinder array types modelled is shown in Figure 7.5, showing their arrangements (top) and volume diffusion coefficients (bottom). These arrangements are based on an aperiodic Penrose tiling [90] (cylinders centred on centres of thin rhomboids only) (a), a 3rd order Apollonian gasket fractal [91] (b) and a logarithmic spiral based on the golden angle [92] (c). It is evident that whilst each structure has potential to diffuse (the performance being comparable to some of the better periodic based cylinder arrays), there are frequencies at which diffusion still suffers. At low frequency this is particularly evident for the Penrose tiling array, since its aperiodic arrangement still displays localised similarities. Further consideration is needed to ascertain whether or not these structures can offer improvements, and if so how more optimal arrays may be created.

7.3.4 Developing the 3D volume diffuser

This thesis has considered the design and implementation of a 2D volume diffuser. This provides a simpler means of approach, and allows for faster computation times and a more straightforward development of design concepts. In practice these arrangements equate to a structure varying in two dimensions, analogous to planar surface diffusers, resulting in scattering in one plane only. Such structures could potentially have a valid use as volume diffusers, though are inherently limited, and ideally a structure should provide scattering in all directions. Potential avenues for extension of the work presented are therefore discussed below, considering equivalent / semi-equivalent 3D structures.

Arrays of slats / percolation structures

A literal translation to 3D for the slat arrays presented would be a simple array of square / rectangular panels similar to those seen in canopy arrays and in hemispherical BAD surface panels [3; 14]. A multi-layer example of this is illustrated in Figure 1.4. This could be extended to include alternative base shapes / arrangements, such as hexagonal panel arrangements, potentially derived from square lattice arrangements using the transformation

matrix method from Section 6.5. These however would make structures more akin to canopy array rather than an isotropic volume diffuser.
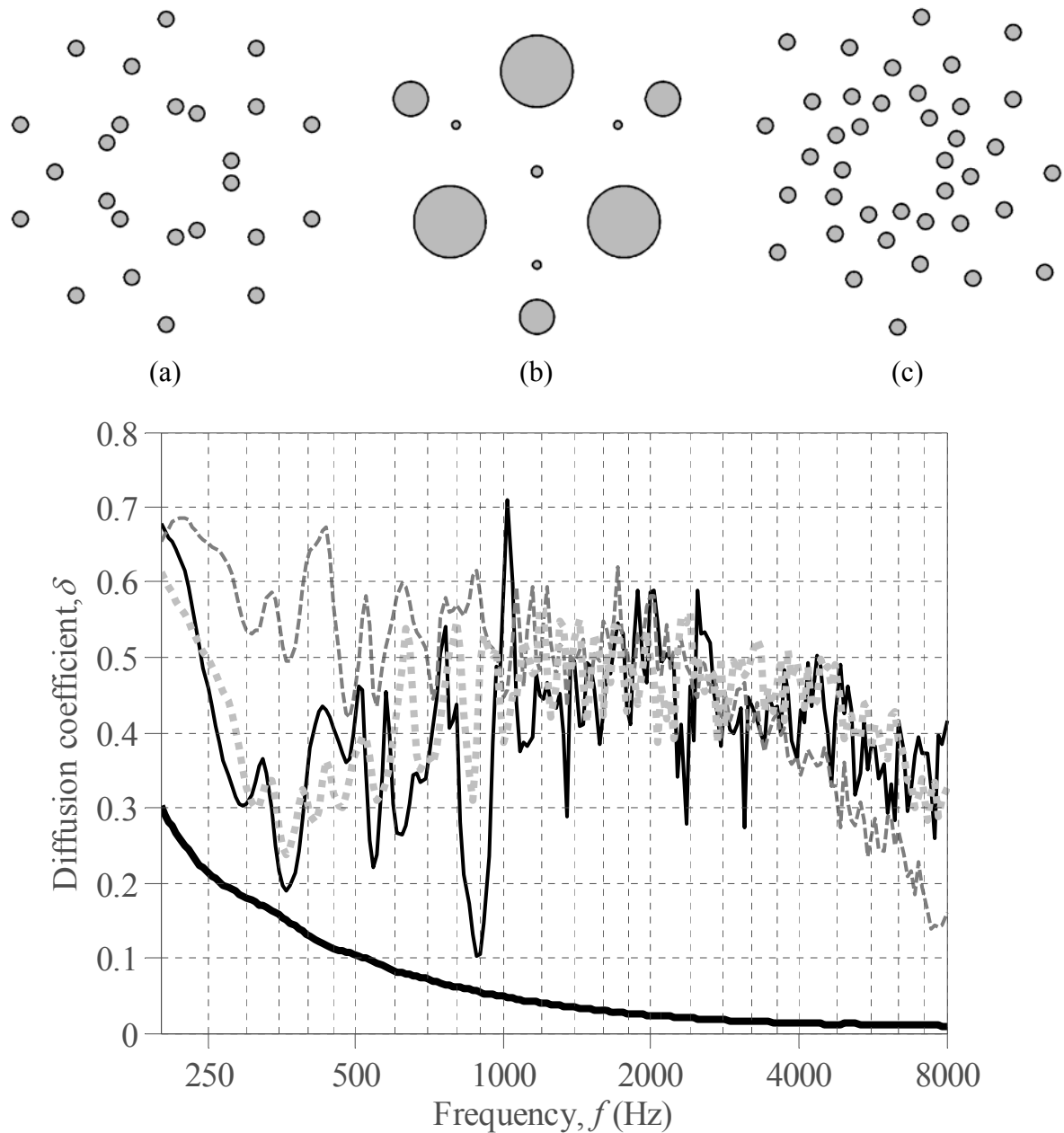
Figure 7.5: Modelled diffusion coefficient (bottom) for cylinder arrays based on a Penrose tiling arrangement (a) (━), an Apollonian fractal (b) (─ ─) and a logarithmic spiral (c) (- - -); $\theta_0 = 0°$, D = 2m; diffusion coefficient of flat plate (▬) shown for reference

Forming a more isotropic array means introducing slats of different orientation. As with the 2D slat arrays this suggests structures more like a percolation structure. A 3D percolation structure would be extremely complex, particularly a complex channelling structure, and so it

is likely that further findings from the 2D case must be found in order to establish what forms an effective percolation structure. An intriguing possibility in 3D is that paths may now overlap without necessarily joining together, since propagation paths may now pass over one another. This means that separate tortuous channels may be possible that do not take up the whole array and stop other channels from being formed. Consequently a 3D structure may provide much greater potential for low frequency diffusion. This however remains untested, and so would need investigation.

Arrays of spheres

The most effective designs presented have been the cylinder arrays; providing a both high level of performance and a relatively simple design concept. A 3D extension to this concept would likely comprise an array of spheres. Spheres scatter in a similar manner to cylinders, though spreading sound in all directions rather than in just one plane. Like the cylinder, their spatial distribution of reflected pressure becomes increasingly more uniform with frequency, though temporally scatters much like a flat plate. Consequently a method is required to break up an incident wavefront in phase which, like the cylinder case, is made possible by using multiple spheres to form an array.

An initial study into sphere arrays was carried out, with arrangements based on a 3D cubic periodic lattice. An example is shown in Figure 7.6, which shows the arrangement (top) and 3D volume diffusion coefficient (bottom) for an array of spheres based on an $N = 17$ Lempel L_2 Costas array. The arrangement was obtained from the cross-product of two orthogonal versions of the same Costas sequence. For simplicity the standard back-scattered diffusion coefficient has been used. The results were modelled using a 3D BEM routine [3] similar to that presented in Section 2.3.1 [32]. Spheres were modelled using a hierarchical triangular mesh [93]. Due to computational restrictions BEM predictions were limited to low frequencies. Results obtained through a 3D Fourier approximation are also shown. This was carried out using a method similar to that presented in Section 6.4, though with the scattering from an individual cylinder replaced with that of a sphere [30], and with the summation altered to include variation in the third dimension (including angle of elevation of the source, φ_0, and lattice spacing in the z (third) dimension, d_z).
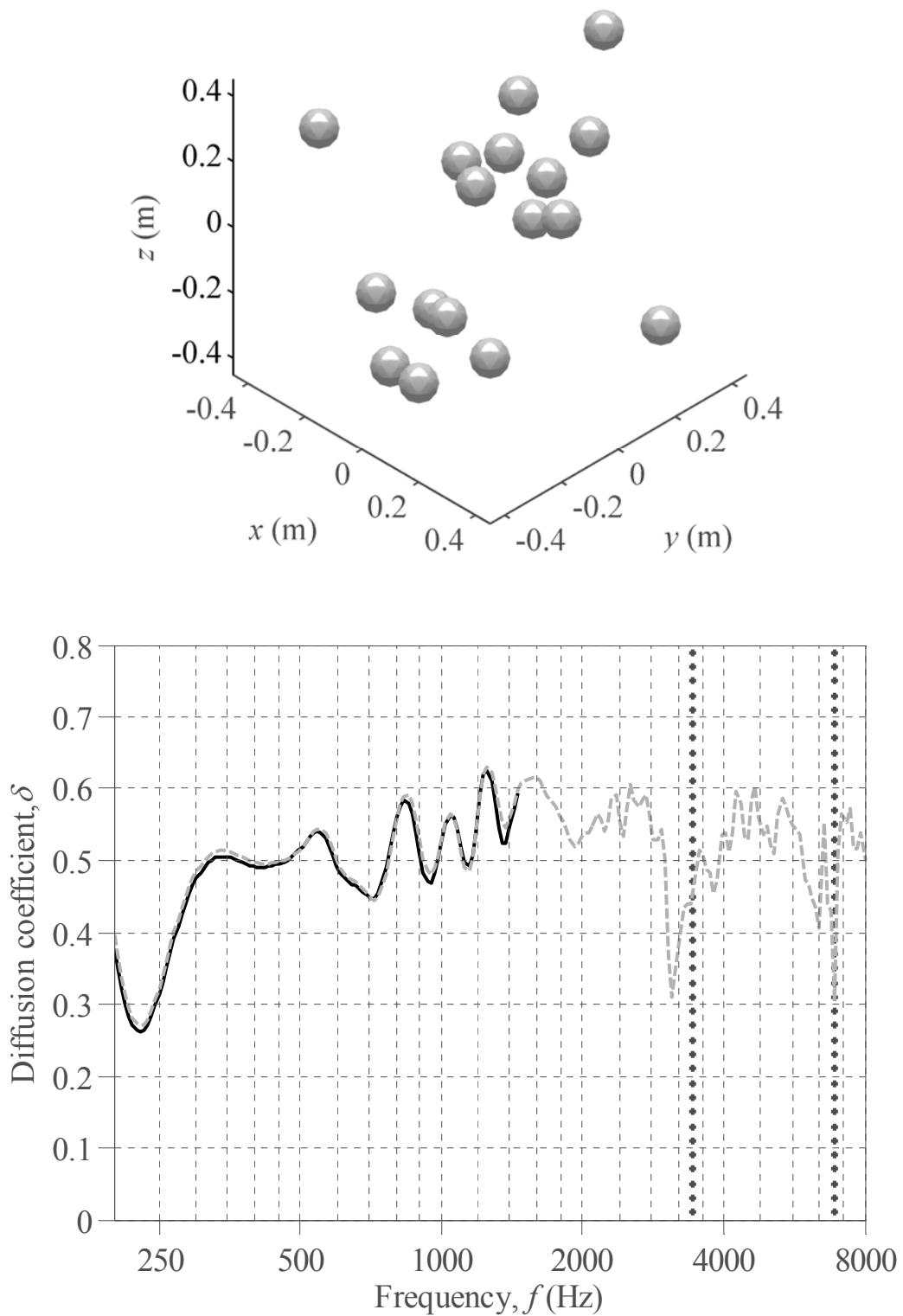
Figure 7.6: Arrangement (top) and 3D back-scattered diffusion coefficient using a BEM model (━) and a Fourier approximation (━ ━) and including predicted Bragg frequencies (•••) (bottom) for an array of spheres based on a 3D square lattice arrangement; $\theta_0 = 0°$, $\varphi_0 = 0°$, $d_e = 10cm$, $d_x = d_y = d_z = 5cm$

The array shown in Figure 7.6 (top) has no redundancies; that is the vector separation between any two spheres is unique. It can be seen from Figure 7.6 (bottom) that, as with the most successful cylinder array designs, the array is able to diffuse well. At low frequency the Fourier model provides a close approximation to the BEM results, though this is likely helped by the relatively low occupancy. The periodicity traits observed in periodic cylinder arrays also seem to apply in three-dimensions; a 3D extension to the Bragg frequency formula given by Eq. 6.13 predicting the first Bragg peak to occur at a frequency of $f = 3.44$kHz (Eq. B.17 in Appendix B). It is likely therefore that the self-similarity findings from 2D arrays will also apply to 3D volume diffusers. This however requires further investigation.

Other areas

In addition to the above the extension to 3D will require further study in several areas. These include the development of equivalent modelling and measurement procedures, and of metrics for analysis. Since 3D models such as the standard BEM may be limited to low frequencies, acceleration schemes or alternative models may need to be considered. In addition a 3D diffuser may allow structures for which 2D equivalents are not possible (for example the percolation 'tube' structure described above). This therefore allows the possibility for new types of volume diffusers to be examined.

8. CONCLUSION

The use of diffusers in acoustics is well established; however they tend to form a surface based treatment. This work has considered a different type of diffuser; a volume diffuser located in the body of a room. A volume diffuser may provide the potential for greater efficiency since, unlike a surface diffuser, it is able to operate on the full hemispherical space. Although some volume diffusers do exist, for instance in reverberation chambers, these tend to be limited in their application. Consequently the work presented here has focussed on the design of a more versatile diffuser, suitable for use in a range of acoustically sensitive environments.

To assess the behaviour of a diffuser, Chapter 2 presented methods for both modelling and measuring a volume diffuser. This extended more conventional procedures commonly used for surface diffusers. Models were introduced that were exploited throughout the thesis, based on both a simple first order scattering Fourier approximation, a more accurate Boundary Element Method (BEM) and Multiple Scattering (MS) techniques. To quantify the models' accuracies, measurements were carried out for each of the diffuser types presented in the proceeding chapters, with each being shown to agree well with measured results. A procedure was developed for receivers close to the back of a volume diffuser, where the standard time windowing techniques used for surface diffuser measurements cannot be applied. This involved the use of a cross-correlation oversampling method to ensure the more accurate estimation of the time of flight, allowing a more accurate separation of the incident and scattered sound.

Suitable metrics were considered in Chapter 3 for diffusive efficacy and power. Building upon the standard diffusion coefficient currently used for surface treatments, the concept was extended to produce a volume diffuser equivalent. This provides a frequency dependent single figure of merit describing scattering uniformity. This volume diffusion coefficient required modifying the existing surface diffuser metric since, due to allowing diffraction around and/or transmission through a structure, the scattered field towards the rear of a volume diffuser changes from reflected to interfering scattering. As the transition between the two behaviour types cannot be described by a simple geometric model, a frequency dependent descriptor was developed defined in terms of Fresnel zones. This, for far-field receivers, was shown to give

consistent values. In addition a measure of scattered power was introduced to provide a measure of scattering efficiency; necessary due to a volume device allowing transmission.

Using the methods above, a volume diffuser based on an array of slats was investigated and presented in Chapter 4. These were based on periodic arrangements and form an extension to surface amplitude diffusers such as the Binary Amplitude Diffuser (BAD), though replacing absorption with transmission (gaps). Consequently, as was illustrated from measurements, the two structures back-scatter in a very similar manner. Both single layer and multi-layered structures were investigated, using number theoretic and array theory concepts to determine slat arrangements; selectively removing or varying the size of the individual slats in an array. The best multi-layer structures were shown to provide typical diffusion coefficient values ranging from 0.1-0.4 (relative to the equivalent reference plate) and scattered power values falling within approximately ±1dB of the -3dB target value over an approximate 4 octave bandwidth.

Based on number theory, aperiodic unipolar and amplitude shading sequences were obtained to determine arrangement. These are different to the periodic sequences more commonly used in diffuser design. Optimal 1D slat diffusers were those whose Aperiodic Autocorrelation (AACF) properties are most desirable, implying a lack of self-similarity. At low frequency runs of (conjoined) slats on the order of a third of a wavelength are required in order to scatter efficiently. Conversely once wavelength becomes comparable to the size of these runs, its scattering becomes more directional. This limits the operational bandwidth of a single slat run, and consequently a range of sizes is required. At high frequency the level of back-scattered power is controlled by line-of-sight through the diffuser, requiring a 50% fill factor to achieve the -3dB target. The best arrangements for diffusion however are both short and sparse, and therefore tend to scatter inefficiently at low frequency. There is therefore a trade-off between the degree of diffusion and the low frequency scattered power.

Multi-layer slat arrays offer improvements due to the addition of depth, allowing cancellation of the back-scattered specular lobe. Once sufficient power is scattered however, due to the narrow bandwidth between when a slat efficiently scatters in a more even manner and when it directionally reflects, little sound is able to propagate into the structure. Consequently performance is dominated by what the source can see, with structures requiring both large

elements and a large open area – two conflicting properties. An array acts much like its equivalent Schroeder diffuser, producing the equivalent of flat plate frequencies due to spatial aliasing when half of a wavelength fits into lattice spacing. In addition due to having open sides this effect varies with angle, causing a form of acoustic iridescence. An alternative structure was therefore presented whereby layers comprise progressively larger elements from front to back, allowing both a range of element sizes and a 50% line-of-sight through the array. This allows sound to propagate further into the array, depending on frequency. In addition, use of oversampling and non-periodic layer spacings were shown to avoid the effects of spatial aliasing within the designed bandwidth. This extends the number theoretic concepts used to determine the depths of an array.

Chapter 5 investigated the use of an alternative diffuser based on a percolation fractal structure. These form a similar structure to an array of slats, though allowing elements of different orientation. This provides potential for channelling sound into an array, producing larger phase changes and hence increased diffusion. In addition, unlike arrays of slats, a more isotropic array may be formed. Structures based on square and triangular periodic lattices were studied before arrangements based on non-periodic lattices were considered. Due to structural complexity, results were presented from a series of Monte Carlo simulations, from which characteristics of a variety of structure types were obtained. Examples of non-periodic percolation diffusers were shown to provide a diffusion coefficient of approximately 0.3-0.5 above the reference plate and a back scattered power value within approximately ±1.5dB of the -3dB target over an approximate 3.5 octave bandwidth.

Initial structures were considered based on a square lattice. At low frequency, below the point at which approximately a half of a wavelength fits into channel width, this structure was shown to allow propagation of sound around corners. This can be used to obtain large phase shifts via complex tortuous paths, though following from Fermat's principle, only when no shorter alternative route exists. Due to these tortuous paths, it was shown that both surface and volume percolation diffusers were capable of diffusing effectively 1-2 octaves below that expected due to overall depth alone. This was best achieved by diffusers with high vertical element occupancy, since these promote lateral propagation and the channelling of sound. In contrast at high frequency a much lower vertical occupancy was required since, once half of a wavelength becomes comparable to element size, little lateral propagation occurs and then a

range of depths is important. Consequently, there is a trade-off between low and high frequency diffusion. In each case channelling into the array is desirable and a high occupancy of horizontal elements is preferred.

At low frequency the most efficient volume diffusers were those comprising tightly packed complex channels. This was illustrated through a measure of tortuosity based on the 'ant in a labyrinth algorithm'. Due to their small range in propagation paths however their diffusive bandwidth is very narrow. In addition due to their high element occupancy structures tend to produce a back scattered power value of approximately 0dB. At high frequency, on the other hand, the best diffusers were those whose 'apparent' well depths result in a set of reflection coefficients with desirable AACF properties. This is due to the directional scattering of a single element; with the structures behaving similarly to the periodic layer spacing slat arrays of Chapter 4. Consequently the same problems arise of incompatible low and high frequency requirements.

By considering alternative lattice shapes it was shown that at high frequency the angle of orientation of elements is important. For a periodic array this results in a distinct set of 'allowed' reflections, and hence uneven scattering. Through use of structures made up of a large number of these orientations however, and by promoting reflection angles which channel sound into an array, more even scattering results. In addition the removal of any underlying periodicity eliminates the effects of spatial aliasing. The best structures however tend to be sparse, and therefore act much like an array of scatterers rather than a tortuous waveguide.

Whilst some arrangements are effective, the slat and percolation structures of Chapters 4-5 respectively are inherently limited by the directional scattering of a flat element. Chapter 6 therefore considered a final diffuser type based on an array of cylinders; an element that scatters in a more even manner. Both single layer and multi-layered structures based on a rectangular and hexagonal lattice were investigated. By removing or altering the cylinder size, diffusers resulting in a diffusion coefficient on the order of 0.3-0.5 above that of the reference plate and a back-scattered power value within approximately ±1dB of the -3dB target were achieved over a bandwidth of at least 5 octaves.

The most even scattering tends to be produced by arrangements based on sequences whose AACF properties are optimal. At low frequency cylinders on the order of approximately a quarter of a wavelength in diameter are required to scatter efficiently, whilst at high frequency scattered power is approximately dictated by line-of-sight through the structure. For single layer structures based on optimal unipolar sequence arrangements this means that the -3dB intensity ratio target cannot be met. By varying the cylinder size through amplitude shading however, fuller arrays may be formed that scatter sufficient power. This, however, tends to result in decreased low frequency diffusion due to an individual cylinder not scattering proportionally to is size and the inherent structural similarity of a full array. Consequently, performance is a trade-off between low frequency diffusion and high frequency scattered power.

The introduction of depth in multi-layered structures allows increased diffusion due to cancellation of the back-scattered specular lobe. When wavelength becomes comparable to lattice spacing however, the inherent redundancy produces strong directional reflections (Bragg scattering). This tends to roughly coincide with the point at which a cylinder begins to scatter efficiently. Consequently at low frequency an array diffuses well though with limited scattered power, whilst at higher frequencies it scatters sufficient power though with reduced diffusion due to the underlying periodicity. This limits the bandwidth of performance to less than an octave.

Diffusion is significantly improved by limiting structural similarity, reducing the effects of Bragg scattering. In addition by producing an effectively oversampled sparse array a cylinder size greater than lattice spacing is allowed, extending the bandwidth of performance by effectively increasing the frequency of the first Bragg peak. An example of this was achieved by using Costas sequences. Additional performance gains may be obtained by transforming to a hexagonal lattice, providing more isotropic behaviour due to the threefold rotational symmetry. Further improvements to both the diffusion and scattered power performance of these arrays can be achieved through amplitude shading, using a variety of cylinder sizes.

In general, as discussed in Chapter 7, the most successful diffusers are those which have some objects on the order of approximately a wavelength in perimeter, display low structural similarity and provide surfaces with a broad range of reflections angles. This allows sound to

be scattered with sufficient power and in a more even manner. A brief analysis of a volume diffuser modelled in a room suggest that there is potential for their use as an effective diffuser. Further investigation is required, however, to determine whether or not a volume diffuser may be successfully applied in a real room; likely requiring a combination of both application specific modelling and measurements, and the extension of the findings presented to three dimensional structures.

APPENDIX A

The following is a derivation of the Specular Zone (SZ) / Geometric Shadow Zone (GSZ) solid angle, φ, referred to specifically in Section 3.2.2 (Eq. 3.1). Consider the diagram below, depicting a flat plate extending from *A* to *B* and centred on *C,* subject to a sound from a source located at *S*. The left hand side shows the image source *S′* which may be used to define the SZ. It is clear that the GSZ defined by the region of the receiver arc R_a' to R_b' is equal in size to that of the SZ covering the region R_a to R_b.
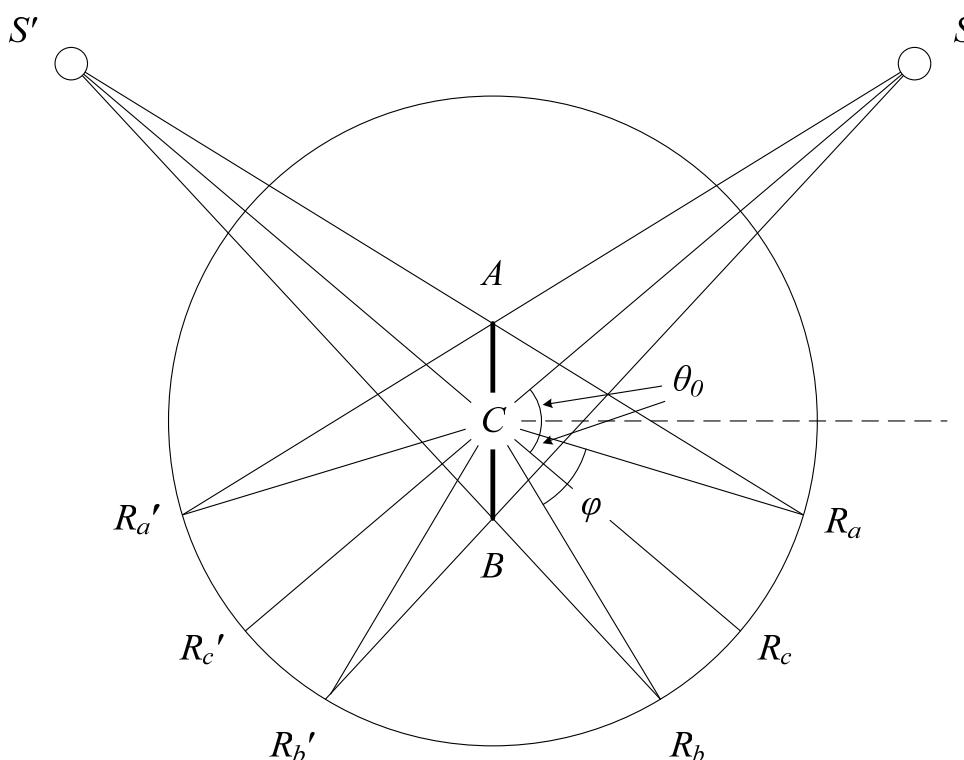
Known parameters

Angle of incidence:	$\theta_0 = \dfrac{\pi}{2} - S\hat{C}A = S\hat{C}B - \dfrac{\pi}{2}$
Source distance:	$r_0 = SC$
Receiver distance:	$r = R_aC = R_bC = R_cC = R_a'C = R_b'C = R_c'C$
Plate width:	$D = AB$
Half plate width:	$D/2 = AC = BC$
SZ / GSZ solid angle:	$\varphi = R_a\hat{C}R_b$

<u>Derivation</u>

Using the cosine rule gives:

$$SA = \sqrt{SC^2 + AC^2 - 2SC.AC.\cos(S\hat{C}A)} = \sqrt{r_0{}^2 + \frac{D^2}{4} - Dr_0\sin(\theta_0)} \qquad \text{A.1}$$

$$SB = \sqrt{SC^2 + BC^2 - 2SC.BC.\cos(S\hat{C}B)} = \sqrt{r_0{}^2 + \frac{D^2}{4} + Dr_0\sin(\theta_0)} \qquad \text{A.2}$$

Using the sine rule gives:

$$\frac{\sin(S\hat{A}C)}{SC} = \frac{\sin(S\hat{C}A)}{SA} \qquad => \qquad \sin(S\hat{A}C) = \frac{SC}{SA}\sin\left(\frac{\pi}{2} - \theta_0\right) = \frac{r_0}{SA}\cos(\theta_0) \qquad \text{A.3}$$

Since $S\hat{A}C + R_a{}'\hat{A}C = \pi$ and $R_a{}'\hat{A}C = R_a\hat{A}C$, then:

$$\sin(\pi - R_a\hat{A}C) = \frac{r_0}{SA}\cos(\theta_0) \qquad \text{A.4}$$

$$R_a\hat{A}C = \pi - \sin^{-1}\left(\frac{r_0}{SA}\cos(\theta_0)\right) \qquad \text{A.5}$$

Again (separately) using the sine rule gives:

$$\frac{\sin(A\hat{R}_aC)}{AC} = \frac{\sin(R_a\hat{A}C)}{R_aC} \qquad => \qquad \sin(A\hat{R}_aC) = \frac{AC}{R_aC}\sin(R_a\hat{A}C) \qquad \text{A.6}$$

Which substituting in the result from A.4 gives:

$$\sin(A\hat{R}_aC) = \frac{AC}{R_aC}\frac{r_0}{SA}\cos(\theta_0) = \frac{D}{2r}\frac{r_0}{SA}\cos(\theta_0) \qquad \text{A.7}$$

$$A\hat{R}_aC = \sin^{-1}\left(\frac{D}{2r}\frac{r_0}{SA}\cos(\theta_0)\right) \qquad \text{A.8}$$

Similarly, for the opposing side the equivalent angles to those given by A.5 and A.8 may also be derived, given as:

$$R_b\hat{B}C = \pi - \sin^{-1}\left(\frac{r_0}{SB}\cos(\theta_0)\right) \qquad \text{A.9}$$

$$B\hat{R}_bC = \sin^{-1}\left(\frac{D}{2r}\frac{r_0}{SB}\cos(\theta_0)\right) \qquad \text{A.10}$$

The required angle, φ, may be given as:

$$\varphi = R_a\hat{C}R_b = \pi - R_a\hat{C}A - R_b\hat{C}B$$

$$\Rightarrow \pi - (\pi - R_a\hat{A}C - A\hat{R}_aC) - (\pi - R_b\hat{B}C - B\hat{R}_bC) \qquad \text{A.11}$$

$$\Rightarrow R_a\hat{A}C + A\hat{R}_aC + R_b\hat{B}C + B\hat{R}_bC - \pi$$

By substituting the angles A.5, A.8, A.9 and A.10 into the above, and by substituting in the lengths given by A.1 and A.2, the solid angle may be given by:

$$\varphi = \left[\sin^{-1}\left(\frac{Dr_0\cos(\theta_0)}{2r\sqrt{r_0{}^2 + \frac{D^2}{4}} + Dr_0\sin(\theta_0)} \right) + \sin^{-1}\left(\frac{Dr_0\cos(\theta_0)}{2r\sqrt{r_0{}^2 + \frac{D^2}{4}} - Dr_0\sin(\theta_0)} \right) \right]$$

$$- \left[\sin^{-1}\left(\frac{r_0\cos(\theta_0)}{\sqrt{r_0{}^2 + \frac{D^2}{4}} + Dr_0\sin(\theta_0)} \right) + \sin^{-1}\left(\frac{r_0\cos(\theta_0)}{\sqrt{r_0{}^2 + \frac{D^2}{4}} - Dr_0\sin(\theta_0)} \right) \right] + \pi \qquad \text{A.12}$$

For the specific case of normal incidence the above may be simplified to give:

$$\varphi = 2\left[\sin^{-1}\left(\frac{Dr_0}{2r\sqrt{r_0{}^2 + \frac{D^2}{4}}} \right) - \sin^{-1}\left(\frac{r_0}{\sqrt{r_0{}^2 + \frac{D^2}{4}}} \right) \right] + \pi \qquad \text{A.13}$$

The above is equal to that defined in Section 3.2.2 Eq. 3.1.

APPENDIX B

The following is a derivation of the Bragg frequencies for a periodic rectangular lattice of scattering elements, referred to in Section 6.4.2 (Eq. 6.13) and Section 7.3.4.

2D Laue Conditions

Considering the 2D rectangular periodic grid of point scattering elements depicted in Figure 2.8. Constructive interference due to the periodicity in a given dimension will occur when the path difference between waves scattered from adjacent elements is equal to a multiple of a wavelength. For the orthogonal directions x and y these will occur at (azimuth) angles:

$$\theta_x = \cos^{-1}\left(\frac{\dfrac{\alpha\lambda}{d_x} - \cos\theta_0\cos\varphi_0}{\cos\varphi}\right) \qquad \text{B.1}$$

$$\theta_y = \sin^{-1}\left(\frac{\dfrac{\beta\lambda}{d_y} - \sin\theta_0\cos\varphi_0}{\cos\varphi}\right) \qquad \text{B.2}$$

Where α and β are integers (including negative integers and zero), and θ_x and θ_y are the angles for which constructive interference occurs between elements in the x and y directions respectively. The angles of elevation φ_0 and φ for the incident and scattered fields respectively are included for generality. Constructive interference occurs when $\theta_x = \theta_y$, giving:

$$\cos^{-1}\left(\frac{\dfrac{\alpha\lambda}{d_x} - \cos\theta_0\cos\varphi_0}{\cos\varphi}\right) = \sin^{-1}\left(\frac{\dfrac{\beta\lambda}{d_y} - \sin\theta_0\cos\varphi_0}{\cos\varphi}\right) \qquad \text{B.3}$$

Using the identity $\sin\left(\cos^{-1}(x)\right) = \left[1 - x^2\right]^{1/2}$ gives:

$$\frac{\dfrac{\beta\lambda}{d_y} - \sin\theta_0\cos\varphi_0}{\cos\varphi} = \left[1 - \left(\frac{\dfrac{\alpha\lambda}{d_x} - \cos\theta_0\cos\varphi_0}{\cos\varphi}\right)^2\right]^{1/2} \qquad \text{B.4}$$

$$\Rightarrow \left(\frac{\beta\lambda}{d_y}\right)^2 + \sin^2\theta_0\cos^2\varphi_0 - 2\frac{\beta\lambda}{d_y}\sin\theta_0\cos\varphi_0 = ...$$

$$\cos^2\varphi + 2\frac{\alpha\lambda}{d_x}\cos\theta_0\cos\varphi_0 - \left(\frac{\alpha\lambda}{d_x}\right)^2 - \cos^2\theta_0\cos^2\varphi_0$$

B.5

$$\Rightarrow \lambda^2\left(\frac{\alpha^2}{d_x{}^2} + \frac{\beta^2}{d_y{}^2}\right) + \cos^2\varphi_0\left(\sin^2\theta_0 + \cos^2\theta_0\right) = ...$$

$$2\lambda\cos\varphi_0\left(\frac{\alpha}{d_x}\cos\theta_0 + \frac{\beta}{d_y}\sin\theta_0\right) + \cos^2\varphi$$

B.6

Using the identity $\sin^2 x + \cos^2 x = 1$ gives:

$$\lambda^2\left(\frac{\alpha^2}{d_x{}^2} + \frac{\beta^2}{d_y{}^2}\right) + \cos^2\varphi_0 = 2\lambda\cos\varphi_0\left(\frac{\alpha}{d_x}\cos\theta_0 + \frac{\beta}{d_y}\sin\theta_0\right) + \cos^2\varphi$$

B.7

For the 2D case $\varphi_0 \equiv 0$, $\varphi \equiv 0$, giving:

$$\lambda\left(\frac{\alpha^2}{d_x{}^2} + \frac{\beta^2}{d_y{}^2}\right) = 2\left(\frac{\alpha}{d_x}\cos\theta_0 + \frac{\beta}{d_y}\sin\theta_0\right)$$

B.8

The frequencies therefore (as given by Eq. 6.13) may be given by:

$$f = \frac{c\left(\dfrac{\alpha^2}{d_x{}^2} + \dfrac{\beta^2}{d_y{}^2}\right)}{2\left(\dfrac{\alpha}{d_x}\cos\theta_0 + \dfrac{\beta}{d_y}\sin\theta_0\right)}$$

B.9

3D Laue Conditions

Following the same convention as Eq. B1-B2, grating lobes due to periodicity in the z dimension will occur at angle of elevation:

$$\varphi_z = \sin^{-1}\left(\frac{\gamma\lambda}{d_z} - \sin\varphi_0\right)$$

B.10

Where γ is an integer. For constructive interference in three dimensions, these angles must coincide with those defined by Eq. B.7.

Defining φ_{xy} to be the angle of elevation for which constructive interference occurs between grating lobes due to periodicity in the x and y dimensions gives:

$$\varphi_{xy} = \cos^{-1}\left(\left[\lambda^2\left(\frac{\alpha^2}{d_x{}^2} + \frac{\beta^2}{d_y{}^2}\right) + \cos^2\varphi_0 - 2\lambda\cos\varphi_0\left(\frac{\alpha}{d_x}\cos\theta_0 + \frac{\beta}{d_y}\sin\theta_0\right)\right]^{\frac{1}{2}}\right) \qquad \text{B.11}$$

Constructive interference will therefore occur when $\varphi_{xy} = \varphi_z$, giving:

$$\sin^{-1}\left(\frac{\gamma\lambda}{d_z} - \sin\varphi_0\right) = \dots$$

$$\cos^{-1}\left(\left[\lambda^2\left(\frac{\alpha^2}{d_x{}^2} + \frac{\beta^2}{d_y{}^2}\right) + \cos^2\varphi_0 - 2\lambda\cos\varphi_0\left(\frac{\alpha}{d_x}\cos\theta_0 + \frac{\beta}{d_y}\sin\theta_0\right)\right]^{\frac{1}{2}}\right) \qquad \text{B.12}$$

Using the same procedure as for Eq. B.4, this becomes:

$$\left(\frac{\gamma\lambda}{d_z} - \sin\varphi_0\right) = \left(1 - \lambda^2\left(\frac{\alpha^2}{d_x{}^2} + \frac{\beta^2}{d_y{}^2}\right) + \cos^2\varphi_0 - 2\lambda\cos\varphi_0\left(\frac{\alpha}{d_x}\cos\theta_0 + \frac{\beta}{d_y}\sin\theta_0\right)\right)^{\frac{1}{2}} \qquad \text{B.13}$$

Expanding gives:

$$\lambda^2\left(\frac{\gamma}{d_z}\right)^2 + \sin^2\varphi_0 - 2\lambda\sin\varphi_0\frac{\gamma}{d_z} = \dots$$

$$1 - \lambda^2\left(\frac{\alpha^2}{d_x{}^2} + \frac{\beta^2}{d_y{}^2}\right) - \cos^2\varphi_0 + 2\lambda\cos\varphi_0\left(\frac{\alpha}{d_x}\cos\theta_0 + \frac{\beta}{d_y}\sin\theta_0\right) \qquad \text{B.14}$$

$$\Rightarrow \lambda^2\left(\frac{\gamma}{d_z}\right)^2 + \lambda^2\left(\frac{\beta^2}{d_y{}^2} + \frac{\alpha^2}{d_x{}^2}\right) + \sin^2\varphi_0 + \cos^2\varphi_0 = \dots$$

$$1 + 2\lambda\cos\varphi_0\left(\frac{\alpha}{d_x}\cos\theta_0 + \frac{\beta}{d_y}\sin\theta_0\right) + 2\lambda\sin\varphi_0\frac{\gamma}{d_z} \qquad \text{B.15}$$

$$\Rightarrow \lambda\left(\frac{\alpha^2}{d_x{}^2} + \frac{\beta^2}{d_y{}^2} + \frac{\gamma^2}{d_z{}^2}\right) = 2\left(\frac{\alpha}{d_x}\cos\theta_0\cos\varphi_0 + \frac{\beta}{d_y}\sin\theta_0\cos\varphi_0 + \frac{\gamma}{d_z}\sin\varphi_0\right) \qquad \text{B.16}$$

Thus the frequencies for grating lobes from a simple orthorhombic 3D lattice are given as:

$$f = \frac{c\left(\dfrac{\alpha^2}{d_x{}^2} + \dfrac{\beta^2}{d_y{}^2} + \dfrac{\gamma^2}{d_z{}^2}\right)}{2\left(\dfrac{\alpha}{d_x}\cos\theta_0\cos\varphi_0 + \dfrac{\beta}{d_y}\sin\theta_0\cos\varphi_0 + \dfrac{\gamma}{d_z}\sin\varphi_0\right)}$$

B.17

APPENDIX C

The following refers to the allowed reflections in an array with an underlying lattice constructed from regular polygons, referred to specifically in Section 5.5.5 (Eqs. 5.7-5.8).

Geometric reflection from a plane surface

Consider the diagram below where a sound is incident from angle θ_i (relative to the source) upon a plane surface with orientation angle a, resulting in a geometric reflection in the direction described by the angle θ_r.
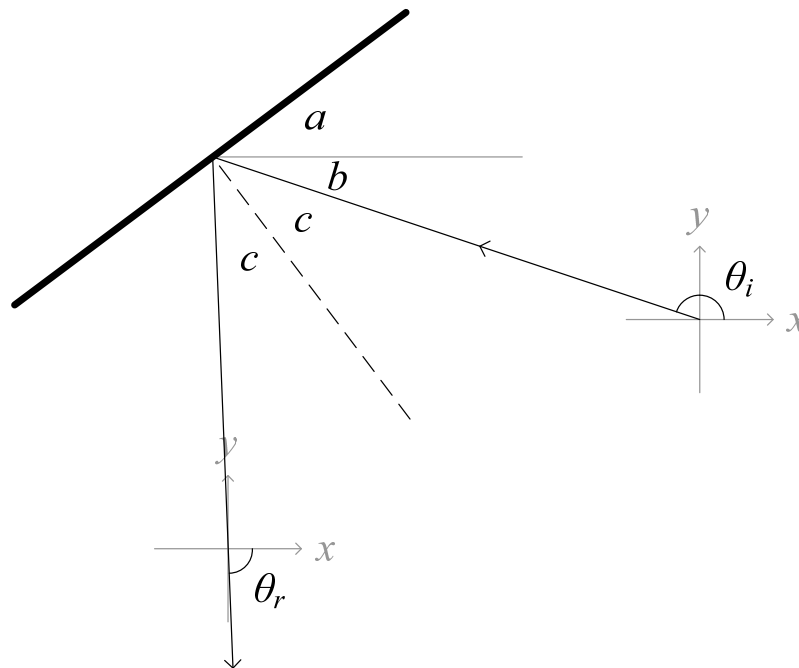
The angle of reflection, θ_r, may be derived as follows (all angles expressed in degrees). Angle b may be given as:

$$b = 180 - \theta_i \tag{C.1}$$

Angle c may be given as:

$$c = 90 - a - b = \theta_i - a - 90 \tag{C.2}$$

Thus the angle of reflection, θ_r, may be given as:

$$\theta_r = -(b + 2c) = -(180 - \theta_i) - 2(\theta_i - a - 90) = 2a - \theta_i \tag{C.3}$$

Geometric reflections from a regular lattice of plane surfaces

Consider a lattice comprising elements whose angles of orientation are given as $a = 360 \times \{\alpha\}/\beta$ (modulo 360), where $\{\alpha\}$ is a set of all possible integer values (positive or

negative) and β is a positive integer of fixed value. Following from Eq. C.3 the fist order geometric angles of reflection, $\theta_{r,1}$ may be given by:

$$\theta_{r,1} = 2a - \theta_i = 2 \times 360 \frac{\{\alpha\}}{\beta} - \theta_i$$

C.4

The angle of incidence relative to the array is given as:

$$\theta_0 = \theta_i - 180$$

C.5

Thus the first order reflection of Eq. C.4 goes to:

$$\theta_{r,1} = 2 \times 360 \frac{\{\alpha\}}{\beta} - \theta_0 - 180$$

C.6

A second order reflection, $\theta_{r,2}$, may be derived by again using Eq. C.3, though by replacing the incident angle, θ_i, with the first order angle of reflection, $\theta_{r,1}$, giving:

$$\theta_{r,2} = 2 \times 360 \frac{\{\alpha\}}{\beta} - \theta_{r,1} = 2 \times 360 \frac{\{\alpha\} - \{\alpha\}}{\beta} + \theta_0 + 180 = 2 \times 360 \frac{\{\alpha\}}{\beta} + \theta_0 + 180$$

C.7

Note the $\{\alpha\}$ integer set remains the same since the difference between two sets of all possible integers will still be a set of all possible integers. Following the same procedure as previously the third order reflections, $\theta_{r,3}$, may be obtained by substituting Eq. C.7 into Eq. C.3 giving:

$$\theta_{r,3} = 2 \times 360 \frac{\{\alpha\}}{\beta} - \theta_{r,2} = 2 \times 360 \frac{\{\alpha\}}{\beta} - \theta_0 - 180 = \theta_{r,1}$$

C.8

Since the third order reflections are equal to the first order reflections and the above process is carried through repeated application of Eq. C.3, it follows that all odd order reflection angles, $\theta_{r,odd}$, and all even order reflections, $\theta_{r,even}$, will be the same. Consequently these may be expressed as:

$$\theta_{r,odd} = 2 \times 360 \frac{\{\alpha\}}{\beta} - \theta_0 - 180$$

C.9

$$\theta_{r,even} = 2 \times 360 \frac{\{\alpha\}}{\beta} + \theta_0 + 180$$

C.10

These angles expressed relative to the angle of incidence, θ_0, may be given as:

$$\theta_{r,odd} = 2 \times 360 \frac{\{\alpha\}}{\beta} - 2\theta_0 - 180$$

C.11

$$\theta_{r,even} = 2 \times 360 \frac{\{\alpha\}}{\beta} + 180$$

C.12

Which are equivalent to Eqs. 5.7-5.8 presented in Section 5.5.5. In total, all possible reflection angles relative to the angle of incidence will be given by:

$$\theta_r = 2 \times 360 \frac{\{\alpha\}}{\beta} \pm (\theta_0 + 180) - \theta_0 \qquad\qquad \text{C.13}$$

REFERENCES

[1]   Angus, J. A. S., "The Effects of Specular Versus Diffuse Reflections on the Frequency Response at the Listener," *J. Audio Eng. Soc.*, Vol. 49(3), pp. 125-33 (2001).

[2]   D'Antonio, P., and Cox, T. J., "Diffusor Application in Rooms," *Appl. Acoust.*, Vol. 60(2), pp. 113-42 (2000).

[3]   Cox, T. J., and D'Antonio, P., *"Acoustic Absorbers and Diffusers: Theory, Design and Application,"* 2nd Ed., London, Taylor & Francis (2009).

[4]   Barron, M., *"Auditorium Acoustics and Architectural Design,"* London, E. & F. N. Spon (1993).

[5]   D'Antonio, P., and Cox, T., "Two Decades of Sound Diffusor Design and Development, Part 1: Applications and Design," *J. Audio Eng. Soc.*, Vol. 46(11), pp. 955-76 (1998).

[6]   Ando, Y., *"Architectural Acoustics: Blending Sound Sources, Sound Field and Listeners,"* Modern Acoustics and Signal Processing, New York NY, Springer (1998).

[7]   Schroeder, M. R., "Diffuse Sound Reflection by Maximum-Length Sequences," *J. Acoust. Soc. Am.*, Vol. 57(1), pp. 149-50 (1975).

[8]   Schroeder, M. R., "Binaural Dissimilarity and Optimum Ceilings for Concert Halls: More Lateral Sound Diffusion," *J. Acoust. Soc. Am.*, Vol. 65(4), pp. 958-63 (1979).

[9]   Cox, T., and D'Antonio, P., "Schroeder Diffusers: A Review," *Building Acoustics*, Vol. 10, pp. 1-32 (2003).

[10]   Schroeder, M. R., "Towards Better Acoustics for Concert Halls," *Phys. Today*, Vol. 33(10), pp. 24-30 (1980).

[11]   Cox, T. J., and Lam, Y. W., "Prediction and Evaluation of the Scattering from Quadratic Residue Diffusers," *J. Acoust. Soc. Am.*, Vol. 95(1), pp. 297-305 (1994).

[12]   Dadiotis, K., "Improving Absorption Grating and Phase Grating Diffusers," Ph.D. Thesis, University of Salford (2010).

[13]   Angus, J. A. S., "Sound Diffusers Using Reactive Absorption Gratings," *Proc. 98th Convention Audio Eng. Soc., Paris, France, February 25-28*, Convention Paper No. 3953 (D-3) (1995).

[14]   Angus, J. A. S., and D'Antonio, P., "Two Dimensional Binary Amplitude Diffusers," *Proc. 107th Convention Audio Eng. Soc., New York, USA, September 24-27*, Convention Paper No. 5061 (D-5) (1999).

[15] Payne-Johnson, E. C., Gehring, G. A., and Angus, J. A. S., "Improvements to Binary Amplitude Diffusers," *Proc. 122nd Convention Audio Eng. Soc., Vienna, Austria*, *May 5-8*, Convention Paper No. 7143 (2007).

[16] Kuttruff, H., *"Room Acoustics "* 4th Ed., London, E. & F. N. Spon (2000).

[17] "Cold Dark Matter: An Exploded View," 1991. A garden shed and contents blown up, by Cornelia Parker, http://www.frithstreetgallery.com/works/view/cold_dark_matter_an_exploded_view (accessed 16/03/2011).

[18] BS EN ISO 354:2003 "Acoustics - Measurement of Sound Absorption in a Reverberation Room."

[19] Sabine, W. C., and Egan, M. D., "Collected Papers on Acoustics," *J. Acoust. Soc. Am.*, Vol. 95(6), pp. 3679-80 (1994).

[20] Cox, T. J., and D'Antonio, P., "Technical Bulletin on the Design of Overhead Canopies for Music and Speech Using the Waveform System," RPG Diffusor Systems, Inc. (2004).

[21] Cox, T. J., and D'Antonio, P., "Canopy Arrays - Density, Size, Shape and Position," *Presented at the 6th International Conference on Auditorium Acoustics (IOA), Copenhagen, Denmark*, *May*, Vol. 28. Pt. 2, pp. 18-23 (2006).

[22] Rindel, J. H., "Design of New Ceiling Reflectors for Improved Ensemble in a Concert Hall," *Appl. Acoust.*, Vol. 34(1), pp. 7-17 (1991).

[23] Robertson, W. M., and Rudy III, J. F., "Measurement of Acoustic Stop Bands in Two-Dimensional Periodic Scattering Arrays," *J. Acoust. Soc. Am.*, Vol. 104(2), pp. 694-9 (1998).

[24] Rubio, C., Caballero, D., Sanchez-Perez, J. V., Martinez-Sala, R. A., Sanchez-Dehesa, J. A., Meseguer, F. A., and Cervera, F. A., "The Existence of Full Gaps and Deaf Bands in Two-Dimensional Sonic Crystals," *J. Lightwave Technol.*, Vol. 17(11), pp. 2202-7 (1999).

[25] Sánchez-Pérez, J. V., Caballero, D., Mártinez-Sala, R., Rubio, C., Sánchez-Dehesa, J., Meseguer, F., Llinares, J., and Gálvez, F., "Sound Attenuation by a Two-Dimensional Array of Rigid Cylinders," *Phys. Rev. Lett.*, Vol. 80(24), p. 5325 (1998).

[26]   Sanchis, L., Cervera, F., Sanchez-Dehesa, J., Sanchez-Perez, J. V., Rubio, C., and Martinez-Sala, R., "Reflectance Properties of Two-Dimensional Sonic Band-Gap Crystals," *J. Acoust. Soc. Am.*, Vol. 109(6), pp. 2598-605 (2001).

[27]   BS ISO 17497-1:2004 "Acoustics - Sound Scattering Properties of Surfaces - Part 1: Measurement of the Random-Incidence Scattering Coefficient in a Reverberation Room."

[28]   AES-4id-2001, "AES Information Document for Room Acoustics and Sound Reinforcement Systems - Characterization and Measurement of Surface Scattering Uniformity," *J. Audio Eng. Soc.*, Vol. 49(3), pp. 149-65 (2001).

[29]   Kinsler , L. E., Frey, A. R., Coppens, A. B., and Sanders, J. V., *"Fundamentals of Acoustics,"* 4th Ed., New York NY; Chichester, John Wiley & Sons (2000).

[30]   Morse, P. M., and Ingard, K. U., *"Theoretical Acoustics,"* Princeton NJ, Princeton University Press (1986).

[31]   Cox, T. J., "Predicting the Scattering from Reflectors and Diffusers Using Two-Dimensional Boundary Element Methods," *J. Acoust. Soc. Am.*, Vol. 96(2), pp. 874-8 (1994).

[32]   Boundary Element Method (BEM) code compiled using Fortran, kindly provided by Professor Trevor Cox of The University of Salford (2006).

[33]   Hargreaves, J. A., and Cox, T., "A Transient Boundary Element Method for Acoustic Scattering from Mixed Regular and Thin Rigid Bodies," *Acta Acust. United Ac.*, Vol. 95(4), pp. 678-89 (2009).

[34]   Terai, T., "On Calculation of Sound Fields Around Three Dimensional Objects by Integral Equation Methods," *J. Sound Vib.*, Vol. 69(1), pp. 71-100 (1980).

[35]   Umnova, O., Attenborough, K., and Linton, C. M., "Effects of Porous Covering on Sound Attenuation by Periodic Arrays of Cylinders," *J. Acoust. Soc. Am.*, Vol. 119(1), pp. 278-84 (2006).

[36]   Wu, T. W., and Seybert, A. F., "A Weighted Residual Formulation for the CHIEF Method in Acoustics," *J. Acoust. Soc. Am.*, Vol. 90(3), pp. 1608-14 (1991).

[37]   Schenck, H. A., "Improved Integral Formulation for Acoustic Radiation Problems," *J. Acoust. Soc. Am.*, Vol. 44(1), pp. 41-58 (1968).

[38]   Balanis, C. A., *"Antenna Theory: Analysis and Design,"* 2nd Ed., New York NY; Chichester, John Wiley & Sons (1997).

[39]   Hammond, C., *"The Basics of Crystallography and Diffraction,"* International Union of Crystallography texts on crystallography: No. 3, Oxford, Oxford University Press (1997).

[40]   Rigelsford, J. M., and Tennant, A., "A 64 Element Acoustic Volumetric Array," *Appl. Acoust.*, Vol. 61(4), pp. 469-75 (2000).

[41]   Rousseau, J.-J., *"Basic Crystallography,"* Chichester; New York NY, John Wiley & Sons (c1998).

[42]   Cox, T. J., and Lam, Y. W., "Evaluation of Methods for Predicting the Scattering from Simple Rigid Panels," *Appl. Acoust.*, Vol. 40(2), pp. 123-40 (1993).

[43]   Abramowitz, M., and Stegun, I., *"Handbook of Mathematical Functions with Formulas, Graphs, and Mathematical Tables,"* 10th Printed Ed., New York NY, Dover Publications (1972).

[44]   Martin, P. A., *"Multiple Scattering - Interaction of Time-Harmonic Waves with N Obstacles,"* Encyclopedia of Mathematics and its Applications (No. 107), Cambridge, Cambridge University Press (2006).

[45]   Rife, D. D., "Transfer-Function Measurement with Maximum-Length Sequences," *J. Audio Eng. Soc.*, Vol. 37(6), pp. 419-44 (1989).

[46]   Cox, T. J., Dalenback, B.-I. L., D'Antonio, P., Embrechts, J. J., Jeon, J. Y., Mommertz, E., and Vorländer, M., "A Tutorial on Scattering and Diffusion Coefficients for Room Acoustic Surfaces," *Acta Acust. United Ac.*, Vol. 92, pp. 1-15 (2006).

[47]   Robinson, P., and Xiang, N., "On the Subtraction Method for In-Situ Reflection and Diffusion Coefficient Measurements," *J. Acoust. Soc. Am.*, Vol. 127(3), pp. EL99-EL104 (2010).

[48]   Hargreaves, T. J., Cox, T. J., Lam, Y. W., and D'Antonio, P., "Surface Diffusion Coefficients for Room Acoustics: Free-Field Measures," *J. Acoust. Soc. Am.*, Vol. 108(4), pp. 1710-20 (2000).

[49]   Hargreaves, T. J., "Acoustic Diffusion and Scattering Coefficient for Room Surfaces," Ph.D. Thesis, University of Salford (2000).

[50]   Hecht, E., *"Optics,"* 4th Ed., London; San Francisco CA, Addison-Wesley (c2002).

[51]   Dadiotis, K., Angus, J. A. S., and Cox, T. J., "Investigation into the Distribution of the Reflected Energy from Absorbing and Hybrid Surfaces," *Presented at the 8th*

European Conference on Noise Control (Euronoise), Edinburgh, Scotland, *October 26-28* (2009).

[52] Bloom, G. S., and Golomb, S. W., "Applications of Numbered Undirected Graphs," *Proc. IEEE*, Vol. 65(4), pp. 562-70 (1977).

[53] Angus, J. A. S., "Using Grating Modulation to Achieve Wideband Large Area Diffusers," *Appl. Acoust.*, Vol. 60(2), pp. 143-65 (2000).

[54] Vertatschitsch, E., and Haykin, S., "Nonredundant Arrays," *Proc. IEEE*, Vol. 74(1), pp. 217- (1986).

[55] Blanton, K. A., and McClellan, J. H., "New Search Algorithm for Minimum Redundancy Linear Arrays," *International Conference on Acoustics, Speech, and Signal Processing, Toronto, Canada*, *14-17 April*, Vol. 2, pp. 1361-4 (1991).

[56] Meurisse, Y., and Delmas, J.-P., "Bounds for Sparse Planar and Volume Arrays," *IEEE Trans. Inf. Theory*, Vol. 47(1), pp. 464-8 (2001).

[57] Hopperstad, J.-F., and Holm, S., "The Coarray of Sparse Arrays with Minimum Sidelobe Level," *The 3rd IEEE Nordic Signal Processing Symposium (NORSIG), Vigsø, Denmark*, *June 8-11*, pp. 137-40 (1998).

[58] Shearer, J. B., "Table of known optimal Golomb rulers," http://www.research.ibm.com/people/s/shearer/grtab.html (accessed 20/04/2011).

[59] Fan, P., and Darnell, M., *"Sequence Design for Communications Applications,"* Electronic and Electrical Engineering Research Studies: No. 1, Taunton, England, Research Studies Press Ltd. (1996).

[60] Van Trees, H. L., *"Optimum Array Processing: Part IV of Detection, Estimation and Modulation Theory,"* New York NY; Chichester, Wiley-Interscience (2002).

[61] Beranek, L. L., *"Acoustics,"* Woodbury NY, Acoustical Society of America (1986).

[62] Rindel, J. H., "Attenuation of Sound Reflections due to Diffraction," *Presented at the Nordic Acoustical Meeting, Aalborg, Denmark*, *20-22 August*, pp. 257-60 (1986).

[63] Cox, T., J., "Acoustic Iridescence," *J. Acoust. Soc. Am.*, Vol. 129(3), pp. 1165-72 (2011).

[64] Van der Wal, M., Start, E. W., and De Vries, D., "Design of Logarithmically Spaced Constant-Directivity Transducer Arrays," *J. Audio Eng. Soc.*, Vol. 44(6), pp. 497-507 (1996).

[65] Jarvinen, A., Savioja, L., and Melkas, K., "Numerical Simulations of the Modified Schroeder Diffuser Structure," *J. Acoust. Soc. Am.*, Vol. 103, p. 3065 (1998).

[66] D'Antonio, P., and Konnert, J., "The QRD Diffractal: A New One- or Two-Dimensional Fractal Sound Diffusor," *J. Audio Eng. Soc.*, Vol. 40(3), pp. 117-29 (1992).

[67] Stauffer, D., and Aharony, A., *"Introduction to Percolation Theory,"* 2nd Ed., London, Taylor & Francis (1994).

[68] Sahimi, M., *"Applications of Percolation Theory,"* London, Taylor & Francis (c1994).

[69] Vukusic, P., Hallam, B., and Noyes, J., "Brilliant Whiteness in Ultrathin Beetle Scales," in *Science*, Advancing Science, Serving Society, p. 348 (2007).

[70] Cox, T. J., Hughes, R. J., Angus, J. A. S., Whittaker, D. M., Pogson, M., and Gehring, G. A., "Volume Diffusers Inspired by Percolation Fractals," *Presented at the 7th International Conference on Auditorium Acoustics (IOA), Oslo, Norway, October 3-5*, pp. 349-58 (2008).

[71] Ten Kate, W. R. T., "On the Bandwidth of Diffusors Based Upon the Quadratic Residue Sequence," *J. Acoust. Soc. Am.*, Vol. 98(5), pp. 2575-9 (1995).

[72] Williams, H. T., Goodwin, L., Desjardins, S. G., and Billings, F. T., "Two-Dimensional Growth Models," *Physics Letters A*, Vol. 250(1-3), pp. 105-10 (1998).

[73] Barber, C. B., Dobkin, D. P., and Huhdanpaa, H. T., "The Quickhull Algorithm for Convex Hulls," *ACM Transactions on Mathematical Software*, Vol. 22(4), pp. 469-83 (1996).

[74] Pritchard, R. L., "Optimum Directivity Patterns for Linear Point Arrays," *J. Acoust. Soc. Am.*, Vol. 25(5), pp. 879-91 (1953).

[75] Schroeder, M. R., *"Number Theory in Science and Communication : With Applications in Cryptography, Physics, Digital Information, Computing, and Self-Similarity,"* 3rd Ed., Springer series in information sciences: No. 7, Berlin; London, Springer (1997).

[76] Romero-Garcia, V., Fuster, E., Garcia-Raffi, L. M., Sanchez-Perez, E. A., Sopena, M., Llinares, J., and Sanchez-Perez, J. V., "Band Gap Creation Using Quasiordered Structures Based on Sonic Crystals," *Appl. Phys. Lett.*, Vol. 88(17) (2006).

[77] Hakansson, A., Cervera, F., and Sanchez-Dehesa, J., "Sound Focusing by Flat Acoustic Lenses Without Negative Refraction," *Appl. Phys. Lett.*, Vol. 86(5), p. 054102 (2005).

[78] Golomb, S. W., and Taylor, H., "Constructions and Properties of Costas Arrays," *Proc. IEEE*, Vol. 72(9), pp. 1143-63 (1984).

[79] Arau-Puchades, H., "An Acoustics Miracle of "Tonhalle St. Gallen" has been Produced. But the Criterion of Gade on Stage has Failed Before and After the Refurbishment of the Hall," *Presented at the 8th International Conference on Auditorium Acoustics (IOA), Dublin, May 20-22*, Vol. 33, pp. 133-40 (2011).

[80] Redondo, J., Pic, R., Roig, B., and Avis, M. R., "Time Domain Simulation of Sound Diffusers Using Finite-Difference Schemes," *Acta Acust. United Ac.*, Vol. 93, pp. 611-22 (2007).

[81] Bilsen, F. A., "Thresholds of Perception of Repetition Pitch. Conclusions Concerning Coloration in Room Acoustics and Correlation in the Hearing Organ," *Acustica*, Vol. 19, pp. 27-32 (1967/68).

[82] ANSI S1.11-1986 (R1993) "Specification for Octave-Band and Fractional-Octave-Band Analog and Digital Filters."

[83] Couvreur, C., "octave," http://www.mathworks.com/matlabcentral/fileexchange/69 (accessed 16th May 2011).

[84] Yasuda, Y., Sakamoto, S., Ushiyama, A., and Tachibana, H., "Reverberation Characteristics in a Room with Unevenly Distributed Absorbers: Numerical Analysis," *Acoust. Sci and Tech.*, Vol. 26(4), pp. 388-90 (2005).

[85] Redondo, J., Pic, R., Avis, M. R., and Cox, T. J., "Prediction of the Random-Incidence Scattering Coefficient Using a FDTD Scheme," *Acta Acust. United Ac.*, Vol. 95, pp. 1040-7 (2009).

[86] Wells, J. J., Murphy, D. T., and Beeson, M., "Temporal Matching of 2-D and 3-D Wave-Based Acoustic Modeling for Efficient and Realistic Simulation of Rooms," *Proc. 126th Convention Audio Eng. Soc., Munich, Germany, May 7-10*, Convention Paper No. 7697 (2009).

[87] Hodgson, M., "Evidence of Diffuse Surface Reflections in Rooms," *J. Acoust. Soc. Am.*, Vol. 89(2), pp. 765-71 (1991).

[88]   Marshall, A. H., "Aspects of the Acoustical Design and Properties of Christchurch Town Hall, New Zealand," *J. Sound Vib.*, Vol. 62(2), pp. 181-94 (1979).

[89]   Stephen, C., and Mike, B., "Sound Level Distribution and Scatter in Proportionate Spaces," *J. Acoust. Soc. Am.*, Vol. 116(3), pp. 1585-95 (2004).

[90]   Ramachandrarao, P., Sinha, A., and Sanyal, D., "On the Fractal Nature of Penrose Tiling," *Curr. Sci. India*, Vol. 79(3), pp. 364-6 (2000).

[91]   Borkovec, M., De Paris, W., and Peikert, R., "The Fractal Dimension of the Apollonian Sphere Packing," *Fractals*, Vol. 2(4), pp. 521-6 (1994).

[92]   Schroeder, M. R., *"Fractals, Chaos, Power Laws: Minutes from an Infinite Paradise,"* New York NY, W.H. Freeman (1991).

[93]   Szalay, A. S., Gray, J., Fekete, G., Kunszt, P. Z., Kukol, P., and Thakar, A., "Indexing the Sphere with the Hierarchical Triangular Mesh," Technical Report MSR-TR-2005-123, Division, M. R. A. T. (2005).